HASAN KALYONCU UNIVERSITY

GAZIANTEP UNIVERSITY

E-ISBN: 978-625-44427-5-9

TICMET'21

05-06 November, 2021 Gaziantep - TURKEY

The 3rd International Conference of Materials and Engineering Technology

3

3. Uluslararası Malzeme ve Mühendislik Teknolojileri Konferansı

https://www.ticmet.org



FACE to FACE

zoom Video Communications

YouTube CANLI YAYIN

CONFERENCE OBJECTIVE

The 3rd International Conference of Materials and Engineering Technology (TICMET'21) will be held on 05-06 November 2021 in partnership with Hasan Kalyoncu University and Gaziantep University.

The main purpose of TICMET'21 is to present the latest research and results of scientists related to materials and engineering technologies. This conference provides different field delegates with opportunities to exchange new ideas and application experiences, build business or research relationships, and find global partners for future collaboration. Due to Covid-19 that shook the world, in addition to face-to-face sessions, ONLINE presentation will be provided to our participants. After this science feast, your abstract/full texts will be published in congress books with ISBNs and will be brought to the world science literature with open access and significant contributions will be made to the scientific field. Webinars will be used in online presentations and will be broadcast live. All participants will be able to ask questions to be answered in the presentations. In the event that more than one session takes place at the same time, it will be possible to follow from parallel rooms.

As an organizing committee we would like to thank to all authors for their valuable contributions. Please note that all papers were reviewed and evaluated by the referees in the field, based on their technical and/or research content, relevance to the conference, contributions and readability.

Selected papers presented at the conference will be published in one of the following journal:

- International Journal of Materials and Engineering Technologies (TIJMET) (Dergipark)
- El-Cezeri Journal of Science and Engineering (TR Directory)

PROGRAM COMMITEES

Honorary Chair

Prof. Dr. Türkay Dereli, Rector, Hasan Kalyoncu University - TR

Prof. Dr. Arif Özaydın, Rector, Gaziantep University - TR

Chair

Prof. Dr. Necip Fazıl Yılmaz, Gaziantep University – TR

Organizing Committee

Prof. Dr. Necip Fazıl Yılmaz, Gaziantep University - TR

Prof. Dr. İbrahim Halil Güzelbey, Hasan Kalyoncu University - TR

Prof. Dr. Adem Kurt, Gazi University - TR

Prof. Dr. Ali Rıza Yıldız, Uludag University - TR

Prof. Dr. Metin Bedir, Gaziantep University - TR

Prof. Dr. Murat Oduncuoğlu, Yildiz Technical University - TR

Prof. Dr. Mustafa Bakkal, Istanbul Technical University – TR

Assoc. Prof. Dr. Halil İbrahim Kurt, Gaziantep University - TR

Lect. Aykut Bilici, Gaziantep University – TR

Lect. Musa Yılmaz, Gaziantep University – TR

Scientific Committee (National Committee)

Prof. Dr. Abdulkadir Ekşi, Cukurova University - TR

Prof. Dr. Abdulkadir Çevik, Gaziantep University – TR

Prof. Dr. Ahmet Erkliğ, Gaziantep University – TR

Prof. Dr. Ali Gürsel, Duzce University – TR

Prof. Dr. Emrah Özahi, Gaziantep University – TR

Prof. Dr. Enver Atik, Celal Bayar University - TR

Prof. Dr. İsmail Sarıtaş, Selcuk University - TR

Prof. Dr. Mehmet Cengiz Kayacan, Süleyman Demirel University - TR

Prof. Dr. Mete Kalyoncu, Konya Technical University - TR

Prof. Dr. Mustafa Bakkal, Istanbul Technical University - TR

Prof. Dr. Mustafa Çiğdem, Yildiz Technical University - TR

Prof. Dr. Oğuzhan Yılmaz, Gazi University - TR

Prof. Dr. Ömer Eyercioğlu, Gaziantep University - TR

Prof. Dr. Rahmi Ünal, Gazi University - TR

Prof. Dr. Serdar Salman, National Defense University - TR

Prof. Dr. Süleyman Can Kurnaz, Sakarya University – TR

Prof. Dr. Sultan Öztürk, Karadeniz Technical University - TR

Prof. Dr. Uğur Cem Hasar, Gaziantep University - TR

Prof. Dr. Yahya Bozkurt, Marmara University – TR

Assoc. Prof. Dr. Abdulcabbar Yavuz, Gaziantep University – TR

Assoc. Prof. Dr. Kürşad Göv, Gaziantep University – TR

Assoc. Prof. Dr. Esin Sarıoğlu, Gaziantep University - TR

Assist. Prof. Dr. Ali Yaşar, Selcuk University - TR

Assist. Prof. Dr. Aziz Barış Başyiğit, Kırıkkale University - TR

Dr. Engin Ergül, Dokuz Eylül University - TR

Scientific Committee (International Committee)

Prof. Dr. Andrey Tsarkov, Moscow State Technical University - RU

Prof. Dr. Bekir Sami Yilbas, King Fahd University of Petroleum and Minerals - SA

Prof. Dr. Fabienne Delaunois, University Of Mons - BE

Prof. Dr. Hazman Seli, University Of Sains Malaysia - MY

Prof. Dr. Heiba Zein, Ain Shams University - EG

Prof. Dr. Marwan K Khraisheh, Hamad Bin Khalifa University - QA

Prof. Dr. Mohamed Elsayed Yahia, International University of Sarajevo - BA

Prof. Dr. Muammer Koç, Hamad Bin Khalifa University - QA

Prof. Dr. Ramazan Asmatulu, Wichita State University - US

Prof. Dr. Şenay Şimsek, North Dakota State University - US

Prof. Dr. Tai Cheng Chen, Institute Of Nuclear Energy Research Iner - TW

Prof. Dr. Vincent Ji, University Of Paris Sud - FR

Prof. Dr. Yousef Haik, Hamad Bin Khalifa University Hbku - QA

Prof. Dr. Yusuf Ozturk, San Diego State University - US

Prof. Dr. Zakaria Boumerzoug, University Of Biskra - DZ

Assoc Prof. Dr. Ahmad Azmin Mohamad, University Of Sains Malaysia - MY

Assoc. Prof. Dr. Mehmet Emin Aydin, UWE Bristol - GB

Assoc Prof. Dr. Mikhail E Semenov, Tomsk Polytechnic University - RU

Assist Prof. Dr. Faten Adel Ismael Chaqmaqchee, Koya University - IQ

Assist Prof. Dr. Nurettin Sezer, Hamad Bin Khalifa University Hbku - QA

Assist Prof. Dr. Sami G Al Ghamdi, Hamad Bin Khalifa University Hbku - QA

Assist Prof. Dr. Shoukat Alim Khan, Hamad Bin Khalifa University Hbku - QA

Assist Prof. Dr. Yusuf Bicer, Hamad Bin Khalifa University Hbku - QA

Dr Abdessalem Bouferrouk, University Of The West Of England - GB

Dr. Fahmi Fariq Muhammad, Koya University - IQ

Dr Mazhar Malik, University Of The West Of England - GB

Dr Mirza Nadeem Baig, Pakistan Welding Institute - PK

Dr. Mohammad Ghaffar Faraj, Koya University - IQ

Dr Peter Kay, University Of The West Of England - GB

Dr Sabir Ghauri, University Of The West Of England - GB

Dr Shahroz Sakhawat, Pakistan Welding Institute - PK

INVITED SPEAKERS



Dr. Tugrul Daim is a Professor in the Department of Engineering and Technology Management. He is also the director of the Technology Management Doctoral program at Portland State University. Dr. Daim leads a research group on Technology Evaluations and Research Applications. His group has had more than 20 PhD graduates. He is currently advising more than 15 PhD students. Over 15 visiting scholars from all around the world have joined his group in the last decade. Dr. Daim is recognized worldwide for his research leadership in roadmapping and forecasting technologies. He has published over 200 refereed journal papers, more than 20 special issues and more than 20 books. He made more than 200 conference presentations and gave several keynote lectures. He sits on the board of many academic institutions and industrial organizations.

Awards & Honors

Honorary Chair Professor title by Chaoyang University of Technology (2019)

R&D Advisory Board member for TUPRAS (Turkey) (2018)

Leading Research Fellowship at National Research University Higher School of Economics in Moscow (2018-2020)

David E Wedge Award for Excellence in Teaching by Portland State University (2017)

President of Omega Rho, International Honor Society in Operations Research and Management Science (2014 - 2016)

INVITED SPEAKERS



Mehmet Lütfi Yola received his MSc and PhD degrees in Faculty of Pharmacy, Hacettepe University, Ankara, Turkey. He was a research assistant at Hacettepe University during his graduate studies where he also served as the researcher on the Nanotechnology Laboratory. His doctoral thesis is about "Development of molecular imprinted nanosensors for determination of biomolecules/drugs in pharmaceuticals and foods". He also remained in the department of Biochemistry as a research associate working on DNA-drug interactions and DNA biosensors based on nanocomposites at Hacettepe University. He then joined the Materials Laboratory at Sinop University, Turkey and was subsequently promoted to research assistant professor. During his tenure, he collaborated on Materials Science and biosensors/nanosensors. He created a new biosensor about cardiac troponin-I recognition and developed a novel methodology for SPR imaging of anticancer drugs and their effect levels. On July 2017, Dr. Yola joined Iskenderun Technical University in Hatay, Turkey as an associate professor. He was the director of Biomedical Engineering. At now, he is working as professor at Hasan Kalyoncu University. While continuing his research on novel biosensors and imaging methods including quartz crystal microbalance (QCM), surface plasmon resonance (SPR) and electroanalytical techniques (CV, SWV, DPV, CA, CC and stripping), he is also working on molecular imprinting technology, validation and optimization of analytical methods.

Dr. Yola received 2018-The Young Scientist Award of the Year (Science Heroes Association) and 2019 Turkish Academy of Sciences (TUBA) Outstanding Young Scientists Awards (GEBİP) in the field of materials science, nanotechnology and biomedical applications. Dr. Yola has published more than 100 research articles in high impact journals including Biosensors and Bioelectronics, Composites Part B: Engineering, Journal of Colloid and Interface Science, Sensors and Actuators B: Chemical, Chemical Engineering Journal, Food Chemistry, Materials Science and Engineering: C, Electrochimica Acta with a total international citation of more than 8000. h-index is 56 (Google Scholar) and h-index is 53 (ISI Web of Knowledge).

CONTENTS

NUMERICAL FLOW FIELD SIMULATION OF COMPACT SPINNING CONDENSING ZONE FOR DIFFERENT AIR PRESSURE LEVELS
MURAT DEMIR 1

DECISION TREE REGRESSION METHOD APPLICATION FOR PREDICTION OF WOVEN FABRICS TEAR STRENGTH
HALIL IBRAHIM CELIK, HATICE KUBRA KAYNAK, ELIF GULTEKIN 7

ELEKTROMANYETİK KORUYUCU ORME KUMASLARIN GELISTIRILMESI
HUSEYIN KADOGLU, DENIZ DURAN, MEHMET KERTMEN, HALIL IBRAHIM OLUCAK, AYBUKE SEN, OZGUR SAMET GIZLENCI, HATICE AKTEKELI YILMAZ 13

FLEXURAL BEHAVIOUR OF HAUNCHED BEAMS REINFORCED WITH GLASS FRP REBAR
SAAD ALMOHAMMAD ALAGOL, MEHMET EREN GULSAN 19

EFFECT OF ELASTANE DIAMETER ON POISSON S RATIO OF HELICAL AUXETIC YARNS
HALIL IBRAHIM CELIK, ESRA CAYMAK 29

MELANJ ELYAF KARISIMLARINDA RENK STANDARDIZASYONU ICIN SISTEM GELISTIRILMESI
MEHMET KERTMEN, HALIL IBRAHIM CELIK, ELIF GULTEKIN, AYBUKE SEN, HALIL IBRAHIM OLUCAK 35

DTY POLYESTER IPLIKLERDE FILAMENT INCELIGININ VE DISK TIPININ IPLIK FIZIKSEL OZELLIKLERINE ETKISI
GULBIN FIDAN, YASEMIN KORKMAZ, HALIL IBRAHIM CELIK 41

Lİ-Fİ İLE UÇAK İÇİ İNTERNET BAĞLANTISINDA FARKLI GEOMETRİK YERLEŞİMLERİN PERFORMANS ANALİZİ
ABDULLAH MURATOGLU, TANSAL GUCLUOGLU 42

A REVIEW ON ALUMINIUM MATRIX COMPOSITES MANUFACTURED BY POWDER METALLURGY
ELIF PESEN, ABDUL KADIR EKSI, AYSE NUR ACAR, AHMET EKICIBIL 54

USING LIGHTWEIGHT EXPANDED GLASS AGGREGATE TO PRODUCE A LIGHTWEIGHT GEOPOLYMER MORTAR
AHMAD AL MOHAMMAD, ABDULKADIR CEVIK 63

DETECTION AND CLASSIFICATION OF FRESH PISTACHIOS USING DEEP LEARNING
AHMET EMIN KARADAG, ALI KILIC 70

COMPARATIVE STUDY ON THE VIBRATION BEHAVIOR OF ALUMINUM ALLOYS USED IN AEROSPACE APPLICATIONS
NURETTIN FURKAN DOGAN, BURAK SAHIN 76

INVESTIGATION OF SURFACE ROUGHNESS FOR INCONEL 718 AS AEROSPACE MATERIAL BY FLOW PEENING GOV PROCESS
KURSAD GOV, NURETTIN FURKAN DOGAN, MURAT KALAK, MEHMET SAIT KOCA 84

OPTIMIZATION OF AN ANTI SWAY CONTROLLER FOR AN OVERHEAD CRANE USING THE BEES ALGORITHM
MAHMUT CIMEN, SAMI YESILBEL, METE KALYONCU 88

INDUCTION SINTERING OF FERROUS MATERIALS AT DIFFERENT TIMES AND INVESTIGATION OF THEIR MECHANICAL PROPERTIES
MEHMET YILDIRIM, ENVER ATIK 96

ASİT BOYARMADDELERLE BOYANMIŞ DENİM KUMAŞLAR ÜZERİNE BİR ARAŞTIRMA
NURIYE KERTMEN, ZEYNEP TEKEREK 103

THE EFFECT OF USING STEEL MESH ON THE INTERLAMINAR FRACTURE TOUGHNESS OF FML COMPOSITES
MEHMET ALI AKELOGLU, MELIH BAYRAMOGLU 109

FAILURE ANALYSIS OF 3D PRINTED AND CONVENTIONALLY MANUFACTURED POLYMER GEARS
ABDURRAHMAN GUNGOR, NECIP FAZIL YILMAZ, MUSA YILMAZ 117

EFFECT OF ELECTRODE GEOMETRY ON OVERCUT OF DRILLED HOLES IN ELECTRICAL DISCHARGE DRILLING PROCESS
ALI TOLGA BOZDANA, NAZAR KAIS AL KARKHI 127

BMG DELİK DELME PROSESİNDE SICAKLIK MODELLEMESİ
AZMI TIMUR, NUREFSAN ELIF KOSEN, M AYBUKE TURKMEN, ELIFNUR KOSEMEN, MUSTAFA BAKKAL 134

ÇOK BİLESENLİ ÖZLÜ İPLİK İCEREN DENİM KUMAŞLARIN YIRTILMA MUKAVEMETLERİNİN İNCELENMESİ
DENIZ VURUSKAN, NAZAN AVCIOGLU KALEBEK, ESIN SARIOGLU 139

CLASSIFICATION OF THE BREAD WHEAT QUALITY WITH ARTIFICIAL NEURAL NETWORK MODELS
BUNYAMIN KAHRAMAN, YUNUS EROGLU 145

VORTEKS İPLİKLERE UYGULANAN FİKSE (VAKUMLU BUHARLAMA) İŞLEMİNİN ÖRME KUMAŞ PERFORMANSINA ETKİSİNİN ARASTIRILMASI
AHMET ORUC, EMEL ILANBEY, KUBRA OZSAHIN, HATICE KUBRA KAYNAK 150

RETROFITTING OF RC STRUCTURES USING NEAR SURFACE MOUNTED FRP
KHALED HAFAR JONEIDI, ABDULKADIR CEVIK 158

BROADBAND MICROWAVE TAPERED MICROSTRIP TRANSFORMERS DESIGN USING COGNITIVE SEEKER OPTIMIZATION ALGORITHM
UGUR CEM HASAR, MONA ALFAQAWI 167

FARKLI ÖZELLİKLERE SAHİP 2605SA1 AMORF VE M27 ELEKTRİK ÇELİĞİ NÜVE MALZEMELERİ KULLANILAN ASENKRON MOTORLARIN VERİMLİLİKLERİNİN SONLU ELEMANLAR YÖNTEMİYLE ANALİZİ
NECIP FAZIL YILMAZ, MUHAMMET YUSUF DULKADİR, MAHMUT FURKAN KALKAN, MUSA YILMAZ 174

KAYNAK GEOMETRISININ LAMINE ELEKTRIK CELIK SACLARI UZERINDEKI ETKISININ SONLU ELEMANLAR YONTEMI ILE INCELENMESI
MAHMUT FURKAN KALKAN, MUHAMMET YUSUF DULKADIR, NECIP FAZIL YILMAZ, SUAT ÖNAL 183

ACPL-332J GATE SÜRÜCÜLÜ FIRÇASIZ DC MOTOR SÜRÜCÜ TASARIMI
UFUK KAYA, HALIL EROL 192

MANUFACTURING OF COPPER WIRE BY THE CONTINUOUS CASTING PROCESS
ZAKARIA BOUMERZOUG 197

S32205 DUBLEKS PASLANMAZ ÇELİKLERDE ISIL İŞLEM SICAKLIKLARININ MİKROYAPI VE SERTLİK ÖZELLİKLERİNE ETKİLERİ
MERVE DUMAN, AZIZ BARIS BASYIGIT, HALIL IBRAHIM KURT 202

EXPLORING THE PHOTOCATALYTIC CAPABILITY OF DMAHDM-MODIFIED ZINC OXIDE AND ITS BISEMA-TEGDMA COMPOSITES
ILKNUR TAS KAZAK, DERYA KAPUSUZ YAVUZ 212

FLEXIBLE ELECTRODES FABRICATED WITH COBALT AND COPPER COATED GRAPHITE FILAMENTS
ALI TUNC, ABDULCABBAR YAVUZ, METIN BEDIR 219

INVESTIGATION OF WEAR BEHAVIOUR OF PLA AND CV 60 MATERIALS
EREF BEDIRHAN AKSOY, NECIP FAZIL YILMAZ, MUSA YILMAZ 228

COBALT AND NICKEL ALLOY ELECTRODE CO DEPOSITED FROM A NON-AQUEOUS ELECTROLYTE
MURAT ARTAN, ABDULCABBAR YAVUZ, NECIP FAZIL YILMAZ 238

RÜZGAR TÜRBİNİ KANATÇIK AÇI KONTROLÜNÜN BULANIK MANTIK İLE ANALİZİ
ATAKAN ARSLAN, HALIL EROL 239

DESIGN AND ANALYSIS OF AN ULTRASONIC SONOTRODE FOR HIGH FREQUENCY VIBRATION ASSISTED SHEET METAL FORMING APPLICATIONS
SADIK OLGUNER, ALI TOLGA BOZDANA 240

MAKINE OGRENME TEKNIKLERI KULLANILARAK HAZIR GIYIM ENDUSTRISINDE IS VERIMLIGININ SINIFLANDIRILMASI
ABDULLAH CALISKAN, ZEYNEL ABIDIN CIL 241

ENERGY, ENVIRONMENT AND ECONOMY INVESTIGATION OF WASTE HEAT RECOVERY TECHNOLOGIES IN MARINE INDUSTRY
HASAN MITHAT DELIBAS, ERHAN KAYABASI 242

A STUDY ON THE MECHANICAL PROPERTIES OF BULK CONTINUOUS FILAMENT YARNS PRODUCED BY MIXING POLYPROPYLENE HOMOPOLYMER WITH POLYPROPYLENE COPOLYMER OR THERMOPLASTIC POLYOLEFIN
CEMILE EMEL YAZ, CEM GUNESOGLU, MEHMET TOPALBEKIROGLU 243

THE HIGH PURITY NANOSIZED STRONTIUM CARBONATE PRODUCTION WITH THE AMMONIUM CARBONATE MEDIA VIA THE MECHANOCHEMICAL SYNTHESIS PROCESS
SULTAN OZTURK, FURKAN ALPTEKIN, SELMINE AKYOL, SEFA EMRE SUNBUL, KURSAT ICIN 244

STRUCTURAL TRIBOLOGICAL ISOTHERMAL OXIDATION AND CORROSION PROPERTIES OF AL CO CR FE NI TI CU HIGH ENTROPY ALLOY
SULTAN OZTURK, SELMINE AKYOL, FURKAN ALPTEKIN, KURSAT ICIN, SEFA EMRE SUNBUL 245

ASSESSMENT OF HEMODIALYSIS MEMBRANES A REVIEW
ADIL GUJRI, OMER NECATI CORA 246

FINITE ELEMENT MODELING AND ANALYSIS OF REPRESENTATIVE WING STRUCTURE FOR STRUCTURAL HEALTH MONITORING PURPOSES
MUHAMMED LATIF BEKCI, OMER NECATI CORA 247

EFFECT OF SURFACE TEXTURING ON TRIBOLOGICAL BEHAVIOR OF SAE 600 BEARING BRONZE
DOGAN ACAR, HASAN ONUR TAN, OMER NECATI CORA 248

INVESTIGATION ON THE SOLID PARTICLE EROSION PERFORMANCE OF TRANSPARENT MATERIALS
MOHAMMAD HUSSAIN DANESH, DOGAN ACAR, OMER NECATI CORA 249

INVESTIGATION OF THE HUB DIAMETER EFFECT ON PROPELLER THRUST
ENES COSKUN, MEHMET HANIFI DOGRU 250

EFFECT OF PROPELLERS NUMBERS AND HORIZONTAL DISTANCE IN DESIGN OF VTOL
MUSTAFA VARKI, EYUP YETER, MEHMET HANIFI DOGRU 251

STRUCTURAL AND SURFACE PROPERTIES OF GLASS POWDER COATED CR STEELS
AYSE NUR ACAR, DOGAN KAYA, ABDUL KADIR EKSI, AHMET EKICIBIL 252

A STUDY ON DETERMINATION OF OPTIMUM AUTOFRETTAGE PRESSURE OF A THICK WALLED CYLINDER WORKING UNDER CYCLIC PRESSURE
HAKAN CANDAR, HALIL KIMSESIZ 253

DESIGN OF FLIGHT CONTROLLER UNIT BASED ON PID CONTROL
HAKAN CANDAR, AHMET OZGUR AYIK 254

IMPLEMENTING THE PMSM RESOLVER INTERFACE ON FPGA
ABDULKADIR SADAY, ILKER ALI OZKAN, ISMAIL SARITAS 255

INVESTIGATION OF MATERIAL REMOVAL RATE FOR INCONEL 718 AS AEROSPACE MATERIAL BY FLOW PEENING GOV PROCESS
KURSAD GOV, BURAK SAHIN, MURAT KALAK, MEHMET SAIT KOCA 256

EXAMINATION OF THE INFLUENCE OF PRINTING PARAMETERS FOR THE CONTINUOUS CARBON FIBER REINFORCED THERMOPLASTICS BASED ON FUSED DEPOSITION MODELING
ALTUG USUN, RECEP GUMRUK, NURI YILDIZ, BAHRI BARIS VATANDAS 257

SURFACE OBSERVATION OF INCONEL 718 TREATED BY FLOW PEENING GOV PROCESS
KURSAD GOV, BURAK SAHIN 258

THE DESIGN OF SOLAR CELLS SENSITIVE TO THE HELICAL BEAMS
KORAY KOKSAL 259

AN EXPERIMENTAL STUDY ON THE PARAMETERS AFFECTING THE THERMAL SEAL FORCE OF COATED BIDIRECTIONAL STRETCHED PET FILM FOR FOOD PACKAGING APPLICATIONS
CAGRI TIKILOGLU, EMRAH OZAHI 260

EFFECT OF DIFFERENT AMOUNTS OF CARBON FIBER ADDITIVE ABS ON THERMAL DISTORTION AND COOLING TIME
OMER EYERCIOGLU, ENGIN TEK, MEHMET ALADAG, GULAGA TAS 261

ELECTROCHEMICAL BEHAVIOUR AND PERFORMANCE OF FLEXIBLE GRAPHITE YARNS IN DIFFERENT ELECTROLYTES WITH WIDE POTENTIAL WINDOW OF 2 V
MAHMUT FURKAN KALKAN, MURAT ARTAN, HASAN MITHAT DELIBAS, NECIP FAZIL YILMAZ, ABDULCABBAR YAVUZ 262

BROADBAND MULTILAYER ABSORBERS DESIGN USING DS-SEEKER OPTIMIZATION ALGORITHM
UGUR CEM HASAR, MONA ALFAQAWI 263

MATERIAL REPLACEMENT AND TOPOLOGY OPTIMIZATION STUDY ON A PVC CUTTING MACHINE COMPONENT
ZEYNEP HANCERKIRAN, UMUT CAN AHLATCI, ERTAN TOPUZOGLU, TAYLAN KASAPCOPUR, ERKAN ALKAN, FIKRET ERTURK, UMUT KARAGUZEL, MUSTAFA BAKKAL 264

ANALYSIS OF MECHANICAL BEHAVIOR OF TERMOPLASTIC COMPOSITES
AYSU HANDE YUCEL, ELIFNUR KOSEMEN, ALI TANER KUZU, MUSTAFA BAKKAL 265

APPLICATION OF FLOW PEENING GOV PROCESS ON INCONEL FROM AEROSPACE MATERIALS
KURSAD GOV, IBRAHIM GOV, BURAK SAHIN, ABDURRAHMAN DOGAN, MURAT KALAK, MEHMET SAIT KOCA 266

AISI 4140 ÇELİĞİNİN FREZELEMESİNİN TAGUCHI-DEAR YÖNTEMİYLE OPTİMİZASYONU
YUSUF FEDAI 267

DENIM KUMASLARIN RENKLENDIRILMESINDE INOVATIF BIR YONTEM
NURIYE KERTMEN, ZEYNEP TEKEREK 268

NUMERICAL FLOW-FIELD SIMULATION OF COMPACT SPINNING CONDENSING ZONE FOR DIFFERENT AIR PRESSURE LEVELS

MURAT DEMIR [1]

[1] Dokuz Eylul University, Engineering Faculty, Textile Engineering Department, İzmir, TURKEY.

Abstract

The basic principle of compact spinning is to condense the fiber bundles before the yarn formation point and to reduce the spinning triangle. Utilizing negative air pressure is one of the ways to condense fiber bundles and pneumatic compact spinning is one of the most widely used compact spinning technology. In this study, condensing zone of pneumatic compact spinning with the perforated drum was numerically simulated for different air pressures. For this purpose, first, essential parts of pneumatic compact spinning, which are air-suction guide, suction insert, and perforated drum, were designed with SolidWorks software. Then, all designed parts were assembled to simulate the condensing zone of pneumatic compact spinning. A numerical flow field simulation was performed on the assembly model for different air pressure levels to investigate the effectiveness of air pressure levels on the condensing zone. 20000 Pa, 40000 Pa, 60000 Pa, and 80000 Pa air pressure levels were used for numerical simulation. Besides two reference lines, named R1 and R2, were introduced at both edges of the condensing zone. Transverse flow velocity components defined in Z-axis direction, static pressure distribution, and streamline diagram were used to compare changing pressure level effectiveness on the condensing zone. Results showed that a successful condensing zone was created for all air pressure levels. However, between 20000 Pa and 60000 Pa, no dramatic changes were observed in the transverse flow components and static pressure levels, but for 80000 Pa air pressure levels, it was seen that the transverse flow components decreased by approximately 23%. Using appropriate pressure levels for compact spinning might be useful for energy savings and final product cost.

Keyword: Numerical simulation, Compact spinning, Flow-field, Air-suction guide, Suction insert

1. Introduction

Condensing fiber bundle before yarn formation point decreases the width of fiber as well as the structure of spinning triangle, provide better yarn properties [1-2]. Utilizing the negative air pressure is one method of condensing fibers besides the twisting roving and mechanical compacting [3]. In pneumatic compact spinning with perforated drum, air-suction guide and suction insert are the auxiliary parts that divert negative air around the fiber bundle. The structures of air slots on these parts are the effective parameter for diverting air and many researchers studied the effect of these slots geometry on the condensing zone [4-5]. The structures of these parts have been also developed by the technology provider for better yarn properties since the first introduction of compact technology (Figure 1). In addition, novel compact technologies were developed by modifying these auxiliary parts [4-5].

Numerical simulation of flow-field in the condensing zone has been studied for the different kinds of compact technologies with computational fluid dynamics which is counted as the most effective tool for flow-field simulation [6-7]. In some studies, the effectiveness of auxiliary parts on the

condensing zone was studied for pneumatic compact spinning with the perforated drum [8-9]. In addition, condensing zone of compact spinning with lattice apron was also studied. There are also studies in the literature that compares flow field distribution of complete compact spinning and lattice apron compact spinning [10-11].

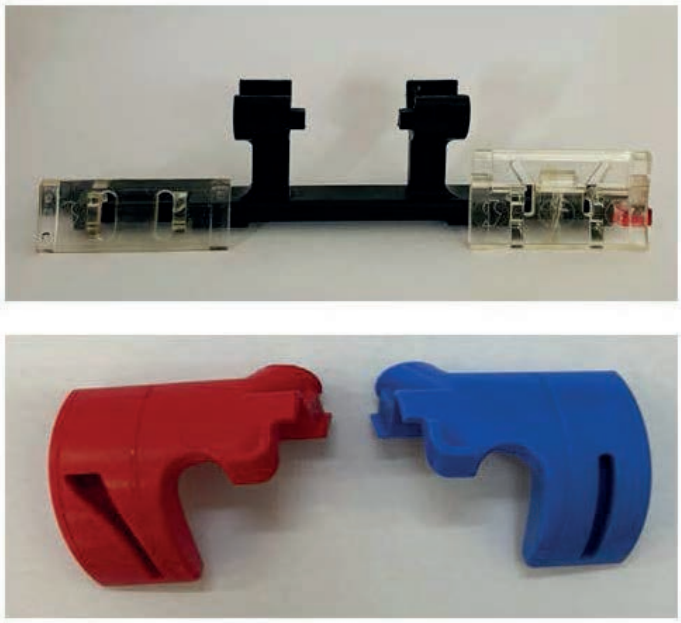


Figure 1. Illustration of different kinds of air-suction guide and suction insert

In this study, regardless of geometrical changes of auxiliary parts, flow-field of compact spinning were numerically simulated for different air pressures that could be effective either on yarn properties or energy consumption. For this purpose, commercially used air-suction guide, suction insert, and perforated drum of compact spinning technology were designed in SolidWorks. Numerical simulations of flow-field were performed for different air-inlet pressures that 20000 Pa, 40000 Pa, 60000 Pa, and 80000 Pa with SolidWorks Flow Simulation software. For each air-inlet pressure, transverse flow velocities on Z- axis, static pressure distribution and streamline diagrams were presented.

2. Methods

To investigate the effect of air inlet pressure on the condensing zone, first, parts of compact spinning were designed. For this purpose, the air-suction guide, suction insert, and perforated drum were designed according to the real part measurement. In the suction insert, the width of air slots was designed in 2 mm, the distance of air-slots at the entry point of fibers was designed in 16 mm and it was 8 mm at the exit point. Length of air-slots was designed in 12 mm in the fiber transportation way. For the suction guide, the width of air-slots was designed in 3 mm width and 20 mm length. For the perforated drum, the width of the maximum condensing zone was designed at 12 mm and 11 air holes were placed in the condensing zone as reported in Demir *et. al*. [4] Figure 2 presents the geometrical measurements of designed parts and assembly model of the condensing zone.

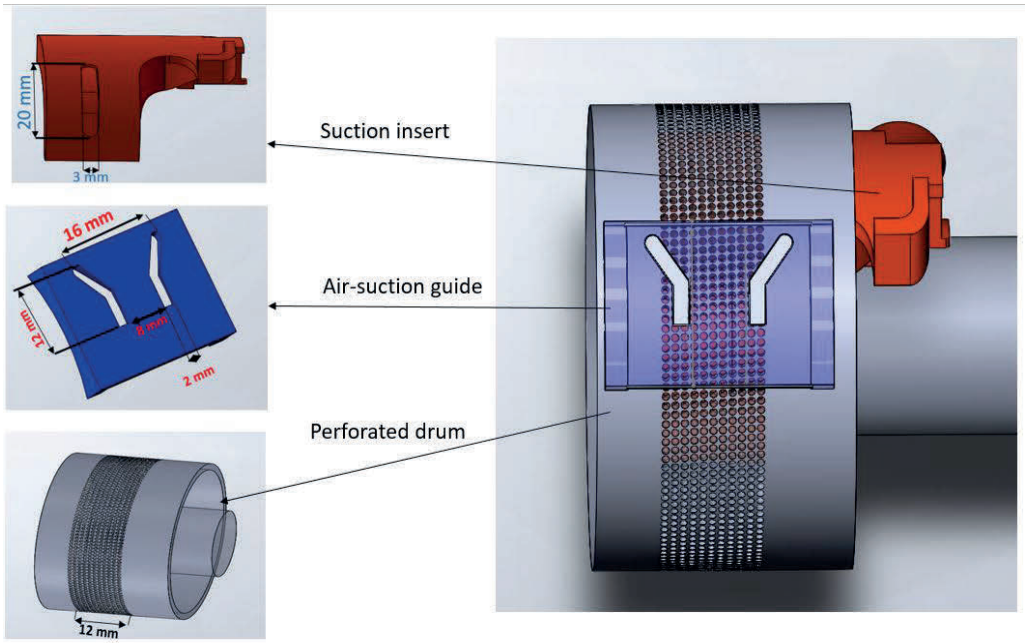


Figure 2. Illustration of design parts and assembly model of compact spinning

In the condensing zone, two reference lines, which are named R1 and R2 were located at the y= -1 mm and both closer edges of the air-suction guide. Air-inlet pressure was defined as standard atmospheric pressure at the air-entry point of the air-suction guide and 20000 Pa, 40000 Pa, 60000, 80000 Pa air-outlet pressures were defined at the air-exit point on the suction insert. In the numerical simulation, flow velocities are comprehensively analyzed in transverse, fiber thickness, and fiber transportation direction. In the designed assembled model, Z-axis is the transverse direction, Y-axis is the fiber thickness direction and X-axis is the fiber transportation direction. Since the changes on the air pressure mostly effective on the transverse condensing zone, flow velocity components on Z-axis, static pressure distribution and stream line diagram were presented for each of the air-outlet pressure levels.

3. Results and Discussion

Flow velocity components on the Z-axis direction for different air pressures were illustrated in Figure 3. From Figure 3, it is seen that actual flow components on the Z-axis direction show a similar trend for the whole condensing zone. It was an expected result, as flow characteristics are mostly related to the geometry of the condensing zone parts. However, changing air pressure affects the magnitude of flow velocity. For the air pressure for 20000 Pa to 60000 Pa, small changes were observed on the magnitudes of flow components on the Z-axis. Increasing air pressure to 80000 PA, resulted greater changes in the magnitudes. The mean value of the flow components on the Z-axis direction was also presented in Table 1. It is seen from Table 1 that, the mean value of the flow components is approximately 49 m/s for 20000 Pa, 48 m/s for 40000 Pa, 45 m/s for 60000 Pa. For the 80000 Pa air pressure, it is seen that the flow components on both reference lines are dramatically decreased by approximately 23% compared to the 20000 Pa.

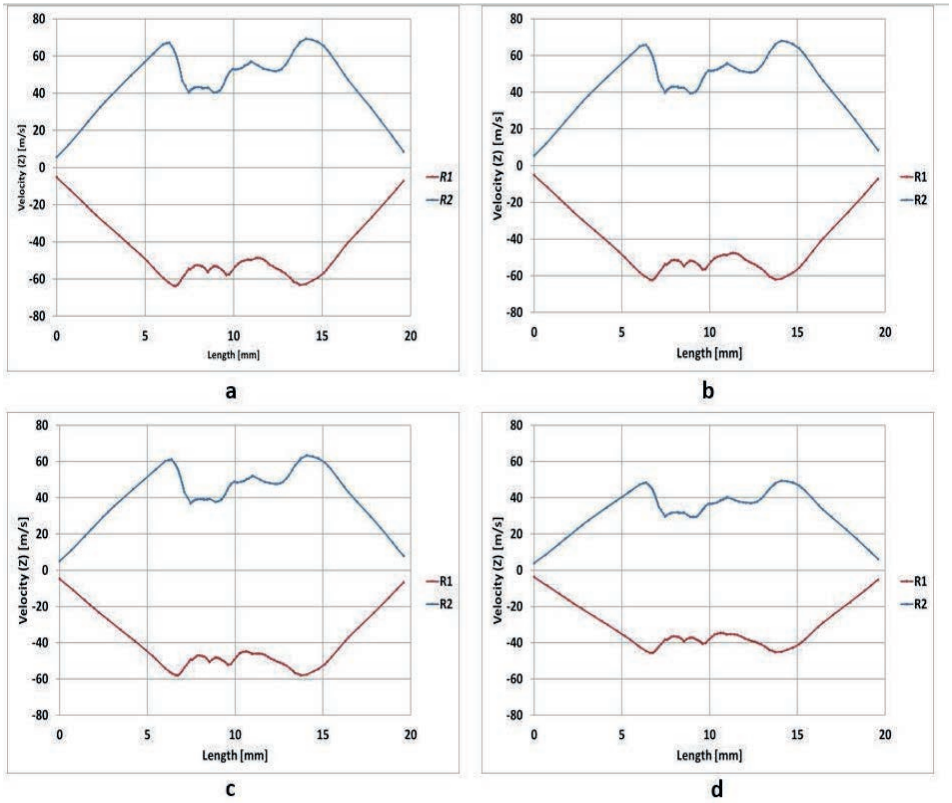


Figure 3. Flow velocities on Z-axis for different air-pressures;
a) 20000 Pa, b) 40000 Pa, c) 60000 Pa, d) 80000 Pa

Table 1. Mean value of flow velocities on Z-axis directions (m/s)

	Air pressure levels (Pascal)			
Reference Line	**20000 Pa**	**40000 Pa**	**60000 Pa**	**80000 Pa**
R1	-49.8808	-48.7123	-45.4646	-35.2705
R2	49.26222	48.35233	45.11268	35.36856

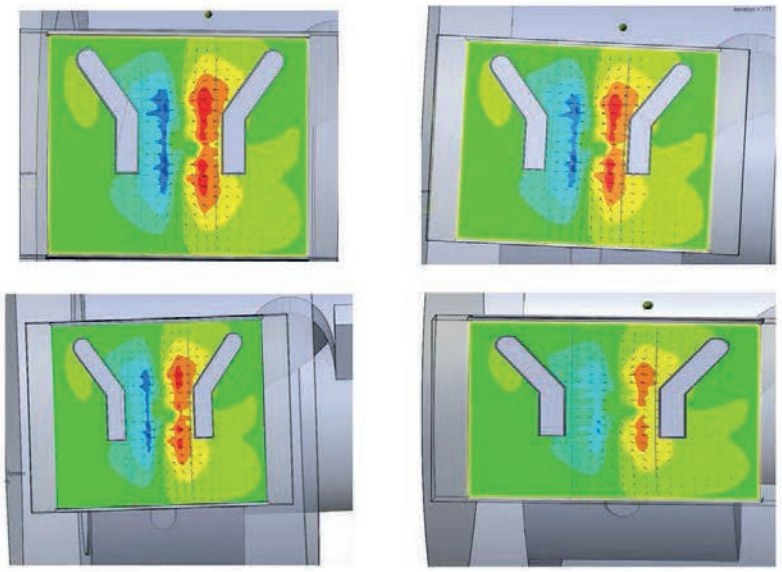


Figure 4. Stream line diagram on the X-Z section

Stream line diagram for the different air pressures was presented in Figure 4. From Figure 4, it is seen that, flow components on the introduced reference lines are in opposite way and towards the center of fiber bundle. It could be concluded that condensing effects were achieved for all pressure levels.

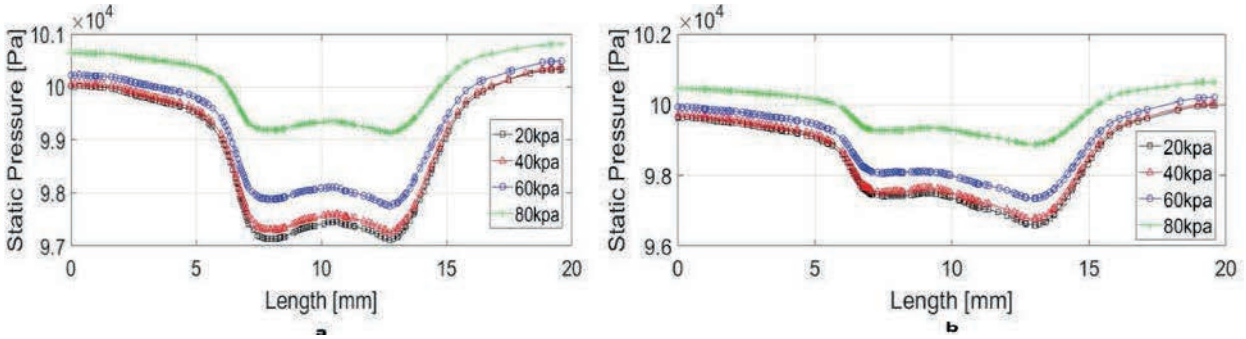


Figure 5. Static pressure distribution on the reference lines for different pressure levels; a)R1, b) R2

Static pressure distribution along the reference lines for different pressure levels was given in Figure 4. From Figure 4 it is seen that for 80000 pa the largest static pressure level is observed, hence it is also assumed that the forces acting on the fibers are the smallest.

4. Conclusions

In this study, condensing zone of pneumatic compact spinning with perforated drum was numerically simulated for different air pressure levels. For this purpose, an air-suction guide, suction insert, and perforated drum, which are the essential part of the condensing zone, was designed and assembly to simulate condensing zone. Numerical flow field simulation was performed for different air-pressure levels. Actual flow components, streamline diagram and static pressure distribution were compared. Results showed that changing air pressure between 20000 Pa to 60000 does not have a major influence on the magnitudes of flow components on the Z-axis direction while for 80000 Pa of air pressure decreased the magnitudes of flow components by approximately 23% compared to 20000 Pa.

The amount of energy consumption is at the center of production decisions of many companies, not only as the production cost reflected in the final product but also with the use of natural resources and environmental effects. The same condensing effects on yarn production with less energy consumption will be beneficial for energy saving. In the future studies, an experimental work will be useful to support the result of this study and investigate the relation between air pressure and yarn properties.

References

1. Zou, Z.Y., Cheng, L.D., and Hua, Z.H. A numerical approach to simulate fiber motion trajectory in an airflow field in compact spinning with a perforated drum. Textile Research Journal. **2010**, 80(5):395-402.
2. Basal, G., and Oxenham, W. Comparison of Properties and Structures of Compact and Conventional Spun Yarns. Textile Research Journal. **2006**, 76(7):567–575.
3. Kumar, A., Ishtiaque, S.M. and Salhotora, K.R. Compact spinning- a critical review. ASME International Mechanical Engineering Congress & Exposition, Washington, USA. **2003**, 59-68.

4. Demir, M., Kılıç, M., Sayın, S., Kıral, Z., Balduk, F. and Denge, K.K. Design of three-strand compact spinning system and numerical flow-field simulation for different structures of air-suction guides and suction inserts. Textile Research Journal. **2021**, 91(15-16):1795-1814.
5. Demir, M. Design and Development of Three Strand Twist Spun Yarn. PhD thesis, Dokuz Eylül University, İzmir, Turkey.**2021**.
6. Liu, X., Zhang, H., and Xuzhong, S. Comparative analysis of pneumatic compact spinning systems. International Journal of Clothing Science and Technology. **2016**, 28(4):400-419.
7. Yinghui, L., Xie, C., and Liu, X. Comparative analysis of two kinds of pneumatic compact spinning using finite element method. International Journal of Clothing Science and Technology. **2017**, 29(4):514-524.
8. Su, X., Gao, W., and Liu, X. Numerical simulation of flow field in complete condensing spinning: effects of suction unit and guiding device. The Journal of the Textile Institute. **2016**, 107:811-824.
9. Su, X., Gao, W., Liu, X., Xie, C., and Xu, B. Numerical simulation of a three-dimensional flow field in compact spinning with a perforated drum: Effect of a guiding device. Textile Research Journal. **2013**, 83(19):2093-2108.
10. Liu, X., Liu, W., Zhang, H., and Su, X. Research on pneumatic compact spun yarn quality. The Journal of the Textile Institute. **2015**, 106(4):431-442.
11. Su, X., Gao, W., and Liu, X. Numerical simulation of flow field in complete condensing spinning: effects of suction unit and guiding device. The Journal of the Textile Institute. **2016**, 107:811-824.

DECISION TREE REGRESSION METHOD APPLICATION FOR PREDICTION OF WOVEN FABRICS TEAR STRENGTH

ELİF GÜLTEKİN[1], HATİCE KÜBRA KAYNAK[1], HALİL İBRAHİM ÇELİK[1]

[1]Gaziantep University, Faculty of Engineering, Textile Engineering Department, Gaziantep, TURKEY.

Abstract

Many tests are applied to determine the mechanical properties of fabrics. Elongation at break, breaking strength, tear strength, bending strength, which determine the behavior of the fabric under the forces affecting in different direction can be given as examples. So many samples must be produced to perform these tests. Many mathematical models and statistical methods can be applied to determine the relationship between the structural parameters of the fabric and the results obtained from mechanical tests. However, due to the complex nature of the textile fabric structure, there are many parameters that affect the mechanical properties. Therefore, there are difficulties in determining the mechanical properties of the fabric with mathematical models. The explanation about the relationship between fabric physical properties and performance can be easily determined by means of artificial intelligence techniques. Data mining includes the steps of cleaning, integrating, selecting, and transforming data to classify and evaluate the information extracted from big data. After these stages, the data is transmitted to databases for analysis and inference, then visualized with machine learning technique solutions and made available for presentation. Clarity is given to the data so that it can be approached with rules and statistics. Statistical methods, genetic algorithms, artificial neural networks, and decision trees are frequently used methods for data mining. In this study, the prediction of static tear strength performance from woven fabric physical parameters using decision trees regression method was conducted. When the results were examined, the tear strength was predicted with 0.97 R^2 from the parameters of weave type, fabric density, filament fineness and weave direction.

Keyword: Decision tree, Machine learning, Tear strength, Woven fabric Prediction.

1. Introduction

The textile industry generates and stores a large amount of data. This data includes raw materials, machine settings, product quality, and fabric performance characteristics. To process textile data, several textile studies have used a variety of classic mathematical and statistical methodologies. Traditional methods, on the other hand, are still incapable of recognizing broad and complex correlations between data instance attributes, as well as anticipating unknown feature values for a new instance. Data Mining (DM) techniques that are used in a variety of technical disciplines have lately been used in textile engineering as a result of this challenge. Data mining is a computer science and statistics interdisciplinary field with the goal of extracting information from a data set using intelligent techniques and translating the data into an understandable structure for later use.

DM methods have been used to a variety of textile challenges in textile printing and dyeing process, including forecasting fabric type [1] and fabric characteristics [2], predicting yarn properties [3–5], fiber identification [6], and color management [7]. Another learning approach,

support vector machine (SVM), has been used in the textile industry for quality control [8,9], particularly for fault categorization [10] in textile textures. Using a Decision Tree (DT) algorithm, Agarwal et al. [11-12] sought to determine the effectiveness of wash-ageing and fabric softener use on the mechanical characteristics (such as tensile extension, shear, bending, stiffness, compression energy, and fabric roughness) of knitted textiles. In this study over 104 varieties of various samples with varied fiber types and fineness, yarn architecture, and fabric structure utilizing a DT algorithm. Some researchers estimated the fabric tearing force from the quantity of softener pickup and its homogeneity [13] by means of linear regression models. It was concluded that the weave type, weft density, ground structure, and ground yarns had the greatest impact on tearing force, while pile form and pile designation have modest impacts. Another research utilized linear regression to estimate fabric tear strength in the warp and weft directions for woven wool textiles, with Pearson correlations of 0.976 and 0.975 for warp and weft, respectively [14]. Eltayib et al. utilized the same linear regression model to predict the relationship between fabric tear strength and additional independent variables including yarn tensile strength, yarn count, and fabric linear density [15]. A flexible nonlinear model based on an Evolutionary Artificial Neural Network was proposed to forecast woven fabric tensile strength, outperforming a linear regression model [16].

In this study, prediction of tear strength of microfilament woven fabrics was carried out by using decision tree method, which is one of the data mining algorithms. The performance characteristics of high-density fabrics were estimated using the weave type, fabric density, number of filaments in the yarn section and weave direction. It is possible to carry out the quality control process of woven fabrics in a faster and more reliable way with such machine learning algorithms.

2. Materials and Methods

Decision Tree Regression Method

One or more branches may exist within a decision node. The root node is the initial node. Both category and numerical data can be used to build a decision tree. Decision trees are a strategy for determining the class of data that is unknown, based on data that has been encountered in the past and whose class has been identified. Decision trees are popular in data mining because they offer predictive and descriptive qualities, are simple to construct and assess, have high reliability, and can be readily incorporated into computer storage units. In data sets with nonlinear connections, heterogeneous data kinds, and outliers, classification modeling with decision trees is possible. Decision theory, classification, prediction, and clustering are all examples of applications for these approaches. Decision trees are known as regression trees when the target variable is continuous, and categorical trees are known as classification trees when the target variable is categorical. Regardless of the circumstance, the methods for creating decision trees remain the same. The initial stage in the decision tree technique, as a statistical method, is to construct a tree structure and then process the data in the data set into this tree. Decision trees are made up of root nodes, nodes, and branches. Questions are asked during the rule-making process, and actions are performed in response to the answers. New rules are formed by combining the responses. The root node, which is the first step of the tree structure, is constructed after choosing on the first variable to ask the question. 'If-then' rules are established in each branch, and the next node is passed based on the decision made. This is how the tree structure is handled until a new query arises. The last node representing a class is finally reached.

Woven polyester multifilament fabrics with Plain, Satin, and Twill types were used in this study. The interlacement points in these different types of weaving are varied. The structural fabric

characteristics were used to predict tear strength performance since the structure of woven fabrics with various junction points will be varied as well. 110 dtex polyester microfilament textured yarns with 0.33, 0.57, and 0.76 dtex filament linear densities, as well as 110 dtex conventional polyester textured yarns with 1.14 and 3.05 dtex filament linear densities used in the fabric. The warp yarn was chosen as 83 dtex polyester yarn with a filament linear density of 1.14 dtex. In order to account for weaveability constraints, four alternative weft sett values were used for each weave type. By this way 60 woven fabric samples were produced. The tear strengths of the samples were determined according to the TS EN ISO 13934-1: 2002 standard, using the Titan Strength device. Each of the produced fabric samples was measured ten times. Fabric measurements were taken in both the weft and warp directions. A total of 1200 strength measurement data were generated as a result. In the prediction model, 720 measurements were utilized for the training set, while 480 measurement results were not included in the training set for use as test data. The Python software was used in this investigation and one of the machine learning topics that is decision tree learning approach was applied. Decision tree is a classification approach that builds a model in the form of a tree structure with decision nodes and leaf nodes. By splitting the data set into smaller or even smaller pieces, the decision tree algorithm is created. While creating the decision tree regression model, the weighted gain calculation of the variables in the data set is performed to ensure that the model is created in a balanced way. Which variable has more effect on the parameter to be predicted is separated as the first root. Then, other roots are formed according to the gain value in the remaining variables. At the last stage, the values showing the prediction results are displayed. Therefore, in this study, it was seen that fabric thread density had the highest gain in the data set (Figure 1). Depending on the fabric thread density, second roots were formed according to the weave type and the number of filaments. Weave direction according to the gain level was used in the estimation process in the third stage.

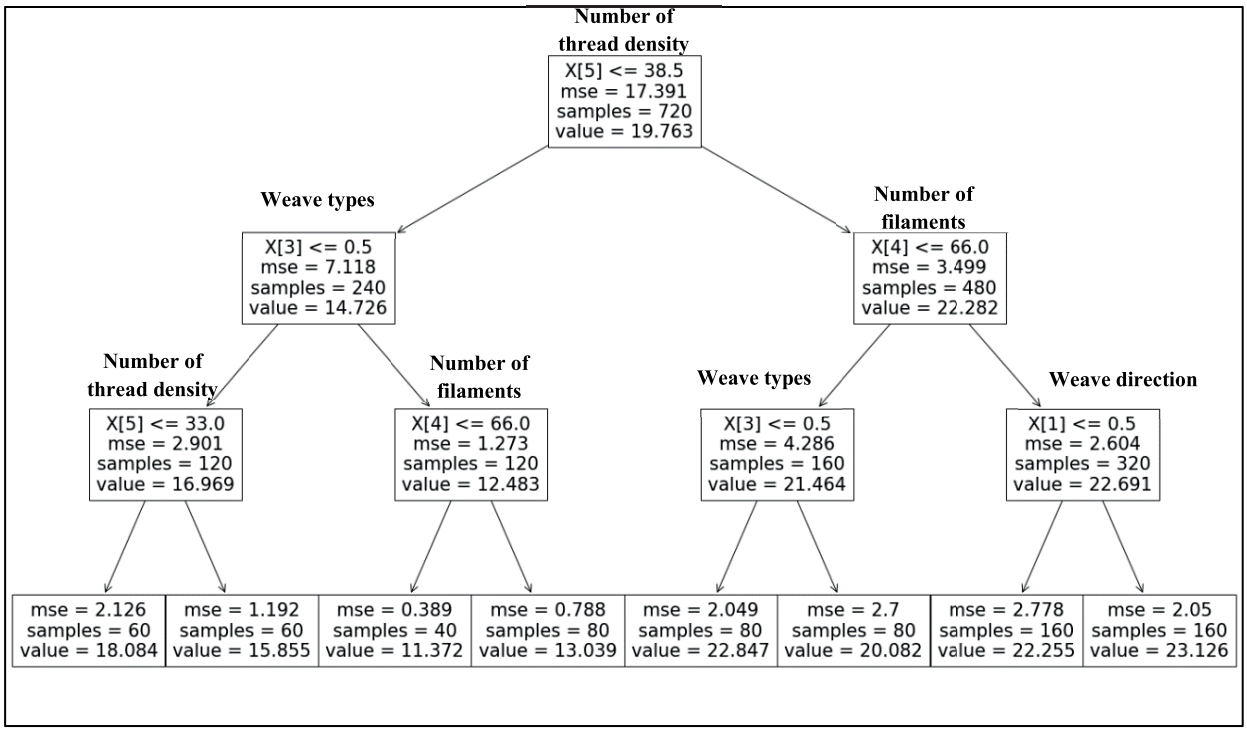


Figure 1. Schematic representation of the Decision tree created in this study

3. Results and Discussion

In order to determine the success ratio of the developed decision tree regression model for tear strength prediction, 12 fabric samples were randomly selected for testing. The tear strength results of those samples were not used for training process. According to Table 1, the lowest and highest error percentage values were obtained as 1.29% and 5.10%, respectively. The mean absolute percentage error of the decision tree regression model is calculated as 2.81%.

Table 1. Tear strength prediction results.

Actual Results	Predicted Results	MAPE
17,33	17,83	2,89
15,99	16,24	1,56
18,04	18,96	5,10
15,96	16,51	3,45
15,38	15,01	2,41
23,85	24,2	1,47
23,36	23,7	1,46
21,52	22,58	4,93
25,36	24,2	4,57
12,38	12,65	2,18
20,17	20,65	2,38
20,89	21,16	1,29
Average: 2,81		

The actual and predicted tear strength results are displayed together in Figure 2. It can be clearly seen that there is high correlation between two value sets; the actual and predicted results are progressing on the same trend. The linear regression between the actual and predicted tear strength results is obtained as R^2 0.97 (Figure 2). This verifies that the tear strength of the woven fabrics could be predicted accurately by using decision tree regression algorithm.

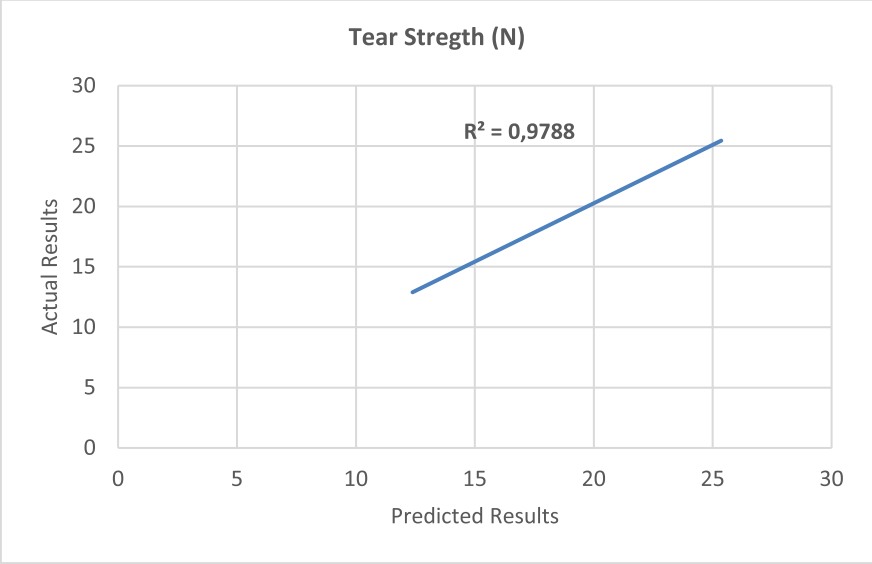


Figure 2. Q–Q plot of the experimental and predicted air permeability values

4. Conclusions

This paper provides an overview of DM techniques intended particularly for textile applications, as well as a description of some experimental work published in the literature. It illustrates how regression techniques may be used to solve an issue in the textile industry. The regression approach is also given more weight in the textile sector, as evidenced by this research. Apart from the fact that ANNs are the most often used prediction or classification methods, it is clear that data mining is equally useful. In this study, the decision tree regression model was employed, which is one of the most often used data mining approaches. Fabric characteristics such as weave type, fabric density, filament fineness, and weave direction were used to predict tear strength. When the results are analyzed, it is clear that the decision tree machine learning approach can be used successfully in the textile industry, which has such a large amount of data. The actual measurement values and the predicted values were found to have a strong correlation.

Considering the latest state of technology today, it is a fact that the quality control process in the textile industry will become increasingly automated, since machine learning can be applied to nearly any business. As a result, one of the responsibilities imposed by the Industry 4.0 era is to generate useful information from data and to utilize that information across departments.

References:

1. Ghosh, A., Guha, T., Bhar, R.B. Identification of Handloom and Powerloom Fabrics Using Proximal Support Vector Machines. Ind J Fibre Text Res, **2015**, (40):87–93.
2. Yap, P.H., Wang, X., Wang, L., Ong, K.L. Prediction of Wool Knitwear Pilling Propensity Using Support Vector Machines. Text Res J, **2009**, (80):77–83.
3. Lü, Z.J., Yang, J., Xiang, Q., Wang, X. Support Vector Machines for Predicting Worsted Yarn Properties. Ind J Fibre Text Res, **2007**, (32):173–178.
4. Abakar, K.A., Yu, C. Performance of SVM Based on PUK Kernel in Comparison to SVM Based on RBF Kernel in Prediction of Yarn Tenacity. Ind J Fibre Text Res, **2014**, (39):55–59.
5. Abakar, K.A.A., Yu, C. Application of Genetic Algorithm for Feature Selection in Optimization of SVMR Model for Prediction of Yarn Tenacity. Fibres Text East Eur, **2013**, (21):95–99.
6. Wan, Y., Yao, L., Zeng, P., Xu, B. Shaped Fiber Identification Using a Distance Based Skeletonization Algorithm. Text Res J, **2009**, (80):958–968.
7. Zhang, J., Yang, C. Evaluation Model of Color Difference for Dyed Fabrics Based on The Support Vector Machine. Text Res J, **2014**, (84):2184–2197.
8. Sun, J., Yao, M., Xu, B., Bel, P. Fabric Wrinkle Characterization and Classification Using Modified Wavelet Coefficients and Support Vector Machine Classifiers. Textile Research Journal, **2011**, 81(9):902-913.
9. Nurwaha, D., Wang, X.H. Using Intelligent Control Systems to Predict Textile Yarn Quality. Fibres Text East Eur, **2012**, (20):23–27.
10. Li, W., Cheng, L. Yarn Dyed Woven Defect Characterization and Classification Using Combined Features and Support Vector Machine. J Text Inst, **2014**, (105):163–174.
11. Agarwal, G., Koehl, L., Perwuelz, A., Lee, K.S. Interaction of Textile Parameters, Wash Ageing and Fabric Softener with Mechanical Properties of Knitted Fabrics and Correlation with Textile Hand I. Interaction of Textile Parameters with Laundry Process. Fibers Polym, **2011**, (12):670–678.

12. Agarwal, G., Koehl, L., Perwuelz, A. The Influence of Constructional Properties of Knitted Fabrics on Cationic Softener Pick Up and Deposition Uniformity. Text Res J, **2010**, (80):1432–1441.
13. Kotb, N. Engineering of Tearing Strength for Pile Fabrics. Journal of Textile and Apparel, Technology and Management, **2009**, 6(1).
14. Malik, Z.A., Malik, M.H., Hussain, T., and Arain, F.A. Development of Models to Predict Tensile Strength of Cotton Woven Fabrics. Journal of engineered fibers and fabrics, **2011**, 6(4).
15. Eltayib, H.E., Ali, A.H., and Ishag, I.A. The Prediction of Tear Strength of Plain Weave Fabric Using Linear Regression Models. International Journal of Advanced Engineering Research and Science, **2016**, 3(11).
16. Zeydan, M. Prediction of Fabric Tensile Strength by Modelling the Woven Fabric. Woven Fabric Engineering, **2010**, 155.

ELEKTROMANYETİK KORUYUCU ÖRME KUMAŞLARIN GELİŞTİRİLMESİ

MEHMET KERTMEN[1], DENİZ DURAN KAYA[2], HÜSEYİN KADOĞLU[2], HATİCE AKTEKELİ YILMAZ[2], HALİL İBRAHİM OLUCAK[1], AYBÜKE ŞEN[1], ÖZGÜR SAMET GİZLENCİ[1]

[1]İskur Tekstil Enerji Tic. ve San. A.Ş., Kahramanmaraş, TÜRKİYE.
[2] Ege Üniversitesi, Mühendislik Fakültesi, Tekstil Mühendisliği, İzmir, TÜRKİYE.

Özet

Elektromanyetik Koruyucu Tekstiller, Koruyucu Teknik Tekstillerin bir alt dalıdır. Elektromanyetik korumanın amacı kişileri ya da hassas elektronik cihazları çevredeki elektromanyetik dalgaların zararlı etkilerine karşı korumaktır. Cep telefonlarından baz istasyonlarına, saç kurutma makinelerinden kablosuz internet ağlarına kadar günlük hayatta çevremizde olan pek çok cihaz etrafa elektromanyetik dalgalar yaymaktadır. Tekstilde elektromanyetik dalgaların etkisini indirgemek için farklı metotlar geliştirilmiştir. İletken maddelerle kaplama yapılarak; kompozit malzemeler ve iletken yapıda polimer malzemeler kullanılarak veya iletken metalleri tekstil yapısına dahil ederek iletken tekstil yüzeyleri elde edilebilir. Bu çalışma kapsamında gümüş içerikli iletken iplikler, hem filament hem de kesikli formda üretilerek bu iplikler kullanılarak süprem ve vanize yapısında örme kumaşlar örülmüştür. Elde edilen farklı tasarımdaki bu örme kumaşların elektromanyetik ekranlama etkinliği özellikleri kıyaslanmıştır. Geliştirilen kumaşların farklı sıklık, farklı konstrüksiyon ve farklı iletken iplik yoğunluklarında üretilmesi gerçekleşmiştir. Böylelikle farklı iletken madde içeriğine, aynı zamanda da farklı görünüş ve kullanım özelliklerine sahip kumaşlar üretilmiştir. Bazı kumaşlarda iletken iplikler her sırada kullanılmayarak, hem elektromanyetik ekranlama etkinliği fonksiyonunu koruyup hem de maliyetin azaltılmasının yolları araştırılmış ve bunun için en uygun kumaş yapıları seçilmiştir. Daha sonra kumaşların koruma özellikleri, cep telefonlarının, tıbbi ekipmanların ve elektrikli ev aletlerinin ve benzeri cihazların yaydığı frekans aralığında (100 MHz - 6 GHz), ekranlı bir odada EMC test sistemi kullanılarak, gerçek elektromanyetik dalgalarla test edilmiştir. Ayrıca kumaşların bazı fiziksel özellikleri, kullanım, konfor ve antibakteriyel özellikleri test edilmiş ve tüm test sonuçları istatistiksel olarak analiz edilmiştir.

Anahtar Kelimeler: Elektromanyetik Ekranlama, Gümüş Filament, Gümüş Elyaf, İletken İplik, Örme Kumaş

1. Giriş

Teknolojinin insan hayatına yoğun entegrasyonu, elektriğin ve elektronik cihazların, aletlerin kullanımının artması elektromanyetik dalgaların artmasına sebep olmuş ve bu da elektromanyetik kirlilikle sonuçlanmıştır. Günlük hayatta kullandığımız cihazların çoğunun elektromanyetik dalgaları yaymakta olduğu ve bu dalgaların insan sağlığına farklı boyutlarda zararlı etkileri olduğu bilinmektedir. Bu nedenle pek çok araştırmacı bu etkileri önlemek için ekranlama çalışmaları yapmaktadır. Tekstiller ile elektromanyetik koruyuculuk sağlama oldukça yeni ve gelecek vaat eden bir konudur. Bu çalışmanın amacı, elektromanyetik dalgalara karşı koruyuculuk özelliğine sahip örme kumaşların geliştirilmesidir.

Elektromanyetik koruyucu tekstiller ile ilgili daha önce literatürde yapılmış olan çalışmalar incelendiğinde, elektromanyetik koruyuculuk özelliğini elde etmek için bakır, çelik, gümüş kaplamalı lifler gibi metalik liflerle yapılmış çalışmalar olduğu görülmüştür. Bu liflerin arasında gümüş kaplı lifler hem yapıya daha yüksek elektromanyetik koruyuculuk özelliği sağlamaları, hem antibakteriyel özellik taşımaları ve hem de daha tekstil karakterli tuşe özelliklerine sahip olmaları bakımından öne çıkmaktadır. Bu nedenlerden dolayı, çalışmada gümüş esaslı iletken materyaller kullanılarak; iletken iplikler üretilecek ve daha sonra bu iplikler örme kumaş üretiminde kullanılmıştır. Bahsedilen iletken iplikler süprem ve vanize kumaş yapısında üretilmiştir. Süprem ve vanize kumaşların farklı sıklık, farklı konstrüksiyon ve farklı iletken iplik yoğunluklarında üretilmesi planlanmıştır. Böylelikle farklı iletken madde içeriğine, aynı zamanda da farklı görünüş ve kullanım özelliklerine sahip kumaşlar üretilmiş olacaktır. Bazı kumaşlarda iletken iplikler her sırada kullanılmayarak, hem elektromanyetik ekranlama etkinliği fonksiyonunu koruyup hem de maliyetin azaltılmasının yolları araştırılmış ve bunun için en uygun kumaş yapıları seçilmiştir.

Bir aygıt, donanım veya sistemin, bulunmuş olduğu elektromanyetik çevre içerisinde, bu çevreyi veya diğer donanımları rahatsız edecek düzeyde bulunmadan elektromanyetik gürültü oluşturmadan ve ortamdaki diğer sistemlerin oluşturduğu girişimden etkilenmeden, kendisinden beklenen işlevi yerine getirebilme yeteneğine elektromanyetik uyumluluk (EMC, Electromagnetic Compability) denilmektedir. Diğer bir deyişle EMC, cihaz ve sistemlerin hedeflenmiş çalışma durumlarında olumsuz şekilde diğer sistemlerden etkilenmeden veya diğer sistemleri de etkilemeden çalışabilme yeteneğini ifade eder [1].

Daha sonra kumaşların koruma özellikleri, cep telefonlarının, tıbbi ekipmanların ve elektrikli ev aletlerinin ve benzeri cihazların yaydığı frekans aralığında (100 MHz - 6 GHz), ekranlı bir odada EMC test sistemi kullanılarak, gerçek elektromanyetik dalgalarla test edilmiştir. Ayrıca kumaşların bazı fiziksel özellikleri, kullanım ve konfor özellikleri test edilecek ve tüm test sonuçları istatistiksel olarak analiz edilmiştir.

Son yıllarda, konfor, özgül ağırlık, yapısal çeşitlilik gibi faktörler, elektromanyetik ekranlama tekstil ürünlerinin geliştirilmesi ve seçilmesinde kriterler olarak dikkate alınmıştır. Bu alanda yapılan örnek çalışmalar literatürde yer almaktadır. Safarova ve Militky (2015), tekstil yapılarının temel özelliklerini koruyarak, teknik amaçlar için kullanıma uygun, çok işlevli, hafif ve esnek, elektromanyetik radyasyona karşı dirençli kumaşların üretimi ve karakterizasyonunu araştırmışlardır. Bu makalede, metal içeriğinin etkisi, iletken ipliğin yerleştirilmesi, geometri, nem içeriği ve frekanslarla ilişkisi incelenmiştir [2]. Çeven ve arkadaşları (2016), Tekstil yüzeylerinin elektromanyetik kalkanlama özelliği göstermesi için sürekli bir iletken yüzey elde edilmesi gerekli değildir. Özünde iletken bir tel (paslanmaz çelik, bakır, vs.) ihtiva eden özlü

ipliklerden oluşturulan yüzeyler, atkı boyunca ve/veya çözgü boyunca iletkenlik sağlarken, kalkanlama etkisi de sağlamaktadırlar. Bu iplikler kullanılarak oluşturulan örme veya dokuma yüzeylerinin kalkanlama verimliliğinin atkı ve çözgü sıklığı artışı ile de arttığı gösterilmiştir [3].

Ekranlama elektrik alanın düşük frekanslarda yansıtılması, yüksek frekanslarda yutulması ile gerçekleşir. Ekranlama manyetik alanın düşük frekanslarda yutulması ile gerçekleşir. Yüksek iletkenlik, yansıma ve yutulmayı pozitif yönde etkiler. Yüksek manyetik geçirgenlik yüksek yutulmaya neden olurken, düşük yansıma oluşturur. Çok düşük frekanslı manyetik kaynakların ekranlanacağı hallerde yüksek manyetik geçirgenlikli malzemeler kullanılır. Ekran kalınlığı arttıkça yutulma artar [4].

Duran ve Kadoğlu (2012), bakır özlü (Cu/Co) ipliklerle elektromanyetik koruyucu tekstil malzemelerinin üretilebilme olanakları araştırılmış ve bu ipliklerle üretilen dokuma kumaşların elektromanyetik ekranlama karakteristikleri incelenmişlerdir. İplik numarası, öz inceliği, atkı sıklığı ve dalga frekansının dokuma kumaşların elektromanyetik koruyuculuğuna etkileri araştırmışlardır. Çalışma sonuçları, hem iplik ve kumaş parametreleri hem de dalga frekansının dokuma kumaşların elektromanyetik ekranlama etkinliğine önemli etkileri olduğunu göstermiştir. Ayrıca üretilen dokuma kumaşlarla 44,4 dB seviyesine kadar ekranlama etkinliği elde edildiği bulunmuştur [5].

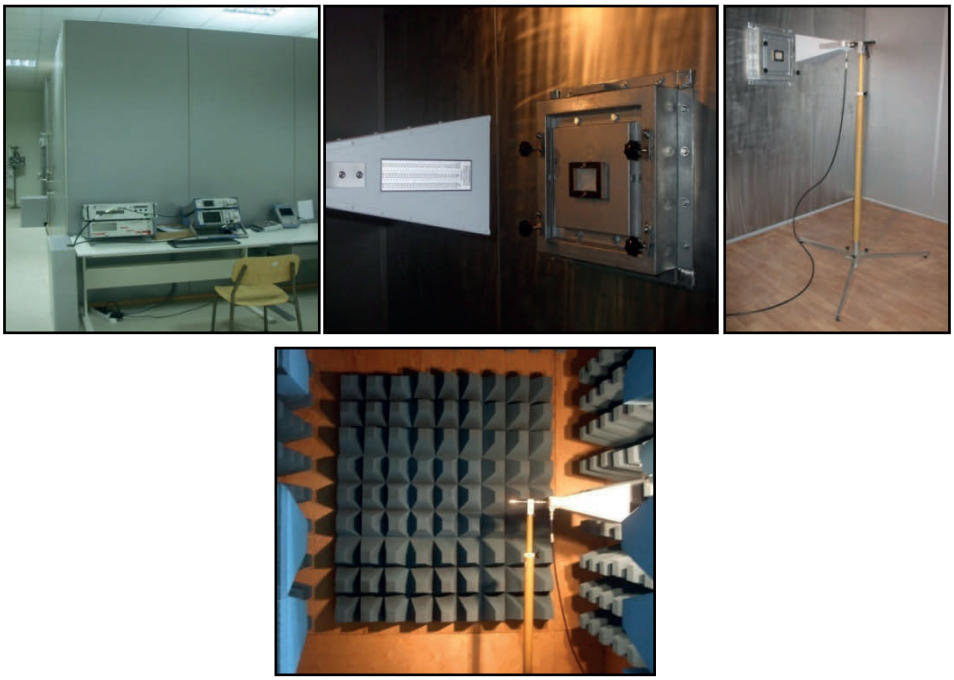
2. Materyal ve Method

Çalışma planındaki numuneler aşağıdaki gibidir;

Tablo1. Çalışma Kapsamında Üretilen Numuneler

Numune No	Kumaş Cinsi	Gramaj (gr/m^2)	Pus/Fe in
1	Ne 20/2 Ring Penye + 30 Denye Gümüş Filament 1x1 Vanize Süprem	265 GR	30/22
2	Ne 20/2 Ring Penye + 30 Denye Gümüş Filament 2x1 Vanize Süprem	336 GR	30/22
3	Ne 20/2 Ring Penye + 30 Denye Gümüş Filament 3x1 Vanize Süprem	340 GR	30/22
4	Ne 20/2 Ring Penye + 30 Denye Gümüş Filament 5x1 Vanize Süprem	316 GR	30/22
5	Ne 20/2 Ring Penye + 100 Denye Gümüş Filament 1x1 Vanize Süprem	292 GR	30/22
6	Ne 20/2 Ring Penye + 100 Denye Gümüş Filament 2x1 Vanize Süprem	312 GR	30/22
7	Ne 20/2 Ring Penye + 100 Denye Gümüş Filament 3x1 Vanize Süprem	323 GR	30/22
8	Ne 20/2 Ring Penye + 100 Denye Gümüş Filament 5x1 Vanize Süprem	340 GR	30/22
9	Ne 40/1 Ring Penye PAMUK-GSM (90-10) Full Likra Süprem +30 Denye	155 GR	32/29
10	Ne 40/1 Ring Penye PAMUK-GSM (90-10) Full Likra Süprem +30 Denye	170 GR	32/29

Elektromanyetik Ekranlama Etkinliği Testleri Gerçekleştirilerek, geliştirilen kumaşların Elektromanyetik Koruyuculuk özellikleri kıyaslanacaktır. Kumaşların koruma özellikleri, cep telefonlarının, tıbbi ekipmanların ve elektrikli ev aletlerinin ve benzeri cihazların yaydığı frekans aralığında (100 MHz- 6 GHz), EN50147-1 standardına göre ekranlı bir odada EMC test sistemi kullanılarak, gerçek elektromanyetik dalgalarla test edilecektir. Ege Üniversitesi Tekstil Mühendisliği Bölümü laboratuvarlarında bulunan Elektromanyetik Ekranlama Etkinliği ölçüm sistemini Şekil 1'te görülmektedir.



Şekil 1. Elektromanyetik Ekranlama Etkinliği Ölçüm Sistemi

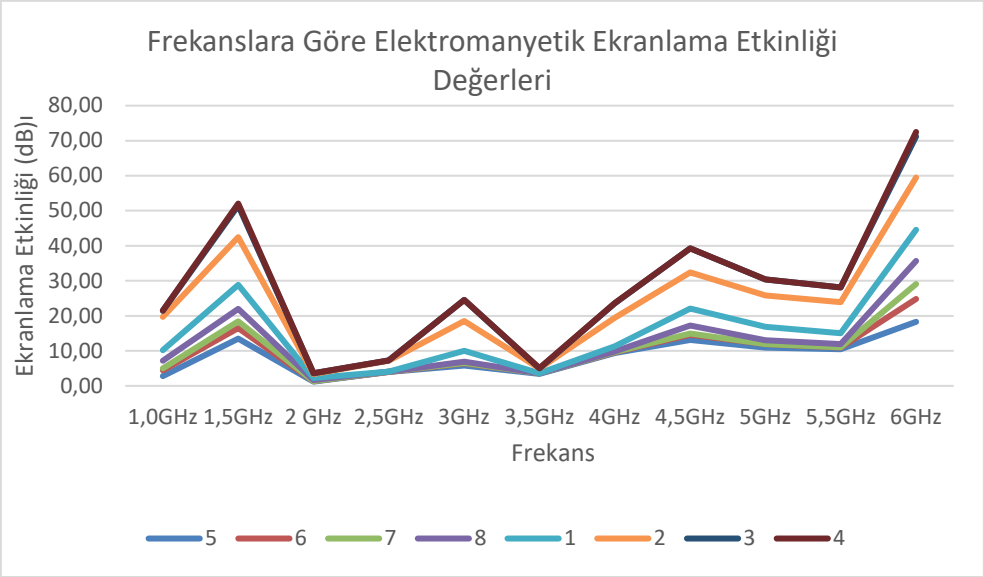
3. Sonuç

Kumaşların elektromanyetik ekranlama etkinliği ölçüm sonuçları Tablo 2, Şekil 2 ve Şekil 3'de verilmiştir.

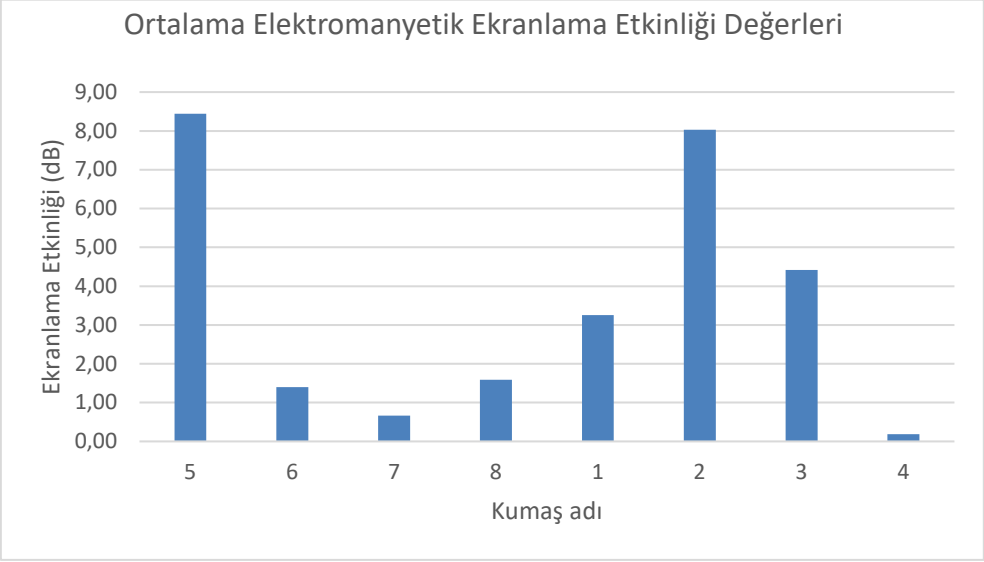
Tablo 2. Ekranlama Etkinliği Ölçüm Sonuçları

	EMSE (dB)									
	1	**2**	**3**	**4**	**5**	**6**	**7**	**8**	**9**	**10**
1,0GHz	2,76	1,72	0,47	2,27	2,94	9,57	1,66	0,15	0,00	0,00
1,5GHz	13,48	2,98	1,97	3,52	6,92	13,57	9,10	0,50	0,00	0,00
2 GHz	1,21	0,13	0,00	0,33	0,59	1,12	0,22	0,01	0,00	0,00
2,5GHz	3,99	0,01	0,03	0,01	0,07	3,03	0,11	0,00	0,00	0,00
3GHz	5,84	0,63	0,04	0,44	3,04	8,53	6,03	0,00	0,00	0,00
3,5GHz	3,41	0,18	0,03	0,00	0,02	1,32	0,05	0,06	0,00	0,00
4GHz	9,33	0,26	0,03	0,18	1,51	8,15	4,11	0,01	0,00	0,00
4,5GHz	13,11	1,45	0,40	2,28	4,85	10,34	6,80	0,00	0,00	0,00
5GHz	10,92	1,04	0,01	1,02	3,83	8,99	4,59	0,00	0,00	0,08
5,5GHz	10,49	0,46	0,10	0,85	3,17	8,80	4,20	0,00	0,00	0,00
6GHz	18,29	6,52	4,27	6,59	8,89	14,93	11,72	1,28	2,00	0,77
Ortalama	8,44	1,40	0,67	1,59	3,26	8,03	4,42	0,18	0,18	0,08

Kumaşların elektromanyetik ekranlama etkinliği değerlerinin frekanslara göre dağılımı Şekil 2'de gösterilmektedir. Grafik incelendiğinde her ne kadar bazı frekanslarda ufak sapmalar gözlense de genel olarak frekans büyüdükçe elektromanyetik ekranlama etkinliğinin arttığı söylenebilir. İleten filament kullanılarak üretilen tüm numunelerde frekansa göre ekranlama etkinliğinin dağılımı bakımından aynı trend gözlenmiştir. Ancak, iletken lifler ile iletken olmayan liflerin karışımından elde edilen iplikler ile üretilen A ve B kumaşları için bu eğilim geçerli olmamış, zaten bu kumaşlarda çok düşük değerle elde edilebilmiştir. En yüksek elektromanyetik ekranlama etkinliği değeri 6 GHz frekansında, her sırasında 30 denye gümüş kaplı PA filamenti içeren Ne 20/2 iplik numara ipliklerle üretilmiş ribana penye vanize kumaş yapısı ile elde edilmiştir.



Şekil 2. Kumaşların elektromanyetik ekranlama etkinliği değerlerinin frekanslara göre dağılımı



Şekil 3. Kumaşların ortalama elektromanyetik ekranlama etkinliği değerleri

Kumaşların ortalama elektromanyetik ekranlama etkinliği değerleri Şekil 3'de gösterilmektedir. Grafik incelendiğinde, genel olarak elektromanyetik ekranlama etkinliğinin kumaş yapısındaki

gümüş içerikli filament miktarı azaldıkça azaldığı görülmektedir. Aynı zamanda gramaj arttıkça elektromanyetik ekranlama etkinliğinin arttığı da gözlenmektedir. BU durum yüksek gramajda daha sıkı bir yapının ortaya çıkmasıyla açıklanabilir. Yapısında 100 denye inceliğinde gümüş kaplı PA filament içeren kumaşların ekranlama etkinliği değerleri 30denye inceliğinde filament içerenlere göre daha yüksek çıkmıştır. Bunun nedeni gümüş kaplı filamentin kalınlığı arttıkça yapıdaki gümüş içeriğinin artmasıdır. Ayrıca kesikli gümüş elyafından üretilen süprem kumaşların elektromanyetik ekranlama etkinlik değerlerinin oldukça düşük olduğu gözlemlenmiştir. Bunun da nedeninin kesikli elyafların birbirleri arasında oluşan boşluklar ve kopukluklardan kaynaklı olduğu düşünülmektedir.

Kaynakça:

1. Cengiz, S. Elektromanyetik Girişimden Korunmada Ekranlama Etkinliği ve Elektromanyetik Uygulama Alanları, Yayınlanmamış Yüksek Lisans Tezi, Isparta: Süleyman Demirel Üniversitesi Fen Bilimleri Enstitüsü, **2009**.
2. Safarova, V., Tunak, M., & Militky, J. Prediction of hybrid woven fabric electromagnetic shielding effectiveness. Textile Research Journal, **2014**, 85(7):673–686.
3. Karaman, Ö. F., Çeven, E. K. & Dırık, A. E. Metal İplikli Dokuma Kumaşlarının Elektromanyetik Kalkanlama Etkinliğinin Mobil Cihazlar İle Tespiti. Uludağ University Journal of The Faculty of Engineering, **2016**, 21(2):85-94.
4. Yılmaz, R. Elektromanyetik Kalkanlama Özelliği Olan Malzemeler. Ejovoc (Electronic Journal of Vocational Colleges), **2014**, 4(1):136-150.
5. Duran, D. Kadoğlu, H. A Research On Electromagnetıc Shielding With Copper Core Yarns. Journal of Textile & Apparel / Tekstil ve Konfeksiyon, **2012**, 22(4):354-359.

FLEXURAL BEHAVIOUR OF HAUNCHED BEAMS REINFORCED WITH GLASS FRP REBAR

SAAD ALMOHAMMAD ALAGOL [*1], MEHMET EREN GULSAN [2]

[1] Gaziantep University, Engineering Faculty, Civil Engineering Department, Gaziantep, TURKEY.
[2] Gaziantep University, Engineering Faculty, Civil Engineering Department, Gaziantep, TURKEY.

Abstract

Fiber reinforced polymer rebar (FRP) has an increasing demand and use worldwide due to its transparency to magnetic fields, along with its higher tensile strength, and lower weights compared to steel. The main aim of this analytical study is to investigate the flexural behaviour of Haunched Beams reinforced with sand-coated Glass FRP rebar. In this paper, three parameters had been taken into consideration, namely, concrete compressive strength, inclination angle, and reinforcement ratio. The analytical program was comprised of twenty- four models. Results of the study were summarized in the form of Load-Deflection curves, whereby the behaviour of the shear beams of higher reinforcement ratio had a significant increase in failure load along with lower deflection patterns, high compressive strengths indicated higher response on both load and deflection axes, and the inclination angle had no significant effect on most of the other parameters.

Keyword: Fiber reinforced plastics, Sand Coat, Haunched Beams, Flexural Behaviour.

1. Introduction

The reinforced concrete haunched beams are getting more popular since the need to optimize the construction process emerged, where they have many advantages when comparing with prismatic beams it can be summarized in: 1) Efficient use of concrete and reinforcement whether it was mild steel or FRP rebar. 2) The lateral stiffness plays a significant role in decreasing the self-weight which is result to a more economic design. 3) Facilitates the utility installment of (Sewage, electricity, and air conditioning). The main disadvantage is the need to skilled labor who are specialized in formwork to cast it and assure its serviceability and aesthetic view [1-2]. However, the serviceability of steel reinforced concrete is subjected to shortness in its life span due to corrosion issues as it can be a major concern in certain cold weather conditions, where the salts are used in deicing process, which accelerates the forming of corrosion [3], alternatively, FRP reinforcement rebar is considered a valid replacement to steel reinforcement [4-5], the present analytical study adopted the Glass FRP reinforcement due to its high chemical resistance, high strength-weight ratio, and high cost efficiency, as well as its superior corrosion resistance [6]. The surface configuration of Glass FRP rebar is sand-coated, since it has a better bond characteristic when compared to other surface configurations [7]

2. Materials and Methods

The analytical program was carried out by ATENA 2D software package, where 18 haunched beams were analyzed, along with 6 prismatic beams, the main model was verified by experimental

article [8] with a user-defined bond-slip model extracted from another article with a focus on same surface configuration and rebar diameter, and its designation was kept as included in literature (Sheehan, T. et al-2019) introduced in figure 2.1 [9] The geometric properties of the verification beam are described below in figure 2.2, the meshed prismatic analytical model was introduced in figure 2.3. The haunched beam variations are followed in figures 2.4-2.5-2.6 respectively. The concrete mechanical properties are described in Table 1. Whereby the Glass FRP reinforcement mechanical properties are listed in table 2, steel plates are introduced in table 3 of the analytical model to avoid stress concentrations between the prescribed deformation of (0.6mm) and the concrete. In the experimental article, the verification beam was subjected to a stroke-controlled rate of (0.6mm/min) with a monotonic load of 500kN up to failure. All the input data used in verification process are extracted from experimental model and applied in ATENA 2D.

Table 1. Input data for concrete properties

Variable	Properties	Magnitude	Units
P	Density	23	kN/m^3
E	Modulus of Elasticity	37280	MPa
ν	Poisson's Ratio	0.2	
f_t	Tensile Strength	3.35	MPa
f_c	Compressive Strength	-43.6	MPa
G_f	Fracture Energy	0.08283	kN/m

Table 2. Input data for Glass FRP Reinforcement mechanical properties

Bar Type	Diameter (mm)	Area (mm^2)	Tensile Strength (MPa)	Modulus of elasticity (GPa)	Ultimate strain (%)
GFRP	16	1407	754 ± 19	42 ± 1	1.8 ± 0.04

Table 3. Input data for steel plates properties

Variable	Properties	Magnitude	Units
E	Modulus of Elasticity	2100000	MPa
ν	Poisson's ratio	0.3	

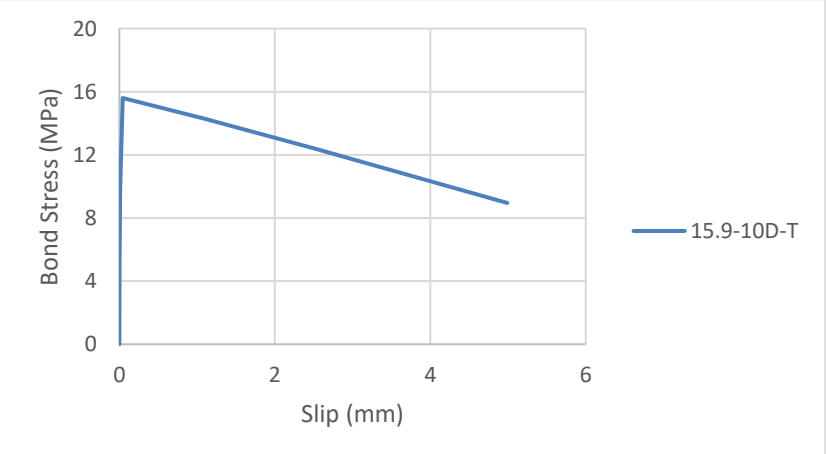


Figure 2.1 Sand coated Glass FRP bond-slip model (Sheehan, T. et al-2019)

2.1 Experimental beam geometry

As shown below in figure 1.2, the beam was 3250 mm long, 250 mm width, 400 mm depth, and a reinforcement ratio of 1.72% with an applied monotonic load of 250 kN at each point load location.

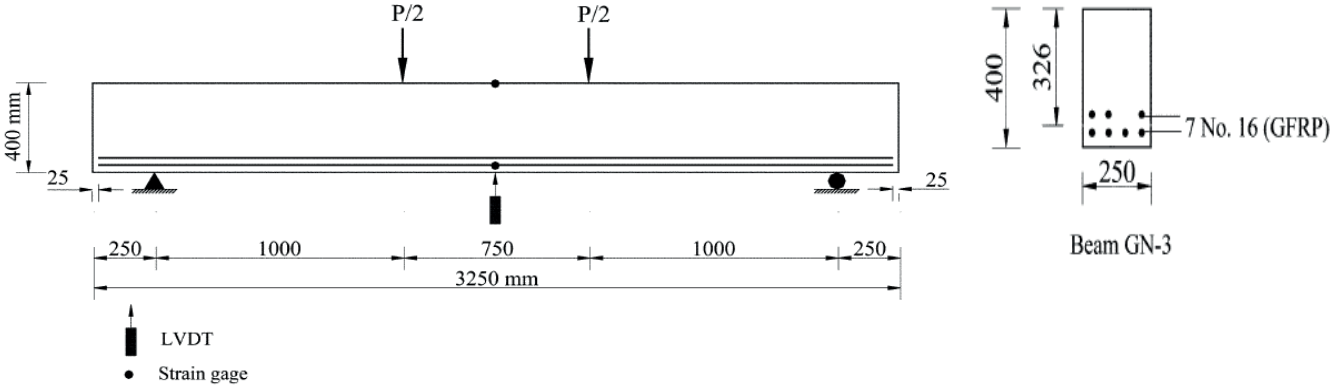


Figure 2.2 Experimental beam geometry (El-Sayed, et al-2006)

2.2 Analytical beams geometry and applied parameters

The analytical models adopted the same mechanical properties prescribed the in previous tables, along with the bond model in figure 2.1. After the verification process was confirmed, the main depth of (400mm) in the experimental was maintained, and the inclination angle was deducted from it. The prismatic beams are denoted by P, three variations of haunch inclination angles were tested, namely 5°,10°, and 15°, and denoted by letter H. The models are associated with different reinforcement ratios of 0.97,1.7, and 2.19 respectively. The compressive strengths used in the analytical study were low compressive strength concrete of (30 MPa) and high compressive strength of (50 MPa) and denoted by C.

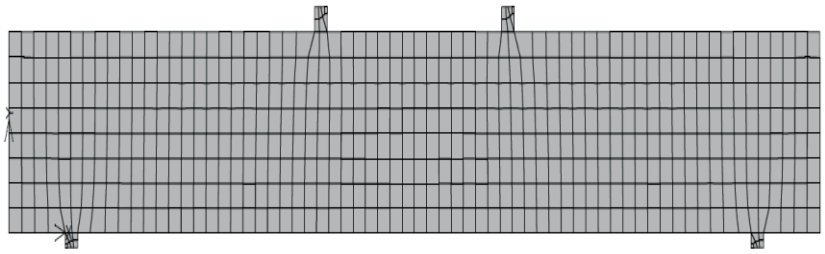


Figure 2.3 Verification model of prismatic beam

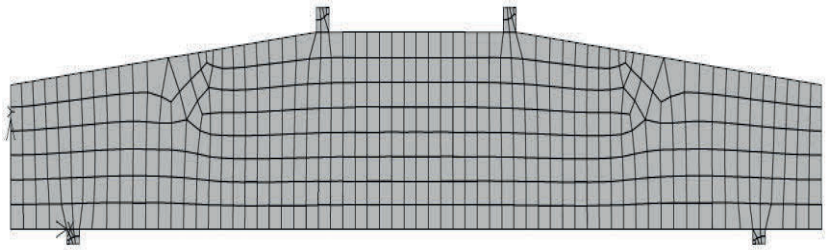


Figure 2.4 Haunched beam model with 5° inclination angle

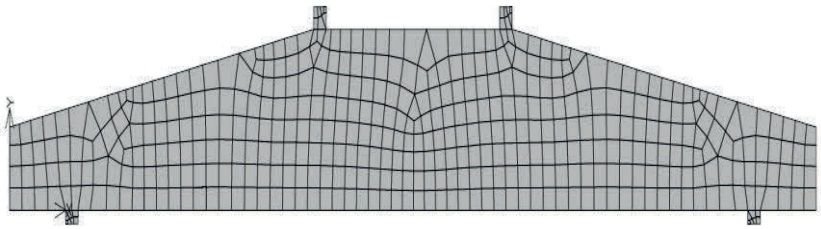


Figure 2.5 Haunched beam model with 10° inclination angle

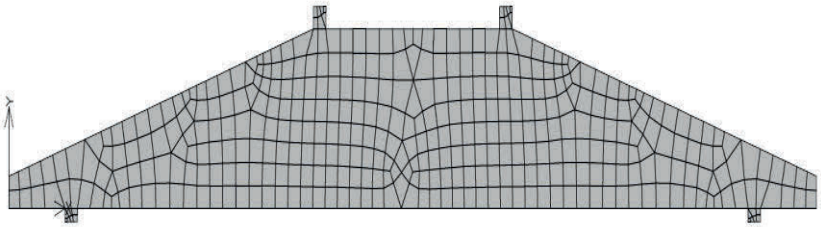


Figure 2.6 Haunched beam model with 15° inclination angle

2.3 Analytical model verification

The experimental beam failure mode was in diagonal tension on its right side, the analytical model experienced almost identical failure mode shown in figures 2.7-2.8 respectively. The field variables of the beam are introduced, whereby it indicated the crack propagation in terms of its displacements in the nodal elements on the right side. The monitoring points had been inserted to capture the reactions of point loads on the location of it exactly, where the deflection captured at the extreme fibers of midspan of the beam and presented in table 4. The load-deflection curves of both experimental and analytical are demonstrated in figure 2.9, the experimental beam designation was kept as in the experimental article., along with table 5 to assess the error percentage between experimental beam and finite element analysis.

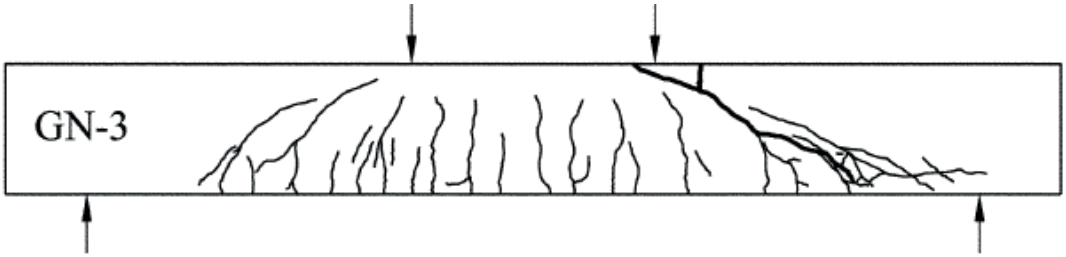


Figure 2.7 Experimental beam failure (El-Sayed, et al-2006)

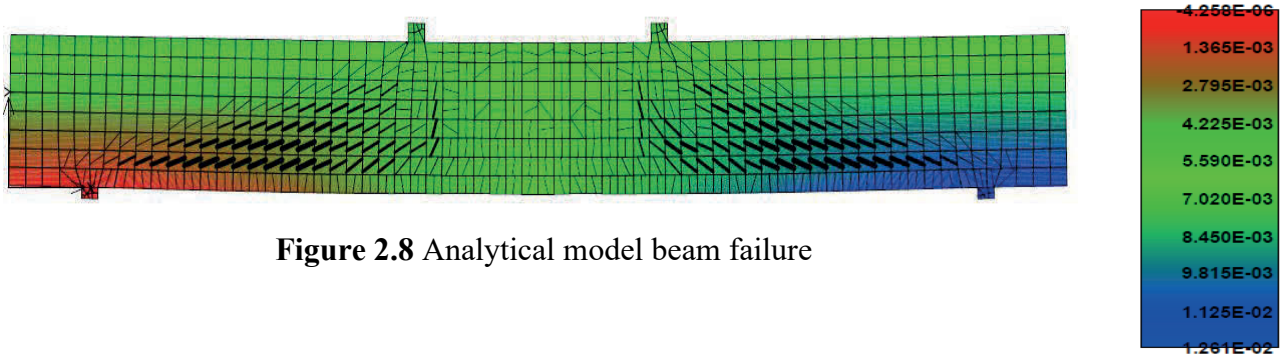


Figure 2.8 Analytical model beam failure

Table 4. Finite element analysis monitoring points description

Monitor Number	Monitor Name	Monitor Type	Monitor Location (mm)	Measured Direction
1	Deflection	Displacement	1625	Component 2 (Vertical)
2	Load	Reactions	1250	Component 2 (Vertical)

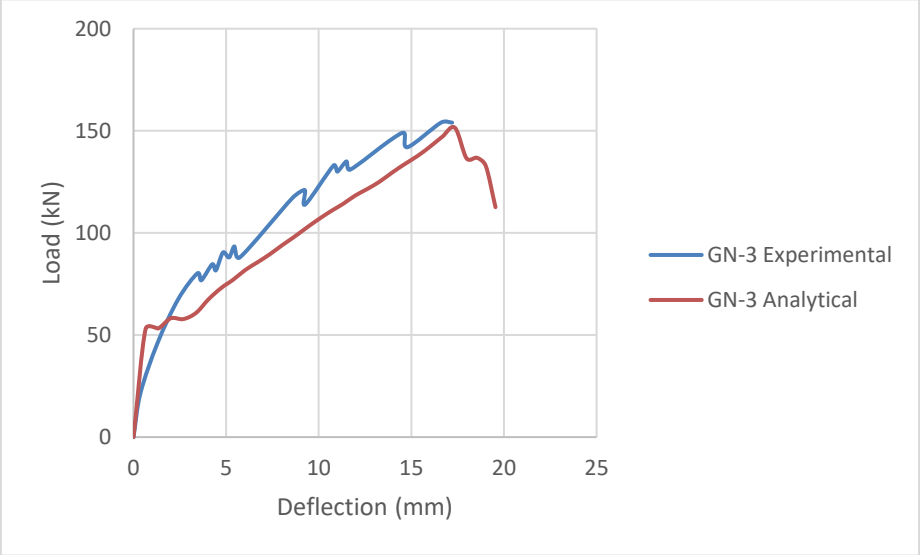


Figure 2.9 Output comparison of experimental versus analytical models' failure

Table 5. Output data for analytical beam verification

Beam Name	Experimental Failure Load (kN)	Analytical Failure Load (kN)	Percent Error	Experimental Displacement (mm)	Analytical Displacement (mm)	Percent Error
GN-3	154.0	151.5	1.65%	17.2	17.35	0.008%

3. Results and Discussion

After the verification process is completed on the four-point loading beam, as well as the percentage errors of both axes are reliable for the intended parameters to be taken into consideration to understand the flexural behavior of Glass FRP reinforcement in haunched beams, the flexural capacity of each featured model was presented in terms of Load-Deflection plot.

3.1 Inclination angle effect at high compressive strength

At the same compressive strength and reinforcement ratio, it was observed that there was no significant effect between 5° -10° inclination, the model of 10° angle reached failure before the

prismatic and haunched beams, however when the inclination angle was set to be 15° the beams experienced a higher failure pattern on both axes.

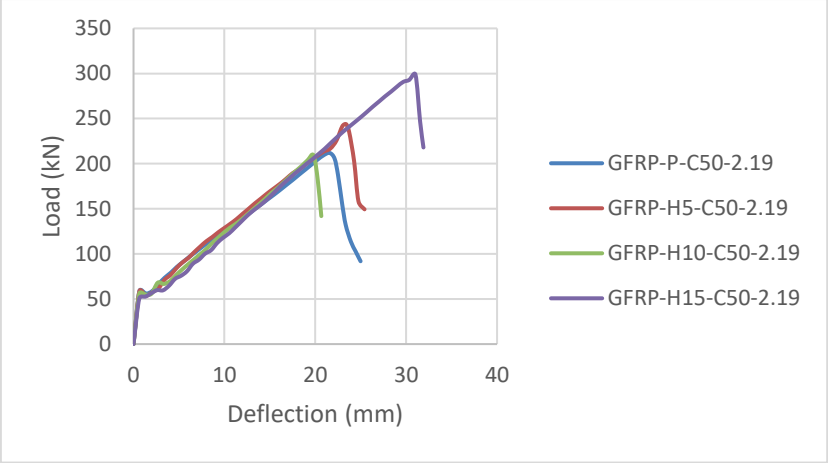


Figure 3.1 Output comparison of inclination angle at high compressive strength

3.2 Compressive strength and reinforcement ratio effect on prismatic beams

Whether the concrete had a compressive strength of 30 MPa or 50 MPa, a negative correlation was found between midspan deflection and reinforcement ratio, that is when the reinforcement ratio is increased, the midspan deflection decreased. This is also had been investigated experimentally [10]. On the other hand, a positive correlation was found between the increase of compressive strength and the models' load-carrying capacity , where the models with higher compressive strength could withstand more load and reached higher midspan deflection when compared to lower compressive strength concrete.

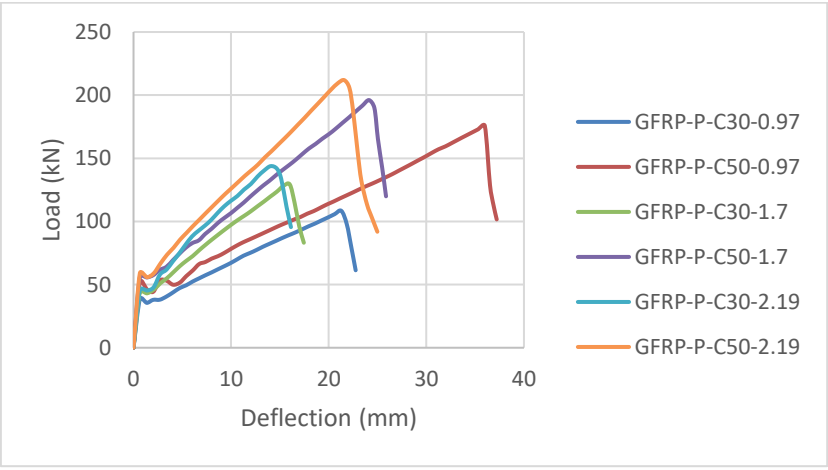


Figure 3.2 Output comparison of compressive strength at different reinforcement ratios of prismatic beams

3.3 Compressive strength and reinforcement ratio effect on haunched beams

The behaviour of haunched beams is similar to prismatic beams in terms of compressive strengths and reinforcement ratios, on one hand the beams of 5° inclination carried more load comparing to the beams of 10°, on the other hand, the beams of 15° experienced a significant increase in load carrying capacity as well as deflection when compared to other beams of lower inclination angles.

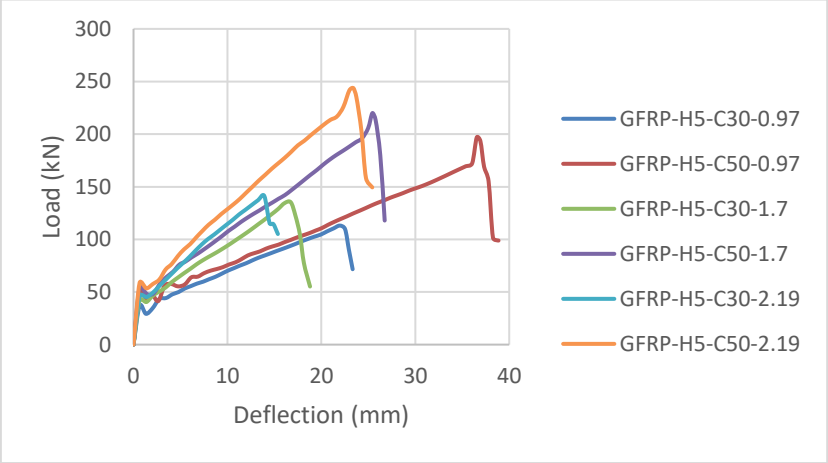


Figure 3.4 Output comparison of compressive strength at different reinforcement ratios of 5° inclination haunched beams

The closest behaviour to prismatic beams is happen to be in haunched beams of 10 ° inclination angle, which they had a similar failure load patterns without a significant difference on midspan deflection amongst them.

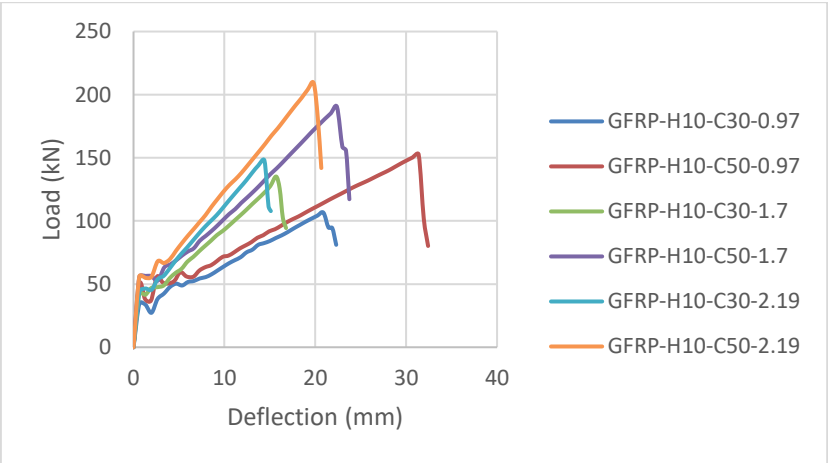


Figure 3.5 Output comparison of compressive strength at different reinforcement ratios of 10° inclination haunched beams

3.4 Summary of output data for load-deflection curves

Sample Name	Inclination angle (α°)	Compressive strength (MPa)	Reinforcement ratio	Failure load (kN)	Midspan deflection at failure (mm)
GFRP-P-C30-0.97	0	30	0.97	108.4	21.29
GFRP-P-C30-1.7	0	30	1.7	129.3	16.01
GFRP-P-C30-2.19	0	30	2.19	143.8	14.05
GFRP-P-C50-0.97	0	50	0.97	175.7	35.99
GFRP-P-C50-1.7	0	50	1.7	196.1	24.13
GFRP-P-C50-2.19	0	50	2.19	211.9	21.58
GFRP-H5-C30-0.97	5	30	0.97	113.1	21.96
GFRP-H5-C30-1.7	5	30	1.7	135.3	16.74
GFRP-H5-C30-2.19	5	30	2.19	141.3	13.92
GFRP-H5-C50-0.97	5	50	0.97	196.9	36.54
GFRP-H5-C50-1.7	5	50	1.7	220	25.43
GFRP-H5-C50-2.19	5	50	2.19	243.8	23.4
GFRP-H10-C30-0.97	10	30	0.97	106.6	20.89
GFRP-H10-C30-1.7	10	30	1.7	135.2	15.69
GFRP-H10-C30-2.19	10	30	2.19	147.9	14.4
GFRP-H10-C50-0.97	10	50	0.97	152.7	31.37
GFRP-H10-C50-1.7	10	50	1.7	190.4	22.38
GFRP-H10-C50-2.19	10	50	2.19	209.2	19.82
GFRP-H15-C30-0.97	15	30	0.97	141.3	26.67
GFRP-H15-C30-1.7	15	30	1.7	161.1	20.22
GFRP-H15-C30-2.19	15	30	2.19	202.1	21.7
GFRP-H15-C50-0.97	15	50	0.97	193.9	38.5
GFRP-H15-C50-1.7	15	50	1.7	273.5	33.9
GFRP-H15-C50-2.19	15	50	2.19	298.8	31.02

Table 6. Output data for analytical beams results

The haunched beams of 15° inclination angle experienced a different behaviour in terms of compressive strength and reinforcement ratio, whereby the midspan deflection of high compressive strength and low reinforcement ratio could deflect more without a significant increase of load when compared with low compressive strength with higher reinforcement ratio.

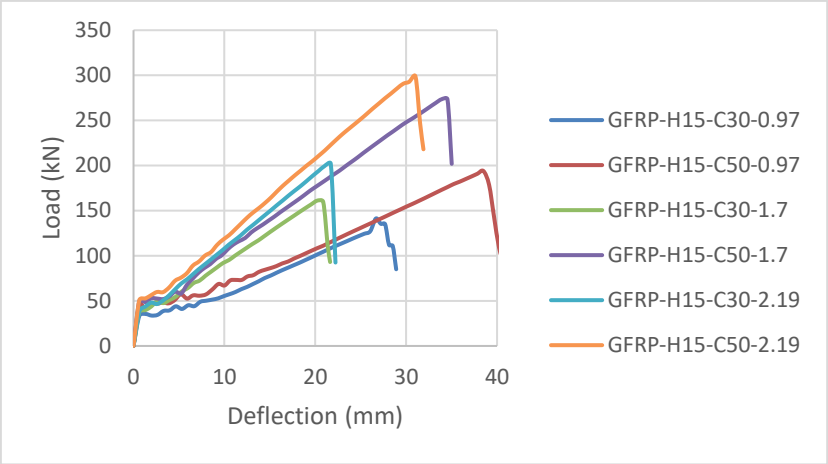


Figure 3.6 Output comparison of compressive strength at different reinforcement ratios of 15° inclination haunched beams

4. Conclusions

In this particular paper, the flexural behaviour of Glass FRP rebar reinforced concrete beams has been investigated analytically by verifying another experimental beam in FEA environment, where various parameters like inclination angle, compressive strength, and reinforcement ratio are considered. To review the findings of the analytical study, it was clear that:

1) The failure mode of prismatic beams reinforced with Glass FRP rebar is in diagonal tension, this has been proved experimentally and analytically.
2) On the same parameters, there was no significant inclination angle effect, except for the models with 15 ° inclination, where the models carried more loads with further failure in deflection axis.
3) High compressive strength positively affects the load carrying capacity in the models, whereby a significant increase in load-deflection curves of the same parameters was observed.
4) The increase of reinforcement ratio resulted a higher load-carrying capacity, yet it was accompanied with premature failure comparing to the models of lower reinforcement ratio.

References:

1. Tena-Colunga, A., Archundia-Aranda, H. I., & González-Cuevas, Ó. M, Behavior of reinforced concrete haunched beams subjected to static shear loading. Engineering Structures. **2008**,30(2), 478-492.
2. Albegmprli, H. M., Gülşan, M. E., & Cevik, A. Comprehensive experimental investigation on mechanical behaviour for types of reinforced concrete Haunched beam. Advances in concrete construction. **2019**, 7(1), 39.
3. Ahmed, E., El-Salakawy, E., & Benmokrane, B. Bond stress-slip relationship and development length of FRP bars embedded in concrete. HBCR Journal. **2008**, 4(3), 1-17.
4. Saadians, H., & Ehsaan, M. R. Application of fiber-composites in Civil Engineering. **1989**, (pp. 526-535)
5. Nannie, A., Al-Zaharani, M., Al-Dulaijan, S., Bakis, C., & Boothby, I. (1995). 17 bond of FRP reinforcement to concrete-experimental results. In Non-metallic (FRP) Reinforcement for Concrete Structures: Proceedings of the Second International RILEM Symposium. **1995**, (Vol. 29, p. 135).

6. Nanni, A., De Luca, A., & Jawaheri Zadeh, H. Reinforced concrete with FRP bars: Mechanics and design. CRC Press **2019**.
7. El-Nemr, A., Ahmed, E. A., & Benmokrane, B. Flexural Behavior and Serviceability of Normal-and High-Strength Concrete Beams Reinforced with Glass Fiber-Reinforced Polymer Bars. ACI structural journal. **2013,** 110(6).
8. El-Sayed, A. K., El-Salakawy, E. F., & Benmokrane, B. Shear strength of FRP-reinforced concrete beams without transverse reinforcement. ACI Materials Journal. **2006**, 103(2), 235.
9. Saleh, N., Ashour, A., Lam, D., & Sheehan, T. Experimental investigation of bond behaviour of two common GFRP bar types in high–Strength concrete., Construction and Building Materials. **2019**, 201, 610-622.
10. Adam, M. A., Said, M., Mahmoud, A. A., & Shanour, A. S. Analytical and experimental flexural behaviour of concrete beams reinforced with glass fiber reinforced polymers bars. Construction and Building Materials. **2015,** 84, (354-366).

EFFECT OF ELASTANE DIAMETER ON POISSON'S RATIO OF HELICAL AUXETIC YARNS

ESRA CAYMAK[1], HALIL İBRAHIM ÇELİK[1]

[1]Gaziantep University, Faculty of Engineering, Textile Engineering Department, Gaziantep, Turkey

Abstract

Auxetic materials exhibit a negative Poisson's ratio (NPR). Auxetic materials have unusual property such as they extend when stretched and contract when applied pressure. This special property makes the auxetic materials very useful for medical and protective textiles. In this study, helical auxetic yarns that is one of auxetic yarn production method were produced by feeding elastane monofilament with three different diameters. The yarn samples were applied tensile force at constant rate of extension and the diameter change of them were recorded. The recorded videos were split into image frames with MATLAB program. Poisson's ratios of the yarn samples were measured via image processing program and the determined values were analyzed with regard to applied tensile force.

Keyword: Helical Auxetic Yarns, Elastane Diameter, Negative Poisson's Ratio, Image Processing

1. Introduction

Nowadays, the need for the smart and high performance materials has increased. The demands from the textile products are over the covering function. To satisfy the custom requirements according to usage area, more sophisticated materials has been introduced to textile products. High performance or functional textiles can be obtained by applying some specific process during manufacture or by using materials that have intrinsically high performance. Auxetic materials are type of novel martials exhibiting negative Poisson's ratio (NPR). Auxetic materials have unusual property such as they extend when stretched and contract when applied pressure (Figure 1). Auxiliary materials have many properties such as enhanced shear resistance [1-3] indentation resistance [4,5], fracture toughness [6] and energy absorption [7]. Taking advantage of these properties of auxiliary materials, it can be used in the products such as seat belts, wearable smart clothing and fabrics, explosion proof curtains, bulletproof vests, smart bandages carrying wound healing agents, filters [8,9].

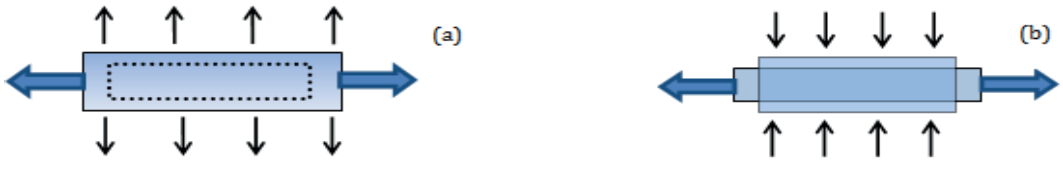


Figure1. (a)Auxetic material, (b)Conventional material[1]

So far, all auxetic yarns have been obtained from non-auxetic components. It was obtained by twisting conventional fibers. Until now, the double-helix yarn (DHY) [10] and helical auxetic yarn (HAY) [11] structures have been used to obtain an auxetic yarn. HAY is a structural material with

a Negative Poisson's ratio which containing a soft yarn with a higher diameter as the core component and a hard yarn with a lower diameter as the winding composition wrapped around the core component yarn (Figure 2). In the unloaded situation, the stiffer component wrapping over the core. As the tensile force applied, the position of the yarn components changes and the core higher diameters yarns wraps over the lower diameter one (Figure 3).

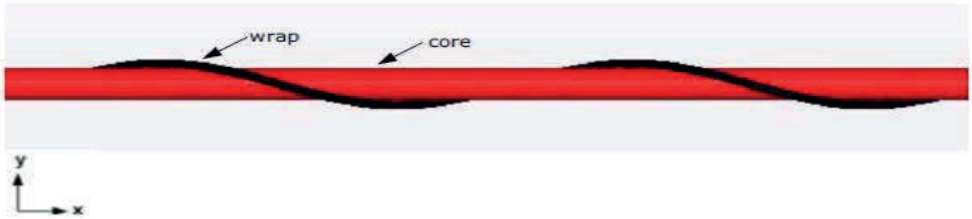


Figure 2. Component of the HAY.[12]



Figure 3. Auxetic behavior under tension.[12]

Many studies have been conducted to study the mechanical behavior of the helical auxetic yarn. Wright et al. (2010) investigated the static behavior of helical auxetic yarn under tensile load [13]. Hook et al. (2006) first created the helical auxetic yarn structure [14]. Sloan et.al. (2011) investigated the effect of geometric and material structure on auxetic yarn [15]. Bhattacharya et al. (2014) investigated the effect of modulus ratio of component on the elastane monofilament and wrap component [16]. Ming and Zhaoqun (2013) investigated the effect of initial helical angle of wrap yarn, diameter ratio of components, modulus ratio of components on and performance of lateral deformation of helical auxetic yarn [17]. In this study, the HAY samples were produced with three different diameters of elastane. The study was conducted with the aim of investigating the effect of core diameter on negative Poisson's ratio properties of yarn samples.

2. Materials and Methods

In the study, 3 different diameter of elastane were used as the core and 100% staple polyester yarn was used as the wrap. In this study, polyurethane elastomer monofilament was selected as the elastane. The elatane samples has three linear densities of 840 Denier, 560 Denier and 420 Denier. The wrap yarn was selected as staple polyester yarn with 32 Tex linear density. The HAY samples were produced by twisting stiffer lower diameter polyester yarn around higher diameter soft elastane. The stiffer yarn component were wrapped with 550 twist/meter and 30% elastane feeding ratio. AĞTEKS (Directwist®) twisting machine was used to obtain a helical auxetic yarn. Tensile strength test was applied to the resulting yarn via Titan 2.0 tensile testing device according to ASTM D 2256 standard.

The video of each sample was acquired during tensile test (Figure 4). The recoded videos were split into image frames for capturing each second view. Before the yarn diameter measure at each second, the image frames were processed and they were applied following algorithm (Figure 5). The image frame was cropped according to the yarn view and then the cropped image was converted to gray scale. The gray image was binarized by applying Otsu's thresholding method. Then, the yarn boundary was made clearer by means of morphological opening process. Finally,

the edges of the yarn body were plotted. The diameter of the yarn sample was determined as pixels between two edge lines. The pixel values were converted to "mm" unit by multiplying proper scale coefficient. The image processing and diameter measurements of the samples were achieved by using MATLAB program. For each yarn sample, 5 diameter measurements were taken and 3 specimens were tested for each sample. Totally, 15 diameter measurement were made for each second of each sample. The Poisson's ratio was calculated using the average diameter values. The extension rate was adjusted as 120mm/min, and so 0.8% axial strain per second was obtained. The camera captured 60 pictures per minute, corresponding to a 0.8% interval axial strain of the yarns. The Poisson's ratios of the yarn samples were calculated for each axial extension second.

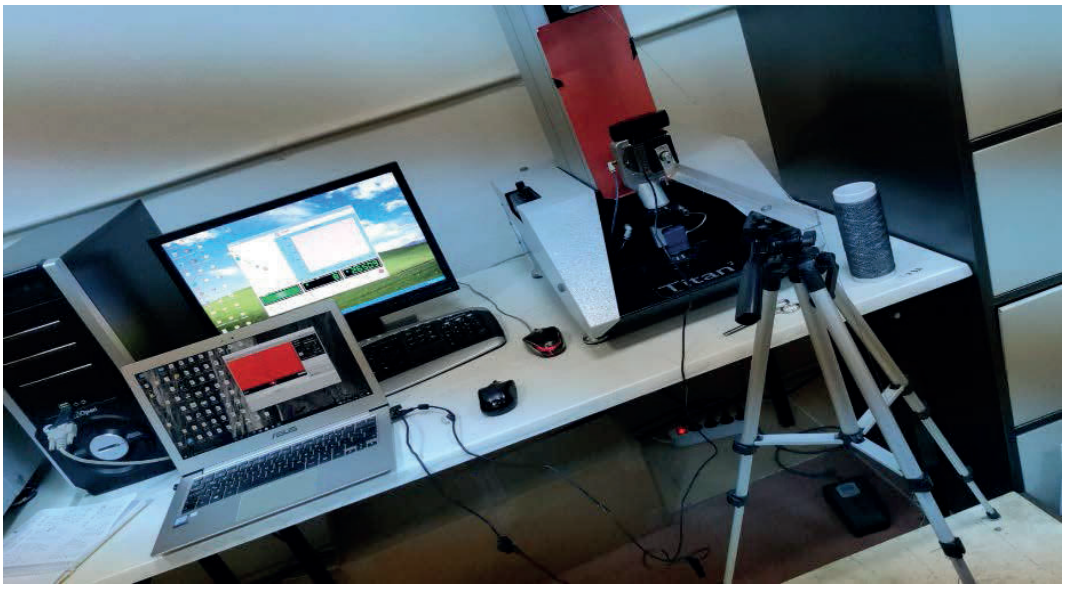


Figure 4. Image acquisition system

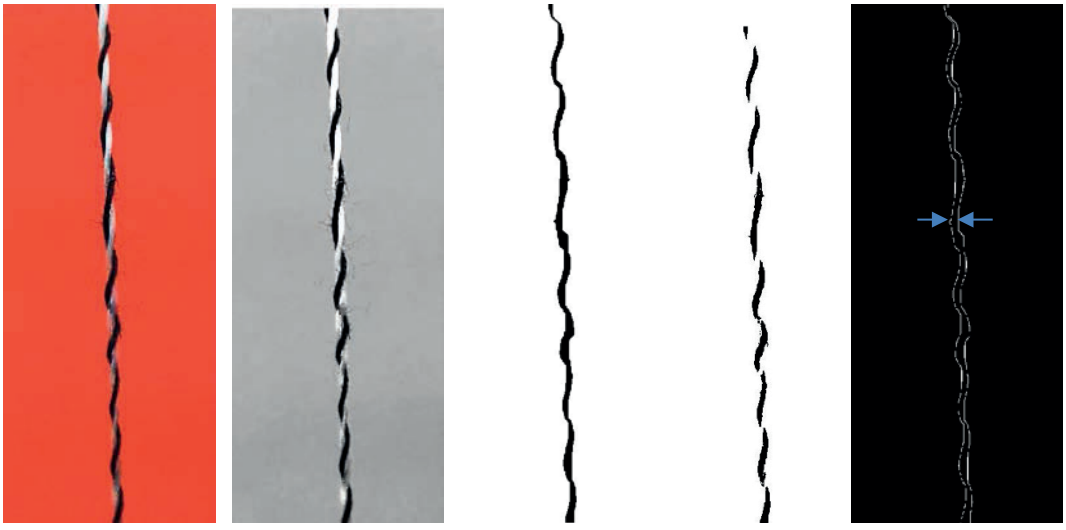


Figure 5. Image processing algorithm application

3. Results and Discussion

The Poisson's ratio vales versus axial stains were given following Figure 6-8. The HAY sample with 420 Denier elastane have high Poisson's ratio at first two second that is 1.6% extension (Figure 6). Then the ratio sharply decreases to nearly 1. After 20% axial strain, the Poisson's ratio values get constant and the Poisson's ratio values are close to zero. It can be stated that after 20% axial strain, diameter of the yarn sample did not deviate from the initial diameter value. Only the elastane and polyester wrap yarn were replaced. When we examined the graph as a whole, it can be seen that any negative Poisson's ratio was not obtained.

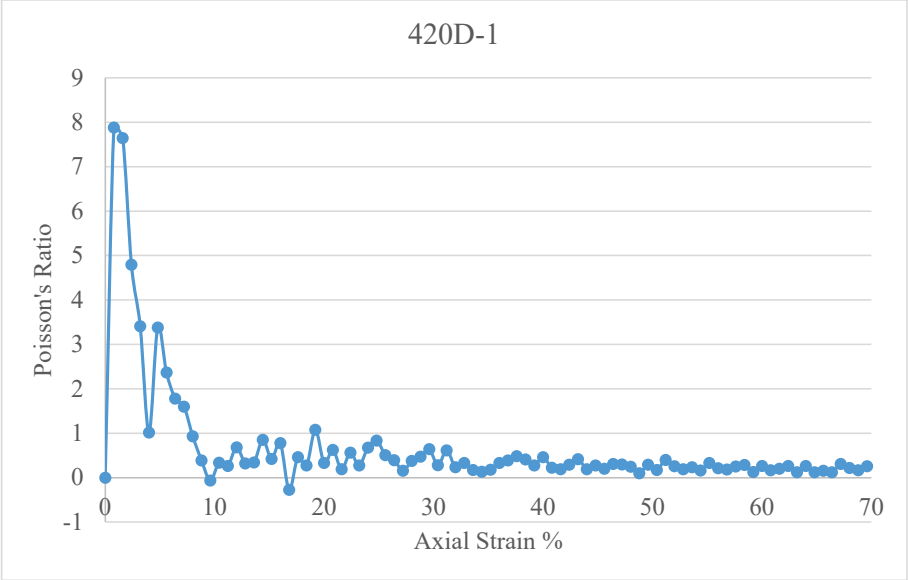


Figure 6. Poisson's Ratio of HAY with 420 Denier elastane

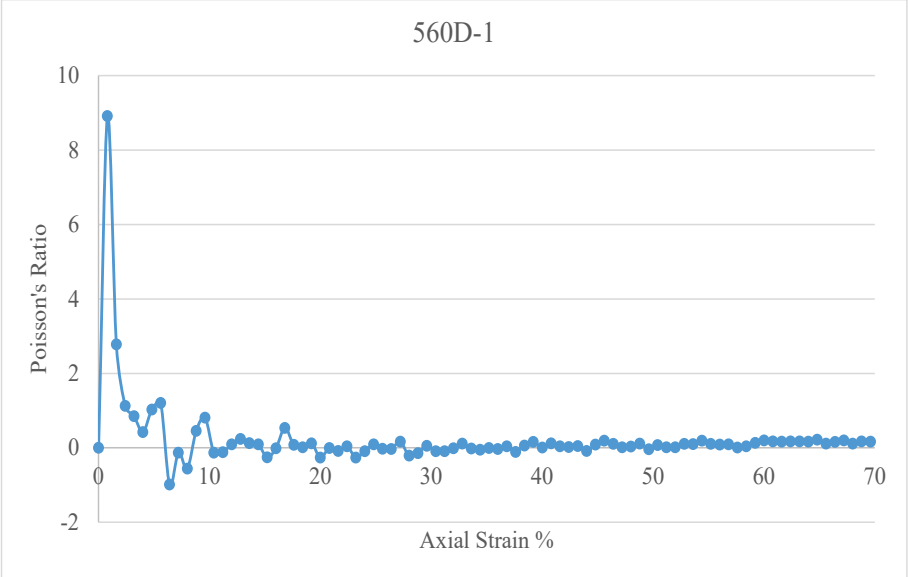


Figure 7. Poisson's Ratio of HAY with 560 Denier elastane

The HAY sample with 560 Denier elastane has similar characteristic with 420 Denier elastane sample (Figure 7). Negative Poisson's ratio was obtained with 560 Denier elastane between 6% axial strain and 36% axial strain. The negative Poisson's ratio values were clearly appeared 6% and 10% axial strains. Other negative Poisson's ratio values are close to zero, so they are not clearly observed.

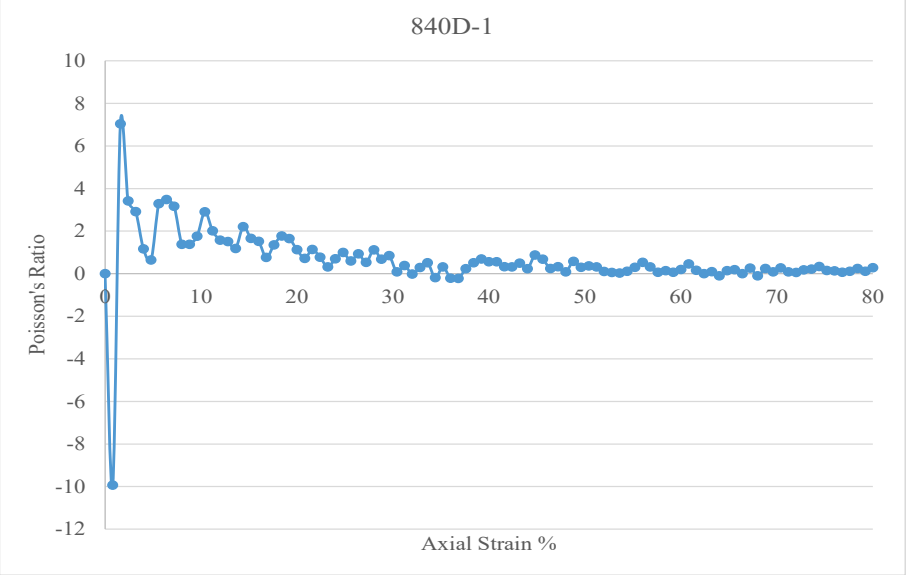


Figure 8. Poisson's Ratio of HAY with 840 Denier elastane

The highest negative Poisson's ratio was obtained with 840 Denier elastane at first axial extension, then Poisson's ratio turns to positive values (Figure 8). After 30% axial strains, the Poisson's ratio values get constant and they are close to zero.

4. Conclusions

In the content of a thesis project study, the effect of elastane diameter, elastane draw ratio and twist per meter on auxeticity property of HAY samples were investigated. In this study, the effect of core elastane diameter on yarn auxeticity were analyzed. Helical auxetic yarns were produced by feeding elastane with three different diameters at constant production parameters. It was revealed that the negative Poisson's ratio values were not obtained with two of yarn samples with 420 Denier and 840 Denier elastane. When yarn auxeticity were analyzed, it can be seen that the yarn sample with 560 Denier elastane provided negative Poisson's ratios at axial strains between 6% and 36%. It was concluded that the obtained auxeticity property can be enhanced with different twist level and elastane draw ratio trials. In future studies, negative Poisson's ratios of HAY samples with different twist level and elastane draw ratio will also be submitted.

References

1. Hu, H., and Zulifqar, A. Auxetic textile materials-a review. J Text Eng Fashion Technol, **2016**, 1(1):00002.
2. Chan, N., Evans, K.E. The mechanical properties of conventional and auxetic foams. Part II: Shear. J Cell Plast, **1999**, 35:166–183.
3. Coenen, V.L., Alderson, K.L. Mechanisms of failure in the static indentation resistance of auxetic carbon fiber laminates. Phys Status Solid B, **2011**; 248: 66–72.

4. Alderson, K.L., Fitzgerald, A., Evans, K.E. The strain dependent indentation resistance of auxetic microporous polyethylene. J Mater Sci, **2000**; 35: 4039–4047.
5. Choi, JB, Lakes, RS. Fracture toughness of re-entrant foam materials with a negative Poisson's ratio: Experiment and analysis. Int J Fract **1996**, 80:73–83.
6. Scarpa, F., Ciffo, L.G., Yates, J.R. Dynamic properties of high structural integrity auxetic open cell foam. Smart Mater Struct, **2004**, 13:49–56.
7. Evans, K.E., Alderson, A. Auxetic materials: Functional materials and structures from lateral thinking. Adv Mater, **2000**, 12:617–628.
8. Wang, Z., Hu, H. Auxetic material and their potential application in textiles. Text Res J, **2014**, 84:1600–1611.
9. Auxetic.com, http://www.auxetic.com (accessed 5 September 2016).
10. Miller, W., Hook, P.B., Smith, C.W., et al. The manufacture and characterisation of a novel, low modulus, negative poisson's ratio composite. Compos Sci Technol, **2009**, 69:651–655.
11. Ge, A., Hu, H., Liu, S. A novel plied yarn structure with negative poisson's ratio. J Text Inst **2015**, 107:578–588.
12. Hu, H., and Zulifqar, A. Auxetic textile materials-a review. J Text Eng Fashion Technol, **2016**,1(1):00002.
13. Wright, J. R., Sloan, M. R., and Evans, K. E. Tensile Properties of Helical Auxetic Structures: A Numerical Study Journal of Applied Physics. **2010**, 108(4):044905.
14. Hook, P.B., Evans, K.E., Hannington, J.P., HartmannThompson, C., Bunce, T.R. **2006**, Patent number: KR20060009826.
15. Sloan, M.R., Wright, J.R., Evans, K.E.The Helical Auxetic Yarn – A Novel Structure for Composites and Textiles; Geometry, Manufacture And Mechanical Properties.Mechanics of Materials. **2011**, 43(9):476-486.
16. Bhattacharya, S., Zhang, G.H., Ghita, O., Evans, K.E. The Variation In Poisson's Ratio Caused By Interactions Between Core and Wrap In Helical Composite Auxetic Yarns. Composites Science and Technology. **2014**, 102:87-93.
17. Ming, Z., Zhaoqun, D. Effects of Structural Parameters and Performance on Poisson's Ratio of Auxetic Yarn. Advanced Materials Research. **2013**, 821:252-258

MELANJ ELYAF KARIŞIMLARINDA RENK STANDARDİZASYONU İÇİN YAPAY ZEKA SİSTEMLERİ ÜZERİNE BİR ÇALIŞMA

MEHMET KERTMEN[1], ELİF GÜLTEKİN[2], HALİL İBRAHİM ÇELİK[2], AYBÜKE ŞEN[1], HALİL İBRAHİM OLUCAK[1]

[1] İskur Tekstil Enerji Tic. ve San. A.Ş., Kahramanmaraş, TÜRKİYE.
[2]Gaziantep Üniversitesi, Mühendislik Fakültesi, Tekstil Mühendisliği, Gaziantep, TÜRKİYE.

Özet

Pamuk melanj renkler değişik renklerin belirli oranlarda harman aşamasında ya da şerit birleştirme aşamalarında karıştırılması sonucu elde edilmektedir. Melanj iplik üretimin renk standardizasyonu çok önemli bir parametredir. Hedeflenen melanj renklerin üretimi lif renk bileşenlerinin karışım oranlarının belirlenmesi amacı ile birçok karışım denemelerinin yapılmasını gerektiren zor ve maliyetli bir işlemdir. Hali hazırda eğirme yöntemlerine, lif özelliklerine ve renk bileşenlerinin karışım oranlarına göre farklı sonuçlar çıkmakta ve istenen renk elde edilmesinde sıkıntılar yaşanmaktadır. Problemin çözümüne yönelik geliştirilecek ona bir yapay zeka modeli ile hedeflenen renk değerlerinin en az karışım denemesi ve en düşük maliyet ile elde edilebileceği düşünülmüştür. Bu çalışmada, farklı karışım oranları ile elde edilen gri tonlu melanj iplik numunelerinin CIELab değerleri spektrofotometre cihazı ile ölçülmüştür. Elde edilen veriler doğrultusunda eğitilen Yapay Sinir Ağı (YSA) modeli ile gri tonlu melanj ipliklerin lif karışım oranları tahmin edilmiştir. Oluşturulan model üzerinden yapılan tahmin sonuçlarının ortalama mutlak yüzde hatası hesaplanmıştır.

Anahtar Kelimeler: Melanj iplik, Renk tahmini, Yapay sinir ağı, CIELab.

1. Giriş

Melanj, önceden boyanmış çeşitli renk nüanslarına sahip liflerin karışımıyla elde edilen bir renk efektidir. Melanj üretim aşamasında renkli elyaflar ile eğirme prosesinden önce, belirli oranlarda harman ya da şerit birleştirme aşamalarında karıştırılır ve eğirme prosesinden sonra elde edilen ipliklerde karışık bir boyama efekti oluşturulur. İşletmelerde yapılan pamuk karışımlı melanj iplik üretimlerinin geneli incelendiğinde her yapılan numune ile üretimden gelen arasında renk farkı sapmasının %17-22 arası olduğu tespit edilmiştir. Renk farklarının oluşmasına etki eden faktörler arasında; ham madde, eğirme yöntemi, boyama farkı, tartım hatası, renk değerlendirme hataları olduğu tespit edilmiştir. Tekstil materyali üretiminde istenilen renk tonunda melanj renkli bir üründe elde edilmesi işletmeler açısından ciddi bir sorun olarak görülmektedir. Mevcut durumda bu efekti elde edebilmek için çeşitli oranlarda renkli elyaf barındıran reçeteler hazırlanır. Yapılan denemelerden elde edilen renk ölçüm değerleri analiz edilerek müşteri talebine en yakın olan karışım oranı belirlenir. Bu şekilde elde edilen çözüm uzun zaman ve maliyet kaybına sebep olduğu gibi aynı zamanda hedeflenen rengin elde edilmesi önemli bir tecrübe gerektirmektedir. Bu yüzden, melanj renkli bir tekstil ürününün renk değerinin önceden tahmin edilmesi zaman ve maliyet açısından işletmelere büyük bir fayda sağlayacaktır.

Bu kapsamda yapılan literatür araştırmasında, Yeşil ve arkadaşlarının sundukları çalışmada, elyaf karışım renklerini tahmin etmek amacıyla farklı elyaf karışım oranlarında beyaz ve siyah renkli, polyester ve viskon elyafları kullanılarak 84 adet renkli melanj numune şerit elde edilmiştir. Bu karışımların renk ölçüm sonuçları CIELab 1976 formülü ile hesaplanmıştır. Renk tahmini için tristimulus renk eşleme algoraitması olan Stearns – Noechel Modeli kullanılmıştır. Ölçülen CIELab ortalama renk farkı 0,98 olarak tespit edilmiştir. Elde edilen sonuç Stearns-Noechel modelinin elyaf karışımlarında renk eşlemede kullanılabildiğini göstermiştir [1]. Bir başka çalışmada Westland ve arkadaşları, melanj reçete tahmini yapabilmek için 31 adet çıktı ile 6 katmanlı, gizli katmanlardaki nöron sayısı 6, 7, 8 ve momentum terimi 0,1 olarak çoklu tabaka algısal yapay sinir ağını oluşturmuşlardır. 123 örnekten oluşan öğrenme veri seti ve 40 örnekten oluşan test kümesi olmak üzere toplam 163 renk örneği kullanılmıştır. Diğer ağlarda 80, 60 ve 40 öğrenme kümesi örnek sayısı kullanılarak öğrenme kümesi örnek sayısının yapay sinir ağları tahminleme performansındaki etkisi incelenmiştir. Aynı sayıda test örneği sayısı için renk tahminlemesinde Kubelka Munk tahminleme sisteminin performansı karşılaştırılmıştır. Test kümesindeki her örnek için CMC (2:1) renk farklılığı belirlenmiştir. Yapay sinir ağları performansında gizlenen tabakadaki nöron sayısının etkisinin az olduğu bulunmuştur. Öğrenme kümesindeki örnek sayısı artarken yapay sinir ağının performansında sürekli bir gelişme gözlenmiştir. Öğrenme kümesi örnek sayısı 123 olduğunda Kubelka Munk modeli yaklaşık 1,5 birim ortalama renk farklılığı verirken yapay sinir ağı kullanıldığında ortalama 1 birim renk farklılığı elde edilmiştir. 40 kalibrasyon örneği için Kubelka Munk modelininin uygun olduğu bulunmuştur. Ayrıca yüksek sayıda öğrenme kümesi örnek sayısı için yapay sinir ağı modeli oldukça uygunken, Kubelka Munk denklemlerine ilave örnekler eklemenin kolay olmadığı belirtilmiştir [2]. Bir diğer çalışmada Bezerra ve arkadaşları, 3 farklı feedforward yapay sinir ağı yöntemini fluoresent boyarmaddelerin konsantrasyonunu tahmin etmek amacı ile kullanmıştır. 238 adet veri yapay sinir ağının eğitim aşamasında ve 28 adet veri yapay sinir ağını test etmek için kullanılmıştır. Bu yöntemde girdi verisi olarak toplam spektral radyans faktörü, XYZ ve L*a*b* değerlerinden faydalanılmıştır. Bu girdileri farklı olan yapay sinir ağlarından yalnızca spektral radyans faktörü değerlerini girdi nöronu olarak kullanılan yapay sinir ağı %3,92 ortalama yüzde relatif hata ile kabul edilebilir sonuç vermiştir. XYZ ve L*a*b* girdileri için yapay sinir ağları sırasıyla %45,66 ve %39,48 ortalama yüzde relatif hata değeri vermişlerdir. Aynı zamanda tersine yönde işlem uygulandığında yani konsantrasyon değerlerinden SRF eğrilerinin üretilmesinde iyi sonuçlar elde edilmiştir. Ayrıca test kümesindeki örnek sayısının 189'dan (%3,56 rölatif hata) 208'e (%4,43, rölatif hata) artırılması ile 400-700 nm arasında tahmin edilen ve ölçülen SRF değerlerinden oluşan eğriler çıkarılmıştır [3].

Bu çalışma kapsamında melanj renkli ürünlerin üretimi sırasında ton farkı hatalarını minimuma indirmek ve çalışma süresinde zaman tasarrufu sağlanması amaçlanmıştır. Hedef melanj renklerin üretilmesinde hali hazırda eğirme yöntemi farklarından ve ara renklerde reçete tahminlemesi doğru bir şekilde yapılamadığı için renk standardizasyonu sağlamak adına bir yapay sinir ağı oluşturulmuştur.

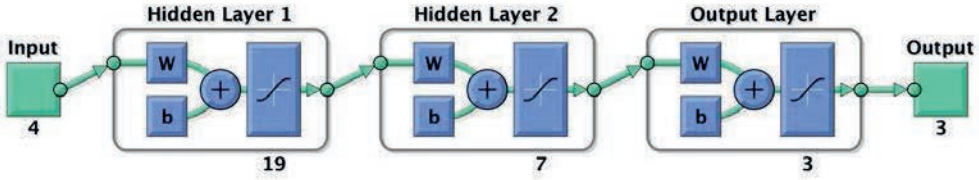
2. Materyal ve Metot

Çalışmada ilk olarak önceden hazırlanmış 7 farklı gri ton rengin CIE lab değerleri spektrofotometre cihazında ölçülüp, boyama sonu, iplik eğirme sonu ve örgü kumaş formu sonrasında renk farkı değerleri ölçülmüştür. Daha sonra reçetesi belirlenmiş olan ana melanj renkli ürünlerin renk değerlerinin yapay sinir ağına öğretilmesi amaçlanmıştır. Böylece yapay sinir ağının eğitim setinde girdi parametreleri olarak reçete de yer alan karışım oranları, çıktı parametresi olarak da CIE Lab değerleri kullanılmıştır. Geliştirilen yapay sinir ağı 3 katmanlı ve

ileri beslemeli şeklinde oluşturulmuştur (Şekil 1). Toplamda 7 farklı gri ton karışımından oluşan numunelere ait veri setinde 5 farklı karışım oranı ağın eğitilmesi amacı ile kullanılırken 2 karışım oranı test amacı ile veri kümesinden ayrılmıştır (Tablo 1).

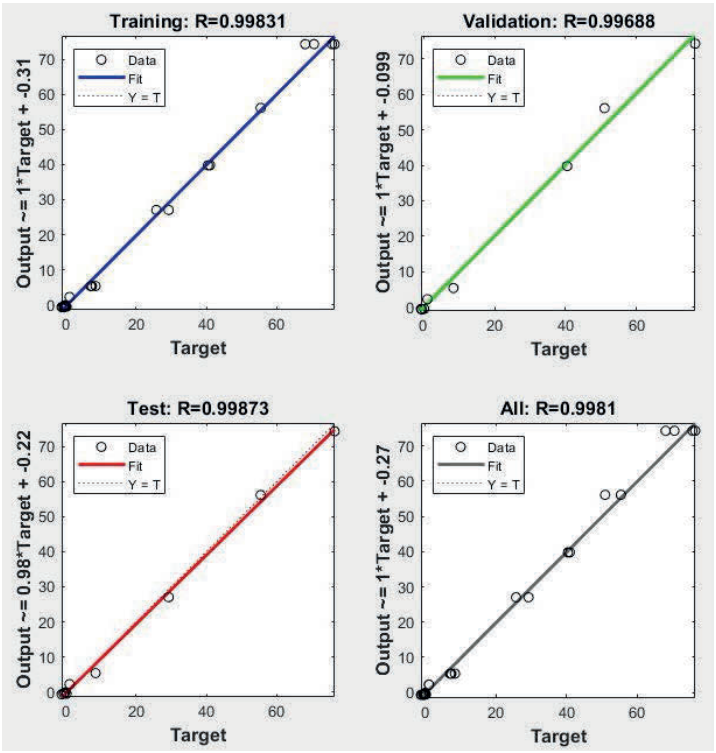
Tablo 1. Eğitim setinde kullanılan girdi değerleri.

	Eğitim Seti					Test Seti	
Karışım Oranı	**1**	**2**	**3**	**4**	**5**	**6**	**7**
Siyah	2	4	16	40	70	8	55
Ham	98	96	84	60	30	92	45



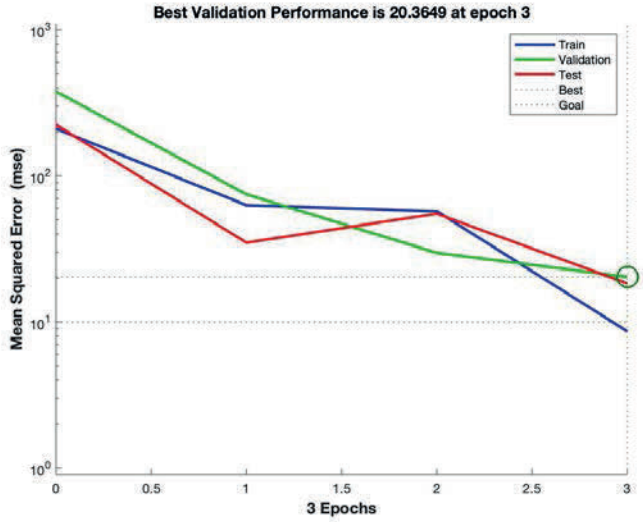
Şekil 1. Geliştirilen yapay sinir ağı tahmin modeli

Eğitilen YSA tahmin modelinin regresyon grafiklerini grafiği Şekil 2'te gösterilmiştir. Bu grafik ağ performansını doğrulamak için kullanılmaktadır. Buradaki sonuçlara en yakın şekilde çizilecek olan doğru regresyon doğrusudur. Bu doğru x=y doğrusuna ne kadar yakınsa o kadar başarılı bir eğitim olduğu anlamına gelir. Her bir grafiğin üstünde görülen değerin 100 ile çarpımı o işlemin başarı yüzdesini ifade etmektedir. Oluşturulan YSA modelinin regresyon grafiğinde eğitim, doğrulama ve test işlemlerinin genel başarı oranının %100 e yakın olduğu görülmektedir. Bu oranı ne kadar yüksek alırsak simülasyon sonuçlarımızın o kadar başarılı olacağı anlamına gelmektedir.



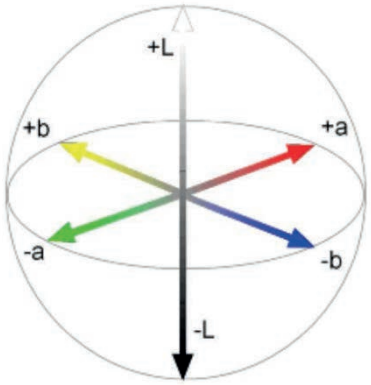
Şekil 2. Yapay sinir ağı regresyon grafikleri

Eğitim setinden elde edilen bir diğer grafik ise devir performansı grafiği Şekil 3'te gösterilmektedir. Hata kareler ortalaması (H.K.O.) ve iterasyon sayıları verilmiş olan bu grafikte performans ölçütü olarak H.K.O. kullanılmıştır. Modelin 0,03'lük değerle en küçük H.K.O. ya sahip olduğu görülmektedir.



Şekil 3. Yapay sinir ağı performans grafiği

CIELab renk uzayı, XYZ renk sisteminden geliştirilmiştir. X, Y ve Z tristimulus değerleri, bir rengi sayısal olarak ifade ederken o renk hakkında bilgi vermemektedir. Rengin daha kolaylıkla anlaşılabilir bir tanımını yapmak için tristimulus değerlerinden hesaplanan L*, a* ve b* şeklindeki üç koordinatı bulunan CIELab renk uzayı tanımlamıştır. Renk uzayında yer alan L*, a* ve b* değerleri renklerin tanımlanmasında kullanılan ana parametrelerdir (Şekil 4).



Şekil 4. CIELab Renk uzayı

L*; ışıklıklık değerini temsil eder. Renk uzayındaki dik eksendir. L* değeri yükseldikçe rengin parklaklığı artar.
a* ve b*; kromatik koordinatlardır. CIELab renk uzayında +a* kırmızı yönü, -a* yeşili, +b* sarı rengi, -b* ise maviyi temsil etmektedir.
Renk farklılıklarının ölçülmesi, bu sistemde daha kabul edilebilir düzeydedir. Belirlenen standart renk ile numune renk arasındaki farklılığının hesaplanmasında bu yöntem kullanılır. Bu sistem tekstil sektöründe yaygın kullanılmaktadır.

3. Bulgular ve Tartışma

Çalışma kapsamında geliştirilen yapay sinir ağı tahmin sonuçları Tablo 2'de verilmiştir. Tablo 2 incelendiğinde iplik ve kumaş formundaki renk ölçümlerinden elde edilen L*, a* ve b* değerlerinin birbirine yakın olduğu görülmüştür. Normal koşullarda sarılan iplik ve kumaş benzer bir yüzey oluşturduğundan, yapılan ölçüm sonuçlarının birbirine yakın olması beklenir. Geliştirilen YSA tahmin sonuçları için her bir numunenin mutlak yüzde hatası hesaplanmıştır. Daha sonra çıktı parametreleri olan tiristimilus değerlerinin ortalama mutlak yüzdesi (MAPE) elde edilmiştir. Tablo 2'ye göre L* değeri için ortalama MAPE 6,17 elde edilirken, a* ve b* değerlerinin sırasıyla ortalama MAPE değeri 81,81 ve 39,01 olarak hesaplanmıştır. En iyi tahmin başarısı renklerin parlaklık değerlerin (L) görülürken en düşük tahmin başarısı kırmızı-yeşil yönlü renk eksenin elde edilmiştir. Özellikle "a" eksenin elde edilen düşük tahin başarısı daha fazla numune ve veri seti ile yükseltilebileceği düşünülmektedir.

Tablo 2. Yapay sinir ağı modelinin tahmin sonuçları.

			L*			a*			b*		
	Karışım Oranı		Gerçek Ölçüm	Tahmin Sonuç	MAPE	Gerçek Ölçüm	Tahmin Sonuç	MAPE	Gerçek Ölçüm	Tahmin Sonuç	MAPE
İplik	8	55	65,96	74,29	0,13	-0,74	-0,48	0,35	3,69	5,12	0,39
	92	45	29,26	27,07	0,07	-0,04	-0,13	2,30	-1,08	-0,62	0,42
Kumaş	8	55	65,25	65,25	0,00	-0,59	-0,61	0,04	4,61	5,12	0,11
	92	45	28,36	27,07	0,05	-0,32	-0,13	0,59	-1,71	-0,62	0,64
Ortalama MAPE					6,17			81,81			39,01

4. Sonuçlar

Bu çalışmada melanj renkli üretim için, farklı karışım elyaf renkleri oranlarından CIELab değerlerinin tahmin edilmesi araştırılmıştır. Pamuk melanj iplik üretimleri için hazırlanan harmanın renk standardizasyonunu sağlamak amacıyla yapay zeka sistemli bir tahminleme modeli geliştirilmiştir. Çalışmanın temelinde çok katmanlı ileri beslemeli bir yapay sinir ağı modeli kullanılmıştır. Çalışmada ilk olarak ring eğirme yöntemi ile hem işletmede hem de laboratuvar şartlarında 7 farklı gri ton renkleri reaktif boyarmaddeler ile boyanan pamuk lifinin tiristimulus değerleri kullanılmıştır. MAPE değerlerinin beklenenden daha yüksek çıkmasının en önemli sebebi numune sayısının ve dolayısı ile veri setinin sınırlı olmasıdır. Çalışma firma bünyesinde bir proje olarak devam etmektedir. Firmanın üretmiş olduğu farklı renk gruplarına ait melanj numuneler ile veri setinin genişletilmesi ve başarı yüzdesinin artırılması hedeflenmektedir.

Sınırlı sayıda iplik numunesi ile elde edilen sonuçlar incelendiğinde eğitilen YSA modelinin sahip olduğu başarı oranı, melanj iplik üretime yönelik renk tahmin yönteminin endüstriyel olarak kullanılabileceğini göstermektedir. Proje kapsamında iplik üretim parametreleri, lif özellikleri ve karışım oranlarını kapsayan geniş bir tahmin çalışması yapılması planlanmıştır. Sunulan çalışma, melanj pamuk iplik üretiminde YSA tahmin modelinin uygulanabilirliğini göstermek adına bir ön çalışma olarak gerçekleştirilmiştir.

Referanslar

1. Yeşil, Y., and Sabır, E.C. Polyester/Viskon Elyaf Karışımlarında Renk Değerlerinin Yeni Bir Algoritma Geliştirilerek Tahmin Edilmesi. Tekstil ve Konfeksiyon. **2010**, 3.

2. Westland, S. Artificial Neural Networks and Colour Recipe Prediction. Proceedings of the International Conference and Exhibition. Colour Science, **1998**.
3. Bezerra, C.M. and Hawkyard, C.J. Computer match prediction for fluorescent dyes by neural Networks. Jsdc, **2000**, 116.

DTY POLYESTER İPLİKLERDE FİLAMENT İNCELİĞİNİN VE DİSK TİPİNİN İPLİK FİZİKSEL ÖZELLİKLERİNE ETKİSİ

GÜLBİN FİDAN[1], YASEMIN KORKMAZ[2], HALIL İBRAHIM ÇELİK[3]

[1]Gaziantep Üniversitesi, Naci Topçuoğlu Meslek Yüksekokulu, Gaziantep, TÜRKİYE.
[2]Kahramanmaraş Sütçü İmam Üniversitesi, Mühendislik Mimarlık Fakültesi, Tekstil Mühendisliği Bölümü, Kahramanmaraş, TÜRKİYE.
[3]Gaziantep Üniversitesi, Mühendislik Fakültesi, Tekstil Mühendisliği Bölümü, Gaziantep, TÜRKİYE.

Özet

Polyester lifi, tekstil endüstrisinde en fazla kullanılan sentetik liftir. Stapel veya filament formda kullanılan polyester, konfeksiyon ürünlerinden teknik tekstillere kadar geniş bir kullanım yelpazesine sahiptir. Halı endüstrisinde ATY (Hava Jetli Tekstüre İplik), DTY (Çekimli Tekstüre İplik), BCF (Hacimli Sonsuz Filament) gibi farklı formlarda halı ipliği olarak kendine kullanım alanı bulmuştur. Hav ipliği üretiminde yaygın kullanılan polipropilene göre, polyester iplikler daha ince filamentler şeklinde üretilebilmektedir. Yumuşak bir tuşeye neden olan bu durumla birlikte polyesterin yüksek dayanıma sahip olması, polipropilene göre artan bir kullanım trendi yakalamasına neden olmaktadır. Filament inceliği, iplik mukavemetine ve elastikiyetine etki eden önemli bir parametredir. Bu bağlamda, farklı filament incelikleri ile üretilen hav ipliklerinin mukavemet, elastikiyet, kıvrım, sıcakta çekme özellikleri ile bu hav ipliklerinden üretilen halıların rezilyans özelliklerinin farklı olması beklenmektedir. Filament inceliğinin yanı sıra, birbirinden farklı yapılardaki poliüretan ve seramik disklerin kullanımı, DTY iplik özelliklerini etkiler. Üretim sırasında uygun disk seçimi bu nedenle önem arz etmektedir. Bu çalışmada, üç farklı filament sayılarında ve farklı disklerle üretilen DTY polyester hav ipliklerinin fiziksel özellikleri incelenmiştir. DTY hav iplikleri, toplam 1200 denye doğrusal yoğunlukta, 3.13, 2.08 ve 1.56 denye inceliğindeki filamentlerin, poliüretan ve seramik disklerle yalancı büküm tekstüre yöntemiyle birleştirilmesi şeklinde üretilmiştir. DTY iplik numuneleri mukavemet, elastikiyet, kıvrım ve sıcakta çekme testlerine tabi tutulmuştur. Test sonuçları istatistiksel olarak analiz edilip filament inceliğinin ve disk tipinin, iplik fiziksel özellikleri üzerine anlamlı bir etkiye sahip olup olmadığı belirlenmiştir. Sonuçlara göre, filament inceliğinin mukavemet üzerinde anlamlı bir etkisi olmazken elastikiyet, kıvrım kısalması ve sıcakta çekme üzerinde anlamlı bir etkisi olduğu görülmüştür. Disk tipinin ise mukavemet, elastikiyet ve kıvrım kısalması üzerinde anlamlı bir etkisi varken, sıcakta çekme sonuçları üzerine etkisinin olmadığı sonucuna varılmıştır.

Keyword: DTY, Polyester, Filament inceliği, Disk tipi, Hav ipliği.

Lİ-Fİ İLE UÇAK İÇİ İNTERNET BAĞLANTISINDA FARKLI GEOMETRİK YERLEŞİMLERİN PERFORMANS ANALİZİ

ABDULLAH MURATOĞLU*[1], TANSAL GÜÇLÜOĞLU [2]

[1]Yıldız Teknik Üniversitesi, Mühendislik Fakültesi, Elektronik ve Haberleşme Mühendisliği Bölümü, İstanbul, TÜRKİYE.
[2] Yıldız Teknik Üniversitesi, Mühendislik Fakültesi, Elektronik ve Haberleşme Mühendisliği Bölümü, İstanbul, TÜRKİYE.

Özet

Kablo karmaşasını ortadan kaldırarak internetin mobil olarak kullanımını herkes için kolaylaştıran Wi-Fi (Wireless Fidelity), hayatımızda önemli bir etki oluşturmuştu. Öte yandan, Wi-Fi ile benzer yeni bir yöntem olan Li-Fi (Light Fidelity) daha hızlı, daha güvenli ve daha tercih edilebilir bir çözüm olarak karşımıza çıkmaktadır. Görünür ışık haberleşmesinin bir uygulaması olan Li-Fi, sızma girişimlerine karşı son derece güvenli olup iletişim kesintisine yönelik problemleri de azaltmasıyla özellikle uçaklardaki her yolcu için aydınlatma lambaları üzerinden yüksek hızlı veri bağlantısı imkânı sağlayabilir. Hassas RF aviyonik komponentler ile elektromanyetik girişim (EMI) olmadan uçakta güvenli bağlantıya izin vermesiyle hava ulaşımında hizmet veren firmalar tarafından müşteri memnuniyetini artırmak için tercih edilebilir. Bu makalede yeni bir internet erişim teknolojisi olarak gelişen Li-Fi ve onun uçakta kullanımı ele alınmış olup, tipik bir B-737 için kabinin farklı noktalarına yerleştirilen Li-Fi verici ve kanalların benzetim sonuçları sunulmuştur.

Anahtar Kelimeler: VLC; Li-Fi; kanal güç dağılımı; kanal impuls cevabı; kanal frekans cevabı;

Abstract

Wi-Fi, which facilitates the use of the internet for mobile by removing the cable clutter, had a significant impact on our lives. On the other hand, Li-Fi, a new method similar to Wi-Fi, emerges as a faster, safer and more preferable solution. Li-Fi, which is an application of visible light communication is extremely secure against leakage attempts and can provide high-speed data connection via lighting lamps for every passenger, especially in aircraft, by reducing the problems of communication interruption. It can be preferred by air transport companies to increase customer satisfaction by allowing secure connection on the aircraft without electromagnetic interference (EMI) with sensitive RF avionic components. In this article, Li-Fi developing as a new internet access technology and its use in aircraft are discussed, and simulation results of Li-

Fi transmitter and channels placed at different points of the cabin for a typical B-737 are presented.

Keyword: VLC; Li-Fi; channel power distribution; channel impuls response; channel frequency response

1. Giriş

Veri iletişimine olan talep son birkaç yıl içinde çarpıcı bir şekilde arttığından, yüksek kapasite ve hızda bilginin iletilebilmesi için elektromanyetik spektrumda çok daha yüksek frekans bandlarına çıkılması gerekmekte ve artan talebi karşılamak için çeşitli yenilikçi yöntemler denenmektedir. Bu bakımdan haberleşmenin optik iletim alanında ağırlık kazanacağı anlaşılmakta ve serbest uzayda ışığın yayılımını kullanarak haberleşmeye olanak sağlayan serbest uzay optik haberleşmesi (FSO) ve görülebilir ışık iletişimi (VLC) hızla gelişmektedir. Optik spektrumun çok yüksek bilgi taşıma kapasitesine sahip olmasından dolayı özellikle aydınlatma amacıyla son yıllarda çok yaygın olarak kullanılan LED'ler (Light Emitting Device) sayesinde görünür ışık haberleşmesinin (VLC) gittikçe popüler bir araç olacağı anlaşılmıştır.

Table 1. Li-Fi'nin Avantajları

Sıra No	Li-Fi'nin Avnatajları	Açıklama
1	Yüksek Hız	1 gigabit hızında iletişim olanağı sağlar.
2	Güvenlik	Li-Fi sinyalleri duvarların ötesine geçmediğinden sızmaya karşı güvenlidir.
3	Akıllı Ortam	Li-Fi ortamdaki mürettebat paneli, havalandırma gibi diğer IP tabanlı araçlara kolayca erişilmesini sağlar.
4	Uygunluk	Li-Fi, Wi-Fi gibi diğer radyo sinyalleri ile girişim yapmaz.

Li-Fi bağlantısı için LED aydınlatma sistemleri ile internet erişimi sağlanabilir. Uçak içi internet erişiminin sağlanmasında Wi-Fi birçok dezavantaja sahip olduğundan hâlihazırda yolculara aydınlatma amacıyla sunulmakta olan tepe lambaları üzerinden Li-Fi yöntemi ile bu ihtiyaç daha efektif biçimde giderilebileceği son dönemlerde görülmüş ve üreticiler tarafından yakından takip edilmektedir.

[1]'de Airbus'ın uçak veri uzmanı Valentin Kretzschmar, Airbus'ın kabinde Li-Fi erişimi sağlamak için çözümler üzerinde çalıştığını, Wi-Fi'nin sebep olduğu sorunları Li-Fi ile aşabileceklerini söylüyor. Öte yandan yine Airbus'ın dijital dönüşüm şefi Eric Peyrucain, "ofislerimizdeki veri akışlarının dışarıdan saldırıya uğramasını istemiyoruz ve Li-Fi benzersiz bir çözüm sağlıyor, çünkü sinyal duvarlardan iletilmiyor", diyor. Peyrucain'e göre, Li-Fi'nin Airbus'taki potansiyel uygulamaları uçaklarla sınırlı değil. Üretim tesisleri için de büyük bir potansiyele sahip. [2]'de Edinburgh Üniversitesi'nde Mobil İletişim Profesörü Harald Haas "havayollarının daha çok ağırlıktan tasarruf ettikleri için Li-Fi ile ilgilendiklerini ve koltukların genellikle kablolarla sabitlenmiş olup esnekliklerinin de sınırlı olduğundan hizmet verdikleri bağlantıya bağlı olarak koltuk aralığını değiştirebilmek istediklerini" ve ayrıca "büyük bir uçak

firmasının, tepe lambasını kullanarak uçak içi eğlence sistemleri için Li-Fi potansiyelini test ettiğini" bildirdiğinden bahsediliyor.

Görülebilir Işık İletişimi (VLC)'nin bir uygulaması olan Li-Fi'nin uygulama alanlarının yaygınlaşması ile birlikte uçak içi kullanımına yönelik araştırmalarda hızlanmıştır. [3]'te uçak için tasarlanmış bir VLC sistemin SNIR (Signal-to-Noise-plus-Interference Ratio) tahminlerine çalışılmıştır. Kendi geliştirdikleri bir MMCA (Modified Monte Carlo) ışın izleme simülatörü kullanarak, farklı koşullar altında sinyal kaynakları, gürültü ve girişimi ele almışlar, ve sonuç olarak SNIR'nin esasen yan koltuklardan gelen girşim kaynaklarından etkilendiğini, güneş gürültüsü ve diğer ışıkların ise nispeten düşük bir etkiye sahip olduğunu göstermişlerdir. [4]'de uçak içindeki LED li aydınlatma lambaları üzerinden iletişimin sağlanabileceğini göstermek için bir laboratuvar uygulaması yapılmıştır. 555 timer entegre devresi LED ile birlikte kullanılarak bir verici ve Texas Instrument tarafından geliştirilen OPT101P-J parça numaralı optik sensor kullanılarak bir alıcı tasarlanmış ve LED'lerin aydınlatma ile birlikte kısa mesafede iletişim içinde kullanılabileceği gösterilmiştir. [5]'te tipik bir dar gövdeli uçak için internet bağlatısı Wi-Fi, LTE ve Li-Fi üzerinden yapılması durumunda data hızlarının nasıl olacağını karşılartıran bir simülasyon çalışması yapılmıştır. Sonuçların sırasıyla, 164 Mb/s, 642 Mb/s ve 3.49 Gb/s ile Li-Fi'nin en iyi performansı ürettiği ve bu sonucun istenilen hız olan 1.2 Gb/s'tan yaklaşık 3 kat daha iyi olduğu gösterilmiştir. [6]'da bir Boeing 747-400 için biri ortada ikisi duvarlarda olmak üzere, ADT (Angle Diversity Transmitter) birimlerine dayalı iki tür okuma ışığı verici olarak düşünülmüş, alıcı tarafında ise dört bacaklı ADR (Angle Diversity Receiver) ve 25 piksel ImR (Imaging Receiver) kullanılarak bir VLC iletişim sistemi kurgulanmıştır. Sonuçta, gecikme yayılması ve SINR belirlenip iki tür alıcı karşılaştırılmış ve her iki alıcı türü de her kullanıcı için 22,8 Gbp/s'ye kadar yüksek veri hızını destekleyen bir SINR sunduğu gösterilmiştir.

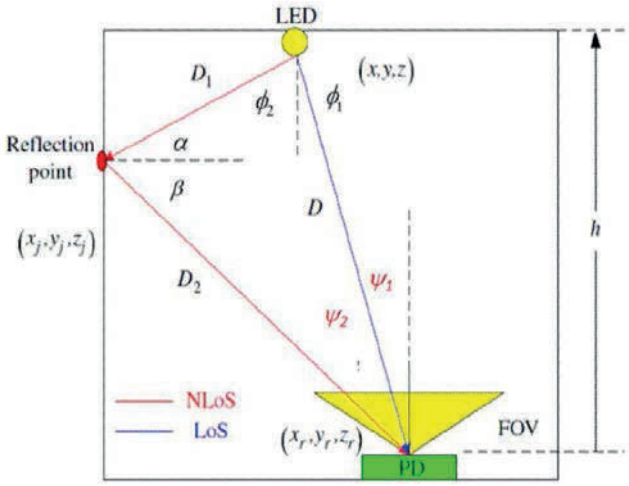
2. Malzeme ve Yöntemler

Bu çalışma tipik bir B-737 dar gövdeli uçak kabini için düşünülmüş olup Li-Fi verici LED'leri ilk durumda; altı kişilik bir sıradaki her bir yolcu için bir adet, ikinci durumda; üç kişilik bir sıradaki her üç yolcu için 1 adet olmak üzere baş üstü paneline, üçüncü durumda ise; altı kişilik bir sıradaki altı yolcu için bir adet tavanın orta kısmına yerleştirilmiştir. Simülasyon çalışması Optisystem V18.0 programında yapılmış olup sistem modeli aşağıda verildiği gibidir.

LED iletim kaynaklarını Lambert'in kosinüs yasasına uyan Lambertian biçimindedir. Bu sebeple Li-Fi kanal modeli, Lambertian kaynak modeli ile modellenmiştir. W/sr cinsinden LED ışıma yoğunluğu şu şekilde verilir:

$$\boldsymbol{R_0}(\emptyset) = \left[\frac{(\boldsymbol{m+1})}{\boldsymbol{2\pi}}\right] \boldsymbol{cos^m}\emptyset \qquad (1)$$

Burada $\emptyset$ alıcıya göre ışıma açısı ve m Lambertian seviyesi olup aşağıdaki gibidir.



Şekil 1- Işık Yayılma Geometrisi [7]

$$\boldsymbol{m} = -\frac{\boldsymbol{log2}}{\boldsymbol{logcos}(\emptyset_{\frac{1}{2}})} \quad (2)$$

Burada $\emptyset_{1/2}$, yarı güçteki verici yarı açısıdır. Radyant yoğunluğu, steradian (sr) cinsinden ölçülen birim katı açı başına yayılan, yansıtılan veya alınan radyant akı (güç) olarak tanımlanır. Vericinin eksenel simetrik ışıma modelinin $P_tR_0(\emptyset)$'yi yaydığını varsayalım. Burada P_t iletilen ortalama optik güçtür. Bu durumda alıcıdaki parlaklık şu şekilde olacaktır.

$$\boldsymbol{I_s(d,\emptyset)} = \frac{\boldsymbol{P_tR_0(\emptyset)}}{\boldsymbol{d^2}} \quad (3)$$

Burada d şekil 1'de gösterilen verici ve alıcı düzlemleri arasındaki mesafedir. Şekil bir yüzeyden yansıma nedeni ile bir LoS ve bir NLoS ışını göstermektedir.
Alınan güç şu şekilde hesaplanır:

$$\boldsymbol{P = I_s(d,\emptyset)A_{eff}(\Psi)} \quad (4)$$

Burada Ψ alıcı eksenine göre olay (incident) açısıdır ve alıcının etkin toplama alanı A_{eff} aşağıdaki şekilde verilir.

$$\boldsymbol{A_{eff}}(\Psi) = \begin{pmatrix} \boldsymbol{A_{det}T_s}(\Psi)\boldsymbol{g}(\Psi)\boldsymbol{cos}(\Psi), & \boldsymbol{0 \le \Psi \le \Psi_c} \\ \boldsymbol{0} & \boldsymbol{\Psi > \Psi_c} \end{pmatrix} \quad (5)$$

Burada Ψ_c alıcının görüş alanı (Field of View-FOV)'dır. A_{det} dedektör alanı, T_s optik filtre iletim kazancı, g alıcı lens kazancı ve n lens kırılma indisidir.
Alıcı lens kazancı aşağıdaki denklem kullanılarak hesaplanabilir.

$$\boldsymbol{g}(\Psi) = \begin{pmatrix} \frac{\boldsymbol{n^2}}{\boldsymbol{sin^2\Psi_c}}, & \boldsymbol{0 \le \Psi \le \Psi_c} \\ \boldsymbol{0}, & \boldsymbol{elsewhere} \end{pmatrix} \quad (6)$$

Tipik olarak, optik alıcı bir yoğunlaştırıcıdan (optik lens), bir optik filtreden, detektör ve transimpedans amplifikatöründen (TIA) oluşur [8].

LOS Lambertian kanalı için DC yakınında nispeten düz yanıt varsayan Li-Fi kanalı frekans yanıtı aşağıdaki gibidir [7].

$$\boldsymbol{H(0)} = \begin{pmatrix} \frac{(m+1)A_{det}}{2\pi d^2} cos^m(\emptyset) T_s(\Psi) g(\Psi) \cos(\Psi), & 0 \le \Psi \le \Psi_c \\ 0, & \Psi > \Psi_c \end{pmatrix} \quad (7)$$

Bir LOS Li-Fi kanal alıcısı için alınan güç şu şekilde verilir:

$$\boldsymbol{P_r} = \begin{pmatrix} \frac{P_t(m+1)A_{det}}{2\pi d^2 sin^2\Psi_c} cos^m(\emptyset) T_s(\Psi) n^2 \cos(\Psi), & 0 \le \Psi \le \Psi_c \\ 0, & \Psi > \Psi_c \end{pmatrix} \quad (8)$$

Hata olasılığı şu şekilde verilir:

$$\boldsymbol{p(e)} = \boldsymbol{Q}(\sqrt{\boldsymbol{SNR}}) \quad (9)$$

Buradaki işaret-gürültü oranı *SNR* aşağıdaki gibidir.

$$\mathbf{SNR} = \frac{P_s}{P_n} = \frac{(RP_r)^2}{\sigma_{tot}^2} \quad (10)$$

Burada *R*, dedektör tepkisidir ve σ^2_{tot}, alıcıda mevcut olan toplam gürültü varyansıdır. Q faktörü şu şekilde tanımlanır[9]:

$$\boldsymbol{Q(x)} = \frac{1}{2\pi} \int_x^\infty e^{\frac{-y^2}{2}} dy \quad (11)$$

Table 2. Simülasyon Parametreleri

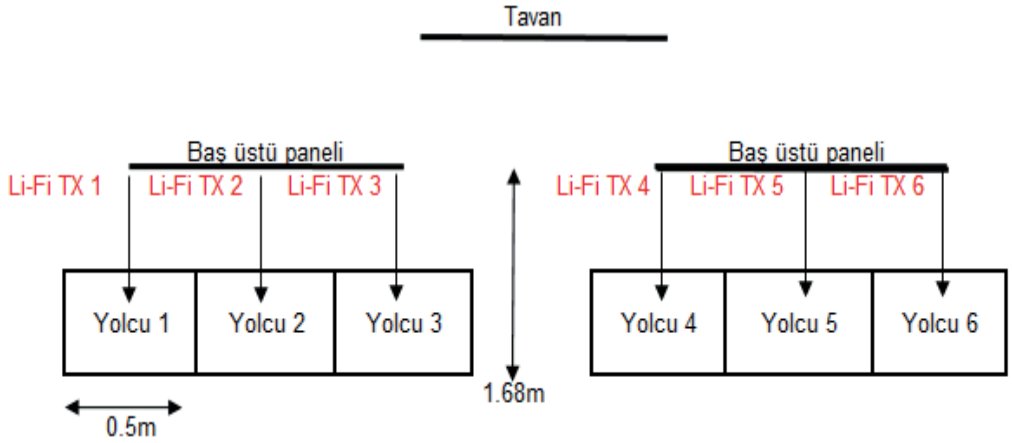
Sıra No	Li-Fi'nin Avnatajları	Açıklama
1	Referans Dalga Boyu	193,75 THz
2	Alıcı Görüş Alanı	70°
3	Alıcı Alanı	0,0001m^2
4	LED Optik Gücü	20mW
5	Verici LED Sayısı	1
6	Optik Filtre Kazancı	1

Table 3. Kabin Boyutları

Sıra No	Li-Fi'nin Avnatajları	Açıklama
1	Koltuk Genişliği	0,5m
2	Koltuklar Arası Mesafe	0,76m
3	Zemin-Tavan Mesafesi	2,2m
4	Zemin-Başüstü Panel Mesafesi	1,68m
5	Zemin Oturma Mesafesi	0,6m
6	Kabin Genişliği	3,54m

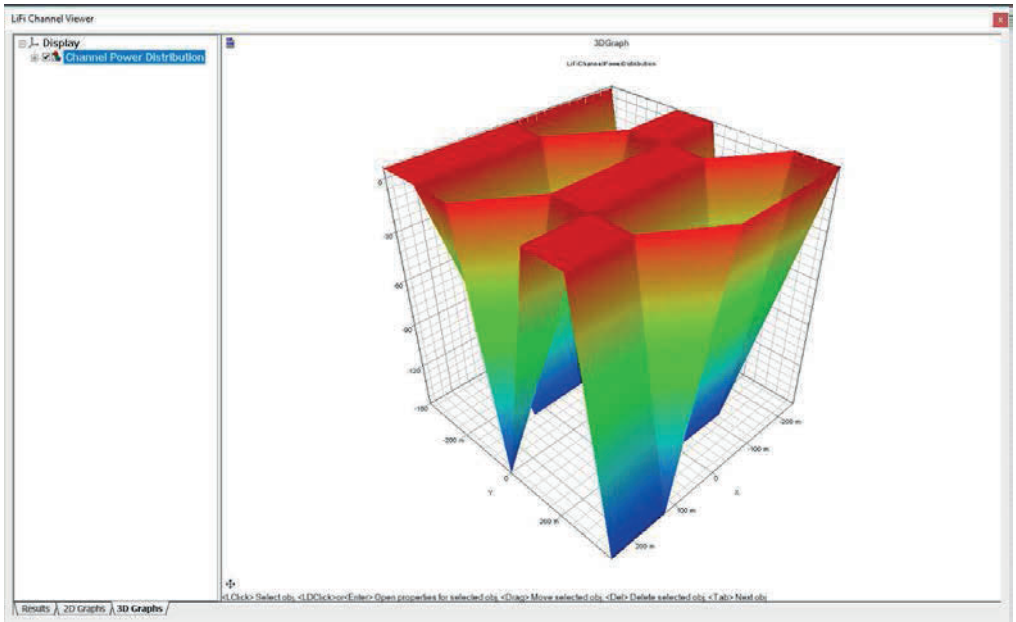
3. Sonuçlar ve Tartışma

Her Yolcuya Bir Li-Fi Bağlantısı Sunulması Durumu

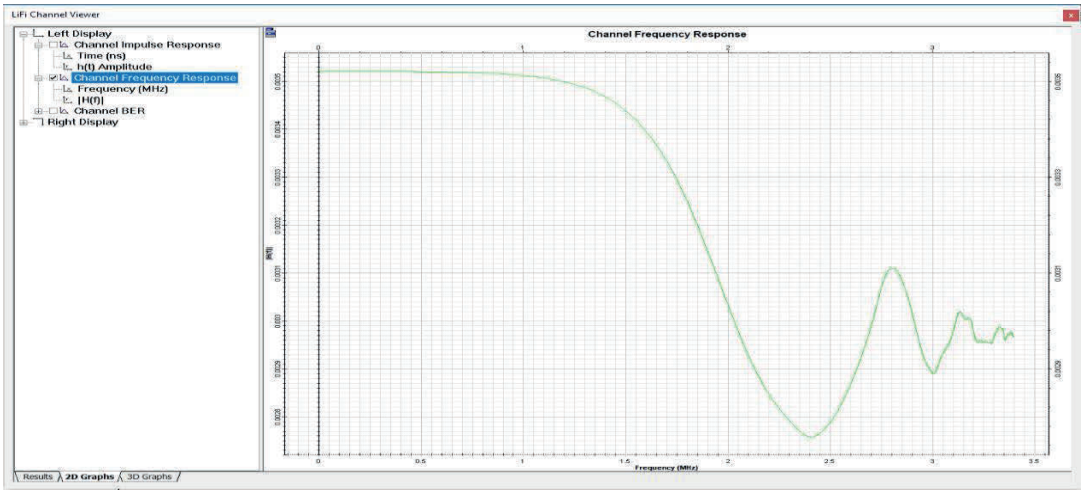


Şekil 2- Birinci Durum İçin Kabin Geometrisinin Temsili Gösterimi

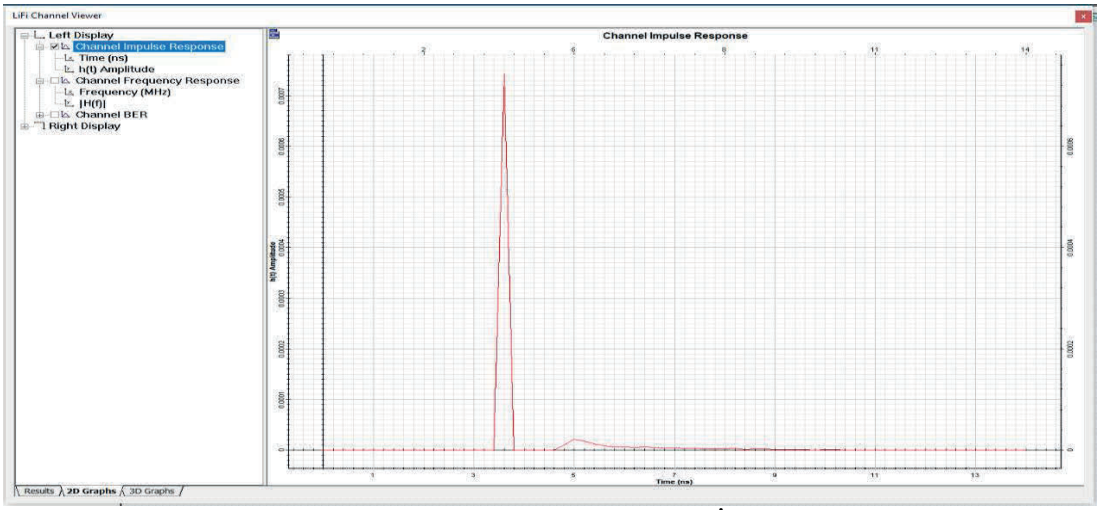
Bu yerleşim planında bir sırada bulunan altı yolcunun her biri için baş üstü paneline bir adet Li-Fi vericisi Şekil 2'de tasvir edildiği gibi konumlandırılmış ve her biri aynı olan altı adet kanalın sadece bir tanesi için benzetim sonuçları aşağıda verilmiştir.



Şekil 3- Birinci Durumda Li-Fi Kanalın Güç Dağılımı

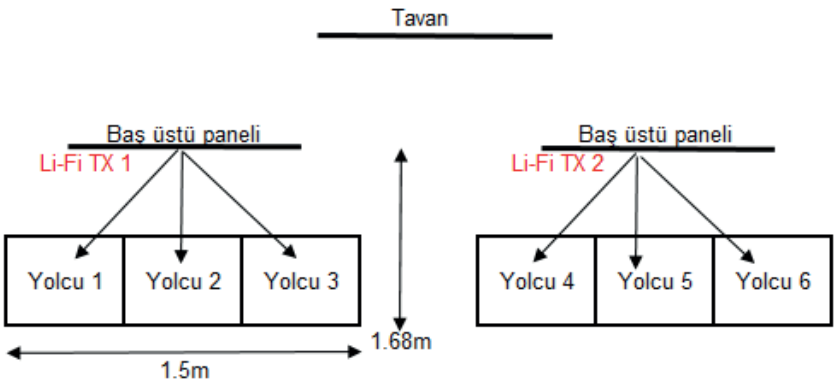


Şekil 4- Birinci Durumda Li-Fi Kanalın Frekans Cevabı



Şekil 5: Birinci Durumda Li-Fi Kanalın İmpuls Cevabı

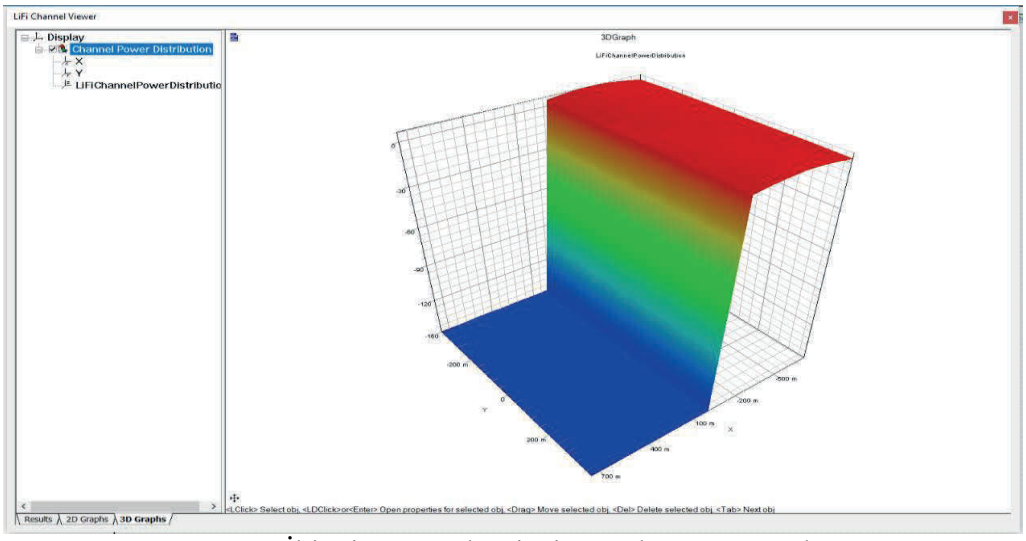
Her Üç Yolcuya Bir Li-Fi Bağlantısı Sunulması Durumu



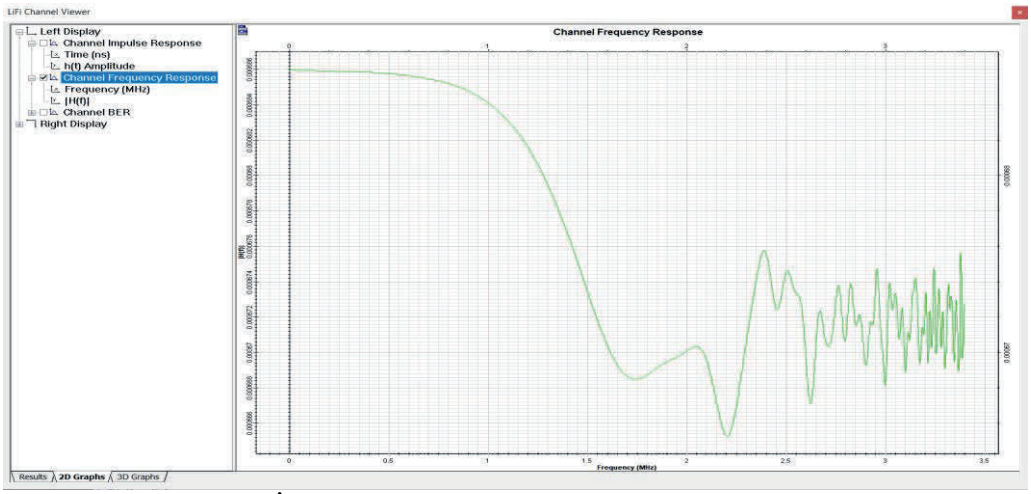
Şekil 6- İkinci Durum İçin Kabin Geometrisinin Temsili Gösterimi

Bu yerleşim planında her bir grupta bulunan üç yolcu için baş üstü paneline bir adet Li-Fi vericisi Şekil 6'da tasvir edildiği gibi konumlandırılmış ve her biri aynı olan dört adet kanalın (yolcu

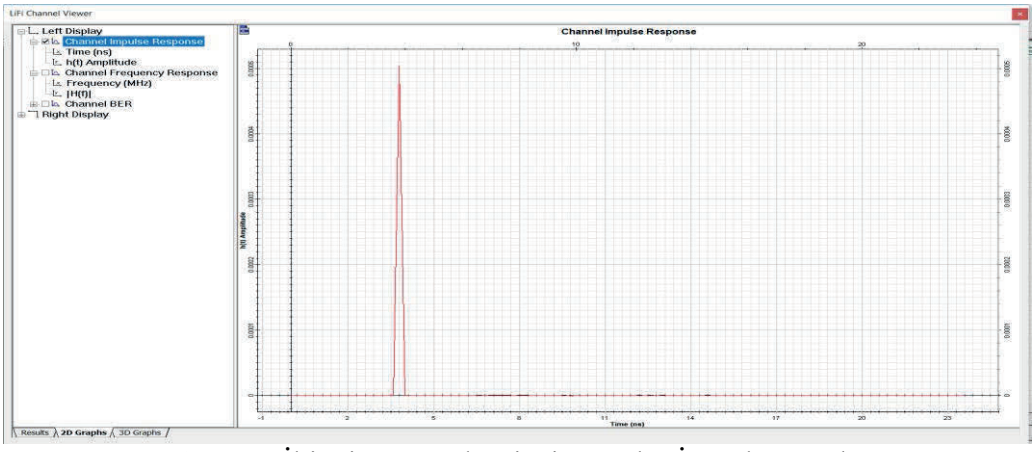
1,3,4,6) sadece bir tanesi için benzetim sonuçları aşağıda verilmiştir. (2 ve 5 nolu yolcular için oluşan kanal parametreleri geometri değişmediğinden bir önceki durum için aynıdır).



Şekil 7- İkinci Durumda Li-Fi Kanalın Güç Dağılımı

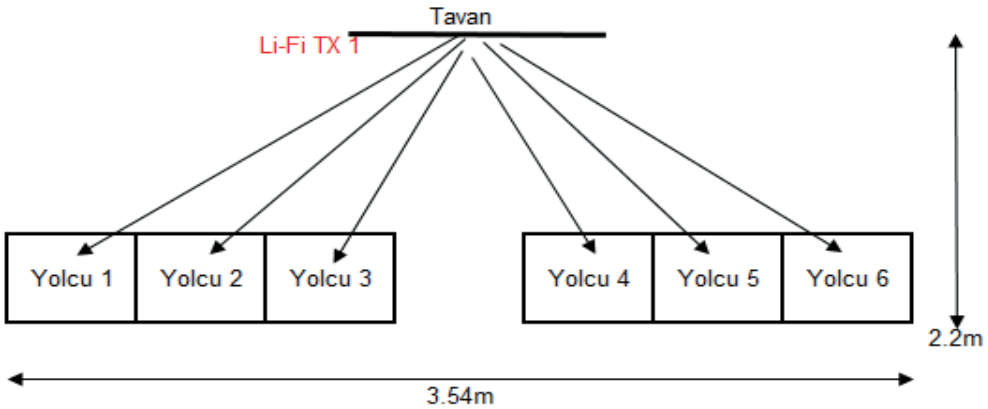


Şekil 8- İkinci Durumda Li-Fi Kanalın Frekans Cevabı



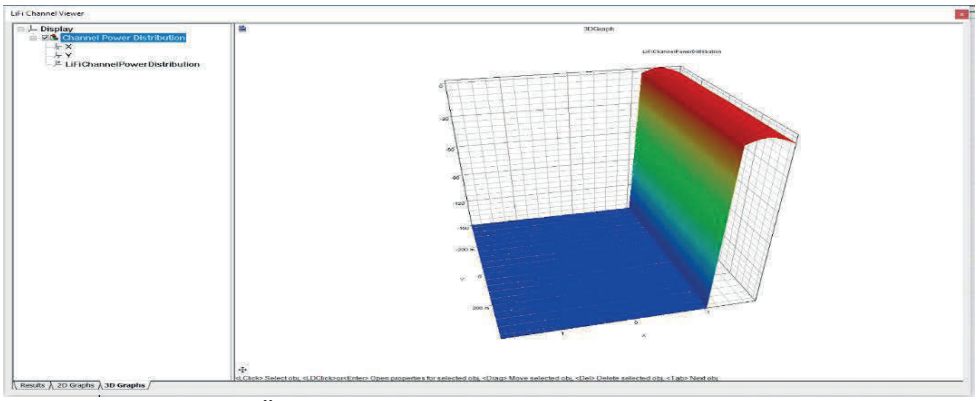
Şekil 9- İkinci Durumda Li-Fi Kanalın İmpuls Cevabı

Her Altı Yolcuya Bir Li-Fi Bağlantısı Sunulması Durumu

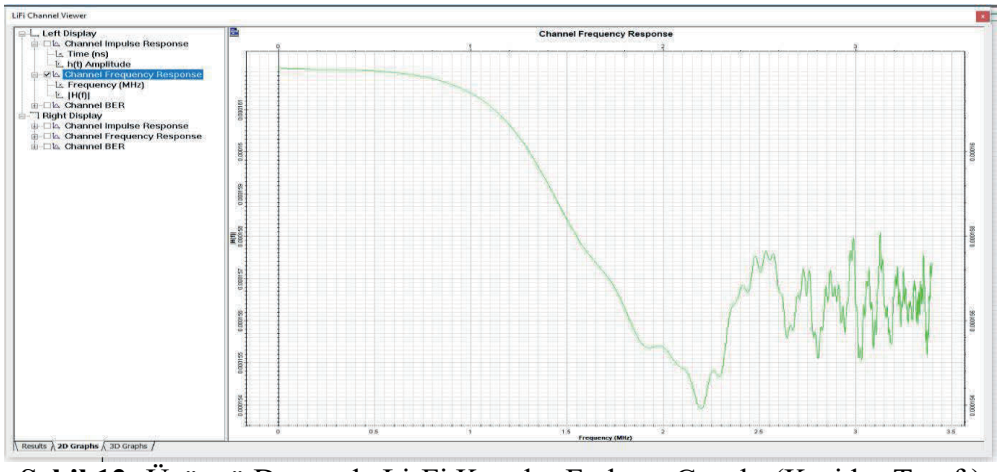


Şekil 10- Üçüncü Durum İçin Kabin Geometrisinin Temsili Gösterimi

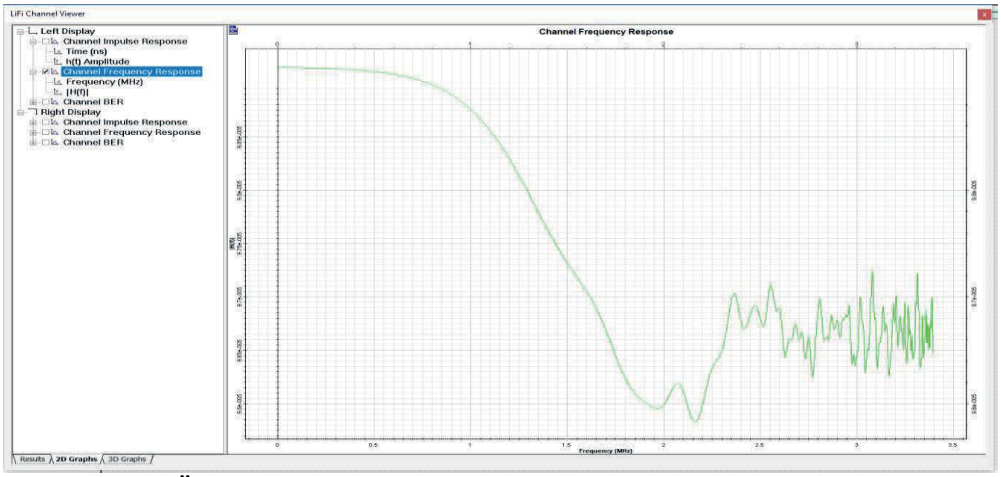
Bu yerleşim planında bir sırada bulunan altı yolcu için bir adet Li-Fi vericisi Şekil 10'da tasvir edildiği gibi ortaya tavana konumlandırılmış ve koridor, orta ve cam tarafı olmak üzere benzetim sonuçları aşağıda verilmiştir.



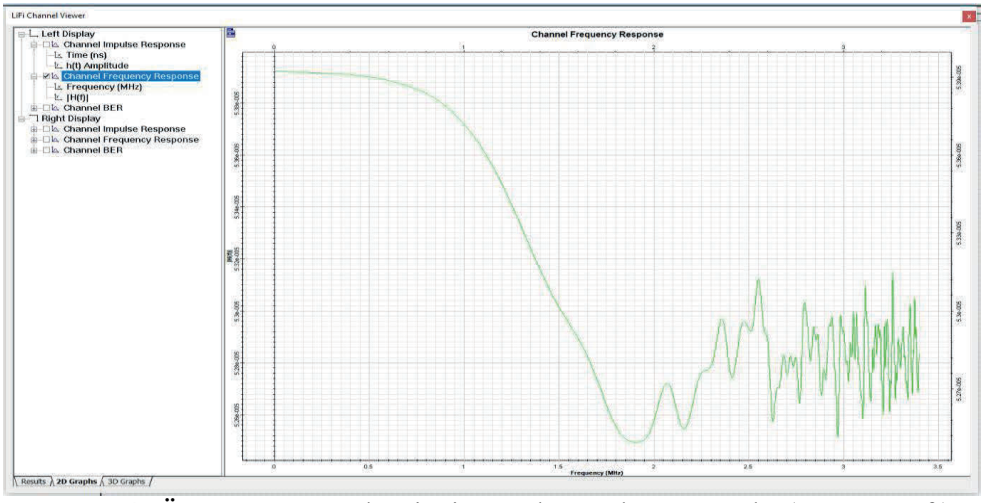
Şekil 11- Üçüncü Durumda Li-Fi Kanalın Güç Dağılımı



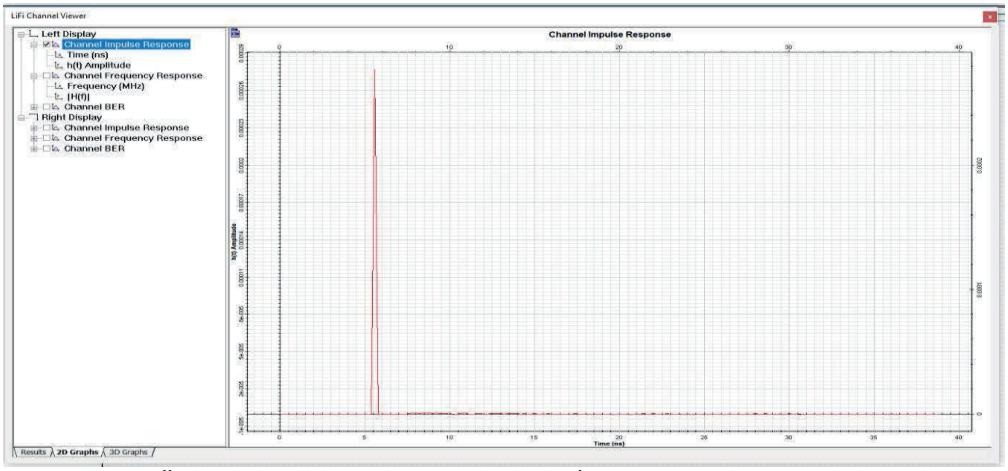
Şekil 12- Üçüncü Durumda Li-Fi Kanalın Frekans Cevabı (Koridor Tarafı)



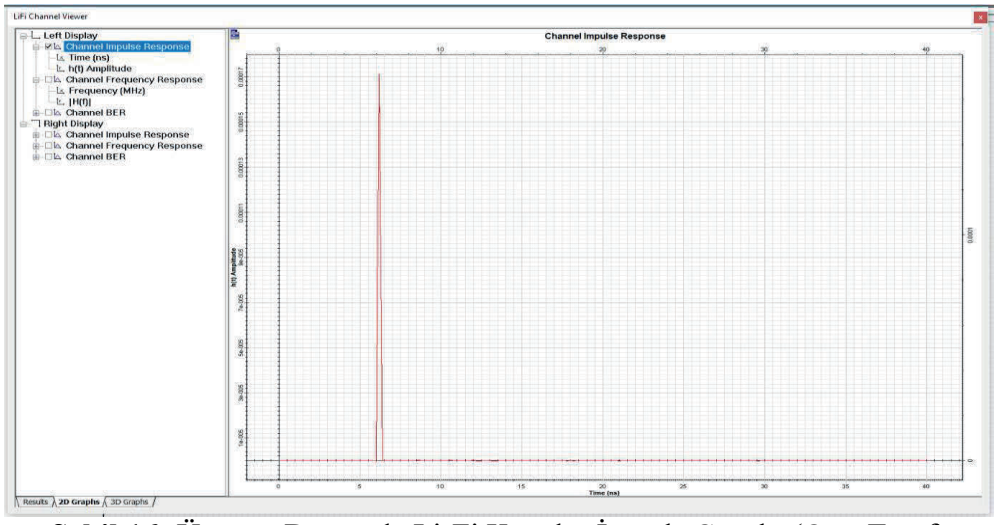
Şekil 13- Üçüncü Durumda Li-Fi Kanalın Frekans Cevabı (Orta Taraf)



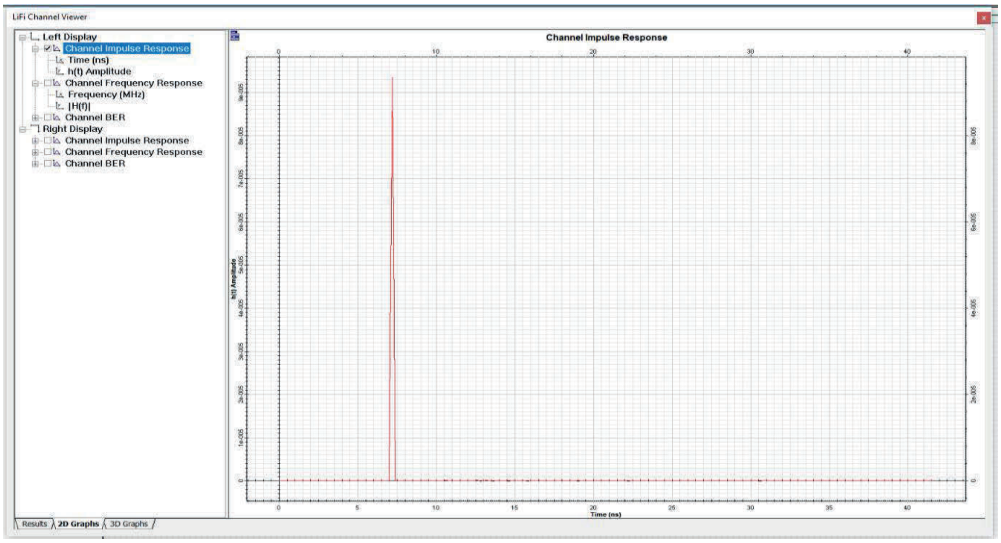
Şekil 14- Üçüncü Durumda Li-Fi Kanalın Frekans Cevabı (Cam Tarafı)



Şekil 15- Üçüncü Durumda Li-Fi Kanalın İmpuls Cevabı (Koridor Tarafı)



Şekil 16- Üçüncü Durumda Li-Fi Kanalın İmpuls Cevabı (Orta Taraf)



Şekil 17- Üçüncü Durumda Li-Fi Kanalın İmpuls Cevabı (Cam Tarafı)

4. Neticeler:

Üreticiler genel olarak her bir kullanıcı için yolcuya özel tepe lambası üzerinden iletişimin sağlanabileceği yönünde uçakta Li-Fi dan bahsediyor. Ancak uçak komponentlerinin pahalı olması ve operasyonel işletmenin de maliyetleri yüksek olması sebebi ile bir bölümdeki her üç yolcuya bir Li-Fi desteği ya da bir sıradaki her altı yolcuya tek bir Li-Fi bağlantısı sunmak suretiyle de iletişim sağlanabilir. Güncel olarak VLC iletim kanal yapıları, farklı alıcı-verici mimariler ve kabin içerisinde farklı planlama yöntemleri araştırılmaktadır.

Bu çalışmada, tipik bir B-737 için kabinin farklı noktalarına yerleştirilen Li-Fi verici ve kanalların benzetim sonuçları sunulmuş olup Li-Fi vericisi olarak kullanılan LED'in kapsadığı hacim büyüdükçe bir uçak kabininde güç dağılımının nasıl olacağı ve alıcı ile verici arasındaki mesafe arttıkça kanalın frekans ve impuls cevabının ne olacağı gösterilmiştir.
Güç dağılımı ilk durumda 6,15dBm'den en uzak köşede 4.85 dBm seviyesine kadar düşerken, ikinci durumda 2.4 dBm ve üçüncü durumda -3.8 dBm olduğu gözlemlenmiştir. Ayrıca kanalın

frekans cevabı |H(f)|'nin ilk durumda 0.00352 seviyesinden sırasıyla, 0.000686, 0.000162, 0.0000995, 0.0000539 seviyesine ve İmpuls cevabı h(t)'nin 0.00075 seviyesinden sırasıyla, 0.00051, 0.00028, 0.00017, 0.00009 seviyesine kadar indiği görülmüştür.

References:

1. https://www.airbus.com/newsroom/news/en/2017/03/Li-Fi.html
2. http://www.techtimes.com/articles/111868/20151130/are-airlines-ready-to-ditch-wi-fi-for-li-fi-on-board-entertainment.htm#
3. D. Tagliaferri, C. Capsoni, "SNIR predictions for on-aircraft VLC systems," International Conference on Broadband Communications for Next Generation Networks and Multimedia Applications (CoBCom), 2016
4. A. Singla, D. Sharma, S. Vashisth, "Data connectivity in flights using visible light communication," International Conference on Computing and Communication Technologies for Smart Nation (IC3TSN), 2017
5. T. Cogalan, S. Videv, H. Haas, "Inflight Connectivity: Deploying Different Communication Networks inside an Aircraft," IEEE 87th Vehicular Technology Conference (VTC Spring), 2018
6. O. Z. Alsulami, M. T. Alresheed, J. M. H. Elmirghani, "Optical Wireless Cabin Communication System," IEEE Conference on Standards for Communications and Networking (CSCN), 2019
7. G. Shi, Y. Li, W. Cheng, L. Dong, J. Yang, W. Zhang, "Accuracy analysis of indoor visible light communication localization system based on received signal strength in non-line-of-sight environments by using least squares method,"Opt. Eng. 58(5), 056102 (2019),doi: 10.1117/1.OE.58.5.056102.
8. J. M. Kahn and J. R. Barry, "Wireless infrared communications," Proceedings of the IEEE, vol. 85, No. 2, pp. 265-298, 1997
9. R. Paudel, Z. Ghassemlooy, H. L. Minh, S. Rajbhandari, E. Leitgeb, " Lambertian source modelling of free space optical ground-to-train communications," 8th International Symposium on Communication Systems, Networks & Digital Signal Processing (CSNDSP), 2012

A REVIEW ON ALUMINIUM MATRIX COMPOSITES MANUFACTURED BY POWDER METALLURGY

ELİF PESEN*[1], ABDUL KADİR EKŞİ[2], AYŞE NUR ACAR[3], AHMET EKİCİBİL[4]

[1] Adana Alparslan Türkeş Science and Technology University, Faculty of Engineering, Department of Materials Science and Engineering Department, Adana, TURKEY.
[2]Çukurova University, Faculty of Engineering, Department of Mechanical Engineering, Adana, TURKEY.
[3]ÇukurovaUniversity, Faculty of Ceyhan Engineering, Department of Mechanical Engineering, Adana, TURKEY.
[4]Çukurova University, Faculty of Art and Sciences, Department of Physics, Adana, TURKEY.
*epesen@atu.edu.tr

Abstract

Recent developments in advanced engineering applications are permanently increasing the demand for new and reliable materials. Aluminum matrix composites are new generation metal matrix composites that have the potential to meet these demands. Due to the developments recorded in studies on Al matrix composites in recent years, such as improving mechanical properties, reducing production costs and adapting to new generation technologies, researches are increasing day by day. Al matrix composites have an important place among engineering materials due to their high strength/weight ratio, high hardness and high corrosion resistance. They used for the production of different parts and equipment, especially in the aerospace industry. Various production techniques and test methods are available for the production of aluminum matrix composites. In this review study, a research conducted on the reinforcing materials in Al matrix composites produced by powder metallurgy technique. The selection of reinforcement materials in the right combinations affects the performance of these materials. In addition, combinations of Al matrix and reinforcing particles used in the design of Al matrix composites is given and how these reinforcing particles affect the mechanical properties of materials.

Keywords: Aluminium Metal matrix composites, SiC, TiO_2, Powder Metallurgy, Mechanical Properties

1. Introduction

Composite materials can be defined as a material structure consisting of at least two macroscopically definable materials working together to achieve a superior result [1]. They composed of matrix and reinforcements. These two materials often called continuous and discontinuous phases, where the discontinuous phase known as the reinforcement phase or reinforcement material, it will be much harder and stronger than the continuous or matrix phase [2]. Composites are classified according to the type of matrix material they contain. There are three main types of matrix materials: polymer matrix composites (PMCs), ceramic matrix composites (CMCs), and metal matrix composites (MMCs). MMCs are the most widely used composite type in industrial applications because of their various advantages over PMCs and CMCs [3]. In MMCs, the matrix material consists of a metal. The metal matrix is the continuous phase of the composite and acts as a binder surrounding the reinforcement. The metal matrix transmits and distributes the load to the reinforcement, which is the dispersed phase [4]. MMCs have been used mainly in the aerospace, automobile, defense, marine, sports and recreation industries due to their properties

such as specific strength/weight ratio and simultaneously cost efficiency, and it is seen that traditional metallic alloys are rapidly replaced in many applications [5].

There are different metallic matrix materials in composite materials that can be selected depending on the type of application and the matrix material needed [6-9]. The main metallic matrix materials used are titanium, aluminum and magnesium. Aluminum matrix composites (AMCs) use pure aluminum or its alloy as the matrix and are increasingly used in industrial applications due to their superior mechanical, material and tribological properties. [10]. There are many reinforcement particles, which selected depending on the type of property, desired from the composite material [11,12]. Predominantly used reinforcement particles are hard ceramics such as silicon carbide, aluminum oxide, graphite or fly ash may be used as reinforcing materials that will form good interfaces with the matrix phase [13]. By reinforcing these composites with the addition of ceramic particles, materials with superior properties that can be used in high temperature applications are produced. Especially among some aluminum alloy series, 6000 series aluminum alloy (heat treatable Al6060, Al6061, Al6063A, Al6065, Al6081, Al6082, Al6105, Al6162 and Al6951) has been extensively researched in the literature. It is noteworthy that Al6061 alloy has high corrosion resistance, moderate strength, and finds many applications in the fields of civil works and automobile applications [14].

In this article, we discussed about research articles on Al MMCs produced by powder metallurgy method. Al MMCs are generally produced by two methods, the solid state method and the liquid state method [15]. These methods are given in detail in the following parts of the study. In addition, studies on the reinforcement materials used in Al MMCs produced by powder metallurgy method and the effects of these reinforcements on the mechanical properties of the produced material are included.

2. Production Methods of Aluminium Metal Matrix Composites (Al MMCs)

Al matrix composites are generally produced in two different routes; solid route and liquid route. While the solid route includes production with powder metallurgy techniques, the liquid route includes production methods such as stir casting, squeeze casting and compo-casting [15].

2.1 Solid State Method

The solid state production process of Al MMCs takes place by bonding the matrix metal and the dispersed phase, as a result of mutual diffusion in the solid state under high temperature and pressure. One of the advantages of this method over the liquid state production method is that undesired reactions can be suppressed at the interface between the matrixes and the reinforcement phases. There are two different solid state production methods, such as diffusing bonding and powder metallurgy, in the production of Al MMCs. The most commonly preferred method is powder metallurgy [15].

2.1.1. Powder Metallurgy Method

The use of powder metallurgy technique has gained great importance in the production of Al MMCs, as it enables the production of composite structures in which the reinforcing particles have a higher volume fraction [16]. In addition, net shaped products that do not require post-production processing can be easily produced with powder metallurgy technique [17]. This technique is based on mixing matrix material with continuous or discontinuous fiber reinforcement. Since metal matrix powders and ceramic reinforcements easily mix and integrate, these materials are produced by mixing, compacting and sintering, respectively [18]. In the powder metallurgy technique, the

first stage is the mixing or blending process. At this stage, reinforcement is incorporated into the matrix by methods such as a ball mill, planetary mill, or roll mill. This step is important as it determines the distribution of the reinforcement in the matrix. The reinforcement material may be in the form of whiskers or particles. There are two types of blending processes, dry blending and wet blending, and the selection of the process is determined by the choice of reinforcement and matrix powder. This process, which seems conceptually simple, has a great role in determining the final properties aimed to be obtained in MMCs [19].

The second stage in the production of MMCs is compression. It is based on the principle of compressing the mixture by means of a mold to obtain the desired shape. The compression process used in powder metallurgy technique includes cold compression, degassing and hot isostatic method. The most widely used compression method among these methods is cold compression. The purpose of this step is to obtain a compact with a certain amount of green strength [15]. The last and most important step in this technique is sintering. The sintering process is the keeping of the parts in a controlled atmosphere at a temperature 1/3 below the melting point of the main component. At this stage, recrystallization and grain growth are observed along with the formation of chemical bonds between the powder particles. The protective atmosphere ensures that the part is freed from oxides and also prevents undesirable reactions between the part and its environment. At this stage, the strength and integrity of the part are greatly increased. The production scheme of MMCs by powder metallurgy technique is shown in Figure 1 [15].

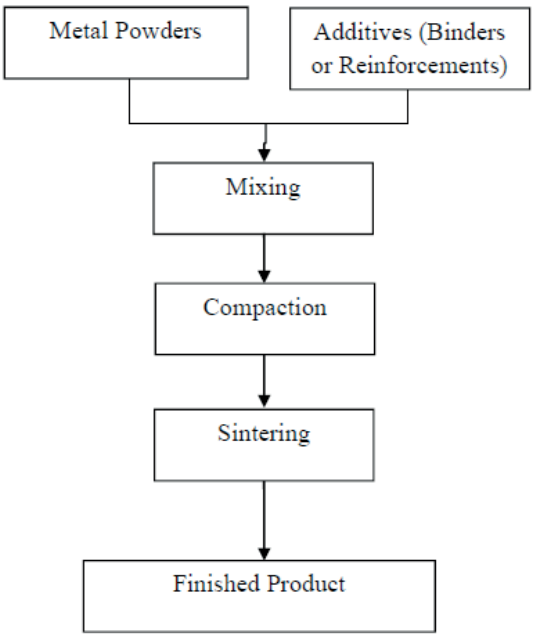


Figure 1. A flowchart of the basic Powder Metallurgy process for structural press and sintered components [20].

2.2 Liquid State Method

Most MMCs are made with low melting point Al alloys. For this reason, liquid state processing methods for MMCs can be applied more easily than solid state processing methods. With the liquid state processing method, reinforcements are included in the molten metal matrix material. During the liquid state processing process, ceramic reinforcements are incorporated into the molten metallic matrix. Afterwards, it is mixed and poured into components in different shapes or billets

for further production stages. In the process, it is essential that the selection is made by considering the compatibility of the ceramic reinforcement with the matrix alloy [15].

Liquid state processing methods commonly used in the production of Aluminum Metal Matrix Composites (Al MMCs) can be classified as stir casting, squeeze casting and compo-casting. Brief information about these methods are presented below.

2.2.1 Stir Casting

In the production of Al MMCs, the simplest and most commercially used technique as the liquid state production method is the stir casting technique. In this method, the solid reinforcement is simply mixed in the liquid metal and then allowed to solidify in a suitable mold. The matrix material is melted at a temperature above its melting temperature before the reinforcement material is added, and reinforcement is added gradually. The mixture can be agitated continuously as the reinforcement is added to the matrix material. The main thing in this process is to create a good wetting between the particle reinforcement and the liquid aluminum alloy melt [20].

2.2.2 Squeeze Casting

Squeeze casting is a fusion metal forming process that combines fixed die casting and die forging in a single operation. In this process, a certain amount of molten phase matrix metal alloy is poured into a pre-heated lubricated mold, and the next step is forging and solidification under hydrostatic pressure [14].

2.2.3 Compo-casting

Compo-casting is a semi-solid processing method in which ceramic reinforcement particles are added to the semi-solid matrix alloy by mechanical mixing. There are two different versions of this technique: semisolid-semisolid (SS) and semisolid-liquid (SL). In both versions, the matrix alloy is semisolid during the mixing step, while during the casting step the matrix is partially liquid or fully liquid for the SS and SL routes, respectively. Porosity and machining difficulties are the biggest disadvantages of the SS method [15].

3. Reinforcing materials in Al MMCs

It is possible to classify the reinforcement materials used in the development of Al MMCs in three broad groups: synthetic ceramic particles, industrial wastes and agricultural waste derivatives [17]. The individual properties of the chosen reinforcement and matrix alloy determine the final properties of Al MMCs [21-23]. The nature of the matrix alloy and reinforcement material is taken into account in the processes applied to synthesize Al MMCs. When the studies are examined, it has been determined that most of the parameters (reinforcement type, size, shape, modulus of elasticity, hardness, distribution of reinforcement in the matrix) taken into account during the design of Al MMCs are related to the reinforcement material used [13]. Based on the reviewed published articles, the reinforcements used in the Al MMCs produced by the powder metallurgy technique examined and the effect on the mechanical properties of the final composite material reported according to the proportions of the reinforcements.

4. Literature Survey

Ravichandran et al. produced TiO_2 reinforced Al-MMCs using liquid powder metallurgy method. The matrix and reinforcements have been verified by metallurgical tests. When the tensile strength and hardness properties of the obtained composite materials were examined, the best mechanical properties were determined in the mixture of pure aluminium with TiO_2 (5% weight) [24]. In

another study, graphene oxide (GO) powder was dispersed into AlMg5 matrix using high energy ball milling. The resulting mixture was then fully densified by hot pressing. They found that 1% vol. of GO addition to the Al alloy matrix led to a significant improvement in the mechanical resistance of the composite. Nevertheless, they found that the ultimate tensile strength (540 MPa) and the macro hardness (166 HV) values are increased by a factor of 2 compared to the same AlMg5 alloy without nanoparticle material and compacted under the same conditions. It was observed that the bending strength increased 4 times and reached a value above 800 MPa [25]. Al-xNi-yCeO_2 (x = 6, 10, 15, 20 and y = 0, 5, 10 wt%) composites were produced by powder metallurgy method. Al, Ni and CeO_2 powder mixtures were produced by mechanical alloying (MA) for 4 hours in a Spex type high energy ball mill. The effects of MA treatment and Ni and CeO_2 amounts on the microstructural, mechanical and tribological properties of sintered composites were determined. The hardness values of sintered composites increased with mechanical alloying and increasing Ni and CeO2 amounts. In addition, according to the reciprocating wear test results showed both the wear resistance and hardness values of the composites increased with increasing Ni and CeO_2 amounts [26].

Amin Azimi et al. studied the mechanical behavior of AA7075/TiC composites produced by powder metallurgy. They reported that the tensile behavior of the investigated composites increased and this was due to the fine distribution of the particles on the matrix material [27]. In another study, the mechanical and thermal behavior of Al/Acrawax lubricant powder was investigated and it was determined that the presence of lubricant on the matrix material caused a decrease in mechanical properties, and that the sintering process created structures with less porosity in composite structures [28]. Sajjad Arif et al. investigated the mechanical behavior and microstructural modifications of pure Al/SiC composites produced by powder metallurgy routine. It was observed that the addition of SiC improved the mechanical and wear behavior of the composites [29]. In another study, the wear behavior of composites developed by AA6061 matrix liquid pressure infiltration process containing 20 vol.% Saffil (Alumina fibers) + SiC was investigated. It was determined that the wear resistance of the composite increased with the increase in weight of SiC compared to the composites containing saffil [30]. Dhanashekar et al. investigated the mechanical properties and wear behavior of AA6061/Silicon Carbide (SiC), varying weight percentage of SiC particles (0, 2. 5, 5 and 7.5 wt%), composites produced by powder metallurgy technique. As a result of the analysis, it was observed that the hardness and compressive strength values of the composite increased with the addition of increasing reinforcement. The produced composites showed a good sintering reaction and the obtained density was maximum. The wear rate of the composites decreased with increasing SiC ratio by weight [31].

Wang et al. produced Al composites reinforced with carbon nanotubes (CNTs) in two aspect ratios using different powder metallurgy methods, followed by spark plasma sintering and hot extrusion methods. The mechanical properties of CNT reinforced Al composites were tested at various loading rates to determine the effect of CNTs on the strength of the composite. Mechanical tests revealed that the addition of CNTs to the Al matrix increased not only the strength but also the strain rate sensitivity compared to pure Al. Under dynamic loading, the composites showed an increase in strength and elongation-to-failure simultaneously due to the increasing strain hardening rates [32]. Surya et al. investigated the microstructure and mechanical properties of SiCp reinforced Al7075 metal matrix composites. Al/SiC composites containing 0, 5, 10, 15, 20, 25 and 30 wt% SiC were produced by compression, mixing and sintering processes, respectively. They found that composites containing 15 wt% SiC had higher mechanical properties such as hardness,

toughness and bending strength compared to other samples due to uniform distribution of SiC particles [33]. In other study, Aluminum-Titanium carbide (TiC) metal matrix composites were produced by powder metallurgy technique in which mechanical alloy powders were sintered in three different volume fractions: 100%-Al, 95%-Al and 5%-TiC and 90%-Al and 10%-TiC. Mechanical tests have shown that the addition of SiC to the Al matrix significantly increases the hardness of the final composite [34]. Mhaske et al. investigated the mechanical properties and microstructural analyzes of Al-SiC composites under different process conditions. The hardness, compression strength and shear strength values of Al-SiC composites containing 5, 10 and 15 wt% SiC were investigated. It was emphasized that the composite containing 15 wt% SiC possesses the optimum mechanical properties desired [35]. Prakash et al. produced multi-walled carbon nanotube (MWCNTs) reinforced Al6061 alloy by powder metallurgy method. The distribution of carbon nanotubes in the Al matrix carried out by microstructure investigations using scanning electron microscopy. When the micro hardness, impact strength and ultimate tensile strength of Al6061 alloy and Al6061 alloy-MWCNTs composites were examined, it was determined that the addition of MWCNTs to the Al6061 alloy improved these properties [36].

The mechanical behavior of Al matrix composites reinforced with 5, 10 and 20 wt% kaolin reinforcements was investigated by Venkatesh et al. tensile strength, compressive strength, density and hardness tests were performed on the produced composite samples. They found that the hardness of the Al matrix composite containing 20% by weight of A-kaolin increased from 77 VHN to 187 VHN. They also determined that the tensile and compressive strength of the final composite increased with the addition of reinforcement from 0% to 20% due to the presence of hard ceramic particles such as Al_2O_3 and SiO_2 in the kaolin reinforcement. In particular, it was found that the tensile strength increased by 54.8% with the addition of 20 wt% compared to pure Al [37]. Zaki et al. aimed to achieve better mechanical properties of the Al composite by mixing boron carbide (B_4C) & manganese (Mn) powders at 2, 4 and 6 wt% to the Al matrix with powder metallurgy technique. They reported that the addition of B_4C from 2% to 4% to the Al matrix increases the hardness of the composite, but the addition of from 4% to 6% B_4C reduces the hardness of the composite. As well as, the Rockwell hardness values of Al-B_4C-Mn was examined, it was revealed that the addition of Mn from 2% to 4% decreased the hardness of the composite, while the addition of Mn from 4% to 6% increased the hardness of the composite [38]. Karabulut et al. produced Al6061 reinforced with 5–20 wt% B_4C using a powder metallurgy method. They reported that the hardness value of the composite samples increased with increasing B_4C content and the maximum hardness value formed for 20% B_4C [39]. Jeevan et al. investigated Aluminum alloy 6082 (AA6082) reinforced with zirconia toughened alumina with different weight fractions. They observed that the increase in the weight fraction of ZTA resulted in a sustained increase in the hardness of the AA6082/ZTA composites due to hard particles obstruct the dislocation motion and increase the strength and hardness of a material [40]. Kumar et al. also mentioned the similar effect of the addition of TiO_2 on the hardness of Al-15wt.%SiC/TiO_2 hybrid composites [41].

5. Conclusions

This paper presents information about Al matrix materials (pure Al, AlMg5, AA7075, AA6082, etc.) and reinforcement materials (TiO_2, GO, TiC, ZTA, B_4C, etc.) used in Al matrix composites produced by powder metallurgy method and detailed information about the effect of reinforcement material selection on the mechanical properties of the produced composites. A wide variety of reinforcement materials, ranging from hard ceramics to nanomaterials have been observed in the production of Al matrix composites. It has been observed that the addition of various hard particles to the Al matrix materials increases the strength and hardness of the composite because it prevents

the dislocation motion. Also ultimate tensile strength and the macro hardness values are increased by a factor of 2 chance in Al MMCs. Bending strength properties almost increased 4 times of base aluminum alloy. In addition, the process techniques for the production of these composites are also included. In the reported studies, it has been understood that the powder metallurgy method is the most widely used process method due to its ease of operation and low cost compared to other production methods. However, there is a clear need to experiment with more matrix and reinforcement configurations in this area in order to produce sustainable, reliable and better service life Al MMCs. In addition, it would be beneficial to focus on improving the properties of Al MMCs, such as fatigue, oxidation behavior and corrosion behavior, which needed in application areas. Still, the field of AI-MMCs is under development. It is obvious that the new generation hybrid composites still show some limitations and are therefore open to future research.

References

1. Nijssen, R.P.L. Composite materials—an introduction. 1st English ed, Delft, the Netherlands: Inholland University of Applied Sciences. **2015**.
2. Puttegowda, M., Rangappa, S.M., Jawaid, M., Shivanna, P., Basavegowda, Y., and Saba, N. Potential of natural/synthetic hybrid composites for aerospace applications. Sustainable Composites for Aerospace Applications, Woodhead Publishing Series in Composites Science and Engineering **2018**, 315-351.
3. Kumar, S.A., Bhandari, R., Aherwar, A., Rimašauskienė, R., Pinca-Bretotean, C. A study of advancement in application opportunities of aluminum metal matrix composites. Mater. Today Proc. **2020**.
4. Mukhopadhyay, P. Alloy designation, processing, and use of AA6XXX series aluminium alloys. ISRN Metall. **2012**.
5. Das, D.K., Mishra, P.C., Singh, S., Pattanaik, S. Fabrication and heat treatment of ceramic-reinforced aluminium matrix composites – a review. Int J Mech Mater Eng. **2014**, 9(1):1–15.
6. Vogt, R.G., Zhang, Z., Topping, T.D., Lavernia, E.J., Schoenung, J.M. Cryomilledaluminum alloy and boron carbide nano-composite plate. J. Mater. Process. Technol. **2009**, 209(11): 5046–5053.
7. Manohar, G., Pandey, K.M., Maity, S.R. Aluminium ({AA}7075) metal matrix composite reinforced with B4C nano particles and effect of individual alloying elements in AL fabricated by powder metallurgy techniques. J. Phys. Conf. Ser. **2020**, 1451:12024.
8. Manohar, G., Dey, A., Pandey, K.M., Maity, S.R. Fabrication of metal matrix composites by powder metallurgy: a review. AIP Conf. Proc. **2018**, 1952.
9. Manohar, G., Pandey, K.M., Maity, S.R. Effect of compaction pressure on mechanical properties of AA7075/B4C/graphite hybrid composite fabricated by powder metallurgy techniques. Mater. Today: Proc. **2020**, 0–4.
10. Kareem, A., Qudeiri, J.A., Abdudeen, A., Ahammed, T., and Ziout, A. A Review on AA 6061 Metal Matrix Composites Produced by Stir Casting. Materials. **2021**, 14(175).
11. Shrivastava, V., Gupta, G.K., Singh, I.B. Heat treatment effect on the microstructure and corrosion behavior of Al-6061 alloy with influence of a nanoalumina reinforcement in 3.5% NaCl solution. J. Alloy. Compd. **2019**, 775:628–638.
12. Niraj, N., Pandey, K.M., Dey, A. Tribological behaviour of Magnesium Metal Matrix Composites reinforced with fly ash cenosphere. Mater. Today: Proc. **2018**, 5(9):20138–20144.
13. Das, D.K., Mishra, P.C., Singh, S., Pattanaik, S. Fabrication and heat treatment of ceramic-reinforced aluminium matrix composites – a review. Int J Mech Mater Eng. **2014**, 9(1):1–15.

14. Saikrupa, C., Chandra M.R.G., and Venkates, S. Aluminium metal matrix composites and effect of reinforcements – A Review. IOP Conf. Series: Materials Science and Engineering. **2021**, 1057:012098.
15. Noor, E.E.M., Syazwani N.S., and Al Bakri, A.M.M. Fabrication Method of Aluminum Matrix Composite (Amcs): A Review. Key Engineering Materials. **2016**, 700:102-110.
16. Miracle, D.B. Metal matrix composites – from science to technological significance. Compos Sci Technol. **2005**, 65(15–16):2526–40.
17. Bodunrina, M.O., Alanemea, K.K., Chown, L.H. Aluminium matrix hybrid composites: a review of reinforcement philosophies; mechanical, corrosion and tribological characteristics. J mater res technol. **2015**, 4(4):434-445.
18. Panwar, N. Development of Aluminum Composites using Red Mud as Reinforcement- A review. **2014**.
19. Tong, X.C. Advanced Materials for Thermal Management of Electronic Packaging. **2011**.
20. Tripathy, S. Studies on Al-Fly ash Composite Produced by Impeller Mixing. Bachelor of Technology. **2007**.
21. Alaneme, K.K., Aluko, A.O. Fracture toughness (K1C) and tensile properties of as-cast and age-hardened aluminium (6063) –silicon carbide particulate composites. Sci Iran. **2012**, 19(4):992–6.
22. Alaneme, K.K., Aluko, A.O. Production and age-hardening behaviour of borax premixed SiC reinforced Al-Mg-Si alloy composites developed by double stir-casting technique. WestIndian J Eng. **2012**, 34(1–2):80–5.
23. Alaneme, K.K., Bodunrin, M.O. Mechanical behaviour of alumina reinforced Aa 6063 metal matrix composites developed by two step – stir casting process. Acta Tech Corvininesis – Bull Eng. **2013**, 6(3):105–10.
24. Ravichandran, M., Dineshkumar, S. Synthesis of Al-TiO2 Composites through Liquid Powder Metallurgy Route. International Journal of Mechanical Engineering. **2014**, 1:12-15.
25. Kwon, H., Mondal, J., AlOgab, K.A., Sammelselg, V., Takamichi, M., Kawaski, A., Leparoux, M. Graphene oxide-reinforced aluminum alloy matrix composite materials fabricated by powder metallurgy. Journal of Alloys and Compounds. 2017, 698:807-813.
26. Akcamlı, N., Senyurt, B. Fabrication and characterization of in-situ Al3Ni intermetallic and CeO2 particulate-reinforced aluminum matrix composites. Ceramics International. **2021**, 47: 21197–21206.
27. Azimi, A., Shokuhfar, A., Nejadseyfi, O. Mechanically alloyed Al7075-TiC nanocomposite: Powder processing, consolidation and mechanical strength. Mater. Des. **2015**, 66:137–141.
28. Gokce, A., Findik, F. Mechanical and physical properties of sintered aluminum powders. J. Achieve. Mater. Manuf. Eng. **2008**, 30:157–164.
29. Arif, S., Alam, M.T., Ansari, A.H., Siddiqui, M.A., Mohsin, M. Investigation of Mechanical and Morphology of Al-SiC composites processed by PM Route. IOP Conf. Series: Mater. Sci. Eng. 2017, 225:012277.
30. Gurcan, A.B., Baker, T.N. Wear behaviour of AA6061 aluminium alloy and its composites. Wear. 1995, 188:185–191.
31. Dhanashekar, M., Loganathan, P., Ayyanar, S., Mohan, S.R., Sathish, T. Mechanical and wear behaviour of AA6061/SiC composites fabricated by powder metallurgy method. Materials Today: Proceedings. **2020**, 21:1008–1012.
32. Wang, M., Li, Y., Chen, B., Shi, D., Umeda, J., Kondoh, K., Shen, J. The rate-dependent mechanical behavior of CNT-reinforced aluminum matrix composites under tensile loading. Materials Science & Engineering A. **2021**, 808:140893.

33. Surya, M.S., Prasanthi, G. Manufacturing, microstructural and mechanical characterization of powder metallurgy processed Al7075/SiC metal matrix composite. Materials Today: Proceedings. **2021**, 39:1175–1179.
34. Albert, T., Sunil, J., Simon Christopher, A., Jegan, R., Anand Prabhu, P., Selvaganesan, M. Preparation and characterization of aluminium-titanium carbide (Al-TiC) composite using powder metallurgy. Materials Today: Proceedings. **2021**, 37:1558–1561.
35. Mhaske, M.S., Shirsat, U.M. An investigation of mechanical properties of aluminum based silicon carbide (AlSiC) metal matrix composite by different manufacturing methods. Materials Today: Proceedings. **2021**, 44:376–382.
36. Prakash, B., Sivananthan, S., Vijayan, V. Investigation on mechanical properties of Al6061 alloy – Multiwall carbon nanotubes reinforced composites by powder metallurgy route. Materials Today: Proceedings. **2021**, 37:336–340.
37. Venkatesh, V.S.S., Deoghare, A.B. Fabrication and mechanical behaviour of Al-Kaoline metal matrix composite fabricated through powder metallurgy technique. Materials Today: Proceedings. **2021**, 38:3291–3296.
38. Zaki, M.U., Hussain, S. Impact of addition of manganese and boron carbide on aluminium metal matrix composites using powder metallurgy process. Materials Today: Proceedings. **2021**, 44:4364–4368.
39. Karabulut, Ş., Karakoç, H., Çıtak, R. Influence of B4C particle reinforcement on mechanical and machining properties of Al6061/B4C composites. Composites Part B. **2016**, 101:87-98.
40. Jeevana, V., Rao, C.S.P., Selvaraj, N., Rao, G.B. Mater. Today: Proc. **2018**, 5:254–260.
41. Kumar, C.A.V., Rajadurai, J.S. Influence of rutile (TiO2) content on wear and microhardness characteristics of aluminium-based hybrid composites synthesized by powder metallurgy. Trans. Nonferrous Met. Soc. China. **2016**, 26:63–73.

USING LIGHTWEIGHT EXPANDED GLASS AGGREGATE TO PRODUCE A LIGHTWEIGHT GEOPOLYMER MORTAR

AHMAD AL MOHAMMAD[a,b]

[a]Department of Civil Engineering, Gaziantep University, Gaziantep, TURKEY.
[b]Department of Civil Engineering, Aleppo University, Aleppo, SYRIA.

Abstract

The effects of utilizing lightweight (expanded glass) aggregate (LEGA) on the characteristics of lightweight geopolymer mortar are investigated in this study. The mechanical characteristics of LWGM are also investigated as a function of temperature (room temperature, 250°C, and 500°C). With 10% and 20%, LEGA can be utilized as a partial replacement for river sand. Slag was used as the basic material for LWGM, which was activated with a solution of sodium silicate and sodium hydroxide. At room temperature, three distinct combinations were produced and cured. The characteristics of workability and density were tested for the fresh situation. To examine the mechanical characteristics of LWGM, a number of experiments were carried out, including compression tests. The study discovered that when the degree of LEGA replacement increases, the density and compressive strength of the LWGM decreases. The mechanical characteristics of examined materials exposed to extreme temperatures of 500°C altered considerably, according to the experimental data.

Keywords: Lightweight Geopolymer Mortar (LWGM), Lightweight Expanded Glass Aggregate (LEGA), Elevated Temperatures, Mechanical Characteristics.

1. Introduction

The tremendous need for basic Portland cement concrete (OPC)) results in an ecological imbalance due to the emission of large amounts of carbon dioxide (CO2) and the continuous consumption of natural resources. As you know, the cement manufacturing process pollutes the air by releasing carbon dioxide gases into the atmosphere. OPC production's contribution to carbon dioxide emissions accounts for approximately 6% of total output of greenhouse gases[1]. In order to reduce the carbon footprint in buildings industry and use industry by-product materials it is necessary to create alternative binders. Geopolymer (GP) is a new kind of eco-friendly inorganic binder produced from industrial by-products and a concrete replacement binder [2] Compressive strength rises as the curing temperature and time rise. The full-strength value can be achieved by curing at temperatures ranging from 60 to 90 degrees Celsius for a period of 24 to 72 hours [3].

2. Experimental Study

2.1 Materials

2.1.1 River Sand

The locally available river sand is utilized. River sand has been partially replaced by LEGA in this study. River sand is 2.68 in particular, 2.86 in the fine module and 0.58 % in all geopolymer mixtures, in water absorption is used. Figure 1 shows the river sand used in this study.



Figure 1. River sand used in this study

2.1.2 Expand glass

Expanded glass granulates, made from recycled glass residues, are used as lightweight aggregates as illustrated in Table1.

Table 1. Expanded glass granulates

Chemical Analysis - XRF Method	
Constituent	%
Loss on Ignition (LOI)	2,33
CaO	4,35
SiO_2	72,95
Al_2O_3	0,41
TiO_2	0,03
FE_2O_3	0,09
Mn_2O_3	0
MgO	0,89
K_2O	0,2
Na_2O	18,74
SO_3	0
Cl	0

2.1.3 Slag

In an alkaline setting, a pozzolanic material, GGBFS, was used as a binding material to produce lightweight geopolymer mortar. (Slag) that met standards was used. As determined by X-ray fluorescence, the physical and chemical properties of GGBFS are described in Table 2.

Table 2. Properties of GGBFS. (slag)

Compounds	Slag (%)
CaO	34.12
SiO_2	36.4
Al_2O_3	10.39
Fe_2O_3	0.69
MgO	10.3
SO_3	0.49
K_2O	0.97
Na_2O	0.35
TiO_2	-
L.O.I	1.64

2.1.4 Water
To make NaOH solution, this kind of water is used to dissolve sodium hydroxide

2.2 Experimental Study
(Mix Design, casting and curing of samples)
The three stages of an experimental investigation are the most important. The first stage focuses on the production of geopolymer mortar using local slag and the growth of compressive power over various curing periods and temperatures. The alkaline is a 1:2.5 mixture of 12M NaOH solution and $Na_2 SiO_3$.

2.2.1 Preparation of Alkaline Activator Solution
By dissolving NaOH beads in water, the NaOH solution was created. The solid weight of sodium hydroxide in a solution change depending on the solution concentration, which is typically expressed in molarity (M). The concentration of NaOH used in this study was 12M. First, dissolve 495 gm of NaOH solid in 505 gm water per liter to produce an alkaline solution. The solution was then allowed to cool at room temperature. The final alkaline solution for geopolymer mortar manufacturing was made by mixing NaOH solution with Na2SiO3 solution and leaving it for at least 24 hours.

2.2.2 Mixing and Casting
As saturated surface dry (SSD) conditions, limestone crushed aggregates were used. First, dry materials (fine, coarse aggregates, and GGBFS) were combined in a pan mixer for 2.5 minutes. The alkali activator solution, which included NaOH and Na2SiO3, was then slowly applied to the superplasticizer and mixed for 3.5 minutes. Using cube specimens 70*70*70 mm^3, specimens were cast and compacted in two layers as test specimens. All specimens have been vibrated for 35 seconds to eliminate the air vacuum. To avoid the evaporation of the alkali activator solution, the GPM specimens were covered with a plastic bag for 24 hours to minimize water evaporation during curing and then kept at room temperature for a rest time. Table 3 depicts all of the data of mix designs.

Table 3. Lightweight geopolymer mortar mix designs

Mix Code	Mixture ID	Binder	Na2SiO3/ NaOH	Molarity	Aggregates		Superplasticizer (gm)
		Slag (gm)			Sand (gm)	Lightweight Aggregate (gm)	
Mix design (For 1L)	Mix design LWGM 10% (1L)	500	2.5	12M	1350	150	25
Mix 1	LW10%EG	10000	2.5	12M	27000	3000	500
Mix 2	LW20%EG	7500	2.5	12M	18000	4500	860

2.2.3 Curing
The GPM specimens were covered with a plastic bag for 24 hours after casting to prevent the alkali activator solution from evaporating. The GPM specimens were oven cured for 48 hours at 250°C before being increased to 500°C. However, the first 24 hours are crucial. The molds were removed and the specimens were wrapped in plastic bags before being returned to the oven.

3. Results and discussion

3.1 Workability

As one may observe, the workability for the First Mix is (12) cm which is higher than the Second Mix (10) cm. As we notice that Mix 1 contains 10% of the lightweight aggregates (expanded glass) got higher workability than Mix 2 that contains 20% of the lightweight aggregates (expanded glass) as illustrated in Table 4 and Figure 2. Consequently, the flow percentage increases with the decrement of the percentage of lightweight aggregates.

Table 4. LWGM's flow table

Mix Code	Mixture ID	Binder Slag (gm)	Na2SiO3/ NaOH	Molarity	Superplasticizer (gm)	Workability (Cm)
Mix design (For 1L)	LWGM 10%(1L)	500	2.5	12M	25	
Mix 1	LW10%EG	10000	2.5	12M	500	12
Mix 2	LW20%EG	7500	2.5	12M	860	10.7

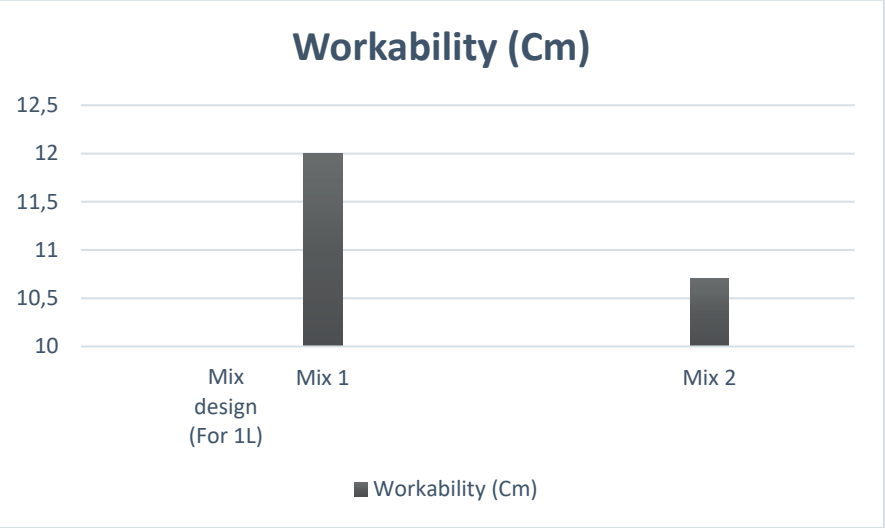


Figure 2. Flow table of different percentage mixes of lightweight aggregates

3.2 Density Test

For all mixes, the density was measured. Table 5 shows the results that the unit weight is decreasing over time beginning from the fresh unit weight until 28 days unit weight because of the evaporation that happens over time. Additionally, the fresh unit weight for the First Mix is (2.02) g/cm^3 which is higher than the Second Mix (1.734) g/cm^3. As one can observe that Mix 1 contains 10% of the lightweight aggregates (expanded glass) got higher fresh unit weight than Mix 2 that contains 20% of the lightweight aggregates (expanded glass). The 20% EG specimen had a fresh density that was 14.16% lower than the 10% EG specimen. Furthermore, increasing the age of the LWGM from 1 to 28 days results in a slight drop in dry density values, as seen in the table. When comparing the dry density of the 20% EG sample to that of the 1day sample, there was a 3.22% drop in 28 days as presented in Figure 3. Consequently, the fresh unit weight percentage increases with the decrement of the percentage of lightweight aggregates in the mixture due to the decrease of mixture weight. Due to the much lower density of LWA, the density of the mixtures drops as the volume replacement of sand by LWA increases.

Table 5. Unit Weight of LWGM

Mix Code	Mixture ID	Fresh unit weight (g/cm^3)	1-day	7-day	28-day
Mix 1	LW10%EG	2.02	2.015	2.011	1.99
Mix 2	LW20%EG	1.734	1.73	1.72	1.676

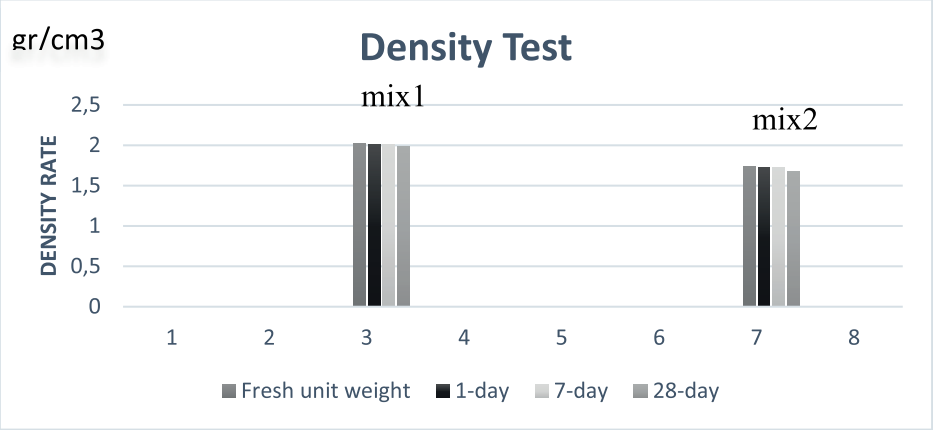


Figure 3. Unit Weight of LWGM

3.4 Effect of the LWA percentage (expanded glass) LEGA on the Strength of compressive for cubes

Three specimens were tested in order to get an average of the results. Cubes were tested for compressive strength after 1, 4, 7, and 28 days. Figure 4 illustrates that regardless of the LEGA content in the mixture, the compressive strength of samples increased with age. However, as the LEGA replacement amount was increased, the compressive strength gradually decreased. The 28-day compressive strength of the geopolymer mortar containing 10% LEGA was 17.9 MPa, whereas that of the geopolymer mortar containing 20% LEGA was just 6.9 MPa, indicating a 61.45% drop in strength as demonstrated in Table 6 and Figure 4.

Table 6. Compressive strength of geopolymer mortar (MPa) with different LWA percentages

		Geopolymer mortar compressive strength (MPa)			
		1 day	4 days	7 days	28 days
Mix 1	LW10%EG	1.58	5.37	7.37	17.9

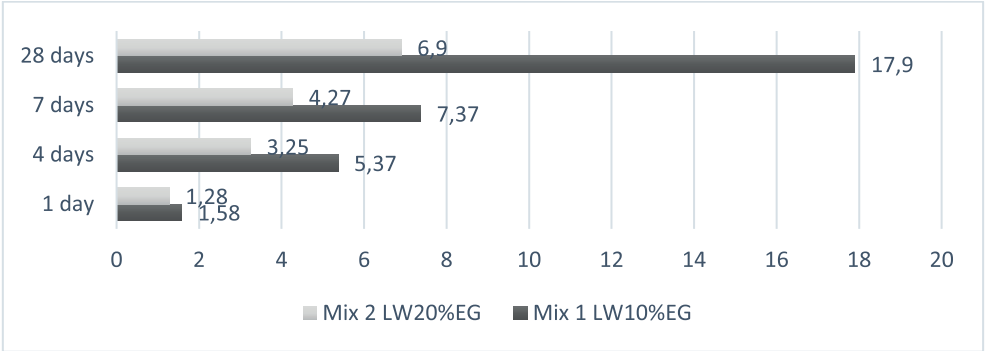


Figure 4. Geopolymer mortar compressive strength (MPa) at various LWA percentages

• When the sand was replaced with LWA (expanded glass), the compressive strength was reduced. The stronger the effect, the higher the replacement. This could be due to the LWA's reduced crushing resistance when compared to sand.
• When a larger volume of sand is replaced by LWA, the strength grows after 7 days slower. Because of the LWA's water absorption. The rate of polycondensation may be slower with time, resulting in a porous microstructure and decreased compressive strength.

3.5 Effect of the Curing Temperature on the compressive strength for cubes:

Table 7. Results of compressive strength before and after exposure to high temperatures

Compressive strength of geopolymer mortar (MPa)				
		ambient	250 °C	500 °C
Mix 1	LW10%EG	17.9	16.78	9.02
Mix 2	LW20%EG	6.9	7.16	3.68

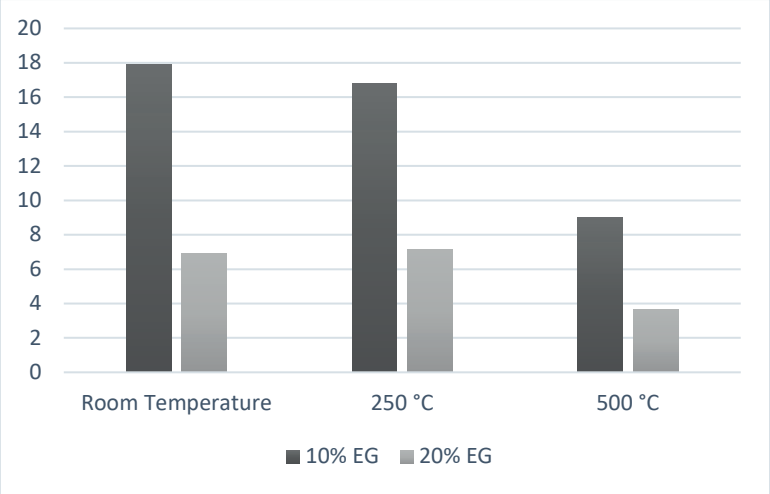


Figure 5 Results of compressive strength before and after exposure to high temperatures

The compressive strength results after exposure to elevated temperatures of 250°C and 500°C are shown in Figure 5. The compressive strength values for samples at room temperature (10% EG) were higher than the compressive strength findings after exposure to elevated temperatures of 250°C and 500°C, as shown in the Figure. The results for 10% EG at room temperature, for example, were 6.26% and 49.61% higher than the same samples at 250°C and 500°C, respectively. However, the compressive strength values for samples at 250°C (20% EG) were higher than the compressive strength findings after exposure to elevated temperatures of room temperature and 500°C [3]. The results for 20% EG at 250°C were 3.63% and 48.6% higher than the same samples at room temperature and 500°C, respectively, as illustrated in Table 7.

The significant thermal shrinkage caused by the vaporization of water from the geopolymer structure was attributed to the decrease in strength at 500°C. As the heating temperature rises, the water is converted into water vapor, and the pressure of the water vapor rises. When the vapor pressure reaches its absolute limit, the matrix with lower permeability will be unable to withstand the high thermal stresses, resulting in extreme thermal cracks on the surfaces or within sections of the samples and a decrease in compressive strength [4]. The difference in thermal expansion between the geopolymer matrix and lightweight aggregate is another reason for the loss of strength

[3] confirmed a similar finding regarding the deterioration of compressive strength of lightweight geopolymer mortar (Expanded Glass) after exposure to high temperatures [5].

However, the greatest compressive strength percentage of lightweight geopolymer mortar for 20% EG samples was 7.16 MPa at 250°C, while the compressive strength reduced to 3.63% and 48.6% at ambient temperature and 500°C, respectively. The factors in the increase in strength at 250°C were evaporation of free water due to sintering at this temperature, as well as a mix of geopolymer matrix and aggregates. Additionally, bonding and strength at 250°C, were improved as well.
When the temperature was raised to 500°C, however, all of the samples' strength declined, as shown in Figure 5. The compressive strength of the 10% EG sample declined from 17.9 MPa at ambient temperature to 9.02 MPa at 500°C.

4. Conclusion

Based on the experimental findings of this study, the following conclusions can be summarized:

- According to the most recent LWGM test findings, raising the LECA replacement amount lowers LWGM workability.
- Due to its low density, the fresh and dry density of geopolymer mortar dropped as the LEGA concentration rose. According to the findings, all of the geopolymer mortar mixes created in this study may be classified as lightweight by ACI committee 213R.
- When river sand was replaced with LEGA, the compressive strength of the geopolymer mortar was reduced at 1, 7, and 28 days. The porous nature of the LEGA particles was to blame for this.

References

1. Davidovits, J. Global warming impact on the cement and aggregates industries. World Resource Review. **1994**, 6(2):263–278.
2. Bnhussain, M., Nizar, K.I., Rafiza, A.R., and Zarina, Y. The processing, characterization, and properties of fly ash based geopolymer concrete. Reviews on Advanced Materials Science. **2012**, 30(1):90–97.
3. Oleiwi, S. M. Mix optimization and experimental evaluation of lightweight geopolymer mortars. Hasan Kalyoncu Üniversitesi. **2017**, 1-172.
4. Abdulkareem, O. A., Abdullah, M.M.A.B., Hussin, K., Ismail, K. N., and Binhussain, M. Mechanical and microstructural evaluations of lightweight aggregate geopolymer concrete before and after exposed to elevated temperatures. Materials. **2013**, 6(10):4450–4461.
5. Ameri, F., Shoaei, P., Zareei, S.A., and Behforouz, B. Geopolymers vs. alkali-activated materials (AAMs): A comparative study on durability, microstructure, and resistance to elevated temperatures of lightweight mortars. Construction and Building Materials. **2019**, 222:49–63.

DETECTION AND CLASSIFICATION OF FRESH PISTACHIOS USING DEEP LEARNING

AHMET EMİN KARADAĞ [*1], ALİ KILIÇ [1]

[1] Gaziantep University, Engineering Faculty, Mechanical Engineering Department, Gaziantep, TURKEY.

Abstract

In marketing, quality of a product has a prominent role in sales. In order to ensure the quality of a product, quality inspection is necessary step on the production line. The purpose of this study is to detect red hulled pistachios and yellow hulled pistachios in an image. The reason for this detection us to help a system to separate blank pistachios without submerging them in water. In order to achieve this a deep learning algorithm specialized in object detection was trained. Accuracy achieved with the detection algorithm was satisfactory, for both red hulled pistachio and yellow hulled pistachio.

Keyword: Classification of Pistachio, Deep Learning, Object Detection

1. Introduction

Quality inspection was and always going to be one of the most important part of any type of product. The reason behind it is the benefits it provides for the producer. One such benefit is quality inspection may provide insight for the production line before the inspection. The producer my use the data from this inspection to adjust the prior steps in the production line. This in turn may shorten some steps or may result in decrease in the amount of product used in a production step. Another benefit is, no matter how good a marketing of a product is, lasting impression comes from the quality of product the consumer receives.

Pistachio, a type of fruit, is an agricultural product that has importance for Turkey. According to the Food and Agriculture Organization, Turkey is the third biggest pistachio producer through 1994 to 2019 [1]. Pistachio is not only important for exporting, it also has a cultural importance in Turkey. It is eaten as a snack, but it is also widely used in desserts, especially in baklava, most commonly known dessert from Turkey. Production steps of salted pistachio are as following:

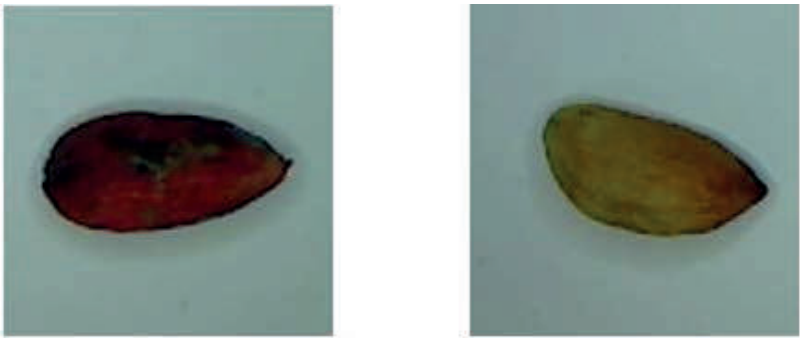
- Dehulling,
- Thrash removing,
- Drying
- Cracking,
- Salting and roasting.

Although, all the processing mentioned can be done on a dry environment, such as dehulling pistachio with abrasive plates or removing thrash with pressurized air, one step cannot be done without using water: blank separation. Blank separation can be done between any steps before cracking and it is done by submerging pistachio into water and separating the floating ones as

blanks. This creates two problems. Firstly, increased moisture will add the time for drying of pistachios. Secondly, moisture content, as is commonly known, will increase the probability of molding and causes aflatoxin formation.

With the advancements in both computer processors and machine learning algorithms there are plethora of researches on quality inspection on food. Siddiqi [2] trained two separate algorithms called YOLOv2 (You Only Look Once) and Single Shot Detection (SSD) to detect defected areas on apples. Dataset contains 244 images, 218 of them for training and remaining for testing. End result is passable but needs some improvements. Wang et al. [3] have trained machine vision system to determine defected areas on fruits. It's done on the idea of fruits having a brownish area where defection is. The algorithm that is trained is called SVM using 600 images, 300 hundred of them are defected. End result is 96.7% detection rate. Thuyet et al. [4] trained a convolutional neural networks (CNN) algorithm called Mask-RCNN to inspect processed garlics. In Japan, garlic roots are trimmed for marketing reasons but this operation is tedious, such as if it is trimmed too much, it harms the garlic, but when trimming is not enough it goes to cutting again. In the project, detection accuracy was average of 98%.

Purpose of this research is to detect pistachios in a given image pistachios according to its hull color (see Figure 1). The reason for it is because yellow hulled pistachios are more prone be blank pistachios. This way, producer may submerge only the yellow hulled pistachios (which in turn lowers the water consumption) or may sell them as "low grade" product. The aim is achieved by training a deep learning algorithm specialized on object detection.



(a) (b)

Figure 1. (a) Red hulled pistachio, (b) yellow hulled pistachio

2. Detection Algorithm

In this research, it was desired to detect pistachios even when they are clustered together, i.e. pistachios are too close to each other to be separated from background easily. So, for that purpose, it was decided to use an object detection algorithm. Object detection algorithms are algorithms that classifies an object in the image, and give its position in pixel values. Object detection algorithms uses CNN as its backbone for classification.

CNNs are specialized deep learning algorithms that are used for image classification. At the basic, what is done with image processing, i.e. extracting features from an image, using this features the determine the object in the image, is done automatically. These algorithms mainly consist of two layers: convolution layer and fully connected layer. In convolution layer, algorithms processes images with kernels. In fully connected layer, a decision is made based on the information collected from convolution layer.

CNN algorithms are used in image classification. These algorithms do not say where the object is placed on the image and are used on the cropped section of an image. But the aim of this research is to classify the pistachios even when they are clustered. So, for that reason the algorithm should be able to give the position of the object in the image. This is the reason why an object detection algorithm was used.

Object detection algorithms are algorithms, as the name suggests, that are able to find the position of the object in an image as it classifies it. There are multiple object detection algorithms such as MobileNet [5] or YOLO [6]. Although the techniques are varied, general idea behind object detection algorithms are the same. What is done by the object detection algorithm is to proffer an area on the image that is likely to have an object in it. Next, object detection algorithm uses an CNN algorithm as its backbone to inspect that proposed region to determine whether there is object in that region. How the region is proposed depends from algorithm to algorithm.

The object detection algorithm used in this research is Faster R-CNN [7]. This algorithm was taken from Tensorflow (open souse deep learning algorithm library for Python) detection zoo. Faster R-CNN used here uses Inception V2 [8] as its backbone. Region proposal is done by the algorithm with an artificial neural network algorithm called Region Proposal Network. So, Faster R-CNN learns from the training how to propose a region for the image given.

In this research, Python programming language was used. The computer used had Windows 10 64-bit Operation System. It had 16GB ram capacity, Intel Core i7-4710HQ processor with 2.50 GHz clock speed and Nvidia GeForce GTX 860M with 2GB Vram graphics card.

2.1 Pre-Training Preparations and Training

As this is a supervised learning, there are pretraining preparation, otherwise known as dataset annotation. Dataset annotation means that preparing a training dataset for the network. This dataset helps the algorithm to learn the properties of the object. How it's done is, firstly dataset is labeled. These labels contain information about the objective such as, for image detection, dataset is prepared by labeling the objects inside image. This way when the network is training, it knows where to look and what to learn.

Images of the pistachios were taken with Logitech Quickcam Pro for Notebooks. It has a resolution of 640x480 (or 480P). Since it was desired that this research to be real world applicable, in this research pistachios are clustered together. 232 images were used for training step, 185 of it for training and 47 for validation. Training dataset had 2125 objects (845 yellow hulled and 1280 red hulled pistachio) and validation dataset had 555 objects (203 yellow hulled and 352 red hulled pistachio) in the images.

When creating annotation, in general there are two types of annotation file format: json and xml and most of the time annotating the images in this format is enough. After the annotations, images and annotations are feed to the training platform and training starts. But the library that used in this research, tensorflow, requires the xml files to be turned into tfrecord format. Tfrecord is a type of file format that combines images and annotations under a single file. According to tensorflow, this makes the file reading more efficient.

After the annotation, configurations are made inside the configuration text file (it is for tensorflow, may show difference from library to library) belonging to that particular CNN. Configuration file

contains informations about where are training files and training values such as learning rate and batch number. After this step, training is started.

Training was stopped when the loss value was no longer changing which had happened at 0.7. It took algorithm 30.000 iteration to reach this value. And result of the training is shown in Figure 2. The algorithm can also be trained to ignore other objects in the image as shown in Figure 3 (Note that because algorithm was trained both under environment light and artificial light, shadows don't affect the detection).



(a) (b)

Figure 2. (a) Original image, (b) pistachio detection (rp: red pistachio, yp: yellow pistachio)



(a) (b)

Figure 3. (a) Original image, (b) pistachio detection (rp: red pistachio, yp: yellow pistachio)

2.2 Instance Segmentation and Length Measurement

In this research, measuring the length, width and area of pistachios were also aimed. In order to achieve this, pistachios were to be segmented from the image. Although it is possible to segment objects using image processing methods, the process of it takes a lot of trial and error. Another problem is, one method can work perfect for one condition but may not so much for another. Furthermore, if the objects are intersecting or overlapping too closely, segmentation process can become far more problematic. In this kind of situations, it is more suitable to use more sophisticated algorithms, namely machine learning algorithms. Even though, there is k-means clustering algorithm for segmenting object according to their color, basic machine learning algorithms are not enough for the job. For that reason, a deep learning algorithm is again needed for a trough segmentation. These kinds of algorithms are called instance segmentation algorithms.

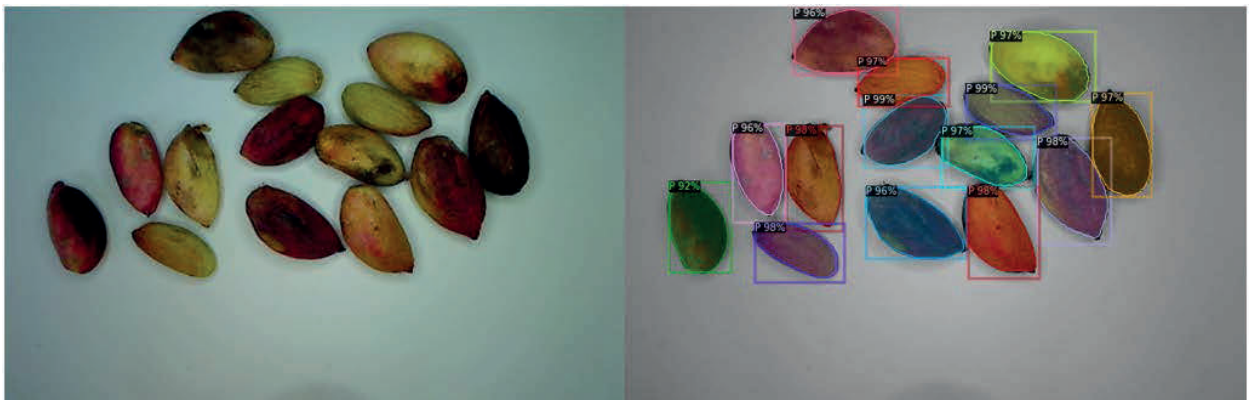
Here, aim is not only to find in what region there is object, it is also to find the exact pixels of the object in question. Instance segmentation is not a standalone idea but a complimentary to object

detection algorithm. The algorithm used in this research is called Mask R-CNN [9], is a upgraded version of Faster R-CNN [7].

Object detection part detects the object on the image, and instance segmentation part suggests a binary mask for the object detected. Mask R-CNN can be used with Python under the library called Detectron2.

2.3 Training of the Instance Segmentation Algorithm

Although algorithm can be trained for classification and segmentation, it would be hard to created a dataset for classification as dataset is created by drawing polynomials around the object. So the algorithm was trained only to detect pistachios without classifying. Training was done using 22 images which contains 181 objects. The algorithm was iterated 300 times and stopped when the loss was 0.3. And result of the training is as Figure 4.



(a) (b)

Figure 4. (a) Original image, (b) instance segmentation.

3. Results and Discussion

Testing of the object detection algorithm was done with 20 images containing 200 pistachios (10 per image) on different positions. Confusion matrix is as shown in able 1.

Table 1. Confusion matrix of object detection algorithm.

Ground Truth\Classification	Red Hulled Pistachio	Yellow Hulled Pistachio
Red Hulled Pistachio	92(98.9%)	1(1.1%)
Yellow Hulled Pistachio	3(2.8%)	104(97.2%)

To test the accuracy of measurement 20 pistachio images were used. Pistachios were placed in different positions, and measured by the algorithm itself. Mean absolute percentage error (MAPE), which is Equation (20) where Re is real measurement, P is predicted measurement and n is number of examples, was used to assess the accuracy. MAPE for prediction found to be 1.77%.

$$MAPE = \frac{100}{n}\sum_{i=1}^{n}\left|\frac{Re-P}{Re}\right| \quad (20)$$

4. Conclusions

Object detection algorithm used shows in this research show capability on par with human eye with 98.9% and 97.2% accuracies for red and yellow hulled pistachios respectively. What is done with this algorithm very hard, if not impossible with conventional image processing algorithms.

Measuring algorithm used here is also very capable algorithm. Measurement taken from the images are satisfactory and can be further used for measuring the weights of the pistachios in the image. Similar experiment was done by S. K. Vidyarthi et al. [10] on pistachio kernels with good accuracy rate.

Only problem has been observed in this research is the detection time required, which is 4 second per image on average. This slowness is the result of the GPU used. It is a 7 years old card. For further understand the capabilities of the algorithm, in future more powerful processing module types such as processors called Tensor Processing Unit (TPU).

References

1. FAO. Food and Agriculture Organization of the United Nations. FAOSTAT 2018 pistachio production data, Retrieved from.: https://www.fao.org/faostat/en . **2018**.
2. Siddiqi, R. Automated apple defect detection using state-of-the-art object detection techniques. SN Applied Sciences. **2019,** 1(11):1–12.
3. Wang, L., Li, A., and Tian, X. Detection of fruit skin defects using machine vision system. Proceedings - 2013 6th International Conference on Business Intelligence and Financial Engineering. https://doi.org/10.1109/BIFE.2013.11. **2014,** 44–48.
4. Thuyet, D. Q., Kobayashi, Y., and Matsuo, M. A robot system equipped with deep convolutional neural network for autonomous grading and sorting of root-trimmed garlics. Computers and Electronics in Agriculture, 178, 105727. https://doi.org/10.1016/j.compag.2020.105727. **2020**.
5. Howard, A., Sandler, M., Chen, B., Wang, W., Chen, L. C., Tan, M., Chu, G., Vasudevan, V., Zhu, Y., Pang, R., Le, Q., and Adam, H. Searching for mobileNetV3. Proceedings of the IEEE International Conference on Computer Vision. https://doi.org/10.1109/ICCV.2019.00140. **2019**,1314–1324.
6. Redmon, J., Divvala, S., Girshick, R., and Farhadi, A. You only look once: Unified, real-time object detection. Proceedings of the IEEE Computer Society Conference on Computer Vision and Pattern Recognition. https://doi.org/10.1109/CVPR.2016.91. **2016**, 779–788.
7. Ren, S., He, K., Girshick, R., and Sun, J. Faster R-CNN: Towards Real-Time Object Detection with Region Proposal Networks. IEEE Transactions on Pattern Analysis and Machine Intelligence. https://doi.org/10.1109/TPAMI.2016.2577031. **2017**,39(6):1137–1149.
8. Szegedy, C., Vanhoucke, V., Ioffe, S., Shlens, J., and Wojna, Z. Rethinking the Inception Architecture for Computer Vision. Proceedings of the IEEE Computer Society Conference on Computer Vision and Pattern Recognition. https://doi.org/10.1109/CVPR.2016.308. **2016**, 2818–2826.
9. He, K., Gkioxari, G., Dollár, P., and Girshick, R. Mask R-CNN. IEEE Transactions on Pattern Analysis and Machine Intelligence. https://doi.org/10.1109/TPAMI.2018.2844175. **2020**, 42(2):386–397.
10. Vidyarthi, S. K., Tiwari, R., Singh, S. K., & Xiao, H. W. Prediction of size and mass of pistachio kernels using random Forest machine learning. Journal of Food Process Engineering. https://doi.org/10.1111/jfpe.13473. **2020**, 43(9).

COMPARATIVE STUDY ON THE VIBRATION BEHAVIOR OF ALUMINUM ALLOYS USED IN AEROSPACE APPLICATIONS

NURETTİN FURKAN DOĞAN [*1], BURAK ŞAHİN [2]

[1] Kilis 7 Aralık University, Faculty of Engineering and Architecture, Mechanical Engineering, Kilis, TURKEY.
[2] Gaziantep University, Faculty of Aeronautics and Aerospace, Aircraft and Aerospace Engineering, Gaziantep, TURKEY

Abstract

The dynamic analysis of the structures possesses a critical stage in the design phase. Modal analysis is a popular technique used to investigate dynamic behaviors, such as natural frequency and modes of structures. A beam was numerically modeled as a cantilever beam and the vibration properties of commonly used aluminum alloys were compared using ANSYS Modal Analysis Module. In the first part of the study, natural frequency, and the vibration modes of the 2024, 6013, 6061, and 7075 types of aluminum were recorded and compared. In the second part of the study, a beam with a circular cutout was formed and the vibration response of the beam was investigated by changing on three different locations. Analyses have shown that the natural frequency of the structures was affected by mechanical properties of materials as well as structural properties such as boundary conditions and cutout locations.

Keyword: Modal analysis, Mode shapes, Natural frequency, Aluminum alloy, Cutout.

1. Introduction

Aluminum alloys are the most frequently used non-ferrous metals in many industrial applications, such as aeronautics and automobile industries [1,2]. Structures produced made from aluminum alloys are vastly found in structural parts of aircraft such as wings and fuselage, and parts that require precision such as engines. These parts are exposed to dynamic as well as static forces during operation. For this reason, it is important to have the necessary information about the vibration properties and mechanical properties of materials used in aerospace applications.

The interaction between the inertial and elastic properties of the materials causes resonant vibration. In other words, when periodically applied load is equal or near to natural frequency of a system, resonance occurs. And on the structures in resonant vibration, even small loads can cause large deflections and thus catastrophic damage to structures under resonant conditions. On the other hand, most of the vibration and noise in mechanical structures are caused by resonance vibration. Therefore, the resonance frequencies of the structures should be defined for different materials and boundary conditions [3]. Modal analysis is performed to determine the dynamic behavior of the structures and gives information about the natural frequency, vibration modes, and damping capacity of the material.
In literature, several experimental and numerical studies have been conducted on the vibration properties of the materials by many researchers [4–8]. Nirmall and Vimala [9] have numerically

and experimentally investigated the vibration behavior of three metals: aluminum, brass and mild steel by using ANSYS. They have concluded that the thickness and the natural frequency are inversely proportional. In another study conducted by Demirtaş and Bayraktar [10], an aircraft wing is modelled as cantilever beam and they have compared theoretical results and numerical model analyses. They pointed out that the aircraft wing can be considered as a cantilever beam when loads other than the gravitational load is ignored. In their experimental and theoretical study Erkliğ et al. [11] have investigated the frequency response of the glass fiber reinforced polymer composites. According to their study, the natural frequency is highly affected by the boundary conditions, cutout shape and location.

In aerospace structures, cutouts are inevitable and mostly used for operations such as ventilation, vibration damping, weight reduction, assembly, and wiring. These cutouts weaken the structure dynamically and also serve as an additional source of vibration. For this reason, it is important to investigate the effects of the cavities used in the design of the structures on the dynamic behavior of the structure [12]. To date, many studies have investigated this issue and reported that the cutouts themselves, as well as their location, have major effects on the vibration behavior of the structure [12–16].

In this study, the vibration behavior of various aluminum alloys (2024, 6013, 6061, 7075) used in aerospace applications has numerically been compared by ANSYS Modal Analysis Module. Additionally, the effects of circular cutout location on the vibration response have also been investigated.

2. Numerical Studies

The model is assumed as a beam with a uniform rectangular cross-section of 200 x 20 x 3 mm as shown in Figure 1. The study has two main parts. In the first part of the study, modal analyses were conducted using solid beam for 2024, 6013, 6061 and, 7075 aluminum alloys. The natural frequencies of the beams and vibration modes were compared. In the second part of the study, the effect of cutouts location (CP=50, 100, 150 mm) on the vibration behavior was investigated by comparing the natural frequencies of beams.

The mechanical properties of the aluminum alloys studied in the study and commonly used in aerospace applications are given in Table 1.

Table 1. Material Properties

Properties	**Al 2024**	**Al 6013**	**Al 6061**	**Al 7075**
Density (kg/m^3)	2780	2720	2700	2810
Young's Modulus (GPa)	73.1	71	68.9	71.7
Poisson's Ratio	0.33	0.33	0.33	0.33

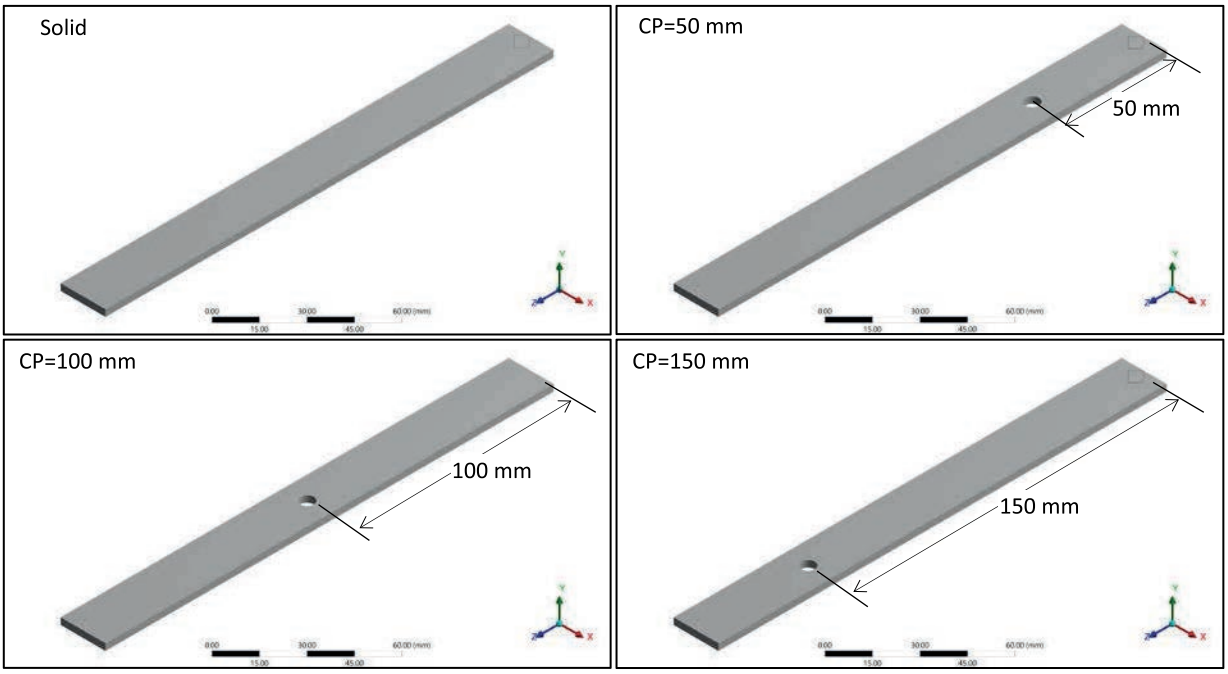


Figure 1. Cantilever beam model.

2.1. Mesh Convergence Analysis

Mesh generation is an important and time-consuming step in the finite element method. Accurate and reasonable meshing will directly determine the speed, accuracy of the final analysis. Before the modal analysis, the mesh convergence analysis was performed to check the accuracy of the mesh. The mesh comparison for solid beam is given in Figure 2. Several element sizes between (0.5 to 10 mm) were considered, and the first mode natural frequency values were compared according to element size. As can be seen in Figure 2, when the element size is 1.0 mm or less, the computed 1st mode natural frequency value converges. Therefore, the cantilever beam was modeled and meshed with an element size of 1.0 mm, which was fine enough to achieve acceptable results as per the convergence criterion.

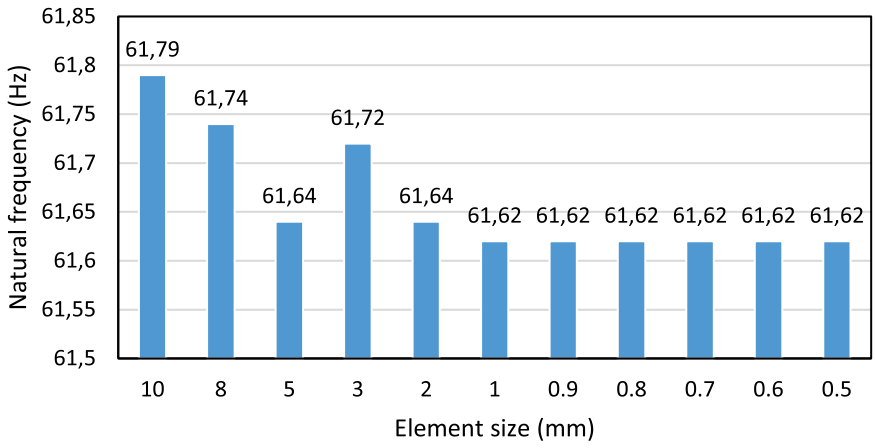


Figure 2. 1st mode natural frequency versus element size

3. Results and Discussion

The first two mode shapes and natural frequencies were obtained for the cantilever beam models with cutout and without cutout. And the mode shapes are presented in Figure 3 for solid and beam with cutout on various cutout positions (CP).

Firstly, the 1st and 2nd natural frequencies of the models were seen quite near to each other for different aluminum alloys as seen in Figures 4 and 5. The 1st mode natural frequencies of the alloys were found as 62.6, 62.3, 61.6, and 61.6 Hz for 2024, 6013, 6061, and 7075, respectively. Although it is a known fact that the natural frequencies of the materials are directly proportional to Young's modulus, it was observed that the natural frequency of the 7075 alloy, which has the second-highest Young's modulus value among the alloys used in this study, was the lowest. On the other hand, in addition to Young's modulus of the materials used, the masses of the structures also affect the natural frequency, and this effect is inversely proportional [17]. Al 7075 alloy has the highest density among the aluminum alloys examined in this study. Therefore, the combined effect of Young's Modulus and material density resulted in the 1st mode natural frequency result of the respective material. The natural frequency results in the same trend have also been observed at the 2nd mode natural frequency.

As presented in Figures 4 and 5, natural frequency values varied under the effect of the cutout. The diameter of the circular cutouts were 6 mm and they located in the distance of 50 mm, 100 mm, and 150 mm from the fixed end of the beam. The 1st mode natural frequency values first decreased with the hole with CP=50 mm, and then showed an increasing trend as it moved away from the support. A possible explanation for this might be that the decrease in the rigidity of the structure. On the other hand, when the position of the circular section opened in the beam is displaced towards the free end of the beam, the decrease in the mass of the structure has led to an increase in the natural frequency. From the graph in Figure 5 we can see that 2nd mode natural frequency is directly affected by the cutout position. As can be seen in Figure 3, the cantilever beam is subjected to bending from its mid-point in the second mode shape. The maximum 2nd mode natural frequency values were obtained when CP=50 mm, while the minimum values were obtained when CP=100 mm. Therefore, while evaluating the position of the cutout in structures, a decision should be made by considering the frequency values (mode shapes) that the structure might be exposed to. In the 1st mode, there is bending at the free end of the beam, while in the 2nd mode, the beam is subjected to bending from its midpoint. However, the change in the natural frequency values of the structure was different in both cases. In short, the position of the hole can have different effects in different mode shapes.

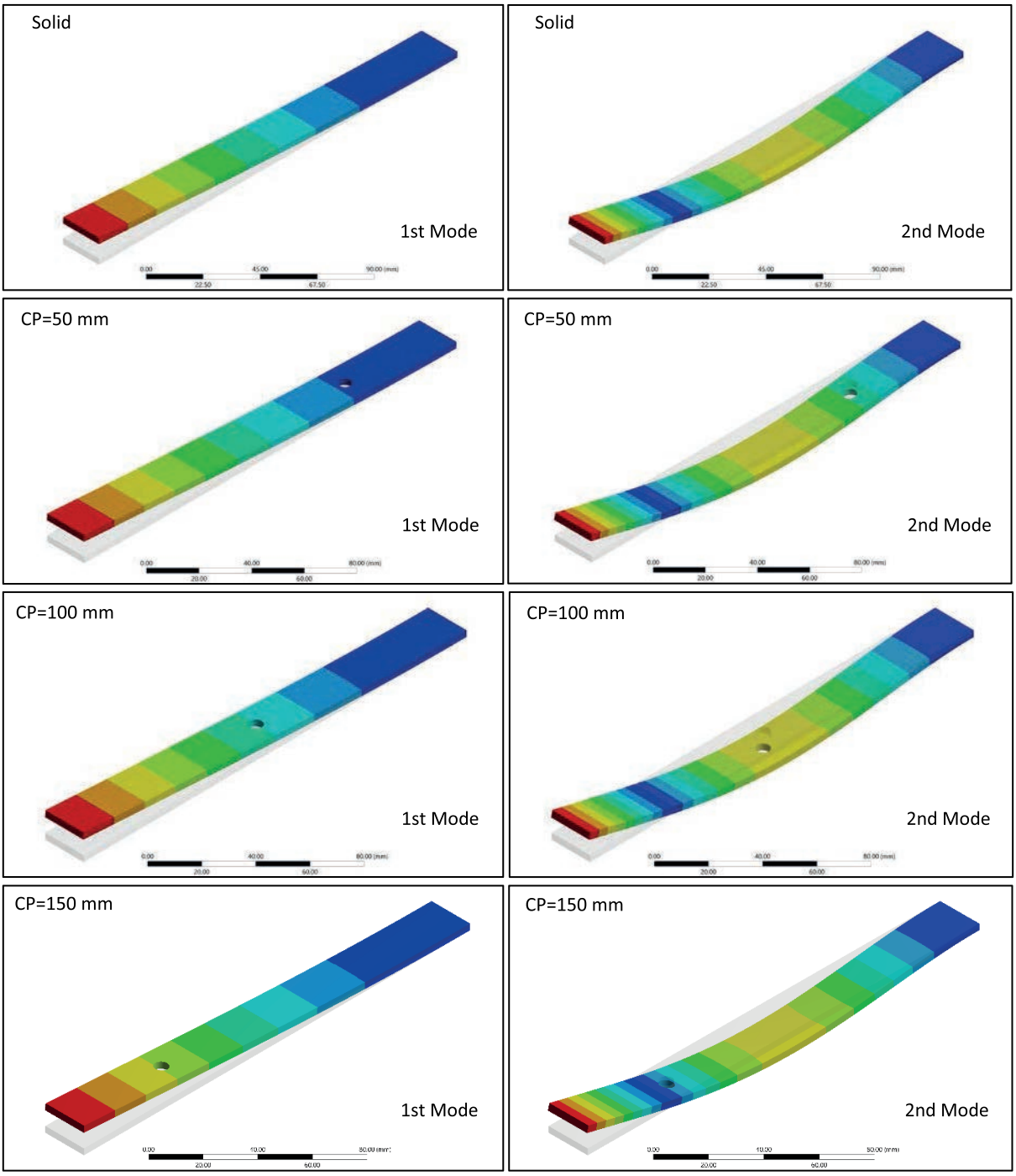
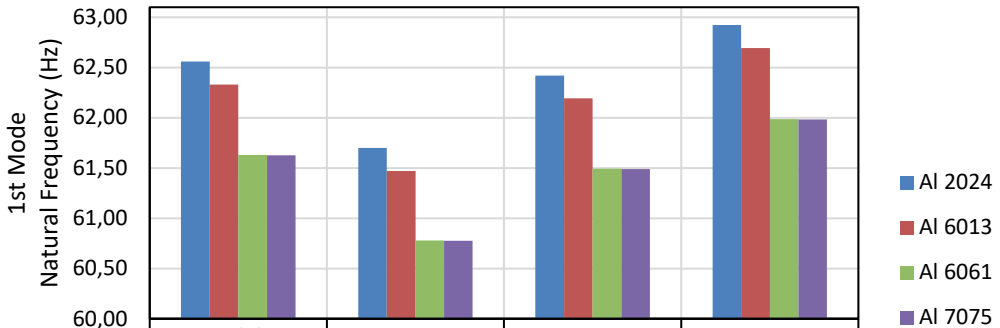
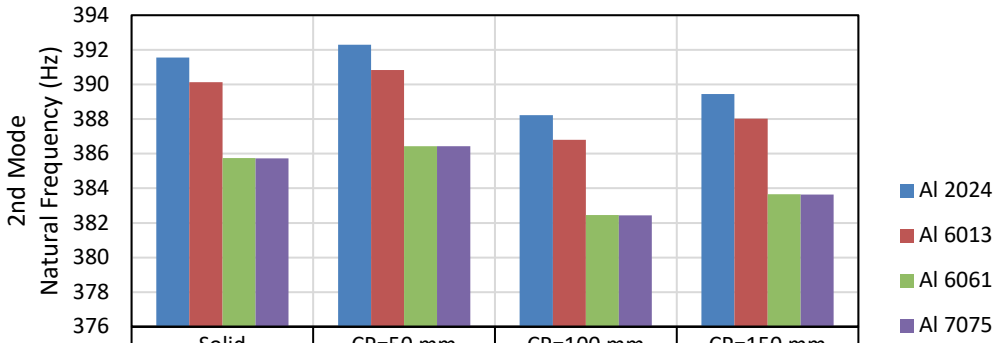


Figure 3. Mode shapes for cantilever beam models



	Solid	CP=50 mm	CP=100 mm	CP=150 mm
Al 2024	62,56	61,70	62,42	62,92
Al 6013	62,33	61,47	62,19	62,69
Al 6061	61,628	60,78	61,49	61,99
Al 7075	61,625	60,78	61,49	61,98

Figure 4. First mode natural frequency variations



	Solid	CP=50 mm	CP=100 mm	CP=150 mm
Al 2024	391,56	392,30	388,22	389,45
Al 6013	390,13	390,84	386,80	388,02
Al 6061	385,74	386,44	382,45	383,65
Al 7075	385,72	386,43	382,43	383,64

Figure 5. Second mode natural frequency variations

4. Conclusions

The present study was designed to examine the vibration response of the cantilever beam made from different aluminum alloys used in aerospace applications by applying modal analysis. In addition, the effect of the cutout and the position of the cutout was also examined and compared with the beam without holes. The following conclusions can be made:

- The natural frequencies of the structures are directly related to Young's modulus and density (hence mass) of the materials used. In addition to these, the boundary conditions and structural rigidity are also effective on the vibration response of the structure.
- Among the solid beam models, the highest 1st mode natural frequency value is 62.6 Hz on the model made from Al 2024 and the lowest is 61.625 on the model of Al 7075.

- The 1st mode natural frequency value of all alloy types reached its lowest value when the cutout was closest to the fixed end (CP=50 mm) and reached its highest value when it was farthest away (CP=150 mm).
- For the 2nd mode natural frequency value, the highest value was reached when the cutout was closest to the fixed end (CP=50 mm). And the value reached its lowest value when it was at the middle point (CP=100 mm).
- According to the findings, the dynamic behavior of the structures is directly related to Young's modulus and density of the materials used, but the boundary conditions also affect this behavior significantly. In particular, the positions of the cutouts to be applied for inspection, ventilation, vibration damping, weight reduction, assembly, and wiring purposes in structures have different effects depending on the vibration mode to which the structure is exposed.

References

[1] Jiang, H. J., Liu, C. Y., Chen, Y., Yang, Z. X., Huang, H. F., Wei, L. L., Li, Y. B., Qi, H. Q. Evaluation of Microstructure, Damping Capacity and Mechanical Properties of Al-35Zn and Al-35Zn-0.5Sc Alloys. J. Alloys Compd. **2018**, 739, 114–121. https://doi.org/10.1016/j.jallcom.2017.12.234.

[2] Bauri, R., Surappa, M. K. Damping Behavior of Al-Li-SiCp Composites Processed by Stir Casting Technique. Metall. Mater. Trans. A **2005**, 36 (3), 667–673. https://doi.org/10.1007/s11661-005-0183-3.

[3] Prashant, S. W., Chougule, V. N., Mitra, A. C. Investigation on Modal Parameters of Rectangular Cantilever Beam Using Experimental Modal Analysis. Mater. Today Proc. **2015**, 2 (4–5), 2121–2130. https://doi.org/10.1016/j.matpr.2015.07.214.

[4] ÖZBEK, Ö., TOKUR BOZKURT, Y. Effect of Cut-Outs on the Free Vibration Response of Basalt/Carbon Hybrid Composites. Afyon Kocatepe Univ. J. Sci. Eng. **2021**, 21 (3), 724–734. https://doi.org/10.35414/akufemubid.889289.

[5] Gautam, A., Sharma, J. K., Gupta, P. Modal Analysis of Beam through Analytically and FEM. Int. jouranal Inov. Res. Sci. Eng. Vol **2016**, No. 2.

[6] Mehdi, H., Mehmood, A. Vibration Analysis of a Cantilever Beam with Crack Depth and Crack Location Effects. Int. J. Res. Eng. Innov. **2016**, 1, 20–28.

[7] Sharma, J. K. Theoretical and Experimental Modal Analysis of Beam. In Engineering Vibration, Communication and Information Processing, Springer, 2019, pp 177–186.

[8] Xu, C., Zhou, H., Mao, Y. Analysis of Vibration and Noise Induced by Unsteady Flow inside a Centrifugal Compressor. Aerosp. Sci. Technol. **2020**, 107, 106286.

[9] Nirmall, T., Vimala, S. Free Vibration Analysis of Cantilever Beam of Different Materials. Int. J. Appl. Eng. Res. **2016**, 5 (4), 612–615.

[10] Demirtaş, A., Bayraktar, M. Free Vibration Analysis of an Aircraft Wing by Considering as a Cantilever Beam. Selçuk Üniversitesi Mühendislik, Bilim Ve Teknol. Derg. **2019**, 7

(1), 12–21.

[11] Erkliğ, A., Bulut, M., Yeter, E. The Effect of Hybridization and Boundary Conditions on Damping and Free Vibration of Composite Plates. Sci. Eng. Compos. Mater. **2015**, 22 (5). https://doi.org/10.1515/secm-2014-0070.

[12] Mahadevaswamy, P., Suresh, B. S. Effect of Flap Position on Transverse Vibration of Rectangular Plate with Cutout. J. Eng. Sci. Technol. **2014**, 9 (2), 233–245.

[13] Kandasamy, S., Singh, A. V. Free Vibration Analysis of Skewed Open Circular Cylindrical Shells. J. Sound Vib. **2006**, 290 (3–5), 1100–1118.

[14] Mandal, A., Ray, C., Haldar, S. Experimental and Numerical Studies on Vibration Characteristics of Laminated Composite Skewed Shells with Cutout. Compos. Part B Eng. **2019**, 161, 228–240. https://doi.org/10.1016/j.compositesb.2018.10.075.

[15] Liew, K. M., Lim, C. W. Vibration of Perforated Doubly-Curved Shallow Shells with Rounded Corners. Int. J. Solids Struct. **1994**, 31 (11), 1519–1536.

[16] Jhung, M.-J., Jo, J.-C. Equivalent Material Properties of Perforated Plate with Triangular or Square Penetration Pattern for Dynamic Analysis. Nucl. Eng. Technol. **2006**, 38 (7), 689–696.

[17] Çakar, O. Mass and Stiffness Modifications without Changing Any Specified Natural Frequency of a Structure. J. Vib. Control **2011**, 17 (5), 769–776. https://doi.org/10.1177/1077546310376084.

INVESTIGATION OF SURFACE ROUGHNESS FOR INCONEL 718 AS AEROSPACE MATERIAL BY FLOW PEENING (GOV) PROCESS

KÜRŞAD GÖV, [*1] NURETTİN FURKAN DOĞAN[*2], MURAT KALAK[*1], MEHMET SAİT KOCA[*1]

[1] : Gaziantep University, Faculty of Aeronautics and Aerospace, Aerospace Engineering Department, Gaziantep, TURKEY.

[2] : Kilis 7 Aralık University, Faculty of Engineering and Architecture, Mechanical Engineering, Kilis, TURKEY.

Abstract

Inconel 718 which is a nickel-based alloy has superior mechanical properties and preferred in aerospace applications. It has high fatigue strength, hardness, wear resistance, corrosion resistance and high strength. Contrary, Inconel 718 has low thermal conductivity and poor processability. It is accepted as a difficult-to-cut material. Because of difficulties, electrical discharge machining (EDM) process is used to cut it. Surface enhancement is very helpful to obtain acceptable level of surface roughness after cutting it by EDM.

Surface roughness is very effective on fatigue strength and their service life under repetitive loads. Keeping roughness at moderate level is very crucial to obtain long service life in engineering applications.

In this study, flow peening (GOV) process is applied for surface enhancement to reduce surface roughness.

Keyword: Inconel 718, Aerospace materials, Material removal rate, Flow peening (GOV) process, Electrical discharging machining (EDM), Abrasssive flow machining (AFM), Surface roughness, fatigure strength, endurance limit, service life.

1. INTRODUCTION

The production method directly affects the life and strength of the material. One of the most important factors in production parameters is undoubtedly the surface quality. Surface roughness has effect on friction losses and decrease in working system efficiency. Therefore, as it was expected high surface quality for the materials of aerospace industry, molding, medical, centrifugal

pump manufacturing are vital. Many different types of materials are currently preferred in the aviation industry.

Inconel 718 is mostly used for aerospace applications owing to its advantageous mechanical properties. On the other hand, because of poor processability, samples of Inconel are cut by electrical discharge machining. Then flow peening (GOV) (Figure 1) process is carried out to improve surface quality by decreasing roughness of aerospace materials.

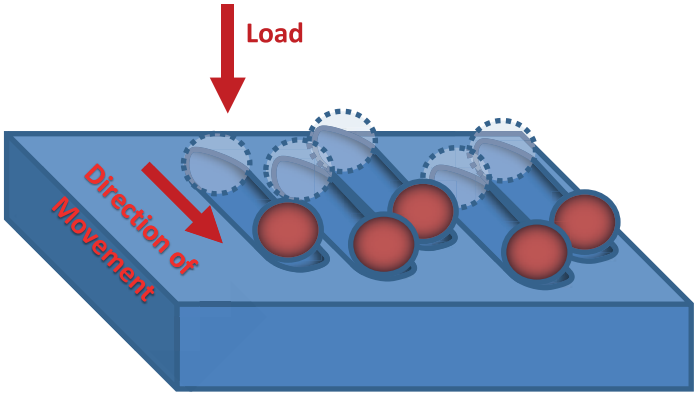


Figure 1. Schematic view of the GOV process

Although this alloy has high strength, it is difficult to cut and process using conventional methods. Inconel 718 is a nickel-based superalloy that is often used in rocket engines, spacecraft, and the marine sector.

The manufacturing method chosen for the material has a significant effect on the surface finish. Advanced manufacturing technologies are mostly used for materials which are processed by mechanical cutting methods. One of the most preferred methods of advanced manufacturing technologies is the EDM method, which can be an alternative to mechanical cutting regardless of the strength and hardness of the materials. Nickel-based superalloys, hardened steels and complex geometries can be easily processed in the EDM method. Gov and Eyercioğlu studied on the hardening of AISI D2 steel and the improvement of the sample surfaces obtained by cutting with the WEDM method from materials with 31,45 and 55 HRC values by using the AFM method [2].

A machine element is often exposed to dynamic loads along in addition to static loading during its service life. The majority of the damages are because of fatigue failure under variable loads. The surface roughness makes it easier for these cracks to progress faster by showing a notch effect during loading. For this reason, the surface roughness has significant effect on the fatigue failure. Surface finishing operations are usually performed after machining to provide a good surface finish to improve surface and fatigue behavior.

In this study, surface enhancement by AFM process and surface strength-stress improvement by shot peening are combined in a single process as flow peening (GOV) process.

2. RESULTS

Dimensions are 5x10x20 mm for the samples (Figure 2) and chemical compositions of samples of Inconel 718 are given in Table 1. The surface roughness values of the surface before and after

applying flow peening (GOV) process for 1 cycle and cycles of 4, 9, 19, 39, 89 and 189 are measured and presented in Figure 3.

Table 1. Chemical composition of Inconel 718 in wt.%

Elem.	Ni	Cr	Mo	Nb	Ti	Al	Co	Mn	Si	Cu	C	Ta	Fe
Min	50.0	17.0	2.8	4.75	0.65	0.2	-	-	-	-	-	-	bal.
Max	55.0	21.0	3.3	0.65	1.15	0.8	1.0	0.35	0.35	0.3	0.08	0.05	bal.



Figure 2. Inconel-718 sample

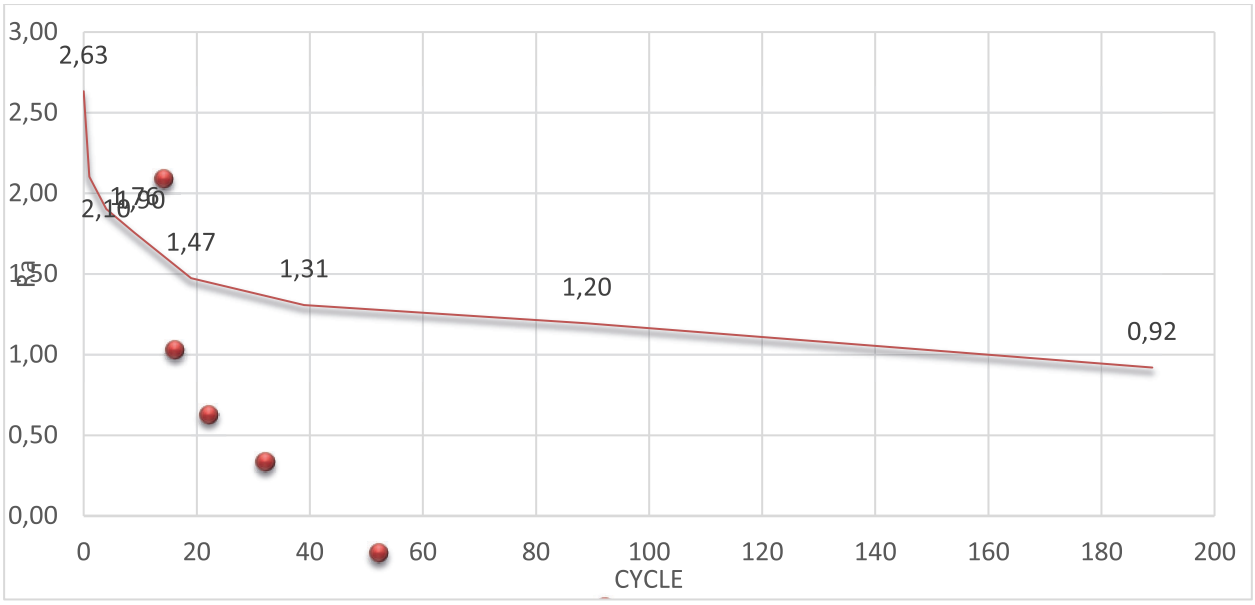


Figure 3. Ra values measured after flow peening (GOV) process

3. CONCLUSIONS

It this study the effect of flow peening (GOV) process on the surface roughness of Inconel 718 as an aerospace material has been investigated. The surface roughness values measured after applying process has been revealed that the surface quality of Inconel 718 alloy increases by depending on number of process cycles. The Ra value decreased from 2.63 μm to 0.92 μm with the increase in the number of process cycles. Increasing the abrasive-polymer ratio also decreased the Ra value.

4.REFERENCES

1. Zahoor S., Ameen F., Abdul-Kader W., Stagner J., Environmentally conscious machining of Inconel 718: surface roughness, tool wear, and material removal rate assessment, The International Journal of Advanced Manufacturing Technology (2020) 106:303–313

2. Gov K, Eyercioglu O – Cakir M. V., Hardness Effects on Abrasive Flow Machining, Jcurnai of Mechanicai Engineering 59(2013)10,626-631

3. Thakur, D. G., Ramamoorthy, B., Vijayaraghavan, L., A Study on the Parameters in High-Speed Turning of Superalloy Inconel 718, Materials and Manufacturing Processes, 24: 497–503, 2009.

4. Unune, D. R., Mali, H. S., Artificial neural network–based and response surface methodology–based predictive models for material removal rate and surface roughness during electro-discharge diamond grinding of Inconel 718, Proc IMechE Part B: J Engineering Manufacture.

5. Devillez, A., Le Coz, G., Dominiak, S., Dudzinski, D., Dry machining of Inconel 718, workpiece surface integrity, Journal of Materials Processing Technology 211 (2011) 1590–1598

OPTIMIZATION OF AN ANTI-SWAY CONTROLLER FOR AN OVERHEAD CRANE USING THE BEES ALGORITHM

MAHMUT ÇİMEN[1], SAMI YEŞİLBEL[1], METE KALYONCU[2]

[1] Sekizli Makina ve Vinç Sanayi Ticaret A. Ş., 42050 Karatay, Konya, TURKEY.
[2] Mechanical Engineering Department, Engineering and Nature Science Faculty, Konya Technical University, 42250 Selçuklu, Konya, TURKEY.

Abstract

This paper presents the design of a hierarchical PID controller for an overhead crane using the Bees Algorithm. The algorithm optimizes the gains of the hierarchical PID controller so that it can move the overhead crane to a desired position with the minimum amount of payload sway during the movement and lifting a payload. Following a description of the algorithm, the paper gives the numerical results obtained for the overhead crane demonstrating the efficiency and robustness of the controller design.

Keyword: Overhead crane, Anti-sway controller, The Bees Algorithm, Optimization.

1. Introduction

Overhead cranes are important tools used in some modern industrial sectors such as construction, manufacturing, mining and transportation. These are extremely basic equipment that requires good knowledge of safety practices and operating competencies. They are used to transport heavy loads from one place to another. Due to industrialization and high productivity, modern industries have adopted the use of overhead cranes to speed up project deliveries. Safety is very important when using overhead cranes because any slip could result in serious injury or untimely death. However, if used carefully, you can reach all your goals quickly. While overhead cranes are highly adaptable to many environments, they are extremely reliable. Here are some benefits of using overhead cranes in modern industries. It is very important to design an anti-sway controller of overhead crane for eliminating pendulum of hook-headed [1-14].

Error detection of a load in position is not a problem. Nothing is moving and any distortion is a value that can be easily detected and corrected. The main question in managing a stable position is what gain should be applied. This becomes a complex problem that must be solved on its own, even before considering the dynamics of movement. The biggest factor is the load mass. The load mass estimates the time allowed for acceleration. A large mass can only be made to accelerate to a certain extent, and there isn't much you can do to change the situation. If the load has a time constant, then the proportional gain required to stabilize the load while "in position" must be based on the time constant of the mass. In a step and direction system, position can be maintained without PID controller.



Figure 1. An overhead crane manufactured by Sekizli Makina ve Vinç Sanayi Ticaret A. Ş.

Editing the move usually follows some simple rules. There is no acceleration or deceleration when the load is moving at a constant speed. That is, velocity is a ratio of the change in position. The speed of the load can only be disturbed by changes that will appear as the following error, the difference between the commanded instantaneous position and the actual. Again, the gain adjustment required for proper regulation will be related to the mass and time allowed for system corrections. In many systems, an allowable tracking error value is programmed and no PID is required. The simplified approach to looking at individual motion states within a given profile is not an end in itself, but the possibility to suggest that other rule bases can be derived and tested as an alternative to the traditional PID approach. At the end of the day, the regulation of a mechanical load can be simplified according to the state of motion, stationary, constant speed or acceleration and deceleration [15-17].

In this paper, a hierarchical PID control system is proposed to control the trolley motion. First of all, the paper obtains a mathematical model of crane motion system in two-dimensional space. Then the paper advances a new controller optimization method and designs a controller for eliminating pendulum of hook-headed and accurately fixing position. In general, it is difficult to design an appropriate control law because of the crane motion system's nonlinearity and strong coupling. However, the control method the paper put forward is simple and effective, and ensures the transient state performance of closed-loop system preferable and stable. The paper will introduce the design steps of anti-sway controller of overhead crane and give a satisfying simulation result.

2. Dynamic Modelling of the Overhead Crane

The overhead crane on a two-dimensional xy plane as shown in Figure 2. The system contains a trolley moving on a rail, a payload that is considered as a point mass and a hoisting cable. It is assumed that the static friction and elasticity are trivial while stiffness and mass of the hoisting cable are neglected, and the overhead crane operates in indoor environments, hence the effects of disturbances caused by wind are not examined. Furthermore, both the trolley and payload are considered as material particles.

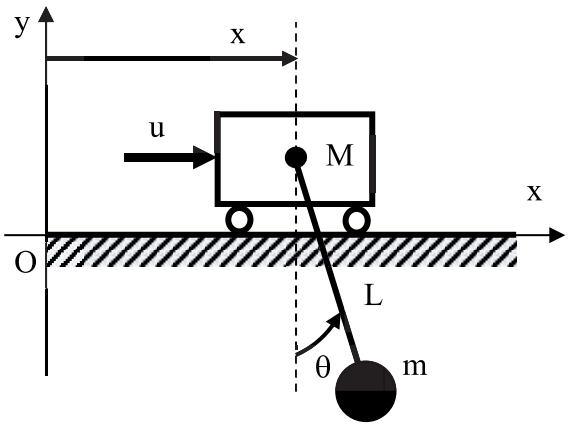


Figure 2. Overhead crane physical model

In Figure 2, x, θ and u are variables presenting for the trolley position, the sway angle of the payload with respect to the vertical line and the trolley driving mechanical force, respectively. On the other hands, M, m and L are also defined as constant parameters delineating the total mass of the trolley, the mass of the payload and the rope length. From Figure 2, it is seen that there are four main variables to control the overhead crane system: sway angle (θ), angular velocity (dθ/dt), trolley position (x) and trolley velocity (dx/dt). The nonlinear mathematical dynamic model of the two-dimensional overhead crane can be specified by

$$(M+m)\ddot{x} - m\ddot{L}\sin\theta - 2m\dot{L}\dot{\theta}\cos\theta - mL\ddot{\theta}\cos\theta + mL\sin\dot{\theta}^2 = u$$
$$\ddot{x}\cos\theta - L\ddot{\theta} - g\sin\theta - 2\dot{L}\dot{\theta} = 0 \qquad (1)$$

3. Hierarchical PID Controller Design

A closed-loop block diagram of the proposed hierarchical PID control system is shown in Figure 3. The controller has two subsystems. The "PID for anti-sway" subsystem reduces the vibrations of the payload, and the "PID for position" subsystem controls the attainment of the desired position. The hierarchical PID controller has six gains which need to be tuned. As can be seen in Figure 3, in the PID controller, the error signal e(t) and sway angle θ(t) are employed to generate proportional, integral, and derivative actions. The resulting signals are summed to form the control signal u(t) applied to the overhead crane model. The mathematical description of the hierarchical PID controller is:

$$u(t) = K_P^X.e_X(t) + K_I^X.\int_0^t e_X(\tau)d\tau + K_D^X.\frac{de_X(t)}{dt}$$
$$+K_P^\theta.\theta(t) + K_I^\theta.\int_0^t \theta(\tau)d\tau + K_D^\theta.\frac{d\theta(t)}{dt} \qquad (2)$$

where u(t) is the input signal to the overhead crane model, K_P, K_I, and K_D the proportional, integral and derivative gains of the PID controllers, respectively. The error signal $e_X(t)$ is defined as $e_X(t)=r(t)-x(t)$, and r(t) is the desired input signal.

4. The Bees Algorithm for Hierarchical PID Controller Design

This section summarizes the main steps of the Bees Algorithm. Figure 4 shows the pseudo code for the algorithm in its simplest form. As detailed in [18, 19], the algorithm requires a number of

parameters to be set, namely: number of scout bees (*n*), number of sites selected out of *n* visited sites (*m*), number of top-rated (elite) sites among the *m* selected sites (*e*), number of bees recruited for the best *e* sites (*nep*), number of bees recruited for the other (*m-e*) selected sites (*nsp*), initial size of each patch (a patch is a region in search space that includes a visited site and its neighborhood) and stopping criterion.

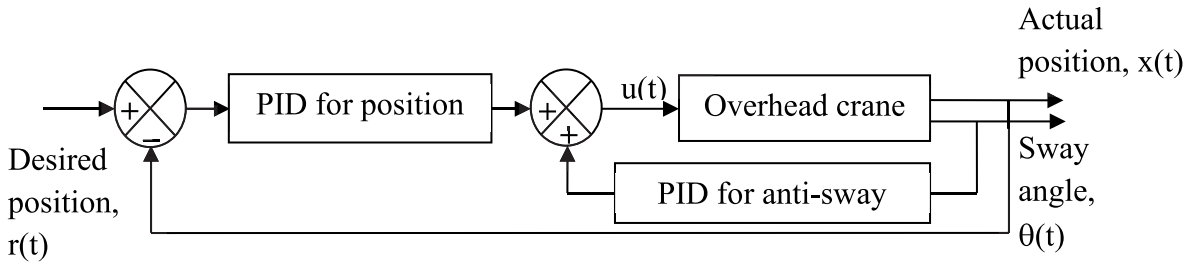


Figure 3. Block diagram of the hierarchical PID controller

The algorithm starts with the *n* scout bees being placed randomly in the search space. The fitnesses of the sites visited by the scout bees are evaluated in step 2. In step 4, the *m* sites with the highest fitnesses are designated "selected sites" and chosen for neighborhood search. In steps 5 and 6, the algorithm conducts searches in the neighborhood of the selected sites, assigning more bees to the best *e* sites. Selection of the best sites can be made directly according to the fitnesses associated with them. Alternatively, the fitness values can be used to determine the probability of the sites being selected. Searches in the neighborhood of the best *e* sites which represent the most promising solutions are made more detailed by recruiting more bees for them than for the other selected sites. Together with scouting, this differential recruitment is a key operation of the Bees Algorithm.

1. Initialize population with n random solutions.
2. Evaluate fitness of the population.
3. While (stopping criterion not met)
   //Forming new population.
4. Select m sites for neighborhood search.
5. Recruit bees for selected sites (more bees for the best e sites) and evaluate fitnesses.
6. Select the fittest bee from each site.
7. Assign the remaining bees to search randomly and evaluate their fitnesses.
8. End While.

Figure 4. Pseudo code of the basic Bees Algorithm

In step 6, for each patch, only the one bee that has found the site with the highest fitness (the "fittest" bee) will be selected to form part of the next bee population. In step 7, the remaining bees in the population are assigned randomly around the search space scouting for new potential solutions. These steps are repeated until a stopping criterion is met. At the end of each iteration, the colony will have two parts to its new population – representatives from each selected patch and other scout bees assigned to conduct random searches.

5. Numerical Results and Discussion

In this work, the aim was to investigate the PID controller gains tuned using the Bees Algorithm and to assess the response of the system. Parameters of the Bees Algorithm have been set as in Table 1.

Substituting the physical parameters in Table 1 of the overhead crane and the other components of the system into the dynamic model equations (1), the linearized state-space form of the system can be obtained as:

$$\dot{X} = AX + Bu$$
$$Y = CX + Du \quad (3)$$

where
$X = [x \quad \dot{x} \quad \theta \quad \dot{\theta}]^T$
A = [0 1 0 0;0 0 m*g/M 0;0 0 0 1;0 0 -((M+m)/(M*l))*g 0],
B = [0;1/M;0;-1/(M*l)],
C = [1 0 0 0;0 0 1 0],
D = [0;0]

The objective function is:

$$J = w_1.t_d + w_2.t_r + w_3.t_p + w_4.M_x + w_5.e_{ss} + w_6.|A_\theta|_{max} \quad (4)$$

where w_i 's are weight factors, t_d is delay time, t_r is rise time, t_p is peak time, M_x is maximum over-shoot, e_{ss} steady state error, and A_θ is amplitude of the sway angle. The weight factors used in this work are given in Table 2.

Table 1. Physical and Geometric Characteristics of the Overhead Crane

Symbol	Parameter	Value	Unit
M	Total mass of the trolley	40.000	kg
m	Mass of the payload	10.000	kg
L	Rope length	5	m
g	Gravity acceleration	9,81	m^2/s

Eqs. (3) and (4) were employed by the Bees Algorithm to find the best values for the gains of the PID controller. The gains of the hierarchical PID controller were tuned using the dynamic model of the overhead crane. The gains of the hierarchical PID controller optimized using the Bees Algorithm are given in Table 3.

Table 2. Values of the Weight Factors

w1	w2	w3	w4	w5	w6
1	1	50	150.0	50	500

In the simulation studies, the gains obtained by using the Bees Algorithm. The desired input signal for the position of the trolley was assumed to be a step function and its final value was defined as 2 meter. While the trolley moved, the sway angle of the payload must be close to zero degree. Figures 5, 6 and 7 show the results obtained by the Bees Algorithm for the position of the trolley, the sway

angle of the payload, and the trolley driving mechanical force. Figures 5, 6 and 7 contain the 10 different results obtained by the Bees Algorithm.

Table 3. Gains of the Hierarchical PID Controller

K_P^X	K_I^X	K_D^X	K_P^θ	K_I^θ	K_D^θ	Objective function value
21.336,7	515,7	32.222,9	42.546,3	39.298,1	36.841,6	1.354,42
22.800,7	177,9	34.487,2	47.217,7	11.945,2	25.027,6	1.359,15
24.509,5	750,1	46.988,7	10.960,4	43.341,8	14.124,6	1.402,24
27.100,3	2.128,5	40.808,8	33.207,9	34.812,5	44.678,0	1.420,79
20.566,2	2.019,9	42.860,3	10.569,4	12.865,6	24.643,2	1.422,29
23.792,5	575,3	38.157,9	11.623,9	35.621,6	16.605,7	1.423,67
20.941,1	243,9	22.841,9	34.124,5	10.753,7	31.734,8	1.428,91
29.542,7	170,9	39.240,5	10.843,7	33.217,9	47.645,6	1.435,18
16.991,3	1.268,2	33.608,9	26.735,5	43.975,7	36.292,7	1.444,44
30.019,0	2.357,5	49.373,1	45.278,1	26.576,6	11.047,6	1.458,64

The trolley position control is shown in Figure 5. It can be seen that, with the Bees Algorithm, the trolley can move fast and reliably. Figure 6 shows that the gains optimized using the Bees Algorithm produced small sway angle. The trolley driving mechanical force for the each PID controller are given in Figure 7. The controllers tuned by the Bees Algorithm have small and smooth control forces.

The mean objective value for 10 different runs of the Bees Algorithm was found to be 1.354,42 and (see Table 4). Also, the standard deviation of all runs was calculated as 32,38 which proves the reliability of the algorithm.

6. Conclusions

The design of a hierarchical PID controller for an overhead crane in this paper. Using the controller, it was aimed to bring the trolley of the overhead crane to a desired position and minimize sway angle of the payload while it moved. The controller had two subsystems. The "PID for anti-sway" subsystem reduced the sway angle of the payload, and the "PID for position" subsystem controlled the attainment of the desired position. The six gains of the hierarchical PID controller were tuned using the Bees Algorithm to minimize the sway angle and positioning errors. Simulation results show that the PID controller design thus obtained was both efficient and robust.

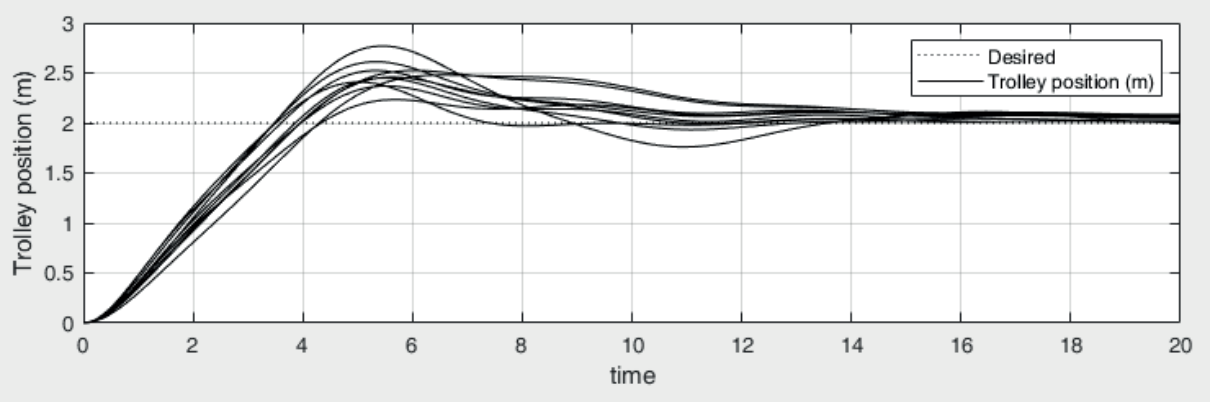


Figure 5. Position of the trolley

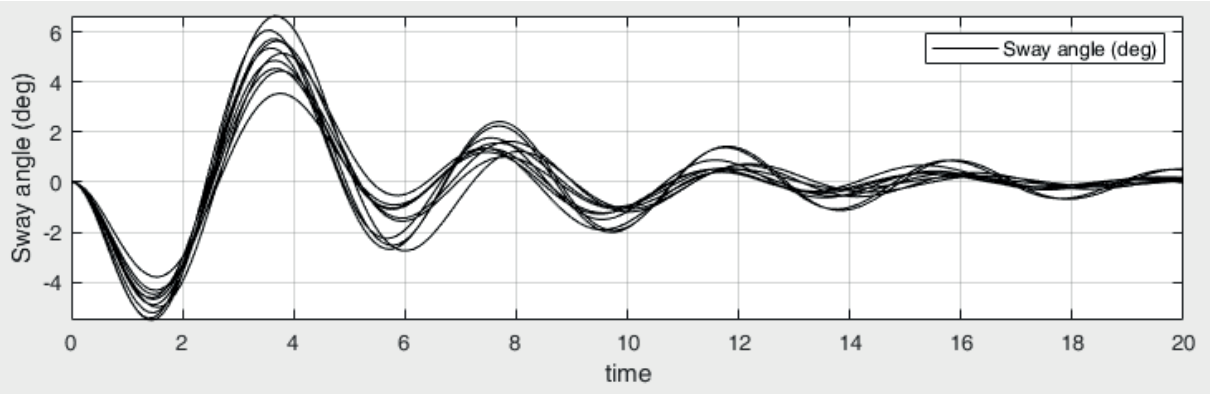


Figure 6. Sway angle of the payload

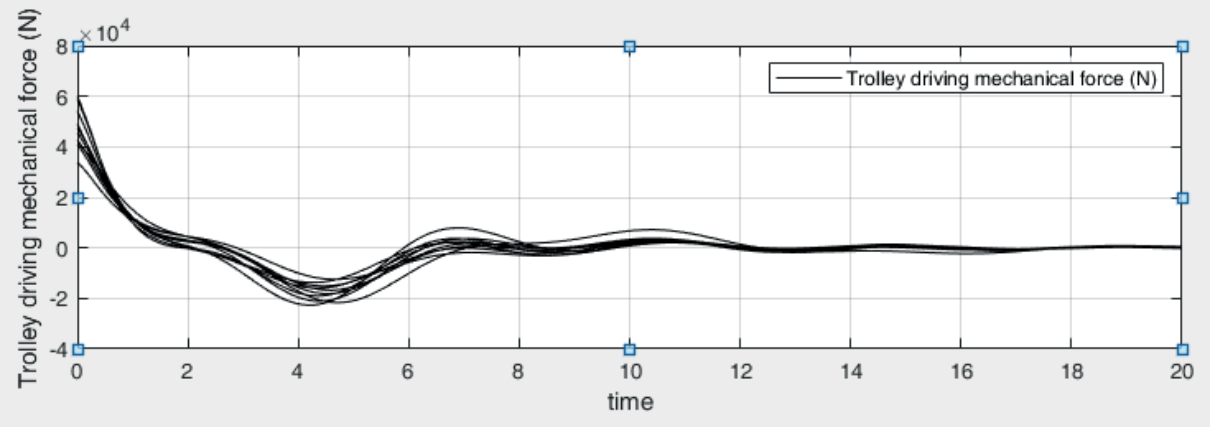


Figure 7. Trolley driving mechanical force

References

1. Esleman, E.A., Önal, G., Kalyoncu, M. Optimal PID and fuzzy logic based position controller design of an overhead crane using the Bees Algorithm. SN Appl. Sci. https://doi.org/10.1007/s42452-021-04793-0. **2021**, 3:811.
2. Tınkır, M., Kalyoncu, M., Önen, Ü. and Şahin, Y. Modeling and Control of Scaled a Tower Crane System, 2011 International Conference on System Engineering and Modeling (ICSEM 2011). Shanghai, China. **2011**, 93-98.
3. Yılmaz, U., Kalyoncu, M., Mobil Hidrolik Teleskobik Vinçlerde Yük Salınım Kontrolü, Selçuk Ü. Müh. Bilim ve Tekn. Derg. **2014**, 2(2):55-64.
4. Yeşilbel, S., Çimen, M., Kalyoncu, M. Gezer köprülü vinç konstrüksiyonunun Arı Algoritması kullanılarak optimum tasarımı. The International Conference of Materials and Engineering Technology, Gaziantep/TURKEY. **2020**, 104-117.
5. Önen, Ü., Çakan, A. Anti-swing Control of an Overhead Crane by Using Genetic Algorithm Based LQR.International Journal of Engineering and Computer Science, ISSN:2319-7242. **2017**, 6(6):21612-21616.
6. Zhu, F., Shan, Y. Anti-Disturbance State Feedback Controller Based on Disturbance Reconstruction for Underactuated Overhead Crane, this work is supported by the National Natural Science Foundation of China under Grant 61573256, IFAC-Papers on Line. **2020**, 53(2):4151-4156.

7. Roger, M.C., Aguilar, L.T. A family of anti-swing motion controllers for 2D-cranes with load hoisting/lowering. Mechanical Systems and Signal Processing. **2019**, 133:106253.
8. Sorensen, K., Singhose, W., Dickerson, S. A Controller Enabling Precise Positioning and Sway Reduction in Cranes with On-Off Actuation. IFAC Proceedings Volumes. **2005**, 38(1):580-585.
9. Trabia, M.B., Renno, J.M. and Moustafa, K.A.F. Generalized design of an anti-swing fuzzy logic controller for an overhead crane with hoist. Journal of Vibration and Control. **2008**, 14(3):319-346.
10. Chai, L., Guo, Q.H., Liu, H.K., Ding, M.B. Linear Active Disturbance Rejection Control for Double-Pendulum Overhead Cranes. IEEE Access. **2021**, 9:52225-52237.
11. Sun, Z., Ling, Y.W., Tan, X., Zhou, Y., Sun, Z.X. Designing and application of type-2 fuzzy PID control for overhead crane systems. International Journal of Intelligent Robotics and Applications. **2021**, 5(1):10-22.
12. Sun, Z., Ling, Y.W., Qu, H.B., Xiang, F., Sun, Z.X., Wu, F. An Adaptive DE Algorithm Based Fuzzy Logic Anti-swing Controller for Overhead Crane Systems. International Journal of Fuzzy Systems. **2020**, 2(6):1905-1921.
13. Ouyang, H., Xu, X., and Zhang, G. Tracking and load sway reduction for double-pendulum rotary cranes using adaptive nonlinear control approach. International Journal of Robust and Nonlinear Control. **2020**, 30(5):1872-1885.
14. Guo, H., Feng, Z.Y., and She, J. Discrete-time multivariable PID controller design with application to an overhead Crane. International Journal of Systems Science. **2020**, 51(14):2733-2745.
15. https://www.konecranes.com/en-us/equipment/overhead-cranes/safe-features-for-overhead-cranes/sway-control
16. http://www.hoistmagazine.com/features/anti-sway-systems/
17. https://dvesta.com/en/technical-solutions/special-cranes-functions-in-the-control-systems/anti-sway-controller/
18. Pham, D.T., Ghanbarzadeh, A., Koc, E., Otri, S., Rahim, S.and Zaidi, M. The Bees Algorithm. Technical Note. Manufacturing Engineering Centre, Cardiff University, UK. **2005**.
19. Pham, D.T., Ghanbarzadeh, A., Koc, E., Otri, S., Rahim, S.and Zaidi, M. The Bees Algorithm – A novel tool for complex optimisation problems. Proceedings of the 2nd Virtual Int. Conference on Intelligent Production Machines and Systems (I*PROMS-06), Cardiff, UK. **2006**, 454-459.

INDUCTION SINTERING OF FERROUS MATERIALS AT DIFFERENT TIMES AND INVESTIGATION OF THEIR MECHANICAL PROPERTIES

MEHMET YILDIRIM[1*], ENVER ATİK[2]

[1]*Institute of Science, Department of Mechanical Engineering, Manisa Celal Bayar University, Manisa, TURKEY.
[2]Engineering Faculty, Mechanical Engineering Department, Manisa Celal Bayar University, Manisa, TURKEY.

Abstract

In this study, Högenas ASC 100.29 iron powder was added to 0.8% zinc sterate and mixed for 30 minutes in a V-type mixer and compressed in a single-action press under 600 MPa pressure. The raw powder metal materials obtained were sintered in different seconds by induction sintering. Three-point bending, hardness, density, electrical resistance measurements were made on the obtained materials and their microstructures were examined.

Keywords: Materials Production, Powder Metallurgy, Induction Sintering

1. Introduction

Powder metallurgy (P/M) method is the process of converting metal or metal powders into useful engineering parts by processing them with thermal effects [1-2]. With powder metallurgy, it is possible to produce economical, cheap and materials with desired properties to be used in different areas of automotive, machinery and industry [2-4]. One of the most important steps in powder metallurgy is sintering. The sintering method is done in conventional furnaces. There are fast sintering methods in the sintering method. These; Induction sintering, microwave sintering, laser sintering, plasma sintering, discharge sintering and rapid sintering are methods. Induction sintering method is widely used in sintering applications. The most important advantage is that they have fast heating/cooling rates and can obtain fine-grained and high-density structures by preventing the materials from being exposed to high temperatures for a long time. In addition, the temperature gradients that occur due to the inward diffusion of heat from the surface in conventional heating are prevented by fast sintering methods [5-10]. There are many studies using ferrous metal with powder metallurgy method. [10-20]. In this study, the effects of induction sintering time of materials produced with iron powder, which is one of the most common metals, were investigated. Högenas ASC 100.29 iron powders were compressed in a single-acting press under 600 MPa pressure. It was sintered by induction sintering at different times. Three point bending, hardness, density and electrical resistance measurements of the sintered samples were made and their microstructures were examined.

2. Materials and Methods

In experimental studies, ASC 100.29 iron powder was used. The chemical properties, physical properties and sieve analysis of the powder used are given in Table 1.

Table 1. Chemical, physical properties and sieve analysis of Högenas ASC 100.29 iron powder [7]

Chemical Properties (%)		Physical Properties		Dimension Analysis (%)	
C	0,5	Apparent Density	2,42 g/cm^3	45 µm<	23
O	0,7			45-150 µm	69
Cu	3	Flow	31s/50 g	150-180 µm	8
Iron	Balance			>180 µm	0

ASC 100.29 iron powder and 0.8% zinc stearate added iron-based mixtures were formed and mixed in a V-type mixer for 25 minutes. Mixture powders were pressed under 600 MPa pressure and 10X10X55 mm samples were obtained. The pictures and dimensions of the obtained candles are given in Figure 1.

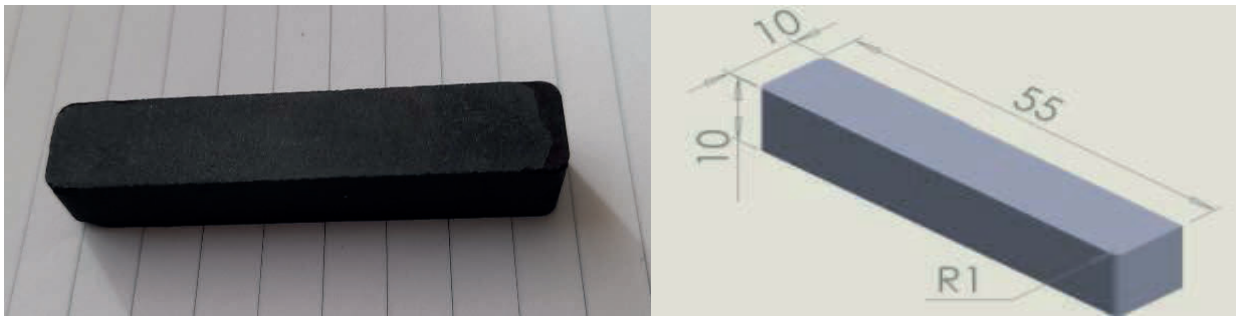


Figure 1. Photograph of a sintered sample, b) Dimensions of samples

In medium frequency induction sintering and argon environment, pre-sintering at 600 C for 10 minutes and sintering at 1120 C in argon environment at 8 different induction sintering times (30, 60, 90, 120, 180, 240, 300, 360 seconds) were carried out.
Electrical resistance measurements were measured with the Hioki 3541 Electrical Resistance Meter. Density measurements of the samples were measured with Archimedes Balance in accordance with ASTM B962-08 standard. Rockwell-B hardness measurements of the samples were carried out in BMS 200 RB brand device with 981 Newton force in accordance with ASTM E18-12 standard. Vickers hardness measurements of the samples were made in accordance with ASTM: E 92-82 standard by applying 50 g load for 10 seconds in Future-Tech FM-700 micro hardness tester. Three-point bending tests of the samples in Schimadzu brand Universal Tensile-Compression Tester were performed at a maximum support distance of 44 mm and a compression speed of 10 mm/min. regression values were determined. The cross-sectional microstructure images of the samples broken in the three-point bending tests were taken using a Nicon Eclipse LV150 brand optical microscope.

3. Results and discussion

The electrical resistance measurement results (µΩm) of the samples produced by sintering at different times are given in Figure 2.

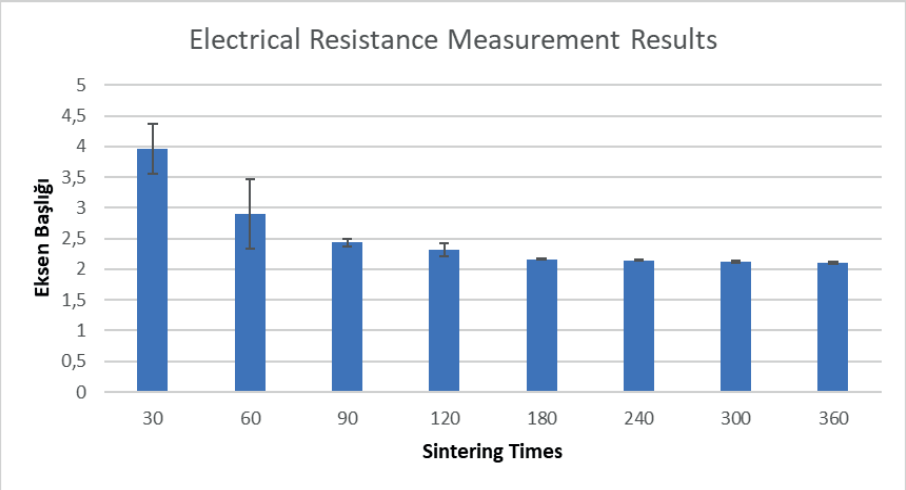


Figure 2. Electrical resistance measurement results

The density values of these samples measured by Archimedes' principle are given in Figure 3.

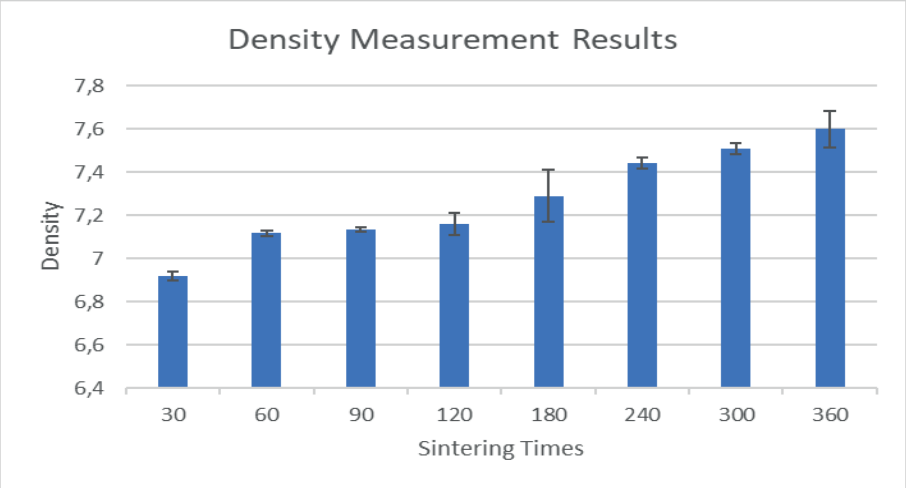


Figure 3. Density measurement results

Rockwell B hardness measurement results are given in Figure 4.

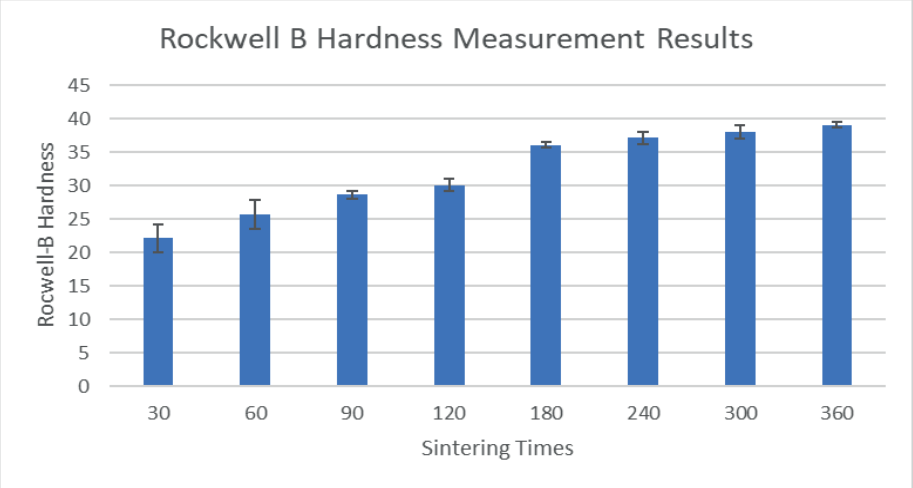


Figure 4. Rockwell-B hardness measurement results (HRB)

Vickers hardness measurement results of the samples are given in Figure 5.

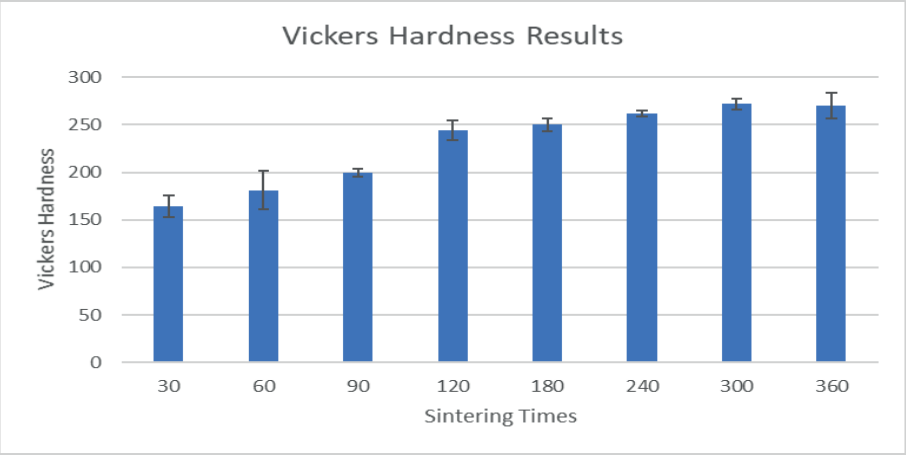


Figure 5. Vickers hardness measurement results of samples

The three-point bending test results of the samples are given in Figure 6.

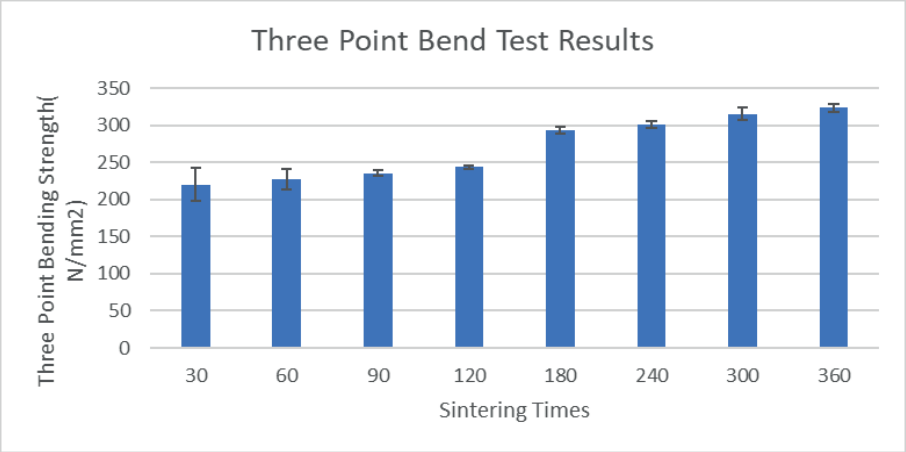


Figure 6. Three-Point Bend Test Results

The deflection values of the specimens obtained in three-point bending tests are given in Figure 7.

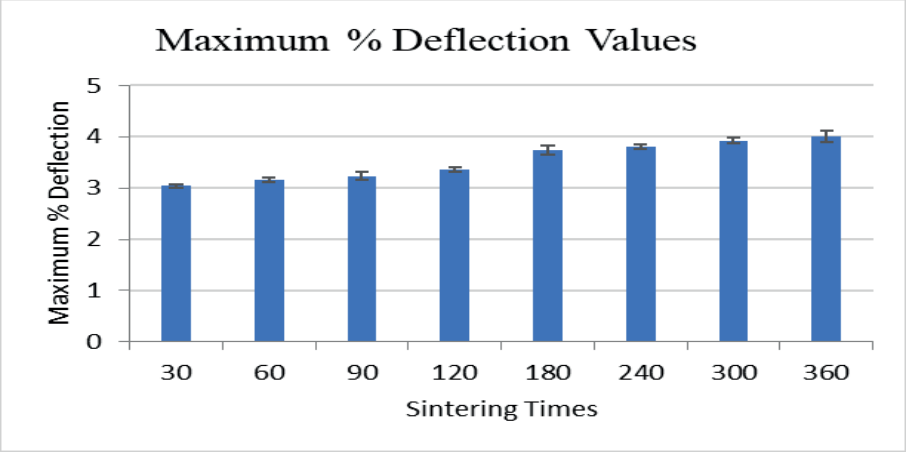


Figure 7. Maximum % Deflection Values

In Figure 8 and Figure 9, there are optical microscope images of the broken cross-sections of the samples sintered by induction at different times, resulting from the three-point bending test.

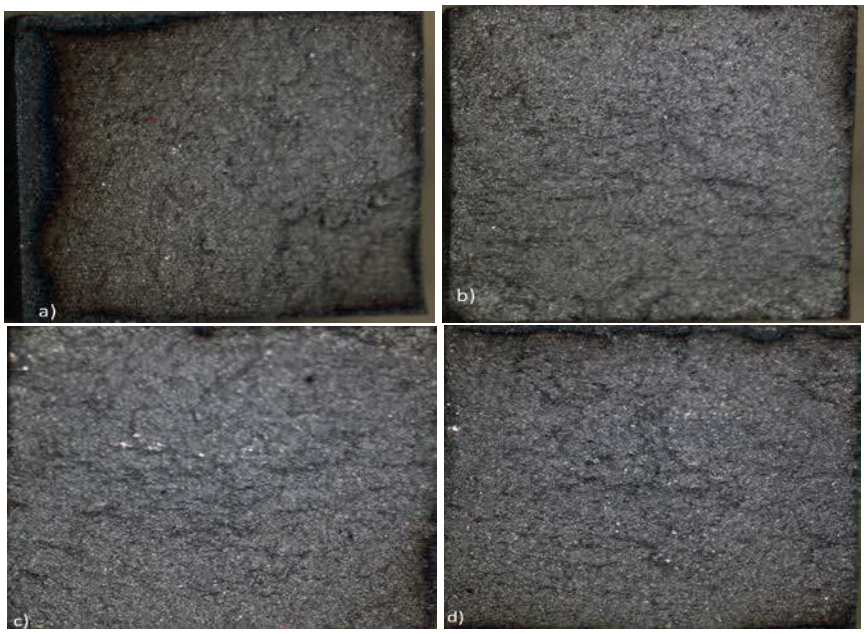


Figure 8. Broken Section Optical Microscope Images of Samples Sintered by Induction at Different Times as a result of Three-Point Bending Test a) 30 Seconds b) 60 seconds c) 90 seconds d) 120 seconds

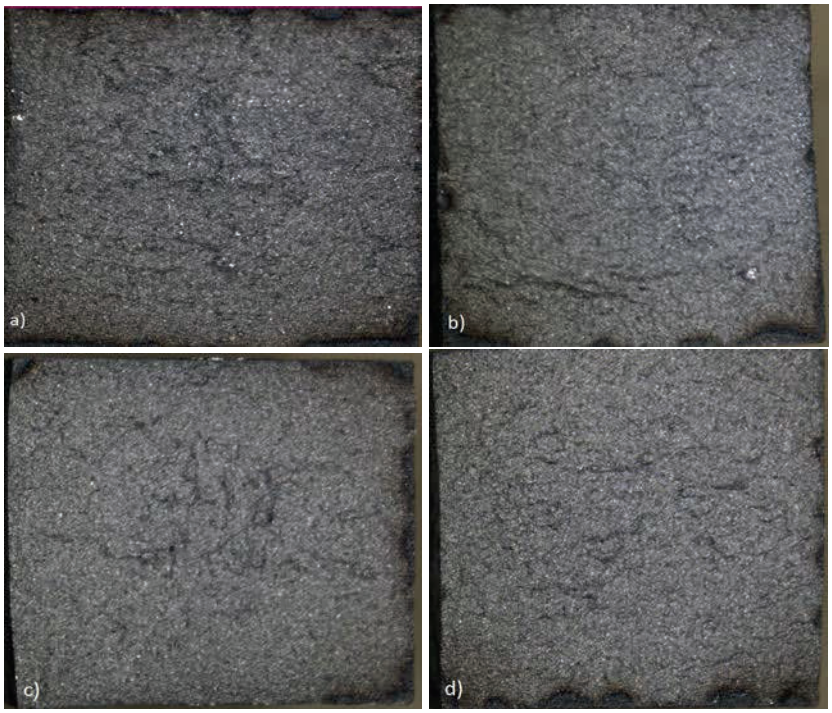


Figure 9. Optical Microscope Images of Broken Sections of Three-Point Bend Test of Induction Sintered Samples at Different Times a) 180 Seconds b) 240 seconds c) 300 seconds d) 360 seconds

4. Results

When we examine the electrical resistance measurement results, the electrical resistance generally decreases as the sintering time increases. In the Rockwell B hardness results, the hardness generally increases as the sintering time increases. In Vickers hardness results, as the sintering time increases, the hardness generally increases, but a decrease of 360 seconds has been observed. In the three-point bending test results, the bending strength and deflection values increased as the sintering time increased. When the fractured surfaces were examined with an optical microscope, it was observed that there was brittle fracture. When we look at the results in general, it is seen that all properties increase and increase up to 180 seconds, and after 180 seconds, except for the result of vickers hardness, it decreases. In this study, samples were produced by induction sintering.

References

1. Randall M. G., Durlu, N., Sarıtaş, S., Türker, M. Powder and Particulate Material Processes. TMMD, Ankara/Turkey. **2007**.
2. Erden, M.A. Effect of Pressing Pressure on Mıcrostructure and Mechanical Properties of Non-Alloyed Steels Produced By Powder Metallurgy Method. OHU J. Eng. Sci. **2017**, 6(1): 257-264.
3. Erden, M.A. The Effect of Mixing Time On Microstructure and Mechanical Properties of Non Alloyed Steels Produced by Powder Metallurgy Method, European Journal of Science and Technology. **2016**, 5(9):62-65.
4. Arık, H., and Orhun, D.Z. Investigation of Dry Sliding Wear Behavior of Powder Metal (P/M) Materials Produced from Mixture of Fe-Cu-C Powders. GU J Sci, Part A. **2018**, 5(1): 37-48.
5. Altuntaş, O., and Güral, A. A Study on Austempering a High Carbon Powder Metal Steel. International Journal of Engineering Research and Development. **2017**, 9(3):6-12.
6. Pingale, A.D., Owhal, A., Katarkar, A.S., Belgamwar, S.U., Rathore, J.S. Recent researches on Cu-Ni alloy matrix composites throughelectrodeposition and powder metallurgy methods: A review. Materials Today: Proceedings. **2021**.
7. Çivi, C., and Atik, E. Effect of the Sintering Temperature to Mechanical Properties of Fe Based Copper and Graphite Containing Materials. CBU J. of Sci. **2017**, 13(2):467-472
8. Atik, E., Çivi, C., Kökey, C., Eyici, G. Joining of Powder Metal Parts with Steel Parts by Induction Sintering Method. **2016**, 31(1):117-122.
9. Çivi, E., and Atik, E. The effect of inductive sintering to iron based powder metal parts. Journal of Alloys and Compounds. **2018**, 753:517-524.
10. Çivi, Tahralı, N., Atik, E. Reliability of mechanical properties of induction sintered iron based powder metal parts. Materials and Design. **2014**, 53:383-397.
11. Shi, H., Duan, L., Tan, S., Fang, X. Influence of pre-alloying on Fe-Cu based metal matrix composite. Journal of Alloys and Compounds. **2021**, 868:159134.
12. Lee, S.M., Jung, J.H., Fleury, E., Kim, W.T.,and Kim, D.H. Metal matrix composites reinforced by gas-atomised Al-Cu-Fe powders. Materials Science and Engineering. **2000**, 294:99-103.
13. Shin, D.S., Lee, C.H., Kim, S.H., Park, D.Y., Oh, J.W., Gal, C.W., Koo, J.M., Park, S.J., Lee, S.C. Analysis of cold compaction for Fe-C, Fe-C-Cu powder design based on constitutive relation and artificial neural networks. Powder Technology. **2019**, 353:330-344
14. Shi, H., Duan, L., Tan, S., and Fang, X. Influence of pre-alloying on Fe-Cu based metal matrix composite. Journal of Alloys and Compounds. **2021**, 868:159134.

15. Zafari, A., and Xia, K. Laser Powder Bed Fusion of Ultrahigh Strength Fe-Cu Alloys Using Elemental Powders. Additive Manufacturing. **2021**, 47:102270.
16. Li, Y., Lv, K., Shen, N., Chen, X., Chen, L., Li, F., and Hui, X. Novel Fe-C-B-P-Cu Nanocrystalline Alloys with Superb Magnetic Properties and Processability. Journal of Magnetism and Magnetic Materials. **2021**, 530:167915.
17. Wang, M., Jiang, Y., Li, Z., Xiao, Z., Gong, S., Qui, W. Microstructure evolution and deformation behaviour of Cu-10 wt%Fe alloy during cold Rolling. Materials Science & Engineering A. **2021**, 801:140379.
18. Liu, S., Xu, S., Jie, J., Zhang, J., Dong, Y., Li, X., and Li, T. Microstructure evolution and magnetic properties of metastable immiscible Cu-Fe alloy with micro-alloying B element. Journal of Alloys and Compounds, **2021**, 888:161627.
19. Wang, W.F. Effect of alloying elements and processing factors on the microstructure and hardness of sintered and induction-hardened Fe–C–Cu alloys. Materials Science and Engineering A. **2005**, 402:92–97.
20. Fu, S., Liu, X., Jin, J., Zhang, Z., Liu, Y., and Yan, M. Magnetic properties evolution with grain boundary phase transformation and their growth in Nd-Fe-Cu-Ga-B sintered magnet during post-sinter annealing process. Intermetallics. **2021**, 137:107303.
21. Zhang, D., Wu, T., Jia B., Wu, H., Zhang, L., Qin, M., Qu, X. Properties of intragranular-oxide-strengthened Fe alloys fabricated by a versatile facile and scalable route. Powder Technology. **2021**, 384:9-16.

ASİT BOYARMADDELERLE BOYANMIŞ DENİM KUMAŞLAR ÜZERİNE BİR ARAŞTIRMA

NURİYE KERTMEN [*1], ZEYNEP TEKEREK[1]

[1] İskur Denim İşletmeleri San. ve Tic. A.Ş., Kahramanmaraş, TÜRKİYE.

Özet

Bu çalışma kapsamında denim kumaşlar, farklı konsantrasyonlarda katyonik madde ve çapraz bağlayıcı ile katyonikleştirildikten sonra asit boyarmaddeleri ile boyanmışlardır. Boyanmış denim kumaşlara ait renk değerleri ve sürtme haslıkları, işlem görmemiş denim kumaşlara ait değerlerle karşılaştırılmıştır. Elde edilen sonuçlara göre, katyonikleştirici ve çapraz bağlayıcı miktarı artırıldığında denim kumaşlardan elde edilen renk verimi daha fazla olmuştur. Tüm denim kumaşlar için kuru sürtme haslıkları, yaş sürtme haslıklarından yüksek bulunmuştur. İşlem görmemiş kumaşlara kıyasla, asit boyarmaddeleriyle boyanan denim kumaşların yaş sürtme haslıkları değişmemekle birlikte, kuru sürtme haslıkları için de yaklaşık olarak benzer sonuçlar elde edilmiştir. Dolayısıyla denim kumaşların asit boyarmaddeleriyle boyanması mümkün olup, denim kumaşların renklendirilmesi bakımından yenilikçi bir alternatif olarak değerlendirilmiştir. Ayrıca denim kumaşların asit boyarmaddeleri ile boyanması, sürtme haslıkları bakımından bir dezavantaj oluşturmamıştır.

Anahtar Kelimeler: Asit Boyarmadde, Denim Kumaş, Kükürt Boyarmadde, Sürtme Haslığı.

1. Giriş

Geçmişte dayanıklılıkları ve rahatlıkları ile bilinen denim kumaşlar, günümüzde fonksiyonel ve yenilikçi yönleriyle de sıkça karşımıza çıkmaktadır. Denim kumaşlar, temel giysiler olarak algılanmasının yanında yüksek moda ürünü olarak da görülen her yaş ve cinsiyete uygun tekstil ürünleridir. Denim, çözgü ipliği indigo ile mavi boyalı, atkı ipliği boyanmamış pamuk ipliğinden oluşan ve genel olarak 3/1 veya 2/1 dimi konstrüksiyonuyla dokunan kumaş olarak bilinmektedir. Standart denim üretiminde çözgü iplikleri her durumda boyalı iken atkı iplikleri renksiz olmaktadır. Denim kumaşların ön ve arka yüz görünümleri birbirinden farklı olup, ön yüzde boyalı çözgü iplikleri arka yüzde ise renklendirilmemiş atkı iplikleri hâkimdir. Denim kumaşların çözgü iplikleri, küp boyarmaddelerinin bir üyesi olan ve denim için karakteristik olarak tanımlanan indigo boyarmaddesi ile boyansa da, çözgü ipliklerinin boyanmasında kükürt boyarmaddeleri de kullanılmakta veya her iki boya aynı denim kumaşın renklendirilmesinde kullanılabilmektedir. Denim kumaşların overdye olarak adlandırılan boyama işlemi, arka yüzde ağırlıklı olan atkı ipliklerinin kumaş formunda boyanması işlemidir [1].

Pamuğun boyanmasında yaygın olarak kullanılan boyarmaddeler; reaktif, direkt, küp ve kükürt boyarmaddelerdir. Pamuğun asit boyarmaddelerle boyanması, selüloz ve boyarmaddenin kimyasal yapıları ve iyonik yükleri bakımından uygun değildir. Pamuk liflerinin katyonize edilmesiyle anyonik boyarmaddelere afiniteleri artmakta ve pamuğu boyamakta kullanılmayan farklı boyarmaddeler ile boyama işleminin gerçekleştirilmesi mümkün olmaktadır. Katyonik pamuğun asit boyarmaddelerle boyanması ile klasik boyamaya göre daha iyi sonuçlar elde

edilmektedir. Çünkü anyonik boyarmaddenin katyonik pamuğa afinitesi daha fazla olmaktadır [2-3].

Asit boyarmaddeleri çoğunlukla organik sülfonik asitlerin sodyum tuzlarıdır ve anyon aktif renkli bileşenlerdir. Asit boyarmaddeleriyle boyama, asidik ortamda (pH 2-6 aralığında) gerçekleşmekte ve bu özelliklerinden dolayı bu tip boyarmaddelere asit boyarmaddesi denilmektedir. Pamuk lifleri ise bazik ortamda, tuz ve soda kullanarak boyanabilirler. Pamuk liflerinin katyonizasyonu sırasında, katyonik reaktif maddeler kullanılmakta ve liflerin sulu ortamda, hafif anyonik karakterdeki yüzeyi katyonik hale getirilerek anyonik boyarmaddelere afinitesi artırılmaktadır [4]. Oktav ve Dayıoğlu (2009) çalışmalarında, pamuk liflerine katyonikleştirme işlemi uygulamışlardır. Katyonikleştirilmiş pamuklu kumaşları asit boyarmaddelerinin yanı sıra, reaktif ve substantif boyarmaddeleri ile boyamışlar ve kontrol kumaşı olarak sadece merserizasyon uygulanmış pamuklu kumaş kullanmışlardır. Boyama işlemlerinden sonra kumaşların renk değerleri, haslıkları ve bazı kullanım özelliklerini incelemişlerdir. Sonuç olarak, katyonize edilmiş pamuklu kumaşlar daha yüksek renk koyuluğunda boyanmış olup, daha az boyarmadde ile daha yüksek renk verimi elde etmişlerdir. Kumaşların ışık haslıkları ise yeterli seviyede bulunmuştur [3]. Özdemir (2014) çalışmasında, asidik ve bazik ortamda tuzlu-tuzsuz ve soda kullanmadan katyonizasyon işlemi uygulanmış pamuğu direkt ve reaktif boyarmaddeler ile boyamıştır. Buna göre, katyonizasyon işlemi sayesinde pamuk liflerinin, reaktif ve direkt boyarmaddeleri ile standart boyamadan farklı olarak asidik ortamda da boyanabildiğini ve standart boyamadaki gibi soda ve tuz kullanımına ihtiyaç duyulmadığını vurgulamıştır. Ayrıca, boyama sonrası ard işlemler de azaldığından, yöntemin maliyet bakımından avantajlı olduğunu ifade etmiştir [5]. Özdemir (2017) diğer bir çalışmasında, katyonize edilmiş pamuk liflerini asidik, nötr ve bazik ortamda asit boyarmaddeleri ile boyamış ve pamuk liflerinin terbiye işlemleri karşısındaki davranışlarını, yıkama haslıklarını ve katyonize pamuğun boya tüketim özelliklerini inceleyerek sonuçları işlem görmemiş pamukla karşılaştırmıştır. Buna göre, daha çok yün ve poliamid boyamacılığında kullanılan asit boyarmaddelerinin pamuk lifleri için de kullanılabileceğini vurgulamış ve katyonik pamuğun asidik ortamda da boyanabilmesinin yaygınlaştırılabileceğini ortaya koymuştur [2]. Erkan ve ark., (2017) yaptıkları çalışmada, boyanmamış ve indigo boyalı iki farklı denim kumaşı, kökboya ekstraktı ile boyamışlardır. Kumaşları altı farklı mordan ile mordanlamışlar ve kumaşların renk değerlerini spektrofotometre ile ölçmüşlerdir. En açık renk değerleri, demir ile mordanlama yapılmış boyamalardan elde edilmiştir. Mordan ve boya konsantrasyonundaki değişikliklerin kumaşların yıkama haslıklarına olan etkisini de incelemişler ve iki tip kumaş için de yıkama haslıklarını iyi olarak değerlendirmişlerdir. İndigo boyalı denim kumaş ile yapılan denemelerde kuru sürtme haslıklarında düşüş gözlemişlerdir [6]. Yüce ve ark., (2020) çalışmalarında, kitosan ile ön işlem uygulanmış ve işlem görmemiş pamuklu kumaşları asit boyarmaddeleri ile boyamışlardır. Farklı reçetelerle boyadıkları kumaşların renk değerlerini, yıkama haslıklarını ve boyama flottesinin iletkenlik değerlerini karşılaştırmışlardır. Sonuç olarak, kitosan ile ön işlem uyguladıkları pamuklu kumaşların renk verimlikleri, tuz ile yapılan standart boyamalara göre daha yüksek bulunmuştur. Böylece kitosan ile ön işlem uygulanmış pamuklu kumaşların asit boyarmaddeleri ile boyanabileceğini ortaya koymuşlardır. Kitosanla işlem görmüş pamuklu kumaşların yıkama haslıklarını daha iyi olarak değerlendirmişler, ek olarak atık boyama flottesinin iletkenlik değerlerinin düştüğünü ifade etmişlerdir [7].

Bu çalışmanın amacı ise, denim kumaşları kuaterner amonyum bileşiği kullanarak katyonikleştirmek ve denim kumaş üretiminde en çok kullanılan indigo ve kükürt boyarmaddelerinden farklı olarak asit boyarmaddeleri ile kumaşı boyayarak, sınırlı bir

renklendirme olanağı bulunan denim kumaşlarda renk çeşitliliğini arttırmaktır. Diğer yandan boyanan denim kumaşların renk değerleri ve kuru/yaş sürtme haslıkları da incelenmiştir. Bu çalışma, 120M943 nolu TÜBİTAK 1005 projesi kapsamında devam etmekte olup, çalışmada asit boyarmaddesiyle boyanan denim kumaş özelliklerinin yalnızca bir kısmı sunulmuştur.

2. Materyal ve Metot

2.1. Materyal

Çalışma kapsamında kullanılan denim kumaş özellikleri Tablo 1' de verilmektedir.

Tablo 1. Çalışmada kullanılan denim kumaş özellikleri

Çözgü İpliği			Atkı İpliği				
Hammadde	**İplik Numarası (Ne)**	**Çözgü Rengi**	**Hammadde**	**İplik Numarası (Ne)**	**Renk**	**Kumaş Konstrüksiyonu**	**Birim Ağırlık (gr/m²)**
Pamuk	10,5/1 Ring	Kükürt Boyalı	Pamuk+Elastan	16/1 Ring+78 dtex Elastan	Ekru	3/1 Z Dimi	347

Çözgü iplikleri siyah kükürt boyarmadde ile boyalı denim kumaşlar emdirme-kurutma-fiksaj yöntemiyle katyonize edildikten sonra asit boyarmadde ile emdirme aplikasyonu yöntemiyle boyanmışlardır. Denim kumaşların katyonizasyonunda; katyonikleştirici olarak Benzalkonyum Klorür (% 50) (50 g/l ve 85 g/l), katalizör (30 g/l) ve çapraz bağlayıcı (30 g/l ve 50 g/l) kullanılmıştır. Asit boyama işleminde ise; asit boyarmadde (Triaset Bordeaux B) (% 3), egalizatör (10 g/l), kırık önleyici (10 g/l) ve sodyum sülfat (3 g/l) kullanılmıştır.

2.2. Metot

Denim kumaşların katyonizasyon ve boyama işlemlerine ait detaylı bilgiler, Tablo 2' de verilmektedir.

Tablo 2. Katyonizasyon ve boyama işlemlerine ait teknik bilgiler.

Kumaş Kodu	Katyonizasyon		Boyama	
Kontrol Kumaşı	Katyonik Madde	0	Asit Boyarmadde	% 0
	Çapraz Bağlayıcı	0		
A	Katyonik Madde	50 g/l		% 3
	Çapraz Bağlayıcı	30 g/l		
B	Katyonik Madde	50 g/l		% 3
	Çapraz Bağlayıcı	50 g/l		
C	Katyonik Madde	85 g/l		% 3
	Çapraz Bağlayıcı	30 g/l		
pH	4		4-5	
Flotte Oranı	1/30		1/30	
Sıcaklık	Oda Sıcaklığı		80°C	
Ard İşlemler	Durulama-Kurutma		Ön Yıkama-Deterjanlı Yıkama-Durulama-Kurutma	

Denim kumaşların ön ve arka yüz görünümleri James Heal marka ışık kabininde D65 gün ışığı altında fotoğraflanmış ve aynı oranda küçültülerek değerlendirilmiştir. Denim kumaşların L*

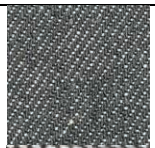
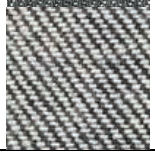
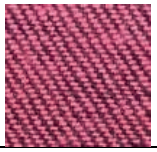
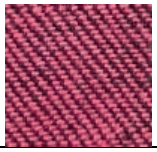
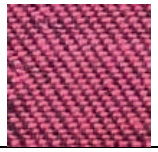
(açıklık-koyuluk), a* (a+; kırmızı, a-; yeşil), b* (b+; sarı, b-; mavi), C (renk doygunluğu) ve h (ton açısı) değerleri ise Datacolor 600 marka spektrofotometre ile D65 ışık kaynağı altında, 10° bakış açısı ile ölçülmüştür. Katyonikleştirilmiş ve boyanmış denim kumaşların yaş ve kuru sürtmeye karşı renk haslıkları TS 717 EN ISO 105- X12 test standardına göre James Heal Crockmaster cihazı ile ölçülmüştür. Kumaşlar, haslık testlerinden sonra gri skala (ISO 105-A03:1993) ile karşılaştırılarak test sonuçları değerlendirilmiştir. Gri skalaya göre 1, en kötü; 5, en iyi değeri ifade etmektedir.

3. Bulgular ve Tartışma

3.1. Kolorimetrik Ölçümler

Denim kumaşların ön ve arka yüzlerine ait görüntüler Tablo 3' te; kolorimetrik ölçüm değerleri ise Tablo 4' te verilmiştir.

Tablo 3. Denim kumaşların ön ve arka yüz görünümleri.

	Kumaş Kodu			
Kumaş Yüzü	**Kontrol Kumaşı**	**A**	**B**	**C**
Ön Yüz				
Arka Yüz				

Tablo 4. Denim kumaşlara ait renk değerleri.

	Kumaş Kodu	L*	a*	b*	C	h
Ön Yüz	**Kontrol Kumaşı**	21,36	0,57	-0,44	0,72	322,04
	A	16,72	3,40	-1,42	3,69	337,32
	B	29,15	24,61	-3,60	24,88	351,69
	C	15,87	3,26	-1,19	3,47	339,98
	Kumaş Kodu	**L***	**a***	**b***	**C**	**h**
Arka Yüz	**Kontrol Kumaşı**	55,95	-0,26	0,99	1,02	104,74
	A	31,69	22,99	-4,95	23,52	347,66
	B	16,29	4,36	-1,50	4,61	341,06
	C	28,80	23,77	-4,04	24,11	350,35

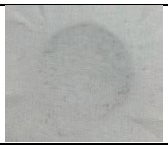
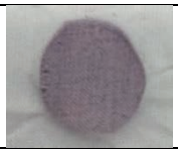
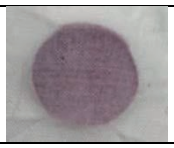
Denim kumaşların ön yüzünde bir miktar kırmızı renk nüansı alınsa da yaşanan değişim belirgin değildir. Esas renk değişimi beklenildiği gibi, kumaşın ekru renkli atkı ipliklerinin yoğunluklu olduğu arka yüzünde meydana gelmiştir. A ve B kodlu kumaşlara uygulanan tüm işlemler aynı olup, yalnızca çapraz bağlayıcının miktarı değiştirilmiştir. Buna göre aynı miktarda katyonik madde kullanılmasına rağmen çapraz bağlayıcı miktarı artırıldığında arka yüze ait L* değeri azalmıştır, yani renk koyulaşmıştır. Aynı şekilde A ve C kodlu kumaşlar için çapraz bağlayıcı miktarı aynı tutulmasına rağmen katyonik madde miktarı artırılmıştır ve yine kumaşın arka yüzüne ait L* değeri azalmış ve renk koyulaşmıştır. Dolayısıyla çapraz bağlayıcı veya benzalkonyum klorür miktarı arttıkça daha fazla boyarmadde life bağlanabildiğinden elde edilen renk verimi daha yüksek olmakta ve renk koyuluğu artmaktadır. En yüksek L* değeri ise

katyonik madde ve çapraz bağlayıcının eşit oranda kullanıldığı B kumaşından elde edilmiştir. Denim kumaşların a* değerleri, kırmızı eksende; b* değerleri ise mavi eksendedir. Asit boyarmaddeleriyle boyanan denim kumaşların renk parlaklığı daha fazla olmuştur. A, B ve C kumaşlarının tümünde ton açısı değerleri artmıştır ve boyamaların, ön ve arka yüz için kırmızı renk düzleminde olduğu görülmektedir.

3.2. Sürtme Haslıklarının Değerlendirilmesi

Denim kumaşların yaş ve kuru sürtme haslıkları için elde edilen sonuçlar Tablo 5' te verilmiştir.

Tablo 5. Denim kumaşların yaş ve kuru sürtme haslık değerleri.

Kumaş Kodu	Sürtme Haslığı	
	Yaş	**Kuru**
Kontrol Kumaşı		
	1/2	**4**
A		
	1/2	**4**
B		
	1/2	**3/4**
C		
	1/2	**3/4**

Kumaşların kuru sürtme haslığı değerleri 3/4 ve 4 arasında oynamaktadır. Kontrol denim kumaşı da dahil olmak üzere tüm denim kumaşların yaş sürtme haslığı değerleri oldukça düşük bulunmuştur. Ancak kontrol kumaşın yaş sürtme haslığı ile kıyaslandığında asit boyarmaddelerle boyanan denim kumaşların yaş sürtme haslıkları değişmemiştir. Diğer yandan kuru sürtme haslıklarının genel olarak iyi ve kontrol kumaşına benzer olduğu görülmüştür. Kontrol kumaşı haricinde diğer 3 denim kumaş arasından en yüksek kuru sürtme haslığı A kumaşından elde edilmiştir.

Patent

Bu çalışmanın konusu ile ilgili olarak Türk Patent Enstitüsü' ne 2020/22850 numaralı patent başvurusu yapılmış olup, araştırma ve inceleme süreci devam etmektedir.

Teşekkür
Bu çalışma, İskur Denim İşletmeleri San. Ve Tic. A.Ş. bünyesinde gerçekleştirilmiş olup; TÜBİTAK-1005 Ulusal Yeni Fikirler ve Ürünler Araştırma Destek Programı-120M943 numaralı proje kapsamında desteklenmektedir.

Kaynaklar

1. Kurban, S. N., Babaarslan, O. Süper streç denim kumaşların özelliklerine dair literatür incelemesi. Tekstil ve Mühendis. **2019**, 26(113):104-115.
2. Özdemir, H. Katyonize ve normal pamuğun asit boyarmaddeler ile boyanması ve boyama sonuçlarının karşılaştırılması. Ulusal Çukurova Tekstil Kongresi-UÇTEK. **2017**, 80-88.
3. Oktav, M., Dayıoğlu, H. Pamuk liflerinin iyonik modifikasyon yardımıyla boyanabilirlik özelliklerinin incelenmesi. Süleyman Demirel Üniversitesi, Fen Bilimleri Enstitüsü Dergisi. **2009**, 13(3):277-296.
4. Şahin, Y. Asit boya banyosu atık sularının kimyasal prosesler ile ön arıtabilirliğinin incelenmesi. Yüksek Lisans Tezi, İstanbul Teknik Üniversitesi, Fen Bilimleri Enstitüsü. **2006**.
5. Özdemir, H. Katyonize ve normal pamuğun çeşitli boyarmaddeler ile boyama sonuçlarının karşılaştırılması. Adıyaman Üniversitesi Mühendislik Bilimleri Dergisi. **2014**, 1:14-22.
6. Erkan, G., Şengül, K., Kaya, S. Denim kumaşların Rubia Tinctorum l. (kökboya) ile boyanması üzerine bir araştırma. Tekstil ve Mühendis. **2010**, 17(80):1-10.
7. Yüce, İ., Erdoğan, S., Becenen, N., Şen, H. Kitosan ile ön işlem görmüş pamuklu kumaşın asit boyalarla tek adımda renklendirilmesi. Trakya Üniversitesi Mühendislik Bilimleri Dergisi. **2020**, 21(1):1-14.

THE EFFECT OF USING STEEL MESH ON THE INTERLAMINAR FRACTURE TOUGHNESS OF FML COMPOSITES

MEHMET ALİ AKELOGLU*[1], MELİH BAYRAMOGLU*[2]

[1] Gaziantep University, Engineering Faculty, Mechanical Engineering Department, Gaziantep, TURKEY.
[2] Cukurova University, Engineering Faculty, Mechanical Engineering Department, Adana, TURKEY.

Abstract

Fiber metal laminate (FML) composites were created primarily to improve the fatigue strength of modern civil aviation industry. And further studies show that, it provides additional advantages such as, excellent impact and damage tolerance, fire resistance and impact resistance with the aid of different configurations, while having a low weight. However, the production of a FML composite is a significant challenge, due to poor bonding at the fiber-metal interface. In this study, the interfacial bond behavior at the fiber-metal interface was investigated by determining their Interlaminar Fracture Toughness values. Test specimens were produced by using, extremely thin stainless steel mesh materials, instead of sheet metal layers as a traditional composition of FML composites. Specimens were produced as FML (Fiber Metal Laminate) composites with steel meshes, and FRP (Fiber Reinforced Polymer) composites in the same combination without steel mesh layer. In experimental stage, specimens were investigated with "DCB (Double Cantilever Beam) Tensile Testing" in "Mode I", and their "Interlaminar Fracture Toughness" values are examined in accordance with ASTM 5528-01 Standards. Finally, test results obtained from FRP and FML specimens were compared in order to show the effectiveness of using steel mesh layer for a better Interlaminar Fracture Toughness.

Keywords: Composites, fiber reinforced polymer (FRP), Fiber metal laminate (FML), Steel mesh, Interlaminar fracture toughness.

1. Introduction

In the industry of nowadays, there is a need for light, high-strength new materials with superior and specific properties to be used in the field of advanced technology. Laminated composites have a wide area of use in the industry due to their high rigidity and strength as well as their lightness. Fiber Metal Laminate (FML) is a family of hybrid composite structure formed from the combination of metal layers, sandwiching a fiber-reinforced plastic layer. FML's are composed of alternatively stacked metal and fiber reinforced composite layers, with advantages of hybrid nature from two different constituents (metal and fiber), the FML's gives excellent mechanical properties like high corrosion resistance, outstanding strength to weight ratio compared to conventional composite lamina.[1] Fibrous composite materials are as strong as steel, have a lower density than magnesium, and can be tailored to have maximum strength and stiffness in specific directions. Thus, composite structures are potentially much lighter than conventional metallic structures, but they're also very notch sensitive because of the linear-elastic fibers that carry most of the load. [2]

Parts produced with composite materials may break due to incorrect designs, material defects, unexpected loads, manufacturing defects and other complex and inexplicable reasons, or separation between layers may occur. At this point, delamination, which is an important damage type that reduces the performance of composites, occurs, and fracture toughness between layers is needed in damage tolerance analyzes to prevent this situation. Fracture toughness is an indication of the amount of stress required to propagate a preexisting flaw. It is a very important material property since the occurrence of flaws is not completely avoidable in the processing, fabrication, or service of a material/component. Fracture toughness is a quantitative way of expressing a material's resistance to brittle fracture when a crack is present. Determination of fracture toughness in FML composites, is very important to perform an analysis of structural integrity to estimate damage tolerated and residual strength of the material against the propagation of cracks. It should be noted that this fracture toughness criteria with its respective testing techniques shows limitations and discussion about the representativeness to determine the residual strength of FML composite materials having mechanical anisotropy, thin thickness, dependence on the geometry and a mechanism of fracture associating the metal fracture propagation and delaminate between metallic sheet and the resin layers reinforced with nonmetallic fibers.[3] The interlaminar fracture toughness "G_C "is the total energy absorbed per unit increase in crack length per unit thickness. G_C is also called the energy release rate or crack driving force. G_C; matrix toughness/brittleness, fiber volume ratio/orientation changes with composite production and experimental conditions. The stress intensity factor "*K*" is a parameter related only to the stress state and the geometry of the crack and does not depend on the properties of the material. Therefore, the G_C and K values are usually found from experiments with using standard samples in order to determine what errors are permissible in real structures and in the material under certain conditions. Different type of metallic materials have been in FMLs as metallic layers to investigate their effects on the mechanical properties. In this work stainless steel mesh have been used as a metallic layer and its effect on the interlaminar fracture toughness has been investigated.

2. Material and Methods

2.1 Material

Carbon-fiber woven orientation were used for the FML production with AISI 304 stainless steel with 100 and 500 mesh sizes were used as a metal layer in FML. During the manufacturing of FML samples, carbon fiber woven fabrics with a density of 400 gr/m^2 and thickness of 0.30 mm were used. The chemical composition and pyhsical properties of the metallic material used in this work are given in Table 1. and Table 2. respectively.

Table 1. The chemical composition of AISI 304 stainless steel

%C	%Cr	%Fe	%Mn	%Ni	%P	%S	%Si
0-0,8	18-20	65,8-74	0-2	8-11	0-0,045	0-0,03	0-1

Table2. The physical properties of AISI 304 stainless steel 100&500 mesh

Mesh Size	Thickness, mm	Wire Diameter, mm	Number of Holes/cm^2	Open Area, %
100	0,154	0,10	39	37
500	0,025	0,025	206	25

In this study, 16 layer of carbon fiber woven fabrics are combined together with epoxy resin to produce Fiber Reinforced Polymer (FRP) plates. And also, 1 layer of extremely thin steel mesh

is placed into the middle of structure to produce FML plates. The values in the material properties table given above belong to pure carbon fiber woven fabric and, AISI 304 stainless steel mesh material. Changes in the mechanical properties of the material will occur for different compositions of layers.

2.2 Vacuum Assisted Resin Transfer Molding (VARTM) Process

Traditionally, composites have also been fabricated by similar methods. However, infusing liquid resin into dry fabric layers solely by vacuum pressure to produce high quality materials has proven to be a more cost-effective process for preparing composites. This process, known as vacuum assisted resin transfer molding (VARTM), utilizes a flow distribution media to allow the resin to proceed rapidly on the surface over the length of the part followed by the slower through the thickness infusion through the part, thereby decreasing infusion times. Figure 1, illustrates a typical VARTM set-up.[4], [7]

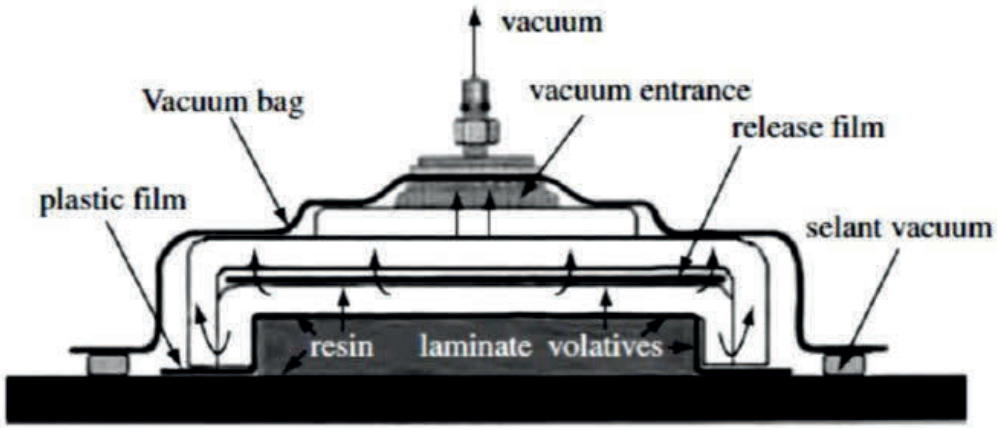


Figure 1. Schematic representation of VARTM Process

The fabrication of FRPs were carried out by using L160 epoxy and its H160 hardener with a mixing ratio of 4:1 by weight. The total amount of resin set was determined equal to the total amount of fiber fabrics.[5] The prepared resin was applied to each fiber fabric with hand lay-up before VARTM process as shown in Figure 2.

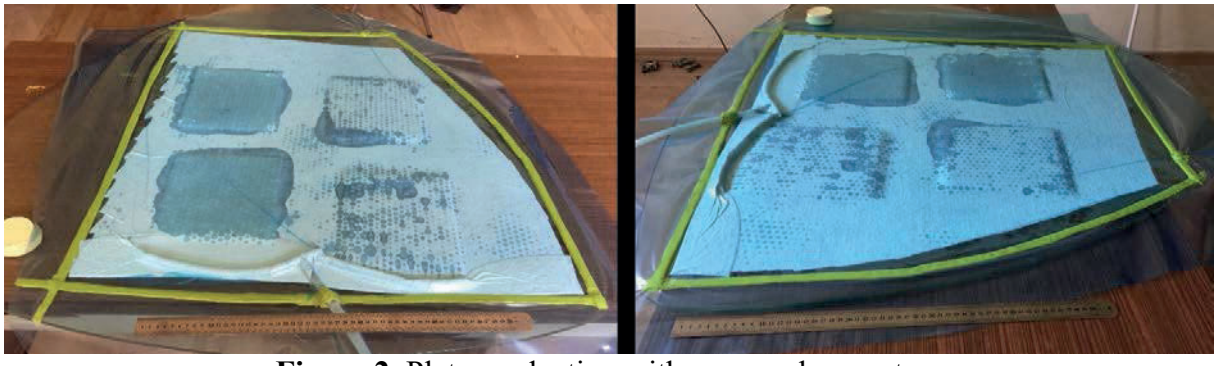


Figure 2. Plate production with vacuum bag system

The curing process was completed for about 24 hours under vacuum. After curing process, the FRP laminates were cut to standard test dimensions by using CNC milling machine. Plates and cutted specimens are shown in Figure 3.

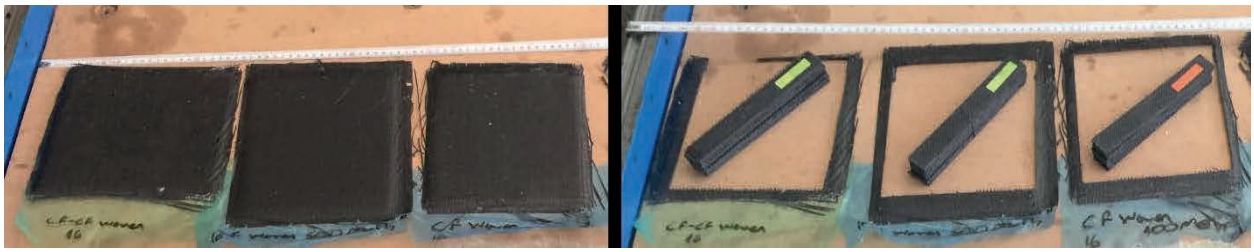


Figure 3. Produced plates and specimens cutted out from them

2.3 Experimental Study; Double Cantilever Beam (DCB) Testing

The Mode-I testing follows the standard specimen of ASTM D5528-01 to measure the Mode-I fracture toughness, G_C, of continuous fiber reinforced composite material. The specimens used in this testing are the double cantilever beam (DCB) specimen shown in Figure 4. The position for delamination opening should be inserted between the plies using a non-adhesive film which approximately 13 µm thickness, and the length of the film is 50 mm, plus the extra length of the hinges. The length of the specimen should be at least 125 mm and 20 to 25 mm wide. The specimen used a constant crosshead rate between 1 to 5 mm/min to promote delamination. Delamination lengths are determined visually, but for more accurate readings, a travelling microscope is recommended.[6]

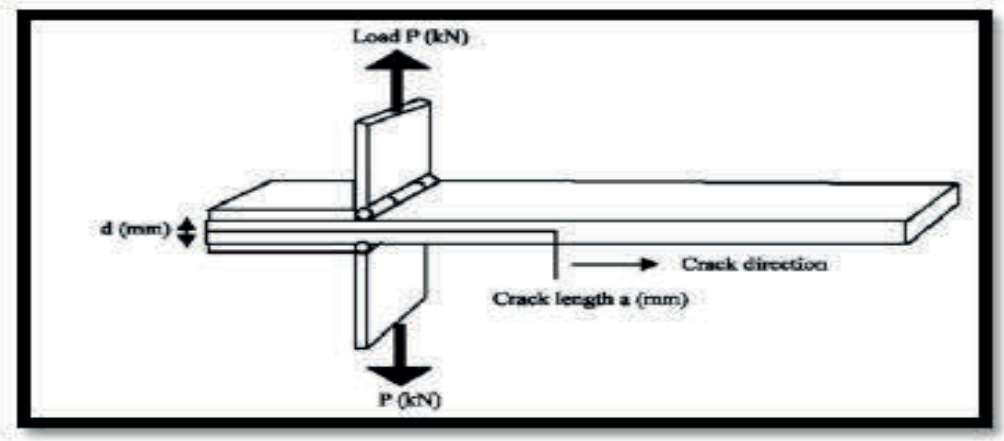


Figure 4. DCB specimen geometry mode 1

In the study, DCB specimens are produced according to ASTM 5528-01 standarts. Plates are produced with 5mm thickness and specimens are cutted out with 25 mm wide and 175 mm long. First 50 mm from tip is inserted with non-adhesive thin film to start pre-crack progress.[8] Total 15 specimens are prepared with 3 different types and 5 specimens for each. Which are, carbon-fiber woven FRP, carbon-fiber woven 100 mesh FML and carbon-fiber woven 500 mesh FML. Furthermore, specimens are marked with certain lengths from side according to ASTM 5528-01 standarts by using millimetric paper and also, brass piano hinges are fixed from tip with epoxy glue as shown in Figure 5.

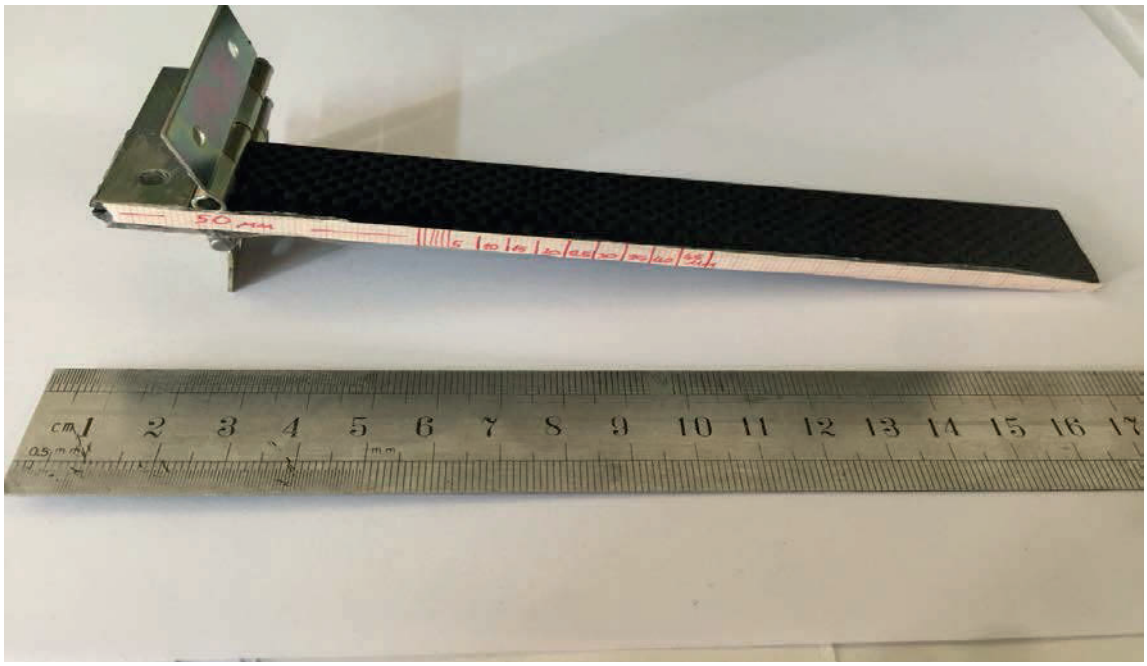


Figure 5. DCB specimen.

All tests were conducted according to ASTM-D 5528-01 standards.at temperature of 22 ºC and relative humidity of 50% by a universal testing machine with a 300 kN capacity as seen in Figure 6.



Figure 6. SHIMADZU tensile test device.

The specimens were connected to jaws of tensile and crack propagation along the z-axis amounts for certain points were determined after loading the specimens at constant speed of 2 mm/min as shown in Figure 7.

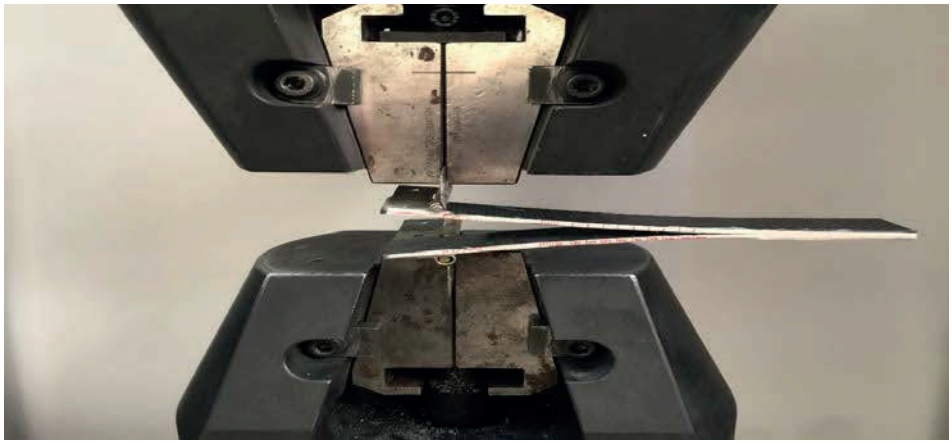


Figure 7. DCB specimen under loading.

20 data per second for each loading-displacement situation were taken and load-displacement curves were created automatically on the screen of the machine. According to ASTM 5528-01 standard, the loading process consists of 2 stages. First stage of loading ended at a displacement of approximately 10 mm and initial crack propagation of 2-3 mm. Then, test was continued with a constant 2 mm/min jaw displacement speed until it became a natural pre-fracture has been created. In the second stage, the loading was constant until the crack length of 45 mm from pre-crack and 95mm from the tip of the specimen. Finally, jaws were returned to the zero point with a constant displacement velocity of 25 mm/min. A video camera with a program build with python code was also used for observing crack propagation as shown in Figure 8.

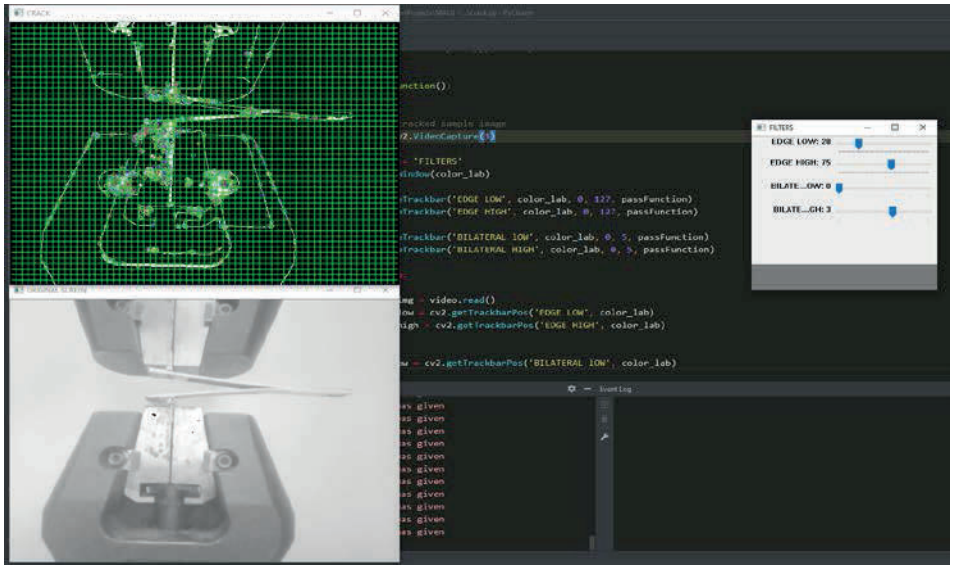


Figure 8. Crack propagation imaging with video camera.

3. Result and Discussion

In this study, total length of crack was fixed to 95 mm total. Which is, 50 mm initial crack from non-adhesive part (pre-crack section), plus 45mm crack length for each specimen. Displacement values were recorded as stroke parameters between two jaws of device. Test has ended for each specimen when, they reached to its total length of 95 mm. The experimental results obtained from DCB test and a load-displacement table are presented in order to evaluate the results clearly. The fracture toughness capacity of each featured specimen was plotted in terms of stress

and strain. Load point displacement curves are given for Carbon-fiber woven FRP, carbon-fiber woven FML with 100 mesh and carbon-fiber FML with 500 mesh in Figure 9.1., Figure 9.2. and Figure 9.3 respectively. As shown in these figures, the changes in the displacements were as expected under recorded load points.

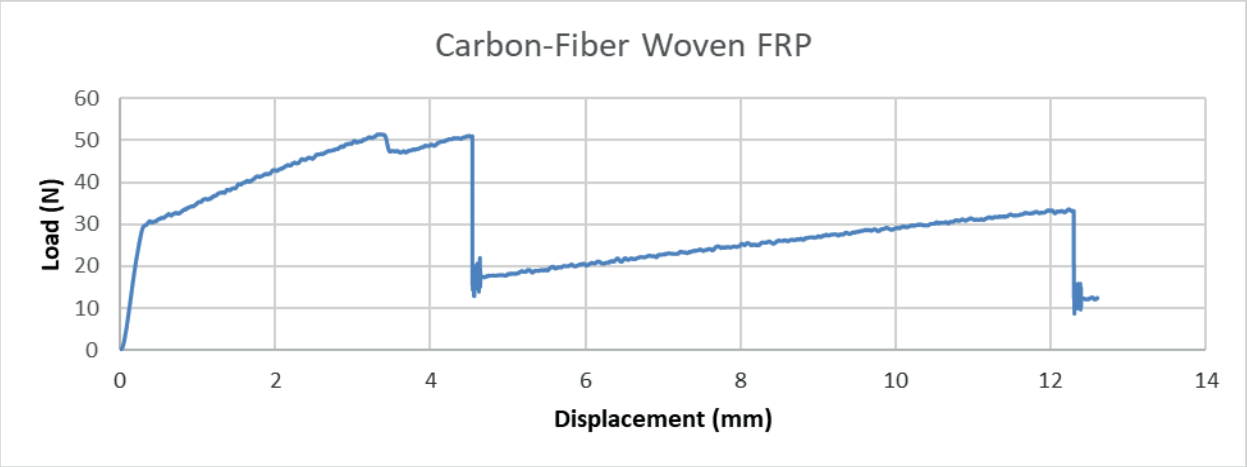


Figure 9.1. Carbon-fiber woven load point displacement graph

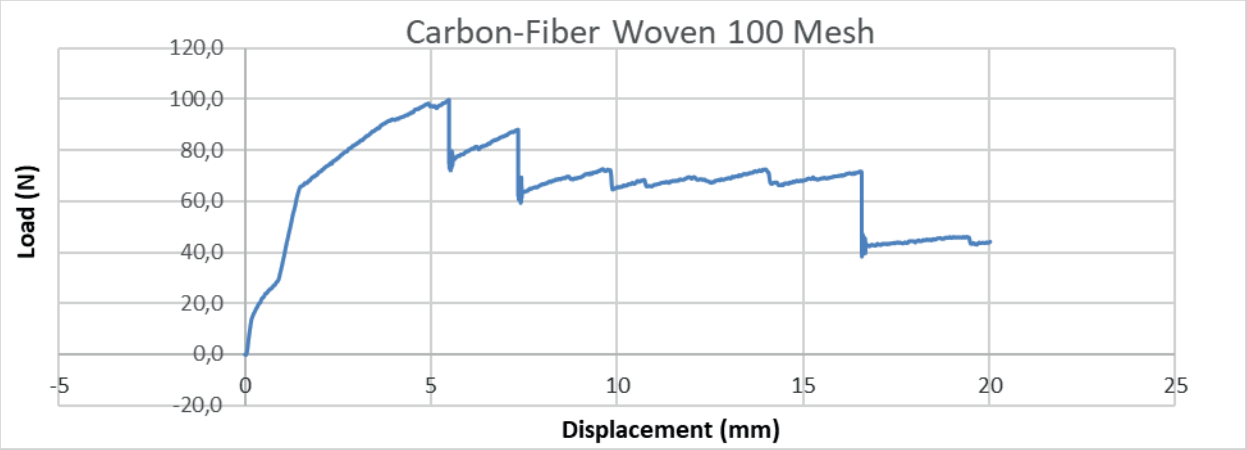


Figure 9.2. Carbon-fiber woven 100 Mesh load point displacement graph

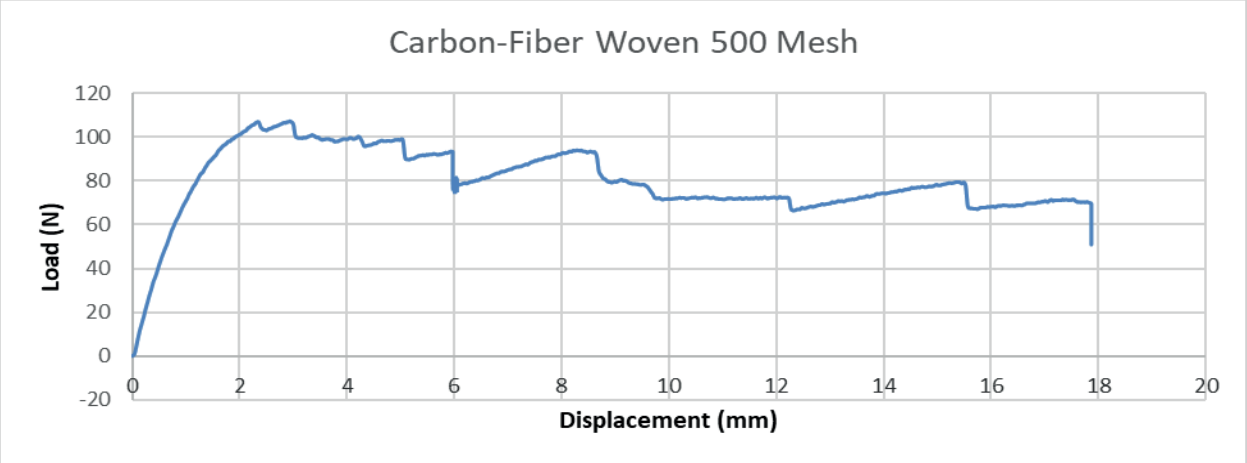


Figure 9.3. Carbon-fiber woven 500 Mesh load point displacement graph.

4. Conclusions

In this study, a steel mesh layer was added to the middle of FML composites and its effect on the fracture toughness has been investigated by conducting tests on universal tensile testing machine. Tensile tests were carried out on the specimens according to the ASTM 5528-01. The followings may be concluded from the results of the study. According to load point displacement curves for each type of specimens, it can be said that using steel meshes as a middle layer of composition resulted an increase in the fracture toughness strength of FML material. While interpreting load point displacement curves, they showed that, FMLs with a steel mesh layer created more resistance against the loads compared to samples produced without using steel mesh. It was also observed that FMLs with steel mesh layers were resisted against same amount of loads longer than other specimens. Finally, it can be concluded that, steel meshes are useful parameter to improve interlaminar fracture toughness of fiber metal laminate (FML) composites.

5. References

1. Salve, A., Kulkarni, R., Mache, A. A Review: Fiber Metal Laminates (FML's) Manufacturing, Test Methods and Numerical Modeling. International Journal of Engineering Technology and Sciences (IJETS). **2016.**
2. Poe, C.C. Fracture Toughness of Fibrous Composite Materials. NASA Technical Paper, NASA-TP-2370. **1984**
3. Rios, J., Chomik, E., Balderrama, J., Cambiasso, F. Determination of fracture toughness J on fiber-metal laminate type CARALL with sheets of aluminium 6061. International Congress of Science and Technology of Metallurgy and Materials, (CONAMET). **2014**.
4. Jensen, B. J., Cano, R. J., Hales, S. J., Alexa, J. A. Fiber Metal Laminates Made by The VARTM Process. NASA Langley Research Center, Hampton, VA 23681-0001. **2009**.
5. Boztepe, M., Bayramoglu, M., Uzay, C., Geren, N. Improving the Adhesion Bonding Strength for FML Composites by Using an Extremely Thin Mesh Steel. European Mechanical Science. **2017**, 1(4): 111-116.
6. Nasuha, N., Azmi, A., Tan, C. A review on mode-I interlaminar fracture toughness of fibre reinforced composites. Journal of Physics: Conference Series 908 012024. **2017.**
7. Sinmazcelik, T., Avcu, E. Bora, M., Coban, O. A review: Fibre metal laminates, background, bonding types and applied test methods. **2011**.
8. Standard Test Method for Mode I Interlaminar Fracture Toughness of Unidirectional Fiber-Reinforced Polymer Matrix Composites. ASTM International, Designation: D 5528 – 01. **2007**.

FAILURE ANALYSIS OF 3D-PRINTED AND CONVENTIONALLY MANUFACTURED POLYMER GEARS

ABDURRAHMAN GÜNGÖR*[1], NECIP FAZIL YILMAZ[1,2], MUSA YILMAZ[1]

[1]Gaziantep University, Engineering Faculty, Mechanical Engineering Department, Gaziantep, TURKEY.
[2]Board of Trustees, Hasan Kalyoncu University, Gaziantep, 27410, TURKEY.
*abdurrahmangungor10@gmail.com

Abstract

Gear is a very important machine element used for power/motion transmission. In the past few decades, polymer gears have gained importance due to the increasing demand for lighter, quieter, durable and cost-effective products. In many applications, polymer gears have advantages such as ease of manufacture in bulk quantities, noiseless operation, low cost, light weight, less maintenance, etc. It has been effective in being preferred over metal gears day by day. Polymer gears are used in motion and power transmission under different loads and speeds. Polymer composite gear finds more applications due to low material, manufacturing cost and weight compared to metal gears, even polymeric materials suffer from poor mechanical strength compared to metals. In this study, Polyoxymehtylene (POM) gear produced with traditional methods and CarboflexV60 gear produced with 3D printer were used. Temperature, surface roughness, noise and torque values while the system is running. In the gear test, it was observed that the performance of the gear produced with the 3D printer was better. During its operation, its most distinctive feature is that it instantly throws out the heat on its surface and does not reach a high temperature.

Keywords: POM, Carbon powder added thermoplastic polyurethane (CV60), Wear Gear

1.Introduction

Gear systems are found in many mechanical systems from simple systems to complex systems. There is a huge shift in the industry from metal gears to polymer, thermoplastic gears. Polymer gears have replaced metal gears in many ways and these gears have unique advantages over metal gears, for example; price-performance, quiet operation, operation without lubrication, etc..(Bı, 2019) Thermosets, on the other hand, have better bout stability, heat resistance and electrical properties. It is more difficult to mold. For this reason, injection is used in the molding of thermoplastics and printing and transfer methods are used in thermosets. Engineering plastics are generally a group of plastics that are resistant and resistant to heat, chemicals, impact, flame.(Kim et al., 2019) These plastics are replacing metal gears every day. It is a group of plastics that are resistant to higher temperatures, also called performance plastics (high performance and super thermal resistant). Thermoplastics deform when pressure and/or heat are applied.(Schuhler et al., 2018)(Singh et al., 2018) Thermoplastic polyurethane (TPU) material also has a higher wear resistance and a higher resistance to oils and greases. Unlike other rigid thermoplastics, TPU filament has qualities that include flexibility and conformability. It also has excellent interlayer adhesion, and there is no curling or delamination during the 3D printing process. Thermoplastics deform when pressure and/or heat are applied.

POM, also known as acetal, polyacetal and polyformaldehyde, is a thermoplastic used in precision parts that require high hardness, low friction and excellent dimensional stability.[5]

POM's engineering applications include fasteners such as threads, screws and nuts, and it is used in the construction of moving machine parts that need to work in water and humid environments without lubrication. Among its main features; It has higher hardness, low friction, high wear and heat resistance, higher friction resistance than nylon. It is resistant to higher temperatures than the polyamide group.[6]Thermoplastic gear materials come to the fore with their features such as lightness, resistance to high heat and impacts and excellent surface quality. There are many production ways of plastic gears. CV60 TPU black filament gear is used. This black filament TPU [7] structured filament is preferred. TPU is the most common type of TPE (Thermoplastic Elastomer) used in 3D printing. It can be printed more easily than other flexible filaments, and at the same time, a good hardness and durable material is obtained. Extensive research to achieve high power transmission and to understand gear behavior should be done predominantly with metal-polymer gear pairs.

Prashant Kumar Singh et al. [8] investigated the behavior of three different thermoplastic gears at different torques and speeds. The materials used in this plastic gear application are Acrylonitrile Butadiene Styrene (ABS), High Density Polyethylene (HDPE) and POM.The POM gear has run 2 million cycles with no signs of failure. Some of the results are as follows; They found that the specific wear rate of polymer gears increases with torque and decreases with rotational speed. A higher rotational speed increases the strain rate, which increases the wear resistance of the gear material. They observed that the higher the rotational speed, the lower the gear tooth wear rate. Tavcar et al.[9] Nylon 6 Nylon 66 investigated life tests for various materials and reinforced materials, including POM and PPS, and the results showed that reinforced materials last longer when lubricated. R.Mohzendadeh et al.[10] POM and POM/CB (Polyoxymethylene Carbon black) produced carbon reinforced gears by injection molding. Their aim is to examine the wear and temperature behavior of these gears at different speeds of 6Nm and 8Nm different torques. As a result of these studies, they found that the POM/CB gear has a low temperature and this gear has a longer life. Tuğçe Tezel et al.[11] They worked on the failure of 3D-printed steel gears. They examined 420 steel gears, produced by both tempered and conventional methods. They investigated the effects of rotational speed, torque, manufacturing technique, and post-production surface treatment. The use of Carbon Fiber Reinforced Polymer (CFRP) composite materials is in greater demand due to their high strength, excellent strength-to-weight ratio and corrosion resistance.

Kenmao et al. [12] examined amplified GFR POM. They focused on the wear performance of POM and 28% GFR POM (glass fiber reinforced POM) gear pairs. Glass fiber reinforced polymers are preferred because of their high damping resistance and self-lubricating properties. As a result of the study, they also observed that GFR POM has 50% more load carrying capacity and longer life than POM gear. K.Mao [13] investigated the relationship between wear rate and surface temperature. Based on this, Acetal (POM -55 Nylon, 30% GFR, 15% PTFE) gear was produced by injection molding. Polymer composite gear versus polymer composite gear operated at different torques and speeds in the test setup. In terms of thermal behavior, the focus is on wear on the tooth surface. It has applied torque in the range of 5 Nm-35 Nm. Root and pitch breakage has been observed in the acetal gear, and temperature has a net effect.

The two most relevant parameters in assessing the load carrying capacity of polymer gears are root and fatigue strength [14]. Damijan Zorko et al. [15] showed that autoclave-hardened woven CFRP gears have higher load carrying capacity compared to polymer and polymer composite gears. Their main focus is to investigate the fatigue behavior of long fiber CFRP composite gears. In their studies, they have shown that woven CFRP gears last 6 times longer at the same fatigue load compared to high-performance PEEK gears. Gear damage in general; wear, tooth

breakage, root and pitch cracking, and thermal deformation. When the gear operates at high torque, the temperature increases locally and accordingly, heat accumulates on the tooth surface and thermal deformation occurs in that region [16].

In this study, the carbon powder added TPU black filament obtained by 3D printing and the POM gear produced by machining were compared. Considering the noise, temperature, and roughness values, the wear amount and results were obtained at the end of 1.5 million cycles.

2. Materials and Method

2.1 Gear design

The first stage of 3D printing of polymer spur gears in Solidworks program and the production of Polyoxymethylene (POM) gears by machining with the same tooth properties. Gear specifications are given in Table 1. The gear produced by machining also worked against the steel gear. Both gears worked 1.5 million revolutions. Another gear material to be used in this study is the carbon powder added TPU structured gear produced with a 3D printer. 4 teeth are marked on CV60 and POM gears and the surface roughness of these marked places is taken into account every 250000 revolution. Details for AISI1040, POM and CV60 gear specifications are given in Table 1. CV60 gear carbon additive provides extra strength and durability.

Table 1. Specifacition of AISI 1040/POM/CV60

Module	2
Number of teeth	20
Pressure angle (°)	20
Face width (mm)	8
Hub Diameter (mm)	20

TPU material is a flexible, wear-resistant thermoplastic. It is used in a number of manufacturing processes for both consumer and industrial use. Parts produced by 3D printing with TPU are durable and can withstand ambient temperatures up to 80°C. The TPU filament is resistant to abrasion, impact and many chemicals. There are different versions of TPU material but it can basically be classified into two types. It is known firstly as Polyether Polyurethane and secondly as Polyester Polyurethane. Both have different features that can meet a specific need. Some properties of TPU filament make it an excellent choice. Its resistance to abrasion, oil, chemicals and abrasion makes it perfect for use in industries such as the automotive industry.

2.2. Gear testing rig

The gear test rig is designed to test gear wear while the gears are engaged and running. 3D printed gears can be tested in the same way as injection molded and machining gears. Electromagnetic powder brake can also be preferred to apply a counter torque to the running gear if necessary. With the change of the magnetic field created by the coil, the viscosity of the powder changes, so that the ideal current moment linearity is achieved regardless of the speed. The diagram of the test setup is presented in Figure 2. Gear wear tests were used against AISI 1040 steel gear, CV60, POM gears were used. torque values were recorded. OPTRIS CS LT / CSmed LT pyrometer was used to measure temperature.

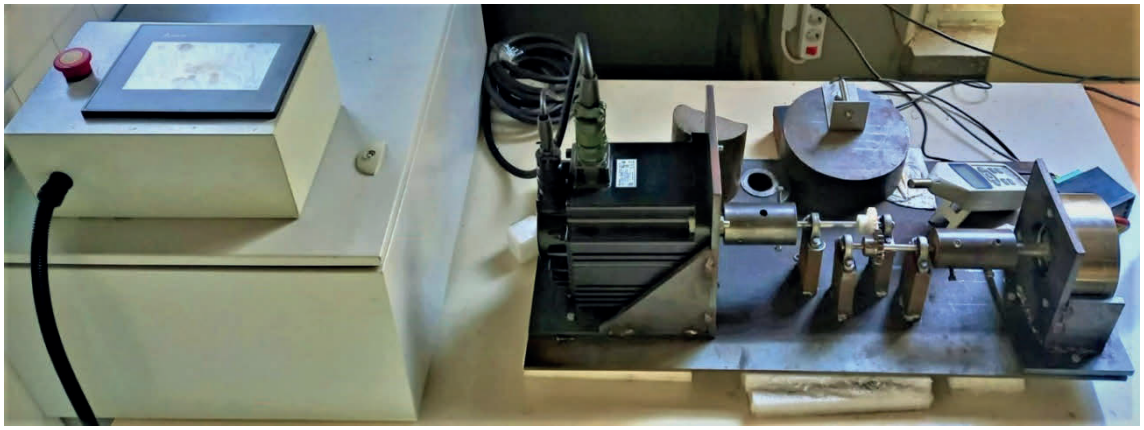
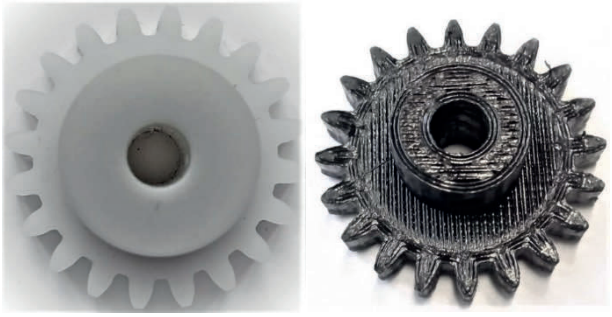


Figure 2. Test rig for Polymer gears

Table 2. Properties of CV60 material and POM [17][18] 19]

Material	Carbon powder added TPU	Density (kg / m3)	1420
Diameter	1,75 mm	Tensile Modulus (MPa)	3100
Print Temperature	230-250°C	Flexural Modulus (MPa)	2900
Bed Temperature	60-80°C	Deflection Temperature (°C)	158
Color	Black	Melting Temperature (°C)	176

The hardness of TPU may depend on the blend of polymers. The extruder temperature of the TPU filament is 230-250 degrees. TPU filament is a medium strength 3D printing material, but can withstand higher compression and tensile forces than the more common PLA and ABS. When it comes to 3D printing, TPU filament requires a greater amount of energy transfer than most other filaments.



(a) (b)

Figure 3. (a) POM and (b) CV60 gear

In this study, gear test rigs were used to investigate the performance of thermoplastic gears. During the test, measurements were taken every second. The surface roughness was also measured at every 250000 revolutions. Surface roughness was made with Mitutoyo SJ-400 model tester. 5 experiments were made for each gear and they worked for a total of 1500000 revolutions. Temperature, sound, surface roughness, torque and wear values are noted every 250 thousand cycles. Another issue to be said for surface roughness is; The Ra and Rz values of the gear produced with a 3D printer were measured higher, but then a noticeable improvement occurred on the surface as it worked against the metal gear, while the other gear was produced by machining, the surface roughness was seen to be smoother with the test device. The values measured here are Ra and Rz. Ra (Arithmetic Average Roughness) (based on DIN EN ISO 4287) is the arithmetic mean of the absolute values of the y-coordinates corresponding to the surface roughness profile. Ra also defines the mean arithmetic deviation of the y-

coordinates of the surface roughness on the centerline. Rz (Maximum Depth of Roughness) Based on the DIN EN ISO 4287 standard. Rz, or the vertical distance between the highest and lowest points of the surface roughness profile, leads to the measurement of the y-coordinate intervals corresponding to the surface roughness. Because, as a rule, Rz is five The dimension division is calculated as the arithmetic average of the IR based on the maximum roughness depth, this parameter expresses the average roughness according to DIN 4768. The leveling depth Rp refers to the previously defined DIN 4762.

3.Results and Discussions

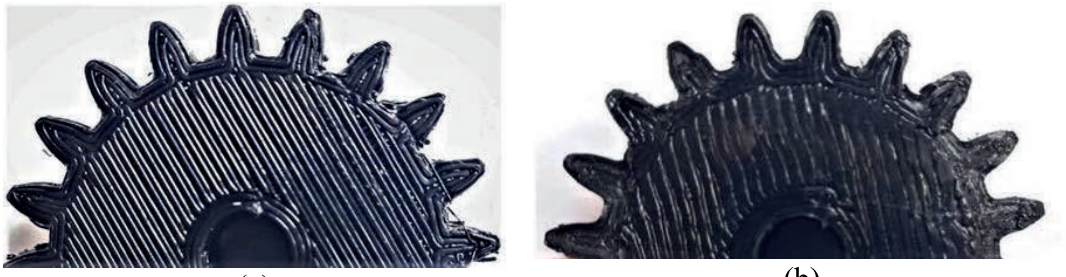
Considering the results obtained after the testing of the selected gear pairs, the most striking values were the noise and temperature results. These results, noise values of POM and CV60 gear are presented in Figure 7. Each gear was worked at 1.5 million revolutions and the temperature, noise and torque values were recorded every second at 250000 revolutions. In this study, a noticeable thinning occurred especially in the teeth of the POM gear. POM gear dimensional stability is good compared to polyamide group. Gears produced by machining, especially POM gear; It provides better surface quality than gears produced by additive manufacturing production method as its excellent machining and lubricity properties. Since the CV60 gear produced by 3D printer is produced in a layered manner, this surface gets better after every 250000 working cycles as there are notches on the tooth surface. It also means longer life. As it works against the steel gear, more heating and friction occurred and it worked at 1000 rpm. When delrin reaches a temperature of 100°C due to its chemical structure, losses occur on its surface, thinning and wear are observed on the tooth surface. The initial and final state of the gear is shown in Figure 4. However, there is less loss and wear in the tooth structure of the CV60 gear compared to the POM gear. The CV60 gear is made of carbon powder added TPU filament. It has shown that it has higher wear resistance than POM gear.



(a) (b)

Figure 4. The (a) initial and (b) final state of the POM gear are shown

As a result of the study, as seen above, wear on the tooth surface and failure in some teeth were experienced. We saw that the POM gear is a gear that should not be preferred as a result of warming up against the heat.



(a) (b)

Figure 5. The (a) initial and (b)Final state of the CV60 gear are shown

Figure 5 shows the initial and final state of the CV60 gear. There is no breakage or deterioration in the tooth bottoms or pitch. The friction coefficient of the CV60 made gear is ,93ShA, that is, a value between 1-2µ. POM material is 85ShA (N.mm2). As can be understood from this, it is understood that TPU is more resistant to friction [20]. As a result of three 1.5 million revolutions of the POM gear against the steel gear, tooth breakage occurred and the tooth surface was also damaged. While the POM gear is in the temperature range of 85 ± 5°C, the CV60 gear is in the temperature range of 25 ± 5°C. Temperature measurements were made with an infrared thermometer at room temperature. The CV60 gear showed that it is more durable and more resistant to temperature, according to the test results. The most important thing in gear business is longevity, wear resistance, warmth and durability. The temperature resistance of CV60 was found to be better than POM and there was no breakage.

Due to its chemical structure, POM wears on its surface for long periods of time at temperatures close to 100°C. Measurements were taken every 4 hours. Better results can be obtained by adding glass fiber to the POM gear. When you examine the graph, it shows that it can work longer. The POM gear showed an increasing graph up to the 1.5 million cycle result, but the CV60 gear kept the temperature range from the beginning to the end of the 1.5 million cycles, no continuous increase was observed. This is shown in Figure 6.

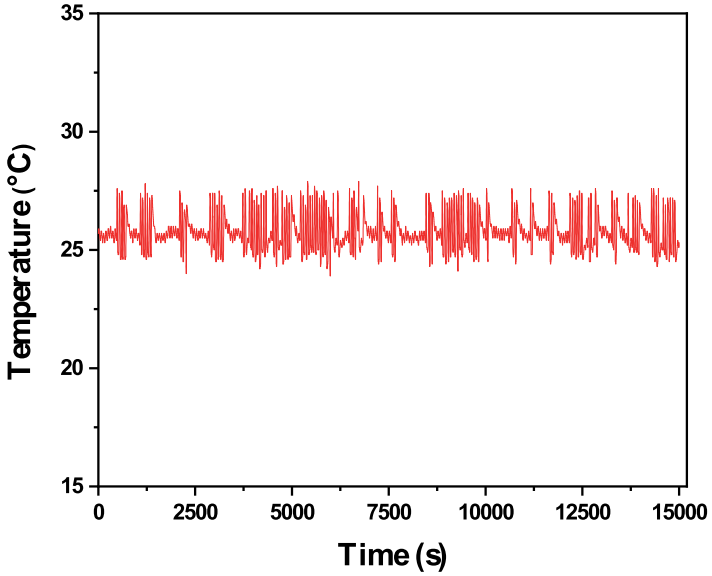


Figure 6. Temperature distribution of CV60

Figure 6 shows the temperature behavior of the CV60 gear. Since the CV60 gear contains TPU containing carbon powder, its impact resistance and strength have increased. This steel dampens the impact resistance from the gear. Impact resistance is better than POM gear. The operating temperature was in the range of 24-28°C. The CV60 gear has completed 1.5 million cycles of

temperature behavior at the same level as the baseline. It did not show a noticeable increase. Its temperature remained constant within a certain range.

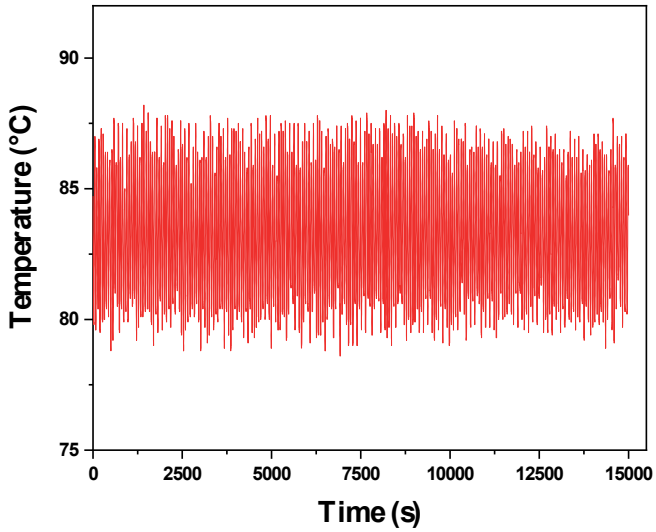


Figure 7. Temperature distribution of POM

Figure 7 shows the temperature behavior of the POM gear. POM gear started at 2 times higher temperature than CV60 gear. The impact resistance and damping of the POM gear is slightly lower than that of the CV60 gear. After 1.5 million cycles, the temperature fluctuation of the POM gear increased in some places and then followed a decreasing graph. There is a torque effect at the rise points. Torque has friction force and impact from steel gear. POM gear could not absorb impact strength as much as CV60 gear. While CV60 gear is 95A shore hardness, POM gear has 75-80A shore hardness value range.

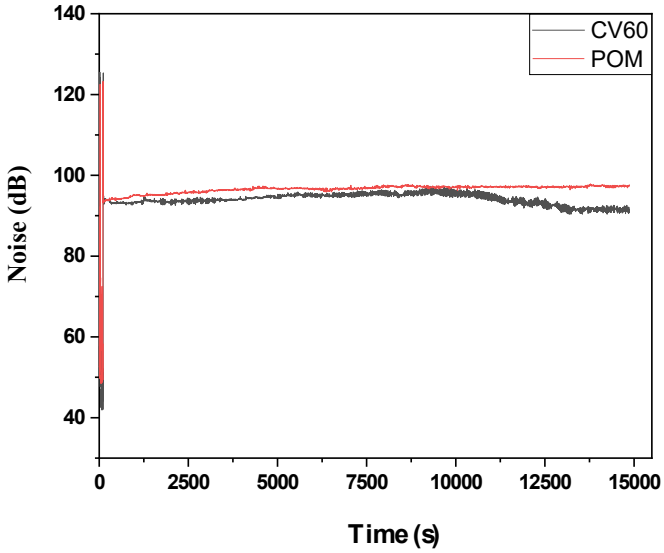


Figure 8. Noise results POM and CV60 gear

Noise results of CV60 and POM gears are given in Figure 8.CV60 At first, it rose to a high value. He then lowered his voice because of his strength. Since it is produced with additive manufacturing, there are gaps between the layers in its structure, which makes the sound more comfortable. The CV60 gear has better shock absorption than the POM gear, which affects the noise parameter results. Both worked against the steel gear. The POM gear initially weighs 22,274 g. However, there was some loss of mass as it was exposed to heat, torque and wear.

Table 6 shows that the maximum loss is the result of 1500000 cycles. Considering the reason for this; Both temperature and torque were higher than at other revs. It was concluded that more temperature factors play a role. Because although the torque value is high at 1250000 rpm, the temperature value is low. The temperature factor plays an effective role at 1500000 rpm and there is not much difference between the torque values. As a result, wear on the tooth surface has occurred. Thermal behavior was more effective in POM gear. Ra and Rz. These values are presented in Table 5. It is understood that the recesses and protrusions on the surface are reduced and smoothed. Surface measurements were made on these 4 randomly selected teeth in the CV60 gear. In the initial state, the Rz value was measured as 150.5µm, but after 250000 runs there was a decrease in the Rz value and this also applies to the Ra value.

Table 6. Mass&Cycle relation

Cycle x10^3 (rev/min)	POM	CV60
250	22,23 gr	12,58 gr
500	22,20 g	12,56 gr
750	22,18 gr	12,54 gr
1000	22,15 gr	12,44 gr
1250	22,13 gr	12,44 gr
1500	22,08 gr	12,39 gr

Since the CV60 gear is produced by additive manufacturing, there are too many indentations and protrusions on its surface. This was also seen in the surface roughness measurement. For this reason, the mass loss was high after 250000 cycles and the surface was smoothed in subsequent studies. The torque value is also measured as 2.86 Nm. No extra counter-torque braking was applied during the gear test. Material losses were observed in the range of the highest torque and temperature values. POM and CV60 gears were worn at constant torque values (3 ± 0.6 Nm). All experiments were carried out at room temperature, the temperature difference in measurements was ±5°C. The noise results of these gears; POM gear measured 94±2 dB, CV60 gear 85±2 dB. Considering the other parameter, noise, the results were close to each other, but the 3D printed gear produced slightly better results. Considering the results of the temperature and noise parameters, the CV60 gear showed superior properties compared to the machining POM gear, and both gears were 1000 rpm AISI 1040 worked stably against the steel gear. CV60 gear can also be preferred.

4. Conclusion

In this study, the operating results of two different plastics, POM and 3D printed gear were examined. If additives such as Glass fiber are added to the POM gear, its strength increases and consequently reduces thermal linear deformation. This makes it more resistant to heat. The findings did not mislead our predictions. Looking at the results in general, gears produced by additive manufacturing are more preferred in terms of temperature, wear and noise.

It was determined that there were noticeable losses in the teeth of the POM gear. A fracture has occurred on the tooth surface of the POM gear. When the CV60 gear was operating, it reached a maximum of 40°C, this is an excellent thing. Polyamide, POM was found to be in a more advantageous position in terms of temperature compared to the Ultem gear. TPU filament PLA is superior to ABS printed gears in terms of strength, rigid structure and temperature. The CV60 gear with TPU structure and carbon additives showed that it could work longer, moreover, it worked against the steel gear (AISI 1040). The use of thermoplastic gears instead of metal gears is increasing in industry. it has been shown that the gear produced by 3D printing has superior

properties compared to the POM gear, and is also in a more advantageous position in terms of production. 3D printed gears is definitely an area of future study and needs to be tested on a wider range of parameters to achieve optimum results. First, more material analysis of current printing materials is required to better understand the key factors affecting wear behavior. Secondly, optimization methods for 3D printing parameters need to be investigated to improve the performance of 3D printed gears. Third, a much broader analysis and comparison of the properties of polymer gears produced by different manufacturing processes, including injection molding, machining and 3D printing, is required.

References

1. Bîrcă, A., Gherasim, O., Grumezescu, V., & Grumezescu, A. M. Introduction in thermoplastic and thermosetting polymers. In Materials for Biomedical Engineering. **2019**, 1-28.
2. Kim, G., Barocio, E., Pipes, R. B., & Sterkenburg, R. 3D printed thermoplastic polyurethane bladder for manufacturing of fiber reinforced composites. Additive Manufacturing. **2019**, 29:100809.
3. Schuhler, E., Coppalle, A., Vieille, B., Yon, J., & Carpier, Y. Behaviour of aeronautical polymer composite to flame: A comparative study of thermoset-and thermoplastic-based laminate. Polymer Degradation and Stability. **2018**, 152: 105-115.
4. Singh, A. K., Siddhartha, & Singh, P. K. Polymer spur gears behaviors under different loading conditions: A review. Proceedings of the Institution of Mechanical Engineers, Part J: Journal of Engineering Tribology. **2018**, 232(2):210-228.
5. Peters, E. N.. Engineering thermoplastics—materials, properties, trends. In Applied Plastics Engineering Handbook, William Andrew Publishing. **2017**, 3-26.
6. Farag, M. M. Quantitative methods of materials selection. Handbook of materials selection. **2002**, 1-24.
7. Evlen, H. Doluluk oranının 3B yazıcıda üretilen TPU ve TPE numunelerinin mekanik özellikleri üzerine etkilerinin incelenmesi. Dokuz Eylül Üniversitesi Mühendislik Fakültesi Fen ve Mühendislik Dergisi. 2019, 21(63):793-804.
8. Singh, P. K., & Singh, A. K. An investigation on the thermal and wear behavior of polymer based spur gears. Tribology International. **2018**, 118:264-272.
9. Tavčar, J., Grkman, G., & Duhovnik, J. Accelerated lifetime testing of reinforced polymer gears. Journal of Advanced Mechanical Design, Systems, and Manufacturing. **2018**, 12(1).
10. Mohsenzadeh, R., Shelesh-Nezhad, K., & Chakherlou, T. N. Experimental and finite element analysis on the performance of polyacetal/carbon black nanocomposite gears. Tribology International. **2021**, 160:107055.
11. Tezel, T., Topal, E. S., & Kovan, V. Failure analysis of 3D-printed steel gears. Engineering Failure Analysis. **2020**, 110:104411.
12. Mao, K., Greenwood, D., Ramakrishnan, R., Goodship, V., Shrouti, C., Chetwynd, D., & Langlois+, P. The wear resistance improvement of fibre reinforced polymer composite gears. Wear. **2019**, 426:1033-1039.
13. Mao, K. A new approach for polymer composite gear design. Wear. **2007**, 262(3-4):432-441.
14. Kalin, M., & Kupec, A. The dominant effect of temperature on the fatigue behaviour of polymer gears. Wear. **2017**, 376:1339-1346.
15. Zorko, D., Tavčar, J., Bizjak, M., Šturm, R., & Bergant, Z. High cycle fatigue behaviour of autoclave-cured woven carbon fibre-reinforced polymer composite gears. Polymer Testing. **2021**, 102:107339.
16. Mao, K., Li, W., Hooke, C. J., & Walton, D. Friction and wear behaviour of acetal and nylon gears. Wear. **2009**, 267(1-4):639-645.

17. Guo, Y., Yan, L., Zeng, Z., Chen, L., Ma, M., Luo, R., ... & Chen, D. TPU/PLA nanocomposites with improved mechanical and shape memory properties fabricated via phase morphology control and incorporation of multi-walled carbon nanotubes nanofillers. Polymer Engineering & Science. **2020**, 60(6):1118-1128.
18. Bedoui, F., & Fayolle, B. POM mechanical properties. **2014**.
19. Şahin, Y., Yalçınkaya, S., & Mirzayev, H. The effect of load on the tribological property of polyacetal and metallographic observation. In Proceedings of the International Symposium of Mechanism and Machine Science. **2017**, 11-14.
20. Mehrabzadeh, M., & Rezaie, D. Impact modification of polyacetal by thermoplastic elastomer polyurethane. Journal of applied polymer science. **2002**, 84(14):2573-2582.

EFFECT OF ELECTRODE GEOMETRY ON OVERCUT OF DRILLED HOLES IN ELECTRICAL DISCHARGE DRILLING PROCESS

ALI TOLGA BOZDANA*[1], NAZAR KAIS AL-KARKHI [2]

[1] Gaziantep University, Engineering Faculty, Mechanical Eng. Dept., Gaziantep, TURKEY.
[2] Baghdad University, Al-Khwarizmi College, Automated Manuf. Eng. Dept., Baghdad, IRAQ.

Abstract

Electrical Discharge Drilling is a process in which small-diameter holes with certain aspect ratios can be produced on difficult-to-machine materials. During drilling operation, an enlargement in diameter of a drilled hole occurs due to formation of side-sparking between the walls of electrode and hole. This refers to overcut that causes the production of holes larger than electrode diameter. It is desirable that overcut should be minimum for producing accurate holes. This study presents an experimental investigation on the effect of electrode geometry on the formation of overcut. Several holes were drilled at various process conditions by using electrodes having four different geometries. Diameters of the drilled holes were measured, and the overcut for each hole was determined. The results showed that electrode geometry has a great influence on the formation of overcut. The overcut of holes could be reduced with use of suitable electrode geometry.

Keyword: Electrical Discharge Drilling, Electrode Geometry, Overcut.

1. Introduction

Electrical Discharge Drilling (EDD), a variation of Electrical Discharge Machining (EDM), is an electro-thermal process based on the eroding effect of electric sparks occurring between tool electrode and workpiece [1]. It is used for production of small-diameter holes on electrically conductive materials. Drilling is conducted by means of rotating hollow electrodes through which the dielectric fluid is flowing for clearing the debris, as shown in Figure 1.

During drilling operation, primary-sparking occurs between bottom of electrode and surface of workpiece, leading to removal of certain amount of debris per unit time. In addition, there is secondary-sparking (side-sparking) between the walls of electrode and workpiece, which causes an enlargement in hole diameter. Thus, the diameter of drilled hole is always larger than that of electrode, which is called Overcut (OC). It is determined based on the amount of enlargement in hole diameter with respect to electrode diameter as given in Equation 1, where D_h and D_e are diameter of drilled hole (measured near the hole entrance) and electrode diameter, respectively.

$$OC\ (\%) = \frac{D_h - D_e}{D_e} * 100$$

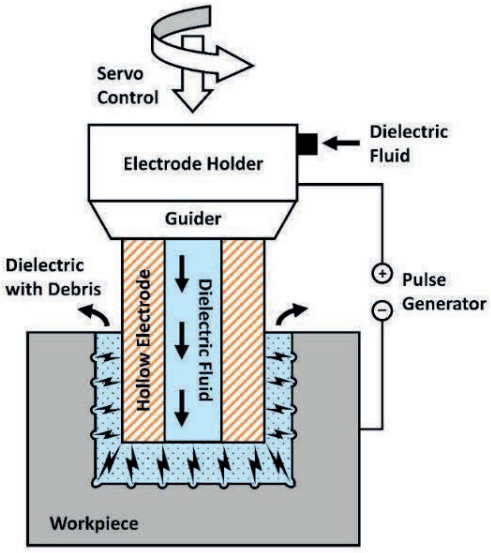


Figure 1. Schematic illustration of EDD process [1]

It is desirable that OC should be the minimum for producing accurate holes. There are number of works on the experimental analysis of OC in drilling of different materials at various conditions. Huang et al. [2] conducted an experimental investigation on the effect of electrode rotation on process performance and hole accuracy in drilling of AISI 304 using micro-EDM. The experiments conducted at different discharge energies showed that OC was relatively smaller at lower rotational speeds. Shastri et al. [3] studied the effect of cryogenically treated copper and brass electrodes on EDM of Ti-6Al-4V. It was showed that OC was reduced due to cryogenic treatment of electrode. An experimental investigation on the effect of process parameters on the machining accuracy of EDM of Inconel 718 using copper electrode was carried out by Ahmad et al. [4]. It was shown that OC varies with settings of certain process parameters.

Some researchers focused on the analysis and optimization of OC based on an experimental plan. Singh et al. [5] studied on Taguchi optimization of performance characteristics in drilling micro-holes using micro-EDM. Holes were produced on brass plates using tungsten electrode. The effects of process parameters were analyzed using ANOVA. Another study on optimization of process performance of EDM using Taguchi was performed by Nagaraju et al. [6]. Workpiece and tool electrode was 17-7 PH stainless steel and copper, respectively. Uyyala [7] studied multi-response optimization of EDM of RENE80 nickel alloy with rotary copper electrode. Taguchi and Grey Relational Analysis (GRA) were used as hybrid approach in order to analyze the effects of process parameters on process outputs, including OC. Another study on optimization of process outputs of EDM was performed by Rajamanickam et al. [8]. They used Taguchi and TOPSIS approach for analysis of machining Ti-6Al-4V and Inconel 718 plates using tubular brass and copper electrodes. In addition to these research, Response Surface Methodology (RSM) was also used for modeling and optimization of process outputs. Hanash and Ali [9] conducted research on EDD of stainless steel using brass electrode. The effects of certain process parameters on OC was investigated, and an empirical equation for OC was obtained based on RSM. Another study on RSM was performed by Yadav et al. [10] on the machining characteristics of near-dry EDM. Drilling experiments on HSS using copper electrode were performed based on central composite design in order to analyze the effects of several parameters on process outputs, including OC.

There is also research on utilization of Artificial Intelligence (AI) techniques for modeling and optimization of EDM process outputs. Belloufi et al. [11] performed experimental and predictive study for modeling input-output relationships using multi-output fuzzy models. Several drilling experiments on AISI 1095 were conducted at various conditions using cupro-nickel electrodes. The experimental data were used for building fuzzy models for prediction of process outputs. Sharma et al. [12] studied on experimental investigation and optimization of parameters using grey-fuzzy-based hybrid approach for prediction of process outputs. Workpiece and electrode were pearlitic SG iron and hexagonal-shaped copper, respectively. Similar work on pearlitic SG iron was done by Kumar et al. [13]. They performed teaching-learning-based parametric optimization of process outputs. In other study by Sharma et al. [14], optimization of machining characteristics for EDMing of various nickel-based alloys using copper electrodes was performed utilizing fuzzy, GRA and Taguchi techniques.

Despite of research on predictive modeling and optimization of process outputs, the sole effect of electrode geometry on OC was not studied. In this study, new electrode geometries were utilized for minimization of OC by reducing or preventing the side-sparking. Drilling experiments were conducted at various conditions, and the corresponding OC values were compared.

2. Materials and Methods

Hollow brass electrodes were used in drilling operations. The electrode geometries are shown in Figure 1. The commercially available circular electrode is the most commonly used in EDD operations. The other electrode geometries were manufactured from circular electrode by means of machining and forging processes. All electrodes have the identical inner and effective outer diameters of Ø1 and Ø3 mm, respectively. This makes it possible to compare their flushing and side-sparking characteristics.

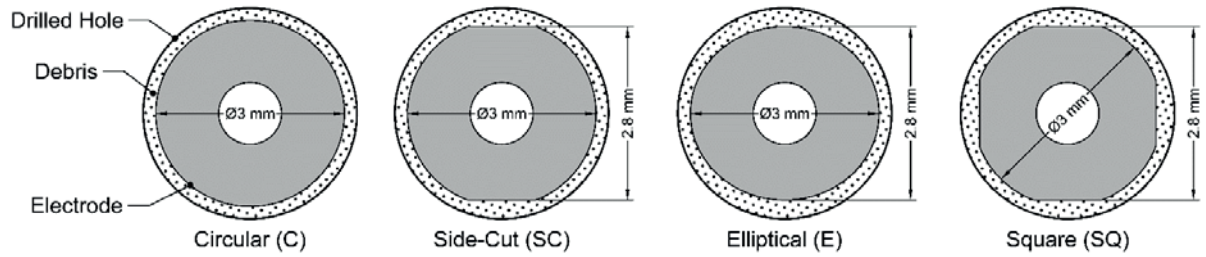


Figure 1. Four electrode geometries used in drilling operations

Workpiece material was AISI 304 stainless steel having chemical composition given in Table 1. Holes were drilled on mating interface of rectangular block specimens, as illustrated in Figure 2. After drilling, specimens were separated and the surface with drilled holes was scanned at high resolution for accurate measurements. OC for each hole was determined based on the effective outer diameter of electrode (i.e. Ø3 mm) and the measured diameter of drilled hole.

Table 1. Chemical composition *(in wt. %)* of AISI 304

C : 0.08 (max)	**Mn :** 2 (max)	**Cr :** 18-20	**S :** 0.03 (max)
N : 0.1	**Si :** 0.75 (max)	**Ni :** 8-10.5	**P :** 0.045 (max)

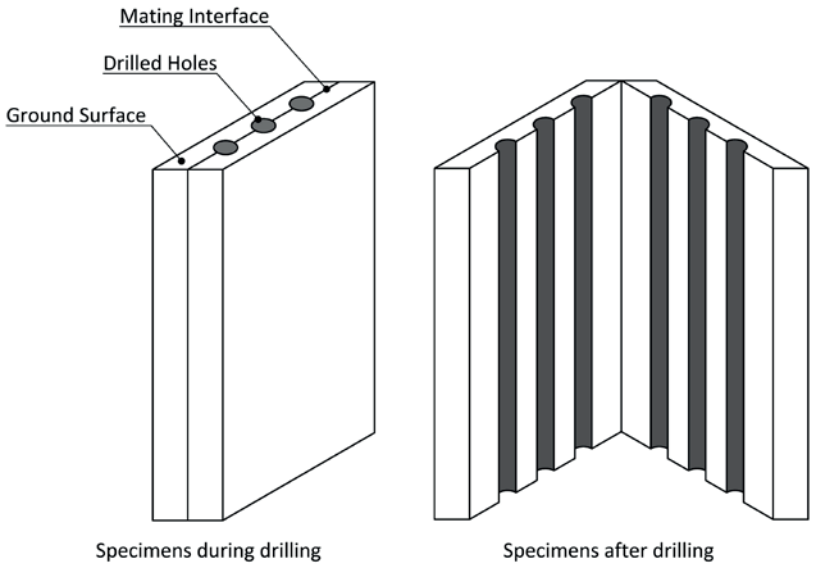


Figure 2. Sketch of specimens before and after drilling

Table 2 presents the details for drilling experiments based on L9 orthogonal array. Holes were drilled at certain levels of current, pulse-on time, and pulse-off time while other process parameters were kept fixed. The levels of parameters were determined based on preliminary drilling trials. Drilling time was kept as 3 minutes for all holes so that a reliable comparison in the corresponding results could be made.

Table 2. Experimental plan with variable and fixed parameters

Hole No.	Current (A)	Pulse-On (µs)	Pulse-Off (µs)
1	16	27	16
2	16	35	20
3	16	44	26
4	20	27	20
5	20	35	26
6	20	44	16
7	24	27	26
8	24	35	16
9	24	44	20

Fixed Parameters	
Voltage:	50 V
Capacitance:	1476 µF
Dielectric Fluid:	deionized water
Dielectric Pressure:	30 kg/cm^2
Electrode Rotation:	200 rpm
Electrode Polarity:	negative

3. Results and Discussion

The diameter of each hole after drilling using four different electrodes as well as the corresponding OC values are given in Table 3. The comparison of OC results is shown in Figure 3. As seen from results, regardless of drilling conditions, it is evident that circular electrode caused the largest OC among all electrode geometries. This is due to the fact that there is insufficient gap between side walls of electrode and workpiece, which leads to side-sparking arising from short circuits and arcs, resulting in enlargement in the perimeter of drilled hole.

Table 3. Measured hole diameters and corresponding OC values

Hole No.	Hole Dia. (mm)				OC (%)			
	C	SC	E	SQ	C	SC	E	SQ
1	3.34	3.13	3.17	3.08	11.33	4.33	5.67	2.67
2	3.33	3.18	3.19	3.06	11.00	6.00	6.33	2.00
3	3.31	3.16	3.18	3.11	10.33	5.33	6.00	3.67
4	3.26	3.12	3.17	3.11	8.67	4.00	5.67	3.67
5	3.39	3.19	3.22	3.15	13.00	6.33	7.33	5.00
6	3.42	3.16	3.28	3.13	14.00	5.33	9.33	4.33
7	3.27	3.18	3.25	3.09	9.00	6.00	8.33	3.00
8	3.24	3.15	3.16	3.15	8.00	5.00	5.33	5.00
9	3.37	3.21	3.22	3.18	12.33	7.00	7.33	6.00

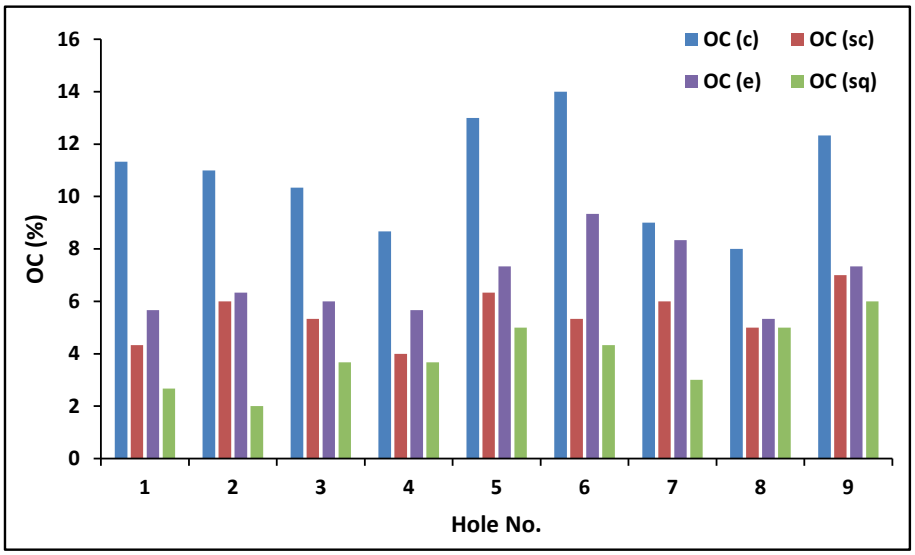


Figure 3. OC values in drilled holes

On the other hand, the other electrode geometries (i.e. side-cut, elliptical, and square) provided relatively less OC than the circular electrode. This is because of improved flushing performance due to increased inter-electrode gap in such electrode geometries, which reduces the possibility of side-sparking generated from debris accumulation.

Among all electrode geometries, the lowest OC was achieved with use of square electrode. The reason for this is that side-sparking occurs only in the vicinity of corners of square electrode, leading to less erosion on its perimeter, and hence less enlargement occurs in hole diameter. Depending upon drilling conditions, up to 80% reduction in OC was obtained in case of square electrode in comparison with circular electrode.

4. Conclusions

The results in this study reveal that enlargement in diameter of holes (overcut, OC) in EDD process can be reduced by use of appropriate geometry of tool electrode. For this purpose, several holes were produced using electrodes having different geometries. The main outcomes of research are summarized as follows:

- OC is caused by the occurrence of side-sparking between side walls of electrode and workpiece. It can be minimized with prevention of debris accumulation at inter-electrode gap.
- This is possible by utilization of proper electrode geometry that provides improved flushing performance for washing the debris away from machining zone.
- The results showed that, in comparison with commercial circular electrode, special designs of electrodes (side-cut, elliptical and square geometries) provided significant reduction in OC, regardless of drilling conditions.
- Among all electrode geometries, the lowest OC was achieved with square electrode because of the minimum degree of erosion occurring in the perimeter of hole during process.
- This study proves the effectiveness of tool geometry in EDD process for production of holes with higher accuracy.

References

1. Bozdana, A.T., Ulutas, T., The effectiveness of multi-channel electrodes on drilling blind holes on Inconel 718 by EDM process, Mat. Manuf. Proc., **2016**, 31:504-513.
2. Huang, Y., Zhang, Q, Xing, Q, Yao, Z., Li, J., Effects of electrode rotational speed on processing performances of AISI 304 in micro-electrical discharge machining, Int. J. Adv. Manuf. Technol., **2019**, 105:1665-1674.
3. Shastri, R.K., Mohanty, C.P., Jadhav, P.S., Study of the effect of cryogenically treated tools during rapid drill electro-discharge machining of Ti-6Al-4V alloy, Materials Today: Proceedings, **2019**, 18:3122-3127.
4. Ahmad, S., Chendang, R.N., Supawi, A., Lajis, M.A., Zaman, M.H.K., Material removal rate and machining accuracy of electrical discharge machining (EDM) of Inconel 718 using copper electrode, IOP Conf. Series: Mat. Sci. Eng., **2019**, 607:1-10.
5. Singh, A.K., Patowari, P.K., Chandrasekaran, M., Experimental study on drilling micro-hole through micro-EDM and optimization of multiple performance characteristics, Journal of Brazilian Society of Mech. Sci. Eng., **2020**, 42(506):1-14.
6. Nagaraju, N., Prakash, N.S., Kumar, V.A., Ujwala, N.G., Optimization of electrical discharge machining process parameters for 17-7 PH stainless steel by using Taguchi technique, Materials Today: Proceedings, **2020**, 24:1541-1551.
7. Uyyala, S.B., An hybrid approach for multi-response optimization of rotary electrical discharge machining of nickel super alloy, Materials Today: Proceedings, **2020**, 23:626-631.
8. Rajamanickam, S., Prasanna, J., Sastry, C.C., Analysis of high aspect ratio small holes in rapid electrical discharge machining of superalloys using Taguchi and TOPSIS, Journal of Brazilian Society of Mech. Sci. Eng., **2020**, 42(99):1-13.
9. Hanash, E.A.H., Ali, M.Y., Experimental study of electrical discharge drilling of stainless steel UNS S30400, IOP Conf. Series: Mat. Sci. Eng., **2018**, 290:1-8.
10. Yadav, V.K., Kumar, P., Dvivedi, A., Effect of tool rotation in near-dry EDM process on machining characteristics of HSS, Mat. Manuf. Proc., **2019**, 34(7):779-790.
11. Belloufi, A., Mezoudj, M., Abdelkrim, M., Rezgui, I., Chiba, E., Experimental and predictive study by multi-output fuzzy model of electrical discharge machining performances, Int. J. Adv. Manuf. Technol., **2020**, 109:2065-2093.
12. Sharma, A., Kumar, V., Babbar, A., Dhawan, V., Kotecha, K., Prakash, C., Experimental investigation and optimization of electric discharge machining process parameters using grey-fuzzy-based hybrid techniques, MDPI Materials, **2021**, 14:1-21.
13. Kumar, V., Diyaley, S., Chakraborty, S., Teaching-learning-based parametric optimization of an electrical discharge machining, Facta Universitatis Series: Mechanical Engineering, **2020**, 18(2): 281-300.

14. Sharma, S., Vates, U.K., Bansal, A., Optimization of machining characteristics for EDM of different nickel-based alloys by embodying of fuzzy, grey relational and Taguchi technique, World Journal of Engineering, **2021**, 18(1):23-26.

BMG DELİK DELME PROSESİNDE SICAKLIK MODELLEMESİ

NUREFŞAN ELIF KOSEN[1], AZMI TIMUR[1], M. AYBUKE TURKMEN[1], ELIFNUR KOSEMEN[1], MUSTAFA BAKKAL[1]

[1]Istanbul Technical University Mechanics Faculty Mechanical Engineering Department, Istanbul/TURKEY

Özet

Bu çalışmada BMG malzemesinin yüksek sıcaklık nedeniyle amorf karakterini kaybetmesine neden olmadan delme işlemi parametrelerinin tespiti hedeflenmiştir. Bu amaçla sıcaklık dağılımı ve modelleme elde etmek için bir delik delme deneyinin tasarımı yapılmış ve bu deneyler gerçekleştirilmiştir. Deneylerinin tasarımı için ilerleme hızı ve devir parametreleri ile faktöriyel metodu kullanılmış ve yapılan literatür araştırmasıyla birlikte ilerleme hızı ve devir parametreleri için referans değerler belirlenmiştir. Deney setinde 50 mm uzunluğunda ve 5 mm çapında Zr bazlı ($Zr_{52,5}Cu_{17,9}Al_{10}Ni_{14,6}Ti_5$ (% olarak)) ark ergitme ve enjeksiyonla kalıplama yöntemleri kullanılarak üretilen bir BMG numunesi kullanılmıştır. Test sonuçları, artan ilerleme hızının düşük kesme hızlarında (4 ve 8 m/dk) yüksek sıcaklığa neden olduğunu göstermektedir. En yüksek kesme hızında (16 m/dk), ilerleme hızı sıcaklık değişimini ters yönde etkilemiştir. En yüksek sıcaklığın (180 °C) en düşük ilerleme hızında (12,5 mm/dk) ve beklendiği gibi en yüksek kesme hızında olduğu kaydedilmiştir. Elde edilen veriler ile birlikte delik delme işleminin sıcaklık modellemesi çalışmalarına başlanmıştır.

Anahtar Kelimeler: Camsı metaller, delik delme işlemi, termal modelleme.

1.Giriş

Günümüzde yüksek performansa sahip, endüstriyel alanda kullanılmak üzere yeni malzemelere ihtiyaç duyulmaktadır. Bu ihtiyaçları karşılamak için laboratuvar ortamlarında yeni malzemeler üretilmeye çalışılmakla beraber hali hazırda bulunan malzemeler üzerine araştırma ve geliştirme çalışmaları da yapılmaktadır. Metal malzemelerin özelliklerini iyileştirmek için alaşımlandırma oldukça kolay ve ekonomik bir yöntemdir. Bununla birlikte başvurulan imalat yöntemi de üretilen malzemelerin yapısını ve mekanik özelliklerini etkilemektedir.

Dökme metalik camlar (BMG) süper-soğutulmuş sıvı bölgelerinde süper-elastisite ile birlikte oda sıcaklığında yüksek sertlik ve mukavemete sahip olan gelişmiş malzemelerdir. Bu doğrultuda BMG, çelik ve plastikler gibi yaygın olarak kullanılan yapısal malzemelerin avantajlarına sahiptir. Termoplastik şekillendirilebilirlik sayesinde, karmaşık şekilli BMG parçaları, mühendislik uygulamalarını destekleyen termoplastik şekillendirme ile imal edilebilmektedir. BMG malzemelerin termoplastik şekillendirilebilirliğinin daha çok alaşım bileşimine bağlı olduğu bulunmuştur. Literatürde yapılan çalışmalara göre bazı Zr bazlı BMG'lerin yüksek termoplastik şekillendirmeye sahip olduğu görülmüştür [1].

Zr bazlı dökme metalik camlar (BMG), tane sınırı ve diğer dislokasyon türlerini içermez ve böylece kristal metallere kıyasla daha yüksek sertlik, yüksek kırılma mukavemeti, yüksek tokluk,

yüksek elastik limit, mükemmel korozyon direnci gibi üstün özelliklere sahiptirler [2,3]. Fakat bu gelişmiş malzeme düşük faz geçiş sıcaklıkları (~420 ºC kristalleşme sıcaklığı ve ~710 ºC erime sıcaklığı) ve zayıf ısı iletkenliği (~4 W/mK) nedeniyle, kesim sırasında yüksek sıcaklıklara maruz kaldığında amorf yapısını kaybetmektedir [3]. Yüksek sıcaklıkta amorf yapısının kaybolması sebebiyle bu malzeme için işleme operasyonları çok sınırlıdır. Bu malzemeyi güvenli bir şekilde üretmek için gelişmiş işleme stratejileri geliştirilmelidir.

Delme, delik açmak için karmaşık şekil ve yüksek boyutsal hassasiyetle BMG parçaları üretmek için yaygın olarak kullanılan bir işleme prosesidir. Kesme hızı ve kesici uç eğimi, delme işleminde talaş oluşumu sırasında bir helisel matkabın kesme kenarları boyunca değişir [4].

Bakkal ve arkadaşları, Zr esaslı dökme metalik cam (BMG) malzemesinin delinmesinde talaş ışık emisyonu, talaş morfolojisi, çapak oluşumu ve işlenmiş yüzeyi incelemişlerdir. 6,35 mm çapında, 2 mm kalınlığında bir disk numune ile 7 deney gerçekleştirilmiş ve HSS ve WC-Co takım malzemelerinin BMG'yi çeşitli besleme hızlarında, iş mili hızlarında ve matkap boyutlarında delme için etkileri incelenmiştir. Yavaş besleme hızı ve yüksek iş mili hızı, spesifik kesme enerjisini, talaşın ekzotermik oksidasyonunu ve ışık emisyonunu arttırdığı gözlenmiştir. Çalışmada yapılan BMG delme işleminde altı çeşit talaş morfolojisi (toz, kısa şerit, uzun şerit, uzun spiral, uzun şerit karışık ve fan) gözlenmiştir. Uzun şerit karışık talaş morfolojisi BMG malzemesine özgüdür. Hızlı durma koşulu altında işlenmiş yüzeyde, metalik camlara özgü kırılma, boşluk ve damar kırılma topografyası gözlenmiştir. Giriş üzerinde yuvarlanma şekli ve çıkış kenarında taç şeklinde farklı çapak oluşumları ve çıkış kenarındaki çapak boyutunun tipik olarak giriş kenarındaki boyuttan daha büyük olduğu gözlenmiştir. Yüksek ilerleme hızının hem giriş hem de çıkış kenarlarındaki çapak boyutunu azaltmaya yardımcı olduğu tespit edilmiştir. Bu çalışmada ayrıca, BMG delme işleminde yüksek termal iletkenliği ve sertliği nedeniyle WC-Co takım malzemesinin yüksek hız çeliği takımdan daha iyi performansa ulaştığı sonucuna varılmıştır.

Bu çalışma, delme işlemi sırasında sıcaklık dağılımı ve modelleme elde etmek için bir delme deneyinin tasarımını içermektedir. Çalışmada malzemenin yüksek sıcaklık nedeniyle amorf karakterini kaybetmesine neden olmadan Zr bazlı BMG malzemesi için optimum delme parametreleri incelenmiştir.

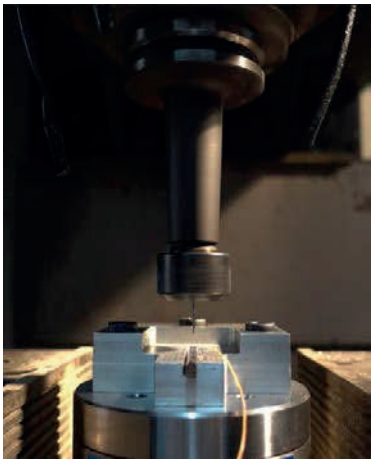
2.Deneysel Çalışma

Bu çalışmada BMG malzemesinin amorf yapısının delik delme prosesinde oluşan sıcaklıklardan etkilenmemesi için parametrelerin tespiti üzerinde çalışılmıştır. Deneysel prosedürün tasarımında literatür araştırmasına göre besleme hızı ve devir parametreleri için referans değerler seçilerek deneyler gerçekleştirilmiştir.

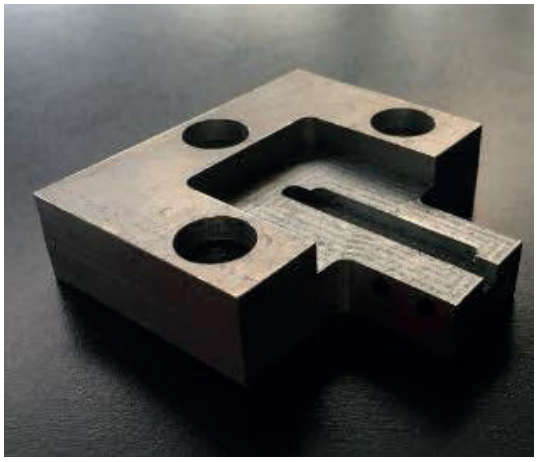
Deneyde Zr bazlı ($Zr_{52,5}Cu_{17,9}Al_{10}Ni_{14,6}Ti_5$) BMG malzemesi kullanılmıştır. Numune 50 mm uzunlukta ve 5 mm çapında olup ark eritme ve enjeksiyonla kalıplama yöntemleriyle üretilmiştir. Deneyler sırasında numune bir fikstür aracılığıyla tezgaha sabitlenmiştir. Delik delme prosesi esnasında sıcaklık verilerinin kaydedilebilmesi için numune üzerinde delinecek her deliğe özgü bir termokupl deliği açılmıştır. Numune ve fikstür sırasıyla Şekil 1 ve Şekil 2'de, fikstür ile tezgaha sabitlenen numuneyi içeren deney düzeneği Şekil 3'de gösterilmiştir.



Şekil 1-Deney Numunesi



Şekil 2-Deney Düzeneği



Şekil 3-Fikstür

Yapılan deneylerde kullanılacak parametreler deneyin yapıldığı tezgah kapasitesi sınırları içerisinde belirlenmiştir. Deneylerde kullanılan parametreler Tablo 1'de verilmiştir.

Tablo 1. Deney Parametreleri

Hız (m/dk)	Devir	Besleme Hızı[mm/dk]
4	1250	3,125
4	1250	6,250
4	1250	12,500
8	2500	6,250
8	2500	12,500
8	2500	25,000
16	5000	12,500
16	5000	25,000
16	5000	50,000

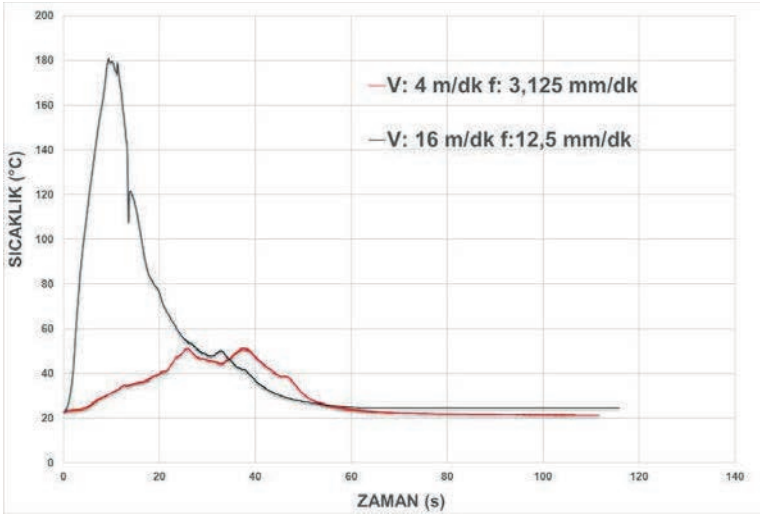
1. Deney Sonuçları

1 mm'lik WC takım ile yapılan delik delme testindeki sıcaklık ölçümü ve bu ölçümler ile birlikte alınan kuvvet değerleri sonuçları Tablo 2'de verilmiştir.

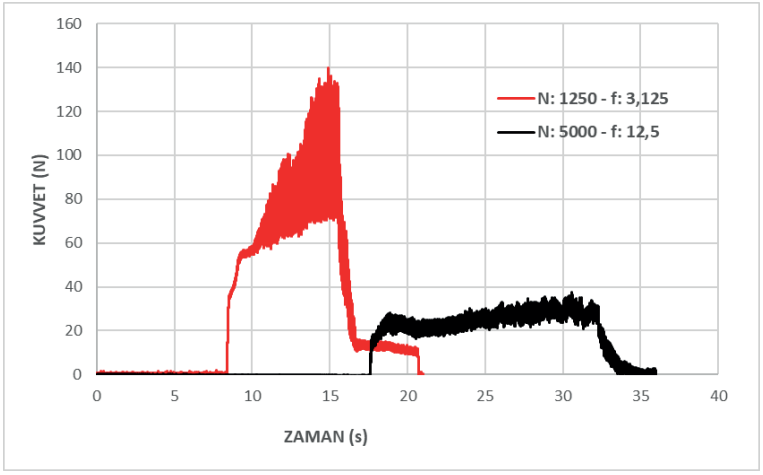
Tablo 2.Sıcaklık Ölçümü Sonuçları

Hız (m/dk)	Devir	Feed Rate [mm/dk]	Max. Temp [°C]	Maksimum Kuvvet [N]
4	1250	3,125	50	140
4	1250	6,250	85	42,4
4	1250	12,500	110	76,1
8	2500	6,250	125	42,4
8	2500	12,500	100	46,1
8	2500	25,000	170	48,4
16	5000	12,500	180	37,4
16	5000	25,000	120	40,1
16	5000	50,000	135	40,9

Test sonuçları, artan besleme hızının düşük kesme hızlarında (4 ve 8 m/dk) yüksek sıcaklığa neden olduğunu göstermektedir. En yüksek kesme hızında (16 m/dk), besleme hızı sıcaklık değişimini ters yönde etkilemiştir. En yüksek sıcaklığın (180 °C) ve en düşük kuvvetin (37,4 N) 5000 devirde en düşük besleme hızında (12,5 mm/dk) ve beklendiği gibi en yüksek kesme hızında olduğu kaydedilmiştir. En düşük sıcaklığın (50°C) ve en yüksek kuvvetin (140 N) 1250 devirde en düşük besleme hızında (3,125 mm/dk) olduğu kaydedilmiştir. Deneyler sonuçta en yüksek ve en düşük sıcaklık değişimleri Şekil 4'te, en yüksek ve en düşük kuvvet değişimleri Şekil 5'te gösterilmiştir.



Şekil 4. En Yüksek ve En Düşük Sıcaklık Değişimleri



Şekil 5.En Yüksek ve En Düşük Kuvvet Değişimleri

Yapılan deneyler sonrasında takımda meydana gelen değişimlerin gözlenebilmesi için SEM görüntüleri alınmıştır. Bu görüntüler Şekil 5'te gösterilmiştir.



Şekil 6. Deney Sonrası Takım Sem Görüntüleri

2.Sonuç

Genel sonuç, kuru delme işleminin test edilmiş koşullarda herhangi bir kristalleşmeye neden olamayacağını göstermektedir. Bir sonraki adım, farklı kesme koşulları için sıcaklık modellemesi olacaktır.

2. Referanslar

1. Gong,P., Kou,H., Wang,S., Deng,L.,Wang,X., and Jin,J., "Research on thermoplastic formability and nanomoulding mechanism of lightweight Ti-based bulk metallic glasses," *J. Alloys Compd.*, **2019**, vol. 801, pp. 267–276.
2. Li, T.H.., Tsai,P.H..,Hsu, K.T.., Liu,Y.C.., Jang,J.S.., and Huang,J.C., "Intermetallics Signi fi cantly enhanced drilling ability of the orthopedic drill made of Zr-based bulk metallic glass composite," , **2016** , vol. 78, pp. 18–21**.**
3. Stief, P.., Dantan, J.., Etienne,A.., and Siadat,A.., "ScienceDirect High performance cutting of Zr-based metallic France a review of chip formation A new methodology to analyze the functional and physical architecture of products for an assembly oriented product family identification," *Procedia CIRP*, **2018** , vol. 77, no. Hpc, pp. 421–424 .
4. Bakkal,M.., Shih,A. J.., Mcspadden, S.B.., Liu, C.T.., and Scattergood,R.O.., "Light emission , chip morphology , and burr formation in drilling the bulk metallic glass,", **2005** ,vol. 45, pp. 741–752.

ÇOK BİLESENLİ ÖZLÜ İPLİK İCEREN DENİM KUMAŞLARIN YIRTILMA MUKAVEMETLERİNİN İNCELENMESİ

DENIZ VURUŞKAN[1], NAZAN AVCIOĞLU KALEBEK[1], ESIN SARIOĞLU[1]

[1]Gaziantep Üniversitesi, Güzel Sanatlar Fakültesi, Tekstil ve Moda Tasarımı Bölümü, Gaziantep, TÜRKİYE

Özet

Günümüzde teknolojik gelişmeler sayesinde tüketicilerin taleplerini karşılayabilmek mümküne hale gelmiştir. Tekstil ürünlerinden en yaygın olarak kullanılan denim kumaşların dayanıklılık ve rahat giyim vb. özelliklerinin iyileştirilmesi noktasında bu teknolojik gelişmelerin katkısını görmekteyiz. Denim kumaşa elastikiyet kazandırmak amacıyla atkı ipliği olarak elastan özlü ipliğin kullanımının yaygın olduğu görülmektedir. Ancak tekrarlı kullanım ve yıkama sonucunda elastanda meydana gelen deformasyon sebebiyle denim kumaşlarda özellikle potlanma problemi oluşmaktadır. Günümüzdeki teknoloji sayesinde artık atkı ipliğinde öz olarak sadece elastan değil elastan ile birlikte filamentin iplik üretim esnasında aynı anda ipliğin merkezine beslenmesiyle çok bileşenli özlü iplik üretimi gerçekleştirilebilmektedir. Bu çalışmada, çok bileşenli özlü ipliklerden öz ve sargı lif değişkenlerinin ve iplik numarasının, denim kumaşların yırtılma mukavemeti üzerine etkilerinin incelenmesini içermektedir. Bu kapsamda, sargı lifi olarak %100 Polyester ve %60/40 Pamuk/Polyester kullanılmıştır. Çalışma kapsamında, 1. öz materyali olarak da 55 dtex T400, PBT ve PET ile birlikte 2. öz materyali olarak 78 dtex elastan iki bileşenli öz materyalleri kullanılmıştır. Çok bileşenli özlü iplik numuneleri aynı üretim parametrelerinde ring iplik eğirme sisteminde Ne 12/1 ve 18/1 numaralarında üretilmiştir. Üretilen bu iplik numuneleri atkı ipliği olarak kullanılarak denim kumaş numuneleri üretilmiş ve bu numunelere çözgü ve atkı yönünde yırtılma mukavemet testleri uygulanmıştır. Analiz sonucunda sargı lifinin ve öz materyalinin ve iplik numarasının denim kumaş yırtılma kuvveti üzerinde istatistiksel olarak anlamlı bir etkisi olduğu belirlenmiştir.

Keyword: Denim, Dual-Core, Özlü İplik, Ring Eğirme Sistemi.

1. Giriş

Denim tüm dünyada günlük kullanımda tüketicilerin tercih ettiği yüksek kullanım potansiyeline sahip bir tekstil ürünü olarak karşımıza çıkmaktadır. Denim sektörü bu yüksek kullanım potansiyeli neticesinde tüketici taleplerine cevap verebilmek amacıyla sürekli olarak bir gelişim içerisindedir. Özellikle kullanım açısından tüketicilerin giyim konforu açısından rahat, esnek ve dayanım özellikleri iyi olan denim ürünlerini talep etmeleri üreticiler üzerinde araştırma ve geliştirme konusunda itici bir güç oluşturmaktadır. Özlü iplikler; iki ve ya daha fazla birleşenin özelliklerinden aynı anda optimum düzeyde faydalanabilmek amacıyla geliştirilmiş öz (ipliğin merkezinde) ve kılıf (öz ipliğinin etrafına sarılan) liflerinden oluşan bir iplik türüdür. Elastan özlü iplikler denim endüstrisinde yaygın olarak kullanılmaktadır. Ancak tekrarlı kullanım ve yıkama neticesinde denimde potlanma ve kalıcı uzama vb. deformasyonlar meydana gelmektedir. Bu problemin çözümüne yönelik günümüzde iplik üretiminde öz de kullanılan elastana ek ikinci bir öz olarak takviye bir filamentin (T400, Polyester (PET), Polybutylene terephthalat (PBT) vb.) iplik üretimi esnasında özde beslenmesiyle çok bileşenli özlü iplik üretimi gerçekleştirilmektedir. Bu sayede elastanın denime sağladığı elastikiyet özelliğine ek

olarak ikinci öz olan filament etkisiyle kumaşın boyutsal dayanımının arttırılması mümkün hale gelmektedir. Çok bileşenli özlü iplik üretimine yönelik literatürde birçok çalışma mevcuttur [1-15]. Aydoğdu ve Yılmaz çalışmalarında farklı numaralarda (12/1 Ne, 16/1 Ne ve 20/1 Ne) X55 (50 ve 70 denye) ve spandex (70 denye) öz içerikli çok bileşenli özlü iplikler (dual-core) elde edilmiştir. Çalışmada aynı zamanda da sargı lifi olarak %100 pamuk, %100 viskon ve %50/50 pamuk/tencel lifleri kullanılmıştır. Çok bileşenli özlü ipliklerin üretimleri ring iplik eğirme sisteminde gerçekleştirilmiştir. Üretilen ipliklerden örme ve dokuma kumaşlar elde edilmiştir. İplik özellikleri (iplik düzgünsüzlük, mukavemet-uzama, tüylülük, iplik hataları), örme kumaş özellikleri (patlama mukavemeti) ve dokuma kumaş özellikleri (boncuklanma dayanımı, çekme mukavemeti ve uzaması, eğilme dayanımı) belirlenmiştir. Çalışma neticesinde sargı lif tipi, iplik numarasının iplik düzgünsüzlük, kalın yer, neps, iplik tüylülüğü ve örme kumaş patlama mukavemeti üzerinde istatistiksel olarak anlamlı etkisinin olduğu, sargı lif tipi, iplik numaarsı ve öz filament doğrusal yoğunluğunun çok bileşenli özlü iplik ve dokuma kumaş özellikleri üzerinde anlamlı bir etkisinin olduğu sonucuna ulaşılmıştır [1]. Babaarslan ve ark. farklı filament inceliğine sahip yalancı büküm tekstüre polyester filamenti kullanarak özlü ve çok bileşenli özlü (polyester+elastan) iplik üretmişlerdir. Elastan çekimi ve filament inceliğinin değişkenlerinin etkisinin incelendiği bu çalışmada ipliklerden denim kumaşlar elde edilmiştir. Elastan çekim oranının kumaş kopma kuvveti ve uzaması, yırtılma kuvveti, kılcallık oranı, kalıcı uzama özellikleri üzerinde etkisinin olduğu ve filament inceliğinin ise kopma kuvveti ve uzaması, yırtılma kuvveti, kılcallık oranı, kalıcı uzama ve su emilimi özellikleri üzerinde istatistiksel olarak anlamlı bir etkiye sahip olduğu sonucuna ulaşmışlardır [14]. Bedez Ute ve Kadoğlu, çalışmalarında farklı elastan ve filament kombinasyonlarında elde ettikleri tek ve çift özlü ipliklerin performans özelliklerini incelemişlerdir. Elastan doğrusal yoğunluğunun ve öz değişkeninin iplik özellikleri üzerinde etkilerinin olduğu sonucuna ulaşmışlardır. Daşan ve Babaarslan çalışmalarında filament tipi (Xa, PES ve PA 6.6) ve elastan çekim oranı (3, 3.5, 4 ve 4.5) değişkenlerinde ring iplik eğirme sisteminde çok bileşenli özlü iplik üretimleri gerçekleştirmişlerdir. Daha sonrasında ise bu iplikleri atkı ipliği olarak kullanarak denim kumaş numuneleri elde etmişlerdir. Denim kumaşların mukavemet, uzama, potlanma, elastikiyet ve kumaş çekme özellikleri belirlemişlerdir [15].

Çalışma kapsamında öz ve sargı lif tipi ve iplik numarası değişkenleri ile üretilen çok bileşenli özlü ipliklerinin denim kumaş yırtılma performansı üzerine etkisi incelenmiştir. Bu amaçla elde edilen iplikler denim kumaş üretiminde atkı ipliği olarak kullanılmıştır. Öz ve sargı lif değişkenleri ve iplik numarasının çözgü ve atkı yönü yırtılma kuvveti üzerindeki etkisini belirleyebilmek amacıyla SPSS paket programı kullanılarak % 95 güven aralığında varyans analizi (ANOVA) gerçekleştirilmiştir.

2. Materyal ve Metot

2.1. Materyal

Sargı lifinin, öz materyalinin ve iplik numarasının denim kumaş yırtılma mukavemeti üzerindeki etkisinin incelendiği bu çalışmada sargı lifi olarak %100 Polyester, %60/40 Pamuk/Polyester ve %100 Pamuk kullanılmıştır. Çalışma kapsamında, 1. öz materyali olarak 55 dtex T400, PBT ve PET ile birlikte 2. öz materyali olarak 78 dtex elastan kullanılmıştır. Bu hammaddeler kullanılarak Tablo 1'de verilen çok bileşenli özlü iplik numuneleri aynı üretim parametrelerinde ring iplik eğirme sisteminde Ne 12/1 ve 18/1 numaralarında Ne 0.70 fitil numarasında fitil kullanılarak 3.62 elastan çekim oranı, 1.08 filament çekim oranı ve 12.600 iğ devrinde gerçekleştirilmiştir. Bununla birlikte, Ne 12/1 numara iplik üretimleri 620 tur/m (tpm) bükümde, Ne 18/1 numara iplik için ise 760 tpm bükümde gerçekleştirilmiştir [16].

Tablo 1. Çalışma kapsamında üretilen iplik numuneleri

İplik Numarası (Ne)	Sargı Lif Tipi	Öz Materyali			
		1.Öz Bleşeni	Doğrusal Yoğunluk (dtex)	2. Öz Bileşeni	Doğrusal Yoğunluk (dtex)
18	100% Polyester	T400	55	Elastan	78
		PBT	55	Elastan	78
		PET	55	Elastan	78
12	100% Polyester	T400	55	Elastan	78
		PBT	55	Elastan	78
		PET	55	Elastan	78
18	60/40% Pamuk/Polyester	T400	55	Elastan	78
		PBT	55	Elastan	78
		PET	55	Elastan	78
12	60/40% Pamuk/Polyester	T400	55	Elastan	78
		PBT	55	Elastan	78
		PET	55	Elastan	78

Toplamda üretilen 12 farklı iplik numunesi kullanılarak denim kumaş numuneleri elde edilmiştir. Denim kumaş üretimleri tarak numarası 70/4 olan Picanol 550 mm/dk dokuma makinasında Ne 12/1 atkı ipliğindeki numunelerin atkı sıklığı 12 atkı/cm, Ne 18/1 atkı ipliğindeki numunelerin atkı sıklığı ise 20 atkı/cm olacak şekilde gerçekleştirilmiştir. Çözgü iplik numarası ise denim üretiminde sıklıkla tercih edilen Ne 20/1 seçilmiştir. Dokunan kumaşlara daha sonra ön yüz teğet yakma, 10 bome kostik ve en son olarak da standart apre sanfor işlemleri uygulanmıştır.

2.2. Metot

Kumaş üretim aşamasında çözgü yönü parametreleri sabit tutularak çift özlü iplikler kumaşın atkı yönünde kullanılmıştır. Yırtılma mukavemeti testi ASTM D1424 standardına göre Dijital Elma Tear Test Cihazı (James Heal/İngiltere) kullanılarak gerçekleştirilmiştir. Çalışmada atkı ipliği olarak farklı özelliklere sahip çok bileşenli özlü iplikler kullanıldığından ve çözgü yönünde kullanılan iplik özellikleri aynı olduğundan kaynaklı kumaş yırtılma mukavemet testi atkı yönünde uygulanmıştır. Analizde atkı yönünde diyagonal olarak 5 adet numune üzerinde ölçüm alınmıştır.

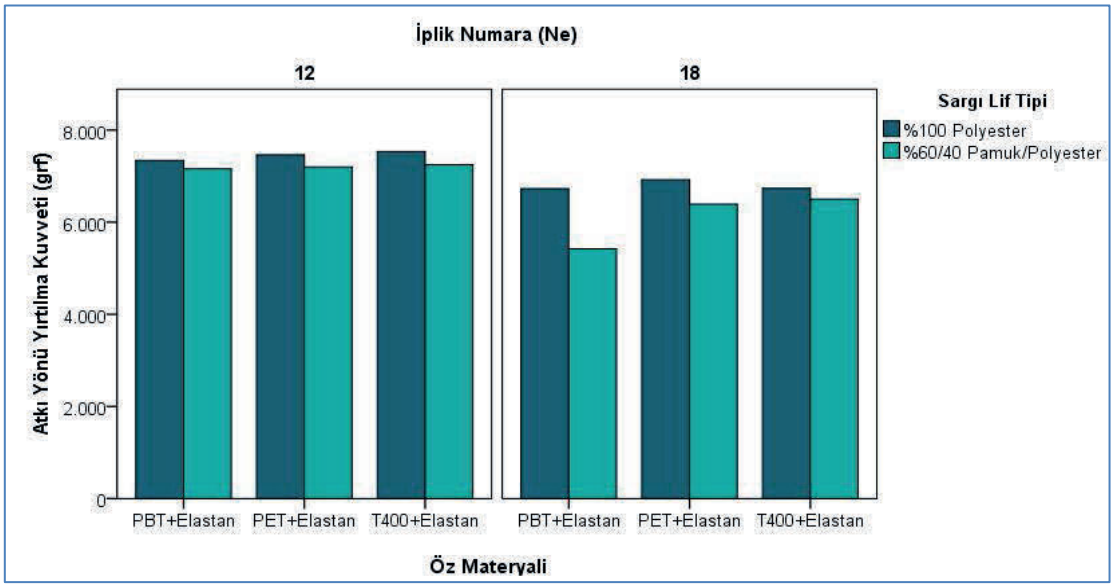
Sargı lif tipi, öz materyal değişkeni ve iplik numarası değişkenlerinin denim kumaş numunelerinin yırtılma mukavemeti üzerinde anlamlı bir etkisinin olup olmadığını belirlemek amacıyla SPSS 21.0 paket programı kullanılarak varyans analizi uygulanmıştır. Tüm sonuçlar %95 güven aralığında değerlendirilmiştir.

3.Bulgular ve Tartışma

Denim kumaş numunelerine ait yapısal özellikler Tablo 2'de verilmiştir. Denim kumaş numunelerinin atkı yönü yırtılma kuvveti Şekil 1'de gösterilmiştir.

Tablo 2. Denim kumaş numunelerinin yapısal özellikleri

İplik Numarası (Ne)	Sargı Lif Tipi	Öz Materyali	Çözgü Sıklığı (çözgü/cm)	Atkı Sıklığı (atkı/cm)	Gramaj (g/m^2)
18	100% Polyester	T400+Elastan	42,6	21,8	313,2
		PBT+Elastan	43,0	21,8	320,0
		PET+Elastan	42,4	22,2	307,4
12	100% Polyester	T400+Elastan	40,2	12,8	284,6
		PBT+Elastan	40,0	13,0	288,0
		PET+Elastan	39,6	13,0	278,2
18	60/40% Pamuk/Polyester	T400+Elastan	41,4	22,2	306,2
		PBT+Elastan	40,4	22,2	307,0
		PET+Elastan	40,0	23,0	297,4
12	60/40% Pamuk/Polyester	T400+Elastan	40,4	12,8	278,4
		PBT+Elastan	39,8	12,8	271,6
		PET+Elastan	40,4	12,6	274,8



Şekil 1. Denim kumaş numunelerinin atkı yönü yırtılma kuvveti

Atkı yönü yırtıma kuvveti incelendiğinde %100 polyester sargı lifinden elde edilen denim kumaş numunelerinin yırtılma kuvvetinin %60/40 pamuk/polyester sargı lifinden elde edilen denim kumaş numunelerinin yırtılma kuvvetinden daha yüksek olduğu belirlenmiştir. Öz materyal değişkeni incelendiğinde atkı yönü yırtılma kuvvetinin yüksekten düşüğe doğru sırasıyla T400+Elastane>PET+Elastan>PBT+Elastan olduğu görülmektedir. Bununla birlikte, Ne 18/1 numara ipliklerden elde edilen denim kumaşların atkı yönü yırtılma kuvvetinin Ne 12/1 numara ipliklerden elde edilen denim kumaşların çözgü yönü yırtılma kuvvetinden daha düşük olduğu belirlenmiştir. Tablo 3'te verilmiş olan ANOVA analiz sonuçlarına göre iplik numarası (A), öz materyal değişkeni (B) ve sargı lif tipinin (C) atkı yönü yırtılma kuvveti üzerinde istatistiksel olarak anlamlı bir etkisinin olduğu görülmektedir ($p<0,05$). Ayrıca A*B, A*C ve B*C parametrelerinin etkileşimlerinin de atkı yönü yırtılma kuvveti üzerinde istatistiksel olarak anlamlı etkilerinin olduğu sonucuna ulaşılmıştır.

Tablo 3. Atkı yönünde yırtılma kuvveti için varyans analiz (ANOVA) sonuçları

Kaynak	Kareler Toplamı	df	Ortalama Kareler	F	Anlamlılık
İplik Numarası (A)	11443286,817	1	11443286,817	155,976	0,000*
Öz Materyal Değişkeni (B)	1516682,033	2	758341,017	10,336	0,000*
Sargı Lif Tipi (C)	3279278,817	1	3279278,817	44,698	0,000*
A*B	700800,233	2	350400,117	4,776	0,013*
A*C	755554,817	1	755554,817	10,298	0,002*
B*C	627457,433	2	313728,717	4,276	0,020*
A*B*C	926737,233	2	463368,617	6,316	0,004*
a. R^2= 0,845 (Düzenlenmiş R^2= 0,810)					

4.Sonuçlar

Bu çalışmada iplik numarasının, öz materyalinin ve sargı lif tipinin denim kumaşların atkı yönü yırtılma kuvveti üzerinde etkisinin belirlenmesi amaçlanmıştır. Bu kapsamda aynı üretim parametrelerinde Ne 12/1 ve Ne 18/1 iplik numarasında, T400+Elastan, PBT+Elastan ve PET+Elastan öz materyalleri kullanılarak %100 Polyester ve %60/40 Pamuk/Polyester sargılı çok bileşenli özlü iplikler ring iplik eğirme sisteminde aynı üretim koşullarında üretilmiştir. Bu ipliklerden daha sonra denim kumaş üretiminde atkı ipliği olarak kullanılmıştır. Denim kumaşların atkı yönü yırtılma kuvveti değerleri tespit edilmiştir. Sonuçlar incelendiğinde, etkisi incelenen bütün parametrelerin (iplik numarası, öz materyali ve sargı lif tipi) atkı yönü yırtılma kuvveti üzerinde istatistiksel olarak anlamlı bir etkisi olduğu sonucuna ulaşılmıştır ($p<0,05$). Ne 12/1 T400+Elastan özlü %100 Polyester sargılı iplikten üretilen denim kumaşın en yüksek yırtılma kuvveti değerine sahip olduğu belirlenmiştir.

Referanslar

1. Çelikhan Aydoğdu, S.H., Yılmaz, D. Analyzing Some of the Dual-Core Yarn Spinning Parameters on Yarn and Various Fabric Properties. Tekstil ve Konfeksiyon, **2019**, 29(3):197-207.
2. Shaw, V.P., Mukhopadhyay, A., Impact of Abrasion on Strength, Elasticity and Elastic Recovery Properties of Stretch-Denim Fabric. International Journal of Clothing Science and Technology. DOI 10.1108/IJCST-12-2020-0205.
3. Pannu, S., Ahirwar, M., Jamdigni, R., Behera, B.K. Effect of Spandex Denier of Weft Core Spun Yarn on Properties of Finished Stretch Woven Fabric. International Journal of Technologies and Management Research. **2020**. 7(07):21-32.
4. Türksoy, H.G., Kılıç, G., Üstündağ, S., Yılmaz, D. A Comparative Study on Properties of Dual-Core Yarns. The Journal of The Textile Institute. **2019**. 110(7):980-988.
5. Erbil, Y., Babaarslan, O., Islam, M.R., Sirlibaş, S. Performance of Core & Dual-core Cotton Yarn Structures on Denim Fabrics. Journal of Natural Fibers. DOI 10.1080/15440478.2021.1982837.
6. Elrys, S.M.E., El-Habiby, F.F., Elkhalek, R.A., Eldeeb, A.S., El-Hossiny, A.M. Investigation Into The Effect of Yarn Structure and Yarn Count on Different Types of Core-Spun Yarns. Textile Research Journal. **2021**. DOI 10.1177/00405175211021447.
7. Türksoy, H.G., Yıldırım, N., Ertek Avcı, M. Comparative Evaluation of Some Comfort

Properties of Denim Fabrics Including Dual-Core Yarns Containing Wool and Elastane Yarn. The Journal of The Textile Institute. **2021**. DOI 10.1080/00405000.2021.1964195.
8. El-Tantawy, S., Sabry, M., Bakry, M. The Effect of Weft Yarn Production Technique on The Pilling Property of Jeans Fabrics. International Design Journal. **2017**. 7(3):161-169.
9. Babaarslan, O., Daşan, Y. Stretch and Physical Properties of Weft Stretch Denim Fabrics Containing Elastane and Filament Yarn. J Textile Sci & Fashion Tech. **2020**. 4(4): 1-10.
10. Fidan, G., Korkmaz, Y., Kaynak, H.K. Bi-Streç Denim Kumaşlarda Buruşma Özellikleri. Pamukkale Üniversitesi Mühendislik Bilimleri Dergisi. **2020**. DOI 10.5505/pajes.2020.74044.
11. Su, X., Liu, X. Research on Performance of Twin-Core Spun Yarns and Fabric. International Journal of Clothing Science and Technology. **2020**. 32(3):338-355.
12. Bedez Ute, T., Kadoğlu, H. The Effect of Single and Dual-Core Yarns Produced with Different Core Materials on the Elasticity and Recovery Properties of Denim Fabrics. Text Leath Rev. **2019**. 2(4):174-182.
13. Babaarslan, O., Sarıoğlu, E., Kaynak, H.K., Ertek Avcı, M., (2018), Air permeability analysis of denim fabrics form dual-core spun yarns, 18th World Textile Congress (AUTEX 2018), 20-22 Haziran **2018**, İstanbul, Türkiye.
14. Babaarslan, O., Sarıoğlu, E., Çelik, H.İ., Ertek Avcı, M., Denim Fabrics woven with dual core-spun yarns, Engineered Fabrics, Ed:Mukesh Kumar Singh, IntechOpen, **2018,** Chapter 2, 19-39, DOI: 10.5772/intechopen.80286.
15. Ertaş, O.G., Zervent Ünal, B., Çelik, N. Analyzing The Effect of The Elastane Containing Dual-Core Weft Yarn Density on The Denim Fabric Performance. The Journal of Textile Institute. **2016**. 107(1):116-126.
16. Vuruşkan, D. Sargı Lifi ve Öz Materyalinin Çift Özlü İpliklerin Kalite Özelliklerine Etkileri. Tekstil ve Mühendis. **2019**. 26(115):289-298.

CLASSIFICATION OF THE BREAD WHEAT QUALITY WITH ARTIFICIAL NEURAL NETWORK MODELS

BÜNYAMİN KAHRAMAN*[1], YUNUS EROĞLU[2]

[1] Gaziantep University, Graduate School of Natural and Applied Sciences, Industrial Engineering Department, Gaziantep, TURKEY.
[2] İskenderun Technical University, Engineering and Natural Sciences Faculty, Industrial Engineering Department, Hatay, TURKEY.

Abstract

Many food factories waste time and money because they do not have accurate and continuous information about raw materials, production, and end products. Large laboratories must be established to have this information. There is also a need for a large number of specialist personnel. These studies in the food sector should be non-contact, hygienic, and practical. Correct classification is one of the most important criteria for the storage process. Correct classification of raw materials is a laborious and highly experienced job. In order to make this decision, a series of analyzes should be made and all results should be interpreted by experts. The wrong decisions can result in high costs. In this study, we proposed artificial neural network-based models to classify wheat which is used as a raw material by bread flour factories. According to the standard TS-2974, bread wheat can be classified into four qualities, Class I (Elite Quality), Class II, Class III, and low-quality wheat (class four). Establishing an automatic classification system that uses laboratory analysis in order not to depend on the expert is very important for profit-making businesses. Therefore, models have been developed in this study that use laboratory analysis as input and allocate the appropriate class for bread wheat. The proposed models were tested with bread wheat obtained from a licensed warehouse in Şanlıurfa, Türkiye. The results of the study showed that it is possible to automate the bread wheat classification using artificial intelligence, independent of the expert. This system, which will reduce the labor force, will also be useful for non-contact and fast results. Thus, a decision support mechanism that can guide decision-makers will be established. It is the beginning of the digital transformation in food factories with artificial intelligence technologies, which are important for Industry 4.0 transformations.

Keyword: Bread Wheat, Artificial Neural Network, Classification, Quality.

1. Introduction

Wheat is one of the basic foodstuffs. It is preferred by farmers as it is easy and effortless to produce. It can be grown easily in wet or arid lands. Storage and transportation costs are low. The most important advantage is that it has high nutritional values [1]. Wheat is used in various ways around the world. For example, the final products obtained by processing wheat are flour, pasta, semolina, and starch. This situation actually makes wheat a commercial value throughout the world. While converting this commercial value into price, of course, determining the wheat quality will be essential.

Wheat is an herbaceous plant that is cultivated in summer and winter. The yield of wheat planted in winter is much higher. Therefore, farmers do not prefer summer planting. Wheat has a long shelf life due to its low moisture content. Generally, wheat is purchased and stored in high tonnages. Before entering the storage process, quality control analyzes and wheat quality classification are required. Physical and chemical analysis are performed to determine the wheat quality. When classifying bread wheat, the most important factors affecting quality are defective grain, other miscellaneous substances, hectoliter and protein values. While defective grain and other miscellaneous substances can be detected by eye, measurement tools are needed for hectoliters, and protein analysis. Hectoliter data expresses the value of 100 liters of wheat in kilograms. Kjeldahl and Near Infrared (NIR) methods are used for protein analysis. NIR Method is used as a method that gives results in a shorter time. Instead of ordinary methods, it gives realistic results by measuring the absorption of radiation at certain wavelength ranges [2].

Researchers have also tried different methods for food classification. By performing image analysis, it has been ensured that wheat can be classified and distinguished from different grains by size and shape analysis [3]. In another study using the Dense Scale Invariant Features (DSIFT) Method, studies were carried out on automatic classification of wheat [4]. Artificial neural networks have been used in the studies on durum wheat using artificial intelligence methods. In another study, estimation studies were carried out based on the physical properties of wheat [5]. The studies conducted are aimed at minimizing the laboratory processes in food factories. The number of laborious analyzes is decreasing day by day. In particular, a raw material analysis should be done very quickly and reliably. In this way, the purchasing and storage processes in factories or warehouses will be easier.

2. Materials and Methods

In this study, analysis results obtained from 412 different bread wheat samples were used to create a data set. The analyzes were obtained from the licensed warehouse using the Perten Inframatic 9500 device. In the obtained data from the device, the variables such as (V1) Moisture, (V2) Broken kernel, (V3) Suni bug damaged kernel, V(4) Germination, (V5) Glume, (V6) Rye, (V7) Vernier grain, (V8) Remains of animal origin, (V9) Hectoliter, and (V10) Protein values were collected for each wheat sample. Also, expert decisions on the quality of the wheat are matched with the collected data sample. Then, we create artificial neural networks methods to determine the class of bread wheat quality. Modeling was done using the Alyuda NeuroIntelligence program.

2.1 Artificial Neural Network

Artificial Neural Networks are computer programs that imitate human nerve cells. There are process elements, each connected by weighted links and each with its own memory [6]. Through these process elements, artificial neural networks generate some outputs by activating a number of functions. Artificial neural networks have a structure that can be trained, verified, and predicted the result [7]. Artificial nerve cells consist of Output, Addition function, Activation function, and weights. A general architecture of artificial neural networks consist of inputs, outputs, and hidden layers between them as represented in figure 1. Each layer has a certain number of components called neurons. Each neuron receives a large number of signals and creates an output signal with its own algorithm [8].

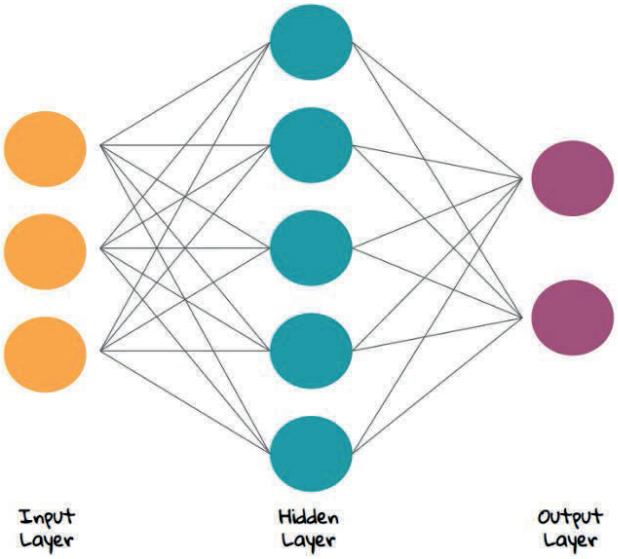


Figure 1. The Artificial Neural Network Architecture

Another important feature of artificial neural networks is their adaptability. Networks have the ability to adapt their synaptic weights to changes in their environment. A previously trained neural network can be easily retrained for even the slightest change in the surrounding conditions. In addition, the synaptic weights of the neural network operating in an unstable environment can also be changed in real time [9].

ANN is a widely used technique in wheat studies. The current studies are found as follows. Jadhav (2021) proposed an ANN model to predict wheat and jowar yield prediction model [10]. Monjezi (2021) suggests a data mining model using ANN to predict energy required in wheat production [11]. Halwani and Bachinger (2021) suggested four different ANN based models to predict grain yield response of winter wheat under organic farming system [12]. By the way, unlike the current literature, we propose a novel ANN based approach to wheat classification.

2.2 Application

The application part was made using the Alyuda NeuroIntelligence program. First of all, the data was uploaded to the system to be completely selected. Estimation of the class of wheat in the data was determined as the target and all other values were specified numerically. Randomly; 290 samples (70%) for Training, 61 samples (15%) for Validation, and 61 samples (15%) for Test were selected. In the proposed ANN models, only V2 (Broken kernel), V3 (Suni bug damaged kernel), V4 (Germination), V9 (hectoliter), and V10 (Protein) parameters were accepted as input data instead of the whole parameters. Because the others (V1, V5, V6, V7, and V8) were not affecting the classification of the wheat according to TSE-2974 which is the standard of bread wheat classification. It means the spec value of these variables are the same for Elite, Class II, and Class III of bread wheat. The units of data used in artificial neural networks can be different, as well as their volumes. Some data can take values in the range of [0, 1], while some can take values between 1 and 1000. It is an appropriate approach to pull these data used in the artificial neural network to a similar value range (such as [0, 1] or [-1, 1]) in order to better model them. In this study, all values are taken between -1 and +1 values by preprocessing. Although the network model can be selected manually, a model structuring has been worked on through the software. The model suggested by the software is selected as 5 input layers, 13 hidden layers, and 3 output layers.

3. Results and Discussion

In this study, the Quick Propagation algorithm has been selected for network training. 500 iterations were found sufficient for this classification. The model was trained 10 times and its accuracy results as in Correct Classification Rate (CCR) for training, validation, test, and all data were recorded, separately. Table 1 gives the results for 10 training runs. According to the CCR results for each run, the highest training rate was 98.29%, the lowest training set was 97.27%, the highest validation rate was 93.22%, and the lowest validation rate was 91.52%. The average training rate was 98.25% and the average validation rate was 91.86%.

Table 1. Test Results of Training

	RUN 1	RUN 2	RUN 3	RUN 4	RUN 5	RUN 6	RUN 7	RUN 8	RUN 9	RUN 10	Max	Min	Mean
Train	97.95	98.29	94.21	98.29	97.27	98.29	98.29	98.29	98.29	97.27	98.29	97.27	97.64
Validation	93.22	91.52	91.52	91.52	91.52	93.22	91.52	91.52	91.52	91.52	93.22	91.52	91.86
Test	96.61	98.3	96.61	96.61	94.91	94.91	100	100	94.91	96.61	100	94.91	96.94
All	97.08	97.33	94.17	97.08	96.11	97.08	97.57	97.57	96.84	96.35	97.57	94.17	96.71

4. Conclusions

The food industry is a system based entirely on quality analysis. There are large laboratories established within the factories and many technicians employed to perform these analyzes. Besides,, examining the analyzes and making an expert decision present a separate difficulty. It is indispensable for food factories that the decision is made quickly and the production is not interrupted. This study proposes a decision support system for people or institutions that buy, sell and stock wheat with artificial neural network models, so that they can control the decision they make.

The study was carried out by making use of real data in order to be suitable for real life. In this way, the process from sampling to classification decision was evaluated through the system and the results were shared.

In this study, ANN models have been developed for the bread wheat classification, which must be determined during the wheat stocking process and the decision is made by the experts. The developed model was able to predict the data obtained by laboratory analysis with an accuracy of 96.71% as Elite, Class II, and Class III. This model can provide a high level of support to experts in their decision-making process. It can set an example for other scientists working in this field and can be developed.

References

1. Bonfil, D. J., and E. S. Posner. "Can bread wheat quality be determined by gluten index?." Journal of Cereal Science, **2012**, 56(2) :115-118.
2. Osborne, Brian G. "Near-infrared spectroscopy in food analysis." Encyclopedia of analytical chemistry: applications, theory and instrumentation. **2006**.
3. Sapirstein, H. D., et al. An instrumental system for cereal grain classification using digital image analysis. Journal of Cereal Science. **1987**, 6(1): 3-14.
4. Olgun, M., et al. Wheat grain classification by using dense SIFT features with SVM classifier. Computers and Electronics in Agriculture. **2016,** 122:185-190.

5. Taner, A., Ali A., and S. A. U. K. Hüseyin. Yapay sinir ağları ile makarnalık buğday çeşitlerinin sınıflandırılması. Anadolu Tarım Bilimleri Dergisi. **2015**, 30(1):51-59.
6. Akkoyun, S., Tuncay B., and Tugba T. Estimations of beta-decay energies through the nuclidic chart by using neural network. Radiation Physics and Chemistry. **2014**, 96:186-189.
7. Civalek, Ö. Dairesel plaklarin nöro-fuzzy tekniği ile analizi (the analysis of circular plates via neuro-fuzzy technique).
8. Lorenz, A., et al. Comparison of different neuro-fuzzy classification systems for the detection of prostate cancer in ultrasonic images. 1997 IEEE Ultrasonics Symposium Proceedings. An International Symposium (Cat. No. 97CH36118). **1997**, 2.
9. Sharma, S., Gurvinder S., and Manik S. A Comprehensive Review and Analysis of Supervised-Learning and Soft Computing Techniques for Stress Diagnosis in Humans. Computers in Biology and Medicine. **2021**, 104450.
10. Jadhav, V. Wheat and Jowar Crop Yield Prediction Model using Ensemble Technique. **2021**.
11. Monjezi, N. Energy Prediction of Wheat Production Using Data Mining Technique in Iran. Basrah Journal of Agricultural Sciences. **2021**, 34(1):14-27.
12. Halwani, M., and Johann B. Using four data mining techniques to predict grain yield response of winter wheat under organic farming system. 41. GIL-Jahrestagung, Informations-und Kommunikationstechnologie in kritischen Zeiten. **2021**.

VORTEKS İPLİKLERE UYGULANAN FİKSE (VAKUMLU BUHARLAMA) İŞLEMİNİN ÖRME KUMAŞ PERFORMANSINA ETKİSİNİN ARAŞTIRILMASI

AHMET ORUÇ[1], EMEL İLANBEY*[1], KUBRA ÖZŞAHİN[1], HATICE KUBRA KAYNAK[2]

[1]MEM Tekstil San. Ve Tic. A.Ş., Kahramanmaraş, TURKEY
[2]Gaziantep Üniversitesi, Tekstil Mühendisliği Bölümü, Gaziantep, TURKEY

Özet

Bu çalışmada, Vorteks eğirme sisteminde üretilen pamuk- viskon karışımlı ipliklere uygulanan fikse (vakumlu buharlama) işleminin iplik mukavemeti, iplik kopma uzaması ve örme kumaş performans parametrelerine etkilerinin araştırılması amaçlanmıştır. Bu kapsamda, %60-40 pamuk-viskon ve %50-50 pamuk-viskon iplik numuneleri Vorteks eğirme sistemi kullanılarak üretilmiştir. Elde edilen ipliklerin bir kısmına fikse işlemi uygulanmıştır. Sonrasında fikseli ve fiksesiz olarak elde edilen ipliklerin kopma mukavemeti ve kopma uzaması özellikleri test edilmiştir. Elde edilen fikseli ve fiksesiz ipliklerden süprem örme kumaş numuneleri elde edilerek boyanmıştır. Daha sonra elde edilen boyalı kumaşların ev tipi yıkama sonrası boyutsal dayanım ve dönme, patlama mukavemeti, boncuklanma dayanımı ve renk haslığı performansları ölçülmüştür. Renk haslığı testlerinden (asit ve baz) ter haslığı, su haslığı, kuru sürtme ve yaş sürtme haslığı testleri uygulanmıştır. Çalışma sonucunda uygulanan fikse işleminin iplik mukavemeti üzerinde önemli bir değişikliğe sebep olmadığı ancak fikse işlemi uygulanan ipliklerin kopma uzamasında ise az miktarda artış olduğu görülmüştür. Elde edilen sonuçlar, bu çalışma kapsamında seçilen lif karışımları için, Vorteks ipliklere uygulanan fikse işleminin örme kumaş performansında bir iyileşme sağlamadığını göstermektedir.

Anahtar Kelimeler: vorteks eğirme sistemi, vakumlu buharlama, patlama mukavemeti, boncuklanma dayanımı, renk haslığı

1.Giriş

Günümüzde iplik üretimi için birçok farklı eğirme sistemi kullanılmaktadır. En yaygın iplik eğirme sistemi Ring eğirme sistemi olmakla birlikte, sıklıkla kullanılan diğer sistemlerden Rotor ve Vorteks eğirme sistemleri de hızla yaygınlaşmaktadır. Her bir eğirme sisteminin farklı avantaj ve dezavantajları bulunmaktadır. Vorteks eğirme sistemi, Ring eğirme sistemindeki fitil ve bobinleme basamaklarının elimine edilmesi sebebiyle daha hızlı üretim ve daha düşük maliyet avantajı sunmakta ve gün geçtikçe yaygınlaşmaktadır. Vorteks eğirme sistemi, tekstil endüstrisinde kullanılan lif tiplerinin birçoğunun kullanılabildiği bir eğirme sistemidir. Bu eğirme sisteminde üretilen iplikler hem örme hem de dokuma kumaş üretiminde kullanılabilmektedir.

İplik canlılığı olarak da bilinen ipliğin kendi üzerinde kıvrılarak büküm alması eğilimine hem kısa hem de uzun stapel iplikçiliğinde rastlanmaktadır. Bu durum örme ve dokuma kumaş üretiminde birçok zorluk yaratmakta ve kumaş hatalarını arttırarak kaliteyi olumsuz yönde etkilemektedir. Bu problemleri ortadan kaldırmak için, ipliğe fikse işlemi olarak da bilinen vakum ortamında buharlama uygulanabilmektedir. Fikse işlemi, iplik üzerinde eğirme prosesinden kaynaklanan gerilimleri gidermek, bükümü sabitlemek, mukavemeti arttırmak ve kumaş üretimi esnasında

ipliğin kendi üzerine büküm alarak kıvrılmasından kaynaklanan kumaş hatalarını gidermek amacıyla uygulanmaktadır.

Çelik ve Kadoğlu [1] yaptıkları çalışmada, ham madde, eğirme sistemi, iplik numarası, büküm katsayısı ve fikse işleminin hem uzun hem de kısa stapel iplikçiliğinde büküm canlılığı üzerine önemli etkileri olduğunu görmüşlerdir. İpliklere fikse işlemi uygulanmasının iplik canlılığında azalmaya sebep olduğunu bildirmişlerdir. Şardağ ve Özdemir [2], çalışmalarında %100 pamuk, %100 viskon ve %100 poliester ipliklerin, farklı büküm, iplik numarası ve fikse sıcaklığı ve süreleri için büküm canlılıklarını incelemişlerdir. Yapılan çalışma, hammadde, büküm, iplik numarası ve fikse işleminin büküm canlılığı üzerinde önemli derecede etkili olduğunu göstermiştir. İlaveten, çalışmada kullanılan her bir hammadde için fikse sıcaklığı ve süresi koşullarının optimize edilebileceği ve fiksesiz ipliklere nazaran büküm canlılığı değerlerinin önemli derecede azaltılabileceği belirtilmiştir. Şardağ vd. [3], %100 pamuk ve %100 viskon ipliklerde fikse işleminin iplik mukavemet özelliklerine etkilerini incelemişlerdir. Çalışma kapsamında, Ne 16/1 ve Ne 30/1, %100 pamuk ve %100 viskon ipliklerde, üç farklı büküm katsayısı uygulayarak ürettikleri iplik numunelerini farklı sıcaklık ve sürelerde fikse işlemine tabi tutumuşlardır. Çalışma sonucunda %100 pamuk iplik numunelerinde büküm katsayısının arttırılması durumunda, mukavemeti arttırmak için, fikse işlemi sıcaklığının arttırılması gerektiğini ve bu ipliklerde fikse süresinin arttırılmasının anlamlı bir etki yaratmadığını vurgulamışlardır. %100 viskon iplik numunelerinde ise, sadece yüksek büküm katsayısı uygulanması durumunda, fikse işleminin uygulanması gerektiğini ve fikse sıcaklığının 70°C'yi aşmaması gerektiğini bildirmişlerdir. İlaveten, viskon iplik numunelerinde fikse süresinin artmasının iplik mukavemetini arttırıcı bir etkisi olmadığını belirtmişlerdir. Şardağ ve Özdemir [4], bir diğer çalışmalarında, %100 poliester ipliklerde fikse işleminin iplik kalite parametreleri, iplik mukavemeti ve büküm canlılığı üzerine etkilerini incelemişlerdir. Bu amaçla, farklı büküm katsayısı ve iplik numaralarında ürettikleri poliester iplik numunelerine, farklı sıcaklık ve sürelerde fikse işlemi uygulamışlardır. Çalışma sonucunda stapel poliester ipliklerde, iplik inceldikçe fikse işleminin mukavemete olumlu etkisi olduğunu, kalın ipliklerde ise olumsuz etki gördüklerini belirtmişlerdir. Fikse işlem sıcaklığının iplik kopma mukavemeti üzerinde anlamlı bir etkisi olmazken, fikse süresinin artmasıyla kopma işinin arttığını bildirmiş ve bu sonucun örme ve dokuma işlemleri için bir avantaj sunacağını vurgulamışlardır. Nabi vd. [5], farklı bölgelerden alınan Özbekistan pamuğundan, Ne 30/1 iplik numarasında üretilmiş pamuk ipliklerinin tüylülük, kopma mukavemeti ve kopma uzaması özelliklerine fikse işleminin etkilerini incelemişlerdir. Çalışma sonucunda fikse işleminin ipliklerin nem miktarını %7'den yaklaşık %12'ye çıkardığını, tüylülük değerlerinin az seviyede azaldığını, kopma mukavemeti ve uzaması değerlerinin ise düşük seviyede iyileştiğini belirtmişlerdir. Çeven ve Özdemir [6], akrilik ve viskon şönil ipliklere, farklı sıcaklık ve sürelerde uygulanan fikse işleminin iplik kopma mukavemeti ve uzamasına etkilerini incelemişlerdir. İlaveten bu ipliklerin atkı yönünde kullanıldığı dokuma kumaş numuneleri üretmişler ve bu kumaşların aşınma dayanımını incelemişlerdir. Çalışma sonucunda, fikse işleminin ipliklerde kopma mukavemeti ve uzamasını arttırıcı bir etkisi olduğunu bildirmişlerdir. Şönil ipliklerde fikse işlemiyle bükümün iyi seviyede sabitlenmesinin sağlandığını ve bu durumun iplik yapısındaki hav liflerinin yapıda tutunmasını sağladığını ve bu şekilde kumaşların aşınma dayanımının iyileştiğini belirtmişlerdir.

Literatürdeki çalışmalar değerlendirildiğinde fikse (vakumlu buharlama) işleminin iplik bükümünün sabitlenmesi ve bu şekilde büküm canlılığının azaltılması, tüylülüğün azaltılması, kopma mukavemetinin ve uzamasının iyileştirilmesi üzerine kayda değer etkiler sağladığı görülmektedir. Yapılan çalışmaların bir çoğunun, büküm açılması probleminin daha çok yaşandığı

ring iplik eğirme sisteminde üretilen iplikler üzerine yoğunlaştığı ve az sayıda çalışmada farklı eğirme sistemleri üzerinde durulduğu görülmektedir. İlaveten fikse işleminin son ürün olan boyalı veya bitmiş haldeki kumaştaki etkilerinin incelendiği çalışmaların oldukça az sayıda olduğu görülmektedir. Bu çalışma kapsamında literatürdeki çalışmalardan farklı olarak, tekstil endüstrisinde en çok kullanılan pamuk-viskon lif karışımından, günümüzde hızla yaygınlaşan Vorteks eğirme sistemiyle iplik numuneleri üretilmiş ve üretilen bu numunelere uygulanan fikse işleminin son ürün olan boyalı örme kumaş performansına etkileri araştırılmıştır.

2. Materyal ve Metot

Bu çalışmada, %60-40 pamuk-viskon ve %50-50 pamuk-viskon karışımlarından, vorteks iplik eğirme teknolojisi ile üretilen ipliklerin fikse işlemi sonrasındaki iplik mukavemeti ve uzaması özellikleri incelenmiştir. İlaveten, fikseli ve fiksesiz ipliklerden üretilerek boyanan örme kumaşların performans özellikleri karşılaştırılmıştır. Çalışmada kullanılan viskon ve pamuk lif özellikleri sırasıyla, Tablo 1 ve Tablo 2'de verilmiştir.

Tablo 1. Çalışmada kullanılan viskon lifinin özellikleri

Lif inceliği, denier	1,14
Lif uzunluğu, mm	37,5
Lif mukavemeti, g/d	2,91

Tablo 2. Çalışmada kullanılan pamuk lifinin özellikleri

Lif inceliği, mic.	4,01
Lif uzunluğu, mm	31,57
Lif mukavemeti, g/tex	31,8

Bu çalışmada Ne 28/1 ve Ne 30/1 iplik numaralarında %60-40 pamuk-viskon ve %50-50 pamuk-viskon karışım oranlarında vorteks eğirme sistemiyle üretilmiştir. İpliklerin düzgünsüzlük, ince yer, kalın yer, neps, tüylülük gibi kalite parametreleri USTER Tester ile 5 bobinden numune alınarak test edilmiş ve Tablo 3'te verilmiştir. Üretilen ipliklere 58°C'de 55 dakika fikse işlemi uygulanmıştır. Daha sonra, elde edilen fikseli ve fiksesiz iplik numunelerinin mukavemet ve kopma uzaması özellikleri USTER Tensojet ile test edilmiş ve Tablo 4'te verilmiştir.

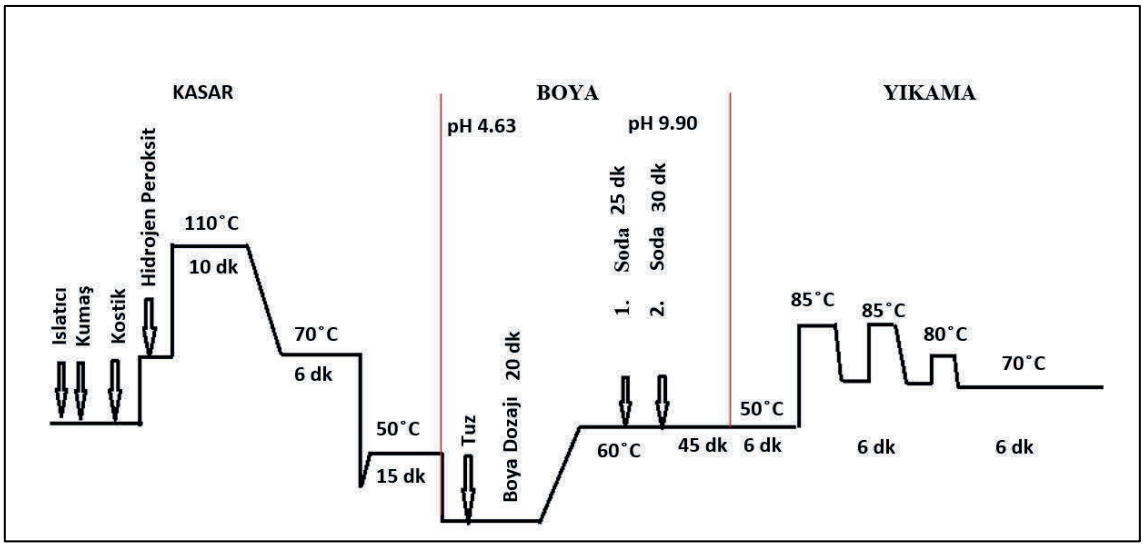
Tablo 3. İplik kalite parametreleri

	U%	**CVm %**	**İnce -50% /km**	**Kalın +50% /km**	**Neps +280% km**	**H**
Ne 28/1 %50-50 pam-vis	10,05	12,66	3,5	20,5	3,5	3,55
Ne 28/1 %60-40 pam-vis	10,32	13,06	3,5	27,5	3,0	3,41
Ne 30/1 %60-40 pam-vis	11,07	13,98	16,0	49,6	7,0	3,37

Tablo 4. Fikseli ve fiksesiz ipliklerin mukavemet ve uzama değerleri

		Mukavemet, cN/tex	**Uzama, %**
Fiksesiz	Ne 28/1 %50-50 pam-vis	13,44	6,17
	Ne 28/1 %60-40 pam-vis	13,03	5,90
	Ne 30/1 %60-40 pam-vis	12,99	5,54
Fikseli	Ne 28/1 %50-50 pam-vis	13,01	6,70
	Ne 28/1 %60-40 pam-vis	13,20	5,99
	Ne 30/1 %60-40 pam-vis	12,81	6,25

Fikseli ve fiksesiz olarak elde edilen ipliklerden daha sonra, 32 pus ve 28 fein süprem yuvarlak örme makinesi ile örme kumaş numuneleri üretilmiştir. Daha sonra elde edilen kumaş numunelerine, Şekil 1'de verilen işlem aşamalarına uygun olarak, ağartma, boyama ve yıkama uygulanmıştır.



Şekil 1. Numunelere uygulanan ağartma, boyama ve yıkama işlemleri

Test ve ölçümlerden önce tüm kumaş numuneleri TS EN ISO 139'a [7] göre şartlandırılmıştır. Testler, 20±2℃ sıcaklık ve %65±4 bağıl nem standart atmosferinde gerçekleştirilmiştir. Kumaş yapısal parametreleri olarak; kumaş gramajı, ilmek yoğunluğu ve ilmek uzunluğu özellikleri sırasıyla TS EN 12127 [8], TS EN 14971 [9] ve TS EN 14970 [10] standartlarına göre belirlenmiş ve Tablo 5'te verilmiştir.

Tablo 5. Üretilen kumaş numunelerinin yapısal parametreleri

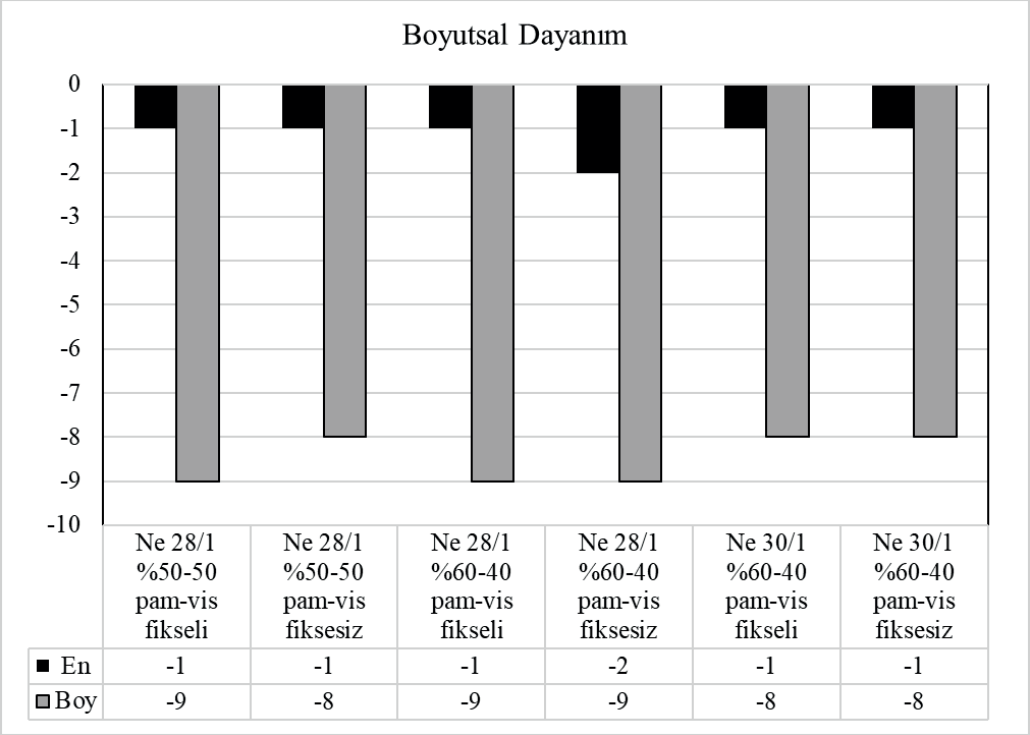
Numune		Kumaş gramajı (g/m^2)	Çubuk sayısı (adet/cm)	İlmek sayısı (adet/cm)	İlmek iplik uzunluğu LFA(cm)
Fiksesiz	Ne 28/1 %50-50 pam-vis	169	14	21	0,29
	Ne 28/1 %60-40 pam-vis	168	14	22	0,29
	Ne 30/1 %60-40 pam-vis	162	14	23	0,28
Fikseli	Ne 28/1 %50-50 pam-vis	170	13	22	0,29
	Ne 28/1 %60-40 pam-vis	160	14	19	0,29
	Ne 30/1 %60-40 pam-vis	160	14	23	0,28

Elde edilen kumaşların ev tipi yıkama sonrası boyutsal dayanım performansı TS EN ISO 6330 [11] standardına göre ve çarpılma performansı AATCC 179 [12] standardına göre belirlenmiştir. Ayrıca numunelerin patlama mukavemeti ve boncuklanma direnci sırasıyla TS EN ISO 13938-2 [13] ve TS EN ISO 12945-2 [14] standartlarına göre test edilmiştir.

3. Bulgular ve Tartışma

3.1. Yıkama Sonrası Boyutsal Dayanım

Elde edilen kumaş numunelerinin boyutsal dayanımları Şekil 2'de verilmiştir.



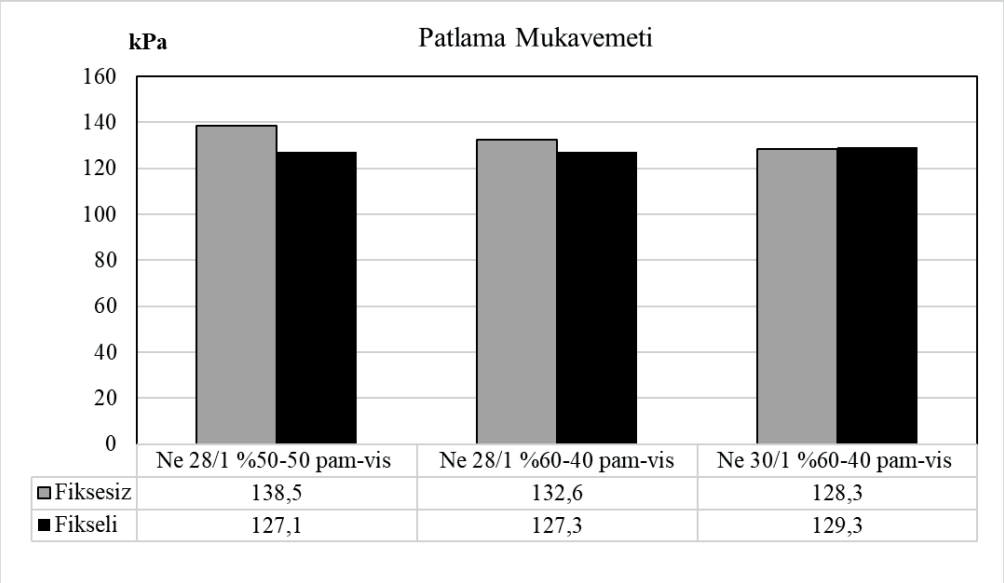
	Ne 28/1 %50-50 pam-vis fikseli	Ne 28/1 %50-50 pam-vis fiksesiz	Ne 28/1 %60-40 pam-vis fikseli	Ne 28/1 %60-40 pam-vis fiksesiz	Ne 30/1 %60-40 pam-vis fikseli	Ne 30/1 %60-40 pam-vis fiksesiz
■ En	-1	-1	-1	-2	-1	-1
▨ Boy	-9	-8	-9	-9	-8	-8

Şekil 2. Kumaş numunelerinin boyutsal dayanım değerleri

Şekil 2'de görüldüğü gibi tüm numunelerde görülen boyutsal değişim çekme şeklindedir. Diğer yandan, tüm numunelerde en yönündeki çekme, boy yönündeki çekmeden oldukça düşüktür. Ancak numunelerde, karışım oranının değişmesi ve fikse işleminin uygulanmasına bağlı olarak boyutsal dayanım değerlerinde önemli bir değişiklik görülmemiştir. İlaveten, boyutsal dayanım numuneleri üzerinde yapılan çarpılma testi sonucunda, fikseli ve fiksesiz olarak üretilen tüm numuneler için çarpılma saptanmamıştır. Diğer bir ifadeyle ipliğe uygulanan fikse işleminin boyutsal dayanımı iyileştirici bir etkisi saptanmamıştır.

3.2. Patlama Mukavemeti

Numunelerin patlama mukavemeti test sonuçları Şekil 3'te verilmiştir. Şekil 3'te verilen patlama mukavemeti değerleri incelendiğinde, numunelerde karışım oranı değişiminin ve fikse işlemi uygulamasının patlama mukavemeti üzerine belirgin bir etkisi olmadığı görülmektedir. Ne 28/1 %50-50 pam-vis ve Ne 28/1 %60-40 pam-vis numunelerde fikseli numunelerin patlama mukavemeti değerlerinde düşük miktarda azalma görülmesine rağmen Ne 30/1 %60-40 pam-vis numunede azalmaya rastlanmamıştır. Bu nedenle tutarlı bir değişim olmadığı görülmektedir.



Şekil 3. Kumaş numunelerine ait patlama mukavemeti değerleri

3.3. Boncuklanma Direnci

Numunelerin boncuklanma direnci değerleri Tablo 6'da verilmiştir. Numunelerin boncuklanma dayanımının değerlendirilmesinde Martindale test metodu kullanılmıştır. Nunumelerin boncuklanma dayanımı Martindale test cihazının 2000 devri sonrasındaki numunelerin görünümlerinin, ASTM standart görünümleri ile karşılaştırılması suretiyle değerlendirilmiştir.

Tablo 6. Kumaş numunelerine ait boncuklanma direnci değerleri

	Fiksesiz	**Fikseli**
Ne 28/1 %50-50 pam-vis	4	4
Ne 28/1 %60-40 pam-vis	4	4
Ne 30/1 %60-40 pam-vis	4	4

Numune kumaşlara uygulanan boncuklanma dayanımı testi sonucunda tüm numunelerde az miktarda boncuklanma görülmüştür. İpliklere uygulanan fikse işleminin ve karışım oranı değişiminin boncuklanma dayanımı üzerine herhangi bir etkisi saptanmamıştır. Fikse işleminin boncuklanma dayanımı üzerinde bir iyileştirme etkisi olmamıştır.

3.4. Renk Haslığı

Numunelerin renk haslığı değerleri Tablo 7'de verilmiştir.

Tablo 7. Nunumelere ait renk haslığı değerleri

	Ter Haslığı (Asidik)	**Ter Haslığı (Alkali)**	**Su Haslığı**	**Kuru sürtme haslığı**	**Yaş sürtme haslığı**
Ne 28/1 %50-50 pam-vis fikseli	4/5	4/5	4/5	4/5	4
Ne 28/1 %50-50 pam-vis fiksesiz	4/5	4/5	4/5	4/5	3/4
Ne 28/1 %60-40 pam-vis fikseli	4/5	4/5	4/5	4/5	3/4
Ne 28/1 %60-40 pam-vis fiksesiz	4/5	4/5	4/5	4/5	4
Ne 30/1 %60-40 pam-vis fikseli	4/5	4/5	4/5	4/5	4
Ne 30/1 %60-40 pam-vis fiksesiz	4/5	4/5	4/5	4/5	3/4

Numunelere uygulanan haslık testleri incelendiğinde, numunelere bilinen ve sıklıkla kullanılan haslık testlerinin tamamının yapıldığı görülmektedir. Haslık test sonuçları incelendiğinde, numunelerin yaş sürtme haslığı testi dışında herhangi bir farklılık göstermediği görülmektedir. Yaş sürtme haslığı testlerinde ise görülen değişimin çok az bir farklılık olmasının yanı sıra fikse işlemi açısından tutarlı bir etkinin olmadığı saptanmıştır. Diğer bir ifadeyle, fikse işleminin üretilen kumaşların renk haslığı değerleri açısından bir iyileştirme etkisi görülmemiştir.

4. Değerlendirme

Bu çalışmada, Vorteks eğirme sisteminde üretilen ipliklere uygulanan fikse işleminin iplik mukavemeti, iplik kopma uzaması ve örme kumaş performans parametrelerine etkilerinin araştırılması amaçlanmıştır. Çalışma sonucunda uygulanan fikse işleminin iplik mukavemeti üzerinde önemli bir değişikliğe sebep olmadığı ancak fikse işlemi uygulanan ipliklerin kopma uzamasında ise az miktarda artış olduğu görülmüştür. Kumaş performans özellikleri açısından; fikse işleminin patlama mukavemetinde bazı numunelerde önemsiz miktarda artışa sebep olduğu tespit edilmiştir. Ev tipi yıkama sonrası boyutsal dayanım ve dönme, boncuklanma dayanımı, renk haslığı değerlerinde fikse işleminden kaynaklanan bir etki görülmemiştir. Elde edilen sonuçlar, fikse işleminin Vorteks eğirme sisteminde üretilen pamuk-viskon karışımlı iplikler için, örme kumaş performansında bir iyileşmeye neden olmadığını göstermektedir. Çalışma kapsamında kullanılan Vorteks iplik eğirme teknolojisinin büküm yapısı düşünüldüğünde, büküm açılması eğiliminin Ring iplik eğirme teknolojisi ile üretilenlere nazaran düşük olabileceği bilinmektedir. Ancak elde edilen sonuçlara rağmen, fikse işleminin örme kumaş üretimi esnasında sağladığı faydalar unutulmamalıdır. Fikse işlemi, ipliğin bükümünü sabitleyerek bobin üzerindeki ipliğin kolay sağılmasını ve örgü makinesine daha düzgün bir akışla beslenmesi sağlar ve daha efektif bir kumaş üretimi sağlamaktadır. İlaveten, fikse işlemi örme kumaş üretiminde ipliğin kendi üzerinde kıvrılmasını engelleyerek, hatalı kumaş üretiminin engellenmesine de yardımcı olur.

Kullanılan lif karışımındaki pamuk ve viskon lif tiplerinin, polimer yapısındaki amorf/kristalin bölge oranı farklılığına bağlı olarak, nem miktarının artması sonrasındaki mukavemet durumları düşünüldüğünde, fikse işlem parametrelerinin bu harman özelinde çok hassas bir şekilde ayarlanarak optimize edilmesi gerektiği düşünülmektedir. Bu bağlamda, sonraki çalışmalarda, farklı sıcaklık ve süre şartlarında uygulanan fikse işlemlerinin pamuk-viskon karışımlı ipliklerde ipliğin nem miktarındaki değişime etkisi detaylı bir şekilde araştırılarak, iplik ve kumaş performansına etkilerinin incelenmesi faydalı olacaktır.

Kaynaklar

1. Çelik, P., Kadoğlu, H. "A Research on Yarn Liveliness Tendency of Staple Yarns", TEKSTİL ve KONFEKSİYON , 3/2009, **2009,**189-196.
2. Şardağ, S., Özdemir, Ö. (2013) Effects of Vacuum Steaming Process on the Twist Liveliness of Staple Yarns, FIBRES & TEXTILES in Eastern Europe, **2013,** 21, 5(101): 49-53.
3. Şardağ, S., Özdemir, Ö., Kanık, M. The Effects of Vacuum Steaming Process Parameters on Tenacity Properties of Cotton and Viscose Yarns, TEKSTiL ve KONFEKSlYON, 4/2011,2011, 343-348.
4. Şardağ, S., Özdemir, Ö.Effects of vacuum steaming processes on the properties of continuous and staple polyester yarns, Textile Research Journal 2015**, 2015**,Vol. 85(12) 1247–1257.
5. Nabi K.A., Nafis, A., Ramij, H. Comparison of Several Cotton Yarn Properties before and after Conditioning International Journal of Textile Science 2017,**2017**, 6(3): 88-91..
6. Çeven, E.K., Özdemir, Ö. The Effect of Vacuum Steaming Parameters on the Physical Properties of Chenille Yarns, FIBRES & TEXTILES in Eastern Europe April/June 2008,**2008**, Vol. 16, No. 2 (67), 35-40.

7. TS EN ISO 139: Textiles-Standard atmospheres for conditioning and testing ,**2008**.
8. TS EN 12127: Textiles- Fabrics - Determination of mass per unit area using small samples,**1999**.
9. TS EN 14971:Textiles - Knitted fabrics - Determination of number of stitches per unit length and unit area, **2006**.
10. TS EN 14970:Textiles – Knitted fabrics - Determination of stitch length and yarn linear density in weft knitted fabrics,**2006**.
11. TS EN ISO 6330 Tekstil- Tekstil deneyleri için- Ev tipi çamaşır makinesi ile yıkama ve kurutma işlemleri
12. AATCC 179 Skewness Change in Fabric and Garment Twist Resulting from Automatic Home Laundering
13. TS EN ISO 13938-2:2003 Textiles- Bursting properties of fabrics- Part 2: Pneumatic method for determination of bursting strength and bursting distension.
14. TS EN ISO 12945-2 Tekstil - Kumaşlarda yüzey boncuklanması, tüylenmesi ve matlaşması yatkınlığının tayini - Bölüm 2: Geliştirilmiş Martindale metodu

RETROFITTING OF RC STRUCTURES USING NEAR SURFACE MOUNTED FRP

KHALED HAFAR JONEIDI[1*]

[1]Sanaa university, Engineering Faculty, Civil engineer department, Sanaa, Yemen,
[*]khahaff@gmail.com

Abstract

Reinforced concrete is considered as the most widely used material for various types of constructions worldwide, it has many advantages including high strength, ability to cast in place, durability and many other advantages, But too many RC constructions reached its life time and many others damaged by different natural disasters ,led to the need of strengthening of these buildings, this paper studies retrofitting of RC members using near surface mounting technique (NSM) with FRP bars, describing materials ,the whole procedure, the failure modes that accompanies this method of retrofitting and In particular, the factors affecting the strength of the retrofitted element.

Keyword: NSM, FRP, Shear, Rehabilitation, Retrofitting.

1. Introduction

Strengthening may be achieved by retrofitting of RC elements using different methods and techniques giving the ability to extend the life time of old buildings or to upgrade the design loads of structures need to be used for different usage to a higher values , many techniques were adopted for this purpose and varied during time according to the technologies and materials manufacturing within each period, example of these materials is “Steel” since it’s already one of the components of RC, many methods were developed for using steel in retrofitting of RC elements, Later new materials with higher properties arised ,”FRP” is an example of these new materials and the assessment of these materials is considered as one of the important subjects of new researches, the decision of retrofitting a structure and selecting the best technology is mainly affected by the economic feasibility since that the replacement of a structure is in some cases more feasible than strengthening it if no economical option is available.

Most of retrofitting methods can be classified under one of two classifications : Externally bonded retrofitting (EBR) and Near surface mounted (NSM), different materials can be used for each one of these types, some of these materials were tested and came in to service and some are still under studying and testing by researchers worldwide, (Steel plates, Steel bars, Fiber reinforced mat, Mesh-Epoxy, FRP) are example of these materials that can be used for EBR or NSM or for both techniques [1], FRP is found to be as one of the most effective material for retrofitting which firstly used with EBR technique for column and beam jacketing, but since that full jacketing of already built elements cannot be achieved to provide full bond between FRP and the retrofitted element a new method for attaching FRP was invented, this method (NSM) will be explained in detail in the next section.

2. Materials and Methods

2.1 Near surface mounting technology

NSM can be defined as the application of reinforcement within the surface area of the strengthened element, this installation requires opening grooves in different shapes, adding adhesive of a special type to insure bonding between concrete and reinforcement, Early use of NSM technology was in Europe in 1948, a bridge in Sweden was to be upgraded in its negative moment region due to settlement, grooves were made in concrete surface then steel bars inserted, cement mortar was injected to fill the grooves and achieve bonding between steel bars and concrete, later, steel was replaced by FRP since that the latest is resistant to corrosion and has higher yielding strength in a great difference.

NSM technique has many advantages over other techniques, better strain distribution achieving improved efficacy, better resistance to environmental effects due to embedment of reinforcement bars or strips in to concrete cover, increased anchorage capacity caused by larger bond surface resulting in better resistance against peeling-off, also less time consuming since it needs no preparation work other than grooving, Experiments showed also improved ductility [2].

2.1.1 Procedure for NSM

The whole procedure can be described as follow, after specifying the targeted area the surface is cleaned and prepared, rectangular grooves is opened using cutter with saw blade in straight lines, air blower can be used to clean inside the grooves, then it's half-filled with filler (adhesive material), bars then installed inside and adhesive material is filled so it surrounds the bar and fill the groove totally and then surfaced to the element's surface level,(figure 1).

The following section, the main three elements of NSM procedure (FRP reinforcement, groove and adhesive (epoxy or groove filler)) will be explained in detail.



Figure 1. – Near surface mounting of reinforcing bars [3]

2.1.1.1 FRP reinforcement

It is a kind of composite material that is compound of Fiber Reinforced Polymers that is manufactured in many shapes like films, Strips and bars , it has a high stress capacity and linear elastic behavior, many types of FRP are available today, some are sensitive to moisture and some

do not absorb water but all FRP types are high strength compared to many other materials, the sensitivity to moister and heat can be overcome by using the suitable filler surrounding the FRP when attached to grooves, another advantage is its light weight compared to its strength , The strength and elasticity of FRP is affected by its shape, dimensions and chemical composition, it's produced in many shapes: Sheets, fabrics, grids, ropes and bars, Mainly there are 3 common types of fibers: Carbon, Glass and Aramid, the main difference between the three types are stiffness and tensile stress, giving them different properties including price and usage purpose, as shown in figure(2) all types of fibers have greater strength than steel and have elastic behavior until failure [4] figure (2) Stress-strain diagram for different materials [4].

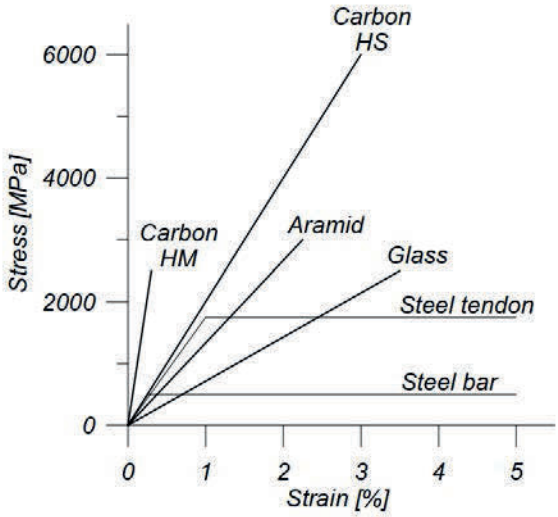


Figure 2. Stress-strain diagram for different materials [4]

2.1.1.2. Groove (properties and preparation)

The dimension, width to height ratio of the groove, distance between grooves and the distance between the groove and the edge of the element are of great effect on bond behavior between FRP and concrete.

let k = b_g /d_b, Lorenzis et al.[5] suggested that for square grooves, k should be no less than 1.5 for smooth bars or 2 for deformed bars, Parretti and Nanni [6] suggested that minimum value of both b_g and h_g is 1.5d_b

For NSM strips, Blaschko [7] suggested that the dimension of the groove in each direction should be about 3 mm larger than the corresponding FRP strip to achieve an adhesive layer thickness of about 1–2 mm. in general studied showed that increasing the groove width can increase the bond strength in a small ratio if adhesive is used, some studies showed that using cement as groove filler can decrease the bond strength if groove width is increased [2]. The surface of the bars is the first surface responsible to transfer the stresses between bars and adhesive, the second surface is the groove surface that is responsible to transfer the stresses between adhesive and concrete, for this reason the groove surface preparation is of great important to insure maximum stress transfer, grooves are usually created by cutting two adjacent saw cuts using saw blades then the concrete between the two cuts can removed by a hummer leading to form a groove with two smooth sides and a rough bottom, these surfaces should be cleaned carefully using compressed air to insure

removing all the dust formed during grooving, this dust can form a separation layer between concrete and the adhesive causing the bars to slip, roughness of the surface is important too, studies showed that smoothing the surfaces can reduce the bond slip strength between concrete and adhesive [8].

2.1.1.3 Groove filler

Groove filler, adhesive or matrix are all refer to the substance used to fill the groove and surround the strengthening bars attached in NSM technology, filler has a great effect to the final strength of the strengthened element since it has the roll of transferring stress between reinforcing bars and concrete, filler also has a great importance of protecting the reinforcing bars since it surrounds the bars from all sides providing a kind of isolation against heat and moisture, it is well known that failure always occurs in the weakest point exposed to stress and filler should be studied well since it is a part of the stress chain.

Cement mortar was the first to use while strengthening the bridge in Sweden in 1948, cement has a lower cost and higher heat resistance compared to other materials like epoxy but unfortunately it's low tensile strength and durability make it unfavorable choice for filling groove in NSM, Täljsten et al. [9]Performed a study to investigate the effectiveness of cement paste as a groove filler in an attempt to lower the cost and to have better results with high temperatures summarizing that cement paste has some limitations regarding it's tensile strength and durability to be used as groove filler, Soliman et al.[10] tested specimens with cement based filler and stated that the failure mode for these specimens is splitting of concrete-cement interface and showed failure load of about 40-56% of that filled with epoxy adhesive.

Vinyl ester and Epoxy are the most common used adhesives, Epoxy is preferred over Vinyl ester but more costly [4], De Lorenzis and Teng [11] suggested that the best performing adhesive is the two component epoxy with the option of using the low viscosity epoxy for negative moment regions since it can be poured easily and the high viscosity one for the positive moment region to avoid dripping.

The modulus of Elasticity of the Epoxy is of great effect on bond and slip behavior of the strengthened element, tests performed by Rizzo and De Lorenzis [12] showed that using an Epoxy with higher strength and stiffness causes lower FRP contribution to the shear capacity of the strengthened element, since that lower stiffness leads to a better stress distribution to the bond slip area between FRP bars and concrete.

Unlike concrete, epoxy showed a good creep behavior [13] concluded that instantaneous and time dependent properties of the tested adhesive can be observed as roughly constant (under constant temperature and humidity) if the applied stress levels are under 50% of the material's tensile strength.

A reduction in mechanical properties of Epoxy was observed in moist environments, Fernandes et al.[14] conducted environmental test to a number of specimens and observed the reduction in mechanical properties for specimens exposed to water, this reduction was due to water absorption of epoxy which causes plasticization leading to volume increase resulting to mechanical properties reduction, On the other hand a significant increase in mechanical properties was noted when the specimens exposed to cyclic temperature (from -15 to +60), the author indicated that the reason

for this increase is the post curing of epoxy achieved by the high temperature experienced after the initial temperature of first curing.
Cement mortar and epoxy are an example of the most famous materials used as fillers, new materials are being tested and some new others are being invented representing an attempt to enhance the bond behavior of NSM reinforcing material (Steel, aluminum, FRP….) to the surrounding concrete.

2.1.2. Failure modes of structural elements retrofitted with FRP using NSM:
Many different failure modes were recorded during tests of structural elements retrofitted with near surface mounted FRP, there are many factors affecting the failure mode like (FRP ratio, concrete strength, epoxy type….), defining the factor controlling the failure mode of each case is still an interested subject for researchers, common modes of failure are listed below:

Debonding Failure
Debonding can occur between FRP and the adhesive Figure (3a) or between the adhesive and the concrete Figure (3b), the FRP-adhesive failure can happen as interfacial failure that usually occurs due to smooth face of bars with insufficient development length that in term causes weak mechanical interlocking between bars and adhesive resulting in bar slipping, this type of failure can be identified by the absence of epoxy residuals on FRP surface, another type of FRP-adhesive failure is the shear failure of the adhesive or epoxy material happens when the shear strength is exceeded, this type can be identified too by the presence of epoxy residuals on FRP surface or on concrete surface or on both surfaces [15].

Adhesive(epoxy)-concrete failure is another type of debonding failure, the first type of this failure is the epoxy-concrete interface interfacial failure, this failure type can be critical for pre-cast grooves due to the smoothness of their surfaces, or For spirally wound bars or ribbed bars with low rib protrusions [11], the other type of adhesive (epoxy)-concrete failure is the cohesive shear failure in the concrete that usually happens with bending stresses within the strengthened region [11].

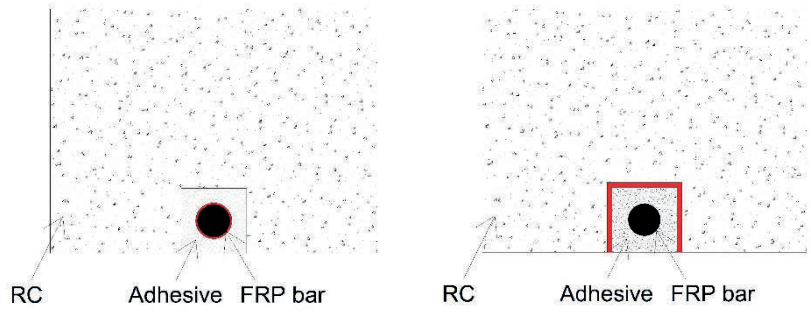


Figure 3. (a) FRP-adhesive failure region. (b) Adhesive-Concrete region.

Epoxy cover splitting
The radial component of the stresses causes this type of failure Figure (4), the surrounding concrete fails when it reaches maximum tensile strength due to these stresses applied by the epoxy cover, the mechanism of failure is similar to that one happens with steel bar internal reinforcement, but

the difference is that longitudinal steel bars benefit from the restraints of shear reinforcement which are not exist in case of NSM FRP retrofitting [11], there are two types of this failure, the first one happens when the splitting occurs only in epoxy cover and no visible cracks on concrete is exist, the second failure type happens with the presence of concrete cracks along the inclined planes of stresses, according to experiment's observations the angle of these cracks is about 30.

Edge splitting
This type of failure occurs when the bars are attached in close distance to the edge of the retrofitted element, minimum distance shall be provided to avoid such type of failure[15].

FRP rupture
This type of failure happens when FRP reaches its maximum tensile stress, it is usually occurring when FRP is prestressed [15].



Figure 4. Epoxy cover splitting [15]

2.1.3 NSM FRP strengthening application field:
During the time, FRP near surface mounting technique has proved its effectiveness for strengthening in different structural elements like beams, columns, slabs and even masonry walls [16][17], the strengthening involved flexure, shear and fewer studies were performed to increase the torsional resistance using this technique [18], unfortunately the precise evaluation of the FRP contribution has not achieved yet due to the many factors influencing this contribution, example of these factors will be discussed in the next section.

2.1.3.1 Factors affecting NSM FRP shear strengthening:
Figuring an equation describing FRP effect on shear strength of beams may pass through analytical derivation based on shear theories and bond equations or any other, these equations then compared to the results of experiments to check its reliability, another method is to obtain the equation from database of large number of experiments performed during the literature using regression-based models using statistic methods or artificial intelligence software , [19][20][21] are example of these methods.

H. Naderpour and S. A. Alavi [20] suggested the following factors affecting the contribution of FRP: ultimate tension strain of FRP, FRP effective depth, width of FRP, spacing steps of FRP strips, angle of inclination of FRP fibers, compressive strength of concrete, elastic modulus of

FRP, thickness of FRP layers, effective depth of the concrete beam and beam shear span length, the most affective parameter is the ultimate tension strain of FRP according to the study,
H. Baghi and J. A. O. Barros [21] suggested a design procedure then a sensitivity analysis was performed to check the effect of 17 input parameter figure (5), the most effective parameters found to be: shear percentage of steel stirrups, longitudinal steel reinforcement ratio, the yield stress of steel stirrups, the concrete compressive strength, ultimate tensile strength of FRP, and shear percentage of FRP.

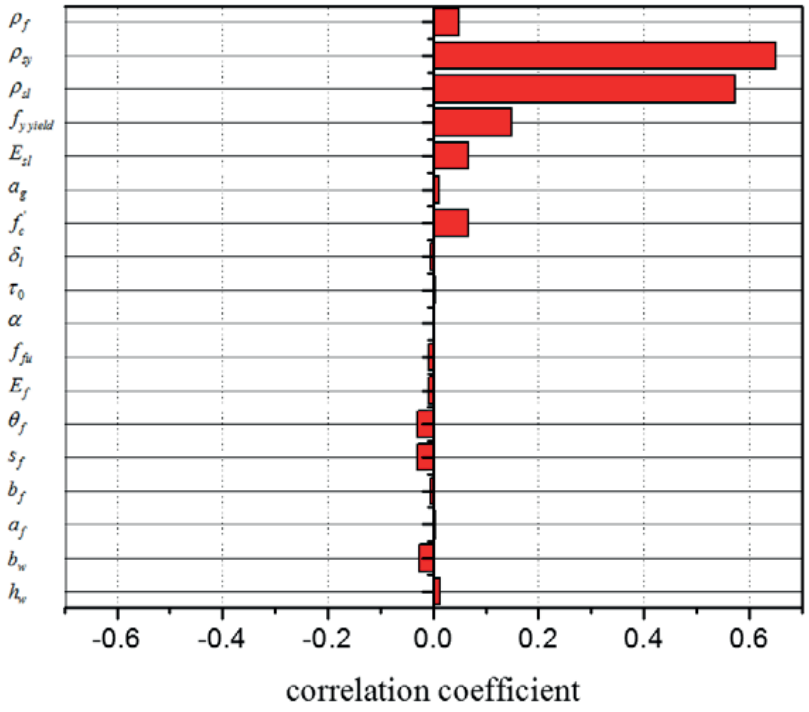


Figure 5. input parameters sensitivity analysis [21]

- Experiments showed the direct effect of some of these parameters:
  - angle of inclination of FRP fibers: results showed that 45^o inclined bars are more effective than vertical ones [22][23][24][2][25][26].
  - effective depth of the beam: the shear strength increases with the increase of beam depth [24].
  - longitudinal steel reinforcement ratio: it was also found that shear strength increases with the increase of longitudinal steel ratio due to dowl action [24].
  - compressive strength of concrete: effectiveness of FRP reinforcement increases with increase of Fc'[25][27][28].
  - shear percentage of steel stirrups: although the total shear capacity is increased with the increase of shear steel stirrups, the effectiveness of FRP contribution is reduced. [25][27][28].
  - spacing steps of FRP strips: increasing the spacing will decrease the ratio of FRP reinforcement which decreases the section shear strength capacity.
  - Until today the effect of parameters related to the FRP contribution is still investigated to reach the most accurate result.

3. Conclusions

Near surface mounting FRP retrofitting is an effective method for strengthening structural elements including beams, columns, slabs and masonry and for both flexure and shear strength. Application of this method do not require qualified labor or even special tools which can be considered as an advantage, on the other hand the estimation of the FRP contribution using this method is still a challenging subject.

References

1. Joseph, J. P.., Jose, A.., and Varghese,G. M., "Retrofitting of RC Beams: A Review," *Appl. Mech. Mater.*, **2016** ,vol. 857, pp. 206–211, doi: 10.4028/www.scientific.net/amm.857.206.
2. Parvin, A.., and Shah,T. Q.., "Near-surface mounted FRP reinforcement for structural strengthening," *Third Conf. Smart Monit. Assess. Rehabil. Civ. Struct.*, **2015,**vol. p., p. 8,
3. Thamrin,R.., Haris,S.., and Haris, Z.., "Shear strengthening of reinforced concrete beams with near surface mounted steel bars," *MATEC Web Conf.*, vol. 276, p. 01004, **2019**, doi: 10.1051/matecconf/201927601004.
4. Carolin,A.., *Carbon Fibre Reinforced Polymers for Strengthening of Structural Elements*, ,**2003** ,vol. 1992, no. 10.
5. De Lorenzis, L.., Nanni,A.., and La Tegola, A..,"Strengthening of Reinforced Concrete Structures with Near Surface Mounted FRP Rods," *ACI Struct. J.*, **2014** , vol. 1948, no.,pp.1–8,2000,[Online].Available: http://www.concrete.org/Publications/InternationalConcreteAbstractsPortal.aspx?m=details&i=11534.
6. Parretti, R.., and Nanni, A.., "Strengthening of RC members using near-surface mounted FRP composites: Design overview," *Adv. Struct. Eng.*, vol. 7, no. 6, pp. 469–483, 2004, doi: 10.1260/1369433042863198.
7. Blaschko, M.B.., "Bond Behavior of CFRP Strips Glued into Slits," **2003**.
8. Novidis, D.., and Pantazopoulou,S.., "Bond tests of short NSM-FRP and steel bar anchorages," *J. Compos. Constr.*, vol. 12, pp. 323–333, **2008**, doi: 10.1061/(ASCE)1090-0268(2008)12:3(323).
9. Täljsten, B.., Carolin, A.., and Nordin, H.., "Concrete Structures Strengthened with near Surface Mounted Reinforcement of CFRP," *Adv. Struct. Eng.*, vol. 6, no. 3, pp. 201–213, **2003**, doi: 10.1260/136943303322419223.
10. Soliman, S. M.., El-Salakawy, E..,and B. Benmokrane, "Bond Performance of Near-Surface-Mounted FRP Bars," *J. Compos. Constr.*, vol. 15, no. 1, pp. 103–111, **2011**, doi: 10.1061/(asce)cc.1943-5614.0000150.
11. De Lorenzis, L.., and Teng, J.G..,"Near-surface mounted FRP reinforcement: An emerging technique for strengthening structures," *Compos. Part B Eng.*, vol. 38, no. 2, pp. 119–143, 2007, doi: 10.1016/j.compositesb.2006.08.003.
12. Rizzo,A.., and De Lorenzis, L.., "Behavior and capacity of RC beams strengthened in shear with NSM FRP reinforcement," *Constr. Build. Mater.*, **2009**, vol. 23, no. 4, pp. 1555–1567, doi: 10.1016/j.conbuildmat.2007.08.014.
13. Costa,I.., and Barros, J..,"Creep of structural adhesives - An overview," *Proc. 6th Int. Conf. FRP Compos. Civ. Eng. CICE 2012*, pp. 1–8, **2012**.
14. Fernandes,P.., Sena-Cruz, J.., Xavier, J.., Silva, P.., Pereira, E.., and Cruz, J.., "Durability of bond in NSM CFRP-concrete systems under different environmental conditions," *Compos.PartBEng.*,**2017**,vol.138,no,pp.19–34,2018,doi: 10.1016/j.compositesb.2017.11.022.
15. Szabó , Z.K.., and Balázs, G.L..,"Near surface mounted FRP reinforcement for strengthening

of concrete structures," *Period. Polytech. Civ. Eng.*, **2007**, vol. 51, no. 1, pp. 33–38, doi: 10.3311/pp.ci.2007-1.05.
16. Behzard, P.., Sharbatdar, M.K.., and Kheyroddin, A..,"Strengthening of Existing RC Two-Way Slabs using New Combined FRP fabric/rod Technique," *J. Rehabil. Civ. Eng.*, **2015** ,vol. 3, no. 2, pp. 30–44, doi: 10.22075/jrce.2015.368.
17. Turco,V.., Secondin,S.., Morbin,A.., Valluzzi,M.R.., and Modena,C.., "Flexural and shear strengthening of un-reinforced masonry with FRP bars," *Compos. Sci. Technol.*, **2006**, vol. 66, no. 2, pp. 289–296, doi: 10.1016/j.compscitech.2005.04.042.
18. Al-Bayati,G.., Al-Mahaidi,R.., and Kalfat,R.., "Experimental investigation into the use of NSM FRP to increase the torsional resistance of RC beams using epoxy resins and cement-based adhesives," *Constr. Build. Mater.*,**2016**,vol.124,pp.1153–1164,doi: 10.1016/j.conbuildmat.2016.08.095.
19. Bianco,V.., Monti,G.., and Barros,J.A.O.., "Design formula to evaluate the NSM FRP strips shear strength contribution to a RC beam," *Compos. Part B Eng.*, vol. 56, pp. 960–971, **2014**, doi: 10.1016/j.compositesb.2013.09.001.
20. Naderpour,H.., and Alavi,S.A.., "A proposed model to estimate shear contribution of FRP in strengthened RC beams in terms of Adaptive Neuro-Fuzzy Inference System," *Compos. Struct.*, vol. 170, pp. 215–227, **2017**, doi: 10.1016/j.compstruct.2017.03.028.
21. Baghi ,H..,and Barros, J.A.O.., "Design Approach to Determine Shear Capacity of Reinforced Concrete Beams Shear Strengthened with NSM Systems," *J. Struct. Eng.*, vol. 143, no. 8, p. 04017061, **2017**, doi: 10.1061/(asce)st.1943-541x.0001793.
22. Cisneros,D.., Arteaga,A.., De Diego, A.., Alzate,A.., and Perera, R.., "Experimental study on NSM FRP shear retrofitting of RC beams," *Proc. 6th Int. Conf. FRP Compos. Civ. Eng. CICE 2012*, pp. 1–8, **2012.**
23. Al-Issawi ,A.S.H..,and Kamonna, H.K.., "Experimental study of RC deep beams strengthened by NSM steel bars," *Mater. Today Proc.*,**2020**, vol. 20, pp. 540–547, doi: 10.1016/j.matpr.2019.09.186.
24. Barros ,JA.O..,and Dias,S.J.E.., "Near surface mounted CFRP laminates for shear strengthening of concrete beams," *Cem. Concr. Compos.*, **2006** ,vol. 28, no. 3, pp. 276–292, doi: 10.1016/j.cemconcomp.2005.11.003.
25. Dias,S.J.E.., and Barros, J.A.O.., "NSM shear strengthening technique with CFRP laminates applied in high T cross section RC beams," *Compos. Part B Eng.*, **2017,** vol. 114, pp. 256–267, doi: 10.1016/j.compositesb.2017.01.028.
26. Dias, S.J.E.., and Barros,J.A.O.., "Performance of reinforced concrete T beams strengthened in shear with NSM CFRP laminates," *Eng. Struct.*, **2010** ,vol. 32, no. 2, pp. 373–384, doi: .10.1016/j.engstruct.2009.10.001.
27. Dias ,S.J.E..,and Barros,J.A.O.., "Shear strengthening of RC beams with NSM CFRP laminates: Experimental research and analytical formulation," *Compos. Struct.*, **2013** , vol. 99, pp. 477–490, doi: 10.1016/j.compstruct.2012.09.026.
28. Dias,S.J.E.., and Barros, J.A.O.., "Shear strengthening of RC T-section beams with low strength concrete using NSM CFRP laminates," *Cem. Concr. Compos.*, **2011**, vol. 33, no. 2, pp. 334–345, doi: 10.1016/j.cemconcomp.2010.10.002.

BROADBAND MICROWAVE TAPERED MICROSTRIP TRANSFORMERS DESIGN USING COGNITIVE SEEKER OPTIMIZATION ALGORITHM

UĞUR CEM HASAR[1], MONA ALFAQAWI [2]

[1] Gaziantep University, Engineering Faculty, Electric and Electronic Department, Gaziantep, Turkey.
[2] Gaziantep University, Engineering Faculty, Electric and Electronic Department, Gaziantep, Turkey

Abstract

This work applies a bio-inspired searching algorithm of Seeker Optimization Algorithm (SOA) for designing broadband microwave tapered microstrip lines that maximally match real load impedance to a transmission line in a pre-described range of frequencies. SOA algorithm has been verified to be very effective in finding the solutions for such multi-objective functions. Herein the design process aims to select the values of the matching impedances between real load and transmission line among a continuous range of values under tapering constraints. The obtained results have been verified and the design parameters have been calculated using the PUFF microwave simulator.

Keyword: Tapered Transmission line, matching, Optimization, Seeker Optimization Algorithm.

1. Introduction

Recently, near-optimal solutions for many complex engineering problems have been enabled using efficient computational algorithms. Hence, optimization techniques take their pivotal role in many raising electromagnetic problems. In particular, bioinspired search optimization algorithms have been successfully applied in constrained and unconstrained electromagnetic design problems, due to their ease of application, and robustness [1-7].

In this paper modified version from the SOA as we called cognitive Seeker Optimization Algorithm (CSOA) [8] has been used to find the design values of the tapered impedances among pre-defined continuous limited intervals. Under the constraint of the decreasing order from the load to the transmission line.

This paper is organized as follows: In section II we describe the CSOA algorithm and also present brief advantages over the other evolutionary-based algorithms when applied to various benchmark functions. In section III we formulate the design problem and the design constraints. In section IV optimization results have been presented and verified by the PUFF simulator, and finally, in section V, we conclude the work.

2. Materials and Methods

Optimization is the process of making something better [15]. In engineering, optimization consists of trying variations of parameters and using information gained in different iterations to get the best results, those best results (solution) are relative to the problem in hand, the solving method,

and the tolerance allowed. Search algorithms, and specifically bio-inspired search algorithms [16] seem to be superior in solving hard and complex optimization problems, particularly where the mathematical approaches stop and fail. Bio-inspired search algorithms imitate the nature strategies. The two most predominant and successful classes in bio-inspired search algorithms are the Evolutionary Algorithms (EA) and Swarm Intelligence (SI) based algorithms, which are inspired by the natural evolution and collective behavior in animals, respectively. In this work, we will compare the result of the SOA with a member from each class, Genetic Algorithm (GA)[17] which is one of the most successfully applied EAs, and the particle swarm optimization algorithm (PSO)[18] as an SI algorithm.

Seeker Optimization Algorithm (SOA), originally proposed by Dai et al. in 2006 [14] is a new promising technique for the real parameter optimization. SOA is based mainly on the concept of simulating the act of humans intelligent searching with their memory, experience, and uncertainty reasoning. SOA divides the set of solutions (search populations) randomly into K subpopulations with the same size; the individual of this population is called seeker or searcher, where all seekers in the same subpopulation constitute a neighborhood socially sharing the search information. After given start point, search direction, search radius (step length), and trust degree, every seeker moves to a new position (next solution) based on his social learning, cognitive learning, and uncertainty reasoning. SOA operates on a search population of s D-dimensional position vectors [19], which represent the solutions to the optimization problem at hand, i.e., $\overrightarrow{x_i} = [x_{i1}, \dots, x_{ij}, \dots, x_{iD}]$; $i = 1, 2, \dots, s$ where x_{ij} is the j^{th} element of $\vec{x}_i$ and s is the population size. The flow chart of the seeker optimization is shown in Figure 1. Firstly, it generates s positions uniformly and randomly in the search space, and calculates the fitness of each seeker, then calculates the search direction $dij(t)$ and the step length $\alpha_{ij}(t)$, for the i^{th} seeker at time step t. Then the j^{th} element of the i^{th} seeker is updated by [19]:

$$x_{ij}(t+1) = x_{ij}(t) + \alpha_{ij}(t) d_{ij}(t) \qquad (1)$$

To avoid converging to a local minimum, SOA uses an intersubpopulation strategy, i.e., the worst k-1 positions of each subpopulation are combined with the best position of each other k-1 subpopulations by the following crossover operator:

$$x_{k_n j,worst} = \begin{cases} x_{lj,best} & if\ R_j \le 0.5 \\ x_{k_n j,worst} & else \end{cases} \qquad (2)$$

Where R_j is a uniformly random real number in the interval [0,1], $x_{k_n j,worst}$ is the j^{th} element of the n^{th} worst position in the k^{th} subpopulation, $x_{lj,best}$ is the j^{th} element of the best position in the l^{th} subpopulation.

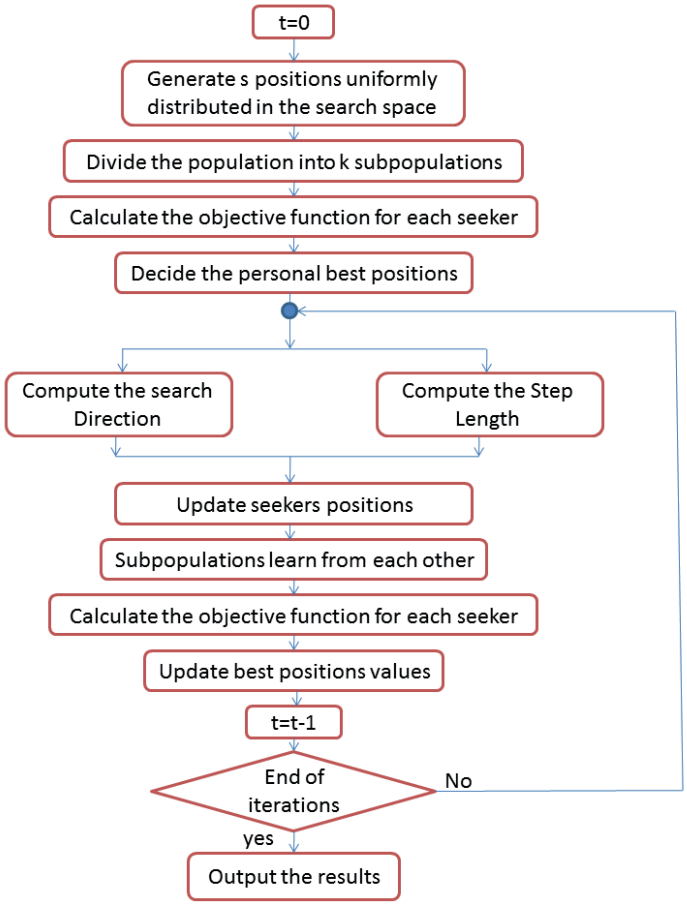


Fig. 1. SOA flow chart.

A. Search Direction

When the fitness function can't be differentiated, a so called empirical gradient can be used [20], by evaluating the response to increments and decrements in each direction. In this way, the seekers will lead their search. Search direction can be determined by the signum function of a better position minus a worse position, keeping in hand that the seekers must take into consideration their own current or historical positions and their neighbors' positions to determine their search direction. So, SOA models three different behaviors to determine search direction: egotistic, altruistic and proactive.

Egotistic, is an entirely proself behavior, in which each seeker i, as a single sophisticated agent, trying to direct toward his historical best position $\vec{p}_{i,best}(t)$ through cognitive learning [21]. Then, an empirical gradient from $\vec{x}_i(t)$ to $\vec{p}_{i,best}(t)$ can be adopted for the i^{th} seeker at time t, and thus each seeker i has an egotistic direction $d_{i,ego}(t) = [d_{i1,ego}, d_{i2,ego}, \dots, d_{iD,ego}]$ calculated as:

$$\vec{d}_{i,ego}(t) = sgn(\vec{p}_{i,best}(t) - \vec{x}_i(t)) \qquad (3)$$

On the other hand, based on their altruistic behavior, the neighboring seekers communicate with each other to adjust their behavior to achieve their goal, the neighbors' historical best position $\vec{g}_{best}(t)$ and the neighbors' current best position $\vec{l}_{best}(t)$ are used as the attraction signal source

of the self-organized aggregation behavior. Thus, each seeker i is associated with two altruistic directions, i.e., $\vec{d}_{i,alt1}(t)$, $\vec{d}_{i,alt2}(t)$

$$\vec{d}_{i,alt1}(t) = sgn(\vec{g}_{best}(t) - \vec{x}_i(t)) \quad (4)$$
$$\vec{d}_{i,alt2}(t) = sgn(\vec{l}_{best}(t) - \vec{x}_i(t)) \quad (5)$$

Moreover, seekers exploit the properties of pro-activeness; they are able to exhibit a goal-directed behavior [22]. Also, future behavior can be predicted and guided by past behavior [23]. As a result, each seeker will be proactive to vary his search direction and exhibit a goal-directed behavior according to his past behavior. Hence, any seeker i is associated with an empirical direction called proactiveness direction $\vec{d}_{i,pro}(t)$:

$$\vec{d}_{i,pro}(t) = sgn(\vec{x}_i(t_1) - \vec{x}_i(t_2)) \quad (6)$$

Where $t_1, t_2 \in t, t-1, t-2$ and $\vec{x}_i(t_1)$ is better than $\vec{x}_i(t_2)$. According to human rational judgment, the actual search direction of the i^{th} seeker, i.e., $d_i(t) = [d_{i1}, d_{i2}, \dots, d_{iD}]$ is based on a compromise among the aforementioned four empirical directions. In this work, the j^{th} element of $d_i(t)$ is selected by applying the following selection rule:

$$d_{ij}(t) = \begin{cases} 0 & if\ r_j \le p_j^{(0)} \\ +1 & if\ p_j^{(0)} < r_j \le p_j^{(0)} + p_j^{(1)} \\ -1 & if\ p_j^{(0)} + p_j^{(1)} < r_j \le 1 \end{cases} \quad (7)$$

$p_j^m, m \in (0,1,-1)$ is defined in the set $(d_{ij,ego}, d_{ij,alt1}, d_{ij,alt2}, d_{ij,pro})$ let $num^{(m)}$ is the number of "m" then $p_j^{(m)}/4$.

B. Step Length

Among the continuous space, there are often fitness points that are closer to the extremum point, such that the fitness values of the input variables are proportional to their distances from the extremum point, so the search must be intensified in regions with relatively good solutions [24]. Hence, from the standpoint of human searching, it could be believed that one may find near-optimal solutions in a narrower neighborhood of the point with lower fitness value and vice versa, less chance to find the optimum in a wider range far away from the points with higher fitness values. Fuzzy systems arose from the need to describe real complex systems by linguistic terms [25]. According to human focusing search aforementioned, the uncertainty reasoning of human searching can be described by natural linguistic variables and a simple control rule as *"If fitness value is small"* (i.e., the conditional part), then *"step length is short"* (i.e., the action part). The linguistic description of human search makes the fuzzy system a good candidate for simulating human focusing search behavior.

Optimization problems often have different ranges of fitness values. To design a fuzzy system that can be applicable to a wide range of optimization problems, the fitness values of all the seekers are firstly sorted in descending order and then turned into the sequence numbers from 1 to s as

inputs to a fuzzy reasoning system. A linear membership function is then used in the conditional part. The expression is presented as

$$\mu_i = \mu_{max} - \frac{s-I_i}{s-1}(\mu_{max} - \mu_{min}) \qquad (8)$$

Where I_i is the sequence number of $\vec{x}_i(t)$ after sorting the fitness values and μ_{max} is the maximum membership degree value that is equal to or little less than 1.0, in this work, $\mu_{max} = 0.95$. In the action part, the Bell membership function $\mu^{\alpha_{ij}^2/2\delta_j^2}$, $(i = 1, \ldots., s; j = 1, \ldots., D)$ is used for the j^{th} element of the i^{th} seekers step length. For the Bell function, the membership degree values of the input variables beyond $[-3\delta, 3\delta]$ are less than 0.0111[26]. Thus the minimum value $\mu_{min} = 0.0111$ is often used. Moreover the parameter δ_j of the Bell membership function is the j^{th} element of the vector $[\delta_1, \delta_2, \ldots, \delta_j]$, which is given by

$$\delta_j = \omega \,.\, abs(\vec{x}_{best} - \vec{x}_{rand}) \qquad (9)$$

Where abs() returns a vector in which each element is the absolute value of the corresponding element in the input vector. The parameter ω is used to decrease the step length with increasing time step such that it gradually improves the search precision. In this work, ω is linearly decreased from 0.9 to 0.1 during the run time. $\vec{x}_{best}, \vec{x}_{rand}$ are the best seeker and a randomly selected seeker in the same subpopulation to which the i^{th} seeker belongs (must differ from $\vec{x}_{best}$,), respectively. Then, the action part of the fuzzy reasoning system gives the j^{th} element of the i^{th} seeker's step length

$$\alpha_{ij} = \delta_j \sqrt{-\log(RAND(\mu_i - 1))} \qquad (10)$$

Where δ_j is the j^{th} element of vector δ in equation 9, RAND (μ_i, 1) returns a uniform random number within the range of [μ_i,1], which is used to improve local search capability.

3. PROBLEM FORMULATION AND DESIGN CONSTRAINTS

Matching circuits have been considered as an essential parts in microwave systems design. Basically impedance matching circuits are lossless circuit placed between a load impedance and a transmission line (Fig. 2) to avoid the unnecessary transmission losses when the load is mismatched from the line as well as to protect the generator from the effects caused by the reflected waves at the load and in some applications (such as antenna arrays) it is used to reduce amplitude and phase errors. Matching network is usually designed so that the impedance seen looking into the matching network is Z0 then the reflection will be eliminated on the transmission line to the left of the matching network. [17]. Matching Networks can be categorized into four main design shapes; Lumped elements, shunt stubs, series transmission lines and coupled transmission lines.

According to many different considerations different matching methods can be applied, the most important factors in selecting particular matching are the complexity, bandwidth, implementation and adjustability. Regarding the Bandwidth aspects; impedance matching network can be designed to be effective for specific frequency of operation (narrowband) or for a given frequency spectrum (broadband) [18]. In this work we will use the multi-section technique in tapered manner for enhancing the bandwidth of the quarter wave transformer. So that it can be considered as simplified combination between the multi-section and the tapered design. Bandwidth enhancement for the matching circuit has been considered in the literature using graphical techniques [19-21] or by

optimization techniques [22], [23]. The motivation of this work is to propose a simple and broadband matching circuit alternative to [24] where narrowband design has been considered. Using the tapered multisectiona impedances bandwidth will be enhanced in a given range of frequencies. Where the SOA optimization algorithm has been used to specify the values of the matching impedances values.

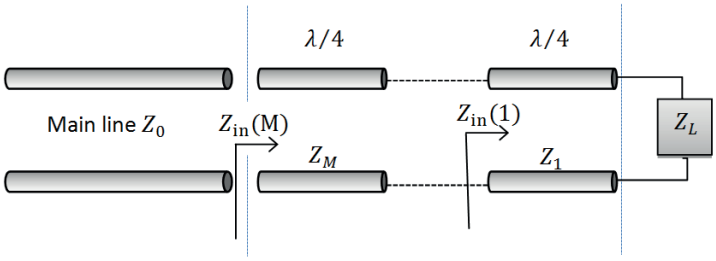


Fig. 4. Multi-section transformer model

In this work we will consider the tapering condition in designing the matching network, which means that successive impedances in the network will be increased from the line impedance up to the load impedance. Mathematically tapering can be described as: So, to minimize the reflection coefficient over the selected range of frequencies, the impedance seen looking into the matching network has to be as near as possible to Z0.

4. Conclusions:

In this work the PSO algorithm has been used to obtain the values of multi-sectional quarter wave transformer that match real load to transmission line in pre determined frequencies Two examples of three and of five segments has been considered, where it has been demonstrated that the five segment model works better due to the fact of the smother the transition between the impedances the better obtained response.

References

1. Cui, S., D. Weile, and J. Volakis, "Novel planar electromagnetic absorber designs using genetic algorithms," IEEE Trans. on Antennas and Propagation, **2006,** 54, 18111817.
2. Chammani S, Mirtabheri S, Shooredeli M,"Design of a very thin wide band absorbers using modified locaol best particle swarm optimization ". AEU-Int. J. Electron Commun **2008**, 62:549-556.
3. Goudos S., Zaharis ZD, Baltzis KB, Hilas CS, Sahalos JN, "A comparative study of a particle swarm optimization and differential evolution on radar absorbing materials design for EMC applications", Electromagnetic Compatibility-EMC Europe,**2009**.
4. Goudos S. "Design of microwave broadband absorbers using a selfadaptive differential evolution algorithm," Int. J.RF and Microwave CAE **2009.**
5. Jiang LY,Li XY, Zhang J."Design of high performance multilayer microwave absorbers using fast genetic algorithm", Science in china Series E-Technological Sciences, **2009,** 2749-2757.
6. Dib, N, Asi M, Sabbah M, "On the optimal design of multilayer microwave absorbers," Progress In Electromagnetics Research C, **2010,** 13, 171-185.
7. Jiang L, Cui J, Shi L, Li X, "Pareto optimal design of multilayer microwave absorbers for wide-angle incidence using genetic algorithms," IET Microwave Antennas Propagation, **2009**, 3, No. 4, 572-579.

8. K. Sridevi; A. J. Rani "Particle Swarm Optimization versus Genetic Algorithm for Adaptive Uniform Circular Array" Electric, Electronic, Signals, Communication and Optimization (EESCO), **2015**.
9. P. Tomasek; Y.V. Shestopalvo; V. Kresalek, "Comparison of selected evolutionary techniques used in reconstruction of permitivity" Electromagnetics in advance applications international conference (ICEAA), **2015**.
10. Kennedy J, Eberhart R, "Particle Swarm Optimization," Proceedings of IEEE International Conference on Neural Networks, **1995**, 1942-1948.
11. R. L. Haupt and S. E. Haupt, "Practical Genetic Algorithms," (2nd edition). Wiley**, 2004**.
12. S. Binitha and S. S. Sathya, "Survey of Bio Inspired Optimization Algorithm," International Journal of Soft Computing and Engineering, **2012**, 2, 137-151.
13. Y. Liu, Z. Gin, and Z. Shi, "Hybrid particle swarm optimizer with line search," in Proc. IEEE Int. Conf. Syst., Man, Cybern., **2004**, 3751-3755.
14. Yilmaz A. E., Kuzuoglu M."Calculation of Optimized Parameters of Rectangular Microstrip Patch Antenna Using Particle Swarm Optimization," Microwave Optical Technology Letters, **2007**, 49, 2905-2907.
15. J. Robinson and Y. Rahmat Samii. "Particle Swarm Optimization in electromagnetics," IEEE Trans Ant Propagat 52, **2004**, 397-407.
16. Yilmaz A. E., Kuzuoglu M. "Calculation of Optimized Parameters of Rectangular Microstrip Patch Antenna Using Particle Swarm Optimization," Microwave Optical Technology Letters, **2007**, 49, 2905-2907.
17. Pozar D. M. "Microwave Engineering," 3rd Edition, Wiley, New York, **2005**.
18. Khare R., Nema R. "Review of impedance Matching Networks for Bandwidth Enhancement," IJETAE, **2012**, 2.
19. Mhala M. M., Desai P. and Kumar G. "Broadband Impedance Matching Netowrk for RF Power Amplifiers," **2008.**
20. B. A. Munk "Finite Antenna Arrays and FSS," **2003**.
21. A. A. R. Townsend "The Smith Charts and Its Applications," **1995**.
22. Jianfie A., Kezhu S., Shuangxi Z., Junfeng Y. and Ping C. " Design of Broadband Electrical Impedance Matching Network for Piezoelectric Ultrasound Transducer Based on Genetic Algorithm," Sensors **2014**.
23. Rengoli C. "Impedance Matching by Using Multi-stub System," International conference on simulation, modeling and optimization, **2007**.
24. Ulker E. D.,Ulker S. " Application of Particil Swarm Optimization to Microwave Tapered Microstrip Lines,",CSEIJ, **2014**, 4, No. 1.
25. Wedge S. W., Compton R. C., Rutledge D. B., Gerstlauer A. PUFF: Computer Aided Design for Microwave Integrated Circuits, version 2.1, California Institute of Technology, Pasadena CA **1998**.

FARKLI ÖZELLİKLERE SAHİP 2605SA1 AMORF VE M27 ELEKTRİK ÇELİĞİ NÜVE MALZEMELERİ KULLANILAN ASENKRON MOTORLARIN VERİMLİLİKLERİNİN SONLU ELEMANLAR YÖNTEMİYLE ANALİZİ

NECİP FAZIL YILMAZ[*1, 2], MUHAMMET YUSUF DULKADİR[1], MAHMUT FURKAN KALKAN[1], MUSA YILMAZ[1]

[1]Gaziantep Üniversitesi, Mühendislik Fakültesi, Makine Mühendisliği Bölümü, Gaziantep, Türkiye
[2]Mütevelli Heyeti, Hasan Kalyoncu Üniversitesi, Gaziantep, 27410, Türkiye
*nfyilmaz@gantep.edu.tr

ÖZET

Asenkron motorlar endüstride sıklıkla tercih edilen elektrik motorlarıdır. Sanayide kullanılan elektrik enerjisinin büyük bir kısmı bu motorlar tarafından tüketilmektedir. Asenkron motorların artan kullanım oranı sonucunda tüketilen enerji miktarı artmaktadır. Yüksek verimlilikteki elektrik motorları enerji tüketimini azaltmaktadır. Asenkron motorlarda mekanik, bakır ve demir kayıpları olmak üzere üç temel kayıp bileşeni bulunmaktadır. Malzeme biliminin gelişimi ile stator ve rotor parçalarında alternatif manyetik nüve malzemeler kullanılmaktadır. Nüve malzemelerin manyetik ve elektriksel özellikleri demir kayıplarını doğrudan etkilemektedir. Bu çalışmada farklı malzeme özelliklerine sahip nüve malzemelerin 1,1 kW gücündeki asenkron motorların verimliliğine ve demir kayıplarına olan etkisini sonlu elemanlar yöntemi (SEY) ile araştırılmıştır. Nüve malzeme olarak M27 elektrik çelik sacı ve 2605SA1 amorf malzeme kullanılarak birbiri ile kıyaslanmıştır. Demir kayıpları açısından, M27 elektrik çeliğinin 2605SA1 amorf nüve malzemesinden yaklaşık olarak 5,5 kat fazla olduğu görülmüştür. M27 nüve malzemeli modelde bakır kayıpları da diğer modele göre daha fazla çıkmaktadır. Mekanik kayıp açısından, her iki nüve malzemeli modelde kayıplar birbiri ile çok yakın çıkmaktadır. Bu sonuçlar neticesinde asenkron motorda kullanılan 2605SA1 amorf nüve malzeme sayesinde verimlilik yaklaşık olarak %2,5 arttığı görülmektedir. Ayrıca, her iki asenkron motor modeli birbiri ile karşılaştırıldığında amorf nüve malzemeli modelde yaklaşık 1 kg ağırlık azalması sağlanmıştır.

Anahtar Kelimeler: Amorf Malzeme, Elektrik Çeliği, Asenkron Motor, Demir Kayıpları, Bakır Kayıpları

1. Giriş

Sincap kafesli asenkron motorlar, endüstride yaygın olarak tercih edilen bir motor türüdür [1,2]. Sincap kafesli asenkron motorlar ticari uygulamalarda kullanılan elektrik motorlarının %90'ından fazlasını temsil eder [3]. Mekanik bileşenlerdeki sürtünmeden kaynaklanan mekanik kayıplar, sargı direncinden kaynaklanan bakır kayıpları ve manyetik nüve malzemeden kaynaklanan demir kayıpları asenkron motorlardaki üç ana kayıp şeklidir [4]. Mekanik ve bakır kayıpları kapsamlı bir şekilde çalışılmış olmasına rağmen, demir kayıpları olgusunun anlaşılması henüz gerekli seviyeye ulaşmamıştır [5]. Ayrıca, rotor ve statordaki demir kayıpları sincap kafesli asenkron motor kayıplarının yaklaşık %25'ini oluşturur [6,7]. Bu nedenle asenkron motorların karakteristik performansını iyileştirmek için demir kayıplarını düşük bir seviyeye indirme çalışmaları yapılmaktadır [8].

Elektrik motorlarında birçok farklı alternatifte yumuşak manyetik malzeme kullanılmaktadır. Bunlardan bir tanesi de elektrik çelikleridir. Hali hazırdaki ticari uygulamalarda stator ve rotor nüve malzemesi olarak elektrik çeliği tercih edilmektedir. Silisyum takviyeli bu çeliklerde silisyum oranının arttırılması, yüksek verimli (düşük demir kayıplı) Si-Fe çeliğini geliştirmek için uygun bir tekniktir. Hou [9] lamine çeliklerde silikon oranının kayıp dağılımı ve manyetik geçirgenlik üzerindeki etkilerini araştırmıştır. Döküm külçelerinin silikon oranı ağırlıkça %0.21 ile %2.00 arasında değişim göstermektedir Silisyum içeriği ağırlıkça %2'ye ulaştığında demir kayıpları minimum ($P_{1.5/50}$ yaklaşık 4,2 W/kg) özellik sergilemektedir.

Son yıllarda elektrik çeliğinin yanı sıra amorf yapıdaki yumuşak manyetik malzemeler ön plana çıkmaktadır. Elektrik çeliğine kıyasla yüksek elektriksel özdirenç ve düşük zorlayıcı kuvvet gibi üstün özelliklere sahiptirler [10]. Yüksek elektriksel özdirenç sayesinde girdap akım kayıplarını azaltmada etkin rol oynamaktadırlar. Amorf manyetik malzemeler transformatör uygulamaları için başarıyla kullanılmaktadır. Tane yönelimli silikon çelik yerine amorf nüve malzeme kullanımı sayesinde yüksüz kayıpların %70'e kadar azaltılabileceği gözlemlenmektedir [5]. Ek olarak, amorf nüve malzemeler çok ince yapıda olup mekanik gerilimlere karşı hassastır [11]. Amorf nüve malzemeler yüksek mekanik sertliği nedeni ile zorlu bir üretim sürecine sahip olmaktadırlar. Bununla birlikte, amorf şerit üretimindeki teknolojik gelişmeler, daha yüksek laminasyon faktörü ile sonuçlanan yüzey kalitesinde iyileştirmelere izin vermektedir [12].

Bu neden ile amorf manyetik malzeme kullanılan birkaç çeşit elektrik motoru geliştirilmiştir. Çekirdek kayıpları motor hızıyla arttığından, amorf manyetik malzemeler, yüksek hızlı uygulamalar için geleneksel elektrikli çelik saclara göre önemli bir gelişme sağlayabilmektedir [13,14]. Ayrıca, mıknatısların maliyeti nispeten yüksek olduğundan, radyal alan anahtarlamalı relüktans motor için de amorf nüve kullanılmaktadır [15].

Bu çalışmada, asenkron elektrik motorlarında kullanılan farklı nüve malzemelerinin kayıp türlerine ve verimliliğe etkileri sonlu elemanlar yöntemi ile gözlemlenmiştir. Ansys-RMxprt modülünde asenkron motor modelleri oluşturulmuştur. Asenkron motorlarda M27 elektrik çeliği ve 2605SA1 amorf nüve malzeme kullanılmıştır. Sonlu elamanlar analiz sonucunda stator ve rotor kısmındaki bakır kayıpları araştırılarak, bunlara neden olan faz akımları değerlendirilmiştir. Bunun yanı sıra, demir kayıpları incelenmiş ve verimlilik değişimleri gözlemlenmiştir. Amorf nüve malzeme ve elektrik çelik malzemeden oluşturulan motor modelleri ağırlık bakımından karşılaştırılmıştır.

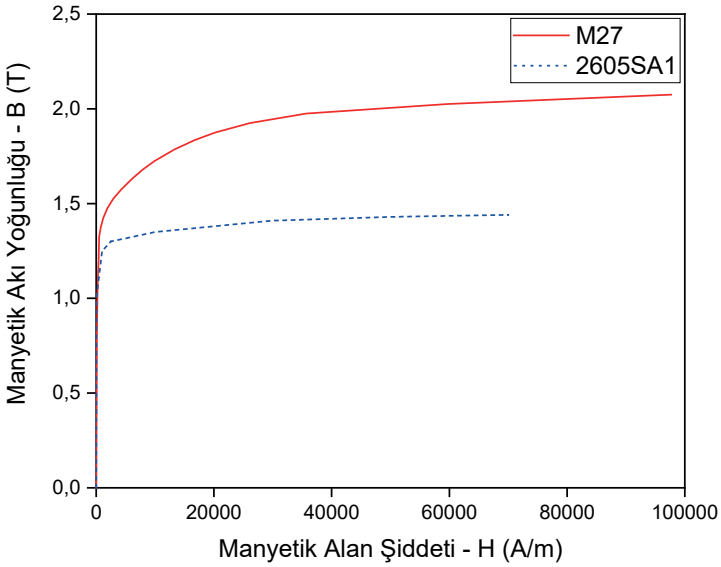
2. Nüve Malzeme

Bu çalışmada, asenkron motor modellerinde nüve malzeme seçiminde M27 elektrik çeliği ve 2605SA1 amorf malzeme kullanılmıştır. Nüve malzemelerin kimyasal kompozisyonları Tablo 1'de gösterilmektedir. Elektrik çeliğinde ana alaşım elementi olarak mangan, alüminyum ve silisyum kullanılarak demir elementi ile alaşım oluşturulmuştur. Amorf malzemede ise demir silisyum ve bor elementi ile alaşım oluşturmuştur.

Tablo 1. M27 ve 2605SA1 nüve malzemelerinin kimyasal bileşimi [14,16]

	Mn (%)	Si (%)	Al (%)	B (%)	Fe (%)
M27	0.25	2.6-3.0	0.12-0.20	-	96.5-97
2605SA1	-	13	-	9	78

Amorf nüve malzeme ve elektrik çeliğine ait manyetik akı yoğunluğu (B) - manyetik alan şiddeti (H) eğrisi Şekil 1'de gösterilmiştir. M27 elektrik çeliği manyetik doyma noktası 2T seviyesinde olmasına rağmen 2605SA1 amorf nüvenin manyetik doyum noktası 1.5T seviyesindedir. B-H eğrisindeki bu farklılık malzemelerin kimyasal kompozisyonundan kaynaklanmaktadır. Alaşım malzemesinde bulunan manyetik olmayan elementler malzemenin histerezis döngüsündeki doyum noktasını aşağı seviyelere düşürmektedir. Bu nedenden dolayı amorf nüve malzemeler elektrik çeliğine kıyasla daha düşük manyetik indüksiyonlarda performans gösterebilmektedirler.



Şekil 1. B-H eğrisi [17]

3. Sonlu Elemanlar Yöntemi (SEY)

Bu araştırmada, asenkron motorda kullanılan nüve malzemelerin etkilerini incelemek için Ansys-RMxprt yazılımı kullanılmıştır. Asenkron elektrik motoruna ait parametreler Tablo 2'de verilmiştir. Modellenen motor çıkış gücü 1.1 kW olarak seçilmiştir. Çalışma frekansı 50Hz olarak seçilmiştir. Asenkron motor modellerinde kullanılan nüve malzeme değiştirilerek sonlu elemanlar analizleri gerçekleştirilmiştir. Modellenen asenkron motor sanayide sıklıkla tercih edilen sincap kafesli asenkron motor olarak belirlenmiştir.

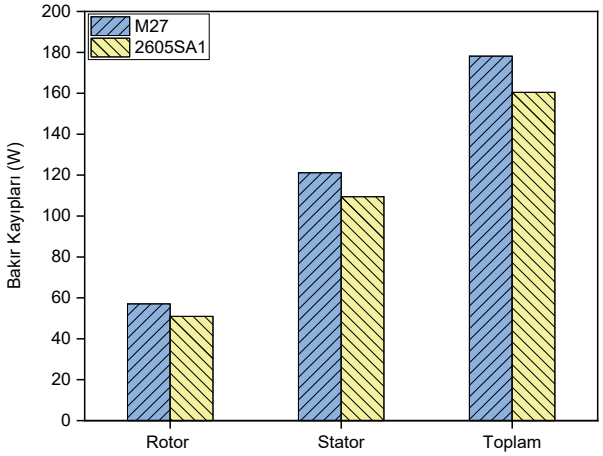
Tablo 2. Asenkron motor parametreleri [8]

			Stator	Rotor
Faz Sayısı	3			
Kutup Sayısı	2	Dış Çap (mm)	140	76
Çıkış Gücü (kW)	1.1	İç Çap (mm)	78	32
Voltaj (V)	400	Paket Boyu (mm)	250	250
Hız (d/dak)	1500	Slot Sayısı	36	28
Çalışma Sıcaklığı (°C)	75			
Frekans (Hz)	50			
Paketleme Faktörü	0.95			

4. Bulgular ve Tartışma

Bu çalışmada kullanılan asenkron motorun farklı nüve malzemelerinden kaynaklanan bakır kayıpları Şekil 3'de gösterilmektedir. M27 silisli sac nüve malzemeli asenkron motor modelinde stator kısmında gerçekleşen bakır kaybı 121 W ve rotor kısmında gerçekleşen bakır kaybı 57 W

olmaktadır. 2605SA1 amorf nüve malzemeli modelde ise bakır kayıpları stator ve rotor kısmında sırası ile 110 W ve 51 W olmaktadır. Sonuç olarak toplam bakır kayıpları M27 silisli sac modelinde yaklaşık olarak 17 W daha fazla olduğu görülmektedir. Sonlu elemanlar analizinde amorf nüve malzeme kullanımı bakır kayıplarını düşürücü bir etki göstermektedir.



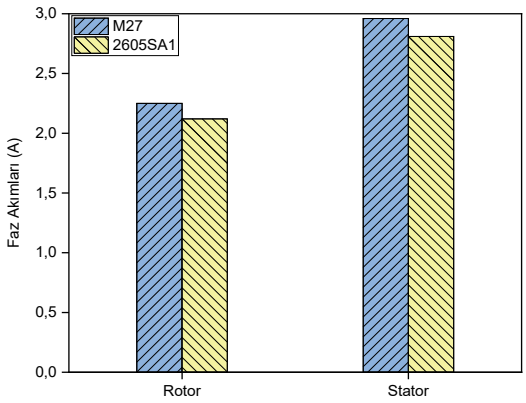
Şekil 3. Amorf malzeme ve elektrik çeliği bakır kayıpları karşılaştırması

Elektrik motorlarında bakır kayıpları (sargı ve direnç kayıpları) makinenin sargılarından kaynaklanır [4,18]. Temel olarak, bakır kayıpları Denklem 1 kullanılarak belirlenmektedir.

$$P_{Cu} = R_{phase} I^2 M_{\Phi} \quad (1)$$

P_{Cu} (W) bakır kayıplarını, R_{phase} (Ω) tek fazlı sargının direncini, I (A) sargının akım değerini ve M_{Φ} elektrik makinesinin faz numarasını temsil etmektedir.

Bakır kayıplarını belirleyici en önemli özellik stator ve rotor bileşenlerindeki faz akımıdır. Şekil 4'de görüldüğü gibi stator kısmındaki faz akımı M27 malzemeli modelde 2.96A değerinde iken amorf malzemeli modelde 2.81A seviyesindedir. Aynı şekilde rotor bileşendeki faz akımı M27 elektrik çelik modelinde daha yüksektir. M27 ve 2605SA1 manyetik malzemeli modellerde rotor faz akımları sırası ile 2.25A ve 2.12A olmaktadır. Bakır kayıplarının amorf malzemede düşük olmasının gerekçesi stator ve rotor faz akımlarının diğer motor modeline kıyasla daha düşük olmasından kaynaklanır.



Şekil 4. Stator ve rotor faz akımları

Asenkron motorlarda meydana gelen kayıp türlerinde, demir kayıpları üzerine araştırmalar yoğunluk göstermektedir. Demir kayıplarını hesaplamak için birkaç farklı analitik metot kullanılmaktadır. Bertotti [19] modeli demir kayıplarını histerezis, girdap akımı ve aşırı kayıpların bileşeni olarak tanımlamaktadır. Her üç kayıp türü manyetik akı yoğunluğunun genliğinden etkilenmektedir. Demir kayıpları Denklem 2 kullanılarak belirlenmektedir.

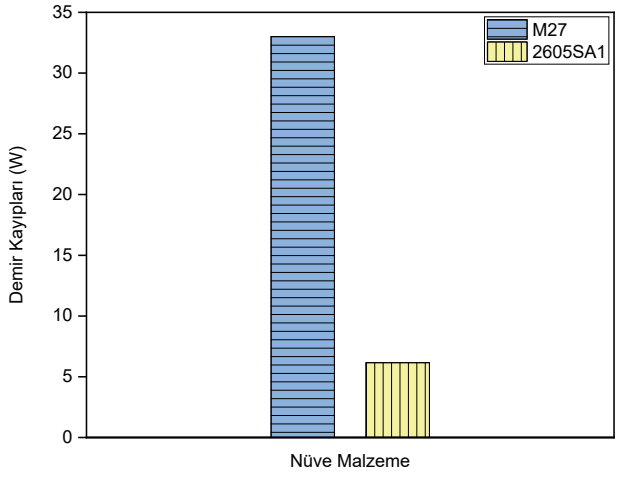
$$P_{Fe} = P_{hyst} + P_{ec} + P_{exc} = k_{hyst} f B^2 + k_{ec} f^2 B^2 + k_{exc} f^{1.5} B^{1.5} \quad (2)$$

P_{Fe} (W/m^3) toplam demir kaybını, P_{hyst} (W/m^3) histerezis kaybını ve P_{exc} (W/m^3) aşırı kayıpları belirtmektedir. F (Hz) frekans değerini ve B (T) manyetik akı yoğunluğunu tanımlamaktadır. Histerezis kaybı için k_{hyst} (W/m^3), girdap akım kaybı için k_{ec} (W/m^3) ve aşırı kayıplar için k_{exc} (W/m^3) katsayıları kullanılmaktadır. M27 elektrik çeliği ve 2605SA1 amorf malzemeye ait histerezis kayıplarının, girdap akımı kayıplarının ve aşırı kayıpların sabitleri Tablo 3'de gösterilmektedir.

Tablo 3. M27 ve 2605SA1 nüve malzeme kayıp sabitleri

	k_{hyst} (W/m^3)	k_{ec} (W/m^3)	k_{exc} (W/m^3)
M27	196.8	4.2×10^{-1}	0
2605SA1	0.44	7.9×10^{-5}	6.9

Şekil 5'de amorf nüve malzemeli ve elektrik çelik nüve malzemeli motor modellerindeki demir kayıpları sunulmuştur. M27 elektrik çeliğinde demir kayıpları 33 W olmaktadır. Ancak, amorf malzemeli modelde 6 W olduğu görülmektedir. Sonlu elemanlar analizlerine göre asenkron motor modelinde, amorf nüve malzeme kullanımı ile demir kayıpları %82 oranında azaldığı gözlemlenmektedir.



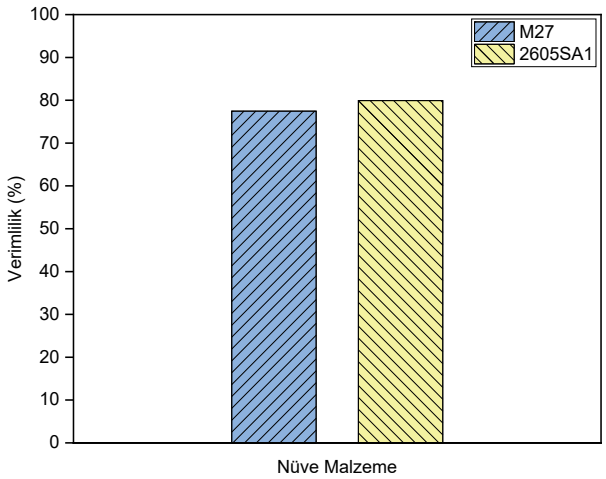
Şekil 5. M27 ve 2605SA1 nüve malzemeleri demir kayıpları

Elektrik motorları elektrik enerjisini mekanik enerji dönüştüren makinelerdir. Bu dönüşüm sırasında enerji kayıpları meydana gelmektedir. Ortaya çıkan bu kayıplar sonucunda verimlilik hesaplanmaktadır. Denklem 3'de gösterildiği gibi mekanik gücün (çıkış gücü) elektrik gücüne (giriş gücü) oranı elektrik motor verimliliğini belirlemektedir.

$$\eta\ (\%) = \frac{P_{mekanik}}{P_{elektrik}} x100 = \frac{P_{mekanik}}{P_{mekanik} + P_{kayıplar}} x100 \quad (3)$$

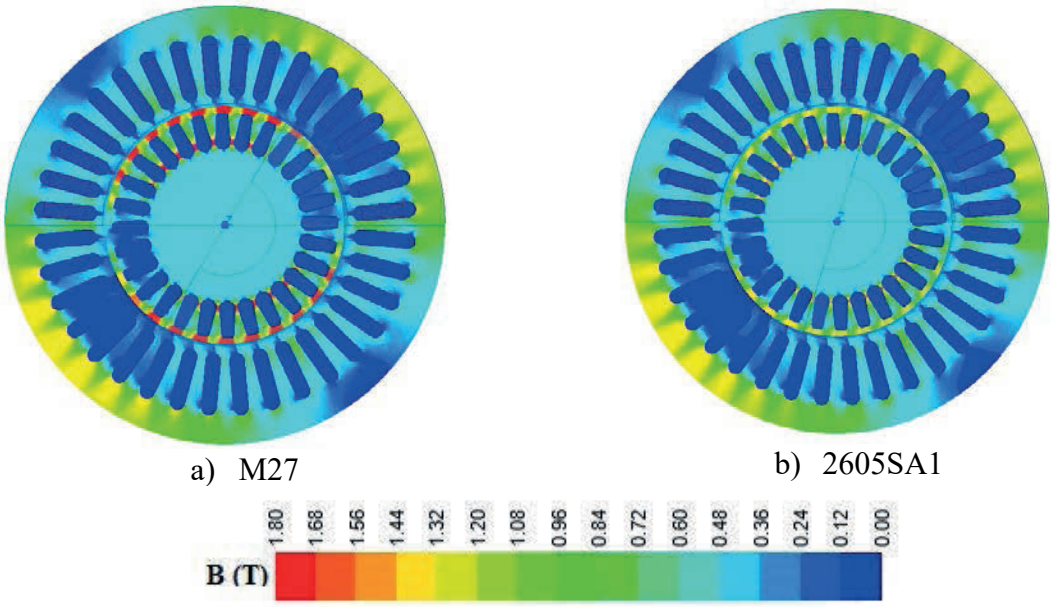
η (%) elektrik motor verimliliğini, $P_{mekanik}$ (W) çıkış gücünü, $P_{elektrik}$ (W) giriş gücünü, $P_{kayıplar}$ (W) kayıpları ifade etmektedir.

M27 malzemeli asenkron motor modelinde elektrik gücü (giriş gücü) 1419.7 W iken 2605SA1 amorf malzemeli modelde elektrik gücü (giriş gücü) 1376.4 W olmaktadır. Sonlu elemanlar analizlerine göre M27 malzemeli asenkron motorda bakır kayıpları 17 W fazla olmaktadır. Ancak demir kayıplarına göre kıyaslandığında, M27 malzeme seçimi yapılan asenkron motor modelinde demir kayıplarının 27 W fazla olduğu görülmektedir. Farklı nüve malzemeler ile oluşturulan asenkron motor modellerine ait verim değerleri Şekil 6'da gösterildiği gibidir. M27 elektrik çeliği modelinde enerji verimliliği 77,5% seviyelerindedir. Amorf nüve malzemesi ile oluşturulan asenkron motor modelinde ise enerji verimliliği 80% olduğu analizler sonucunda gözlemlenmiştir. Nüve malzeme olarak amorf malzeme seçimi, kayıpları azaltarak motor verimliliğini geliştirici bir özellik sunmuştur.



Şekil 6. Asenkron motor modelleri enerji verimliliği

Şekil 7'de elektrik çeliğine ve amorf malzemeye ait motor modellerinin manyetik akı yoğunluğu dağılımı gösterilmektedir. M27 elektrik çeliğinde ve 2605SA1 amorf malzemede manyetik akı rotor bölgesinde yoğunlaşmaktadır. Hava boşluğunda her iki modelde manyetik akı yoğunluğu düşük seviyede olmaktadır. M27 ve 2605SA1 nüve malzemelerinin manyetik doyum noktası sırasıyla 2T ve 1.5T seviyesindedir. Amorf malzemedeki düşük doyum seviyesinin ana nedeni kimyasal bileşimindeki manyetik olmayan elementlerin elektrik çeliğine kıyasla daha fazla olmasından kaynaklanmaktır. Nüve malzeme seçiminde elektrik motorunun çalışma şartlarının dikkate alınması gerekmektedir. Analizleri yapılan elektrik motorlarının düşük indüksiyon seviyesinde performans gösterdiği görülmektedir. Asenkron motorların manyetik akı yoğunluğu dağılımları incelendiğinde her iki malzeme için doyum noktası aşılmamıştır. Bu nedenle, modellenen motorlarda malzeme seçiminde elektrik çeliği gibi amorf malzeme kullanımında uygun olacağı gözlemlenmiştir.



Şekil 7. Manyetik akı yoğunluğu dağılımı; a) M27 nüve malzeme, b) 2605SA1 nüve malzeme

Tablo 4'de farklı nüve malzeme kullanılarak modellenen asenkron motorlara ait sonlu elemanlar analiz sonuçları gösterilmektedir. 2605SA1 amorf malzemede toplam bakır kayıpları 161 W olarak çıkmaktadır. M27 malzemede bakır kayıplarının 178 W olduğu görülmektedir. Bakır kayıplarında iletken olarak seçilen bakır malzeme aynı olmasına rağmen M27 elektrik çeliği kullanılan asenkron motor modelinde bakır kayıpları amorf malzemeli elektrik motoruna göre %10 fazla olmaktadır. Bunun temel nedeni, asenkron motor modelinin 1.1 kW çıkış gücüne ulaşabilmesi için gereken akım değerinin, M27 nüve malzemeli modelde hem stator hem de rotor kısımları için daha fazla faz akımına ihtiyaç duymasından kaynaklanmaktadır. Asenkron motor modelinde seçilen amorf malzemenin bakır kayıplarına olumlu etkisi demir kayıpları açısından da benzerlik göstermektedir. Amorf malzemeli modeldeki demir kayıpları elektrik çeliği kullanılan modele kıyasla 27 W daha düşük seviyede olmaktadır. Bunun temel nedeni, nüve malzemelerin kimyasal bileşimlerinin ve kristal yapısının farklı olmasındandır. Amorf alaşımlar, iç yapıdaki düzensizlikten dolayı kristal yapı gösteren alaşımlara göre çok daha düşük elektrik iletkenliği gösterirler. Amorf nüve malzemelerin atomik bir düzende olmaması amorf malzemelerin, kristal yapıdaki elektrik çeliklerine kıyasla yüksek elektriksel öz direncine sahip olduğunu göstermektedir. Bunun sonucunda 2605SA1 amorf malzemede girdap akımları düşük seviyeye ulaşarak düşük demir kaybı özelliği sergilemektedir.

Tablo 4. Sonlu elemanlar analiz sonuçları

	2605SA1	M27
Stator Bakır Kayıpları (W)	110	121
Rotor Bakır Kayıpları (W)	51	57
Toplam Bakır Kayıpları (W)	161	178
Stator Faz Akımı (A)	2.81	2.96
Rotor Faz Akımı (A)	2.12	2.25
Demir Kayıpları (W)	6	33
Giriş Gücü (W)	1376.4	1419.7
Verimlilik (%)	80	77.5

Demir kayıpları ve bakır kayıplarının 2605SA1 amorf nüve malzemeli motor modelinde düşük çıkması nedeni ile şebekeden çekilen güç M27 malzemeli modele nazaran amorf malzemeli modelde 43.3 W daha düşük olmaktadır. Bu sayede, 2605SA1 malzemeli motor modelinde verimlilik %80 seviyesinde olur iken M27 malzemeli modelde verimlilik %77.5 seviyesinde olmaktadır. Elektrik motor modellerinde stator ve rotor parçalarında amorf malzeme kullanımı asenkron motor modelinin enerji verimliliğini elektrik çeliği kullanılan modele kıyasla %2.5 geliştirdiği gözlemlenmiştir.

5. Sonuçlar

Bu çalışmada, 1.1 kW gücündeki sincap kafesli asenkron motorlar farklı manyetik nüve malzemelerin kullanımı ile modellenmiştir. Stator ve rotor kısımları için M27 silisli sac ve 2605SA1 amorf nüve malzemeler seçilmiştir. Elektrik motor modellerinin sonlu elemanlar yöntemi ile analizleri gerçekleştirilmiş ve birbirleri ile karşılaştırılmıştır. Elektrik motor modellerinin verimlilikleri ve kayıp türleri incelenmiştir. Elektrik motor modellerinin çalışma koşulundaki manyetik akı yoğunluğu değerlendirilmiştir.

Sonlu elemanlar analiz sonuçlarına göre, stator ve rotor kısımlarında bakır kayıpları M27 elektrik çelik modelinde daha fazla çıkmaktadır. Bakır kayıplarına neden olan faz akımları incelendiğinde, M27 sac malzemeli modelde stator ve rotor faz akımları amorf malzemeli modele nazaran daha fazla olduğu görülmektedir. Demir kayıpları açısından amorf nüve malzeme elektrik çelik malzemeye göre daha üstün özellikler sergilemektedir. Bu sonuçlar doğrultusunda, 2605SA1 amorf nüve malzeme asenkron motor modelin verimliliğini geliştirerek enerji verimliliğine olumlu katkılar sunmaktadır. Manyetik akı yoğunluğu dağılımları incelendiğinde her iki malzemede manyetik doyum bölgesinin aşılmadığı görülmüştür. Sonlu elemanlar analizlerinin çıktıları, nüve malzeme seçiminde 2605SA1 amorf malzeme kullanımın M27 elektrik çeliğine kıyasla çeşitli avantajlar sunduğunu göstermektedir.

6. Kaynaklar

1. T. Vaimann, A. Belahcen, and A. Kallaste, "Changing of magnetic flux density distribution in a squirrel-cage induction motor with broken rotor bars," *Elektron. ir Elektrotechnika*, **2014**,vol(20, no. 7), pp. 11–14, 2014.
2. O. Yaman, "An automated faults classification method based on binary pattern and neighborhood component analysis using induction motor," *Measurement*, **2021**,vol. 168, p. 108323.
3. F. J. T. E. Ferreira and A. T. de Almeida, "Novel multiflux level, three-phase, squirrel-cage induction motor for efficiency and power factor maximization," *IEEE Trans. energy Convers.*, **2008**,vol. 23, no. 1, pp. 101–109.
4. A. Krings, *Iron losses in electrical machines - Influence of material properties , manufacturing processes , and inverter operation*. **2014**.
5. S. Okamoto, N. Denis, Y. Kato, M. Ieki, and K. Fujisaki, "Core loss reduction of an interior permanent-magnet synchronous motor using amorphous stator core," *IEEE Trans. Ind. Appl.*,**2016,** vol. 52, no. 3, pp. 2261–2268.
6. R. Saidur, "A review on electrical motors energy use and energy savings," *Renew. Sustain. Energy Rev.*, **2010,** vol. 14, no. 3, pp. 877–898.
7. J. Kartigeyan and M. Ramaswamy, "Effect of material properties on core loss in switched reluctance motor using non-oriented electrical steels," *J. Magn.*, **2017**,vol. 22, no. 1, pp. 93–99.
8. Y. N. Fazıl, M. Y. Dulkadir, M. Yılmaz, and M. F. Kalkan, "The effects of electrical steel

properties on energy efficiency in electric motors with the finite element method," in *The International Conference of Materials and Engineering Technology*, **2020**, pp. 322–327, [Online]. Available: https://www.ticmet.org/uploads/files2/ticmet20-proceeding-book201120.pdf.
9. C. K. Hou, "Effect of silicon on the loss separation and permeability of laminated steels," *J. Magn. Magn. Mater.*,**1996**, vol. 162, no. 2–3, pp. 280–290, doi: 10.1016/S0304-8853(96)00268-5.
10. H. Fujimori, H. Yoshimoto, T. Masumoto, and T. Mitera, "Anomalous eddy current loss and amorphous magnetic materials with low core loss," *J. Appl. Phys.*, **1981**,vol. 52, no. 3, pp. 1893–1898.
11. Y. Okazaki, "Loss deterioration in amorphous cores for distribution transformers," *J. Magn. Magn. Mater.*, **1996**,vol. 160, pp. 217–222, 1996.
12. R. Hasegawa, "Present status of amorphous soft magnetic alloys," *J. Magn. Magn. Mater.*, **2000**, vol. 215, pp. 240–245.
13. Z. Wang, Y. Enomoto, R. Masaki, K. Souma, H. Itabashi, and S. Tanigawa, "Development of a high speed motor using amorphous metal cores," in *8th International Conference on Power Electronics-ECCE Asia*, **2011**, pp. 1940–1945.
14. R. Kolano, K. Krykowski, A. Kolano-Burian, M. Polak, J. Szynowski, and P. Zackiewicz, "Amorphous soft magnetic materials for the stator of a novel high-speed PMBLDC motor," *IEEE Trans. Magn.*, **2012** ,vol. 49, no. 4, pp. 1367–1371.
15. A. Chiba *et al.*, "Test results of an SRM made from a layered block of heat-treated amorphous alloys," *IEEE Trans. Ind. Appl.*, **2008**,vol. 44, no. 3, pp. 699–706.
16. S. K. Gupta *et al.*, "Cold rolled non-oriented (CRNO) silicon steel production at Rourkela Steel Plant, SAIL."
17. A. Najafi and I. Iskender, "Reducing losses in distribution transformer using 2605SA1 amorphous core based on time stepping finite element method," *2015 Int. Sib. Conf. Control Commun. SIBCON 2015 - Proc.*, pp. 0–3, 2015, doi: 10.1109/SIBCON.2015.7146963.
18. D. A. Gonzalez and D. M. Saban, "Study of the copper losses in a high-speed permanent-magnet machine with form-wound windings," *IEEE Trans. Ind. Electron.*, **2013**,vol. 61, no. 6, pp. 3038–3045.
19. G. Bertotti, "General properties of power losses in soft ferromagnetic materials," *IEEE Trans. Magn.*, **1988**, vol. 24, no. 1, pp. 621–630,.

KAYNAK GEOMETRİSİNİN LAMİNE ELEKTRİK ÇELİK SACLARI ÜZERİNDEKİ ETKİSİNİN SONLU ELEMANLAR YÖNTEMİ İLE İNCELENMESİ

MAHMUT FURKAN KALKAN[1], MUHAMMET YUSUF DULKADİR[1], NECİP FAZIL YILMAZ*[1,2], SUAT ÖNAL[3]

[1]Gaziantep Üniversitesi, Mühendislik Fakültesi, Makine Mühendisliği Bölümü, Gaziantep, Türkiye
[2]Mütevelli Heyeti, Hasan Kalyoncu Üniversitesi, Gaziantep, 27410, Türkiye
[3]Osmaniye Korkut Ata Üniversitesi, Osmaniye Meslek Yüksekokulu, Osmaniye, Türkiye
*nfyilmaz@gantep.edu.tr

ÖZET

Kaynak işlemi elektrik motoru, trafo ve jeneratörlerde lamine olarak kullanılan elektrik çelik saclarının birleştirilmesinde en yaygın kullanılan yöntemlerden birisidir. Geleneksel kaynak yöntemlerinin yanı sıra, lazer kaynağı lamine yapıyı sabitlemek için alternatif bir teknolojidir. Lazer kaynağı geleneksel kaynak metotlarına göre elektrik makinelerinde manyetik özelliklerin korunmasında bilinen en verimli kaynak yöntemlerinden bir tanesidir. Bununla birlikte, kaynak geometrisielektrik makinelerinin çalışma performansında ciddi bir etkiye sahiptir. Bu çalışmanın temel amacı,presleme prosesi sonucunda üst üste gelen lamine sacları farklı kaynak geometrileri ile birleştirerek, geometriden dolayı oluşan manyetik kayıpları birbirleri ile kıyaslamaktır.Farklı kaynak dikiş geometrilerine sahip elektrik çeliği saclarının simülasyonları sonlu elemanlar yöntemi ile modellenmiştir. Kaynak geometrisi olarak yarım daire seçilmiştir ve daire yarıçapı arttıkça girdap akım kayıpları artış göstermiştir. Kayıp dağılımları gözlemlendiğinde kaynak bölgesinde kayıpların daha yoğun olduğu görülmüştür.

Anahtar Kelimeler: Elektrik Çeliği, Sonlu Elemanlar Yöntemi, Manyetik Kayıplar, Girdap Akım Kayıpları, Kaynak Geometrisi

1. Giriş

Elektrik motoru ve trafo gibi elektrik makinelerinde yaygın olarak elektrik sacları kullanılırlar. Elektrik sacları aynı zamanda silisyum içerikli saclar olarak da adlandırılabilirler. Bu sacların yaygın olarak kullanılma sebeplerinden başlıca; yüksek geçirgenlik ve düşük demir kayıpları gibi özelliklere sahip olmalarıdır. Bu malzemelerin temel kullanım amacı enerjinin taşınmasıdır [1]. Bu özellikler ilesilisyum içerikli sacların kullanıldığı elektrik makinelerinde saclar üzerinde oluşan girdap akımı, önemli bir demir kaybı çeşididir. Bu demir kaybı elektrik makinelerinde kullanılan silisyum içerikli saclar gibi malzemelerin tasarımına büyük oranda yön vermektedir. Silisyum içerikli sacların elektrik makinelerinde kullanımı esnasında kalınlık arttıkça girdap akımının sac nüve içerisinde gezindiği alanda artmaktadır. Bu durum elektrik makinelerinde demir kaybına dolayısıyla da verim kaybına sebebiyet vermektedir. Demir kaybının azaltılmasına yönelik atılan adımlardan birisi silisyum içerikli sacların kalınlığının azaltılmasıdır. Piyasada yaygın olarak 0.5 mm kalınlığında silisyum içerikli sac kullanılsa da bazı üreticiler daha ince kalınlıklarda silisyum içerikli saclar kullanmaktadır [2]. Kalınlığın 0.5 olduğu durumlarda girdap akımlarından kaynaklanan verimlilik kaybı azalsa da, düşük sac kalınlığı üretim maliyeti ve işçiliği arttırmaktadır. Elektrik makinelerinde kullanılan silisyum içerikli sacların demir kayıplarının azaltılmasında kullanılan diğer bir yöntem ise silisyum içerikli

sacların kimyasal içeriklerinin değiştirilmesidir. Silisyum oranı arttırıldıkça bu lamine sacların kullanıldığı elektrik makinelerinin çalışma performansında daha düşük demir kayıpları olduğu gözlenmiştir. Bu noktada, yine bazı dezavantajlar ortaya çıkmaktadır. Silisyum içeriğinin manyetik nüve malzemelerdeki artışıyla, nüve malzemelerin haddelenme gibi işlemleri zorlaşmaktadır. Bu sebepten ötürü piyasada yaygın olarak %1 ile %3 arasında silisyum içeren saclar bulunmaktadır. Bu yapılan çalışma ve araştırmaların yanı sıra lamine silisyum içerikli sacların birbirlerine bağlantı yöntemlerinin de elektrik makinelerinin performansına olan etkisi oldukça önemlidir.

Lamine edilmiş saclar kaynak, yapıştırma veya perçinleme gibi yöntemlerle birleştirilerek sabitlenir [3]. TIG ve plazma gibi geleneksel kaynak metotları, kullanım esnekliği ve düşük maliyetlerden dolayı silisyum içerikli sacların kaynağında yaygın olarak kullanılmaktadır [4]. Lazer kaynak yöntemi ise geleneksel yöntemlere kıyasla daha iyi bir kaynak kalitesini ve daha yüksek hızlara sahip imalat süresini sağlamaktadır [5]. Bunlarla birlikte lazer kaynağı TIG ve plazma gibi kaynak metotlarına kıyasla daha küçük ITAB bölgesine sebebiyet vermektedir[6]. Bu sebeplere ek olarak, silisyum içerikli sacların kaynak ile birleştirilme işleminde lazer kaynağının yaygınlaşmasının sebebi lazer kaynak metodunun sağladığı konsantre ısı kaynağı ve düşük deformasyondur. Kaynak yöntemleri kullanılarak yapılan birleştirme işlemlerinde, dikişin kenar düzleminin altında olduğu yerde pürüzsüz bir yüzeyin sağlanması için bir kaynak geometrisi için hazırlık gerekmektedir [7]. Silisyum içerikli sacların kaynağında kaynak geometrisi elektrik makinelerin çalışması esnasında gösterdikleri verimliliğe önemli derecede etkiye sahip olduğu bilinmektedir [8]. Kaynak geometrisinin yanı sıra silisyum içerikli saclar üzerinde kalan çapakların veya yapılan kaynak işlemiyle birlikte silisyum içerikli sacların sahip olduğu yalıtkan kaplamanın tahrip olmasıyla ortaya çıkan manyetik kayıplar bilimsel araştırmalara konu olmuştur [9]. Kaynak esnasında silisyum içerikli saclar üzerinde bulunan elektrik izolasyon kaplamasının zarar görmesiyle, elektrik makinelerinde girdap akım kayıplarının arttığı gözlenmektedir [10,11].

Sonlu elemanlar yöntemi, elektrik makinelerinde manyetik kayıpların ve verimliliğinin araştırıldığı çalışmalarda sonlu elemanlar yöntemi literatürde sıkça kullanılmıştır [12,13]. Zhang ve arkadaşları, sonlu elemanlar yöntemi kullanarak lazer ve TIG kaynağının silisyum içerek sacların birleştirilmesindeki manyetik analizini gerçekleştirmişlerdir. Yaptıkları bu çalışmada TIG kaynağının daha fazla girdap akım kaybına sebebiyet verdiğini gösterdiler [14].Lamprecht ve arkadaşları [15], sonlu elemanlar yöntemi kullanarak silisyum içerikli sacların farklı istifleme yöntemlerinin girdap akımı kayıpları üzerindeki etkileri üzerine çalışmışlardır. Ukwungwu ve arkadaşları ise farklı kaynak yöntemlerinin silisyum içerikli sacların istiflenmesi esnasında manyetik özelliklere etkisi nümerik analiz yöntemleri ile araştırılmıştır [16].

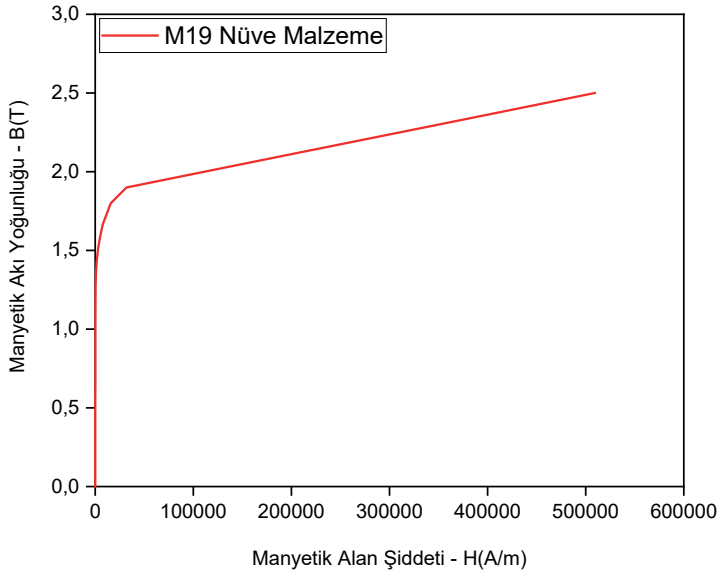
Bu çalışmada, kaynak geometrisi ile manyetik özellikler arasında ilişkiler incelenmiştir. Bu kapsamda silisyum içerikli sacların kaynak işlemi ile istiflenmesi esnasında kullanılan kaynak geometrilerinin manyetik özelliklere olan etkileri incelenmiştir. Belirlenen farklı kaynak geometrilerinde yapılan kaynak ile istiflemesi yapılan modellerin; manyetik akı yoğunlukları, girdap akım yoğunlukları ve girdap akım kayıpları değerlendirilmiştir.

2. Malzeme ve Metot

2.1 Nüve Malzeme

Bu çalışmada, elektrik motorlarda kullanılan tane yönelimli olmayan silisyumlu sacın kaynak geometrisine bağlı olarak değişik manyetik özellikleri sonlu elemanlar yöntemi ile analiz

edilmiştir. Kaynak geometrileriAnsys-Maxwell sonlu elemanlar yazılımında modellenmiştir. Elektrik motorlarda, M19 sacı düşük güç kayıpları ve yüksek manyetik doyum özellikleri nedeni ile tercih edilmektedir. Bu nedenden dolayı, modellemede kullanılan lamine elektrik çeliği olarak M19 malzeme seçilmiştir.Laminasyon sacının elektriksel özdirenci 51 μΩcm ve kütle yoğunluğu 7650 kg/m^3 şeklindedir. M19 sacına ait manyetik akı yoğunluğu (B) – manyetik alan şiddeti (H) eğrisi Şekil 1' de gösterilmiştir. M19 nüve malzeme B-H eğrisinde manyetik doyum noktası 2.5T olmaktadır. Yüksek manyetik alan şiddetlerin yüksek manyetik indüksiyonlara ulaştığı görülmektedir.



Şekil 1. M19 nüve malzeme manyetik akı yoğunluğu (B) – manyetik alan şiddeti(H) eğrisi

Nüve kayıplarının hesaplanması elektrik makinelerinin tasarımının ve analizinin zorlu bir yönü olmaktadır. Çeşitli indüksiyon seviyeleri ve frekansları için nüve kayıplarını hesaplamak için çeşitli analitik metotlar bulunmaktadır. Jordan[17] nüve kayıplarını iki tipe ayırdı; histerezis kayıpları (P_{hyst}) ve girdap akımı kayıpları (P_{ec}).Her iki kayıp biçimi de akıyoğunluğunun genliğinden etkilenmiştir. Histerezis kayıpları (statik kayıplar) f ile orantılı olmasına rağmen, girdap akımı kayıpları f^2 (dinamik kayıplar) ile orantılı olmaktadır. Güç kaybı denklemi şu şekilde yazılmaktadır;

$$P_{Fe} = P_{hyst} + P_{ec} = k_{hyst} f B^2 + k_{ec} f^2 B^2 \quad (1)$$

Denklem 1'de; P_{Fe}(W/m^3) toplam nüve kaybını, f (Hz), B (T) manyetik akı yoğunluğunu temsil etmektedir. Histerezis kaybı için k_{hyst} (W/m^3) ve girdap akım kaybı için k_{ec}(W/m^3)sabitleri kullanılmaktadır. Tablo 1'de M19 nüve malzemeye ait histerezis ve girdap akım kayıplarının katsayıları verilmiştir.

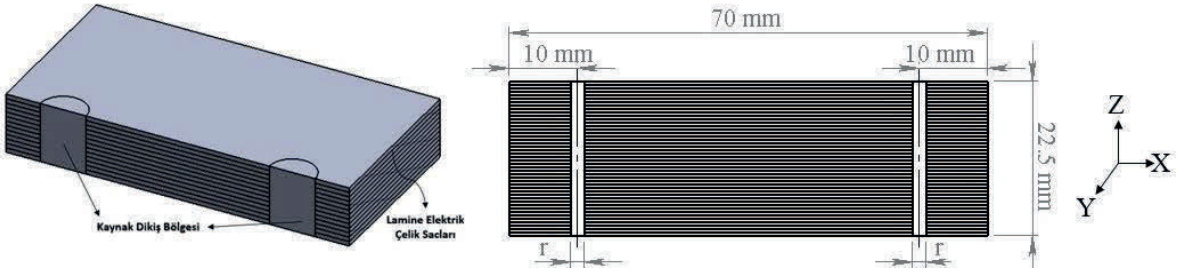
Tablo 1. M19 nüve malzeme histerezis ve girdap akımı kayıp sabitleri

	k_{hyst} (W/m^3)	k_{ec}(W/m^3)
M19	164.2	0.409

2.2 Sonlu Elemanlar Modeli

Bu çalışmada, kaynak geometrilerinin manyetik kayıplara etkisini incelemek için kaynak dikiş bölgesi parametreleri üzerinde değişiklikler yapılmıştır.Laminasyon saclarının kalınlıkları, hali

hazırdaki ticari uygulamalarda kullanılan silisyumlu sacın kalınlığı referans alınarak 0.5 mm olarak seçilmiştir.Şekil 2'de gösterildiği gibi silisyumlu saclar üst üste koyularak iki farklı bölgeden kaynak modellemesi bir cad programı yardımı ile hazırlanmıştır. Kaynak geometrisi her iki bölge içinde yarım daire olarak seçilmiştir. Modellemelerdeki daire yarıçapları sırasıyla 0.25, 0.50, 0.75 ve 1 mm olarak seçilmiştir. Sonlu elemanlar analizinde hesaplama süresini azaltmak için temel ve karmaşık olmayan bir model kurulmuştur. Problemin çözümü zaman bağlı olarak gerçekleştirilmiştir. Problem 100 adımda 0.1 saniyede çözülmüştür. Ansys-Maxwell yazılımında girdap akım kayıpları ve bunların dağılımları gözlemlenmiştir.

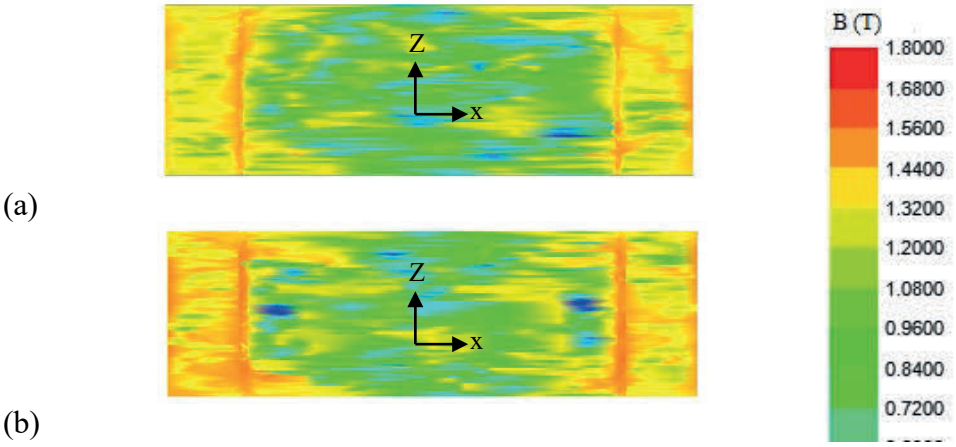


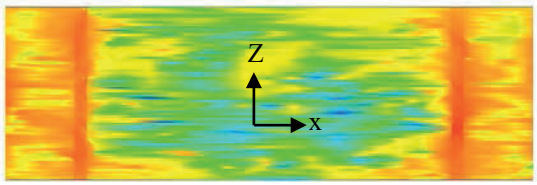
(a) katı model (b) kesit alanı

Şekil 2. Sonlu elemanlar modeli; (a) katı model ve (b) kesit alanı görünümü

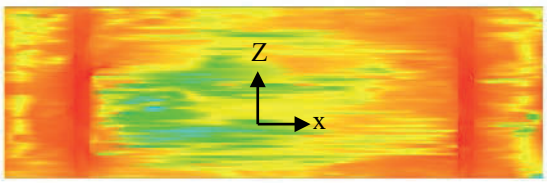
3. Bulgular ve Tartışma

Şekil 3'de farklı kaynak geometrilerine sahip laminasyon saclarının manyetik akı yoğunluğu dağılımları gösterilmektedir. Merkez çevresinde 0.25 mm ve 0.50 mm (Şekil 3.a ve 3.b) yarıçapına sahip modellerde manyetik akı homojen bir şeklide dağılarak daha düşük manyetik indüksiyon seviyelerindedir. Ancak 0.75 mm ve 1 mm (Şekil 3.c ve 3.d) kaynak geometrilerinde ki modellerde merkez bölgedeki homojenlikte bozulmalar meydana gelmekte ve manyetik indüksiyon yüksek seviyelere ulaşmaktadır. Her dört faklı kaynak geometrilerine sahip modellerde manyetik akı yoğunluğu doyma noktasına ulaşmamıştır.0.75 mm ve 1 mm kaynak geometrilerine sahip modellerde kaynak dikiş bölgesinde manyetik indüksiyon dağılımları belirgin bir şekilde artış göstermektedir. Analiz sonuçları göre, kaynak dikiş bölgesinin çevresinde manyetik akı yoğunluklarında artış gerçekleşmektedir. Modellemede nüve malzeme olarak seçilen M19 elektrik çeliğinin manyetik doyum noktası 2.5 T olduğu için her dört farklı model içinde kaynak bölgesi çevresini manyetik doyum seviyesini aşmamaktadır.





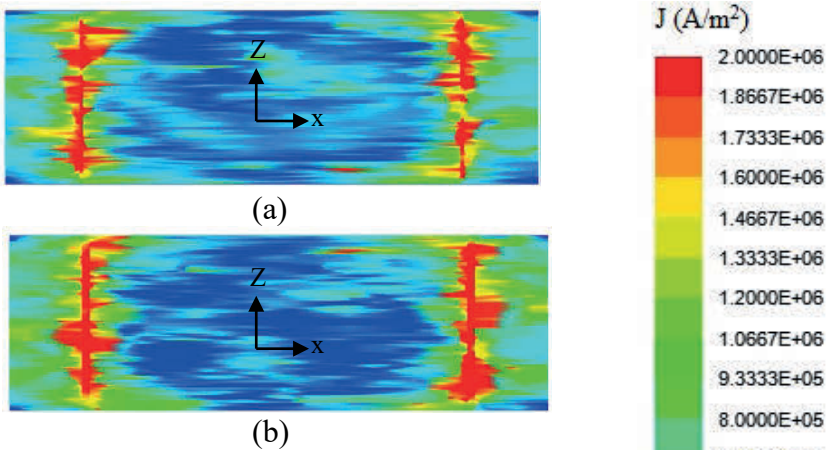
(c)

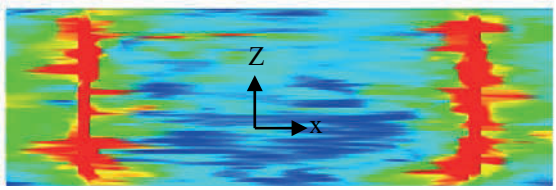


(d)

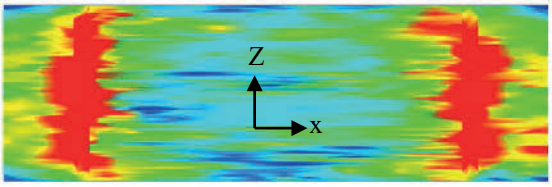
Şekil 3. Manyetik akı yoğunluğu dağılımı;
(a) r = 0.25 mm, (b) r = 0.5 mm, (c) r = 0.75 mm, (d) r = 1 mm

Girdap akım yoğunluğunun dağılımları Şekil 4'te gösterilmektedir. Kaynak dikiş bölgelerinde akım yoğunluğunun dağılımı incelendiğinde her dört modelde girdap akım dağılımın arttığı gözlemlenmektedir. Laminasyon saclarında girdap akımlarını sınırlandırmak için yalıtım kaplaması kullanılmaktadır. Bu sayede girdap akımlarını minimum seviyeye indirmek amaçlanmaktadır. Ancak, laminasyon saclarını birleştirme yöntemi girdap akımlarını arttırıcı etki göstermektedir. 0.25 mm (Şekil 4.a) kaynak dikiş geometrisine sahip modelde girdap akımlarının dağılımları en düşük seviyede olmasına rağmen, 1 mm (Şekil 4.d) kaynak dikiş geometrisine sahip modelde girdap akımın dağılımı artış göstermektedir. 0.25 mm ve 0.50 mm yarıçapındaki modellerde girdap akımlarının dağılımları birbiri ile benzerlik göstermesine rağmen 0.75 mm ve 1 mm yarıçapındaki modellerde girdap akımları dağılımlarındaki artış kaynak dikiş bölgesi çevresinde daha belirgin hale gelmektedir. Kaynak geometri yarıçapındaki artış girdap akımlarını arttırıcı etki göstermektedir. Kaynak dikiş geometrisinden uzaklaştıkça yani merkez bölge çevresinde girdap akımları düşük seviyede olmaktadır. 1 mm yarıçapına sahip modelde merkez bölgenin çevresindeki girdap akım dağılımlarının homojenliğinde bozulmalar meydana gelmiştir. Sonlu elemanlar analizlerine göre 0,75 mm kaynak yarıçapından büyük geometriye sahip modelde (r = 1 mm) girdap akımlarında düzensizlikler gözlemlenmiştir.





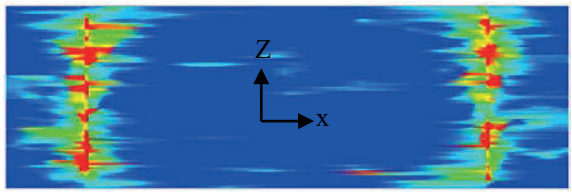
(c)



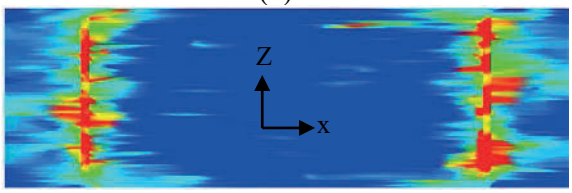
(d)

Şekil 4. Girdap akımı yoğunluğu dağılımı;
(a) r = 0.25 mm, (b) r = 0.5 mm, (c) r = 0.75 mm, (d) r = 1 mm

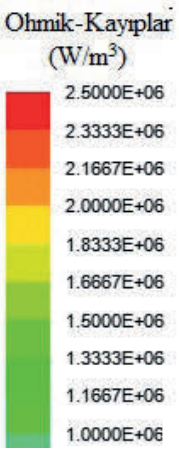
Şekil 5 girdap akımı kayıplarının dağılımlarını sunmaktadır. Her dört modelde kaynak dikiş bölgelerindeki girdap akım kayıpları artış göstermektedir. 0.25 mm (Şekil 5.a) yarıçapına sahip modelde girdap akımlarına bağlı kayıplar düşük seviyedeyken, 1 mm (Şekil 5.d) yarıçapındaki modelde girdap akım kayıpları en yüksek seviyede olmaktadır. Girdap akımı kayıpları 0.25 mm, 0.5 mm ve 0.75 mm yarıçapındaki modellerde kaynak dikiş bölgesinde yoğunlaşmasına rağmen 1 mm yarıçapındaki modelde kaynak dikiş bölgesinin çevresine daha belirgin bir şekilde dağılmaktadır. Bu neden ile 0.75 mm kaynak yarıçapı farklı kaynak geometrilerine sahip modellemeler için kritik bir değer haline gelmektedir. 0.25 mm ve 0.50 mm yarıçap ölçülerindeki modellerde merkez bölge çevresinde girdap akımı kayıplarının dağılımları birbirleri ile benzerlik göstermekte ve homojen bir şekilde dağılmaktadır. 0.75 mm yarıçapındaki modelde nispeten 0.25 mm ve 0.75 mm kaynak yarıçapındaki modeller ile tutarlılık göstermektedir. Ancak, 1 mm yarıçapındaki model incelendiğinde merkez bölge çevresindeki girdap akımı kayıpları daha belirgin duruma gelmekte ve homojenlik bozulmaktadır. Analiz çıktılarına göre 0.75 mm üzerindeki yarıçapa sahip modelleme girdap akım kayıpları açısından olumsuz özellik göstermektedir.

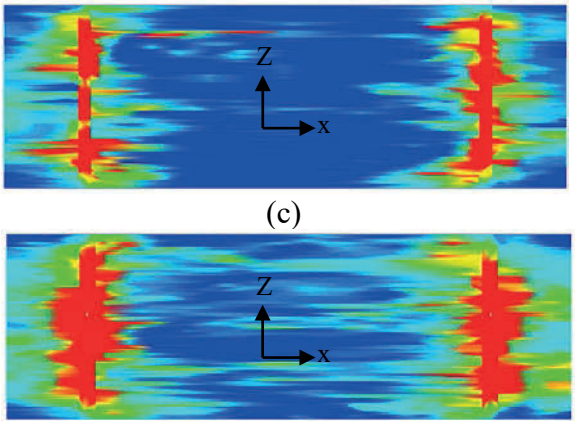


(a)



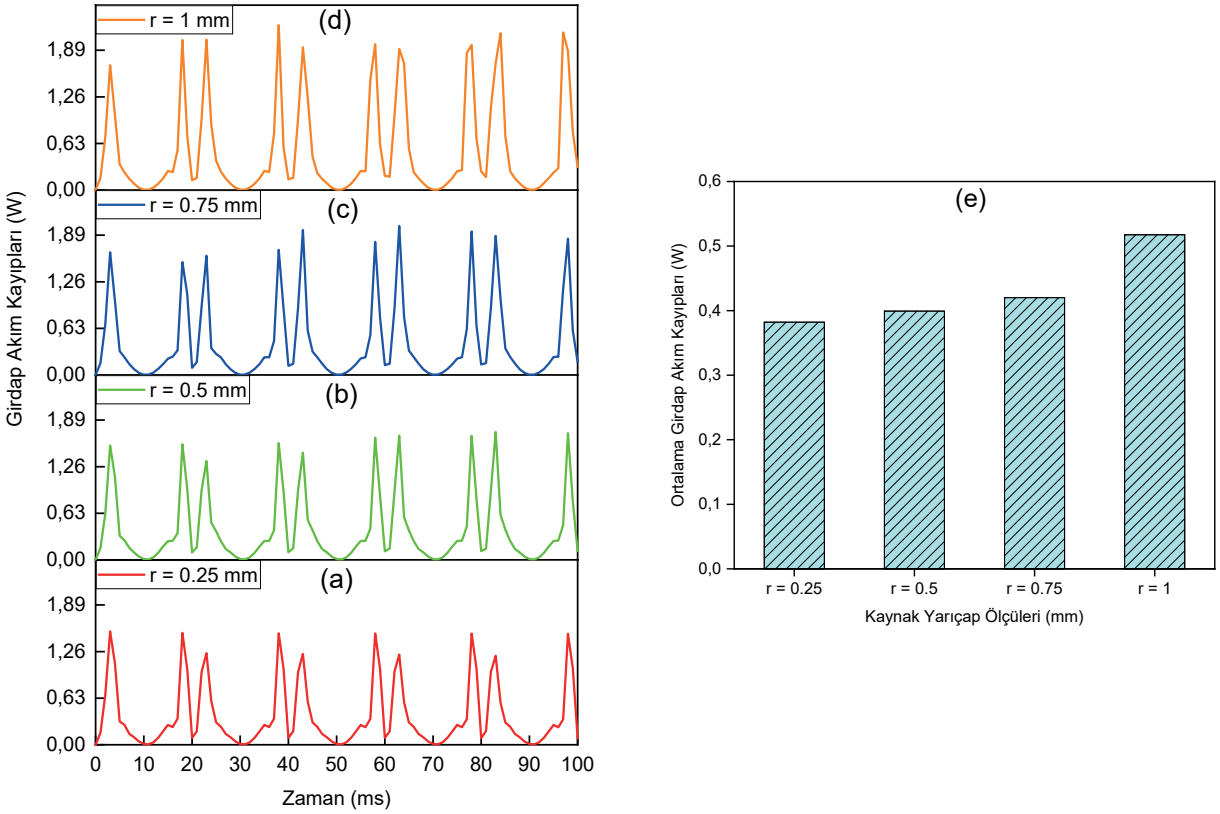
(b)





Şekil 5. Girdap akımı kayıpları dağılımı;
(a) r = 0.25 mm, (b) r = 0.5 mm, (c) r = 0.75 mm, (d) r = 1 mm

Şekil 6'da girdap akım kayıplarının zamana bağlı değişimi ve 100 ms boyunca gerçekleşen girdap akım kayıplarının ortalaması gösterilmektedir. Girdap akım kayıplarının zamana bağlı değişimleri her dört model içinde benzerlik göstermektedir. 30 ms'den sonra girdap akım kayıpları sabitdurumageçmektedir. Ortalama girdap akım kayıpları (Şekil 6.e) incelendiğinde 0.25 mm kaynak yarıçapına sahip modelde girdap akım kayıpları en düşük değerine ulaşırken kaynak yarıçapı 1 mm olduğunda girdap akım kayıpları en yüksek değerine ulaşmaktadır. Ortalama girdap akım kayıplarında 1 mm'den küçük kaynak geometrileri birbirleri ile benzerlik göstermektedir. Lakin kaynak dikişi yarıçapı 1 mm olduğunda kayıplarda keskin bir artış gözlenmektedir. 1 mm kaynak yarıçapına sahip model ile 0.25 mm kaynak yarıçapına sahip model ile karşılaştırıldığında, girdap akım kayıplarında %34 artış olduğu simülasyon sonuçlarında gözlemlenmektedir. Analiz sonuçları karşılaştırıldığında kaynak yarıçapındaki azalış girdap akım kayıpları bakımından olumlu avantajlar sunmaktadır.



Şekil 6. Girdap akım kayıplarının zamana bağlı değişimi; (a) r = 0.25 mm, (b) r = 0.5 mm, (c) r = 0.75 mm, (d) r = 1 mm - (e) ortalama girdap akım kayıpları

3. Sonuçlar

Analiz sonuçlarına göre dört faklı model için manyetik akı yoğunluğu, seçilen nüve malzemenin (M19) manyetik doyum noktasını aşmamıştır. Girdap akımları değerlendirildiğinde 0.75 mm ve 1 mm yarıçaplarındaki modellerde kaynak dikiş bölgesinde yüksek akımlara ulaştığı görülmektedir. Girdap akım kayıp dağılımları simülasyon sonuçlarına göre 0.25 mm, 0.5 mm ve 0.75 mm yarıçapındaki modellerde benzerlik göstermekte ve merkez bölge çevresinde 1 mm yarıçaplı modele nazaran daha homojen bir dağılım göstermektedir. Buna bağlı olarak girdap akım kayıp değerleri 1 mm yarıçaplı modelde en yüksek değeri sergilemektedir. Kaynak dikiş bölgesinin yarıçapındaki artış laminasyon sacları arasındaki iletkenliği artırarak birbirleri arasındaki girdap akımlarını yüksek seviyede tutmaktadır. Bunun sonucunda girdap akım kayıplarında kaynak yarıçapı artışına bağlı olarak kayıplar daha yüksek seviyelere ulaşmaktadır. Laminasyon sacları arasındaki girdap akımlarını sınırlandırmak için düşük kaynak yarıçapına sahip proseslerin tercih edilmesi gerekmektedir. Bu sayede elektrik motorlarındaki girdap akım kayıpları düşük seviyelere indirilerek, enerji verimliliği arttırılacaktır.

4. Kaynaklar

1. Beckley P. Electrical steels for rotating machines. IET; **2002**.
2. Wang H, Zhang Y, Lai X. Effects of interfaces on heat transfer in laser welding of electrical steel laminations. Int J Heat Mass Transf **2015**, 90:665–77. https://doi.org/https://doi.org/10.1016/j.ijheatmasstransfer.2015.07.027.
3. Schoppa A, Schneider J, Wuppermann C-D, Bakon T. Influence of welding and sticking of laminations on the magnetic properties of non-oriented electrical steels. J Magn Magn Mater

2003,254:367–9.
4. Mehdi B, Badji R, Ji V, Allili B, Bradai D, Deschaux-Beaume F, et al. Microstructure and residual stresses in Ti-6Al-4V alloy pulsed and unpulsed TIG welds. J Mater Process Technol **2016**;231:441–8.
5. Reinhart G, Munzert U, Vogl W. A programming system for robot-based remote-laser-welding with conventional optics. CIRP Ann **2008**;57:37–40.
6. Zhang L, Li X, Nie Z, Huang H, Niu L. Comparison of microstructure and mechanical properties of TIG and laser welding joints of a new Al–Zn–Mg–Cu alloy. Mater Des **2016**,92:880–7.
7. Markovits T, Takács J. Edge welding of laminated steel structure by pulsed Nd: YAG laser. Phys Procedia **2010**,5:47–52.
8. Kurosaki Y, Mogi H, Fujii H, Kubota T, Shiozaki M. Importance of punching and workability in non-oriented electrical steel sheets. J Magn Magn Mater **2008**,320:2474–80. https://doi.org/10.1016/j.jmmm.**2008**.04.073.
9. Dharmik BY, Lautre NK. Experimental evaluation on weld zone of thin–laminated stacked sheets post-GTA weld of CRNO electrical steel. Sādhanā **2021**,46:1–15.
10. Eldieb A, Anayi F. Evaluation of loss generated by edge burrs in electrical steels. IEEE Trans Magn **2016**,52:1–4.
11. Wang H, Zhang Y, Li S. Laser welding of laminated electrical steels. J Mater Process Technol,230:99–108.**2016** https://doi.org/https://doi.org/10.1016/j.jmatprotec.2015.11.018.
12. Ruuskanen V, Nerg J, Rilla M, Pyrhönen J. Iron loss analysis of the permanent-magnet synchronous machine based on finite-element analysis over the electrical vehicle drive cycle. IEEE Trans Ind Electron **2016**,63:4129–36.
13. Ruangsinchaiwanich S, Khongseephai K. Investigation of transformer performance by the finite element method. 2009 Int. Conf. Electr. Mach. Syst., IEEE; **2009,** p. 1–6.
14. Zhang Y, Wang H, Chen K, Li S. Comparison of laser and TIG welding of laminated electrical steels. J Mater Process Technol **2017**,247:55–63.
15. Lamprecht E, Hömme M, Albrecht T. Investigations of girdap current losses in laminated cores due to the impact of various stacking processes. 2012 2nd Int. Electr. Drives Prod. Conf., IEEE; **2012,** p. 1–8.
16. Ukwungwu D, Krichel T, Schauerte B, Leuning N, Olschok S, Reisgen U, et al. Electromagnetic assessment of welding processes for packaging of electrical sheets. 2020 10th Int. Electr. Drives Prod. Conf., IEEE; **2020**, p. 1–6.
17. Krings A, Soulard J. Overview and comparison of iron loss models for electrical machines. J Electr Eng **2010**,10:162–9.

ACPL-332J GATE SÜRÜCÜLÜ FIRÇASIZ DC MOTOR SÜRÜCÜ TASARIMI

UFUK KAYA[1], HALIL EROL[*1]

[1]Osmaniye Korkut Ata Üniversitesi, Mühendislik Fakültesi, Elektrik Elektronik Mühendisliği Bölümü, 80050, Osmaniye Türkiye

Özet

Bu çalışmada, ACPL-332J Kapı sürücü ile fırçasız doğru akım motorlarına yönelik motor sürücü tasarlanmış ve uygulaması gerçekleştirilmiştir. Anahtarlama elemanı olarak 2MBI200XAA-065-50 IGBT modül kullanılmıştır. ACPL-332J Kapı sürücü, active miller clamp ve desturation koruma metotlarına sahiptir. Bu bir izolasyonlu kapı sürücü olduğu için, oluşabilecek bir problemde kontrol kartının hasar alması önlenmiştir. Bu kapı sürücünün bir diğer avantajı ise, desaturation metodu ile, devrede bulunan anahtarlama elemanın kısa devre seviyesinde akım çektiği durumda, algılanır ve anahtarlama elamanı kapatılır. Active miller clamp ile ise, anahtarlama elemanının istenmeyen zamanlarda iletime geçmesini önlemekte kullanılmaktadır. Uygulaması gerçekleştirilen sürücünün, faz-faz arası osiloskop ölçümleri ve test aşamalarına ait görüntüleri sonuç olarak verilmiştir.

Anahtar Kelimeler: Fırçasız Doğru Akım Motorları, Motor Sürücüleri, ACPL-332J kapı sürücü.

1.GİRİŞ

Fırçasız Doğru Akım Motorlar her geçen gün daha fazla alanda faaliyet göstermektedir. Elektrikli hava-kara ve deniz araçlarında kullanımı hızla yaygınlaşan bu motorlar beyaz eşyalarda ve üretim araçlarında da gün geçtikçe daha fazla tercih edilmektedir. Verimlilik ve hacim başına momentum ihtiyacı gün geçtikçe artmaktadır.Fırçasız doğru akım motorları, yüksek verimlilik ve moment/hacim oranına sahiptir.[1] Fırçalı Doğru Akım Motorlarına göre verimlilik ve elektromanyetik gürültü gibi konularda avantajlı olan bu motor tipi, fırçalı motorların yerini de doldurmaya devam etmektedir. Konum sensörleri ile sürüşe ihtiyacı olması bir dezavantaj olarak önümüze çıkmaktadır. Piyasadaki asenkron motorlara göre daha maliyetli olması bir diğer dezavantajıdır.Motor sürücüler fırçasız doğru akım motorlarında zorunlu olarak kullanılması gerekmektedir. Bu sürücüler temel olarak kontrol katı, sürücü katı, güç katı, olarak üç gruba ayrılabilir. Bu gruplardan sürücü katında anahtarlama elemanlarını süren kapı sürücüleri ve yardımcı elemanları bulunmaktadır. Anahtarlama elemanın doğru tanınması ve onun ihtiyaçlarına ve çalışma aralıklarına uygun bir kapı sürücü belirlenmelidir. Farklı amaçlara göre özelleşmiş farklı tiplerde kapı sürücüleri bulunmaktadır. Bu uygulamada ACPL-332J kapı sürücüsü kullanılmıştır. Kullanılan bu kapı sürücü anahtarlama elemanımızın ihtiyacı olan akımı sağlayabilmektedir. Ayrıca çalışma gerilimi bakımından anahtarlama elemanımızın çalışma gerilimine uygundur. Ayrıca bu kapı sürücünün, izolasyona sahip olması, simetrik olarak beslenebilmesi, desaturation ve active miller clamp [2] koruma yöntemlerine sahip olması gibi avantajları da bulunmaktadır. Uygulamasının karmaşık olması, maliyeti ve yardımcı devre elemanları sayısının fazla olması dezavantajları olarak sıralanabilir.

Fırçasız DA Motor sürücüleri ile ilgili yapılan benzer çalışmalar gözlemlendiğinde, genellikle, active miller clamp ve desaturation koruma metotlarına sahip olmadıkları gözlemlenmektedir. Bu iki analog koruma metodu yüksek akımlar sürülmesi için gerçekleştirilen uygulamalarda büyük öneme sahiptir.

Desaturation metodu kısa devre durumlarında istenmeyen akımların anahtarlama elemanından geçişini çoğu zaman kontrol elemanından çok daha önce algılayabilir ve istenmeyen akımların geçişine engel olabilir. Bu şekilde anahtarlama elemanı ani akım sıçramalarına karşı korunmuş olur. Active miller clamp metodu ile ise anahtarlama esnasında kaçak kapasitede oluşabilecek gerilim yükü ile anahtarlama elemanının istenmeyen zamanlarda tetiklenmesinin veya akım sızdırmasının önüne geçilmektedir.Böyle bir koruma metodu bulunmadığı çalışmalarda anahtarlama, elamanı kontrolsüz bir şekilde tetiklenebilir. Bu durumda istenmeyen akımlar fazlar üzerinde dolaşabilir ve kısa devre durumu oluşarak anahtarlama elamanları zarar görebilir.Bu çalışmanın diğer çalışmalardan en temel farkı bu iki koruma metodu ile oluşabilecek problemlerin önüne geçilebilecek olmasıdır. Bu özellikleri ile daha güvenli ve daha uzun bir çalışma ömrü gibi avantajlara sahiptir.

2.MATERYAL VE METOD

Motor sürücüler fırçasız doğru akım motorlarında zorunlu olarak kullanılması gerekmektedir. Bir fırçasız doğru akım motoru sürülürken konum sensörlerine ihtiyaç duyulmaksızın back-emf yöntemi de kullanılabilmektedir.[3] Bu yöntem özellikle elektrikli hava araçlarına yönelik yapılan motorların sürücülerinde görülmektedir. Bu uygulamada konum sensörleri kullanılarak sürüş gerçekleştirilmektedir. Fırçasız doğru akım motorlarının hız kontrolünde de çeşitli hız kontrol yöntemleri bilinmektedir. En bilindik yöntemler olarak basitten zora doğru, trapezoidal PWM kontrol[4] space vektor PWM kontrol(SV-PWM) ve field oriented control(FOC) olarak sıralanabilir. Bu uygulamada, trapezoidal PWM kontrol ile hız kontrolü gerçekleştirilmektedir.
Kontrol kartı olarak STM32F-Discovery kullanılmaktadır. Konum sensörlerinden bilgi dijital olarak alınmakta ve GPIO ile okunmaktadır. Hız kontrolü ve akım okuma için ADC modülü kullanılmaktadır. Akım sensörü olarak HAS-200 analog çıkışlı akım sensörü kullanılmaktadır. 12 bit olan ADC1'in 1. kanalı ile analog sinyal okunur ve PWM ayarlamak için bir dönüşüm formülü ile genel sinyal ile duty-cycle ayarlanmaktadır. 2. 3. ve 4. kanallar ile ise akım okunur bir algoritma ile faz akımları belli değerleri geçince pwm belli oranlarda düşürülmektedir. TIM-1'in 3 kanalı ve evrilmiş kanalları ile toplamda 6 çıkış kullanılmıştır. Konum sensörlerinden gelen bilgi kullanılarak bir algoritma ile PWM kanal çıkışları tetiklenmektedir. Aşağıdaki tabloda hall sensörlerden gelen sinyale göre motor ileri yönde sürülür iken TİM1 pwm kanal çıkışları görülmektedir.Anahtarlama elemanları bakımından birçok tip anahtarlama elemanı bulunmaktadır. Frekans, çalışılacak gerilim ve akım değerleri gibi referanslara göre anahtarlama elemanı tipi belirlenebilir. Maliyet çalışma sıcaklıkları iç direnç, kapı kapasitansı gibi spesifik özelliklere göre de hangi anahtarlama elemanın tercih edileceği belirlenebilir.

Bu çalışmada Anahtarlama elemanı olarak ise 2MBI200XAA-065-50 IGBT Modül tercih edilmiştir. Her bir modül 1 adet yarım köprüden oluşmaktadır. Yüksek frekanslı anahtarlama esnasında anahtarlama gerilimi istenmeyen seviyelere yükselebilir. Bunu önlemek amacı ile Snubber kapasitör kullanılır. Bu uygulamada 2.2uF 1000VDC snubber, ve 2 adet 2200uF 400V elektrolit kondansatör kullanılmaktadır.

Tablo 1. Dijtial Hall Sensör Sinyaline Göre PWM Çıkışlarının Tablosu[5] :

HALL Effect Sensör Girdileri			TİM1 PWM Kanal Çıkışları		
HALL A	HALL B	HALL C	CH1	CH2	CH3
1	1	0	0	PWM	N_PWM
0	1	0	N_PWM	PWM	0
0	1	1	N_PWM	0	PWM
0	0	1	0	N_PWM	PWM
1	0	1	PWM	N_PWM	0
1	0	0	PWM	0	N_PWM
1/0	1/0	1/0	0	0	0

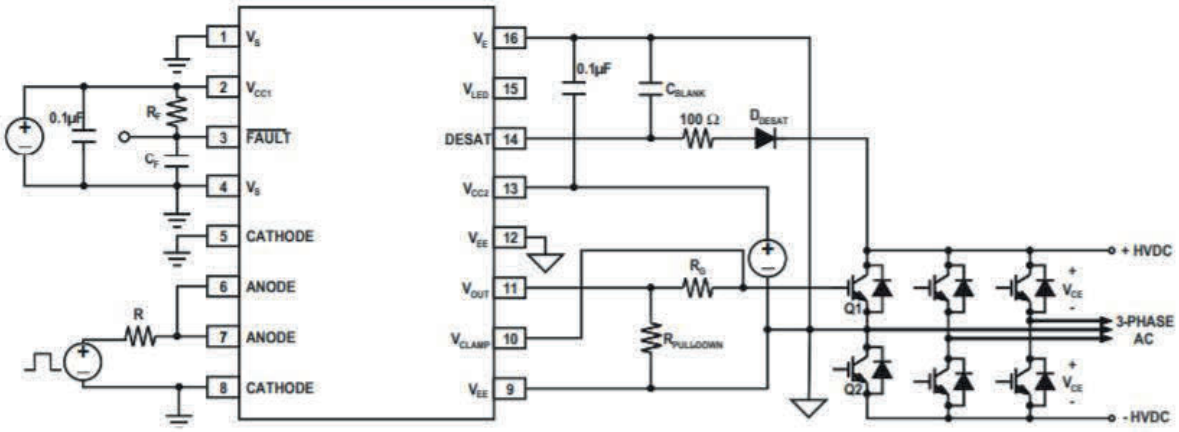
ACPL-332J kapı sürücünün Uygulanması

Kapı sürücüleri güç elektroniği uygulamalarında ihtiyaçtır. Birçok tipte kapı sürücüleri bulunmaktadır. Bunlardan biri ve bu uygulamada kullanılan kapı sürücü tipi izolasyonlu kapı sürücülerdir. İzolasyonlu kapı sürücüler ile,^([6]) yaşanabilecek bir aksilikte kontrol kartının zarar görmesinin önüne geçilmiştir. Sürücünün sağlıklı çalışması için çeşitli yöntemler kullanılmaktadır. Bunlardan ilki izole besleme yöntemidir. Bu yöntemle her kapı sürücü ayrı ayrı beslenmekte ve kaçak indüktanstan dolayı anahtarlama elemanlarının emitter uçlarında oluşabilecek farklı durumlarda, yaşanabilecek problemlerin önüne geçilmiştir. Bir diğeri ise, kapı sürücülerinin +15/-15V ile simetrik olarak beslenmesidir. Bu yöntemle anahtarlama elemanı hızla iletimden çıkarılabilmekte, bu şekilde istenmeyen 2 anahtarlama elemanın aynı anda açık olması durumunda oluşabilecek bir kısa devre durumunun da önüne geçilebilmektedir. Aynı zamanda yüksek akım basabilen bir kapı sürücü ile gecikme olmaksızın anahtarlama elemanı iletime geçebilmektedir.

İleri seviye güç kontrolünde oluşabilecek aksilikleri önlemek amacı ile 2 metoda daha başvurulabilmektedir. Bunlardan ilki desaturation metodu ile korumadır. Bu metodda anahtarlama elemanı normal çalışmada Cblank kapasitörünü boşaltacağı için desat ucundaki gerilim düşük seviyelerde olacaktır. Ancak kısa devre veya anahtarlama elemanın çalışabileceği akım değerlerinden yüksek akım geçmeye başladığında Cblank şarj olup belli bir zaman sonra eşik gerilimini aşacaktır. Bu durumda kapı sürücü kısa devre korumasına geçecektir ve anahtarlama elemanı yüksek akımdan korunabilecektir.

İkinci koruma metodu ise miller clamp metodudur. Anahtarlama elemanı hızlı bir şekilde iletimden çıkarken kaçak kapasite üzerinde istenmeyen gerilimler oluşur. Bu gerilimler bazen anahtarın kontrolsüz bir şekilde açılmasına sebep olabilir. Kontrolsüz açılan anahtarlama elemanı yüzünden, istenmeyen akımlar anahtarlama elemanı üzerinden geçebilir ve anahtarlama elemanı zarar görebilir. Bunu önlemek için, Vclamp ucu anahtarlama elemanın kapısına direkt bağlanır ve sürücü elemanı iletimden çıkarıldığında, kapı ucu gerilimi anahtarlama elemanın iletim eşiğine gelmeden önce, kapı sürücü içerisindeki yapı devreye girer ve anahtarlama elemanın kontrolsüz iletime geçmesinin önüne geçilir.

İkinci ve daha alt seviye başlıklar 10 pt. ve kalın harflerle yazılmalıdır. Tablolardan, şekillerden ve alt seviye başlıklardan önce ve sonra da birer satır boşluk bulunmalıdır. Tablo ve şekil açıklamaları sayfaya ortalı şekilde hizalanmalıdır. Tablo içi metinlerin büyüklüğü için herhangi bir kısıtlama bulunmamaktadır.



Şekil 1. ACPL-332J uygulama şeması.[7]

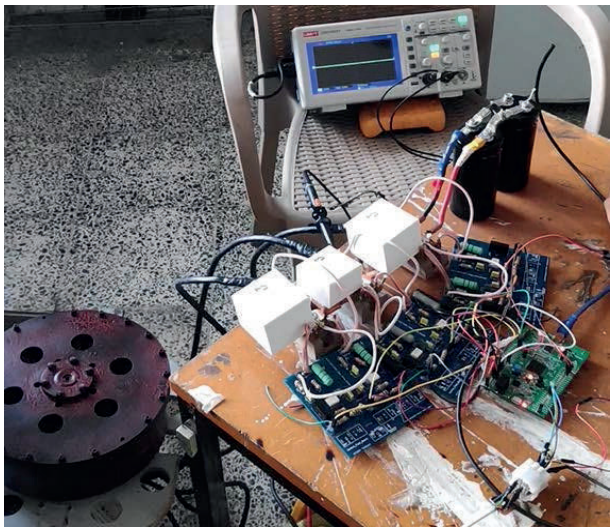
3.BULGULAR

Tasarlanan sürücü bir fırçasız DC motor üzerinde test edilmiştir. Osiloskop ile motorun fazlar arası gerilimi gözlemlenmiştir. Örnek olarak A-B fazları arası gerilimi şekil 3 te gösterilmiştir. Sinyalin salınım seviyesi oldukça düşüktür. Sürücüyü test etmek için kullanılan fırçasız doğru akım motorunun özellikleri tablo 2 de verilmiştir.

Tablo 2. Sürücüyü test etmesi amacı ile kullanılan motorunun özellikleri

Terminal Gerilimi	10V
Çıkış Gücü(P)	1kW
Çift Kutup Sayısı(p)	13
Faz Sayısı	3(yıldız bağlantı)
Yüksüz Hız(ω)	250
Nominal akım (I_n)	120A

Yukarıdaki özellikleri verilen motor ile sürücü test edilmiştir. Test başarı ile tamamlanmıştır. Faz çıkışları osiloskop, faz akımları ise pens ampermetre ile ölçülmüştür. Deney düzeneği, test motoru ve test edilen sürücü devresi şekil 3'te görülmektedir.



Şekil 2. Test motoru, Sürücü ve test düzeneği

Fazlar arasında PWM sinyali oluşan gerilimin şekli osiloskop aracılığı ile ölçülmüştür. Test aşamasında osiloskop aracılığı ile yapılan ölçümün sonuçları şekil 3'te görülmektedir. BLDC motorun ideale yakın bir kare dalga ile sürüldüğü osiloskop ekranında gözükmektedir. Osiloskopta gözüken A-B fazları arası (VAB) besleme gerilimidir.



Şekil 2. V_{AB} gerilimi osiloskop dalga şekli görüntüsü

4. SONUÇLAR

Bu çalışmada ACPL-332J kapı sürücü ve IGBT modüller ile yük altında çalışan fırçasız DA motor sürücü uygulaması gerçekleştirilmiştir. Testler başarı ile tamamlanmıştır. Desaturation ve Active Miller Clamp gibi koruma metotların uygulanması ve etkileri üzerine bir çalışma gerçekleştirilmiştir. Yapılan deneyler, sürücü ile yük altında çalışan fırçasız doğru akım motorlarının güvenli bir şekilde sürülebileceğini kanıtlamaktadır.

Teşekkür

Tübitak, 2209-B Sanayiye Yönelik Lisans Araştırma Projeleri Desteği Programına, çalışmaya sağladıkları destek için teşekkür ederiz.

Kaynakça

1. Yedamale, P., "Brushless DC (BLDC) Motor Fundamentals"
2. "*AN-5073 Active Miller Clamp Technology",* ON Semiconductor İnc., USA **2013.**
3. Shao, Jianwen., "*Direct Back EMF Detection Method for Sensorless Brushless DC (BLDC) Motor Drives"*
4. Şevgin,Eyyup.,Dikici,Zinnur.,Tuntaş,Remzi., "*Fırçasız DC Motoruna PWM Yönteminin Etkisi ve PIC Uygulaması"*
5. Elevich,Leonard N.., "*3-Phase BLDC Motor Control with Hall Sensors Using 56800/E Digital Signal Controllers",* Freescale Semiconductor Inc., USA **2005.**
6. Chen, Baoxing.., "*Isolated Half-Bridge Gate Driver with Integrated High-Side Supply"*
7. Data Sheet, *ACPL-332J,* Avago Technologies İnc., USA **2015**.

MANUFACTURING OF COPPER WIRE BY THE CONTINUOUS CASTING PROCESS

ZAKARIA BOUMERZOUG

University of Biskra, LMSM, Department of Mechanical Engineering, Biskra, Algeria
*z.boumerzoug@univ-biskra.dz

Abstract

Copper is the most widely used metal in the field of electricity transport. For a large production of copper, casting is the most suitable process. The production of copper wires is carried out by continuous casting which is a simple and economical method. In this paper, continuous casting production techniques will be presented. In particular, the vertical continuous casting will be detailed. The metallurgical parameters and problems of the production of copper wires will also be presented. Some solutions for these issues were suggested.

Keyword: Copper, Continuous casting, Solidification, Parameters

1. Introduction

The growing demand for electricity due to the increase in population and the expansion of the construction industry is mainly driving the copper wire market. This is further attributed to the increasing demand for consumer electronics devices, such as mobile devices, telecommunication tools, wearable devices, entertainment devices, etc.[1]. Copper has been and will continue to be vital for power transmission and heat transfer applications. Copper has the best electrical conductivity of all industrial metals except silver (noble metal) and is widely available at a reasonable cost. The ductility of copper allows it to be processed into wire bars and other shapes required for electrical system components [2]. Thousands of tons of copper are produced each year as rods, tubes, rods and other products of various cross sections in the casting-extrusion-drawing processes.In the production of ferrous and non-ferrous metals, copper can be cast in various forms. This can be done in two ways: in molds, or by continuous casting (CC).

In 1857, Henry Bessemer devised a continuous casting production method for sheet steel. Since then, continuous casting has become the main technique for casting steel. Copper today is continuously cast using a design similar to that of steel casting. Continuous casting is a process of melting and continuous solidification. Continuous casting avoids some intermediate steps such as ingot casting, sawing, preheating and hot rolling normally required to reduce ingot dimensions**.**

2. Continuous Casting

Continuous casting processes are divided into two main types, vertical and horizontal continuous casting processes. Figure 1 shows a typical diagram of the continuous casting process. The heart of a continuous casting machine is the mold. The molten metal is poured from the ladle through an inlet nozzle submerged in the tundish, which maintains a constant height for the molten metal to flow into the continuous casting mold. The mold is an open tube into which metal is poured

[3]. The liquid metal is protected either by a gas, inert or reducing, or by a molten compound. The melt is poured into a cooled mold. The casting speed is equal to the solidification speed. The cast wire is then cooled after leaving the mold and if necessary cut into pieces by an automatic displacement saw. Cutting cannot be done until the wire is completely solidified [4].

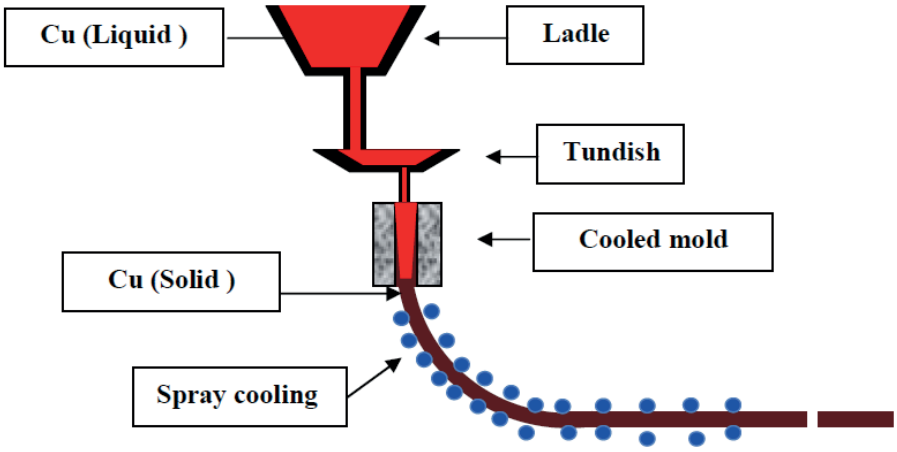


Figure 1. Typical diagram of the curved continuous casting process.

In most cases the mold is in vertical oscillation which facilitate lubrication and to pick up any tears in the skin during bonding, but it causes the formation of defects on the surface of the solidified metal, called oscillation marks. The oscillation marks appear as grooves perpendicular to the pouring direction. The oscillation marks can be used as an initiation point for cracks [3].

3.Manufacturing of Copper Wire

In this part, the fabrication of copper wire will be presented. The process which is adopted by several factories involves two successive processes. The first is the vertical continuous casting followed by the wire drawing process to reduce the section of the wire (Fig.2). The wire obtained from the continuous casting is called wire rod. The production of this wire begins with the insertion of a copper rod into the copper liquid bath through a channel (1) in which water circulates to cause cooling of the liquid metal drawn through this channel (2). The driven wire will pass through a pulley and then undergo the wire-drawing process (3) in order to reduce its section (4).

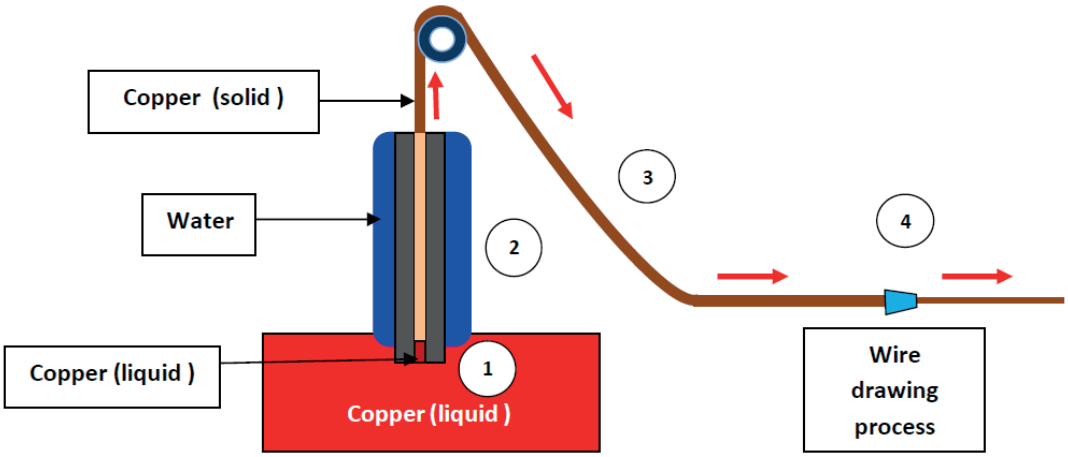


Figure 2. Manufacturing of copper wire by vertical continuous casting.

4. Main casting parameters

The quality of continuously cast copper wire is largely dependent on the microstructure as well as mechanical properties such as tensile strength and percent elongation. Electrical conductivity for wires intended for carrying electricity is an important characteristic. The control of the grain structure, which develops during the solidification process, is a key issue for the optimization of the final mechanical properties. These can be improved by analyzing and optimizing process parameters during the casting process, such as [5]:

– Cooling water flow rate:

Water flow rate is known to affect the structure formation during solidification. For example, when the cooling rate is fast, many more clusters develop and each grows rapidly. As a result more grains form and the grain size in the solid metal is finer [6,7]. According to the literature[5]:

- Low cooling rate result in less homogeneous micro-structure.
- When the cooling rate is fast, many more clusters develop and each grows rapidly. As a result more grains form and the grain size in the solid metal is finer
- Therefore, faster cooling rate will provide a harder material whereas slower cooling rate will make the softer material.

– Casting speed:

Casting speend is a critical parameter in casting process. From industrial aspect, the lower the casting speed, the larger the grains found and vice-versa. Lowering casting speed results in an increase in material conductivity. For example, typical speeds of 1.0- 2 M/min are normal for 20mm diameter Cu-OF-1 copper rod and 3 – 5 M/min for 6 & 8mm diameter rod [8]. It has been found, for oxygen free copper obtained under industrial conditions, an increase in tensile strength was observed with a decrease of casting speed [5]. Experience has shown that success in achieving good quality castings depends on avoiding slow cooling rates [9].

– Melt temperature :

For this parameter, we have two possibilities :

- For high casting temperature, formation of holes, and the solubility of oxygen, hydrogen and other gases in the copper liquid increases.
- For low casting temperature**,** some defects can be formed in the copper wire, such as porosity and component segregation.

For these reasons, the casting temperature is generally controlled at 1120˚C ± 10˚C, and the tundish temperature of the production line is between 1110 ˚C and 1150˚C.

4. Fabrication challenges

Manufacturers of copper wire can face several challenges either in the continuous casting or in the wire drawing process. The main challengers are:

- Surface quality of the wire after casting process

- Inclusions, pores and segregation in the wire after casting process (Fig. 2). Most metals (tin, iron, nickel, aluminum, silicon, cobalt, arsenic) form intermetallic compounds with copper which reduce ductility and some other mechanical properties of the alloys. Oxygen is a harmful impurity since in case of its large content, electrical and thermal conductivity, plasticity and

corrosive properties are sufficiently reduced.In casting process, Boron is an effective deoxidizer for copper, while it has no negative effect on electrical conductivity [ ].

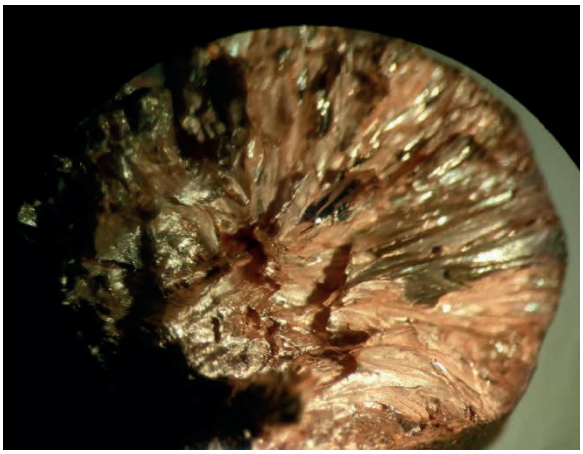


Figure 2. Cross section view of copper wire produced by vertical casting process.

- Cracks of the wire during wiredrawing process. It is also know that the main cause of initiation of hot cracks is saturation of the melt copper with hydrogen and formation of microspores during crystallization of copper.

5. Conclusion

In this scientific contribution, the manufacture of copper wire by continuous casting was introduced. The parameters of this process have been listed and we have shown the importance of each parameter such as cooling water flow rate, casting speed, and melting temperature. In addition, the challenges of producing copper wires were discussed. The main challengers are the cracks observed in copper wire which can be due to high solubility of oxygen. Oxygen is considered as a harmful impurity since in case of its large content, electrical and thermal conductivity, plasticity and corrosive properties are sufficiently reduced. The appropriate solution for this problem is the use of boron in copper liquid, because it is an effective deoxidizer for copper.

References

1. Wilson, M. Copper Wire Manufacturing Project Report , Plant Setup, Industry Trends, Business Plan, Machinery Requirements, Raw Materials, Cost and Revenue 2026 , **2021**
2. Olaru, P. Improving the Electrical Conductivity of Copper. Conference: Journées Annuelles de la SF2M 2011 SF2M Annual Meeting **2011**.
3. Elfsberg, J. Oscillation Mark Formation in Continuous Casting Processes, Casting of Metals. Royal Institute of Technology, Stockholm, Sweden, **2015**.
4. Cuypers, P. F. Continuous Casting in the Copper Industry. (EUT - BDK report. Dept. of Industrial Engineering and Management Science;Technische Universiteit Eindhoven. **1987**. 29..
5. Bagherian, E.R., Fan, Y., Cooper, M., Frame, B., and Abdolvand, A. Effect of Water Flow Rate, Casting Speed, Alloying Elements and Pull Distance on Tensile Strength, Elongation Percentage and Microstructure of Continuous Cast Copper Alloys. Metall. Res. Technol. **2016**, 113, 308.

6. Knych, T., Smyrak, B., Walkowicz, M., Research on the Influence of the Casting Speed on the Structure and Properties of Oxygen-free Copper Wires. AGH University of Science and Technology, Poland, **2011.**
7. Alexander, W.O., Davies, G.J., Reynolds, K.A., Bradbury, E.J., Essential Metallurgy for Engineers. pp. 63-71, Van Nostrand Reinhold (UK) Co.Ltd. ISBN: 0-442-30624-5. **1985 .**
8. Technical Recoprt:Some General Comparison of Small Diameter Copper Wire Rod Products,Download on 01/10/2021 from http://www.conticast.com/documents/CuOF%20or%20CuETP%20--%20GENERAL%20COMPARISONS.pdf
9. Konečná, R., and Fintová, S. Copper and Copper Alloys: Casting, Classification and Characteristic Microstructures, Copper Alloys - Early Applications and Current Performance - Enhancing Processes, Edited by: Luca Collini, **2012**.

S32205 DUBLEKS PASLANMAZ ÇELİKLERDE ISIL İŞLEM SICAKLIKLARININ MİKROYAPI VE SERTLİK ÖZELLİKLERİNE ETKİLERİ

MERVE DUMAN[1], AZIZ BARIŞ BAŞYIGIT[2], HALIL IBRAHIM KURT[3]

[1]Metalurji ve Malzeme Mühendisi, Tedsan Teknik Makine Dişli Ltd.Şti, Ankara, TÜRKİYE.
[2]Kırıkkale Üniversitesi, Mühendislik Fakültesi, Metalurji ve Malzeme Mühendisliği Bölümü, Kırıkkale, TÜRKİYE.
[3]Gaziantep Üniversitesi, Mühendislik Fakültesi, Metalurji ve Malzeme Mühendisliği Bölümü, Gaziantep, TÜRKİYE.

Özet

Dubleks paslanmaz çelikler günümüzde başlıca petrokimya tesisleri, endüstriyel su arıtma sistemleri, köprüler olmak üzere birçok alanda artarak tercih edilmektedir. Dubleks paslanmaz çeliklerin yapısında yaklaşık eşit oranlarda ferrit ve östenit fazları bulunmaktadır. Dubleks paslanmaz çelikler, üstün korozyon dirençleri ve tatminkar mekanik dayanım özellikleriyle öne çıkmaktadırlar. Bu çalışmada; 3 mm kalınlığında ve 10x25 mm ebatlarında S32205 dubleks paslanmaz çelik plakalar hazırlanmış, çeşitli ısıl işlem sıcaklıklarının mikroyapısal değişikliklere ve mikro-sertlik özelliklerine etkileri incelenmiştir. 815°C 'den doğrudan oda sıcaklığına soğutulan numunelerde sigma fazı oluşumundan dolayı en yüksek sertlik değeri gözlenmiştir.

Anahtar kelimeler: Dubleks Paslanmaz Çelikler, Çözeltiye Alma Isıl İşlemi, Dubleks Paslanmaz Çeliklerin Mikro-yapıları.

1.Giriş

Dubleks paslanmaz çelikler, nikel ve krom temel alaşım elementleri içerirler. Krom; ferrit faz yapısını, nikel ise östenit oluşumunu kararlı hale getirmektedir. Dubleks paslanmaz çeliklere ilave edilen azot elementi, östenit oluşumunu desteklemektedir [1]. Dubleks paslanmaz çelikler ferritik paslanmaz çeliklerin sahip olduğu yüksek gerilim korozyon direncine ve östenitik paslanmaz çeliklerin yüksek süneklik, tokluk ve yeterli kaynak kabiliyetine bir arada sahiptirler [2]. Dubleks ikili faz yapısından ve yüksek krom ve molibden içeriğinden dolayı çukur korozyonuna, çatlak korozyonuna ve gerilmeli korozyon çatlağına karşı tatminkar dirence sahiptirler [3]. Dubleks paslanmaz çelikler, yeterli düzeyde mekanik ve korozyon dayanımı özellikleri sergilemelerinden dolayı bu iki hususun birlikte arandığı uygulamalarda güvenli kullanım olanağı sağlarlar [4]. Bu alaşımlar, günümüzde gıda sektöründe de artan miktarlarda tercih edilmektedirler [5].

Dubleks paslanmaz çelikler, Fe-Cr-Ni üçlü faz diyagramından faydalanılarak geliştirilmişlerdir. Yapılarında dengeli miktarlarda bulundurduğu bu temel fazlar dışında ısıtma ve soğutma şartlarında ayrıca sigma ve chi gibi çeşitli ikincil fazlarda oluşabilmektedir [6]. Dubleks paslanmaz çelikler yapılarında, birincil (δ ve ɣ) ve ikincil (ɣ2, σ, χ, π, karbürler ve nitrürler) fazları bulundurabilmektedir. Yüksek sıcaklıklarda yapıda oluşan bu ikincil oluşumlar, metaller-arası fazlar olarak karşımıza çıkmaktadır [7]. Dubleks paslanmaz çeliklere uygulanan ısıl işlem sıcaklıkları ve soğutma hızları; sertlik korozyon dayanımı gibi temel özelliklerin, faz yapılarının ve çeşitli çökeltilerin ortaya çıkmasında rol oynayan önemli etkenlerdir [1, 2, 8].

Dubleks paslanmaz çeliklere uygulanan ısıl işlemler sırasında oluşan ferrit-östenit faz oranına, tane sınırlarında çöken metaller-arası fazlara dikkat edilmeli, ısıl işlemler bu hususlar göz önünde bulundurularak tasarlanmalıdır [9]. İkincil fazların oluşumu malzemede ferrit-östenit dengesini değiştirmekte ve bu da mekanik ve korozyon özelliklerini etkileyebilmektedir [10]. Dubleks paslanmaz çeliklerde uygulanan ısıl işlem sıcaklıklarından oda sıcaklığına soğutma işleminde, artan soğuma hızının delta ferrit fazı oranı lehine bunun yanında östenitin ise aleyhine olacak şekilde sonuçlanmaktadır [1,2].

Bu çalışmada; 3x10x25 mm boyutlarında hazırlanmış olan S32205 dubleks paslanmaz çelik sac numunelerin farklı ısıl işlem koşullarının mikro-sertlik ve mikro-yapı üzerindeki etkileri incelenmiştir.

2. Malzeme ve Deneysel Yöntemler

Çalışmada, deneysel malzeme olarak 3x10x25 mm ebatlarında S32205 dubleks paslanmaz çelik numuneler kullanılmıştır. Deneysel malzemenin Spectromax Amatek Argon Spektral analiz cihazından elde edilen kimyasal kompozisyonu Tablo 1' de verilmektedir.

Tablo 1. S32205 alaşımının spektral analizi (% ağırlıkça)

C	Mn	P	S	Si	Cr	Ni	Mo	Fe	N	Diğerleri
0.032	0.83	0.023	0.0039	0.42	24.9	6.62	3.51	62.9	0.3	0.461

Tablo 2. Isıl işlem koşulları

Numune No.	1. ön ısıtma Sıcaklığı (° C)	1.ön ısıtma süresi (dakika)	2.ön ısıtma sıcaklığı (° C)	2.ön ısıtma süresi (dakika)	Çözeltiye alma sıcaklığı (° C)	Çözeltiye alma süresi (dakika)	Soğutma ortamı	Soğutma süresi (dakika)
1	550	15	800	8	1040	3	Sakin hava	Oda sıcaklığına kadar
2	550	15	800	8	1040	3	Sakin su	Oda sıcaklığına kadar
3	550	15	800	8	1040	3	Sakin yağ	Oda sıcaklığına kadar
4	550	15	800	8	1040	3	Sakin banyo (500° C)	2
5	550	15	800	8	1040	3	(%4.5) Polimerli su	Oda sıcaklığına kadar
6	550	15	800	8	1040	3	Sakin banyo (310° C)	2
7	550	15	800	8	1040	3	Sakin mazot	Oda sıcaklığına kadar
8	550	15	800	8	1040	3	Sakin banyo (200° C)	2
9	550	15	-	-	815	60	--	Oda sıcaklığına kadar

S32205 dubleks paslanmaz çeliğin ısıl işlem görmemiş hali ile ısıl işlemler sonrası mikro-yapısal incelemeleri yapılmıştır. Deneysel malzemelerin çözeltiye alma sıcaklığı 1040°C'de olarak seçilmiş ve 9 farklı koşulda ısıl işlem gerçekleştirilmiştir. Test numunelerine uygulanan 9 farklı ısıl işlem koşulları Tablo '2 de verilmiştir.

2.1. Mikroyapısal İncelemeler

Deneysel numuneler bakalite alma işlemlerinden sonra 240 ile 800 numara aralığında zımparalama kağıtları ile zımparalanmış ve 6µm elmas pasta ile parlatılmışlardır. Ardından elektrolitik dağlama yöntemiyle %20 NaOH çözeltisinde dağlanmıştır [11]. Test numunelerinin mikro-yapıları Leica marka 1000 kez büyütme kapasiteli metalurji mikroskobunda incelenmiştir.

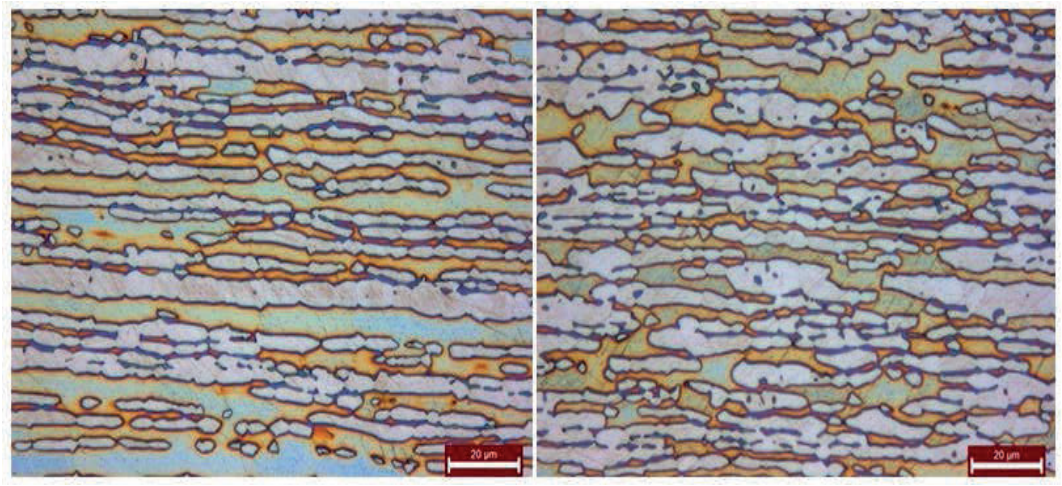
2.2. Mikrosertlik İncelemeleri

Ham malzemenin ve ısıl işlem sonrası bütün test numunelerinin sertlikleri, HV10 kg yük altında vikers sertlik ölçme yöntemiyle laboratuar ortam sıcaklığında 22° C'de taranmıştır [12].

3. Deneysel Bulgular

3.1. Mikroyapısal İncelemeler

Ana malzemenin mikro-yapıları

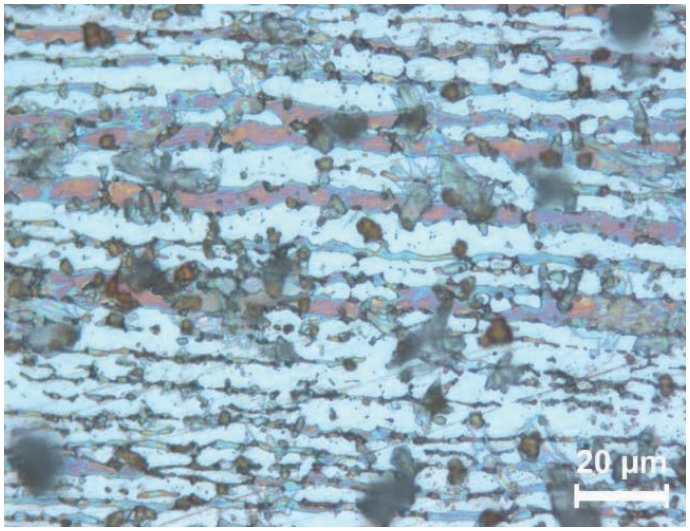


(a) (b)

Şekil 1. S32205 dubleks paslanmaz çeliğin (a) Boyuna (haddeleme yönü), (b) Enine (haddeleme yönüne dik) mikro-yapıları

Şekil 1'de S32205 dubleks paslanmaz çeliğin (işlem görmemiş haliyle ana malzemenin) kullanıma sunulduğu haldeki mikro-yapıları görülmektedir. Haddelenmiş çeliğin tane yönlenmeleri görülmektedir.

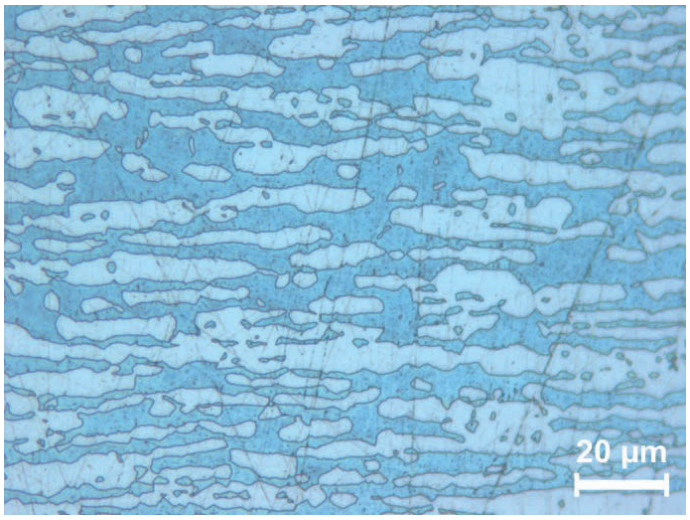
Açık renkli (beyaz) olan faz östeniti, koyu renkli (kahverengi) faz ise delta-ferriti (yüksek sıcaklık ferriti) ifade etmektedir. Östenit ve delta ferrit haricinde başka bir faz veya çökelti tespit edilmemiştir.Sakin havada soğutulan Numune 1'e ait mikro-yapı Şekil 2' de verilmektedir.



Şekil 2. Sakin havada soğutulmuş Numune 1 mikro-yapısı

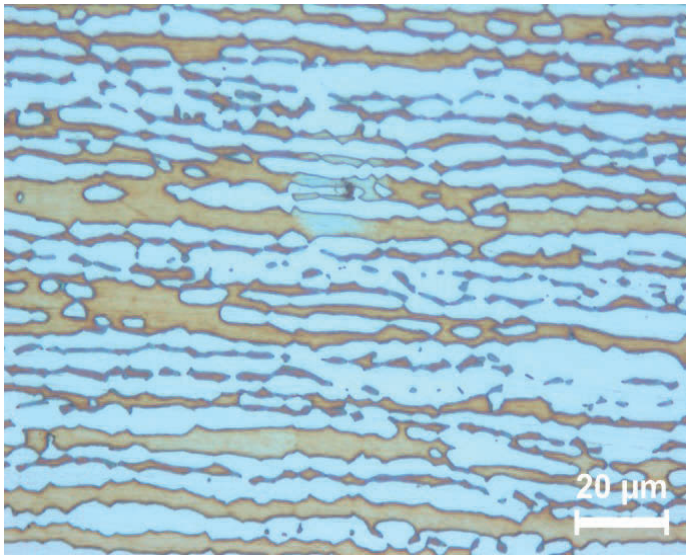
Şekil 2'de sakin havada soğutulan S32205 dubleks paslanmaz çeliğin mikro yapıları incelendiğinde havada nispeten yavaş soğuma neticesinde Fe-Cr bileşiklerinin oluşum sıcaklık aralıkları (yaklaşık 800°C) yavaş geçildiğinden mikro-yapıda en koyu renkli olan bölgelerin sigma benzeri Fe-Cr çökeltilerini oluşturduğu görülmektedir. Açık renkli (beyaz) fazlar östeniti, kahverengi bölgeler ise delta ferriti ifade etmektedir [1,2].

Sakin suda soğutulmuş Numune 2' ye ait mikro-yapı Şekil 3 'de verilmektedir.



Şekil 3. Sakin suda soğutulmuş Numune 2 mikro-yapısı

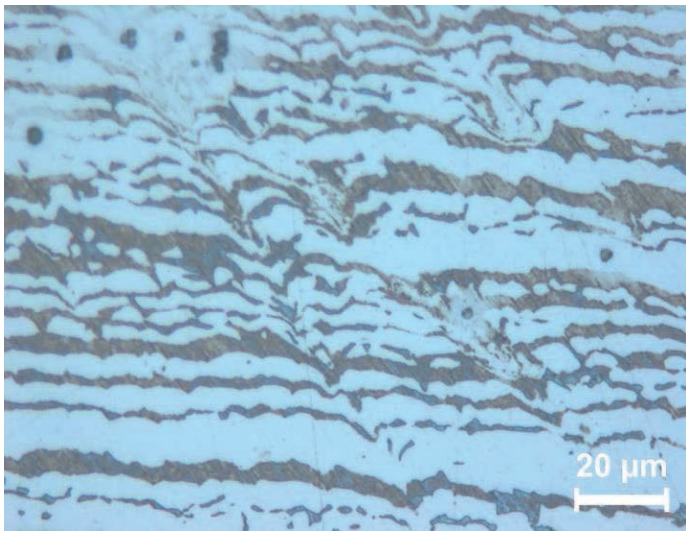
Sakin suda soğutulan numunelerin Şekil 3'deki mikro-yapısı incelendiğinde ana malzemeye benzer olarak yapının östenit ve delta-ferritten oluştuğu anlaşılmaktadır. Açık renkli beyaz yapı östeniti, koyu renkli (mavimsi) yapı ise delta-ferriti ifade etmektedir.
Sakin yağda soğutulmuş Numune 3'e ait mikro-yapı Şekil 4' de verilmektedir.



Şekil 4. Sakin yağda soğutulmuş Numune 3 mikro-yapısı

Yağda soğutulan numuneler, Şekil 4'de görüleceği gibi suda soğutulan numunelere yakın mikro-yapılara sahip olmuştur. Yağda soğutma işlemi soğutma hızını azaltsa da zararlı Fe-Cr çökeltilerinin oluşumuna fırsat vermeyecek şekilde dönüşüm tamamlanmıştır. Ancak suya göre nispeten daha yavaş soğuma hızında dolayı östenit oranının bir miktar arttığı gözlenmiştir.

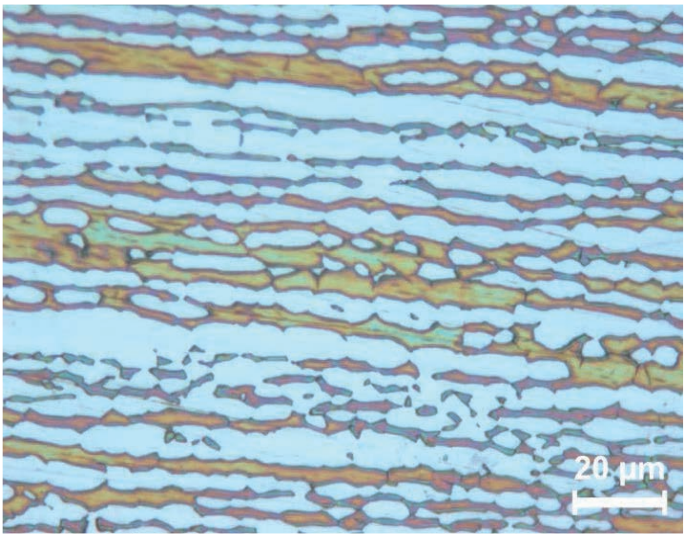
Sakin banyoda 500 °C' de izotermal sıcaklıkta soğutulmuş olan Numune 4'e ait mikro-yapı Şekil 5 'de görülmektedir.



Şekil 5. Sakin banyoda 500 °C' de izotermal sıcaklıkta soğutulmuş olan Numune 4 mikro-yapısı

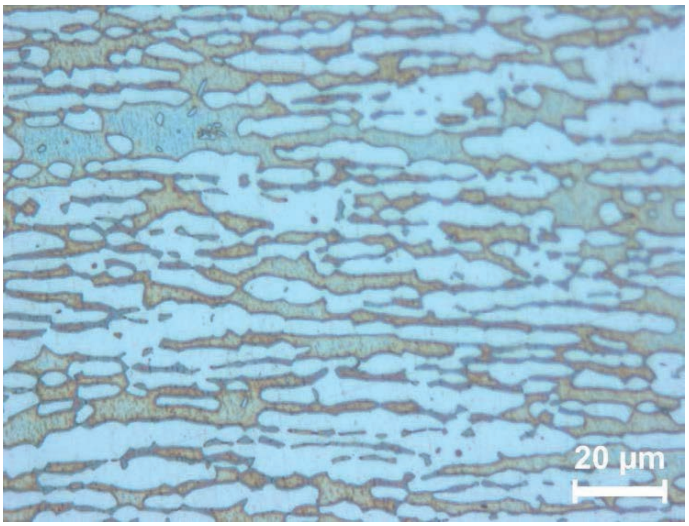
Şekil 5 incelendiğinde; östenitleme sonrası izotermal 500 °C sabit sıcaklıktaki banyoda bekletilip daha sonra havada soğutulan numunelerin faz yapısında bir miktar ikincil fazlar (en koyu bölgeler) tespit edilmiştir [1,2]. Östenit ve delta ferritin yapılarında bir değişiklik gözlenmezken, yapıda açık renk östeniti orta koyu tonda renk ise delta-ferriti ifade etmektedir.

Oda sıcaklığında bekletilen Polimerli suda soğutulmuş olan Numune 5'e ait mikro-yapı Şekil 6 'da verilmektedir.



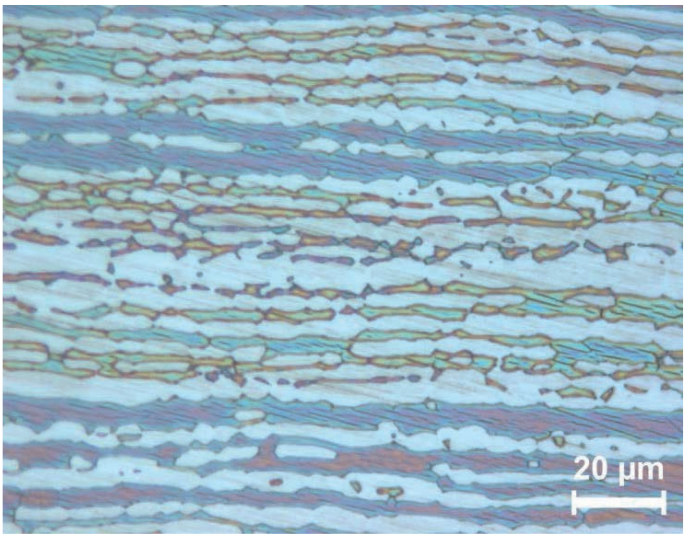
Şekil 6. Polimerli suda soğutulmuş olan Numune 5 mikro-yapısı

Şekil 6 incelendiğinde; Polimer katkılı suda su verilen numunelerde suda su verilenlere benzer bir mikro-yapı dağılımı gözlenmiştir. Benzer şekilde açık renkli (beyaz) faz östeniti, koyu renkli (kahverengi) faz ise delta ferriti ifade etmektedir. Sakin banyoda 310°C sıcaklıkta soğutulan Numune 6'ya ait mikro-yapı Şekil 7 'de görülmektedir.



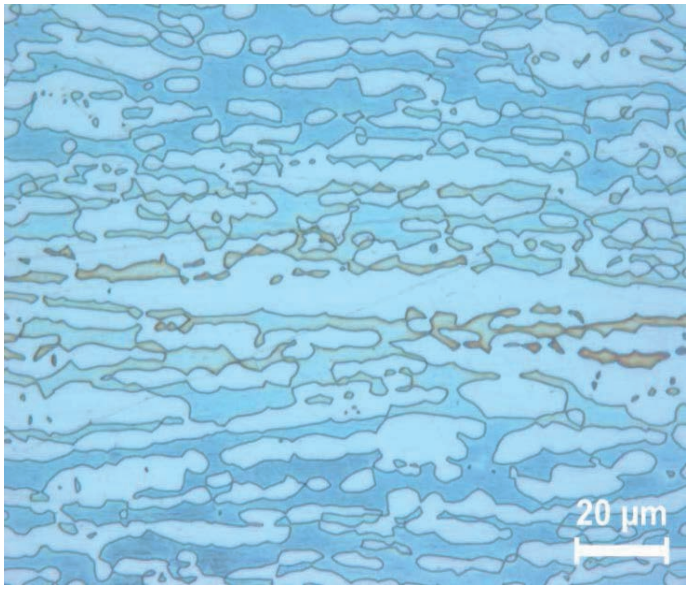
Şekil 7. Sakin banyoda 310°C sıcaklıkta soğutulan Numune 6 mikro-yapısı

Şekil 7 incelendiğinde, östenitleme sonrası 310°C sıcaklıkta izotermal olarak soğutulan ve ardından sakin havada soğutulan numunelerin mikro-yapıları baskın olarak yine östenit ve delta ferritten meydana gelmektedir. Ayrıca başka bir faz veya çökeltiye rastlanmamaktadır. Haddeleme yönü mikro-yapılardan görülmektedir.Sakin mazot ortamında soğutulmuş Numune 7' ye ait mikro-yapı Şekil 8 'de verilmektedir.



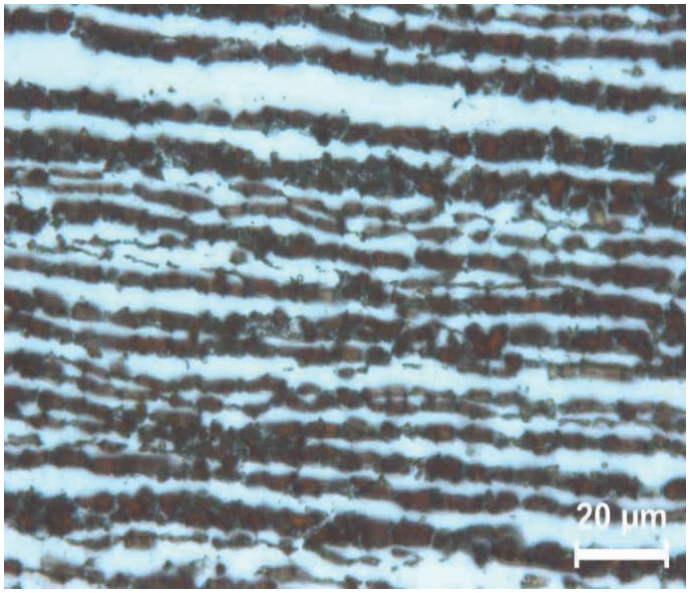
Şekil 8. Sakin mazot ortamında soğutulmuş Numune 7 mikro-yapısı

Şekil 8 incelendiğinde; soğutma ortamı olarak oda sıcaklığındaki mazotta soğutulan numuneler mikro-yapılarında suda soğutulan numunelere benzer östenit ve delta ferrit dağılımı sergileseler de suya göre nispeten daha yavaş soğuma hızı nedeniyle az miktarda da olsa östenit faz içeriğinde artış görülmektedir. Sakin banyoda 200°C sıcaklıkta soğutulmuş Numune 8'e ait mikro-yapı Şekil 9 'da görülmektedir.



Şekil 9. Sakin banyoda 200°C sıcaklıkta soğutulmuş Numune 8 mikro-yapısı

Şekil 9' da östenitleme sonrasında 200°C sıcaklıkta izotermal olarak soğutulan ve ardından sakin havada soğutulan numunelerin mikro-yapıları incelendiğinde östenitik-delta ferritik yapının dışında bir faz veya çökeltiye rastlanmamıştır. Açık renkli fazlar östeniti koyu renkli fazlar ise delta ferriti ifade etmektedir.200°C sıcaklıkta bekletme işlemi oda sıcaklığına soğuma işlemini bir miktar yavaşlatması sonucu az miktarda da olsa östenit lehine bir faz içeriğine sahip olunmasına neden olmuştur. 815 °C sıcaklıkta 1 saat süreyle bekletilmiş ve oda sıcaklığına soğutulmuş Numune 9 mikro-yapısı Şekil 10 'da verilmektedir.



Şekil 10. 815 °C sıcaklıkta 1 saat bekletilip oda sıcaklığına soğutulmuş Numune 9 mikro-yapısı

Şekil 10 incelendiğinde, açık renkli fazlar östeniti kahverengi fazlar delta ferriti koyu kahverengi fazlar ise sigma fazını ifade etmektedir. Zengin bir Fe-Cr bileşiği olan sigma fazı 800°C sıcaklık civarında en hızlı oranda oluşmakta ve matristeki toplam Cr elementi içeriğini düşürmekte bunun bir sonucu olarak korozyon direncini azaltabilmektedir [1,2,9].Bununla birlikte sigma fazı gevrek bir faz olmasından dolayı dubleks paslanmaz çeliklerde istenmemektedir. Östenit, delta ferrit ve sigma dışında başka bir çökelti veya faz içeriğine rastlanmamıştır.

3.2. Mikro-sertlik Taramaları

Isıl işlemler sonrası deneysel numunelerin sertlik değerleri, Vickers Sertlik ölçme cihazında HV 10 kg yük uygulanarak ölçülmüştür. Sertlik değerleri Tablo 3' de verilmiştir. Ham malzemenin sertliği ortalama 302 HV olarak kayıt edilmiştir. Sakin havada soğutulan numunelerde ikinci sırada yüksek sertlik değerleri gözlenmiş bunun temel nedeninin nispeten yavaş soğuma hızı ile muhtemel ikincil sert çökeltilerin oluşumlarına fırsat bulunmasıdır. En yüksek sertlik değeri 815°C de 1 saat süre bekletilerek oda sıcaklığına doğrudan soğutulan numunede tespit edilmiştir. Bu durumun nedeni; bu sıcaklık değerinin dubleks paslanmaz çelikler için sigma fazı gibi gevrek ve sert Fe-Cr bileşiğinin optimum oluşum sıcaklığı olduğu anlaşılmaktadır [1,2,11].

Tablo 3. Test numunelerinin sertlik değerleri

Numune No. (soğutma koşulları)	**Vickers Sertlik Değeri (ortalama HV10)**
1 (Sakin hava)	307
2 (Sakin Su)	284.4
3 (Sakin yağ)	275.4
4 (Sakin banyo 500°C)	290.9
5 (%4.5 polimerli su)	272.9
6 (Sakin Banyo 310°C)	280.1
7 (Sakin mazot)	278.3
8 (Sakin Banyo 200°C)	290.2
9 (815°C 'den oda sıcaklığına soğutma)	428.7

4. Sonuç

Dubleks paslanmaz çeliklerde çözeltiye alma ve su verme (soğutma) teknikleri yardımıyla arzu edilen östenit-delta ferrit faz ve ikincil çökeltilerin dağılımının sağlanması sonucunda gereken sertlik ve korozyon dayanımı değerleri de ayarlanabilmektedir.

Bu çalışmada kullanılan S32205 dubleks paslanmaz çeliğine farklı ısıl işlem ortamlarında farklı soğutma koşulları ile birlikte sigma gibi bazı zararlı çökeltilerin oluşma sıcaklıkları da düşünülerek ısıl işlemler uygulanmıştır. Bu alaşımların tedarik ediliş hali olan 1040°C' de çözeltiye alma ve ardından suda su verme ısıl işlemi ile östenit ve delta ferrit faz dağılımının yakın değerlerde oluşturulduğu gözlenmiştir. Bu alaşımlarda, 800 °C civarındaki ısıl işlem veya kullanım sıcaklıklarında sigma fazı gibi sert ve gevrek bir demir-krom bileşiğinin toplam sertliği artırabildiği tespit edilmiştir.

Sertlik tarama testlerinde; numunelerin tamamının sertlik değerlerinin birbirine yakın olduğu anlaşılmış ancak 815°C de bekletilerek darbe dayancını ve korozyon direncini de düşürebilen zararlı sert ve gevrek sigma fazı oluşturulan numunede sigma fazından dolayı sertlik değerleri diğer tüm deneysel numunelere göre daha yüksek tespit edilmiştir.

Dubleks paslanmaz çeliklerde sigma ve benzeri çeşitli zararlı faz ve çökeltilerin oluşabildiği sıcaklık aralıklarına; ısıl işlem, kaynak, sıcak şekillendirme gibi termal uygulamalarda ve ilgili kullanım ortamlarında dikkat edilmelidir.

Teşekkür

Yazarlar, MKE Mühimmat Fabrikası Isıl işlem atelyesi personeline destekleri için teşekkür ederler.

Referanslar

1. Lippold, J.C.., Kotecki, D.J. Welding Metallurgy and Weldability of Stainless Steels; John Wiley and Sons Inc. Hoboken, NJ, USA, **2005**, 250–251.
2. Gunn, R.N. Duplex Stainless Steels Microstructures Properties and Applications; Abington Publishing: Cambridge, UK, **2005**, 24–76.
3. Liou, H.-Y.; Pan, Y.-T.; Hsieh, R.-I.; Tsai, W.-T. Effects of Alloying Elements on the Mechanical Properties and Corrosion Behaviors of 2205 Duplex Stainless Steels. J. Mater. Eng. Perform. **2001**, 10, 231–241.
4. Kou, S. Welding Metallurgy, 2nd ed.;Wiley Interscience Publications: Hoboken, NJ, USA, **2002**.
5. Stainless, T. M. R.., Practical Guidelines for the Fabrication of Duplex Stainless Steel, International MolybdenumAssociation (IMOA), London, **2009**.
6. Sevilay A., Dubleks Paslanmaz Çelikte Oluşan Sigma ve Chi Fazlarının Oluşum Mekanizmalarının Farklı Isıl İşlem Parametreleriyle Saptanması, Yüksek Lisans Tezi, Yıldız Teknik Üniversitesi, Fen Bilimleri Enstitüsü, İstanbul, **2014**.
7. Türkyılmazoğlu A., Dubleks, Martenzitik ve Ferritik Paslanmaz Çeliklerin Kaynağı, Yüksek Lisans Tezi, Sakarya Üniversitesi Fen Bilimleri Enstitüsü, Adapazarı, **2006**.
8. Kısaöz A., Karaslan A., Dubleks Paslanmaz Çeliklerde Oluşan Yüksek Sıcaklık Fazlarına Genel Bir Bakış, Metalurji , **2012,** 7, 57-61,.
9. Nowacki J., Lukojc A., "Structure and Properties of the Heat-Aff ected Zone of Duplex Steels Welded Joints", Journal of Materials Processing Technology **2005,** 1074–1081**.**

10. Yalçıner,G.., Özer,G.., Kısasöz,A.., and Karaaslan,A.., Influance of the phase balance and cooling conditions on the microstructure and corrosion behaviour of solution-treated 1.4462 duplex stainless steel. Materials Research Express, **2019,** 6(12), 1-9.
11. ASM Handbook Committee. ASM Metals Handbook Volume 9: Metallography and Microstructures of Stainless Steels and Maraging Steels; George, F., Vander, V., Eds.; ASM International: Materials Park, OH, USA, **2004**.
12. ASTM A370, Standard Test Methods and Definitions for Mechanical Testing of Steel Products; ASTM International: West Conshohocken, PA, USA, **2020**.

EXPLORING THE PHOTOCATALYTIC CAPABILITY OF DMAHDM-MODIFIED ZINC OXIDE AND ITS BISEMA-TEGDMA COMPOSITES

ILKNUR TAS KAZAK*, DERYA KAPUSUZ YAVUZ

Dept. of Metallurgical and Materials Engineering, Engineering Faculty, Gaziantep University, 27310 Gaziantep/Turkey

Abstract

Recently, Zinc oxide (ZnO) has become a commonly used material in dental applications owing to its semiconductor structure, biocompatibility and photocatalytic capability. It has been shown that ZnO reinforcement into dental resins increased their mechanical strength and enhanced the aesthetics, structural and antibacterial properties. In this work, ZnO nanoparticles were synthesized using the sol-gel process and coated with dimethyl aminohexadecyl methacrylate (DMAHDM), a quaternary ammonium methacrylate with antibacterial properties. The particles were calcined at 500 and 800°C for 3h. The particles were then dispersed in subsequently prepared BisEMA-TEGDMA co-monomer mixture, at a concentration of 2 wt. %. After the addition of initiator and the co-initiator, the composites were light-cured. The ZnO particles were characterized using x-ray diffraction (XRD) and scanning electron microscopy (SEM). Photocatalytic degradation tests using methyl orange as a model dye was applied on the composites. Results indicated that DMAHDM-coating on ZnO resulted in enhanced photocatalytic activity up to 24h. A remarkable degradation was observed on the composite containing DMAHDM-coated ZnO calcined at 800°C for 3h compared to 500 °C for 3h. It was observed that not only DMAHDM, but also calcination had a profound effect on the photocatalytic performance.

Keywords: Zinc oxide, Sol-gel, Methacrylate, Photocatalytic, Dental resin

1.Introduction

In the last decades, research on hybridizing bioactive ceramics with nontoxic polymers has gained considerable interest for use in biomedical applications. Contrary to their fragile structure; low-strength and durability of polymers, enhanced mechanical and functional properties of ceramic-polymer hybrids increased the utilization potential of them in the biomedical field. High chemical inertness, aesthetic appearance and higher compression strength made them attractive in restorative dentistry [1]. These materials which form the matrix in the composite provided high mechanical strength, antibacterial effect, photocatalytic properties and biocompatibility [2].

ZnO is a nontoxic, bioceramic material with photocatalytic capability that can be modified by controlling the particle morphology and size. It can be synthesized in various sizes and morphologies using several methods. Solvothermal and sol-gel methods are the most common methods for the production of ZnO structures. Compared to the solvothermal method, sol-gel method is the most economical and practical method providing control of the processing parameters such as pH, temperature, and the concentration of additives [3-5]. In this manner, sol-gel derived ZnO has attracted a lot of attention with its photocatalytic degradation capability of pollutants including bacteria for use in self-cleaning applications [6-8].

On the other hand, DMAHDM is a quaternary ammonium methacrylate that is used as an antibacterial additive in dental restoration seals [9]. It increases the bonding efficiency of dentin-restoration interface and can prevent biofilm formation by electrostatically attracting bacteria owing to its positive surface charge, and bursting the cell membrane [10]. Taking the antibacterial requirements in dental restorations to prevent biofilm formation into account, synthesis of hybrids with both antibacterial ingredients and photocatalytic capabilities holds a remarkable promise for developing dental restorations with prolonged service life. In this work, DMAHDM-ZnO hybrids were synthesized by sol-gel method following calcination and an additional solution step. ZnO particles with three distinct morphologies were produced and modified by 2 wt. % DMAHDM. Later on, the hybrids were dispersed in BisEMA-TEGDMA co-monomer. To test the photocatalytic degradation behavior of the particles and composites, methyl orange was used as a model pollutant.

2. Materials and Methods

Materials

For the synthesis reactions, zinc acetate dihydrate (ZAD; Zn(CH3COO)2.2H2O; %, Sigma-Aldrich 98 %379786) was used as the Zn source. Sodium hydroxide (NaOH; 98 %; Isolab969.113) was used as a catalyst. Ethanol (C2H5OH, 99.9%, Sigma-Aldrich 32205) and. deionized water (RNAse free, Human ®) were used as solvent and the dispersing medium. BisEMA (Sigma-Aldrich 455059) and triethylene glycol dimethacrylate (TEGDMA; Sigma-Aldrich 261548) were used as dental monomers. Camphorquinone (CQ, Sigma-Aldrich 124893) and 2-(Dimethylamino)ethyl methacrylate (DMAEMA, Sigma-Aldrich 234907) were used as the initiator and co-initiator, respectively for the polymerization reactions. 1-Bromohexadecane 97% (BHD; Sigma-Aldrich 234451) was used to synthesize DMAHDM. Methyl Orange (MO; 85%, Merck 114510) was used as a model pollutant in photocatalytic degradation tests.

Synthesis of ZnO particles

12 g of ZAD was dissolved in 15 mL DI water and stirred 10 min at 500 rpm. After 8 g NaOH was dissolved in 10 mL DI water, NaOH solution was poured into ZAD solution. Then the solution was stirred for 5 min. After that, 100 mL ethanol was added dropwise and the solution was kept at 75°C for 1h. Lastly, the precipitate formed in the solution were dried at 90°C overnight. The sample was coded as B5. After calcination at 500 and 800 °C for 3h, the samples were coded as B5K5 and B5K8, respectively.

Synthesis of DMAHDM

Using the Menschutkin method, 10 mmol BHD and 10 mmol DMAEMA were dissolved in 3 g of ethanol, respectively in 20 mL autoclavable glass bottle. The solution was kept at 70°C for 24h. Then ethanol was evaporated from the solution and viscous liquid was obtained [12].

DMAHDM modification of ZnO

0.75 g of ZnO (B5, B5K5 and B5K8) particles were added into 2 mL of DMAHDM and sonicated in an ultrasonic water bath at 50°C for 30 min. The mixture was stirred for 12 h at the same temperature then it was dried in an oven at 50°C for 5h. After DMAHDM-modification, sample codes were modified with letter D5, DB5K5 and DB5K8.

Production of DMAHDM modified ZnO reinforced BisEMA-TEGDMA Composites

In a typical composite synthesis, 3.6 g BisEMA and 2.4 g of TEGDMA was mixed at room temperature. When the monomer mixture became homogeneous after 10 min of stirring,

DMAHDM-ZnO particles DB5 was dispersed 2 wt. % and composite monomer was stirred at 800 rpm for 1h. Lastly, 0.06 g CQ and DMAEMA were added in the mixture and stirred additionally for 30 min. After that, it was transferred into molds made of silicone rubber and polymerized from their top surfaces using UltraDent Valo® LED light for 40 s. The same procedure was applied on DB5K5 and DB5K8 incorporated composites.

Characterization and Testing

The ZnO particles were analyzed by XRD using Bruker D8 Advance X-ray diffractometer. Samples were scanned at 2°/min scan rate in 20°–60° 2-theta range using monochromatic Cu-K_α radiation at 40 kV. The ZnO particle morphologies were investigated by SEM.

For the photocatalytic testing, the concentration of mother MO solution was prepared 5 mg/L. The specimens were put in 50 mL MO solution and isolated from day light by keeping them under dark in a UV-lamp (365 nm) equipped box. The distance between solution surface and UV-light was set to 40 cm. Specimens were first stirred under dark for 30 min for obtaining adsorption-desorption equilibrium. Next, UV-light was switched on and the solutions were continuously stirred at room temperature. For testing of particles, 4 mL aliquots were taken after 1h, 3h and 5h and syringe-filtered. For testing of composites, 4 mL aliquots were taken 1h and after 24h. The maximum absorbance (λ_{max}; chromophore) of MO is at 465 nm [13]. The behavior of degradation was observed by monitoring A compared to A_0 vs. time (A is the absorbance at 465 nm at time = t and A is the absorbance of pure MO solution at 465 nm at time = 0).

3. Results and Discussion

The XRD patterns of synthesized particles are shown in Fig. 1. Results demonstrate that the particles were composed of ZnO (ICDD: 80-0075) with some impurities [14-15]. After calcination, there was remarkable change occurred in the crystalline structure, except for the growth of (103) plane (at 66.80°). The morphology of the particles was investigated in the SEM images at Fig. 2. The B5 sample (before calcination) did not exhibit a significant morphology; mainly composed of agglomerated sheet-like irregular particles. Whereas, calcination at 500 °C for 3h (B5K5) resulted in the formation of nanofibers self-assembled in an urchin-like morphology in microscale diameter. Increasing the calcination temperature (B5K8) increased the free energy and promoted growth, therefore caused the nanofibers to attach themselves possibly on their high-energy surfaces, leading to formation of irregular chunks made of ZnO nanofibers and the impurities.

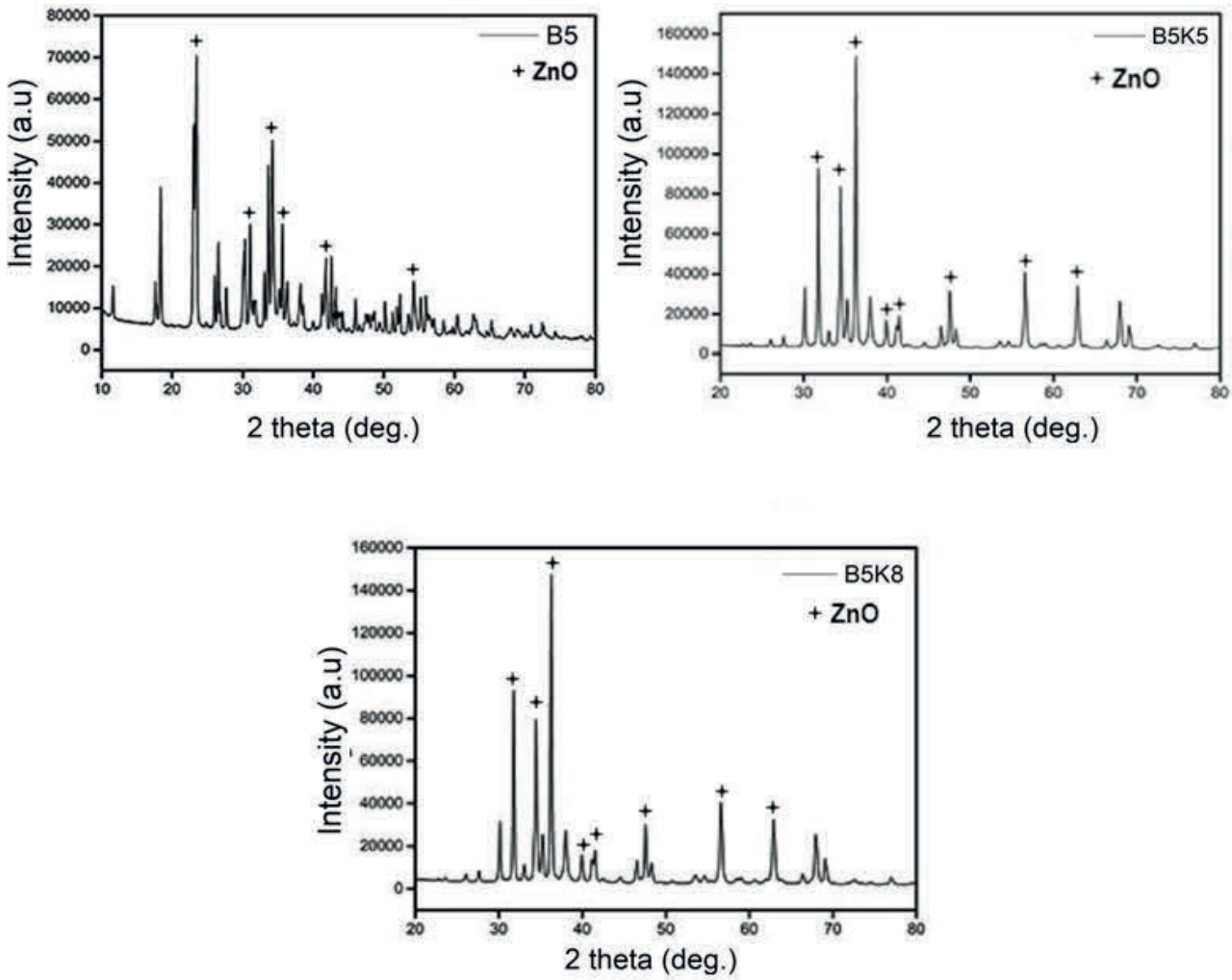


Fig.1. XRD patterns of a) B5, b) B5K5 and c) B5K8

Photocatalytic degradation capability of the ZnO particles is compared in Fig. 3. Fig.3a shows the change in absorbance of MO at 465 nm, after exposure to ZnO with respect to change in time. At time=0, the MO absorbance was at 0.48. Before UV-light was on, it did not change in time, meaning that no remarkable surface adsorption of MO was occurred on ZnO particles. As the light was on, the absorbance decreased slightly, indicating that B5 particles exhibited weak capability of MO degradation. It is known that the photocatalytic effect depends on the crystal structure, size, shape and porosity of the particle [16-17]. In this manner, as shown in Fig. 3b and 3c calcination resulted in fluctuations in degradation, possibly because of the presence of agglomerates and the impurities. B5 showed the highest and most stable performance after 5h. No appreciable absorbance was observed in the calcined samples after 5h.

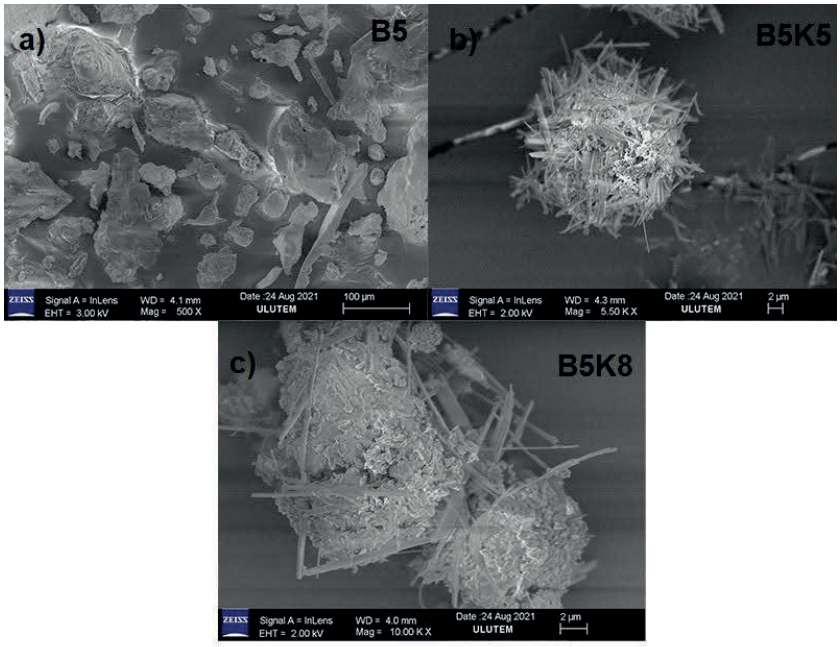


Fig. 2. SEM images of a) B5, b) B5K5 and c) B5K8

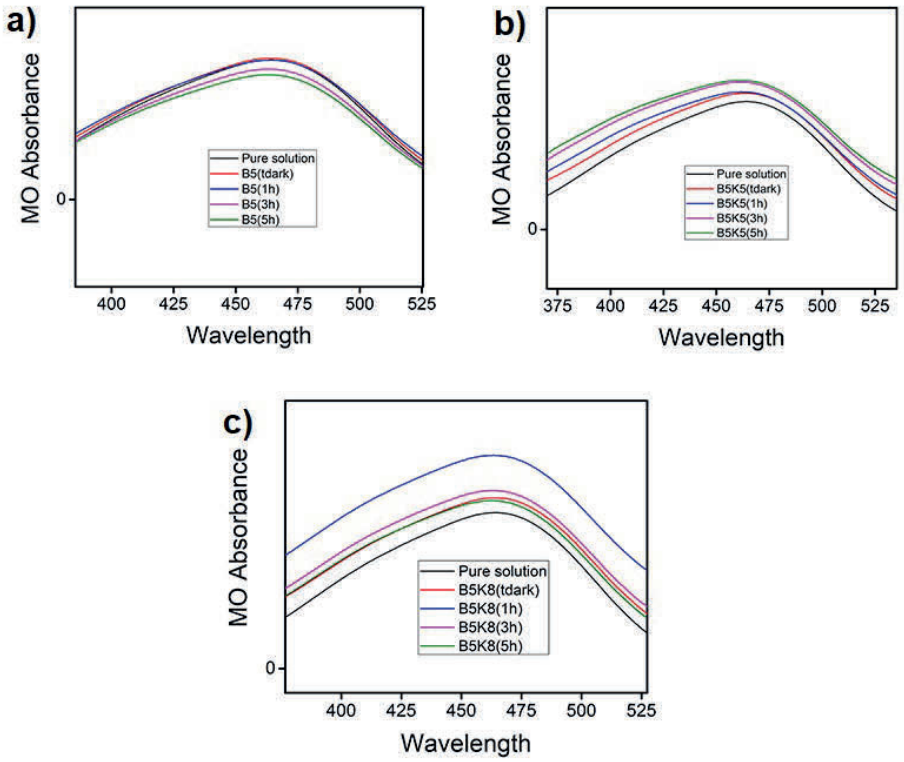


Fig. 3 MO dye adsorption of ZnO particles a) B5, b) B5K5 and c) B5K8

The photocatalytic degradation behavior of DMAHDM-modified ZnO incorporated (2 wt.%) composites were tested for 24 h and results are shown in Fig.4. Results indicated that the degradation performance of B5 decreased after modification with DMAHDM and incorporation

into the copolymer. It was possibly related to the inhibition of electron-hole mobility that was required for formation of the free radicals that degrade the pollutant on the surface. Surprisingly, composites of calcined samples showed more significant performance after 24h possibly because of less agglomeration leading to better dispersion in the matrix.

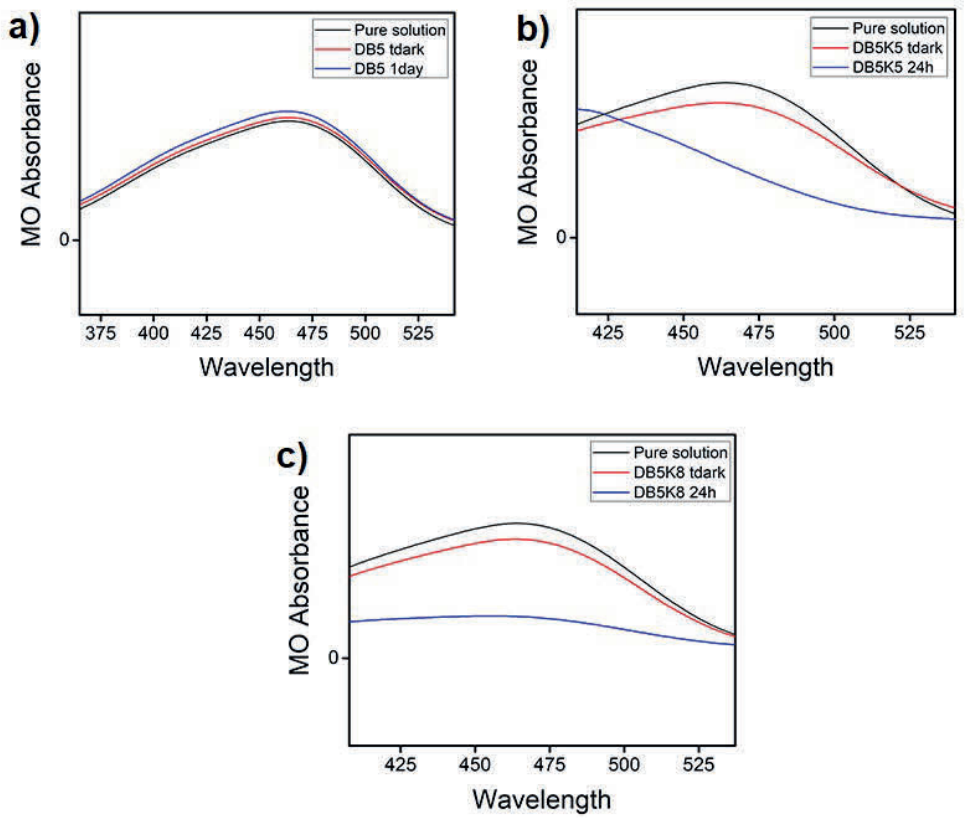


Fig. 4 MO dye degradation behavior of composites a) DB5, b) DB5K5 and c) DB5K8 incorporated BisEMA-TEGDMA

4. Conclusions

This study aimed to obtain a novel composite structure by hybridizing ZnO with antibacterial DMAHDM, and then incorporating them into BisEMA-TEGDMA resin composition. The photocatalytic capability of both the particles and composites were determined. It has also been observed that when the particles dispersed in the composite after calcination, they increased the photocatalytic performance. Results indicated that DMAHDM-modified ZnO particles, themselves and after incorporation into dental resins, show a significant promise for self-cleaning ability.

Acknowledgments

Authors would like to thank TUBITAK for partially funding the work under 1919B012001377.

References

1. Vallet-Regí, M., Ceramics for medical applications. *Journal of the Chemical Society, Dalton Transactions*, **2001**, 97-108.
2. Hojati, S. T., Alaghemand, H., Hamze, F., Babaki, F. A., Rajab-Nia, R., Rezvani, M. B., & Atai, M., Antibacterial, physical and mechanical properties of flowable resin composites containing zinc oxide nanoparticles. *Dental Materials*, **2013,** *29*(5), 495-505.

3. Ba-Abbad, M. M., Kadhum, A. A. H., Mohamad, A. B., Takriff, M. S., & Sopian, K.,**2013**. The effect of process parameters on the size of ZnO nanoparticles synthesized via the sol–gel technique. *Journal of Alloys and Compounds*, *550*, 63-70.
4. Yiamsawas, D., Boonpavanitchakul, K., & Kangwansupamonkon, W..,. Preparation of ZnO nanostructures by solvothermal method. *Journal of Microscopy society of Thailand*, 2009, *23*(1), 75-78.
5. Feng, Y., Zhang, M., Guo, M., & Wang, X.., Studies on the PEG-assisted hydrothermal synthesis and growth mechanism of ZnO microrod and mesoporous microsphere arrays on the substrate. *Crystal growth & design*, 2010, *10*(4), 1500-1507.
6. Ohira, T., Yamamoto, O., Iida, Y., & Nakagawa, Z. E.., Antibacterial activity of ZnO powder with crystallographic orientation. *Journal of Materials Science: Materials in Medicine*, **2008**, *19*(3), 1407-1412.
7. Al-Mosawi, R. M., & Al-Badr, R. M., The study effects of dental composite resin as antibacterial agent which contain nanoparticles of zinc oxide on the bacteria associated with oral infection. IOSR Journal of Dental and Medical Sciences, **2017**, 16(1), 49-55
8. Hojati, S. T., Alaghemand, H., Hamze, F., Babaki, F. A., Rajab-Nia, R., Rezvani, M. B., ... & Atai, M..,.Antibacterial, physical and mechanical properties of flowable resin composites containing zinc oxide nanoparticles. Dental materials, **2013**, 29(5), 495-505.
9. Zhou, H., Li, F., Weir, M. D., & Xu, H. H..Dental plaque microcosm response to bonding agents containing quaternary ammonium methacrylates with different chain lengths and charge densities. Journal of dentistry, **2013,** 41(11), 1122-1131.
10. Dangge, G., Xiying, D., Chen, C., Bin, L., & Jianzhong, M. Synthesis of polymer quaternary ammonium salt containing epoxy group/nano ZnO long-acting antimicrobial coating for cotton fabrics. Industrial & Engineering Chemistry Research, **2015,** 54(43), 10560-10567.
11. Ristić, M., Musić, S., Ivanda, M., & Popović, S. (2005). Sol–gel synthesis and characterization of nanocrystalline ZnO powders. Journal of Alloys and Compounds, 397, (1-2), L1-L4.
12. Wang, S., Wang, H., Ren, B., Li, X., Wang, L., Zhou, H., & Xu, H. H., Drug resistance of oral bacteria to new antibacterial dental monomer dimethylaminohexadecyl methacrylate. Scientific reports, **2018,** 8(1), 1-11.
13. He, Qiaohong, and Hengwu Chen. "Flow injection spectrophotometric determination of anionic surfactants using methyl orange as chromogenic reagent." Fresenius' journal of analytical chemistry 2000, 270-274.
14. Prakoso, S. P., Paramarta, V., Tju, H., Taufik, A., & Saleh, R. (2016, November). The influence of narrow optical gap silver oxide on zinc oxide nanoparticles produced by microwave-assisted colloidal synthesis: photocatalytic studies. In *Journal of Physics: Conference Series*, **2016**, 776, No. 1, p. 012051. IOP Publishing.
15. Bouaslaa, N., Abderrahmanea, S., Athmania, S., Oulabbasa, A., & Bououdinab, M.. ZnO nanoparticles and biocidal effect of nanostructured ZnO films on Escherichia coli. *Desalination and Water Treatment*, **2018**, *104*, 217-224.
16. Chen, C., Jian, H., Mai, K., Ren, Z., Wang, J., Fu, X., ... & Wang, Z.. Shape-and Size-Controlled Synthesis of Mn3O4 Nanocrystals at Room Temperature. *European Journal of Inorganic Chemistry*, *2014,* (19), 3023-3029.
17. Kucio, K., Charmas, B., & Pasieczna-Patkowska, S. Structural, thermal and photocatalytic properties of composite materials SiO 2/TiO 2/C. Adsorption, **2019,** 25(3), 501-511.

FLEXIBLE ELECTRODES FABRICATED WITH COBALT AND COPPER COATED GRAPHITE FILAMENTS

ALI TUNÇ [1], ABDULCABBAR YAVUZ [2], METIN BEDİR*[1]

[1] Gaziantep University, Engineering Faculty, Engineering Physics Department, Sehitkamil, 27310, Gaziantep, TURKEY.
[2] Gaziantep University, Engineering Faculty, Metallurgical and Materials Engineering Department, Sehitkamil, 27310, Gaziantep, TURKEY.
*bedir@gantep.edu.tr

Abstract

Electrodes used for supercapacitor applications are generally rigid. However, flexible electrodes could be also fabricated. New developments in wearable technology require electrical energy for example smart watches, smart glasses, smart bracelets, headgears, smart belts need electrical energy to operate. Flexible electrodes are convenient for these wearable technology devices as they are lighter than conventional electrodes and they can be easily produced in various shapes. The main motivation of this work is to fabricate flexible electrode by using inexpensive materials and methods. Cobalt and copper metals were individually electrodeposited on graphite filament. The specific capacitance of Co based electrode on graphite filament) was 90 F g^{-1} at the scan rate of 5 mV $s^{-}1$. A low-cost carbon with metals-based coating was developed on the basis of simple fabrication method.

Keyword: Cobalt, Copper, Electrodeposition, Graphite, Flexible.

1. Introduction

Energy can be produced from nonrenewable energy sources (including coal, oils, and natural gas) and renewable energy sources (including sun, wind, and hydroelectric). Non-renewable energy sources can be directly used whenever needed in some of the machines, cars, vehicles. However, renewable energy production depends on many parameters like location and climate [1]. Renewable energy sources could have low efficiency and low power densities. Additionally, energy could be used at a different time. Therefore, renewable energy is required to be stored. Electrical energy is the most common energy type in use because we produce electrical energy from almost all non-renewable and renewable energy sources. Produced energy can easily be transferred to a place of demand by energy transmission lines. Transferred electrical energy can be converted to needed energy types, light, sound, heat, kinetic, etc. Electrical energy storage is important for portable devices; vehicles and stationary energy sources. Several types of energy storage systems could be found and energy can be mainly stored electrochemically [2], electromagnetically [3], thermodynamically [4], and mechanically [5]. Some of the energy storage systems are shown in Figure 1. Supercapacitors, which are researched in this study, are the types of electrochemical cells.

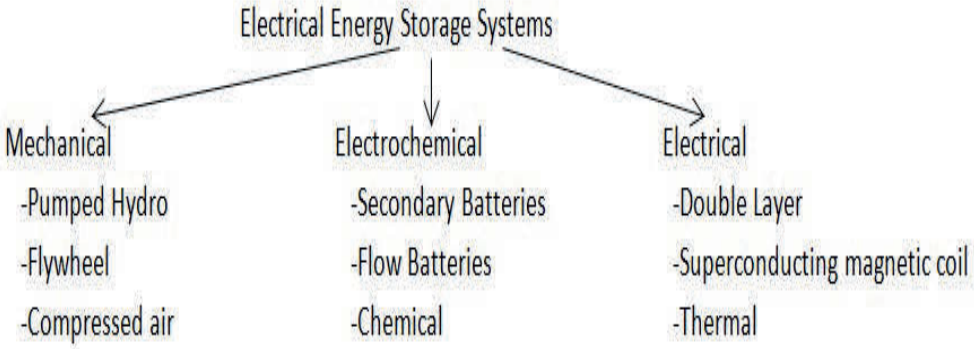


Figure 1. Diagram of electrical energy storage systems

Electrical energy storage is crucial for human life when there are natural disasters, like earthquakes, floods, hurricanes, and tsunamis because electrical energy supply centers or transportation lines could be damaged in these types of disasters. Energy storage devices are essential for hospitals and companies where power cuts could result in the loss of many people's life and data. Electrical energy storage systems are also helpful to reduce energy costs. The electrical energy usage rate is changing during the day and/or days of the week, so energy can be stored during off-peak times while it is cheaper in energy storage devices [6].

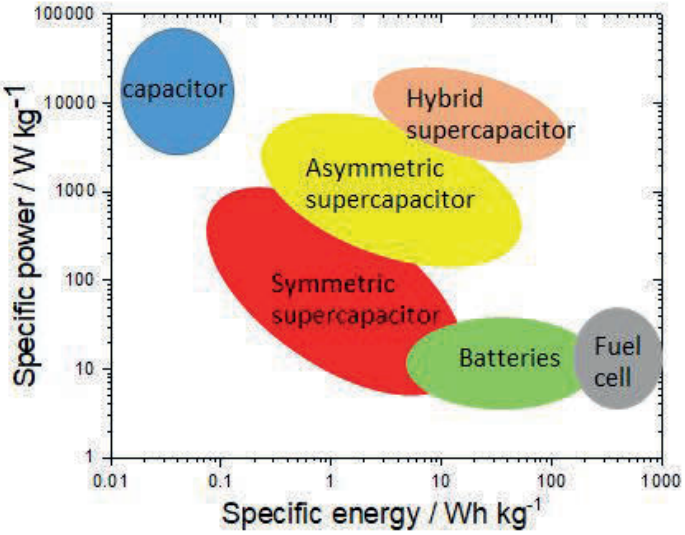


Figure 2. Ragone plots for energy storage devices

Supercapacitors, are also called ultracapacitors, could store charge electrostatically on high surface area electrodes. The main advantage of supercapacitors are long cycle life (high capacitance retention after long charge-discharge cycles), high power density and they could be built with environmentally friendly components (electrodes and electrolytes) [7]. They usually store less energy compared with conventional batteries but they can charge and discharge in a short timescale (typically within several seconds). They can store approximately 100 times more energy per unit of mass than electrolyte capacitors do [8]. The specific energy and power comparisons of some energy storage devices are illustrated by Ragone Plot in Figure 2. There are three types of supercapacitors; electric double-layer capacitors, hybrid capacitors, and pseudocapacitors (faradaic capacitors). Supercapacitors have many advantages over batteries as supercapacitors

have short charging time [9], long cycle life [10], high specific power [11], longer service life [12], and wide operation temperature range during charge-discharge [13]. However, the weaknesses of supercapacitors compared to lithium-ion batteries could be low specific energy and high costs.

Electrodeposition, also known as electroplating, is the process of material growth onto a conducting surface from a solution including a salt. This technique is commonly used to obtain thin films on the surface of an object to change its surface properties. Basically, electrodeposition system has three components: electrode, electrolyte, and a power supply. The electrolyte is the source of ions that will be deposited on the electrode in a solid form. Thickness and surface morphology can be controlled in this technique [14–16]. This method is easy to apply and a cheap method and can be scalable [17–19]. A Three-cell electrode system (explained below) will be used for electrodeposition in this study. Cobalt and copper were electrodeposited from an electrolyte on a graphite surface.

2. Materials and Methods

Firstly, ethaline electrolyte was prepared for electrodeposition medium of metals. Merck Company's (Germany) choline chloride (139.62 g mol^{-1}) and ethylene glycol (62.07 g mol^{-1}) were used to obtain ethaline. Alfa Aesar Company's (Germany) cobalt (II) chloride hexahydrate (98%) was used for the cobalt coating study. 0.02 mole (4.76 gram) of cobalt (II) chloride hexahydrate (237.93 g mol^{-1}) was added to ethaline (until having 100 ml solution) and 0.2 M $CoCl_2$ in ethaline was prepared. Merck Company's (Germany) copper (II) chloride (98%) was used for copper deposition. 0.02 mole (2.69 gram) of copper (II) chloride (134.45 g mol^{-1}) was added ethaline by completing 100 ml solution in order to have 0.2 M Cu^{2+} in Ethaline. KOH electrolyte was used as cycling electrolyte with cyclic voltammetry. 0.5 mole (28.05 gram) of potassium hydroxide (56.11 g $mole^{-1}$) (Merck, Germany) was added to some distilled water until the volume of the solution became 500 ml water was added to the mixture and 1 M KOH electrolyte was obtained. Platinum-coated titanium counter electrode and silver wire reference electrode were used for the deposition of cobalt onto graphite filament.

DowAksa Company's (Turkey) Aksaca brand 3000 K (3000 fibers on cross-section of the rope) carbon fibers were used as graphite filament illustrated in Figure 3. The base material of the electrode in this study was 99.9% pure carbon filament. 1000 meters of this graphite filament is 200 grams and mass per unit length is 0.002 gram per centimeter. Cobalt and copper were coated on graphite filament separately from ethaline including cobalt and copper salts, respectively. For obtaining cobalt coated graphite filament, the filament was immersed in 0.2 M of Co in ethaline and -1.6 V static potential was applied for 500 seconds by using AMATEK Company's (USA) VersaSTAT 3, Princeton Applied Research model potentiostat. 0.2 M of Cu in ethaline and constant -1.1 V potential (applied for 500 seconds) was used for copper-coated graphite filament. Ethaline was on the heater with a temperature of 60 °C during electrodeposition of both metals. All samples were produced in the same process for analysis.

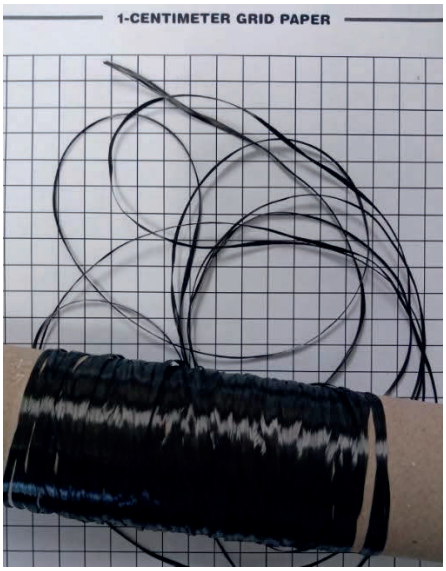


Figure 3. Photo of flexible graphite filament

3. Results and Discussion

Electrolyte which must be a conductor substance is the medium that anode and cathode are immersed in to perform a required reaction. Current and ions in the electrolyte can be controlled with help of external electrical power and hence a material can be tailored through a redox reaction [20–22]. The electrolyte is an important component in energy storage devices as it can cause reaction change. Therefore, the physical properties of electrolytes including flammability, toxicity, volatility are important during the production of electrodes and cycling of electrodes [23–25]. However, the types of electrolytes used so far are limited as aqueous and organic electrolytes are commonly used and the physical properties of these conventional electrolytes could not be changed easily. In order to increase the numbers of electrolytes and control the physical properties of electrolytes, a novel type of electrolyte called ionic liquid electrolyte has been commonly studied for electrochemical applications, recently [26–28].

Ionic liquid's first description has been made by Paul Walden in 1914 [29]. Ionic liquids are salts in liquid states or salts whose melting point is below 100 °C. This is the main difference between ILs and conventional molten salts because classical salts melt at higher temperatures. Molten salts are used for some metal reduction (including lithium, sodium, and titanium) because they are conductive and have wide potential windows [30]. However, melting temperature and extreme operational requirements limits the use of molten salts. Normal liquids such as water or alcohols, mostly consisting of neutral atoms, but ILs are mostly composed of ions (cations and anions). For the last two decades, ionic liquids have attracted researchers' attentions [31–33]. Ionic liquids have high conductivity [34], wide potential window [35], wide thermal stability [36], large liquid phase range (-100°C to 400 °C) [37]. Ionic liquids can also be useful if they are non-volatile, non-flammable, and non-toxic.

Bare graphite filament and cobalt coated graphite filament electrodes were immersed in 1 M KOH and cyclic voltammogram technique was then applied and the results are represented in Figure 4. This graph clearly indicates that bare graphite filament had no significant current when cycled in 1 M KOH between -0.2 V to 0.5 V at a scan rate of 50 mV s^{-1}. When the same conditions were applied to cobalt coated graphite filament electrodeposited from Ethaline medium at -1.6 V, both

oxidation and reduction peaks were observed in KOH electrolyte as seen in Figure 4. From this result, it can be deduced that cobalt-coated graphite filament can be a promising electrode for supercapacitor applications. Therefore, the electrochemical performance of the cobalt-coated graphite filament at many scans and different scan rates was investigated.

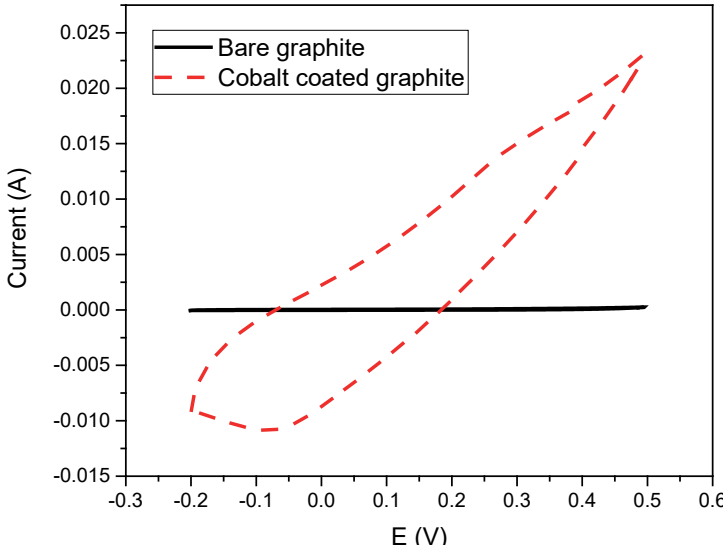


Figure 4. Cyclic voltammogram graph of bare and cobalt coated graphite filament cycled in KOH at 50 mV s^{-1}

Cyclic voltammogram results of cobalt coated graphite filament electrodes at different scan rates (200 mV s^{-1}, 100 mV s^{-1}, 50 mV s^{-1} ,20 mV s^{-1}, 10 mV s^{-1}, 5 mV s^{-1}) in 1 M KOH medium are illustrated in Figure 5. Electrochemical performance comparison makes sense when the current density was used. In order to obtain current density versus applied potential graph, the mass of immersed graphite filament was calculated. As 1000 meters of graphite filament's mass was 200 grams, the graphite filament was 0.02 g cm^{-1}. Current values obtained by cyclic voltammogram were divided by 0.02 to find current density in A g^{-1} because 1 cm of filament was immersed and Figure 5 was obtained. Figure 5 illustrates that the maximum values of oxidation current density and reduction current density decreased upon decreasing the scan rate. This is consistent with the theoretical expectation because declining of scan rate means the rise of time and the increase of time could cause current drops and hence the decrease of current density.

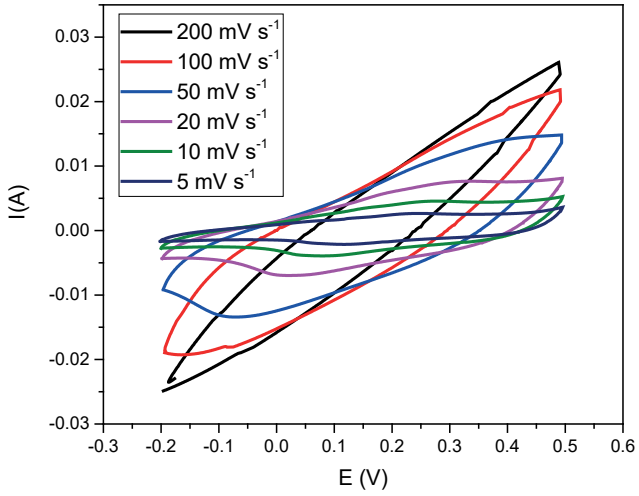


Figure 5. Raw cyclic voltammogram data of cobalt coated graphite filament at different scan rates.

Specific capacitances of cobalt coated carbon-based fiber electrodes were calculated for different scan rates and the results are illustrated in Figure 6. The specific capacitance of cobalt deposited graphite filament was 90 F g^{-1} when scan rate was 5 mV s^{-1} and 15 F g^{-1} when scan rate was 200 mV s^{-1}.

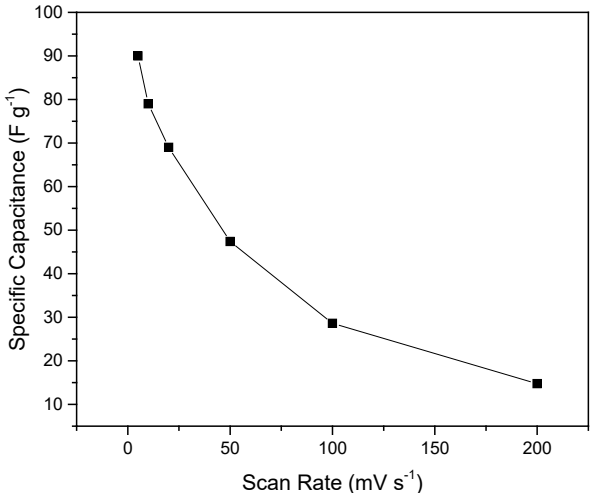


Figure 6. Specific capacitance versus scan rate for cobalt-coated graphite rope.

The cyclic voltammetry graph presented in Figure 5 was used in order to elucidate the reaction mechanism between cobalt-coated flexible graphite electrode and alkaline electrolyte. Logarithm values of oxidation and reduction current peaks for cobalt coated graphite filament and logarithm values of scan rates were calculated and their graph demonstrated in Figure 7 was obtained. Gradients of both logarithms of oxidation and reduction current density peaks as a function of the logarithm of scan rate were close to each other as clearly seen in Figure 7. The slope of logarithm of oxidation current density peaks as a function of the logarithm of scan rate was calculated as 0.64 and the slope of logarithm of reduction current density peaks as a function of the logarithm of scan rate was calculated as 0.67. This result concludes that the reaction mechanism of cobalt-coated graphite filament is controlled by diffusion and surface controlled mechanism.

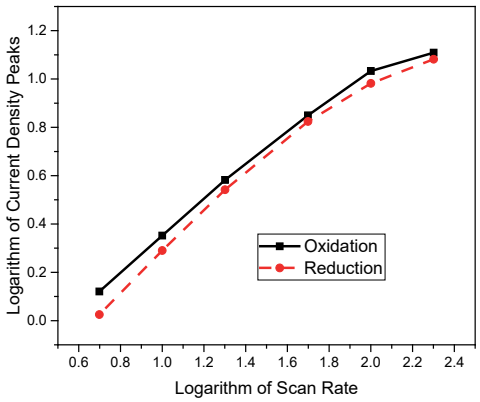


Figure 7. Logarithm of current density values against the logarithm of scan rate for cobalt coated electrode cycled in KOH media.

Bare graphite filament and copper coated graphite filament electrodeposited from ethaline by applying -1.1 V were immersed in 1 M KOH for cycling. The cyclic polarization was applied in 1 M KOH between -0.8 V to -0.3 V at a scan rate of 50 mV s^{-1} and the resulting data are presented in Figure 8. This graph shows that both bare graphite and copper coated graphite had no significant current values and current values were close to each other. This result might occur because of the removal of the coating due to the washing and drying process. Having no significant oxidation or/and reduction values made it unnecessary to investigate the copper-coated graphite filament in ethaline medium for energy storage devices because uncoated and coated graphite had similar results. It is not necessary to coat graphite filament with copper.

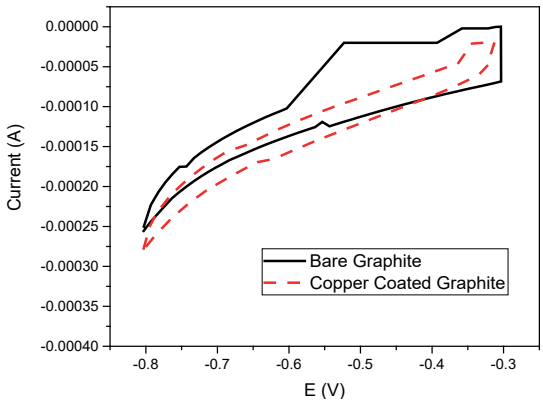


Figure 8. Cyclic voltammogram graph of bare and copper coated graphite filament cycled in KOH electrolyte at 50 mV s^{-1}.

4. Conclusion

The study was regarding the production of cobalt and copper coated graphite filament. Cobalt coated graphite filament electrodes has a specific capacitance of 90 F g^{-1} at the scan rate of 5 mV s^{-1} in 1 M KOH medium. It was observed bare graphite had no significant oxidation or reduction, so it can be concluded that this specific capacitance was the effect of cobalt coating on graphite filament. The slope of current density logarithm and scan rate logarithm values resulted that cobalt-coated graphite filament electrodes in 1 M KOH medium had both diffusional and surface controlled mechanisms. Cycling voltammogram results showed that copper-coated graphite filament was not suitable for supercapacitor applications because there were no significant oxidation or reduction peaks. At the end of this study, it can be concluded that cobalt coating on graphite filament is an inexpensive and easy method in order to fabricate flexible carbon-based electrodes for supercapacitor applications whereas copper coating on graphite filament is not feasible to use for energy storage systems. The work presented in this proceeding was presented in Ali Tunç's PhD thesis [38].

References

1. Siddiqui, R., Bajpai, U., Deviation in the performance of solar module under climatic parameter as ambient temperature and wind velocity in composite climate, Int. J. Renew. Energy Res. 2 , **2012** ,486–490.
2. Goodenough, J.B., Electrochemical energy storage in a sustainable modern society, Energy Environ. Sci. 7 , **2014** ,14–18.
3. Liu,C., Li, L,F., H,Cheng,Ma., Advanced materials for energy storage, Adv. Mater. 22 **2010**, E28–E62.
4. Vollaro, R.D.L.., Faga,F., Tallini,A., Cedola,L.,Vallati,A., Energy and thermodynamical study of a small innovative compressed air energy storage system (micro-CAES), Energy

Procedia. 82 , **2015,** 645–651.
5. Amirante,R.,Cassone,E.,Distaso,E., Tamburrano,P., Overview on recent developments in energy storage: Mechanical, electrochemical and hydrogen technologies, Energy Convers. Manag. 132 , **2017**, 372–387.
6. Arteconi,A.,Ciarrocchi,E., Pan,Q., Carducci,F., Comodi,G., Polonara,F., Wang,R., Thermal energy storage coupled with PV panels for demand side management of industrial building cooling loads, Appl. Energy. 185, **2017 ,**1984–1993.
7. Vangari,M., Pryor,T., Jiang,L., Supercapacitors: review of materials and fabrication methods, J. Energy Eng. 139, **2013** , 72–79.
8. Burke,A., Ultracapacitors: why, how, and where is the technology, J. Power Sources. 91 , **2000** ,37–50.
9. Mondal,A.K.., Su,D., Chen,S., Ung,A.,Kim,H., Wang,G., Mesoporous MnCo2O4 with a flake-like structure as advanced electrode materials for lithium-ion batteries and supercapacitors, Chem. Eur. J. 21 ,**2015**, 1526–1532.
10. Wang,Y., Xia,Y., Recent progress in supercapacitors: from materials design to system construction, Adv. Mater. 25 ,**2013**, 5336–5342.
11. Mastragostino,M., Soavi,F., Strategies for high-performance supercapacitors for HEV, J. Power Sources. 174 , **2007** ,89–93.
12. Zhang,J., Li,Y., Zhang,Y., Qian,X., Niu,R., Hu,R., Zhu,X., Wang,X., Zhu,J., The enhanced adhesion between overlong TiNxOy/MnO2 nanoarrays and Ti substrate: Towards flexible supercapacitors with high energy density and long service life, Nano Energy. 43 ,**2018**,91–102.
13. Hung,K., Masarapu,C., Ko,T., Wei,B., Wide-temperature range operation supercapacitors from nanostructured activated carbon fabric, J. Power Sources. 193, **2009**, 944–949.
14. Amâncio,M.A.., Pinto,E.P.., R.S. Matos, F.X. Nobre, W.R. Brito, H.D. da Fonseca Filho, Nanoscale morphology and fractal analysis of TiO2 coatings on ITO substrate by electrodeposition, J. Microsc. 282 ,**2021**, 162–174.
15. Xia,F., Li, C.,Ma,C., Li,Q., Xing,H., Effect of pulse current density on microstructure and wear property of Ni-TiN nanocoatings deposited via pulse electrodeposition, Appl. Surf. Sci. 538 ,**2021**,148139.
16. Wu,Y., Lian,J., Wang,Y., Sun,J., He,Z., Gu,Z., Potentiostatic electrodeposition of self-supported NiS electrocatalyst supported on Ni foam for efficient hydrogen evolution, Mater. Des. 198 ,**2021**, 109-316.
17. Zhang,M., Yang,D., Li,J., Supercapacitor performances of MnO2 and MnO2/reduced graphene oxide prepared with various electrodeposition time, Vacuum. 178 ,**2020**, 109-455.
18. Saha,S., Johnson,M., Altayaran,F., Wang,Y., Wang,D., Zhang, Q.,Electrodeposition Fabrication of Chalcogenide Thin Films for Photovoltaic Applications, Electrochem. 1 ,**2020,** 286–321.
19. Coelho,D., Gaudêncio,J.P.R.S.., Carminati,S.A.., Ribeiro,F.W.P.., Nogueira,A.F.., Mascaro,L.H.., Bi electrodeposition on WO3 photoanode to improve the photoactivity of the WO3/BiVO4 heterostructure to water splitting, Chem. Eng. J. 399 ,**2020,** 125836.
20. Srimuk,P.., Su,X.., Yoon,J.., Aurbach,D.., Presser,V.., Charge-transfer materials for electrochemical water desalination, ion separation and the recovery of elements, Nat. Rev. Mater. 5 ,**2020**,517–538.
21. Lee,S.., Hong, J.., Kang,K., Redox-Active Organic Compounds for Future Sustainable Energy Storage System, Adv. Energy Mater. 10 ,**2020**,2001445.
22. An, G.., Hong, J.., Pak,S.., Cho,Y.., Lee,S.., Hou,B.., Cha,S.., 2D metal Zn nanostructure electrodes for high-performance Zn ion supercapacitors, Adv. Energy Mater. 10 ,**2020**,

1902981.
23. Lebedeva,N.P.., Boon-Brett, L..,Considerations on the chemical toxicity of contemporary Li-ion battery electrolytes and their components, J. Electrochem. Soc. 163 ,**2016**, A821.
24. Jaumaux,P.., Wu,J.., Shanmukaraj,D.., Wang,Y.., Zhou,D.., Sun,B.., Kang,F.., Li,B.., Armand,M.., Wang,G.., Non-Flammable Liquid and Quasi-Solid Electrolytes toward Highly-Safe Alkali Metal-Based Batteries, Adv. Funct. Mater. 31 ,**2021**, 2008644.
25. Roth,E.P.., Orendorff,C.J.., How electrolytes influence battery safety, Electrochem. Soc. Interface. 21 ,**2012**, 45.
26. Mahanta,U.., Choudhury,S.., Venkatesh,R.P.., Sarojini Amma,S.., Ilangovan, S.S.., Banerjee, T.., Ionic-liquid-based deep eutectic solvents as novel electrolytes for supercapacitors: COSMO-SAC predictions, synthesis, and characterization, ACS Sustain. Chem. Eng. 8 ,**2019**, 372–381.
27. Zhang,C.., Zhang,L.., Yu,G.., Eutectic electrolytes as a promising platform for next-generation electrochemical energy storage, Acc. Chem. Res. 53 ,**2020**, 1648–1659.
28. Huang,Y.., Zhao,L.., Li,L.., Xie,M.., Wu,F.., Chen,R.., Electrolytes and Electrolyte/Electrode Interfaces in Sodium-Ion Batteries: From Scientific Research to Practical Application, Adv. Mater. 31 ,**2019**,1808393.
29. Angell,C.A..,Ansari,Y.., Zhao,Z.., Ionic Liquids: Past, present and future, Faraday Discuss. 154 ,**2012**,9–27.
30. Barron,J.C.., The electrochemistry of Zn in deep eutectic solvents, **2010.**
31. Sasikumar,B.., Arthanareeswaran,G.., Ismail,A.F.., Recent progress in ionic liquid membranes for gas separation, J. Mol. Liq. 266 ,**2018**,330–341.
32. Manjunath,K.., Yadav,L.S.R.., Jayalakshmi,T.., Reddy,V.., Rajanaika,H.., Nagaraju,G.., Ionic liquid assisted hydrothermal synthesis of TiO2 nanoparticles: photocatalytic and antibacterial activity, J. Mater. Res. Technol. 7 ,**2018**, 7–13.
33. Daryayehsalameh,B.., Nabavi,M.., Vaferi,B.., Modeling of CO2 capture ability of [Bmim][BF4] ionic liquid using connectionist smart paradigms, Environ. Technol. Innov. 22 ,**2021**, 101484.
34. Mantravadi,R.., Chinnam, P.R., Dikin,D.A.,Wunder,S.L.., High conductivity, high strength solid electrolytes formed by in situ encapsulation of ionic liquids in nanofibrillar methyl cellulose networks, ACS Appl. Mater. Interfaces. 8 ,**2016**, 13426–13436.
35. Kitazawa,Y.., Iwata,K.., Kido,R..,Imaizumi,S.., Tsuzuki,S., Shinoda,W.., K..,Ueno, T. Mandai, Kokubo,H.., Dokko,K.., Polymer electrolytes containing solvate ionic liquids: A new approach to achieve high ionic conductivity, thermal stability, and a wide potential window, Chem. Mater. 30 ,**2018**, 252–261.
36. Ngo,H.L.., Le Compte,K.., Hargens,L.., McEwen,A.B.., Thermal properties of imidazolium ionic liquids, Thermochim. Acta. 357 ,**2000**, 97–102.
37. Keshavarz,M.H.., Pouretedal,H.R.., Saberi,E.., A novel method for predicting melting point of ionic liquids, Process Saf. Environ. Prot. 116 ,**2018**, 333–339.
38. Tunç,A.., PhD thesis, Fabrication and Characterization of Composite Electrodes for Supercapacitors, Gaziantep University ,**2021.**

INVESTIGATION OF WEAR BEHAVIOUR OF PLA AND CV 60 MATERIALS

EREF BEDIRHAN AKSOY [*1], NECIP FAZIL YILMAZ [1], MUSA YILMAZ[1]

[1] Gaziantep University, Engineering Faculty, Mechanical Engineering Department, Gaziantep, TURKEY.
[*]bedirhanaksoy@mail.com

Abstract

Wear behavior of Poly Lactic Acid (PLA) and Thermoplastic Polyurethanes with carbon powder (TPU) CV60 materials is examined in this work. PLA and CV 60 components created using Fused Deposition Modeling (FDM) technic, one of the additive manufacturing methods. The model can be made with the most appropriate material for the desired mechanical properties thanks to the technology's wide range of thermoplastic materials. The tribological properties of these materials must be known and compared before they can be used as a final product. The aim of this study is to use FDM to determine the friction coefficient and wear behavior of PLA and CV60 parts manufactured using one of the additive manufacturing. Test specimens produced different infill density rates. The wear coefficient was determined using the pin-on-disc test, which was performed according to ASTM G 99. All materials were tested at the same temperature, with the same load, and in the same environmental condition. In this study, two different filling ratios of two different materials were investigated. As a result of the researches, it has been examined whether 3D printed products can be used as a final product or not, and the relevant results have been shared.

Keyword: Additive Manufacturing, Wear, Coefficient of friction, Infill density

1. Introduction

FDM, the technology of the future, is an additive manufacturing technology developed to knit products from thermoplastic materials. The word, which consists of the initials of the words 'Fused Deposition Modeling', is one of the first developed methods of layered production, that is, layered production. It is also used as FFF, one of the initials of the words 'Fused Flament Fabrication'. FDM is a ground-breaking technique that allows for faster printing and is less expensive than other 3D printing processes [1]. Consequently, its printers are now the most popular consumer-level 3D printers for producing polymer composites using extrusion A.M. [2]. A spool of thermoplastic material in the form of filaments is melted and then extruded using a heated nozzle in the FDM process [3]. The use of thermoplastics with higher melting temperatures as 3D printing materials has recently been possible [4].

The usage of thermoplastics in industrial applications, construction, and different vehicle components, such as door panels, dashboards, headliners, package trays, and interior pieces, has gotten a lot of attention in the recent decade [5]. Due to its numerous benefits, such as lower maintenance and setup costs, rapid part production, perfect tolerance, ease of manufacturing complex parts, and minimal post processing, A.M. has gained traction in both modern and academic fields[6].

Although they have many advantages, these materials are used in limited numbers as final products today. There are many reasons for this, one of which is that materials show lower wear behavior than materials used in industry. Functional use in machine elements has become popular in recent years. As a result, it's critical to look into the mechanical properties of these components. There are lots of studies on the wear characteristics of these parts in the literature. Fused Deposition Modeling has been used to study the wear behavior of polymers[1]. Recent technological advancements have increased the possibilities for products created using Additive Manufacturing techniques, particularly by FFF. It produces excellent results at a low cost. Fabrication is done with a variety of thermoplastic filaments. The required parts are designed in CAD software and then converted to STL files for inclusion in the machine. The filament is continually fed. The filament is extruded by the printer head when it is in the molten state. To form the required 3D part, the printer head moves back and forth in vertical and horizontal directions [7]. Researchers are looking for sustainable materials with improved mechanical and tribological properties due to friction and wear in a variety of engineering applications. Bad tribological practices result in significant energy losses, which could result in significant economic losses. Making surfaces smoother can reduce friction between sliding surfaces, but a super-smooth surface can be costly and may cause failure [4]. Material content has a significant impact on the functional performance of various engineered components. The wear mechanisms of various types of filament parts manufactured using FDM are investigated in this paper. The science of tribology is crucial for improving the dependability of materials and mechanical components[6]. Wear behavior is one of the tribological properties. In this study, we have worked on the wear behavior of PLA and CV 60 filaments. Pin-on-disc test was performed according to ASTM G 99 standards.

The carbon and other active chemicals present in the material directly impact the mechanical and tribological characteristics of the material, according to Muammel M. Hanon's experiments on PLA and PTFE material. The laying angle of the test specimens retrieved from the 3D printer generated using the FDM technology has also been shown to have an influence. The term "before" or "after" the microscopic examinations was not used in the text, therefore it is unclear at what stage the experiments were done. Proportional expressions are not included in the wear tests, and it is not stated which methodology or procedure is used to quantify wear[7]. The mechanical and tribological characteristics of the samples, which will be utilized at various temperatures and environmental conditions, will be studied separately from this study using various filaments.

It looks at the possibility of PP as a contender for FDM-based 3D printing. The complete filament manufacturing chain is assessed by printing test samples, starting with PP pellets and ending with filament synthesis via extrusion. This method is based on the use of the same high-quality raw materials. A comparison has been done between the components produced via compression molding. The mechanical characteristics of printed samples, filament orientation, layer thickness, degree of filling, and material impact were all assessed. There were two types of PP tested: one with reinforcement and one without reinforcement. There were two types of PP studied: one with reinforcement and one without. The ability of conventional FDM to compete with manufacturing processes, particularly for tiny parts/components, has been demonstrated to be beneficial for serial production. Furthermore, because this technology allows for the manufacture of components with mechanical performance, it is not restricted to the creation of mock-ups and prototypes [8].

The aim of this research is to see how the FDM 3D-printing process affects the performance of polymers in terms of friction and wear. Several tribology test specimens were fabricated in two different infill designs to investigate the impact of this manufacturing technique. The printed samples were tested using an ASTM G 99-17 reciprocating sliding tribotester in dry sliding conditions. For the entire test samples printed in various orientations, the behavior of friction coefficient and wear versus sliding distance was evaluated. The average wear values among the tested samples, as well as the results of static and dynamic friction coefficients, were compared.

2. Materials and Methods

In this paper, the PLA and CV60 filaments were used in this experiment. PLA layer height is 0.12 mm, extruder temperature is 215 °C, table temperature is 55 °C, and infill rates of 100% and 20% are selected as production settings. The layer height for CV 60 filament is 0.12 mm, the extruder temperature is 230 °C, the table temperature is 60 °C, and the infill ratio is 100% and 20%. The images of the samples were given below according to the infill density ratios used. Materials properties are given Table 1.

Table 1. Material Properties

Properties	**PLA**	**CV60**
Denier (d)	12.857	13.714
Breaking Strength (MPA)	0,5687857	0,45306723
Elongation at break (%)	303	508

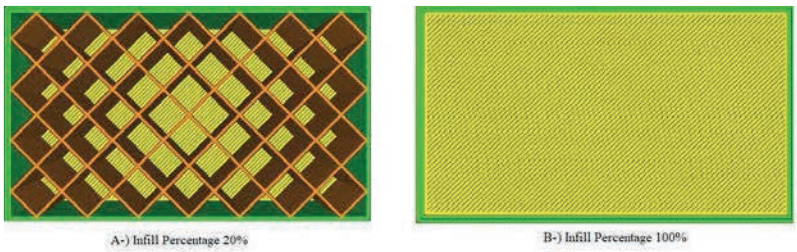


Figure 1. Schematic representation of infill percentage types a) 20% b) 100%

In this paper, the pin specimens' solid model is created in 3D drawing program, 3D modeling software, and exported as STL file. Using PLA and CV 60 filaments and the Creality CR 10 S 04 3D printer with FDM technology, FDM is a 3D printing technology that is produced by flowing and adding the thermoplastic material melted by a hot nozzle on the printing plate layer by layer, pin specimens for wear testing are made in the shape of test bars according to ASTM G 99 standards. Specimen's criteria are 25 mm height and 8 mm diameter.

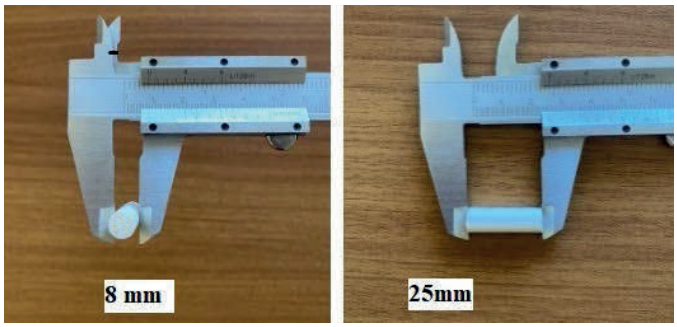


Figure 2. Specimens

The coefficient of friction and wear rate of 3D printed PLA and CV 60 specimens were tested at room temperature under dry sliding conditions using the pin on disc technique [2]. The tests were conducted in compliance with ASTM G99 guidelines. Cast iron and steel were used to make the abrasive counter discs, which have varying surface roughness and hardness. The test performed on TURKYUS Pin- on test machine shown in Figure 4. The wear test parameters, as well as the specifications of counter discs and 3D-printed PLA and CV 60 specimens, are all included in Table 2 and all dimensions shown in Figure 3.

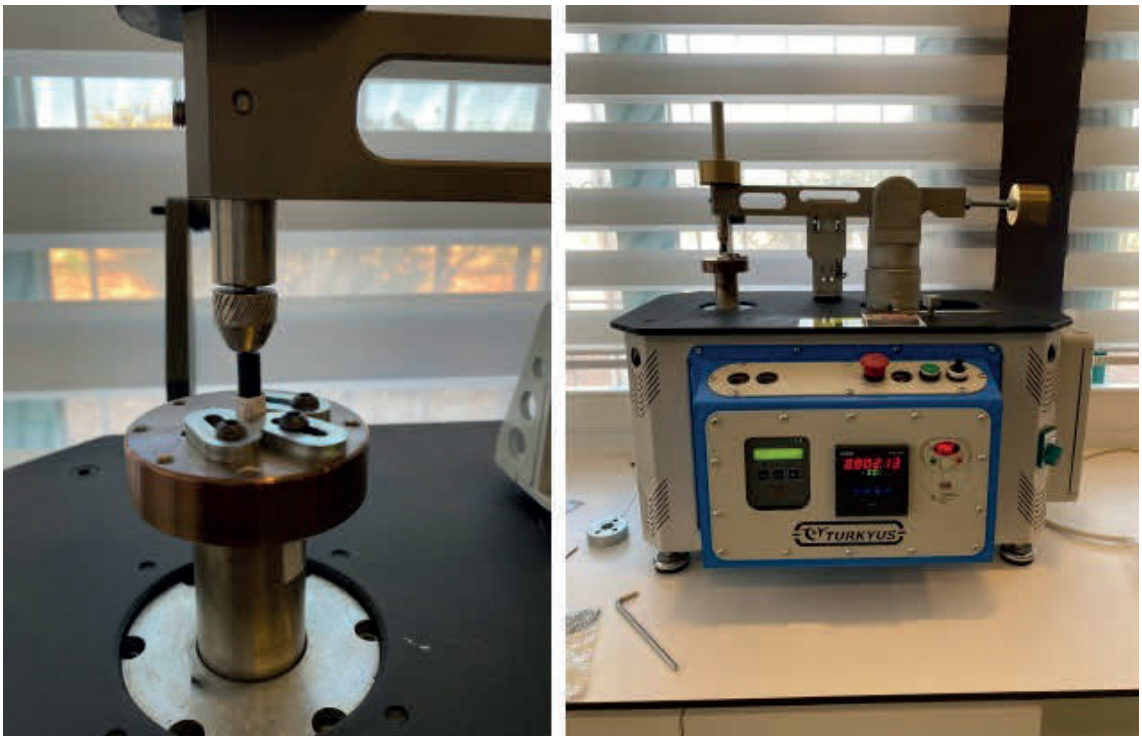


Figure 3. Pin-on-disc Test Machine

All test specimens was performed under the same environmental conditions. Due to the mechanical properties of the device, the test parameters on the part were changed to 15 N. The graphics of the test results are shared in the results section.

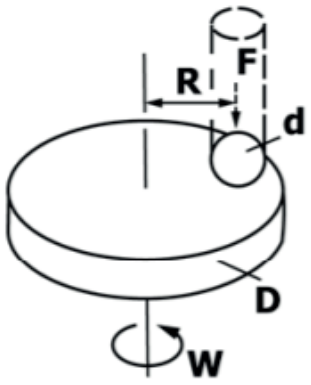


Figure 4. Schematic of Pin-on-Disk Wear Test System [13].

Table 3. Test Parameters

Properties	Levels
Rotation Speed	250 rpm
Track Diameter	6 mm
Speed	79 mm/s
Time	600 s
Road	47122 mm
Load	15 N
Temperature	26°C

3. Results and Discussion

The wear and friction characteristics of 3D printed PLA and CV 60 filaments were examined using a pin-on-disc test machine under dry sliding circumstances. The coefficient of friction during a tribology test with a weight of 15 N as a function of sliding distance. From all specified sample criteria two were produced and tested. All result of specimens is shown as a graph in Figure 5,6,7,8.

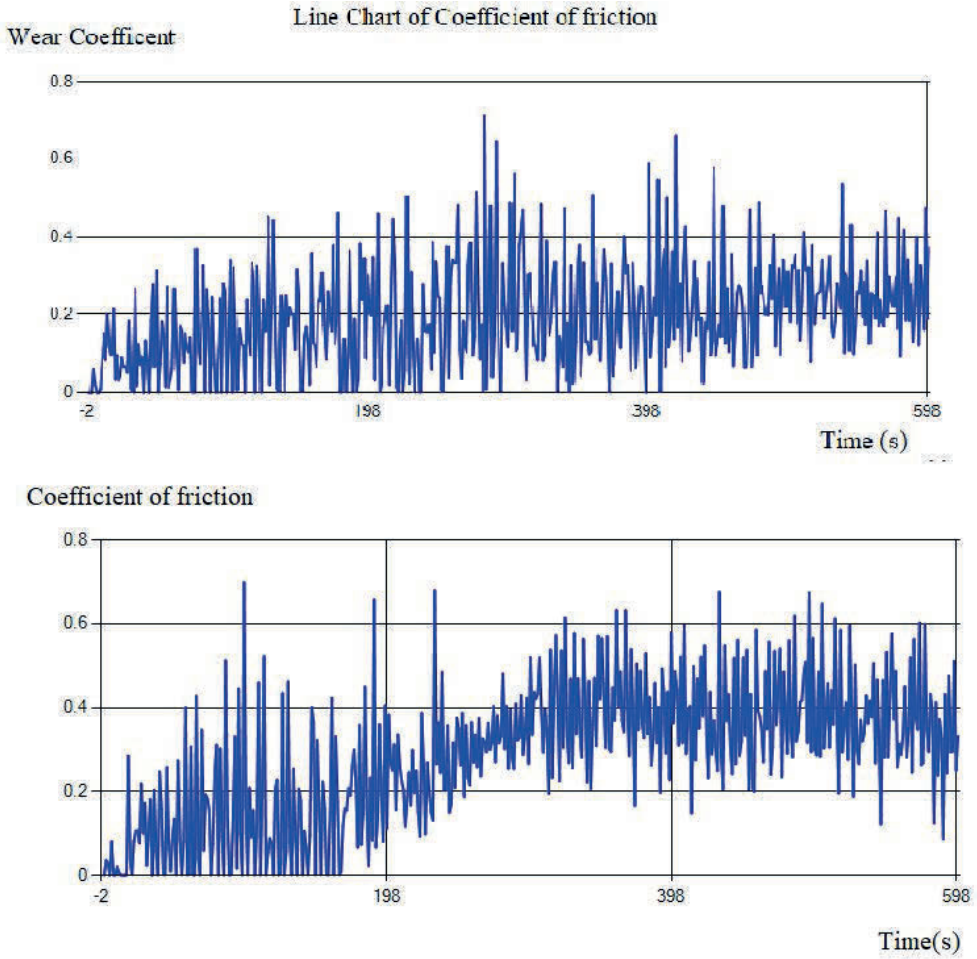


Figure 5. PLA Results for 20% Density Rate

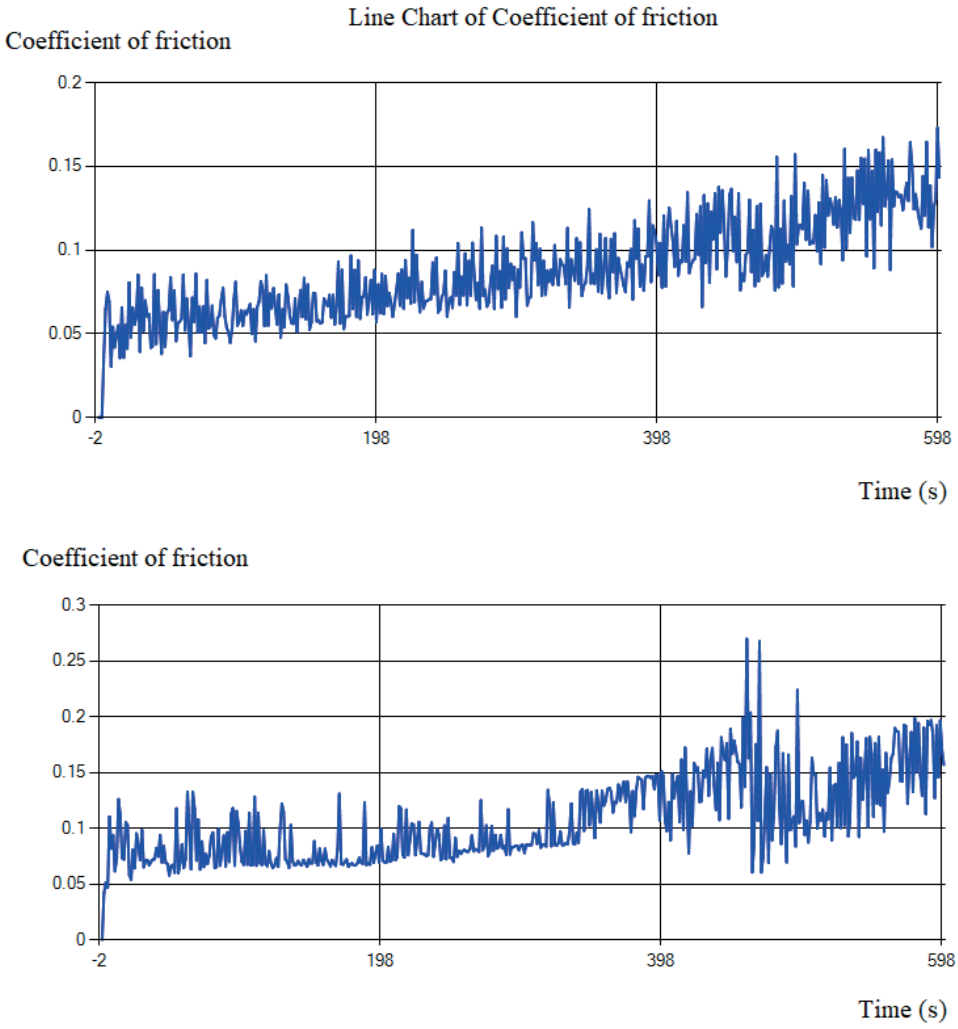


Figure 6. PLA Results for 100% Density Rate

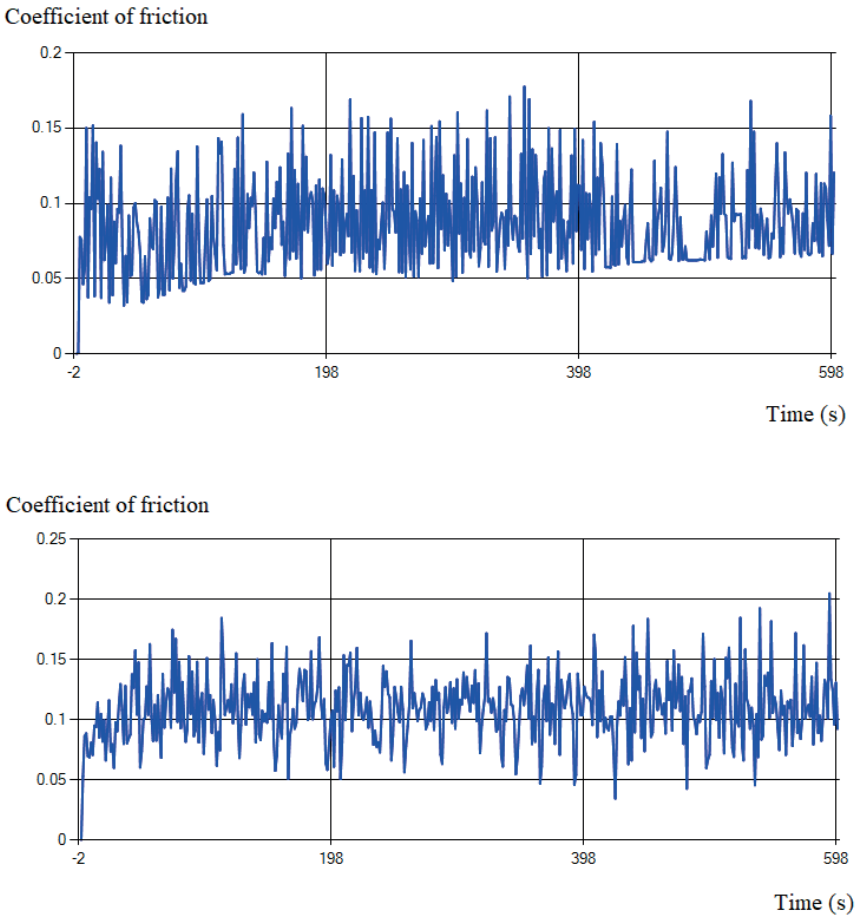


Figure 7. CV60 Results for 20% Density Rate

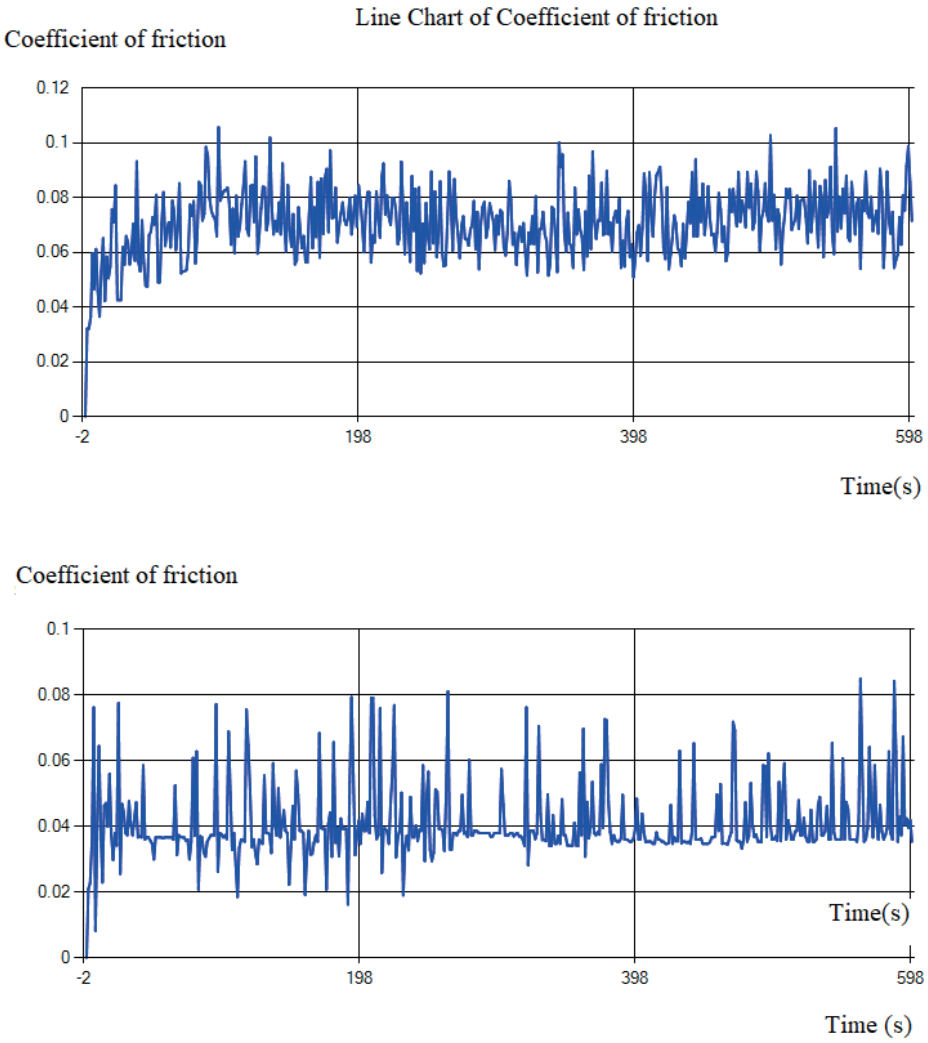


Figure 8. CV60 Results for 1000% Density Rate

Surface texture patterns offer a lot of promise in terms of increasing tribological performance by minimizing friction and wear [10]. Laser and injection molding are the most prevalent technologies for surface texturing. Because texture production via 3D printing is faster, more versatile, and less costly than previous approaches, it is also utilized to produce components, patterns, and molds with fine features for a broad range of applications. There has been no study on textured surfaces created by 3D printing to yet. As a result, improving friction and wear qualities using a novel manufacturing process based on 3D printing is a topic worth investigating. One of the essential criteria in the performance of long-term temporary restorations in the oral cavity is wear resistance. Wear, in contrast to material qualities such as elastic modulus, hardness, or flexural strength, is a system attribute arising from the complex interplay of many elements in the tribosystem employed in wear testing [11]. The results of the Pin-on-Disc test were obtained for both PLA and CV60. For the identical printing settings of the specimens, the wear rates, specific wear rates, and coefficient of friction are calculated. The wear rates were not homogeneous during the first few cycles of the test because the foreign substance and roughness of the specimen disrupted the contact between the specimen surface and the disc surface [12]. After a few cycles, the wear track disc removes the foreign materials and

roughness, which is known as the break in stage. The contact between the pin's bottom surface and the disc was enabled to acquire the genuine wear rates of the specimen. For a direct comparison of PLA and CV60 wear rates, the test data are displayed in a line chart. The wear rates, specific wear rates, and coefficient of friction of the specimens are displayed against their layer thickness, as well as the infill pattern for various infill densities. In terms of layer thickness, the infill densities and patterns of the PLA and CV60 printed specimens are compared [13]. Because layer thickness is directly related to wear rate, it also reduces the specific wear rate and coefficient of friction. In this study, as can be seen in the graphics, a difference was observed between 20% pave rate and 100% pave rate. This difference is thought to have a lower wear coefficient as the material is more in contact with the abrasive tip on the pin-on-disc. Since graphs of both PLA filament and CV60 filament show similar results, the higher the fill rate, the lower the wear coefficient will be. The weights of the materials were measured both before and after the test, and no significant weight difference was detected. The reason for the absence of weight loss is assumed to be high elongation at break, taking into account that the materials are ductile. In addition, the wear coefficient of PLA filament against abrasion is higher than that of CV 60 filament. This difference shows that the use of PLA filament in applications that will show wear may be the reason for preference. This study was carried out under the same ambient conditions at the same temperature. In the next study, the wear behavior of materials under different temperature and ambient conditions will be examined. In the study, the test was started under the 10 N load specified in the asthma standards, and the test results are in the first results. The standards given in ASTM standards were changed and the test continued at 250 rpm under 15 N load.As a result, at a sliding velocity of 79 m/s and a load of 15 N, it is proposed that printing with a minimum layer thickness and increased infill density with a grid pattern can achieve a low wear rate. The wear rate determines the coefficient of friction. It showed a lower wear behavior and a smoother behavior with a high fill rate.The PLA filament has a higher strength property and it is expected to show a higher behavior than the CV 60 filament in terms of durability [14]. As a result of these studies, it has been shown in the graphics that the PLA filament has a higher wear coefficient.

4. Conclusions

In this study, specimens were produced in Creality SR 10 3D printer. Analysis of wear behavior of 3D printed materials investigated with Pin-on-disc test method. In the test, specimens, 8 mm diameter and 25 mm high long, were performed on the ASTM G 99 -17 standards and results were compared. The test result was successful and it was seen that different tip type of materials could be available for final product. It has been concluded that the different type of materials with different infill density can provide varying outcomes with different filling rates, and the material's wear coefficient can vary depending on the application. When all of the data is considered, it is clear that the CV 60 filament has a greater wear coefficient than the PLA filament.

References

1. İstif, İ., Identification of Dry Sliding Wear Behavior of PLA Parts Manufactured by Fused Deposition Modeling. Dicle University Journal of Engineering, 275-283,**2021**.
2. L.M. Galantucci, F. L., Experimental study aiming to enhance. CIRP Ann., 189-192, **2009**.
3. Nagamani Bankupalli, D. S.., Effect of process parameters and butadiene content on friction and wear. Materials Today: Proceedings, 416-421, **2021**.
4. Ruttba Aziz, M. I. Effect of surface texturing on friction behaviour of 3D printed polylactic. Polymer Testing, 1-10., **2020**.

5. A review on tribological performance of natural fibre polymeric composites U. Nirmal, J. Hashim and M.M.H. Megat Ahmad Tribol Int, 83 , pp. 77-104, 10.1016/j.triboint.2014.11.003, **2015.**
6. L.M. Galantucci, F. L.., Experimental study aiming to enhance. CIRP Ann., 189-192, **2009**.
7. Singh, R., & Singh, S. . Investigating the friction coefficient in functionally graded rapid prototyping of Al–Al2O3 composite prepared by fused deposition modelling. Assembly Automation, **2017**.
8. Carneiro, O. S., Silva, A. F., & Gomes, R. . Fused deposition modeling with polypropylene. Materials & Design, 83, 768-776, **2015**.
9. Nedelcu, D., Mazurchevici, S. N., Popa, R. I., Lohan, N. M., Maldonado-Cortés, D., & Carausu, C.., Tribological and Dynamical Mechanical Behavior of Prototyped PLA-Based Polymers. Materials, 13(16), 3615**, 2020**.
10. Hong, Y., Zhang, P., Lee, K. H., & Lee, C. H.., Friction and wear of textured surfaces produced by 3D printing. Science China Technological Sciences, 60(9), 1400-1406, **2017**.
11. Kessler, Reymus, M., Hickel, R., & Kunzelmann, K. H. Three-body wear of 3D printed temporary materials. Dental Materials, 35(12), 1805-1812.) ,**2019**.
12. O. A. Mohamed, S. H. Masood, J. L. Bhowmik, and A. E. Somers, "Investigation on the tribological behavior and wear mechanism of parts processed by fused deposition additive manufacturing process," J. Manuf. Process., vol. 29, pp. 149–159, **2017**, doi: 10.1016/j.jmapro.2017.07.019.
13. S. T. Method, "Standard Test Method for Wear Testing with a Pin-on-Disk Apparatus 1," Wear, 2011.
14. J. C. Middleton and A. J. Tipton, "Synthetic biodegradable polymers as orthopedic devices," Biomaterials, vol. 21, no. 23, pp. 2335–2346, 2000, doi: 10.1016/S0142-9612(00)00101-0.
15. ASTM G 99-17 Standarts

COBALT AND NICKEL ALLOY ELECTRODE CO-DEPOSITED FROM A NON-AQUEOUS ELECTROLYTE

MURAT ARTAN [*1], ABDULCABBAR YAVUZ[2], NECIP FAZIL YILMAZ[1, 3]

[1]Gaziantep University, Engineering Faculty, Mechanical Engineering Department, 27310, Gaziantep, TURKEY.
[2] Gaziantep University, Engineering Faculty, Metallurgical and Materials Engineering Department, 27310, Gaziantep, TURKEY.
[3] Hasan Kalyoncu University, Board of Trustees, 27010, Gaziantep, Turkey
*muratartan@hotmail.com

Abstract

Electrochemical capacitors, also mostly known as supercapacitors, could be novel energy storage systems globally. Their intrinsic properties make them promising energy storage devices, which can have a bridging role between batteries and traditional capacitors. In recent years, researchers paid their attention to produce high performance supercapacitors using different materials and processes. In this paper, fabricating a supercapacitor in an easy and inexpensive way is aimed. Supercapacitive performance of nickel and cobalt mixed film on graphite electrode surface was examined. Electrodeposition of nickel and cobalt from ethaline deep eutectic solvent by electrochemical reduction was investigated using the potentiostatic deposition method coupled with cyclic voltammetry. The Ni-Co based modified electrode on flexible graphite current collector has a specific capacitance of 201 mF cm-2 at the scan rate of 5 mV s-1.

Keywords: Supercapacitor, Graphite, Flexible electrode, Alloy, Metal oxide, Ionic liquid

RÜZGAR TÜRBİNİ KANATÇIK AÇI KONTROLÜNÜN BULANIK MANTIK İLE ANALİZİ

ATAKAN ARSLAN [1], HALIL EROL* [1]

[1]Osmaniye Korkut Ata University, Engineering Faculty, Electrical and Electronic Engineering Department, Osmaniye, TURKEY.

ÖZET

Rüzgâr enerjisi sistemleri (RES), rüzgârdan aldıkları enerjiyi jeneratörde elektriğe çeviren sistemlerdir. Görece çevreye daha az zarar veren RES'ler gelişen radikal iklim değişiklikleri sonrası daha çok itibar edilir duruma gelmiştir. Ancak değişken rüzgâr hızları çeşitli ulaşım zorlukları gibi etkenler RES yapımında ve yatırımında iyi bir planlamanın gerekliliğini ortaya koymuştur. RES'lerden alınan verimi artırmanın birçok yolu vardır. Bunlardan biri de rüzgâr türbini kanatlarının açısını değiştirmektir. Bu çalışmada da rüzgâr türbini kanadı bulanık mantık ile kontrol edilerek daha verimli ve stabil bir çıkış elde edilmeye çalışılmıştır. Bulanık mantık sisteminin parametreleri değiştiğinde oluşan sonuçlar tatmin edicidir.

Keyword: Bulanık Mantık, Rüzgâr Türbini, Rüzgar türbini Kanat Açısı kontrolü

DESIGN AND ANALYSIS OF AN ULTRASONIC SONOTRODE FOR HIGH FREQUENCY VIBRATION ASSISTED SHEET METAL FORMING APPLICATIONS

SADIK OLGUNER[1], ALI TOLGA BOZDANA[2]

[1] Gaziantep University, Turkey ; [2] Gaziantep University, Turkey

ABSTRACT

Ultrasound technology is widely used in welding, metallurgy, food processing, machinery and chemical industries due to its beneficial effects such as temperature increase, reduction in friction and resistance of material against further deformation. A typical ultrasonic system is composed of four main parts: an ultrasonic generator, a transducer (converter), a booster, and a sonotrode (horn). The ultrasonic generator that converts power supply into high frequency voltage signals, the transducer that converts such signals into mechanical oscillations and the booster that serves as an amplitude transformer are generally designed and manufactured as standard in different features and capacities for all applications. However, the sonotrode that transfers ultrasonic vibrations into the tool should be designed and manufactured with specialized geometric and mechanical properties according to the application. Designing sonotrodes for ultrasonically assisted metal forming processes brings some design challenges due to the nature of forming dies. In this study, in order to apply ultrasonic vibrations to sheet metal forming processes, theoretical background of ultrasonic sonotrode design procedure is examined. A novel ultrasonic sonotrode for implementation of high frequency vibrations into the deep drawing process is designed using harmonic finite element analyses. The designed sonotrode is manufactured and vibration amplitude and frequency of vibrations on the sonotrode surface is measured with an accelerometer in order to determine the damping coefficient to be used in harmonic analyses of complete forming system. As a result of the deep drawing tests, it was observed that the formability of the sheet materials significantly increased by applications of ultrasonic vibrations with the designed system. Acknowledgments: This study has been financially granted by Scientific and Technological Research Council of Turkey (TUBITAK) under the grant number of 315M300. The authors would like to express their sincere thanks to TUBITAK for the support.

KEYWORDS - Deep drawing, Ultrasonic vibrations, Ultrasonic sonotrode, Finite element analysis

MAKINE OGRENME TEKNIKLERI KULLANILARAK HAZIR GIYIM ENDUSTRISINDE IS VERIMLIGININ SINIFLANDIRILMASI

ABDULLAH CALISKAN[1], ZEYNEL ABIDIN CIL[2]

[1] Munster Technological University, Ireland ; [2] Izmir Democracy University, Turkey

ABSTRACT

Hazır giyim günümüzde hızla büyüyen endüstrilerin başında yer almaktadır. Hazır giyim endüstrisin' de ürün çeşitliliğinin fazlalığı veya bireysel ürün üretimden dolayı genel olarak emek yoğun bir sektör olarak hizmet vermektedir. Bu sebepten dolayı, bu sektörde iş yapan firmaların verimliliği doğrudan işçilerin verimliğine bağlıdır. Işçi verimliliğini etkileyen birçok sebep bulunmaktadır. Bu çalışmada çalışma günü, saati, mesai saati v.b parametrelerden yola çıkılarak işçilerin verimliği tahmin edilmiştir. Belirtilen parametrelerden yola çıkılarak işçilerin verimli olup olmadıkları ya da hangi koşullarda verimli oldukları çeşitli makine öğrenme teknikleri yardımıyla ölçülmüştür. Bunun yanında hangi özniteliklerin sınıflandırma başarımında ne kadar etkin olduğu belirlenmiştir. Çünkü amacımız verimliği ölçmektir. Eğer verimliği en çok etkileyen öznitelik bulunursa daha az veri toplanarak daha etkin ölçümler yapılmasının önü açılmış olur. Veri setinde toplamda 14 öznitelik yer almaktadır. Bu özniteliklere karşılık gelen işçilerin verimliği yer almaktadır. Önerilen modele giriş verisi olarak 14 farklı öznitelik gönderilerek işçilerin verimliği tahmin edilmiştir. Çalışmada veri setine uygulanan 4 farklı sınıflandırıcı ve bunlara ait istatiksel sonuçlar karşılaştırmalı olarak sunulmuştur. Bu çalışmanın deneysel sonuçları, önerilen modelin 0.86 doğruluk oranı ile umut verici bir tahmin performansı verdiğini göstermiştir.

KEYWORDS - Hazır Giyim, Verimlilik, Makina Öğrenmesi

ENERGY, ENVIRONMENT AND ECONOMY INVESTIGATION OF WASTE HEAT RECOVERY TECHNOLOGIES IN MARINE INDUSTRY

HASAN MITHAT DELİBAŞ [*1], ERHAN KAYABAŞI [2]

[1] Hasan Kalyoncu University, Engineering Faculty, Mechanical Engineering, Gaziantep, TURKEY.
[2] Karabük University, Engineering Faculty, Mechanical Engineering, Karabük, TURKEY.

Abstract

In this study, a review and comparison of the Waste Heat Recovery (WHR) systems in maritime industries are made in detail in terms of energy, environment, and economy (3E) analysis. WHR systems are classified according to types and stroke engines, thermodynamic cycles, waste heat source, types of fluid, heat exchangers, and the pollutants released into the atmosphere by the exhaust gas. Furthermore, while examining WHR systems, criteria such as feasibility, initial investment costs, depreciation periods, depreciation rates, possible energy recovery are considered. It is noteworthy that such a review has not been conducted so far in the comprehensive literature researches. With this study, the most appropriate waste heat recovery systems can be determined in marine industries.

Keyword: Waste heat recovery (WHR), Marine industries, Energy savings, Thermodynamic cycles, 3E analysis

A STUDY ON THE MECHANICAL PROPERTIES OF BULK CONTINUOUS FILAMENT YARNS PRODUCED BY MIXING POLYPROPYLENE HOMOPOLYMER WITH POLYPROPYLENE COPOLYMER OR THERMOPLASTIC POLYOLEFIN

CEMİLE EMEL YAZ[1], CEM GÜNEŞOĞLU [2], MEHMET TOPALBEKİROĞLU[2]

[1] Gaziantep University, Naci Topçuoğlu Vocational School, Machinery and Metal Technologies Department, Gaziantep, TURKEY.
[2] Gaziantep University, Faculty of Engineering, Textile Engineering Department, Gaziantep, TURKEY.

Abstract

Bulked continuous filament (BCF) yarns have an extend usage on machine carpets as pile yarn. Polypropylene (PP) is the major polymer which is preferred as raw material on BCF yarn production, due to its good resistance to abrasion and low price, nevertheless some of the mechanical behaviors are expected to be improved. In other respects, polypropylene copolymer and thermoplastic polyolefin polymers are widely preferred engineering materials in different industrial products to improve some mechanical behavior of polypropylene. In this sense, with the purpose of investigate the effects of mixing polypropylene homopolymer with polypropylene copolymer (coPP) or thermoplastic polyolefin (TPO) polymers on the mechanical properties of BCF yarns, eleven different types of BCF yarn samples with linear density 2100/144 dtex as five types of TPO mixed (5%, 10%, 15%, 20%, 25%), five types of coPP mixed (5%, 10%, 15%, 20%, 25%) and a pure PP as a reference yarn were produced and tensile strength, elongation, shrinkage and crimp contraction properties of the samples were examined. Experimental results and statistical analyses showed that, mixing PP homopolymer with coPP or TPO had a significant effect on the mechanical properties of BCF yarns.

Keyword: BCF Yarn, Polypropylene, Copolymer, Thermoplastic Polyolefin.

THE HIGH PURITY NANOSIZED STRONTIUM CARBONATE PRODUCTION WITH THE AMMONIUM CARBONATE MEDIA VIA THE MECHANOCHEMICAL SYNTHESIS PROCESS

SULTAN OZTURK[1], FURKAN ALPTEKIN[1], SELMINE AKYOL[1], SEFA EMRE SUNBUL[1], KURSAT ICIN[1]

[1] Karadeniz Techical University, Turkey

ABSTRACT

The conversion and production of strontium carbonate from concentrated celestite by mechanochemical synthesis process ore was investigated. Different proportions of ammonium carbonate were used to convert celestite ore to strontium carbonate. Mechanochemical synthesis process was applied with 3 different ratios of 1, 1.5 and 2 between ammonium carbonate and celestite ore and 3 different synthesis times of 10, 100 and 200 minutes. Impurities and contaminations in concentrated celestite ore were removed by acid leaching and calcination. DTA, TGA, XRD, SEM, EDX, TEM and FT-IR analyzes were performed on the produced strontium carbonates. As a result of the mechanochemical synthesis process of 200 minutes, it was observed that the strontium sulfate phase decreased, and the strontium carbonate phase increased. Also, it was determined that carbonate bonds were formed, where the sulfate bonds were destroyed in the FT-IR analysis. The decomposition temperatures of strontium carbonate were decreased with increasing synthesis times

KEYWORDS - Celestite, Strontium carbonate, Mechanochemical synthesis

STRUCTURAL TRIBOLOGICAL ISOTHERMAL OXIDATION AND CORROSION PROPERTIES OF AL CO CR FE NI TI CU HIGH ENTROPY ALLOY

SULTAN OZTURK[1], SELMINE AKYOL[1], FURKAN ALPTEKIN[1], KURSAT ICIN[1], SEFA EMRE SUNBUL[1]

[1] Karadeniz Techical University, Turkey

ABSTRACT

In the present work, Al10Co24Cr10Fe15Ni34Ti6Cu1 (at.%) was obtained high entropy alloy (HEA) with vacuum arc melting. The microstructure, tribological properties, oxidation, and corrosion resistance of the HEA were detailly investigated. The faced-centered cubic solid solution structure was observed in the microstructure. SEM analysis shows that Fe, Co, and Cr elements are dominant in the dendrite region, the interdendritic regions are significantly enriched in Al and Ti elements. The average friction coefficients for 0.5 MPa, 1 MPa, and 1.5 MPa loads were found as 0.59, 0.64, and 0.68, respectively. The specific wear rates generally raised in consequence of the increase in the same applied loads. The time-dependent oxidation amount exponentially increased in our HEA. Oxide formation appeared as TiO2 and AlFeO3 in the oxidation process at 900 °C. The corrosion potential (Ecorr) and the corrosion current density (Icorr) values of the alloy were determined -0.082 V and 2.18 x 10-8 A/cm2, respectively. Acknowledgments This study was supported by The Scientific and Technological Research Council of Turkey (TUBITAK) (Grand Nos. 119M111) and Karadeniz Technical University, Department of Scientific Research Project (Grand Nos. FDK-2018-7685 and FBA-2019-8162). The authors are grateful Barit Maden A.Ş, which is supplied a lot of celestite ore.

KEYWORDS - High entropy alloys; Microstructure; Surface oxidation, Tribological properties; Corrosion resistance

ASSESSMENT OF HEMODIALYSIS MEMBRANES A REVIEW

ADIL GUJRI[1], OMER NECATI CORA[2]

[1] Karadeniz Technical University, Turkey ; [2] Karadeniz Technical University, Turkey

ABSTRACT

Hemodialysis, often known as dialysis, is a blood purification procedure in which uraemic retention solutes in a failing kidney are removed through a semipermeable membrane. Conventionally, hemodialysis membranes are classified based on their composition (cellulosic or non-cellulosic) and permeability (low and high flux). However, with the advancement in material science and the development of new synthetic polymeric materials, traditional membrane classification became obsolete. Advanced polymer chemistry enabled the development of membranes with specific characteristics and refined properties. Hence for a suitable characterization of these new membranes, additional parameters including hydrophilicity and hydrophobicity of membranes, mass transfer properties (diffusion, convection, adsorption, etc.) and electrical potential are taken into consideration. On the other hand, various production parameters could have a huge impact on the final characteristics of the membranes. These include composition of the solution, viscosity, spinning temperature, pumping rates of the solution and the bore fluid, coagulation agents (inside and outside), coagulation temperature, & nascent fiber drawing rate. In this review, we present the most recent cutting-edge developments in the field of hemodialysis membranes, describe the different processes used in membrane production (dry spinning, wet spinning, and dry jet wet spinning) and the solute removal mechanisms. Finally, we discuss various process parameters that impact the morphology of the membranes like, the shape and size of the pores, wall thickness, macro voids, etc.

KEYWORDS - Hemodialysis, Hollow fiber membranes, Dialysis.

FINITE ELEMENT MODELING AND ANALYSIS OF REPRESENTATIVE WING STRUCTURE FOR STRUCTURAL HEALTH MONITORING PURPOSES

MUHAMMED LATIF BEKCI[1], OMER NECATI CORA[2]

[1] Ordu University, Turkey ; [2] Karadeniz Technical University, Turkey

ABSTRACT

Introduction Structural health monitoring (SHM) is widely used in various engineering applications to detect and diagnose failures in real-time. The present study examined the behaviour of the representative wing structure in response to different loading conditions via finite element analysis (FEA) to understand the deformation characteristics of the wing structure and suggest locations for the sensors to be used for SHM purposes. Keywords: Representative wing structure, Carbon fibre reinforced polymer, Finite element analysis. Methods Representative wing structure consists of metal and composite components in general. SHM will conduct on top and bottom composite test panels on the structure, and this will be manufactured from 18 plies of CFRP. The finite element model of the wing structure was established with various solid element types, and about 560.000 elements were used in total. FEA was conducted on a PC with an Intel® Core™ i7-10700F processor and 64 GB RAM. The structure is loaded up to 2000 kN through rectangular bars along the width of the structure on its top. Each analysis lasted 22 minutes of CPU time approximately. Analysis results are used to determine the maximum vertical displacement and stress distribution on the structure, also the critical points for possible failure initiation on the composite test panels of interest. Results and Discussion The displacement of the rectangular loading blocks was obtained with respect to incremental loading values up to 2000 kN. This data will be compared with the actual test data to verify the accuracy of the model established. It was revealed that the top composite test panel fails at 2000 kN loading condition based on the maximum stress failure criterion. Nevertheless, the metallic truss structure was found to fail much earlier compared to composite panels at a load level of 300 kN, approximately. Conclusion: To conclude, the representative structure fails due to the failure of load-carrying frames rather than composite skins. If the composite plate is required to be failed first, either the steel structure should be strengthened, or some pre-cracks need to be introduced in composite plates.

KEYWORDS - FEA, Representative Wing Structure,Structural Health Monitoring

EFFECT OF SURFACE TEXTURING ON TRIBOLOGICAL BEHAVIOR OF SAE 600 BEARING BRONZE

DOGAN ACAR[1], HASAN ONUR TAN[2], OMER NECATI CORA[3]

[1] Karadeniz Technical University, Turkey ; [2] Giresun University, Turkey ; [3] Karadeniz Technical University, Turkey

ABSTRACT

SAE 600 bronze is a general-purpose bearing alloy, which is used in ship propellers, submerged bearings, and in small electric motors due to its good anti-friction properties, high strength and hardness, adequate ductility, and excellent machinability. This study aimed to further improve the frictional properties of SAE 600 Bronze by means of producing micro-features (e.g., lubricant pockets) on contact surface. The micro-pockets were realized through micromachining. First, test specimens were machined to the dimensions of 10x15x26 mm. Then, 40 lubricant pockets with different diameters (0.2 and 0.6 mm) were formed on specimen surfaces. The samples were then tested against AISI 4140 rotating disk using a block-on-disk type of test system. Effect of lubricant-pocket size, normal load value, lubrication conditions on the coefficient of friction and wear performance were investigated. It was measured that coefficient of friction is reduced and stabilized after certain test duration. Decrease in friction coefficient was observed to be decreasing due to increase in lubricant pocket diameter. Besides, temperature measurements showed than presence of lubricant pockets are effective on decrease in temperature values.

KEYWORDS - Surface Texturing, Lubricant Pocket, Lubricated Friction, Wear

INVESTIGATION ON THE SOLID PARTICLE EROSION PERFORMANCE OF TRANSPARENT MATERIALS

MOHAMMAD HUSSAIN DANESH[1], DOGAN ACAR[2], OMER NECATI CORA[3]

[1] Karadeniz Technical University, Turkey ; [2] Karadeniz Technical University, Turkey ; [3] Karadeniz Technical University, Turkey

ABSTRACT

In this study, an investigation on solid particle erosion performances of transparent polycarbonate solid sheet, plexiglass and two types of laminated materials, which are widely used in various industries, were performed. All the experiments were performed using tests system developed per ASTM G76-13 and MIL-STD-3330 solid particle erosion test standards. The influence of impact angle (20°, 30°, 45°, 60° and 90°) and impact velocity (70, 150 and 195 m/s) were taken into consideration on the solid particle erosion behavior. Besides these test parameters, alumina (Al2O3 – 52 µm) and silica sand (SiO2 – 71 and 348 µm) with different particle diameters were used as impinging erodent particle. Polycarbonate material showed higher erosion resistance at all velocity and impact angle parameters when compared to other materials. In addition, polycarbonate material represented an incubation behavior at low velocity tests performed with smaller silica sand size. Impact angle of 30°, for both polycarbonate and laminated glass materials, was noted as the direction that gives the highest erosion rate. Laminated glass samples exhibited different erosion characteristics compared to single sheets.

KEYWORDS - Solid particle erosion, transparent materials, polycarbonate, plexiglass, laminated glass

INVESTIGATION OF THE HUB DIAMETER EFFECT ON PROPELLER THRUST

ENES COŞKUN*[1], MEHMET HANİFİ DOĞRU [2]

[1] Gaziantep University, Aeronautics and Aerospace Faculty, Aeronautics and Aerospace Engineering Department, Gaziantep, TURKEY.
[2] Gaziantep University, Aeronautics and Aerospace Faculty, Pilotage Department, Gaziantep, TURKEY.

Abstract

With the widespread of unmanned aerial vehicles in the aviation industry, the importance of detailed examination of propellers, whose task is to provide thrust, has also increased. A propeller is a part that is formed by attaching more than one aerodynamically shaped blade to a hub and produces thrust by being rotated by a motor. The amount of thrust that is produced by a propeller depends on some parameters such as diameter, number of blades, pitch angle etc. The aim of this study is to investigate the thrust distribution along a propeller diameter section with the gradual increase of the hub diameter. Related studies show that the maximum thrust of a propeller is obtained in the region between 75% and 85% of the propeller length. In order to obtain the necessary data, numerical flow analyzes were made and the results were discussed. As a conclusion, at the very closer to the root of the propeller blade, the amount of produced thrust is considerably low compared to the near tip of propeller. Therefore, the thrust loss due to the increase of the propeller hub diameter is negligible and maximum thrust obtained in the expected region.

Keyword: Propeller, Computational Fluid Dynamics, Hub Effect, Thrust Distribution.

EFFECT OF PROPELLERS NUMBERS AND HORIZONTAL DISTANCE IN DESIGN OF VTOL

MUSTAFA VARKİ [1], EYÜP YETER [1], M.HANİFİ DOĞRU[2]

[1] Gaziantep University, Aeronautics and Aerospace Faculty, Aeronautics and Aerospace Department, Gaziantep, TURKEY.
[2] Gaziantep University, Aeronautics and Aerospace Faculty, Pilotage Department, Gaziantep, TURKEY.

Abstract

Nowadays, unmanned aerial vehicles with vertical take-off and landing (VTOL) capabilities are increasing. One of the reasons is that these vehicles can take off and land even in difficult conditions and does not need any runway. In design stages of unmanned aerial vehicles, certain design criteria are taken into consideration. VTOL vehicles, which are divided into tilt-wing or tilt rotor, used in areas such as operation areas, efficiency and cost advantage. In this study, CFD analysis is performed to determine the optimum configuration of the VTOL vehicle by considering the horizontal distance between the propellers and the number of propellers of a tilt-wing unmanned aerial vehicle. For this aim, effect of aerodynamic parameters such as thrust, velocity etc. of propellers are investigated. As a result of this study, the suitable propeller position on the wing and number of propellers for the VTOL vehicle are determined.

Keywords: VTOL, Propeller, Aerodynamic Parameters, Flow Analysis

STRUCTURAL AND SURFACE PROPERTIES OF GLASS POWDER COATED Cr STEELS

AYŞE NUR ACAR[1*], DOĞAN KAYA[2], ABDUL KADIR EKŞİ[3], AHMET EKİCİBİL[4]

[1]Çukurova University, Ceyhan Engineering Faculty, Mechanical Engineering Department, Adana, TURKEY.
[2]Çukurova University, Adana Vocational School, Electronic and Automation Department, Adana, TURKEY.
[3]Çukurova University, Engineering Faculty, Mechanical Engineering Department, Adana, TURKEY.
[4]Çukurova University, Sciences and Letters Faculty, Physics Department, Adana, TURKEY.

Abstract

The most common used glasses are soda-lime silica glasses, which contain alkaline and alkaline earth oxide materials, such as silicon, sodium, aluminium oxides, *etc*., and these soda lime silica glasses are used in different applications such as windows, bottles, *etc*. Glass powder is acquired by grinding of waste glass cracks and applied as additive in structural materials due to its compositions. In this study, the effect of glass powder on the surface and structural properties Cr steel sheets has been investigated. Cr steels coated with dehydrated glass powder have been annealed at 950 °C temperature in the furnace for various hours and cooled in the furnace. The surface and structural properties of these coated steel sheets have been investigated by optical microscopy images, Scanning electron microscopy images, Energy dispersive x-ray spectroscopy data. The crystal structures of these sheet samples have been recorded with XRD patterns. As a result, glass powder on the surfaces of Cr steel sheets has not melted homogeneously and surface appearances of these steel sheets have been obtained as waved textures.

Keywords: Cr steel, Glass powder, Heat treatment, Structural property, Surface property

A STUDY ON DETERMINATION OF OPTIMUM AUTOFRETTAGE PRESSURE OF A THICK WALLED CYLINDER WORKING UNDER CYCLIC PRESSURE

HAKAN CANDAR[1], HALIL KIMSESIZ[2]

[1] University Of Gaziantep, Turkey ; [2] University Of Gaziantep, Turkey

ABSTRACT

This paper presents an analytical study on determination of optimum autofrettage pressure for the high pressure cylinder of an abrasive waterjet intensifier pump working under cyclic pressure. In this optimization problem, maximization of safety factor (n) for dynamic condition at the elastic-plastic interface is defined as an objective function. For different autofrettage pressures, the safety factors both at the inner diameter of the cylinder and at the elastic-plastic interface are calculated according to Modified Goodman Theory. In the calculations, endurance limit modifying factors are neglected and the endurance limits are considered equal for both regions. In the stress calculations, autofretage equations based on the actual stress-strain curve of the material are used. The safety factors at the inner diameter of the cylinder and at the elastic-plastic interface are compared, and the autofretage pressure for which the safety factor calculated for the inner diameter is small are not taken into account. The autofrettage pressure that gives the highest safety factor at the elastic-plastic interface is defined as the optimum autofretage pressure. Optimum autofrettage pressure for maximum working pressure is also calculated and the results are compared.

KEYWORDS - Autofrettage, thick walled cylinders, fatigue analysis, optimization

DESIGN OF FLIGHT CONTROLLER UNIT BASED ON PID CONTROL

HAKAN CANDAR[1], AHMET OZGUR AYIK[2]

[1] University Of Gaziantep, Turkey ; [2] University Of Gaziantep, Turkey

ABSTRACT

In this study, a flight control board is designed which can be used for various unmanned aerial vehicles (UAV). STM32F411 microcontroller is used as the central processing unit and it is programmed by using special function registers in C language to increase the system performance. High operating frequency and FPU unit are used to perform PID algorithm calculations at high speed. The orientation angles data are obtained from the MPU6050 IMU (Inertial measurement unit) sensor. Radiolink R9D is used as the control receiver module as it supports SBUS data communication protocol. The system is controlled by PID, which is a closed-loop control algorithm. The software is developed using the Keil uVision5 IDE. Board schematic and PCB design are made using KiCad. The model is produced and the software is integrated into the system. It is seen in the performance tests that the PID algorithm gives expected results as in theory and the system is tried to reach the set point accordingly. Also, Pid gain values is investigated for a stable flight.

KEYWORDS - Unmanned aerial vehicles (UAV), Flight control board, Control algorithms, Embeded systems, PID control

IMPLEMENTING THE PMSM RESOLVER INTERFACE ON FPGA

ABDULKADIR SADAY[1], ILKER ALI OZKAN[2], ISMAIL SARITAS[3]

[1] Selcuk University, Turkey ; [2] Selcuk University, Turkey ; [3] Selcuk University, Turkey

ABSTRACT

Permanent magnet synchronous motors (PMSM) are brushless motors with sinusoidal waveforms, which are frequently used in industrial applications. It is generally used in electric and hybrid vehicles, goods such as refrigerators, washing machines, dishwashers, and other devices that require high reliability and efficiency. Compared to standard DC motors, PMSMs are more reliable due to their construction. There are application methods for controlling PMSMs such as vector control and torque control. For each application, the control is calculated over the current position of the motor, current, and voltage values. Precise measurement of the motor position is an important factor for the precision of the control. In addition, problems such as torque fluctuations must be eliminated and the motor must be controlled in real-time for stable operation. The concept of the application is to create a closed-loop motor driver for the PMSM using a solver. In this study, the motor position calculator with the resolver interface is designed on FPGA. With this design, the instantaneous position of the PMSM is provided via the resolver interface, and real-time calculation is provided with the FPGA. As a result, the calculations of the resolver interface has been done on the FPGA and, in order for the application to be a source for further studies, the design has been turned into an IP package.

KEYWORDS - fpga, pmsm, resolver calculator

INVESTIGATION OF MATERIAL REMOVAL RATE FOR INCONEL 718 AS AEROSPACE MATERIAL BY FLOW PEENING GOV PROCESS

KURSAD GOV[1], BURAK SAHIN[2], MURAT KALAK[3], MEHMET SAIT KOCA[4]

[1] Gaziantep University, Turkey ; [2] Gaziantep University, Turkey ; [3] Gaziantep University, Turkey ; [4] Gaziantep University, Turkey

ABSTRACT

Inconel 718 is familiar with its good mechanical properties such as high temperature resistance, temperature strength, fatigue strength, hardness, chemical wear resistance, corrosion resistance, creep resistance, high strength-to-weight ratio. This all makes Inconel 718 a significant candidate material for aerospace applications and many other hostile environments. In addition to these all merits of Inconel 718, there is a big task to machine it because of poor processability of Nickel alloys. In the machining stages of Inconel 718, high temperature, high stress, overheating and burning occur because of its low thermal conductivity. Because of all these difficulties of machining Inconel 718, electrical discharge machining (EDM) is used for cutting and machining of it. There is a high demand for a secondary process for the purpose of surface enhancement to provide required level of surface quality in terms of roughness and hardness after EDM. But material removal rate should be kept at minimum level for surface enhancement process to maintain geometrical and dimensional accuracy. In this study, flow peening (GOV) process is applied to Inconel 718 as an aerospace material for surface enhancement. Then material removal rate (MRR) values are going to be presented. Results will be compared to those of abrasive flow machining (AFM) process.

KEYWORDS - Inconel 718, Aerospace materials, Material removal rate, Flow peening (GOV) process, Electrical discharging machining (EDM), Abrasssive flow machining (AFM), Surface enhancement process

EXAMINATION OF THE INFLUENCE OF PRINTING PARAMETERS FOR THE CONTINUOUS CARBON FIBER-REINFORCED THERMOPLASTICS BASED ON FUSED DEPOSITION MODELING

ALTUĞ UŞUN [*1], RECEP GÜMRÜK [1], NURİ YILDIZ[1], BAHRİ BARIŞ VATANDAŞ[1]

[1*]Karadeniz Technical University, Department of Mechanical Engineering, Trabzon, TURKEY.

Abstract

The continuous carbon fiber-reinforced thermoplastic (CFRTP) printing process has been used more widely in recent years and is an alternative production method, especially in sectors such as aviation, automotive, prototyping, medical applications, and aerospace. Although additive manufacturing reduces the design limitations and makes it easier to manufacture, it is one of the disadvantages of this method: it has relatively low thermal and mechanical properties compared to standard production techniques. Therefore, in this study, printing parameters such as nozzle temperature, printing speed, layer thickness and heated bed temperature was investigated for fused deposition modelling. In this regard, a polymer impregnation line based on the melt impregnation technique was utilized to obtain CFRTP filaments using polylactic acid (PLA) and 3K carbon fiber. Obtained filaments then were used to print three-point bending test samples in order to investigate mechanical performance. The test result showed flexural stress between 108 and 224 MPa and flexural modulus between 9.67 and 17.69 GPa with a 23% fiber ratio. Results from this study proclaim that CFRTP's manufactured with this method and optimized printing parameters have great potential for implementing future production methods.

Keyword: Continuous Fiber-reinforced Thermoplastic (CFRTP), Fused Deposition Modelling (FDM), Additive Manufacturing, Mechanical Properties

SURFACE OBSERVATION OF INCONEL 718 TREATED BY FLOW PEENING GOV PROCESS

KURSAD GOV[1], BURAK SAHIN[2]

[1] University Of Gaziantep, Turkey ; [2] University Of Gaziantep, Turkey

ABSTRACT

Inconel 718 which is a nickel based alloy has superior mechanical properties. It is preferred in aerospace applications due to its high fatigue strength, hardness, wear resistance, corrosion resistance and high strength. On the other hand, it has low thermal conductivity and poor processability. This makes it difficult-to-cut material. So nontraditional manufacturing methods are generally preferred to machine nickel alloys. In this study, Inconel 718 samples are prepared by cutting with electrical discharge machining process. Then flow peening (GOV) process is applied to samples for surface enhancement to obtain required surface quality parameters. SEM images are taken and compared to those of some other methods.

KEYWORDS - Inconel 718, Aerospace materials, Material removal rate, Flow peening (GOV) process, Electrical discharging machining (EDM), Surface enhancement process, SEM images

THE DESIGN OF SOLAR CELLS SENSITIVE TO THE HELICAL BEAMS

KORAY KÖKSAL [1]

[1] Hasan Kalyoncu University, Engineering Faculty, Electrical and Electronics Engineering Department, Gaziantep, TURKEY.

Abstract

The sensitivity of silicon-based solar cells to the polarization of light is mainly weak and ignorable. However, the recent studies show that some organic solar cells can be sensitive to polarization. Circularly polarized or so-called spin-polarized light is a well-described example of the helical beams which are able to carry optical helicity[1-2]. In some organic solar cells, the spin of the photon can be transferred to the electrons, which is called photon spin-electrons spin interaction [3-4]. In our study, we will describe and investigate the theory of the interaction between organic solar cells and helical beams.

Keyword: Solar cells, organic solar cells, helical beam, polarization

AN EXPERIMENTAL STUDY ON THE PARAMETERS AFFECTING THE THERMAL SEAL FORCE OF COATED BIDIRECTIONAL STRETCHED PET FILM FOR FOOD PACKAGING APPLICATIONS

ÇAĞRI TIKILOĞLU [*1], EMRAH ÖZAHİ[2]

[1]Gaziantep University, Graduate School of Natural and Applied Sciences, Product Development and Design Engineering, Gaziantep, TUKEY.
[2]Gaziantep University, Faculty of Engineering, Department of Mechanical Engineering, Gaziantep, TUKEY.
[*]cagritikiloglu@gmail.com

Abstract

Besides the physical and barrier properties of a flexible plastic material to preserve the freshness and shelf life of a product, the heat sealing performance of the packaging also plays an important role. Proper heat sealing is an important requirement in packaging. The main critical control elements for heat sealing are temperature, time and jaw compression force. Adequate pressure on the surfaces must be used for a sufficient time to achieve a reasonable bond. Thus, polymer chains can spread and form bridges across the interface. Since heat sealing is a melt fusion process, time and temperature are two most fundamental parameters that affect sealing performance. Time and temperature are interrelated. The physical evaluation of an adhesion can provide a useful qualitative indicator of the effectiveness of the heat sealing process and is based on optimization of the parameters of dwell time, temperature and process pressure. The aim of this study is to determine the effective jaw temperature and compression time for the seal strength of the surface coated PET film to the APET surface. The effects of parameters, which are thought to be effective on the heat seal performance of the surface coated food packaging film, on the seal strength were analyzed using the Box-Behnken design, which is one of the response surface methodologies (RSM). In this study, the necessary thermal bonding process parameters have been determined to maximize the seal strength.

Keyword: BOPET, Box-Behnken Experiment Design, Response Surface Method, Heat Seal, Coating.

EFFECT OF DIFFERENT AMOUNTS OF CARBON FIBER ADDITIVE ABS ON THERMAL DISTORTION AND COOLING TIME

OMER EYERCIOGLU[1], ENGIN TEK[1], MEHMET ALADAG*[1], GULAGA TAS[2]

[1] Gaziantep University, Engineering Faculty, Mechanical Engineering Department, Gaziantep, TURKEY.
[2] Hasan Kalyoncu University, Engineering Faculty, Mechanical Engineering Department, Gaziantep, TURKEY.

Abstract

This study presents an analysis of the distortions of ABS composites with different amounts of carbon fiber produced by large-scale additive manufacturing (LSAM). Part failures often occur in extrusion-based large-scale additive manufacturing due to thermal contraction. These are called thermal distortions. Undesirable distortions are caused by differential thermal expansion and contraction and corresponding residual stresses. Residual stress and strain analysis require accurate thermo-mechanical material properties. These can be controlled by changing the amount of additives in polymer material. In this study, fiber orientations in Acrylonitrile Butadiene Styrene (ABS) reinforced with 10%, 5%, 0% carbon fiber by weight were modeled using a homogenization technique. The amount of distortion of the parts modeled according to these carbon fiber ratios was examined and, the cooling durations were compared.

Keywords: LSAM, carbon fiber, thermal imaging, ABS

ELECTROCHEMICAL BEHAVIOUR AND PERFORMANCE OF FLEXIBLE GRAPHITE YARNS IN DIFFERENT ELECTROLYTES WITH WIDE POTENTIAL WINDOW OF 2 V

MAHMUT FURKAN KALKAN [*1], MURAT ARTAN[1], HASAN MITHAT DELİBAŞ[2] NECIP FAZIL YILMAZ[1,3], ABDULCABBAR YAVUZ[4]

[1] Gaziantep University, Engineering Faculty, Mechanical Engineering Department, Gaziantep, TURKEY.
[2]Hasan Kalyoncu Univeersity, Engineering Faculty, Mechanical Engineering Deparment, Gaziantep, Turkey
[3] Hasan Kalyoncu University, Board of Trustees, 27010, Gaziantep, Turkey
[4] Gaziantep University, Engineering Faculty, Metallurgical and Materials Engineering Department, Gaziantep, TURKEY.
*mfkalkan@gantep.edu.tr

Abstract

Energy storage systems have received increasing attention in recent years because of the requirements of energy supply with respect to the growing population and technology. Among the technologies of energy storage devices, supercapacitors become popular due to their superior characteristics such as high power density, extremely fast charge-discharge capability and long life cycle. A wide variety of materials are already in use to fabricate supercapacitors. Carbon and its derivatives are common materials among the electrode materials of supercapacitors. In this study, electrochemical behaviour of flexible graphite yarns are investigated in different media in order to elucidate the performance of graphite as a supercapacitor material. Electrochemical experiments of graphite electrode are carried out in sodium sulphate (Na_2SO_4), hydrochloric acid (HCl), potassium hydroxide (KOH) and Ethaline deep eutectic solvent as electrolyte media. Graphite yarn is cycled at wide potential window (from -1 V to 1 V) at various scan rates in the range of 5 to 100 mV s^{-1} in order to observe the associated electrochemical behaviour and performance. Graphite yarn electrodes without any treatment can be used in Ethaline and aqueous Na_2SO_4 electrolytes. However, these electrodes cannot be used in acidic or alkaline media with high potential window of 2 V.

Keyword: graphite, supercapacitor, energy storage, flexible, capacitance

BROADBAND MULTILAYER ABSORBERS DESIGN USING DS-SEEKER OPTIMIZATION ALGORITHM

UĞUR CEM HASAR[1], MONA ALFAQAWI [2]

[1]Gaziantep University, Engineering Faculty, Electric and Electronic Department, Gaziantep, Turkey.
[2] Gaziantep University, Engineering Faculty, Electric and Electronic Department, Gaziantep, Turkey

Abstract

This work the optimization of a broadband absorbers based on multi-layered absorber scheme have been proposed. Non similar to the usual designs of the problem design the number of layers (NL) and their sequence have been determined randomly and fid to the optimization algorithm. By applying such method, we prevent the loss of the best chances by decreasing the number of optimized parameters and give a better randomity in the NL selection. As in the traditional procedure of the pre-determination of the number of layers may prevent the discovery of the global best solution. In this study we called the optimization algorithm a double-stage Seeker Optimization Algorithm (DS-SOA), as the SOA has been used to determine the thicknesses of the randomly selected layers independently during the second stage of the process but not the type of the layers. The pre-selected frequency ranges, incident angles as well as the polarization have been selected as per the ones in the literature for the sake of fare comparison. The results show that the DS-SOA is superior to the designs in the literature in finding the best solutions.

Keyword: Multilayer, Broad band, Optimization, Seeker Optimization Algorithm.

MATERIAL REPLACEMENT AND TOPOLOGY OPTIMIZATION STUDY ON A PVC CUTTING MACHINE COMPONENT

HANÇERKIRAN ZEYNEP[1], AHLATCI UMUT CAN[1], TOPUZOGLU ERTAN[1], KASAPCOPUR TAYLAN[1], ALKAN ERKAN[1],FIKRET ERTURK[2] UMUT KARAGUZEL[3], MUSTAFA BAKKAL[1]

[1]Istanbul Technical University, Department of Mechanical Engineering, Istanbul, TURKEY
[2]Yılmaz Machine, Istanbul, TURKEY
[3] Isik University, Istanbul Department of Mechanical Engineering, TURKEY

Abstract

In this study, it is aimed to lighten the aluminum body of the PVC cutting machine, reduce the production cost and shorten the production time. With this purpose, firstly, literature researches of composite materials were made and the PVC machine was introduced. Then, alternative designs of this body were made in Fusion360, and material selection was discussed in line with the analyzes made on the designs in ANSYS. Designs of this body were reexamined by topology optimization of designs created with selected materials. Test and analyzes are shown step-by-step in order to achieve the final result with the necessary changes to mitigate. As a result the body part has lightened up to %70 with the choice of different materials and design.

Keywords: Lightening project,polymer composite,mass reduction,finite element,reinforced composites

ANALYSIS OF MECHANICAL BEHAVIOR OF TERMOPLASTIC COMPOSITES

AYSU HANDE YUCEL[1], ELIFNUR KOSEMEN[1], ALI TANER KUZU[2], MUSTAFA BAKKAL[1]

[1]Istanbul Technical University, Department of Mechanical Engineering, Istanbul, TURKEY
[2]Isik University, Department of Mechanical Engineering, Istanbul, TURKEY

Abstract

This paper presents the effect of fiber orientation on the tensile, compression, impact, and flexural properties of glass fiber reinforced acrylic-based thermoplastic composites. The mechanical behavior of three different composite plates, produced by the resin transfer molding (RTM) method, with 0º / 90º / 45º, 0º / 90º and ± 45º glass fiber orientations were investigated by carrying out tensile, compression, three-point bending and Charpy impact tests. A Weibull distribution model was implemented to explain the variation in mechanical properties of the acrylic-based composite. According to Weibull analysis results with 63.2 % probability, the highest tensile strength (561 MPa), compressive strength (293 MPa) and impact values (19.44 J) were obtained when the plate with 0º/90º glass fiber orientation was tested, whereas the highest flexural strength was obtained when the plate with 0º/90º/45º was tested.

APPLICATION OF FLOW PEENING (GOV) PROCESS ON INCONEL FROM AEROSPACE MATERIALS

KÜRŞAD GÖV,[*1] İBRAHİM GÖV, [1] BURAK ŞAHİN[1], ABDURRAHMAN DOĞAN[2], MURAT KALAK[1], MEHMET SAİT KOCA[1]

[1]Gaziantep University, Faculty of Aeronautics and Aerospace, Aerospace Engineering Department, Gaziantep, TURKEY.
[2] Gaziantep Islam Science And Technology University, Vocational School of Technical Sciences, Machinery and Metal Technology, Gaziantep, TURKEY.
[*]gov@gantep.edu.tr

Abstract

Surface quality is of great importance for materials used in the aviation industry as it directly affects friction and energy losses. On the surfaces of the parts processed with various production methods, burrs and residual toolpaths occur during shaping. This results in a deterioration in surface roughness that needs to be corrected. For this reason, surface treatment is applied by various methods in aviation materials.

Abrasive flow machining (AFM) is one of the most effective of these methods. The abrasive powders are mixed in a polymer media. Then the media is flowed from the surface with high pressure and the surface finishing is done by removing the chip. As a result, a very smooth surface texture is obtained. Another effective method of surface improvement processes is to increase the surface strength.

These processes are carried out by forging on the surface and sub-surface layers and by increasing the strength in terms of permanent deformation. The shot peening is most commonly used for this purpose. While peening, the surface is strike with balls (metal, ceramic, glass) high pressure, it is seen that the surface texture also deteriorates. Considering these two cases, the balls used for peening are mixed into the polymer and flowed from the surface under high pressure by imitating the AFM method. As a result, the resulting flow peening surface improvement method is called the GOV process.

In this study, the parameters of the GOV process and its application on Inconel 718 material are studied and the results are discussed. In the light of the data obtained, it has been observed that the surface quality has improved and the amount of chip removal has been determined to be negligible.

Keyword: Inconel 718, Aerospace Materials, Flow Peening (GOV) process, AFM, Shot Peening, Surface Treatment, Surface Roughness, Surface Quality.

AISI 4140 ÇELİĞİNİN FREZLEMESİNİN TAGUCHİ-DEAR YÖNTEMİYLE OPTİMİZAYONU

YUSUF FEDAI *[1]

[1]Osmaniye Korkut Ata Üniversite, Mühendislik Fakültesi, Endüstri Mühendisliği, Osmaniye, TÜRKİYE.

Özet

İmalatta, maliyetlerin düşürülmesi ve kalitenin iyileştirilmesi için uygun proses parametrelerinin seçimi için oldukça önemli bir konudur. Farklı çelişkili faktörlerin bir arada bulunduğu parametrelerin seçiminde Çok Kriterli Karar Verme (MCDM) yöntemleri başarıyla uygulanmaktadır. Bu çalışmanın amacı, AISI 4140 çeliğinin Frezelenmesi esnasında çıktı parametreleri olan, üç farklı yüzey pürüzlülük (Ra,Rz ve Rq) ve işleme zamanını en düşük düzeyde tutmak, talaş kaldırma oranını ise en yüksek değere çıkarma için kontrol faktörlerinin etkisini incelemek ve bu faktörlerin doğru ayarlarını seçmektir. Çalışma için seçilen kontrol faktörleri kesme hızı, ilerleme ve kesme derinliğidir. Deneyler, kontrol faktörlerinin çeşitli kesme koşulları altında Taguchi'nin L9 tasarımına göre planlanmıştır. Çoklu kalite karakteristik optimizasyonu için Taguchi-Veri Zarflama Analizi Tabanlı Sıralama tekniği (Taguchi-DEAR) çok yanıtlı optimizasyon yaklaşımı kullanılmıştır. Deneysel araştırmalardan, kesme derinliğinin talaş kaldırma oranı üzerindeki etkisinden dolayı performans ölçümlerinin belirlenmesinden en yüksek etkiye sahip olduğu görülmüştür. Optimum proses parametreleri kombinasyonu A3B3C3 şeklinde kesme hızı 325 m/dak, ilerleme 0,16 mm/dev ve kesme derinliği 1,5 mm değerlerinde bulunmuştur.

Anahtar Kelimeler: AISI 4140 çeliği, Frezeleme, Taguchi Tekniği, Çok kriterli Karar Verme, Optimizasyon, DEAR tekniği

DENIM KUMASLARIN RENKLENDIRILMESINDE INOVATIF BIR YONTEM

NURIYE KERTMEN[1], ZEYNEP TEKEREK[2]

[1] Iskur Denim Isletmeleri San Ve Tic A S, Turkey ; [2] Iskur Denim Isletmeleri San Ve Tic A S, Turkey

ABSTRACT

Günlük hayatın vazgeçilmez giysilerinden olup, her yaşa ve cinsiyete uygun tekstil ürünleri olan denim kumaşlar, rahatlıkları ve dayanımlarının yanı sıra fonksiyonel ve yenilikçi yönleriyle de karşımıza çıkmaktadırlar. Denim, mavi indigo boyalı çözgü ve boyanmamış atkı iplikleriyle 3/1 veya 2/1 dimi konstrüksiyonuyla dokunan % 100 pamuklu kumaş olarak tanımlanmaktadır. Denim kumaşların ön ve arka yüz görünümleri farklı olup, ön yüzde boyalı çözgü; arka yüzde ise renksiz atkı iplikleri hâkimdir. Çözgü iplikleri, denim için karakteristik olan indigo ile boyansa da kükürt boyarmaddeleri de sıklıkla tercih edilmekte veya bu boyarmaddeler birlikte kullanılabilmektedir. Denim kumaşların overdye prosesi, ağırlıklı olarak arka yüzde bulunan atkı ipliklerinin kumaş formunda boyanması işlemidir. Overdye boyamada çoğunlukla kükürt boyarmaddeler tercih edilmektedir. Denim kumaşların asit boyarmaddelerle boyanması, selüloz ile boyarmaddenin kimyasal yapıları ve iyonik yükleri bakımından uygun değildir. Ancak bu çalışmada denimin içeriğinde bulunan pamuk lifleri katyonize edilerek anyonik karakterdeki asit boyarmaddelere afiniteleri artırılmış ve asit boyarmaddeleriyle denim kumaşların boyanması mümkün hale getirilmiştir. Bu çalışmanın amacı, denim kumaşları kuaterner amonyum bileşiği ile katyonikleştirmek ve denim kumaşların üretiminde en çok kullanılan indigo ve kükürt boyarmaddelerinden farklı olarak asit boyarmaddeleri ile kumaşı boyayarak, sınırlı bir renklendirme olanağı bulunan denim kumaşlarda renk çeşitliliğini ve efektlendirmeyi arttırmaktır.

KEYWORDS - Asit Boyarmadde ,Denim ,Denim Yıkama Işlemleri ,Katyonizasyon ,Pamuk

HASAN KALYONCU UNIVERSITY

GAZIANTEP UNIVERSITY

TICMET'21

05-06 November, 2021 Gaziantep - TURKEY

The 3rd International Conference of Materials and Engineering Technology

3

3. Uluslararası Malzeme ve Mühendislik Teknolojileri Konferansı







https://www.ticmet.org